Aalborg Universitet

AALBORG UNIVERSITY
DENMARK

Proceedings of the Twenty Second Nordic Seminar on Computational Mechanics

Damkilde, Lars; Andersen, Lars; Kristensen, Anders Schmidt; Lund, Erik

Publication date:
2009

Document Version
Publisher's PDF, also known as Version of record

[Link to publication from Aalborg University](#)

Proceedings of the Twenty Second Nordic Seminar on Computational Mechanics

Lars Damkilde, Lars Andersen,
Anders Schmidt Kristensen & Erik Lund (editors)

AALBORG UNIVERSITY

Department of Civil Engineering
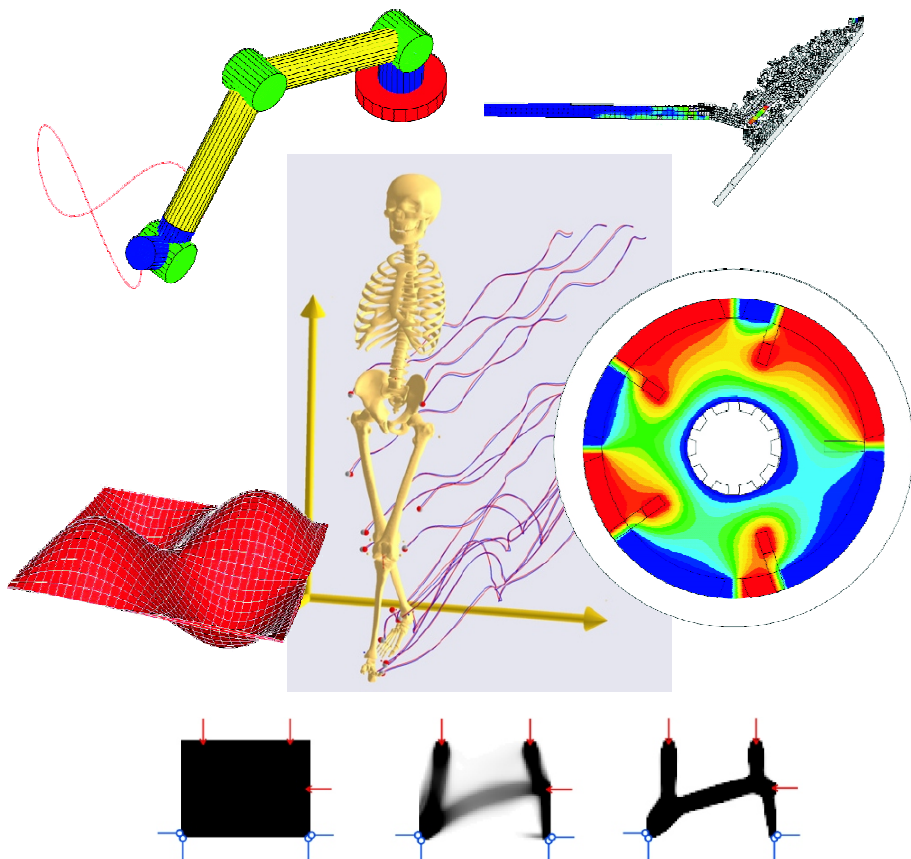
Aalborg University
Department of Civil Engineering
Structural Mechanics

DCE Technical Memorandum No. 11

Proceedings of the Twenty Second Nordic Seminar on Computational Mechanics

edited by

Lars Damkilde, Lars Andersen,
Anders Schmidt Kristensen & Erik Lund

October 2009

Scientific Publications at the Department of Civil Engineering

Technical Reports are published for timely dissemination of research results and scientific work carried out at the Department of Civil Engineering (DCE) at Aalborg University. This medium allows publication of more detailed explanations and results than typically allowed in scientific journals.

Technical Memoranda are produced to enable the preliminary dissemination of scientific work by the personnel of the DCE where such release is deemed to be appropriate. Documents of this kind may be incomplete or temporary versions of papers—or part of continuing work. This should be kept in mind when references are given to publications of this kind.

Contract Reports are produced to report scientific work carried out under contract. Publications of this kind contain confidential matter and are reserved for the sponsors and the DCE. Therefore, Contract Reports are generally not available for public circulation.

Lecture Notes contain material produced by the lecturers at the DCE for educational purposes. This may be scientific notes, lecture books, example problems or manuals for laboratory work, or computer programs developed at the DCE.

Theses are monograms or collections of papers published to report the scientific work carried out at the DCE to obtain a degree as either PhD or Doctor of Technology. The thesis is publicly available after the defence of the degree.

Latest News is published to enable rapid communication of information about scientific work carried out at the DCE. This includes the status of research projects, developments in the laboratories, information about collaborative work and recent research results.

Preface

This book contains the proceedings of the Twenty Second Nordic Seminar on Computational Mechanics (NSCM22), taking event 22–23 October 2009 at Aalborg University, Denmark. The papers presented at the Optimization Seminar in Honour of Niels Olhoff, held 21 October 2009 at Aalborg University, Denmark, are included at the end of the proceedings.

The Nordic Seminars on Computational Mechanics are organized annually by the Nordic Association of Computational Mechanics (NoACM). The association represents the interest of the Nordic countries (Denmark, Finland, Iceland, Norway, Sweden) and the Baltic countries (Estonia, Latvia, and Lithuania) in the International Association for Computational Mechanics (IACM) and the European Community on Computational Methods in Applied Sciences (ECCOMAS).

NoACM was founded in 1988 with the overall mission to promote and stimulate research within the field of computational mechanics. The annual seminars are intended as a meeting place for researchers developing computational methods, and for scientists and engineers focusing on challenging applications in broad aspects of mechanics. Young researchers, including doctorate and graduate students, are particularly welcome.

This year, the Nordic Seminar on Computational Mechanics is organised and hosted by the Department of Civil Engineering and the Department of Mechanical Engineering, Aalborg University, Denmark. The book of proceedings includes four invited papers and a total of 66 other contributions, divided into 18 sessions. Seven invited lectures are given at the Optimization Seminar in Honour of Niels Olhoff. The corresponding papers are included at the end of the proceedings.

Sincere appreciations are extended to all participants in the seminar, not least to the invited speakers and all other lecturers at the NSCM22 and the Optimization Seminar for their efforts in preparing and presenting papers. The success of the event closely relies on these contributions. Especially we would like to thank our main sponsor Siemens Wind Energy A/S and our co-sponsor Medeso AB for their most kind financial contributions to the seminar.

Aalborg, October 2009

Lars Damkilde
Lars Andersen
Anders Schmidt Kristensen
Erik Lund

Table of Contents

Optimization Seminar in Honour of Niels Olhoff

PDE-interpolations in Topology Optimization

O. Sigmund

Department of Mechanical Engineering, Solid Mechanics
Technical University of Denmark, Lyngby, Denmark
e–mail: sigmund@mek.dtu.dk

Summary   The paper discusses recent developments in interpolation schemes for density based multi-physics topology optimization problems. The paper is a slight update of an article that has appeared earlier in the IACM-expressions [1].

Introduction

Since its invention by Bendsøe and Kikuchi two decades ago, the topology optimization method as a computational tool [2] has undergone a tremendous development. In the early days of the method, it was mainly seen as an academic toy for optimizing material distributions in mechanics and lots of post-processing and -interpretation had to be performed before realistic and useful designs could be extracted. In the early 90's, the automotive industry took up the method with mainly in-house codes but since then, the method has spread rapidly into all other mechanical engineering disciplines. By now, all major FE-software houses provide topology optimization functionalities and there exists a small handfull of dedicated topology optimization software providers that offer mechanical design solutions with manufacturing constraints like deep drawing and casting constraints. This expansion process has culminated with the use of the method in the structural design of the new A380 mega-plane by EADS [3]. Whereas the method enjoys great popularity for simple mechanical design criteria like stiffness, buckling, and dynamic eigenfrequencies, the method is only slowly spreading to other physics disciplines - most probably because it is difficult to systematize the transfer of the method to other disciplines. As is, every new application requires reconsideration of modeling aspects, design parameterizations, design goals and penalization schemes. Especially problems involving boundary loads have been difficult to deal with due to the paradox: where to add the boundary loads if the boundaries are unknown? In this article, we will discuss some recent developments in providing a unified scheme for topology optimization in multiple physics and loading settings.

The original topology optimization method consists of repeated finite element analyses, gradient evaluations, and material redistributions based on optimality criteria or Math Programming approaches[1]. For stiffness optimization, the design variables are the individual element material densities. In order to be able to use efficient gradient-based optimization approaches, the design variables are allowed to take any value between zero (void) and one (solid), however, discrete and well-defined solid-void solutions are obtained by choosing appropriate penalization schemes that favor discrete solutions from porous intermediate stiffness solutions [4]. The topology optimization procedure is demonstrated on a wing rib example in Figure 1.

Lately, alternatives to the above described density approach have appeared. In level-set approaches material boundaries are described by the zero level-set surface and boundary optimization is obtained by solving of Hamilton-Jacobi equations [5]. Parameterized level-set functions allowing for

---

[1]The reader is kindly invited to visit the homepage www.topopt.dtu.dk (compliance design) to try out a topology optimization Java applet that illustrates the technique.
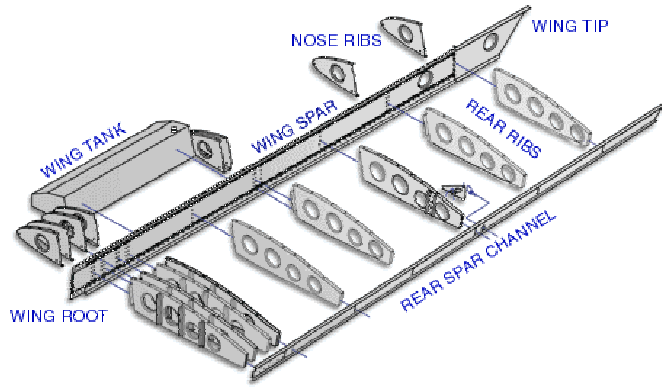
Conventional wing rib design with circular holes

Design domain   FE–discretization

Material redistribution (topology optimization)
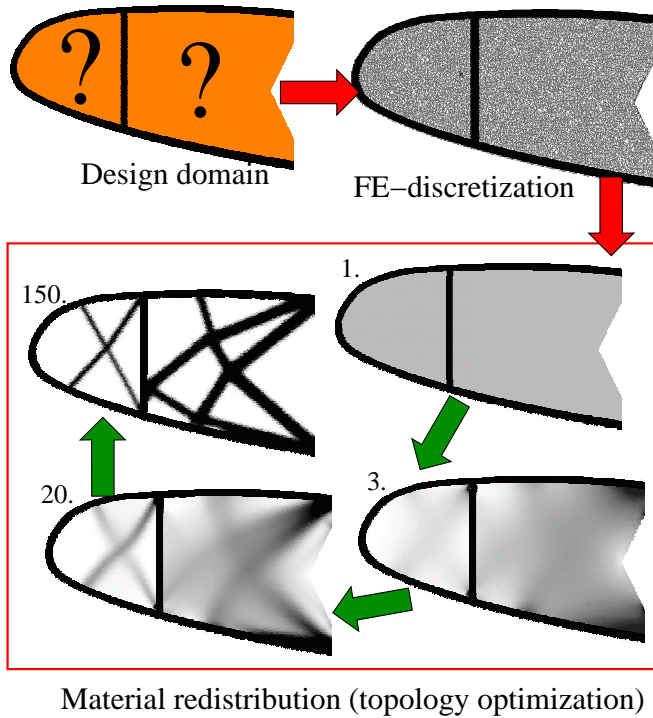
Figure 1: Wing rib design by topology optimization. Top: Conventional design with circular holes for weight reduction. Bottom: definition of design domain, FE-discretization and snap shots from the optimization history.

the use of Math Programming approaches have also been suggested based on the use of radial basis functions [6]. The different approaches each have their pros and cons, however, common for all is that they are based on fictitious domain modeling and hence they require interpolation schemes for the correct modeling of the solid and void domains. In simple stiffness optimization problems this may not be a problem because the void domain has no influence on the structure. However, in other physics cases, the void domain may contain pressurized fluids, moving fluids, acoustic waves, electric fields, etc. If the topology was given, such modeling problems could easily be solved by staggered approaches, i.e. for a structural-acoustic problem, the Helmholtz and

Navier equations could be solved separately in each their subdomains but coupled through boundary terms. In topology optimization, the boundaries are unknown a priori and hence staggered approaches are impractical and must be substituted with monolithic approaches where all physics is modeled on the same mesh. In the following we demonstrate how monolithic (non-staggered) analysis schemes suitable for topology optimization of multiphysics problems can be based on suitable interpolations of PDEs (Partial Differential Equations).

Elasticity

The first examples of topology optimization were based on minimum compliance design of mechanical structures. The PDE for elasticity without volume load is given in Table 1a. The design variable ρ interpolates between empty space ($\rho = 0$) and solid material ($\rho = 1$) governed by the elasticity PDE. In practice, this is done by letting the Young's modulus or the whole stiffness tensor of solid material be a function of ρ. A compliance minimization example for airplane wing-rib design is shown in Figure 1. A range of other design problems are also covered by this simple interpolation between void (empty space) and solid material. Examples are thermal and electric conduction problems and also multiphyscis problems like electrothermomechanical actuators [7].

PDE	Interpolation	Void region $\rho\!=\!0$	Solid region $\rho\!=\!1$
a) Elasticity, compliance minimization			
$\nabla \cdot (\mathbf{C}(\rho)\nabla \mathbf{u}) = \mathbf{0}$	$\mathbf{C}(\rho) = \rho \mathbf{C}_s$	void	$\nabla \cdot (\mathbf{C}_s \nabla \mathbf{u}) = \mathbf{0}$
b) Elasticity and porous flow, bone optimization			
$\nabla \cdot (\mathbf{C}(\rho)\nabla \mathbf{u}) = \mathbf{0}$ $\nabla \cdot (\kappa(\rho)\nabla \psi) = 0$	$\mathbf{C}(\rho) = \rho \mathbf{C}_s$ $\kappa(\rho) = (1-\rho)\kappa_f$	porous flow $\nabla \cdot (\kappa_f \nabla \psi) = 0$	elastic bone $\nabla \cdot (\mathbf{C}_s \nabla \mathbf{u}) = \mathbf{0}$
c) Stokes flow			
$-\nabla \cdot (\mu\nabla\mathbf{u} - \mathbf{I}p) + \alpha(\rho)\mathbf{u} = \mathbf{0}$ $\nabla \cdot \mathbf{u} = 0$	$\alpha(\rho) = (\rho-1)\alpha_f + \rho\alpha_s$	fluid ($\alpha_f = 0$) $\nabla\cdot(\mu\nabla\mathbf{u} - \mathbf{I}p) = \mathbf{0}$ $\nabla \cdot \mathbf{u} = 0$	support ($\alpha_s = \infty$) $\mathbf{u} = \mathbf{0}$
d) Elasticity with pressure loads			
$\nabla \cdot (2G(\rho)\nabla\mathbf{u} - \mathbf{I}p) = \mathbf{0}$ $p = -K(\rho)\nabla \cdot \mathbf{u}$	$K(\rho) = (\rho-1)K_f + \rho K_s$ $G(\rho) = \rho G_s$	fluid $p = -K_f \nabla \cdot \mathbf{u}$	solid $\nabla \cdot (2G_s\nabla\mathbf{u} - \mathbf{I}p) = \mathbf{0}$ $p = -K_s \nabla \cdot \mathbf{u}$
e) Electrostatic actuation			
$\nabla \cdot (\mathbf{C}(\rho)\nabla\mathbf{u}) = \nabla\mathbf{F}$ $\mathbf{F} = \epsilon(\rho)\nabla\phi\nabla\phi - \frac{1}{2}\nabla\phi \cdot \nabla\phi\mathbf{I}$ $\nabla \cdot (\tilde{\epsilon}(\rho)\nabla\phi) = 0$	$\mathbf{C}(\rho) = \rho\mathbf{C}_s$ $\epsilon(\rho) = (1-\rho)\epsilon_0 + \rho\epsilon_0\epsilon_r$ $\tilde{\epsilon}(\rho) = \epsilon_0(1 + \rho\alpha\epsilon_r),$ $\alpha \gg 1$	vacuum $\nabla \cdot (\epsilon_0\nabla\phi) = 0$ $\mathbf{F} = \epsilon_0\nabla\phi\nabla\phi - \frac{1}{2}\nabla\phi \cdot \nabla\phi\mathbf{I}$	solid $\nabla \cdot (\mathbf{C}_s\nabla\mathbf{u}) = \nabla\mathbf{F}$ $\nabla \cdot (\alpha\epsilon_0\epsilon_r\nabla\phi) = 0$ $\mathbf{F} = \epsilon_r\nabla\phi\nabla\phi - \frac{1}{2}\nabla\phi \cdot \nabla\phi\mathbf{I}$

Subscript $_s$ means solid, and subscript $_f$ means fluid. No volume loads assumed.

Table 1: PDE-interpolation schemes for various physics problems.

Photonic crystals

A simple extension of the solid-void scheme is to have the same PDE governing the solid and the void regions, i.e. the design variable interpolates between e.g. a low and a high value of refractive index as seen in the design of photonic crystals governed by Maxwell's equations [8]. A photonic crystal based wave guide nano-scale splitter is shown in Figure 2.

Elasticity and porous flow

It has long been known that human bone structure adapts to external loads and generates anisotropic porous microstructures. However, the exact objective function behind the adaption is still not clearly understood although it is clear that competing objectives such as maximum stiffness
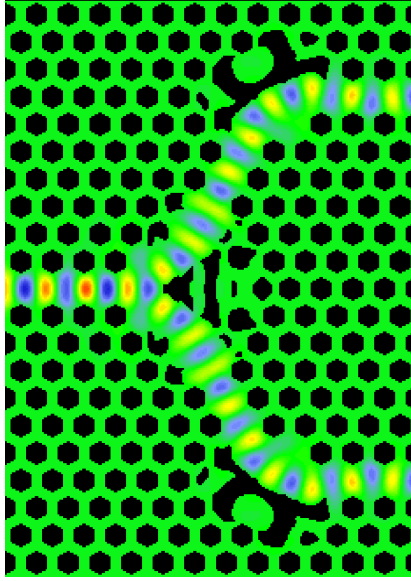
Figure 2: A nano-scale photonic wave guide splitter designed by topology optimization.

or strength as well as nutrition transport are in play. In order to study optimal microstructures governed by the porous flow PDE in the void region and the elasticity PDE in the solid regions, reference [9] suggested to interpolate between the two PDEs as seen in the Table 1b. With $\rho = 0$ we obtain porous flow governed by Poisson's equation and with $\rho = 1$ we obtain solid structure governed by Navier's equation. An example of micromechanical bone design with varying constraints on permeability/conductivity is shown in Figure 3.

Stokes flow

The extension of the topology optimization to fluid mechanics problems was not straightforward and has only been solved recently [10]. Following the ideas from elasticity, a first thought was to interpolate the material property, i.e. the viscosity between fluid and non-fluid region by switching between the physical viscosity of the relevant fluid and an infinitely high viscosity (non-fluid) region. However, this does not work since the high viscosity regions only will stop flow if they are attached to no-slip boundaries. A better solution proved to be to add a dissipation (inverse permeability) term to the Stokes equation, i.e. turning it into the Brinkman equation and then letting the design variable determine the magnitude of the dissipation term. As seen in Table 1c, switching the inverse permeability α between 0 and infinity, one can interpolate between the pure Stokes flow equation ($\rho = 0$) and no flow ($\rho = 1$). Examples of topology optimization for fluids are shown in Figure 4.

Elasticity with pressure loads

Solving pressure load problems using the topology optimization is inherently a problem since it is unclear where to apply the pressure loads if the boundaries are unknown. In order to solve the problem previous works used various shape descriptors and boundary optimization techniques on top of the topology optimization parameterization. However, it has turned out [12] that a reformulation of the standard elasticity formulation into a mixed form makes it possible to solve the problem by simple interpolation between zero shear stiffness but finite bulk modulus (i.e. a com-
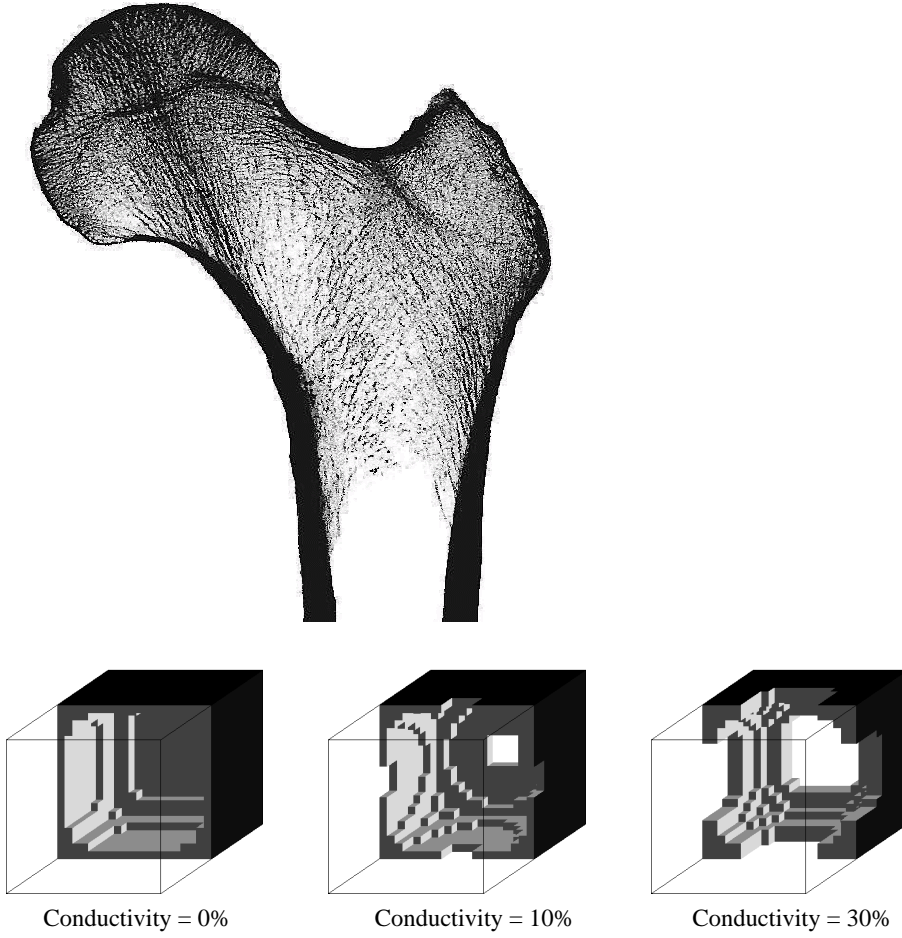
Figure 3: Top: Cut through human hip bone. Bottom: results for topology optimization of bone microstructure with constraints on porosity (from [8]).
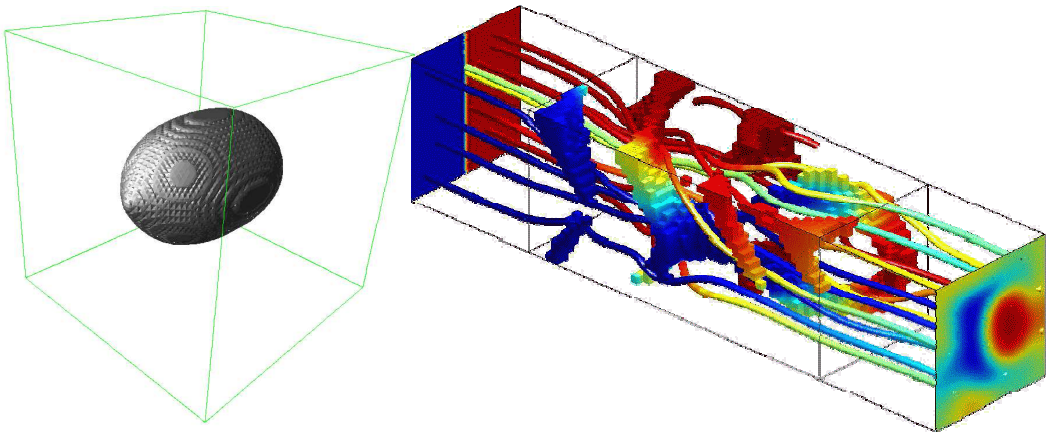
Figure 4: Stokes flow examples. Left: minimizing drag of obstacles of given volume (from [11]). Right: a flow mixer with flow lines and colors indicating temperature from inlet (left) to outlet (right) (from [?]).
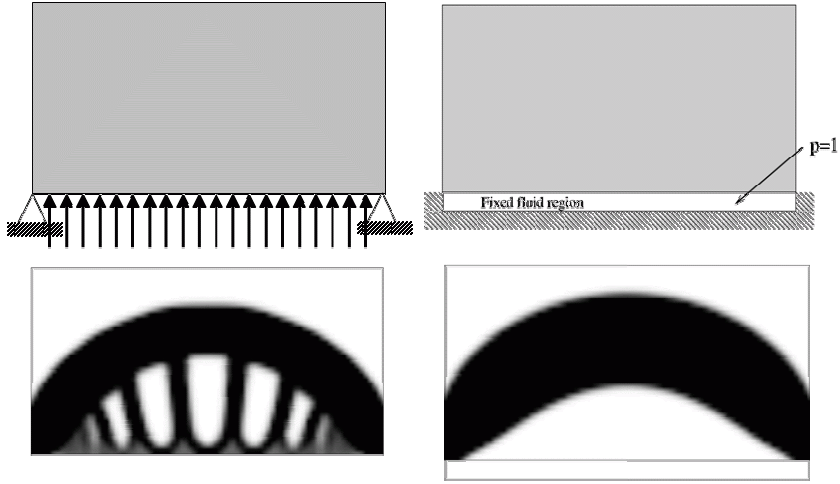
Figure 5: Topology optimization with pressure loads. Left: Suboptimal topology obtained by conventional formulation with fixed pressure load line. Right: Optimized solution based on mixed formulation (from [12]).

pressible stationary fluid) in the pressurized void region and finite shear and bulk moduli in the solid region. The equations are given in Table 1d and an example is shown in Figure 5. The idea can also be extended to structural acoustic problems by the same interpolation of the mixed form but now including inertia terms [13].

Electrostatic actuation

The last and most challenging example of a PDE-interpolation for topology optimization, that we will discuss here, is the design of electrostatically actuated micro systems. Electrostatic forces between two conductors are inversely proportional to the square of the gap between them, hence in micro scale these forces become large enough for mechanical actuation. Normally the electromechanical modeling problem is solved by staggered analysis approaches but recently it was shown that monolithic schemes amenable to topology optimization can be set up [14, 15]. Table 1d shows the scheme that interpolates between the electrostatic Poisson's equation (void regions) and the elasticity equations (solid region). The boundary loads (Maxwell stresses) F generated by the electrostatic field enter the elasticity equation as volume loads. An example of electrostatic actuator design is shown in Figure 6.

Concluding remarks

With these five examples presented in this paper it has been demonstrated how various multi-physics and boundary load problems can be posed in monolithic settings amenable to topology optimization formulations by proper interpolations between the governing PDEs. It is the authors vision that any kind of physical design problem can be formulated in similar monolithic forms. Ideally, one would set up a table of all known PDEs and generate the proper interpolations between them. As long as the PDEs are formulated in the same coordinate systems this should indeed be possible. However, when considering "incompatible PDEs" like for instance the fluid-structure problem where the fluid problem is formulated in an Eularian coordinate system and the elastic problem is formulated in a Lagrangian system, the proper interpolation scheme is not yet clear. Also, the penalization rule that ensures black and white designs for complicated multi-physics
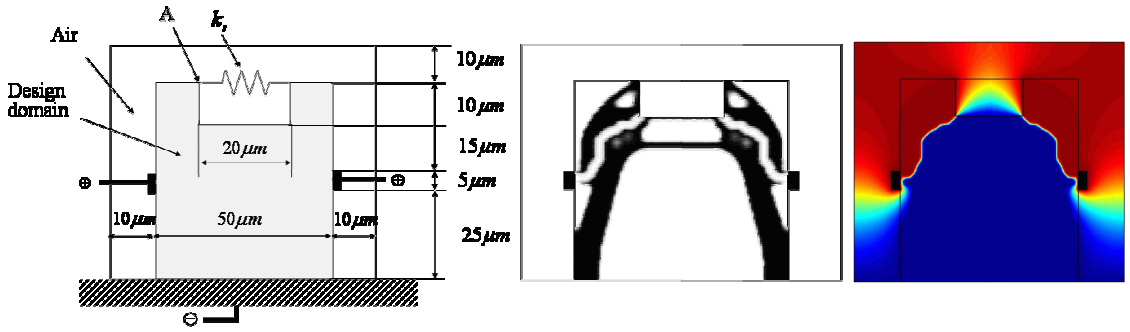
Figure 6: Topology optimization with electrostatics forces for MEMS. Left: design domain. Center: topology optimized micro gripper. Right: Electric field distribution (from [15]).

problems is not easy to find. Amongst others, it is the formulation and solution of such advanced incompatible coupled problems that constitute the future challenges within the field of topology optimization.

Acknowledgments

References

[1] O. Sigmund. PDE-interpolations in topology optimization. In *IACM Expressions*, volume 23, pages 16–20. International Association for Computational Mechanics, June 2008.

[2] M. P. Bendsøe and N. Kikuchi. Generating optimal topologies in structural design using a homogenization method. *Computer Methods in Applied Mechanics and Engineering*, 71(2):197–224, 1988.

[3] G. Schuhmacher. Optimizing aircraft structures. *Concept to Reality, Altair Engineering*, winter:12–16, 2006.

[4] M. P. Bendsøe and O. Sigmund. Material interpolation schemes in topology optimization. *Archives of Applied Mechanics*, 69(9-10):635–654, 1999.

[5] J. A. Sethian and A. Wiegmann. Structural boundary design via level set and immersed interface methods. *Journal of Computational Physics*, 163(2):489–528, 2000.

[6] J. Norato, R. Haber, D. Tortorelli, and M.P. Bendsoe. A geometry projection method for shape optimization. *International Journal for Numerical Methods in Engineering*, 60(14):2289–2312, 2004.

[7] O. Sigmund. Design of multiphysics actuators using topology optimization - Part I: One-material structures. *Computer Methods in Applied Mechanics and Engineering*, 190(49-50):6577–6604, 2001.

[8] P. I. Borel, A. Harpøth, L. H. Frandsen, M. Kristensen, J. S. Jensen, P. Shi, and O. Sigmund. Topology optimization and fabrication of photonic crystal structures. *Optics Express*, 12(9):1996–2001, 2004. http: //www. opticsexpress.org/abstract.cfm?URI=OPEX-12-9-1996.

[9] O. Sigmund. On the optimality of bone microstructure. In P. Pedersen and M. P. Bendsøe, editors, *Synthesis in Bio Solid Mechanics*, pages 221–234. IUTAM, Kluwer, 1999.

[10] T. Borrvall and J. Petersson. Topology optimization of fluids in Stokes flow. *International Journal for Numerical Methods in Fluids*, 41:77–107, 2003.

[11] N. Aage, T. H. Poulsen, A. Gersborg-Hansen, and O. Sigmund. Topology optimization of large scale stokes flow problems. *Structural and Multidisciplinary Optimization*, 35:175–180, 2008.

[12] O. Sigmund and P.M. Clausen. Topology optimization using a mixed formulation: An alternative way to solve pressure load problems. *Computer Methods in Applied Mechanics and Engineering*, 196(13-16):1874–1889, 2007.

[13] G. H. Yoon, J. S. Jensen, and O. Sigmund. Topology optimization for acoustic structure interaction problems. *International Journal for Numerical Methods in Engineering*, 70(9):1049–1075, 2007.

[14] A. Alwan and G.K. Ananthasuresh. Topology optimization of electrostatically actuated micromechanical structures with accurate electrostatic modeling of the interpolated material model. In *DETC2006-99684*, 2006.

[15] G. H. Yoon and O. Sigmund. A monolithic approach for topology optimization of electrostatically actuated devices. *Computer Methods in Applied Mechanics and Engineering*, 197:4062–4075, 2008. doi:10.1016/j.cma.2008.04.004.

Numerical simulations of wall-bounded shear flows

Luca Brandt

Linné Flow Centre, KTH Mechanics,
SE-100 44 Stockholm, Sweden
e–mail: luca@mech.kth.se

Summary   Numerical investigations performed at the Department of Mechanics, KTH Stockholm, are reviewed to show how recent developments in computational capability, both in terms of computer power and algorithm efficiency, have deeply changed our approach to fluid mechanics problems leading to significant improvement of our understanding. After introducing the numerical approach adopted, two different problems will be considered, both concerned with the behavior of wall-bounded shear flows. The interest for this type of flows is also related to our ability to understand and predict the performance of man-made devices. Firstly, we will consider the transition from laminar to turbulent flow in a boundary layer exposed to high levels of external free-stream disturbances. The work is performed in collaboration with *Philipp Schlatter* and *Dan S. Henningson*, also at the Linné Flow Centre in Stockholm, and *Rick deLange* at the Department of Mechanical Engineering, Eindhoven University of Technology. Secondly, numerical simulations of turbulent channel flow seeded with different populations of diluted, tiny particles are presented. The investigation, in collaboration with *Philipp Schlatter*, *Gaetano Sardina* and *Carlo M. Casciola* from the Department of Mechanics and Aeronautics, University of Rome La Sapienza, focuses on the large scale accumulation patterns of inertial particles.

Introduction

The equations of motion for gases and simple liquids, such as water, are well known; nevertheless, exact solutions of the equations are known for only a few cases. The reason for this is twofold, firstly the equations are highly nonlinear, exhibiting solutions with a large range of scales and secondly the boundary conditions are usually not well defined. During the last 30 years, however, a new revolution in fluid mechanics research has been apparent, namely the use of computers, both for numerical simulations and for collecting and analyzing experimental data. The computers have drastically changed the possibilities to understand and analyze complex flow situations. In particular, direct numerical simulations (DNS) have provided physical insight into the phenomena of transitional and turbulent flows, despite the simulations are limited to simple and moderate Reynolds-number flows. Our understanding has significantly improved over the past two decades; in particular, the identification of relevant flow structures and the recognition of their role in the near-wall dynamics are among the major advances in transition and turbulence research. Two showcases will be presented here: simulations of transition to turbulence in the presence of high levels of ambient noise and analysis of inertial particles in turbulent channel flow.

Numerical method

The simulation code (see Chevalier et al. [4]) employed for the simulations presented here has been developed at KTH Mechanics over the last fifteen years and uses spectral methods to solve the three-dimensional time-dependent incompressible Navier-Stokes equations in plane geometries. This is used to study simpler canonical flows like channel flow and the boundary layer over a flat plate. The streamwise, wall-normal and spanwise directions are denoted by x, y and z, respectively, and the corresponding velocity vector is $\mathbf{u} = (u, v, w)^T$. The algorithm is based on Fourier discretization in the streamwise and spanwise directions, and an expansion in Chebyshev polynomials in the wall-normal direction. The nonlinear convection terms are evaluated pseudo-spectrally in physical space using fast Fourier transforms. Aliasing errors from the evaluation of

the nonlinear terms are removed by the 3/2-rule in the wall-parallel x/z plane. In the wall-normal direction, it has been found more convenient to increase resolution rather than to use dealiasing. The time is advanced using a four-step low-storage third-order Runge-Kutta method for the non-linear and forcing terms, and a second-order Crank-Nicolson method for the linear terms. The code is fully parallelized for efficient use on both shared and distributed-memory systems.

In the case of boundary layer flows, the downstream growth of the shear layer thickness must be correctly accounted for, and therefore a so-called spatial technique is necessary. This requirement is combined with the periodic boundary conditions in the streamwise direction by adding a fringe region, similar to that described by Bertolotti et al. [1]. In this region, located at the downstream end of the computational box, the function $\lambda(x)$ in equation (1) is smoothly raised from zero and the flow is forced to a desired inflow solution $\mathbf{v}$ in the following manner,

$$\frac{\partial \mathbf{u}}{\partial t} + (\mathbf{u} \cdot \nabla)\mathbf{u} = -\nabla p + \frac{1}{Re_{\delta_0^*}}\nabla^2 \mathbf{u} + \lambda(x)(\mathbf{v} - \mathbf{u}) + \mathbf{g},\tag{1}$$

$$\nabla \cdot \mathbf{u} = 0,\tag{2}$$

where p indicates the pressure and $\mathbf{u}$ is the solution vector. Both $\mathbf{g}$, which is a disturbance forcing, and $\mathbf{v}$ may depend on the three spatial coordinates and time. The forcing vector $\mathbf{v}$ is smoothly changed from the laminar boundary layer profile at the beginning of the fringe region to the pre-scribed inflow velocity vector. This is normally a boundary layer profile, but can also contain a disturbance. A convenient form of the fringe function is as follows:

$$\lambda(x) = \lambda_{max}[S(\frac{x - x_{start}}{\Delta_{rise}}) - S(\frac{x - x_{end}}{\Delta_{fall}} + 1)],\tag{3}$$

where λ_{max} is the maximum strength of the damping, x_{start} to x_{end} the spatial extent of the region where the damping function is nonzero and Δ_{rise} and Δ_{fall} the "rise" and "fall" distance of the damping function. $S(a)$ is a smooth step function rising from zero for negative a to one for $a \geq 1$. This method damps disturbances flowing out of the physical region and smoothly transforms the flow to the desired inflow state, with a minimal upstream influence. In the case of boundary layers, it is also important to be able to set the free-stream boundary condition closer to the wall. To this aim, the behavior of disturbances approaching the undisturbed flow away from the wall is mimicked. For the simulation of channel flows, conversely, periodic boundary conditions are applied directly, together with no-slip boundary conditions at the wall.

Bypass transition

Transition in boundary layers exposed to moderate to high levels of free-stream turbulence, termed bypass transition, has in recent years been studied by a number of authors. The overall picture of the transition scenario can be deduced from figure 1, where the impinging free-stream turbulence is indicated by the yellow vortical structures at the inlet of the computational domain. This transition scenario is dominated by the – randomly in space and time – appearance of streamwise elongated structures in the boundary layer with alternating positive and negative streamwise disturbance velocity, so-called streaks. The amplitude of the boundary-layer disturbance grows in the downstream direction, and finally – through a rapid process bypassing the exponential growth of Tollmien-Schlichting waves – breakdown into localized turbulent spots occurs. These spots also increase in size and merge until a fully turbulent boundary layer can be observed. A review of
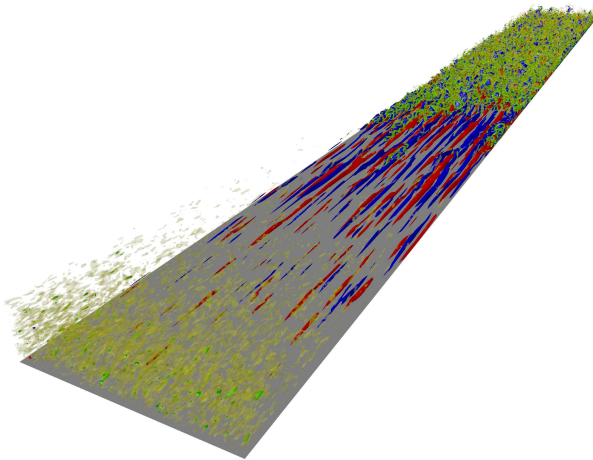
Figure 1: Numerical visualizations of boundary layer transition induced by free-stream turbulence. The flow is from bottom left to top right. The blue and red isosurfaces correspond to low and high velocity while the green and yellow are used to indicate vortical structures by means of the λ_2 vortex identification criterion. The flow is fully turbulent in the second half of the domain.

early experimental work can be found in Matsubara and Alfredsson [9] while more recent experiments focussing on the appearance of turbulent spots are presented by Mans et al. [7, 8]. The first direct numerical simulation (DNS) of bypass transition was performed by Jacobs and Durbin [6], who found good overall agreement with previous experiments. Further numerical simulations have been performed by Brandt et al. [3] and Nagarajan et al. [11].

From the previous work, there is a consensus about the overall features of the bypass-transition process. Free-stream vortical disturbances enter the boundary layer, mainly at the leading-edge area, where their streamwise vorticity components induce transiently growing streamwise streaks by the lift-up effect (see e.g. [14]). The streaks break down locally and growing turbulent spots appear. The spots subsequently merge causing a fully developed turbulent boundary layer further downstream. However, the cause of the breakdown into turbulent spots has generated some controversy, something we aim to clarify by means of large scale numerical simulations.

To understand the mechanisms of streak breakdown, a model problem is considered first. The linear and nonlinear stability of steady and spanwise periodic streaks is analyzed by means of numerical simulations. Two instability modes have been identified: sinuous and varicose, denoted according to the motion of the streak during the disturbance growth. It is also observed that the former type occurs earlier. In figure 2 the streak nonlinear response to a impulse is depicted at different times following the downstream propagation of the perturbation. The localized sinuous oscillations of the low-speed streak, associated to staggered quasi-streamwise vortices are clearly visible.

Results from the numerical simulations of the full transition scenario (see figure 1 and [3, 13]) are presented next. Three-dimensional instantaneous views of four different sinuous spot precursors observed during an integration time of 4000 non-dimensional units, corresponding roughly to four passages through the computational domain, are displayed in figure 3. During that integration time, a total of 22 incipient turbulent spots have been observed. In the plots, red (medium gray) and blue (dark gray) represent surfaces of constant streamwise velocity perturbation $u' = \pm 0.15$,
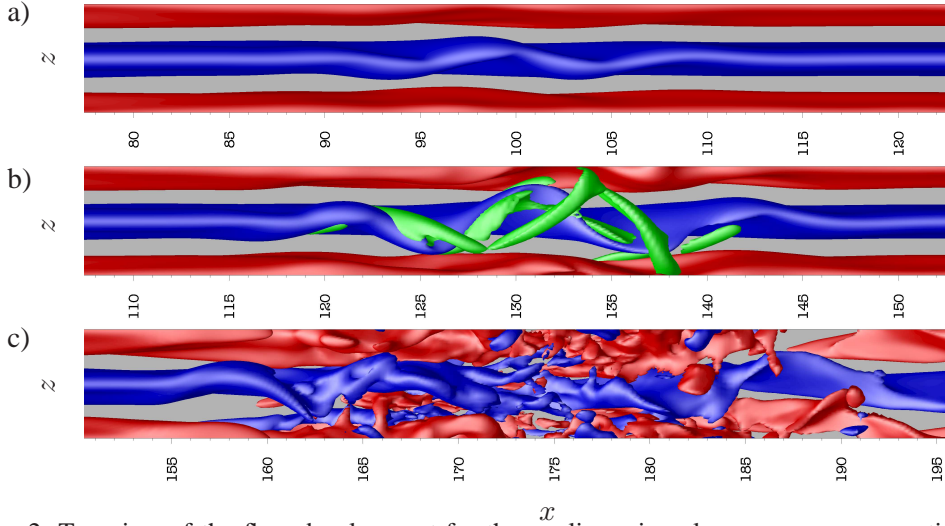
Figure 2: Top view of the flow development for the nonlinear impulse response on a spatially evolving streak at times a) $t = 120$, b) $t = 160$, c) $t = 220$. Low-speed streaks are indicated by dark gray (blue) isocontours, medium gray (red) isocontours correspond to high-speed streaks ($u' = \pm 0.12$). Light gray (green) isocontours in b) correspond to the λ_2 criterion used to identify vortical structures.

whereas the green (light gray) structures indicate negative values of λ_2, used here to identify vortical structures. The flow features common to all cases displayed are the spanwise oscillations of the low-speed streak and the presence of quasi-streamwise vortices on the flank of the low-speed region. The streak instability appears as a wave packet, with staggered patterns of streamwise vortices consisting of three to five structures. The resemblance with the results from the model problem provides evidence that the instability mechanisms have been corrected identified. Note also that the sinuous breakdown was found to be the most likely to occur. The flow structures in the fourth plot of figure 3 are those most similar to the nonlinear impulse response presented in figure 2. The low-speed streak in the first plot in figure 3 is highly asymmetric as observed by the fact that a region of high-speed fluid is found only on its left side. As a consequence, the following instability is also asymmetric and the quasi-streamwise vortices observed are only those bending in the positive spanwise direction. The second plot, Figure 3, depicts the effect of the streak finite length. It can be seen in the figure that the instability is triggered at the head of an incoming region of high-momentum fluid: as this approaches the low-speed streak on its left a region of high spanwise shear is forming and here the instability is first seen. Motivated by these observations, Brandt and de Lange [2] have recently investigated numerically the interaction between optimal streaks assumed periodic but of finite streamwise length. These authors observe that this interaction is able to trigger the streak breakdown and that the following flow structures are very similar to those in bypass transition.

The data collected from linear streak instability, impulse responses on parallel and spatially developing streaks essentially give the same results as full simulations and experiments of bypass transition; not only with respect to flow visualizations but also concerning characteristic measures of the involved instability mechanism. Namely, the streaks break down due to a sinuous secondary instability with a wave length about an order of magnitude larger than the local boundary-layer displacement thickness, a growth rate of the order of one percent of the free-stream velocity over the boundary layer thickness and a group velocity of about 0.8 of the free-stream velocity. The secondary instability manifests itself in all cases as a growing wave packet situated on the low-speed
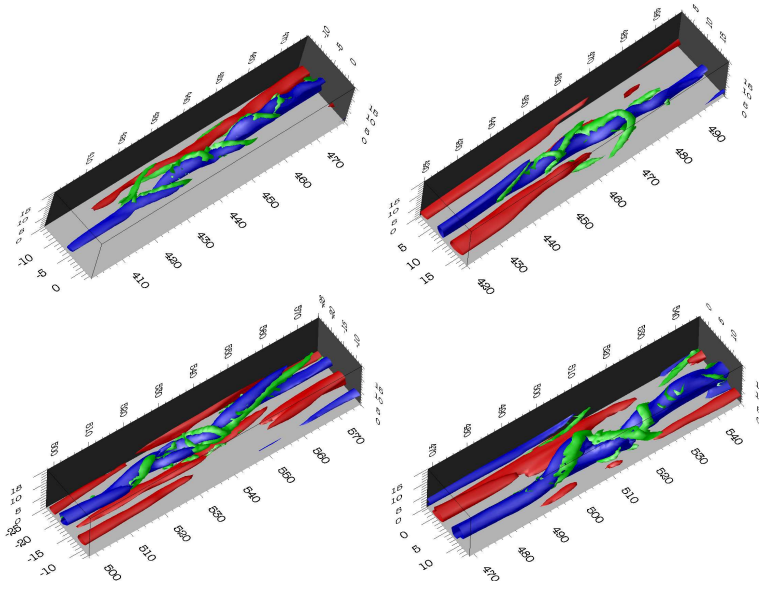
Figure 3: Three-dimensional visualizations of sinuous streak instability prior to the formation of a turbulent spot identified from the numerical simulations of a boundary layer subject to free-stream turbulence. Iso-contours of positive and negative streamwise disturbance velocity $\pm u' = 0.15$ in medium (red) and dark gray (blue), respectively, and surfaces of the λ_2 vortex identification criterion ($\lambda_2 = -0.002$) in light gray (green).

streak, increasing in magnitude as it is dispersing in the streamwise direction. In summary, numerical simulations allowed us to conclude that the streak secondary instability process is responsible for the generation of turbulent spots in bypass transition.

Inertial particles in turbulent channel flow

The dynamics of small inertial particles transported by a turbulent flow is crucial in many environmental and engineering applications. For instance internal combustion engines or rockets as well as diffusion processes in the atmosphere.

Small, diluted particles, much heavier than the carrier fluid, are essentially forced only by the viscous drag. For the dispersed phase we therefore consider the following simplifying assumptions: the particles are rigid spheres, their diameters are much smaller than the viscous scales of the turbulence, they are very diluted, and the density of the solid phase is taken much larger than the fluid one, $\rho_p/\rho = 1000$. In these conditions the feedback acting on the fluid phase and collisions can be safely neglected (one-way coupling) and the only force acting on the particles is the viscous Stokes drag. The particle dynamics is described by a Lagrangian formulation [10] and each particle evolves according to Newton's law: $\dot{\mathbf{v}} = (\mathbf{u} - \mathbf{v})/\tau_p$ where $\mathbf{v}$ denotes the particle velocity and $\tau_p = \rho_p \, d_p^2/(\rho \nu 18)$ is the particle response time (Stokes time), with d_p the particle diameter and ν the fluid viscosity. This leaves the Stokes number, ratio of τ_p and the characteristic time scale of the carrier fluid, as the only parameter defining the particle dynamics for given flow field. In this model Lagrangian fluid particles are recovered in the limit of vanishing Stokes time. The opposite limit of ballistic particles is achieved for τ_p tending to infinity. In wall-bounded flows the viscous time ν/u_*^2 is the natural choice, leading to $St^+ = \tau_p u^{*2}/\nu$. The outer scale Stokes number is than $St = \tau_p R/U_0 = St^+ Re_\tau^2/Re$. Elastic collisions are assumed when the particle surface hits the wall, i.e. when the distance from the particle center to the wall equals the radius. The nominal
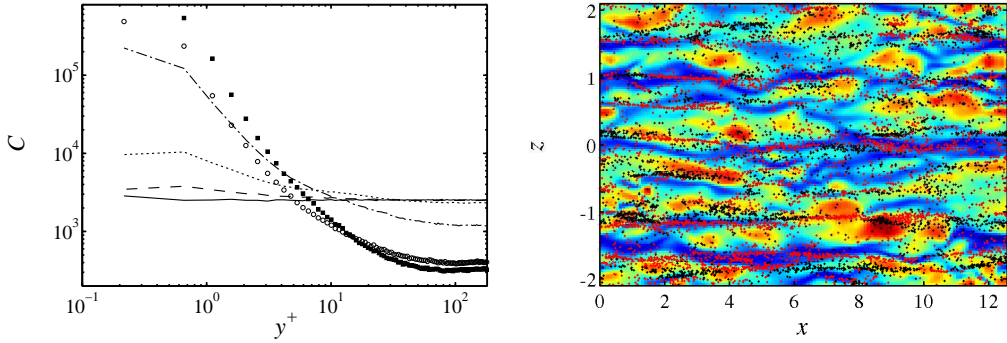
Figure 4: a) Mean concentration (number of particle per volume) of particles in the channel flow simulation at $Re_\tau = 180$, $(-)$ $St^+ = 0$, $(--)$ $St^+ = 0.2$, $(\cdot)$ $St^+ = 1$, $(-\cdot)$ $St^+ = 5$, (o) $St^+ = 10$, $(\square)$ $St^+ = 50$. b) Instantaneous visualization of particles (departing: black points, approaching red ones) with $St^+ = 10$ near the wall ($y^+ = 10$). The background color indicates the instantaneous streamwise fluid velocity (high speed:red; low speed: blue).

particle diameter has then an active role in the interaction with the wall, i.e. d_p^+ is an additional dimensionless parameter of the system. The difference between particle and fluid velocity produces various anomalous phenomena such as small-scale clustering or preferential accumulation at the wall even for incompressible flows, see among others [12].

Inertial particles in turbulent wall flow are characterized by the so-called thurbophoresis phenomena, that is, preferential particles accumulation at the wall. Under appropriate conditions, particles may achieve extremely large concentrations at the wall, up to thousands times the mean value. This turbulence-induced transport and the issuing preferential accumulation as been addressed in a number of paper dealing with a variety of configurations, from boundary layers to plane channels and pipe, attacked both from the experimental and the numerical side. Another peculiarity of these phenomena is represented by the non-uniform instantaneous particle concentrations at the wall; in fact, particles at the wall seem to accumulate in preferential structures and these are extremely long and straight along the mean velocity direction. The specific nature and dynamics of these structures is not understood well enough, so the aim of our work is to investigate the origin of these phenomena and in particular their link with large-scale turbulence motions.

Simulations are run in two different domains, a smaller domain of size $4\pi \times 2 \times 4\pi/3$ (where 2 is the channel height) and a bigger one of dimensions $12\pi \times 2 \times 4\pi$ as in [5]. The latter represents the largest domain used so far for the simulation of particle-laden flows. Both simulations assume a turbulent Reynolds number $Re_\tau = 180$. The effect of turbophoresis is exemplified in Figure 4a) showing the wall-normal profile of the (Eulerian) mean particle concentration C, defined as the number of particles per volume. This figure clearly indicates the well-known behavior of particle-laden flows that heavier particles tend to accumulate close to the wall. Fluid tracers, on the other hand, are equally distributed throughout the channel. The most accumulating particle populations ($St^+ = 10, 50$) show values of particles concentration at the wall a thousand times larger than those at the center of the channel. These mean Eulerian observables are the same in both simulations so it may appear that box dimensions do not affect mean quantities, nonetheless they do influence correlations and particle patterns. The accumulation patterns are shown in figure 4b) where a snapshot of the instantaneous streamwise velocity field is given in a wall-parallel plane at $y^+ \approx 10$. It is apparent the dominance of wall-layer streaks. Particles form streamwise elongated
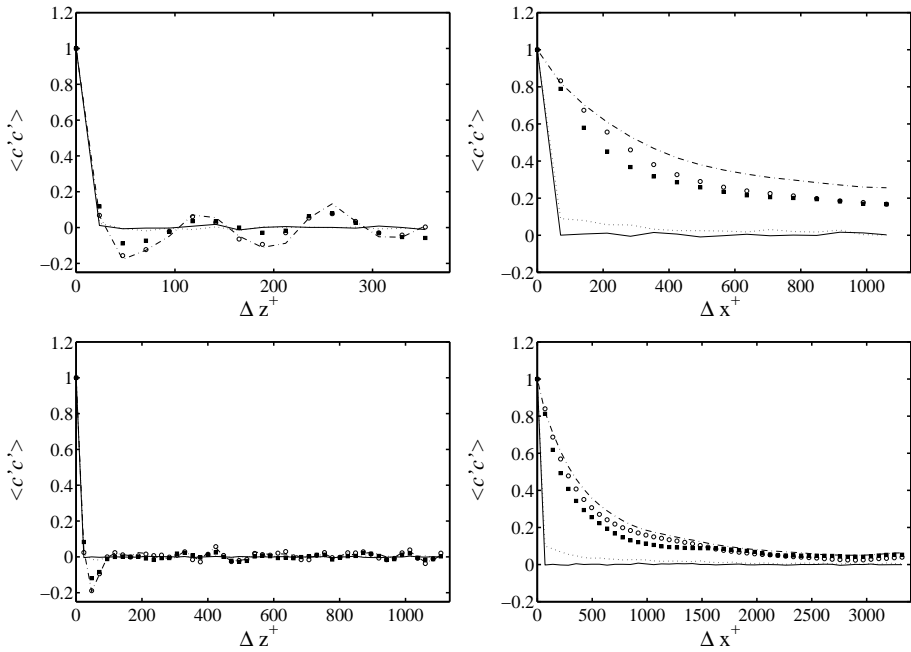
Figure 5: Spanwise autocorrelation functions (left panels) and streamwise autocorrelation functions of particle concentration fluctuations (right panels), top-bottom panels are referred to small-big domain simulation respectively, symbols as in Fig.4.

patterns, which are very thin in the spanwise direction. These particle streaks are predominantly located in low-speed velocity streaks and are characterized by an outward (*i.e.* away from the wall) velocity vector. On the other hand, particles moving towards the wall are mostly found in between the streaks, *i.e.* in the region of the streamwise vortex cores.

To analyze in details the accumulation structures we make use of the concentration function C. In figure 5 streamwise $\langle c'(x)c'(x + \Delta x)\rangle_{x,z,t}(y)$ and spanwise two-point correlations $\langle c'(z)c'(z + \Delta z)\rangle_{x,z,t}(y)$ are shown for particles close to the wall $y^+ = 5$. Concerning the small box simulation, particles with a small Stokes number are correlated neither in the streamwise nor in the spanwise direction. Actually their two-point correlations decay to 0 already at the lowest separation distance. However, heavier particles appear more correlated in both direction. In particular, a clear sinuous behavior can be observed in the spanwise direction. The characteristic length of this structures is $\Delta z^+ \approx 120$ as for the streamwise-velocity spanwise-correlation at similar wall distance. However, unlike for the velocity components, particles show a clear sinusoidal behavior of the two-point correlation also at larger separations (e.g. see at $\Delta z^+ \approx 240$). This indicates that the particle patterns are much more regular and straight than the corresponding velocity streaks. The large domain shows a similar negative peak in the spanwise correlation, although the sinusoidal trend for large separations appears attenuated. As far as the streamwise correlations are concerned, the lightest particles show again virtually no correlation for both simulations. For $St^+ > 5$ the long structures visible in figure 4b) give rise to positive correlations even for large streamwise displacement. Nonetheless the large box computations show smaller values of the streamwise correlation at fixed separation. In particular for $St^+ = 5$ at $\Delta x^+ = 1000$, a value of ~ 0.35 is computed in the small box simulation, while the value of ~ 0.2 emerges from the large domain DNS. These results clearly show that particle streaks extend for very long distances and are influenced by the

periodic boundary conditions if simulations are performed with the typical domain size suited for mono-phase flows.

In summary, we have shown that particles predominantly form narrow, but very long streamwise patterns, located in the low-speed streaks and characterized by an outward wall normal motion. However, the analysis of the streamwise two-point correlations clearly shows that the length of these particle streaks is significantly larger than the corresponding velocity structures. In addition, the spanwise organization is extremely regular and corresponds to a mean spacing of about 120 plus units. The turbulent channel flow simulations with an increased size of the numerical box highlight some significant differences in the correlation of particle concentrations. A possible explanation of this feature can be related to large-scale structures of velocity field, which might carry a considerable amount of energy (see *e.g.*[5]). These structures usually scale with the channel height, and span the whole wall-normal extent. The influence of these structures on the particle pattern has not been studied before and probably is the key to understand the particle pattern formations.

References

[1] Bertolotti, F.P., Herbert, T. and Spalart, P.R., Linear and nonlinear stability of the Blasius boundary layer, J. Fluid Mech. 242, 441-474, 1992.

[2] Brandt, L. and de Lange, H.C., Streak interactions and breakdown in boundary layer flows, Phys. Fluid 20, 024107, 2008.

[3] Brandt, L., Schlatter, P. and Henningson, D.S., Transition in boundary layers subjected to free-stream turbulence. J. Fluid Mech. 517, 167-198, 2004.

[4] Chevalier, M., Schlatter, P., Lundbladh, A. and Henningson, D.S., SIMSON - A pseudo-spectral solver for incompressible boundary layer flows, Tech. Rep. KTH Stockholm, Sweden, TRITA-MEK 2007:07, 2007.

[5] del Álamo J. C. and Jiménez J. (2003), Spectra of the very large anisotropic scales in turbulent channels, Physics of Fluids , vol. 15, L41.

[6] Jacobs, R.G. and Durbin, P., Simulations of bypass transition, J. Fluid Mech. 428, 185-212, 2000.

[7] Mans, J., Kadijk, E.C., de Lange, H.C. and van Steenhoven, A.A., Breakdown in a boundary layer exposed to free-stream turbulence. Exp. Fluids 39, 1071-1083, 2005.

[8] Mans, J., de Lange, H.C. and van Steenhoven, A.A., Sinuous breakdown in a flat plate boundary layer exposed to free-stream turbulence. Phys. Fluids 19, 088101, 2007.

[9] Matsubara, M. and Alfredsson, P.H., Disturbance growth in boundary layers subjected to free-stream turbulence. J. Fluid Mech. 430, 149-168, 2001.

[10] Maxey, M.R., Riley, J.J., Equation of motion for a small rigid sphere in a nonuniform flow, 1983, Physics of Fluids, 26, 883.

[11] Nagarajan, S., Lele, S.K. and Ferziger, J.H., Leading-edge effects in bypass transition. J. Fluid Mech. 572, 471-504, 2007.

[12] Portela L.M., Cota P., Oliemans R.V.A, (2002), Numerical study of the near-wall behaviour of particles in turbulent pipe flow, Powder Technology, vol. 125, pp. 149-157.

[13] Schlatter, P. Brandt, L., de Lange, H.C., and Henningson, D. S. On streak breakdown in bypass transition, Phys. Fluid 20, 024107, 2008.

[14] Schmid, P.J. and Henningson, D.S., Stability and Transition in Shear Flows, Springer, New York, U.S.A., 2001.

Tissue fiber families in the mitral valve - constitutive modelling, numerical analysis and potential clinical application

Bjørn Skallerud

Department of Structural Engineering
Norwegian University of Science and Technology, Trondheim, Norway
e–mail: bjorn.skallerud@ntnu.no

Summary Some hyperelastic constitutive models and solid finite element analyses of the mitral valve are presented herein. Focus is on healthy tissue, but some comments regarding diseased tissue and clinical applications are given. Current state of art on physiology and anatomy of the native mitral apparatus shows that a full understanding and explanation of tissue response is incomplete. Hence, further studies on characterising microstructure, and coupling of this to constitutive modelling, are necessary. With this, one has the potential to develop numerical tools that can be used in the clinic for improved diagnostics and treatment planning.

Introduction

The mitral valve controls the blood flow direction in the left part of the heart, and prevents blood from flowing back into the right atrium during systole. Diseases that affect the mitral valve have severe consequences. Due to the complexity of the valve, surgeons would try to repair before replacement with an artificial valve. The constitutive modeling of the leaflets and chordae is quite well established now, with hyperelastic transverse isotropy defined by a dominating collagen fibre family embedded in an isotropic matrix and incompressibility as the main setting (Kunzelman et al, 1993a, Kunzelman et al, 1993b, May-Newman and Yin, 1998, Liao and Vesely, 2003, Kunzelman and Cochran, 1990, Prot et al, 2009a). It seems that the collagen fibers are oriented parallel to the circumferential (annular) direction for significant parts of the leaflets, see e.g. Einstein et al (2005). Elastin is also contributing to tissue stiffness, and is usually lumped into the the isotropic bulk elasticity of the matrix. Muscle fibers and cells also contribute to the stiffness and motion of the valve (Williams and Jew, 2004).

Most studies on material models for mitral tissue are based on animal tissues and in-vitro tests (May-Newman and Yin, 1995). With this one gets an understanding of the passive response of the material. Some initial studies on human tissue constitutive modeling are provided by Prot et al (2009b).

Constitutive modelling

In this section we briefly introduce the continuum mechanical framework. The purpose is to provide the derivation of the appropriate tensors in order to use the anisotropic hyperelastic constitutive model with solid finite elements. Further details can be found in (Prot and Skallerud, 2009).

Kinematics

Let Ω_0 and Ω be the reference and current configurations, respectively. The deformation map $\varphi(\mathbf{X}) : \Omega_0 \to \mathbf{R}^3$ transforms a material point $\mathbf{X} \in \Omega_0$ into the related current position $\mathbf{x} = \varphi(\mathbf{X}) \in \Omega$. Hence, the deformation gradient $\mathbf{F}$ is defined as $\mathbf{F} = \partial\varphi(\mathbf{X})/\partial\mathbf{X} = \partial\mathbf{x}/\partial\mathbf{X}$, with the volume ratio $J = \det\mathbf{F} > 0$ ($J = 1$ for an incompressible material).
We consider the multiplicative decomposition of the deformation gradient $\mathbf{F}$, first introduced by Flory (1961):$\mathbf{F} = (J^{1/3}\mathbf{1})\bar{\mathbf{F}}$ $\mathbf{C} = (J^{2/3}\mathbf{1})\bar{\mathbf{C}}$. The terms $J^{1/3}$ and $J^{2/3}$ are associated with

volume changing deformation. $\bar{\mathbf{F}}$ and $\bar{\mathbf{C}} = \bar{\mathbf{F}}^T\bar{\mathbf{F}}$, which are called modified deformation gradient and modified right Cauchy-Green tensor, are associated with the volume preserving deformations of the material. The modified left Cauchy-Green tensor then reads $\bar{\mathbf{B}} = \bar{\mathbf{F}}\bar{\mathbf{F}}^T$.

We assume that the anisotropic properties arise from two fibre families embedded in the continuum and that the two directions of the fibres at point $\mathbf{X}$ in the reference configuration Ω_0 are defined by unit vectors $\mathbf{a_0}(\mathbf{X})$ and $\mathbf{b_0}(\mathbf{X})$, respectively. During deformation these fibres move with the material points of the continuum body and arrive at the deformed configuration Ω. Therefore, the new fibre directions at the associated point $\mathbf{x}$ in Ω is defined by the vectors $\mathbf{a} = \mathbf{Fa_0}$ and $\mathbf{b} = \mathbf{Fb_0}$, and the stretch of the fibres in these direction are $|\mathbf{a}|$ and $|\mathbf{b}|$, respectively. For further use, we define the following vectors: $\bar{\mathbf{a}} = \bar{\mathbf{F}}\mathbf{a_0}, \quad \bar{\mathbf{b}} = \bar{\mathbf{F}}\mathbf{b_0}$.

Strain energy function

In order to describe the anisotropic hyperelastic response of mitral valve leaflets with two fiber families, we use the following strain energy function Ψ:

$$\Psi = \Psi(\mathbf{C}, \mathbf{a}_0 \otimes \mathbf{a}_0, \mathbf{b}_0 \otimes \mathbf{b}_0), \tag{1}$$

and adopt the following decomposition of Ψ into two parts (Holzapfel, 2000),

$$\Psi(\mathbf{C}, \mathbf{a}_0 \otimes \mathbf{a}_0) = U(J) + \bar{\Psi}(\bar{\mathbf{C}}, \mathbf{a}_0 \otimes \mathbf{a}_0, \mathbf{b}_0 \otimes \mathbf{b}_0), \tag{2}$$

where U and $\bar{\Psi}$ are the volumetric and isochoric contributions of Ψ, respectively. For the particular case of mitral valve leaflets, we assume that the energy function may be expressed in terms of four invariants:

$$\begin{aligned}\Psi(\mathbf{C}, \mathbf{a}_0 \otimes \mathbf{a}_0) &= U(J) + \bar{\Psi}(\bar{I}_1, \bar{I}_4, \bar{I}_6) \tag{3} \\ &= U(J) + \bar{\Psi}_p(\bar{I}_1, \bar{I}_4) + \bar{\Psi}_a(\bar{I}_6), \tag{4}\end{aligned}$$

where $\bar{I}_1 = \mathrm{tr}\bar{\mathbf{C}} = \mathrm{tr}\bar{\mathbf{B}}$, $\bar{I}_4 = \bar{\mathbf{C}} : \mathbf{a}_0 \otimes \mathbf{a}_0$ and $\bar{I}_6 = \bar{\mathbf{C}} : \mathbf{b}_0 \otimes \mathbf{b}_0$.

We employ the following form for the strain energy function Ψ:

$$\Psi(\bar{I}_1, \bar{I}_4, \bar{I}_6, J) = \underbrace{c_0 \left(e^{c_1(\bar{I}_1-3)^2 + c_2(\bar{I}_4-1)^2} - 1 \right)}_{\bar{\Psi}_p(\bar{I}_1, \bar{I}_4):\text{ passive isochoric part}} + \underbrace{\bar{\Psi}_a(\bar{I}_6)}_{\bar{\Psi}_a(\bar{I}_6):\text{ active isochoric part}} + \underbrace{\kappa(J-1)^2}_{U(J):\text{ volumetric part}},$$
$$\tag{5}$$

where c_0, c_1, c_2 are material parameters, κ is a positive penalty parameter and $(J-1)^2$ is known as the penalty function. Herein, $\bar{\Psi}_p$ and $\bar{\Psi}_a$ are associated with the passive behaviour (May-Newman and Yin, 1998, Prot et al, 2009a) and to the active behaviour of the leaflets due to muscle fiber contraction, respectively.

Stress and elasticity tensors

The second Piola-Kirchhoff stress tensor $\mathbf{S}$ is derived from eq.(4):

$$\mathbf{S} = 2\frac{\partial \Psi}{\partial \mathbf{C}} = 2\underbrace{\frac{\partial U}{\partial \mathbf{C}}}_{\mathbf{S}_{vol}} + 2\underbrace{\frac{\partial \bar{\Psi}}{\partial \mathbf{C}}}_{\mathbf{S}_{iso}} \tag{6}$$

18

The Cauchy stress tensor $\boldsymbol{\sigma}$ is obtained by the push-forward operation of $\mathbf{S}$ to the current configuration, $\boldsymbol{\sigma} = \frac{1}{J}\mathbf{F}\mathbf{S}\mathbf{F}^T$. Thus,

$$\boldsymbol{\sigma} = 2\kappa(J-1)\mathbf{1} + \frac{1}{J}\mathrm{dev}\bar{\boldsymbol{\sigma}}, \quad \bar{\boldsymbol{\sigma}} = 2\psi_1\bar{\mathbf{B}} + 2\psi_4\bar{\mathbf{a}} \otimes \bar{\mathbf{a}} + 2\psi_6\overline{\mathbf{b}} \otimes \overline{\mathbf{b}}. \tag{7}$$

The material elasticity tensor obtained from eq.(4) reads:

$$\mathbb{C} = 4\frac{\partial^2 \Psi}{\partial\mathbf{C}\partial\mathbf{C}} = \underbrace{4\frac{\partial^2 U}{\partial\mathbf{C}\partial\mathbf{C}}}_{\mathbb{C}_{vol}} + \underbrace{4\frac{\partial^2 \bar{\Psi}}{\partial\mathbf{C}\partial\mathbf{C}}}_{\mathbb{C}_{iso}}. \tag{8}$$

We adopt the following notation: $\psi_{ij} = \frac{\partial^2 \Psi}{\partial \bar{I}_i \partial \bar{I}_j}$, $\quad i,j = 1,4,6$. Hence,

$$\mathbb{C}_{vol} = 4\kappa(J^2-J)\frac{\partial\mathbf{C}^{-1}}{\partial\mathbf{C}} + 4\kappa(J^2 - \frac{J}{2})\mathbf{C}^{-1} \otimes \mathbf{C}^{-1}, \tag{9}$$

$$\mathbb{C}_{iso} = 4\psi_{11}\frac{\partial\bar{I}_1}{\partial\mathbf{C}} \otimes \frac{\partial\bar{I}_1}{\partial\mathbf{C}} + 4\psi_{14}\left(\frac{\partial\bar{I}_1}{\partial\mathbf{C}} \otimes \frac{\partial\bar{I}_4}{\partial\mathbf{C}} + \frac{\partial\bar{I}_4}{\partial\mathbf{C}} \otimes \frac{\partial\bar{I}_1}{\partial\mathbf{C}}\right) + 4\psi_{44}\frac{\partial\bar{I}_4}{\partial\mathbf{C}} \otimes \frac{\partial\bar{I}_4}{\partial\mathbf{C}} \tag{10}$$

$$+4\psi_{66}\frac{\partial\bar{I}_6}{\partial\mathbf{C}} \otimes \frac{\partial\bar{I}_6}{\partial\mathbf{C}} + 4\psi_1\frac{\partial^2\bar{I}_1}{\partial\mathbf{C}\partial\mathbf{C}} + 4\psi_4\frac{\partial^2\bar{I}_4}{\partial\mathbf{C}\partial\mathbf{C}} + 4\psi_6\frac{\partial^2\bar{I}_6}{\partial\mathbf{C}\partial\mathbf{C}}.$$

The spatial description the elasticity tensor is obtained by push-forward operation of $\mathbb{C}$:

$$\mathbb{c} = \boldsymbol{\chi}_*(\mathbb{C}), \quad c_{ijkl} = \frac{1}{J}F_{iI}F_{jJ}F_{kK}F_{lL}C_{IJKL}. \tag{11}$$

Finite element models

The above models were implemented in ABAQUS UMAT. All simulation are based on ABAQUS. Fig. 1 shows the finite element model in initial configuration (beginning of systole). Eight noded hybrid solid elements were employed for the two leaflets, and transversely isotropic hyperelastic truss elements were employed for the chordae tendinae (Prot and Skallerud, 2009). The lower attachment points for the chordae were fixed, the attachment of the leaflets along the annulus were fixed with respect to displacements and free with respect to rotations. The left ventricle blood pressure from beginning of systole to peak systole was applied according to a measured history. Quasi-static analyses were performed, only. Fig. 2 depicts the orientation of the collagen fibers on the deformed mesh at peak systole. Contact surfaces were defined on the atrial side of the leaflets in order to account for valve closure.

Results and discussion

Fig. 3 shows three deformed meshes of the valve at peak systole (Prot et al, 2009b). These analyses employed passive material modeling only. The first corresponds to a healhty, but very old, donor (88 years), the second corresponds to a younger (42 years) donor with the HOCM affected heart. Interestingly, the age of the old donor promoted a change in the exponent of the collagen tissue term in the strain energy potential from 2 to 4 in order to capture increased tissue stiffness. It is well documented that collagen stiffness increases with age. Furthermore, the mitral tissue from the HOCM heart was much softer than the old donor, and even softer in some directions than the
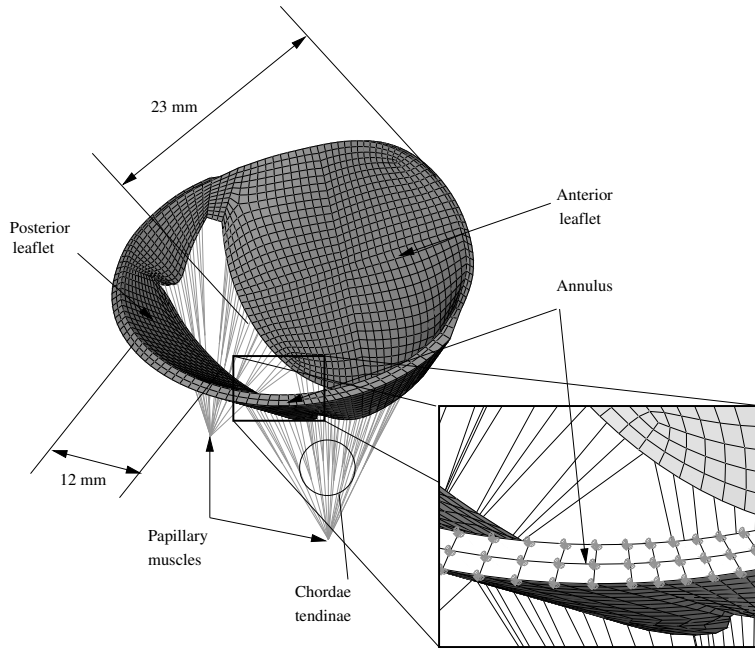
Figure 1: Initial geometry for the healthy mitral valve at the beginning of systole. The finite element mesh is shown with two layers of solid elements for the leaflets.
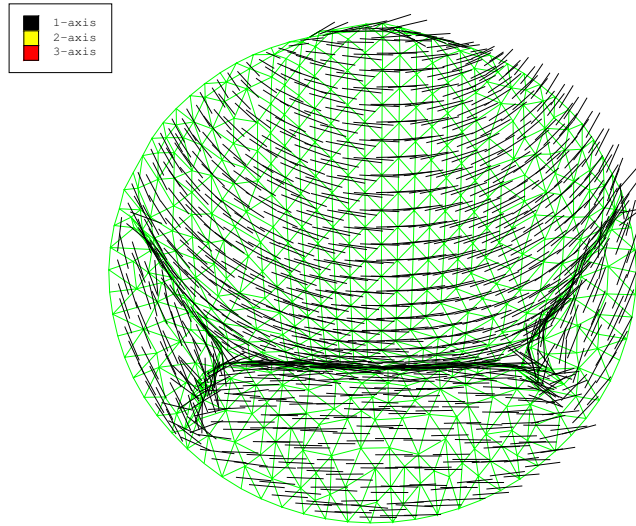
Figure 2: Collagen fiber orientation.

porcine model shown in Fig. 3c, and this affected the resulting material parameters obtained from nonlinear LSQ estimation. Hence, the HOCM condition affects the mitral tissue elasticity significantly. Including muscle fibers in the constitutive model improve the predictions of the deformed shape of the leaflets at peak systole, with a reduced displacement into the left atrium. We believe that this improves the hemodynamics when the blood is pushed out of the left ventricle during systole. Hence, in a fluid structure interaction approach to this system this additional fibre system will be important.

(a) Healthy

(b) HOCM
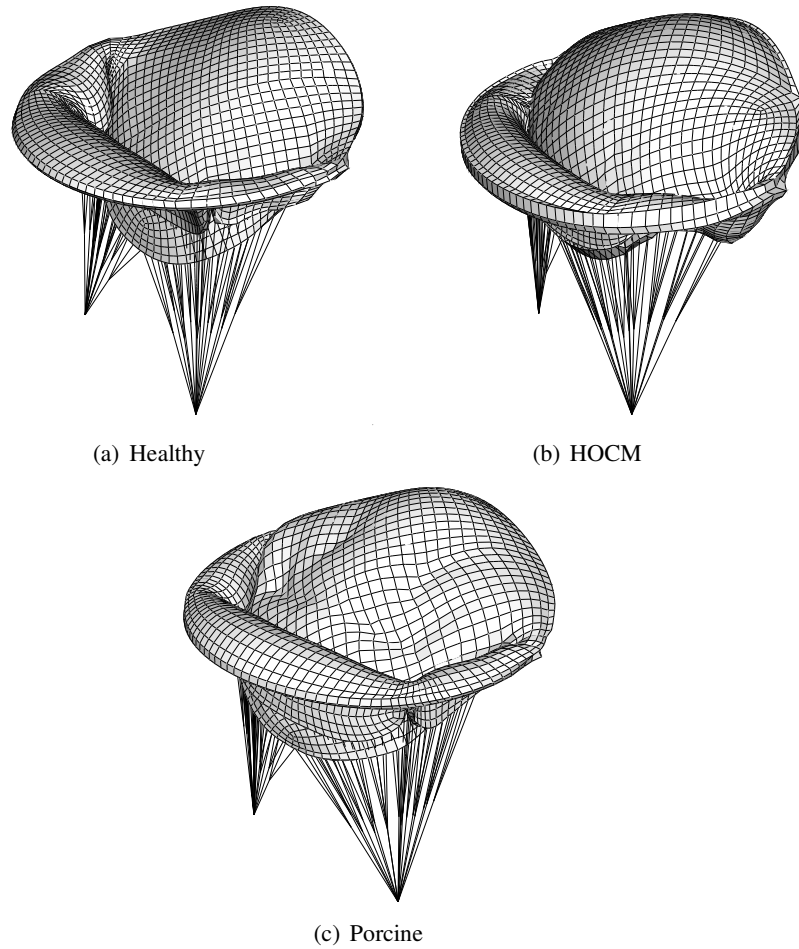
(c) Porcine

Figure 3: Deformed configurations of a) a healthy human, b) hypertrophic obstructive cardiomyopatic (HOCM), and c) healthy porcine mitral valves at 120 mmHg. From Prot et al, (2009b).

With above modelling, one has the possibility to adjust material parameters depending on the state of the tissue. E.g. connective tissue disorders (Marfan's syndrome etc) leads to softer collagen. This then affects the shape and motion of the mitral leaflets, eventually disturbing physiological blood flow. If one can obtain such material parameters, one can carry out numerical simulations studying different disease scenarios and corresponding surgical procedures in order to optimise treatment. However, how to obtain material data by non-invasive means is a big challenge.

References

[1] Einstein DR, Kunzelman KS, Reinhall P, Nicosia M, and Cochran RP (2005) The relationship of normal and abnormal microstructural proliferation to the mitral valve closure sound. *J. biomech. eng.* , **127(1)**:134–147.

[2] Flory PJ (1961) Thermodynamics relations for high elastic materials. *Trans. Faraday Soc.* , **57**:829–838.

[3] Grande-Allen KJ, Calabro A, Gupta V, Wight TN, Hascall VC, Vesely I (2004) Glycosaminoglycans and proteoglycans in normal mitral valve leaflets and chordae: association with regions of tensile and compressive loading. *Glycobiology* ,**14(7)**:621–633.

[4] Holzapfel GA (2000) *Nonlinear Solid Mechanics. A Continuum Approach for Engineering*. John Wiley & Sons, Chichester.

[5] Kunzelman KS, Cochran RP, Chuong C, Ring WS, Verrier ED, and Eberhart RD (1993) Finite element analysis of the mitral valve. *J. Heart Valve Dis.* , **2**:326–340.

[6] Kunzelman KS, Cochran RP, Murphree SS, Ring WS, Verrier ED, Eberhart RC (1993) Differential collagen distribution in the mitral valve and its influence on biomechanical behavior. *J. Heart Valve Dis.* , **2**:236-244.

[7] Kunzelman KS and Cochran RP (1990) Mechanical properties of basal and marginal mitral valve chordae tendineae. *ASAIO Trans.* , **36**:M405–408.

[8] Liao J, Vesely I (2003) A structural basis for the size-related mechanical properties of mitral valve chordae tendineae. *J. Biomech.* , **36(8)**:1125–33.

[9] May-Newman K and Yin FCP (1998) A constitutive law for mitral valve tissue. *J. Biomech. Eng.* , **120**:38–47.

[10] Prot V, Skallerud B, Holzapfel GA (2007) Transversely isotropic membrane shells with application to mitral valve mechanics. Constitutive modeling and finite element implementation. *Int. J. Numer. Meth. Eng.* , **71(8)**, 987–1008.

[11] Prot V, Haaverstad R, Skallerud B (2009a) Finite element analysis of the mitral apparatus: annulus shape effect and chordal force distribution. *J. Biomech Mod in Mechanobiol*, **8**, 43–55.

[12] Prot V, Skallerud B, Sommer G, and Holzapfel GA (2009c) On modelling and analysis of healthy and pathological human mitral valves: two case studies. *J Mech Beh Biomed Mater*, accepted.

[13] Prot V and Skallerud B (2009) Nonlinear solid finite element analysis of mitral valves with heterogeneous leaflet layers.*Comp Mech*,**43**, 353–368.

[14] Votta E, Caiani E, Veronesi F, Soncini M, Montevecchi FV, and Redaelli A (2008) Mitral valve finite element modelling from ultrasound data: a pilot study for a new approach to understand mitral function and clinical scenarios. Phil Trans R Soc A, **366**,pp3411–3434.

[15] Votta E, Maisano F, Soncini M, Redaelli A, Montevecchi FM, and Alfieri O (2002) 3-D computational analysis of the stress distribution on the leaflets after edge-to-edge repair of mitral regurgitation. *J. Heart Valve Dis.* , **11**:810–822.

[16] Williams TH and Jew JY (2004) Is the mitral valve passive flap theory overstated? An active valve is hypothezised. *Medical Hypotheses*, **62**, 605–611.

Computer Methods for Large Deformation Analysis of Multibody Systems

Marko K. Matikainen and Aki M. Mikkola*

Department of Mechanical Engineering
Lappeenranta University of Technology, Lappeenranta, Finland
e–mail: matikain@lut.fi, mikkola@lut.fi

Summary   The study provides a review of computer methods that can be used in the dynamic analysis of large deformations in multibody applications. Particular emphasis is placed on developments of the absolute nodal coordinate formulation. The absolute nodal coordinate formulation is a recently proposed approach to the analysis of multibody systems that takes into account nonlinearities, including large deflections and plasticity. In the absolute nodal coordinate formulation, finite elements are defined in the global coordinate system using position coordinates together with independent global slopes that are, in fact, partial derivatives of the position vector with respect to the element coordinates. Due to the use of a large number of slope coordinates, an arbitrary rigid body motion can be described by the shape function matrix and the vector of nodal coordinates. This unique feature leads to a constant mass matrix in two- and three-dimensional cases. Due to the constant description of the mass matrix, the inertia vector that depends quadratically on velocities vanishes, simplifying the expression of the equations of motion.

Introduction

During the past decades, the dynamic analysis of machines has become important in terms of advanced designs. Increased computational power and enhanced formulations allow for the possibility to solve mathematical models that describe the dynamic performance of complex mechanical systems. These types of complex systems may consist of a number of interconnected rigid or flexible bodies, where an analytical solution may not be available. In the field of multibody dynamics, a large number of formalisms are introduced for the dynamic analysis of mechanical systems [1, 2].

Multibody system dynamics offer a computer-based approach to treat and solve dynamic problems of mechanical systems. The multibody approach can be applied to a wide variety of engineering fields, including robotics, aerospace applications, vehicle dynamics, biomechanics and rotating structures. In these applications, optimization and sophisticated design tools are often required. Generally, a multibody system consists of a number of bodies that are connected together via constraints. Figure 1 illustrates a general multibody system depicted in an abstract form.

In multibody formalism, equations of motion can be formulated in a systematic manner while no assumptions regarding the magnitude of rotations of bodies are made. Equations of motion of a multibody system are based on fundamental laws of systems of particles. This leads to the principal difference between rigid and the flexible bodies that depends on the relative movement of the particles in the body. In the case of rigid bodies, all of the particles in the body are rigidly coupled, while in the case of flexible bodies, particles can exhibit relative movement with respect to each other. By employing multibody formalisms, the system level analysis of mechanical systems can be obtained in a straightforward manner [4, 5, 6].

Usually, the bodies in the multibody system are assumed to be rigid, which may be an acceptable assumption for the analysis of motion and forces in many practical engineering problems. However, in some cases, the deformation of the bodies should be taken into consideration in order to improve the accuracy of the numerical solution. The deformation of bodies can be described using a number of approaches. In simple approaches, linear strain-displacement as well as linear
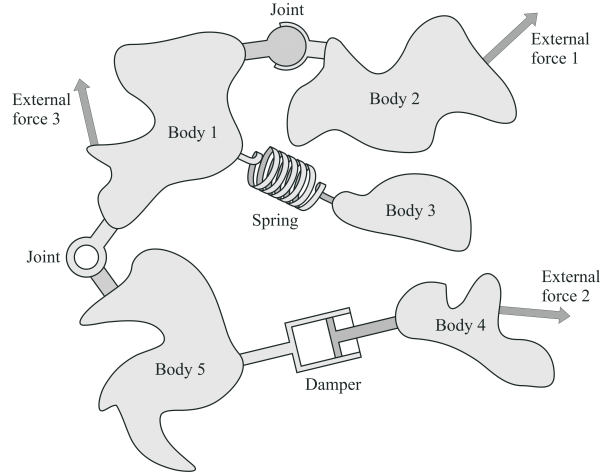
Figure 1: Abstract description of a multibody system. [3]

stress-strain relations are used by assuming that deformations are small and the material behavior is elastic. In some practical applications, the geometric change of a body may become significant in terms of the dynamic response, making it necessary to employ a nonlinear stress-strain relation in the mathematical modeling. In addition to geometrical nonlinearity, advanced modeling approaches are capable of taking material nonlinearities into account by using a nonlinear stress-strain relation [7, 8].

Figure 2 shows helicopter blades, a belt pulley system and a tire. In these practical applications, the flexibility of mechanical components is significant and the deformations of bodies should be accounted for in order to obtain accurate results from the mathematical model.
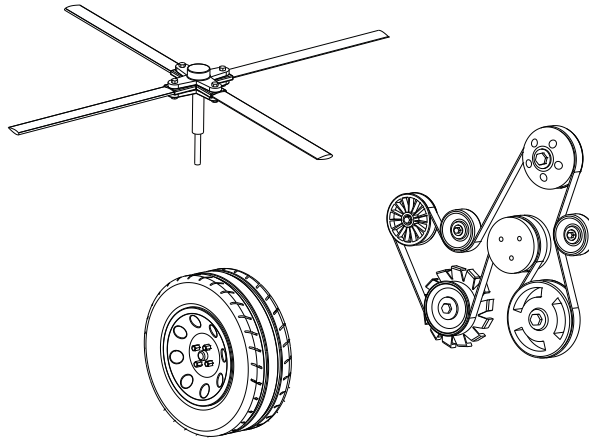
Figure 2: Multibody systems where geometrical nonlinearities and material nonlinearities may occur in some of the bodies. [9]

For flexible bodies, the description of motion can be derived using numerous different formalisms. According to [2], the floating frame of reference formulation, the large rotation vector formulation and the absolute nodal coordinate formulation are widely used formulations in the description of flexible bodies in multibody applications. These formulations differ from each other in a num-

ber of ways, although a common feature of the formulations is that they reproduce exactly zero strain under rigid body movements. This could be considered as a minimum requirement to reach the energy balance in the case of lengthy multibody dynamic simulations. It is noteworthy that nonlinear finite element formulations can also be used in flexible multibody system dynamics. Formulations used in flexible multibody dynamics are often related to finite element formulations. In the floating frame of reference formulation, elastic deformations can be approximated by employing conventional finite elements, whereas in the large rotation vector and the absolute nodal coordinate formulations, the total Lagrangian approach is employed.

Due to the fact that bodies of a multibody system undergo a different magnitude of deformations, it is common to combine different formulations in the multibody simulation. Accordingly, some bodies can be assumed to be rigid while some flexible bodies can be modeled using the floating frame of reference formulation with the assumption of small elastic deformations. For bodies that experience large deformations, such that geometrical and material nonlinearities are involved, the large rotation vector or absolute nodal coordinate formulations can be used in the modeling.

The study provides a review of computer methods that can be used in the dynamic analysis of large deformations in multibody applications. This review is mainly based on doctoral thesis by Matikainen [9]. Particular emphasis is placed on developments of the absolute nodal coordinate formulation.

Floating frame of reference formulation

The floating frame of reference formulation can be applied to bodies that experience large rigid body displacements and rotations and linear deformations. In the formulation, a non-inertial reference frame is used to describe large translations and large rotations with respect to inertial coordination. The deformation of a flexible body is defined with respect to a non-inertial reference frame using a set of elastic coordinates. In the floating frame of reference formulation, the deformations are usually assumed to be linear with respect to the non-inertial reference frame. Elastic deformation within the reference frame can be approximated by using the Ritz-method, or by using the assumed deformation modes of the body. In [10], where the formulation is introduced for the planar flexible mechanisms, the deformation of the body is approximated using the conventional Bernoulli-Euler finite beam elements that are interconnected by constraints. It is possible to obtain the deformation modes of the body through the use of component mode synthesis [11, 12].

Component mode synthesis is a model reduction technique that can be used to decrease the degrees of freedom of the finite element model. The reduction makes the computation more effective and it may decrease the stiffness of the system but unfortunately, it also leads to a loss of accuracy. The usage of the reduction technique in the floating frame of reference formulation is explained in detail in [13, 14]. When the component mode synthesis is used, the floating frame of reference is difficult to apply to geometrically or materially nonlinear problems. If nonlinearities are taken into account, using for example Ritz approximation for the displacement field, the elastic forces are nonlinear. It is demonstrated in [15] that material nonlinearities can be accounted for within the floating frame of reference formulation by using isoparametric finite elements and a body fixed reference frame. Due to the use of a body fixed reference frame, the approach is different than the traditional updated Lagrangian formulation [15].

The use of the floating frame of reference formulation leads to a simple description for strain energy with a constant representation of the stiffness matrix, and a highly nonlinear description of kinetic energy. This is due to coupling between variables of reference and relative motion. In

some cases, the constraint equations may become cumbersome to model due to the kinematics description of a flexible body. The main advantages of this approach are the exact description of rigid body motion and the possibility to decrease the number of degrees of freedom by employing component mode synthesis. It is also notable that the formalism is not limited to beam and plate type structures. However, due to the use of relative variables in the description of deformation, centrifugal and Coriolis terms will occur in the equations of motion.

Geometrically exact formulations

A geometrically exact beam element has been examined in numerous studies. In theory, geometrical approximations, such as the linearization of rotation parameters, are not employed. This formulation is suitable for multibody applications in which large deformations, i.e. large displacements and large strains, need to be accounted for. When the theory is applied to practical applications, the element can be described within the concept of the total Lagrangian formulation. However, to overcome the singularity problem associated with rotation parameters in the total Lagrangian formulation, the updated Lagrangian formulation or quaternions, can be used. Simo and Vu-Quoc present the geometrically exact beam formulation based on the Reissner theory with respect to the large rotation vector formulation in [16, 17]. In this approach, spatial basis functions are used in the element discretization procedure [17].

The large rotation vector formulation is a widely used approach and it has been extensively studied for two and three-dimensional beam elements [18]. The finite elements based on the large rotation vector formulation are discretized using position and rotational nodal coordinates. This discretization leads to a constant description of the mass matrix in the case of two-dimensional elements. However, in three-dimensional cases, discretization leads the mass matrix to no longer be constant, regardless of the choice of rotational coordinates. It is important to note that the cross-section is described by an orthonormal moving basis leading to an orthogonal representation of the rotation matrix. This representation is favorable, as it simplifies the element computation [19].

In [20], the beam element based on the geometrically exact beam theory is introduced within the framework of a total Lagrangian formulation without singularity problems. The element is based on the Timoshenko-Reissner theory, and singularities of the angle 2π and its multiples are avoided by the varying parameterization on the rotation manifold. From a computational point of view, the beam formulation is favorable to be presented in a manner in which the solution can be determined with a constraint free manifold, as it leads to a system of ordinary differential equations. In this formulation, the expression of the mass matrix is simple, but unfortunately, not constant. The three-dimensional element is defined using six degrees of freedom at a node. In the element, linear interpolation is used for displacements and rotations. This formulation appears to be effective since quaternions are not employed. It is noteworthy that the use of quaternions, such as Euler parameters, will result in one extra constraint and one extra rotation parameter at the node when compared to the use of Euler rotations. This type of total Lagrangian parameterization is also introduced for rigid bodies in [21].

Absolute nodal coordinate formulation

The absolute nodal coordinate formulation is a nonlinear finite element approach that is based on the use of a global position and gradient coordinates. Using gradient coordinates, i.e. the components of the deformation gradient, instead of conventional rotational coordinates, the absolute nodal coordinate formulation leads to the exact description for inertia of the rigid body

with a constant mass matrix. Since the presentation of the formulation [2], the numerous finite elements based on the absolute nodal coordinate formulation are introduced; see for example [22, 23, 24, 25, 26]. However, within fully-parameterized elements, different types of locking phenomena may occur due to low order interpolation in the transverse direction [27, 38]. In order to overcome this problem, alternative approaches are introduced to define the elastic forces; see for example [28, 29, 30, 31, 32]. In order to clarify the absolute nodal coordinate formulation, the fully-parameterized element is described at the beginning of this section. Fully-parameterized elements allow for the energy from kinetic, strain and external forces to be defined in a consistent manner.

The kinematics description of an element based on the formulation does not include conventional rotational coordinates. Therefore, the use of quaternions is not needed to avoid the singularity problem of finite rotations under three-dimensional rotations. In this formulation, gradient coordinates that are partial derivatives of the position vector are used to describe the cross-section or fiber orientations and deformations. Therefore, all nodal coordinates are described in an inertial frame allowing for the usage of the total Lagrangian approach, such as in the case of large rotation vector formulations and conventional solid elements. Elements based on the absolute nodal coordinate formulation can be considered as geometrically exact because no geometrical simplifications are necessary. Based on the special features of the formulation mentioned above, elements based on the absolute nodal coordinate formulation can be considered more advanced than classical beam and plate elements. The use of the absolute nodal coordinate formulation leads to benefits including a constant mass matrix, which simplifies the description of the equations of motion. Due to the use of the global description of the element configuration, the estimation for contact surfaces and the description of geometric constraints, such as for a sliding joint, are straightforward - particularly compared to the floating frame of reference formulation [33]. On the other hand, non-conservative forces in the formulation, such as internal damping, lead to a more complex description [34]. Due to the use of positions and their derivatives, the Hermite base functions are usually employed in the elements based on the absolute nodal coordinate formulation.

Kinematics

In elements based on the absolute nodal coordinate formulation, kinematics can be expressed using spatial shape functions and global coordinates. Position of an arbitrary particle p in the isoparametric element (Figure 3) can be defined in the inertial frame as follows:

$$\boldsymbol{r} = \boldsymbol{S}_m(\boldsymbol{x})\boldsymbol{e} = \boldsymbol{S}_m(\boldsymbol{\xi}(\boldsymbol{x}))\boldsymbol{e}, \tag{1}$$

where $\boldsymbol{S}_m$ is a shape function matrix, $\boldsymbol{e} = \boldsymbol{e}(t)$ is the vector of nodal coordinates and vector $\boldsymbol{x} = x\overline{\boldsymbol{e}}_1 + y\overline{\boldsymbol{e}}_2 + z\overline{\boldsymbol{e}}_3$ includes physical coordinates. For the isoparametric elements, the shape functions can be expressed using physical coordinates $\boldsymbol{x}$ or local coordinates $\boldsymbol{\xi}$ in the range -1 ... +1. The kinematics of the element in the reference configuration at time $t = 0$ can be described as $\overline{\boldsymbol{r}} = \boldsymbol{S}_m(\boldsymbol{x})\overline{\boldsymbol{e}}$, where $\overline{\boldsymbol{e}} = \boldsymbol{e}(0)$. The vector $\boldsymbol{e}$ contains both translational and rotational coordinates of the element and it can be written at node i of the three dimensional fully-parameterized element as follows:

$$\boldsymbol{e}^{(i)} = \begin{bmatrix} \boldsymbol{r}^{(i)^T} & \boldsymbol{r}_{,x}^{(i)^T} & \boldsymbol{r}_{,y}^{(i)^T} & \boldsymbol{r}_{,z}^{(i)^T} \end{bmatrix}^T; \tag{2}$$

where the following notations for gradients are used:

$$\boldsymbol{r}_{,\alpha}^{(i)} = \begin{bmatrix} r_{1,\alpha}^{(i)} \\ r_{2,\alpha}^{(i)} \\ r_{3,\alpha}^{(i)} \end{bmatrix} = \frac{\partial \boldsymbol{r}^{(i)}}{\partial \alpha}; \qquad \alpha = x, y, z.$$

In Figure 3, the kinematics of the fully-parameterized beam element is shown. The beam includes two nodes, both of which are defined by 12 degrees of freedom.
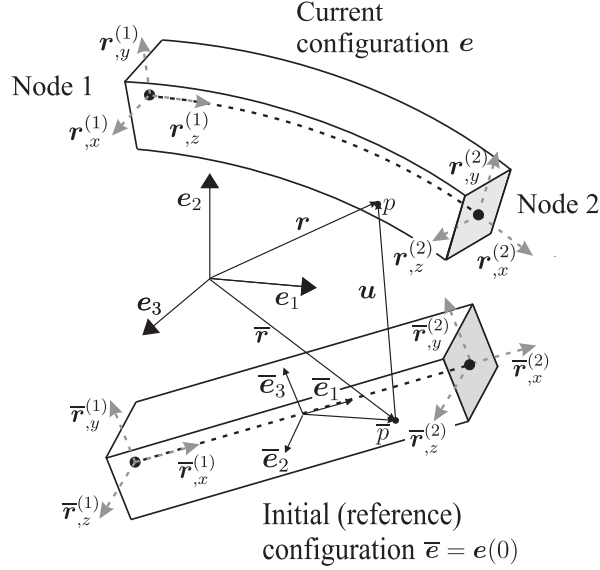
Figure 3: Description of the position of an arbitrary particle in the fully-parameterized beam element. Points $\overline{p}$ and p refer to the same particle at different configurations after displacement $\boldsymbol{u}$. The gradient vectors at nodes are shown by dashed arrows. [9]

Equations of motion

The weak form (variational form) of the equations of motion in the Lagrangian (material) description can be derived from the functional $\mathcal{I}$, see for example [35], which can be written as

$$\mathcal{I} = \int_{t_1}^{t_2} (W_{kin} - W_{pot}) \, \mathrm{d}t, \tag{3}$$

where W_{kin} is the kinetic energy of the element and W_{pot} is the potential energy which includes the internal strain energy W_{int} and the potential energy W_{ext} due to conservative external forces. The potential energy can be written as follows:

$$W_{pot} = W_{int} - W_{ext} \tag{4}$$

In this study, non-conservative forces are not taken into account. The variation of the functional leads to

$$\delta \mathcal{I} = \delta \int_{t_1}^{t_2} (W_{kin} - W_{int} + W_{ext}) \, \mathrm{d}t = 0, \tag{5}$$

The variations of the energies can be written as

$$\delta W_{kin} = \int_V \rho \dot{\boldsymbol{r}}^T \delta \dot{\boldsymbol{r}} \, \mathrm{d}V \tag{6}$$

$$\delta W_{int} = \int_V \boldsymbol{S} : \delta \boldsymbol{E} \, \mathrm{d}V \tag{7}$$

$$\delta W_{ext} = \int_V \boldsymbol{b}^T \delta \boldsymbol{r} \, \mathrm{d}V \tag{8}$$

where : denotes the double dot product, ρ is the mass density, $\boldsymbol{S}$ is the second Piola-Kirchhoff stress tensor, $\boldsymbol{E}$ is the Green strain tensor and $\boldsymbol{b}$ is the vector of body forces. In the special case of gravity, the body forces can be written as $\boldsymbol{b} = \rho \boldsymbol{g}$, where $\boldsymbol{g}$ is the field of gravity. The Green strain tensor can be written as

$$\boldsymbol{E} = \frac{1}{2}(\boldsymbol{F}^T \boldsymbol{F} - \boldsymbol{I}) \tag{9}$$

where $\boldsymbol{I}$ is the identity tensor and $\boldsymbol{F}$ is the deformation gradient tensor, which can be presented in terms of the initial and current configurations $\overline{\boldsymbol{r}}$ and $\boldsymbol{r}$ as follows:

$$\boldsymbol{F} = \frac{\partial \boldsymbol{r}}{\partial \overline{\boldsymbol{r}}} = \frac{\partial \boldsymbol{r}}{\partial \boldsymbol{x}} \left(\frac{\partial \overline{\boldsymbol{r}}}{\partial \boldsymbol{x}} \right)^{-1}. \tag{10}$$

Integrating the variation of the kinetic energy by parts within the time interval t_1 and t_2, the weak form of the equations of motion for an element can be written as follows:

$$\int_V \rho \ddot{\boldsymbol{r}}^T \delta \boldsymbol{r} \, \mathrm{d}V + \int_V \boldsymbol{S} : \delta \boldsymbol{E} \, \mathrm{d}V - \int_V \boldsymbol{b}^T \delta \boldsymbol{r} \, \mathrm{d}V = 0. \tag{11}$$

Using the interpolation for the position vector $\boldsymbol{r}$, the variations of energy with respect to the nodal coordinates can be expressed. The variation of the kinetic energy can be represented as

$$\delta W_{kin} = \int_V \rho \ddot{\boldsymbol{r}}^T \delta \boldsymbol{r} \, \mathrm{d}V = \ddot{\boldsymbol{e}}^T \int_V \rho \boldsymbol{S}_m^T \boldsymbol{S}_m \, \mathrm{d}V \, \delta \boldsymbol{e}, \tag{12}$$

from which the mass matrix of the element can be identified as follows:

$$\boldsymbol{M} = \int_V \rho \boldsymbol{S}_m^T \boldsymbol{S}_m \, \mathrm{d}V. \tag{13}$$

As can be concluded from Equation (13), the mass matrix is constant, as it is not a function of the nodal coordinates. This will save time on computation, especially when the explicit time integration method is used. However, this advantage may be marginal when implicit time integration is required. The virtual work for the externally applied forces can be written as

$$\delta W_{ext} = \int_V \boldsymbol{b}^T \delta \boldsymbol{r} \, \mathrm{d}V = \int_V \boldsymbol{b}^T \boldsymbol{S}_m \, \mathrm{d}V \, \delta \boldsymbol{e}, \tag{14}$$

where $\boldsymbol{b}$ is the vector of body forces. The vector of externally applied forces can be identified from Equation (14) as follows:

$$\boldsymbol{F}_{ext} = \int_V \boldsymbol{b}^T \boldsymbol{S}_m \, \mathrm{d}V. \tag{15}$$

The variation of the strain energy with respect to the nodal coordinates can be written as

$$\delta W_{int} = \int_V \boldsymbol{S} : \delta \boldsymbol{E} \, \mathrm{d}V = \int_V \boldsymbol{S} : \frac{\partial \boldsymbol{E}}{\partial \boldsymbol{e}} \, \mathrm{d}V \, \delta \boldsymbol{e}. \tag{16}$$

The vector of elastic forces can be identified from Equation (16) as follows:

$$\boldsymbol{F}_e = \int_V \boldsymbol{S} : \frac{\partial \boldsymbol{E}}{\partial \boldsymbol{e}} \, \mathrm{d}V. \tag{17}$$

Due to the fact that inertia description is simple and interpolations of rotational parameters are not needed, the formulation has potential to be effective in large deformation multibody applications. Examples where the absolute nodal coordinate formulation performs more effectively than the floating frame of reference formulation are described in [36]. Recently, the usability of elements based on the absolute nodal coordinate formulation in practical applications is considered in belt-drive and pantograph-catenary systems [37, 38]. Furthermore, in order to extend the usage of the absolute nodal coordinate formulation in fluid-structure interaction, a special pipe-element is introduced [39].

Conclusions

A review of computational methods for the dynamic analysis of large deformations in multibody applications was provided in this study. In the floating frame of reference formulation, large reference motions are described using a reference frame, while the deformations of the body are described relative to the reference frame. The use of a reference frame allows coupling of deformations and large reference motions in the inertia description of the body. The geometrically exact formulation can be applied to beam structures where large deformations, i.e. large displacements and large strains, need to be accounted for. In this approach, the element can be described within the concept of the total Lagrangian formulation. The absolute nodal coordinate formulation extends the multibody simulation approach to cases where large deformations and contacts need to be accounted for. In this formulation, the nodal coordinates of finite elements are defined using global positions and components of the deformation gradient of the nodes. Due to the linear relation between nodal coordinates and position coordinates, the element mass matrix is constant and can be defined in the same manner as in the linear finite element approach. Contradictory to the simple expression of the inertia forces, the expression of elastic forces of the elements is highly nonlinear and computationally demanding. However, due to the use of global coordinates, the Coriolis and centrifugal forces are not present simplifying the expression of the equations of motion. It is also important to note that the interpolation of nodal positions and the deformation

gradient components does not restrict the rigid body rotation. In fact, an arbitrary rigid body motion of an element is presented exactly in the absolute nodal coordinate formulation.

References

[1] W. Schiehlen. Multibody system dynamics: Roots and perspectives. *Multibody System Dynamics*, **1**, 149–188, (1997).

[2] A.A. Shabana. Flexible multibody dynamics: Review of past and recent developments. *Multibody System Dynamics*, **1**, 189–222, (1997).

[3] Rami Al Nazer. Flexible multibody simualtion approach in the dynamic analysis of bone strains during physical activity. *Acta Universitatis Lappeenrantaensis, doctoral thesis*, Lappeenranta, Finland, (2008).

[4] E.J. Haug. *Computer aided kinematics and dynamics of mechanical systems. Vol. 1: Basic methods*. Allyn and Bacon, Boston, (1989).

[5] P.E. Nikravesh. *Computer-aided analysis of mechanical systems*. Prentice-Hall, Englewood Cliffs (NJ), (1988).

[6] J. García de Jalón and E. Bayo. *Kinematic and dynamic simulation of multibody systems. The Real-Time Challenge*. Springer-Verlag, New-York (NJ), (1994).

[7] P. Eberhard and W. Schiehlen. Computational Dynamics of Multibody Systems: History, Formalisms, and Applications. *Journal of Computational and Nonlinear Dynamics*, **1**, 3–12, (2006).

[8] W. Pan and E.J. Haug. Dynamic simulation of general flexible multibody systems. *Mech. Struct. & Mach.*, **27**, 217–251, (1999).

[9] M.K. Matikainen. Development of beam and plate finite elements based on the absolute nodal coordinate formulation. *Acta Universitatis Lappeenrantaensis, doctoral thesis*, Lappeenranta, Finland, (in press).

[10] J.O. Song and E.J. Haug. Dynamic analysis of planar flexible mechanisms. *Computer Methods in Applied Mechanics and Engineering*, **24**, 359–381, (1980).

[11] W.C. Hurty. Dynamic analysis of structural systems using component modes. *AIAA Journal*, **3**, 678–685, (1965).

[12] R.R. Graig and M.C.C. Bampton. Coupling of substructures of dynamic analysis. *Int. J. Num. Meth. Eng.*, **6**, 1313–1319, (1968).

[13] A.A. Shabana and R.A. Wehage. Variable degree-of-freedom component mode analysis of inertia variant flexible mechanical systems. *ASME Journal of Mechanisms, Transmissions, and Automation in Design.*, **105**, 371–378, (1983).

[14] A.A. Shabana and R.A. Wehage. A Coordinate Reduction Technique for Dynamic Analysis of Spatial Substructures with Large Angular Rotations. *Mechanics Based Design of Structures and Machines*, **11**, 401–431, (1983).

[15] J.A.C. Ambrosio and P.E. Nikravesh. Elasto-plastic deformations in multibody dynamics. *Nonlinear Dynamics*, **3**, 85–104, (1992).

[16] J.C. Simo and L. Vu-Quoc. On the dynamics of flexible beams under large overall motions - the plane case: Part I. *Journal of Applied Mechanics*, **53**, 849–854, (1986).

[17] J.C. Simo and L. Vu-Quoc. On the dynamics of flexible beams under large overall motions - the plane case: Part II. *Journal of Applied Mechanics*, **53**, 855–863, (1986).

[18] A. Ibrahimbegović. On finite element implementation of geometrically nonlinear Reissner's beam theory: three-dimensional curved beam elements. *Computer Methods in Applied Mechanics and Engineering*, **122**, 11–26, (1995).

[19] J.C. Simo. A finite strain beam formulation. The three-dimensional dynamic problem: Part I. *Computer Methods in Applied Mechanics and Engineering*, **49**, 55–70, (1985).

[20] J. Mäkinen. Total lagrangian Reissner's geometrically exact beam element without singularities. *International Journal for Numerical Methods in Engineering*, **9**, 1009–1048, (2007).

[21] J. Mäkinen and H. Marjamäki. Total lagrangian parametrization of rotation manifold. *The Fifth EUROMECH Nonlinear Dynamics Conference, ENOC-2005*, Eindhoven, The Netherlands, (7 - 12 August 2005).

[22] M.A. Omar and A.A. Shabana. A two-dimensional shear deformable beam for large rotation and deformation problems. *Journal of Sound and Vibration*, **243**, 565–576, (2001).

[23] A.A. Shabana and Y.R. Yakoub. Three dimensional absolute nodal coordinate formulation for beam elements: theory. *Journal of Mechanical Design*, **123**, 606–613, (2001).

[24] A.M. Mikkola and A.A. Shabana. A non-incremental finite element procedure for the analysis of large deformations of plates and shells in mechanical system applications. *Multibody System Dynamics*, **9**, 283–309, (2003).

[25] O.N. Dmitrochenko and D.YU. Pogorelov. Generalization of plate finite elements for absolute nodal coordinate formulation. *Multibody System Dynamics*, **10**, 17–43, (2003).

[26] O. Dmitrochenko and A. Mikkola. Two simple triangular plate elements based on the absolute nodal coordinate formulation. *Journal of Computational and Nonlinear Dynamics*, **3**, 041012–1–8, (2008).

[27] J.T. Sopanen and A.M. Mikkola. Description of elastic forces in absolute nodal coordinate formulation. *Nonlinear Dynamics*, **34**, 53–74, (2003).

[28] K.E. Dufva and J.T. Sopanen and A.M. Mikkola. A two-dimensional shear deformable beam element based on the absolute nodal coordinate formulation. *Journal of Sound and Vibration*, **280**, 719–738, (2005).

[29] A.L. Schwab and J.P. Meijaard. Comparison of three-dimensional flexible beam elements for dynamic analysis: Finite element method and absolute nodal coordinate formulation. *Proceedings of the IDEC/CIE 2005, ASME 2005 International Design Engineering Technical Conferences, Paper Number DETC2005-85104*, Long Beach, USA, (24 - 28 September 2005).

[30] A.M. Mikkola and M.K. Matikainen. Development of elastic forces for a large deformation plate element based on the absolute nodal coordinate formulation. *Journal of Computational and Nonlinear Dynamics*, **1**, 103–108, (2006).

[31] J. Gerstmayr and M.K. Matikainen and A. Mikkola. A geometrically exact beam element based on the absolute nodal coordinate formulation. *Multibody System Dynamics*, **20**, 359–384, (2008).

[32] J. Gerstmayr. A corotational approach for 3D absolute nodal coordinate elements. *Proceedings of the IDETC/CIE 2009, ASME 2009 International Design Engineering Technical Conferences & Computers and Information in Engineering Conference, Paper Number DETC2009-97476*, San Diego, USA, (30 August - 2 September 2009).

[33] H. Sugiyama and J.L. Escalona and and A.A. Shabana. Formulation of three-dimensional joint constraints using the absolute nodal coordinates. *Nonlinear Dynamics*, **31**, 167–195, (2003).

[34] D. García-Vallejo and J. Valverde, and J. Domínguez. An internal damping model for the absolute nodal coordinate formulation. *Nonlinear Dynamics*, **42**, 347–369, (2005).

[35] H. Goldstein. *Classical mechanics*. Addison-Wesley, Reading (MA), Second edition, (1980).

[36] M. Dibold and J. Gerstmayr and H. Irschik. On the accuracy and computational costs of the absolute nodal coordinate and the floating frame of reference in deformable multibody systems. *Proceedings of the IDETC/CIE 2007, ASME 2007 International Design Engineering Technical Conferences & Computers and Information in Engineering Conference, Paper Number DETC2007-34756*, Las Vegas, USA, (4 - 7 September 2007).

[37] K. Kerkkänen and D. García–Vallejo and A. Mikkola. Modeling of belt-drives using a large Deformation finite element formulation. *Nonlinear Dynamics*, **4**, 239–256, (2006).

[38] J. Gerstmayr and A.A. Shabana. Analysis of thin beams and cables using the absolute nodal coordinate formulation. *Nonlinear Dynamics*, **45**, 109–130, (2006).

[39] M. Stangl and J. Gerstmayr and H. Irschik. A large deformation finite element for pipes conveying fluid based on the absolute nodal coordinate formulation. *Proceedings of the IDETC/CIE 2007, ASME 2007 International Design Engineering Technical Conferences & Computers and Information in Engineering Conference, Paper Number DETC2007-34771*, Las Vegas, USA, (4 - 7 September 2007).

Multi-Scale Structural-Acoustic Optimization of a Multi-Functional Vehicle Body Panel

Christopher J. Cameron[*]**, Per Wennhage and Peter Göransson**

Centre for ECO^2 Vehicle Design
Dept. of Aeronautical and Vehicle Engineering
Kungliga Tekniska Högskolan
SE-100 44, Stockholm, Sweden
e–mail: cjca@kth.se

Summary   A novel concept for a multi-layer, multi-functional vehicle body panel is presented and weight optimized to a set of structural and acoustic constraints. Design variables include both macroscopic and microscopic properties of the various layers. Advanced FE software is used which enables the effects of fluid-structure interaction of the open celled porous foam materials to be included in the optimization. Promising weight savings and acoustic improvements over conventional solutions are shown possible.

Introduction

The vast majority of modern automobile structures are constructed by spot welding together pressed metallic components. Body panels, such as the roof, hood, trunk lid, etc, often have large areas of unsupported sheet metal which are prone to vibration. Viscoelastic damping treatments are a common method of controlling such unwanted vibrations[1], and minimizing their impact on the acoustic environment in the vehicle. These treatments are effective, however successful implementation often relies heavily on experimentation and the experience of the engineer [2, 3].

An alternative approach to acoustic damping is the use of porous, light weight, open celled foams. By varying the properties of each layer in a multiple layer foams stack, favourable acoustic behaviour can be achieved at a relatively low weight penalty. More importantly, the treatments can be accurately tuned for a specific behavioural response using models based on numerical methods for poro-elastic media which have recently become available in commercial finite element software.[4]

Within this work, a multi-layered, multi-functional body panel concept has been proposed which includes the functionality of the following conventional components present in the roof of a passenger car: outer sheet metal, panel damping treatments, acoustic absorption treatments, structural reinforcement, and interior trim. The panel consists of composite face sheets, and multiple layers of structural and acoustic foam. This configuration has been suggested as a method of meeting the structural and quality needs present in an existing vehicle design.

The panel is mass optimized to a given set of structural and acoustic constraints. Macroscopic properties examined include layer thickness of various components,and their mechanical properties. The effects of changes to the microstructure of the acoustic foam are also included within the optimization. Results of the optimization are presented and discussed.

Method

The work described herein is an extension of previous work[5] and has been carried out in the following manner.

Firstly, a novel concept is proposed. The novel concept is mass optimized to a set of structural and acoustic constraints. Static deflection and normal vibration behaviour are used as structural

constraints and mechanical properties and thicknesses of the various layers are used as design variables. Acoustic sound pressure levels in a fluid cavity resembling the vehicle interior are the acoustic constraints, and the thickness and cellular construction of the acoustic layers are the design variables.

Calculations are performed using NXNastran FE software in combination with CDH/EXEL software for poro-elastic acoustic calculations. Optimization was performed using tools based on the method of moving asymptotes (MMA) [6]

Concept Proposal

A conceptual design was proposed based upon a five layer construction consisting of the following components:

- Exterior sheet – Glass fibre reinforced vinyl-ester composite laminate
- Structural foam layer – thermoplastic based expanded polymer foam (closed cell)
- Acoustic foam layer – A three component low stiffness open celled elastic foam treatment
- Air Gap– A 1mm thick air gap for increased acoustic performance
- Interior sheet – CSM Glass fibre reinforced sheet, perforated for acoustic functionality
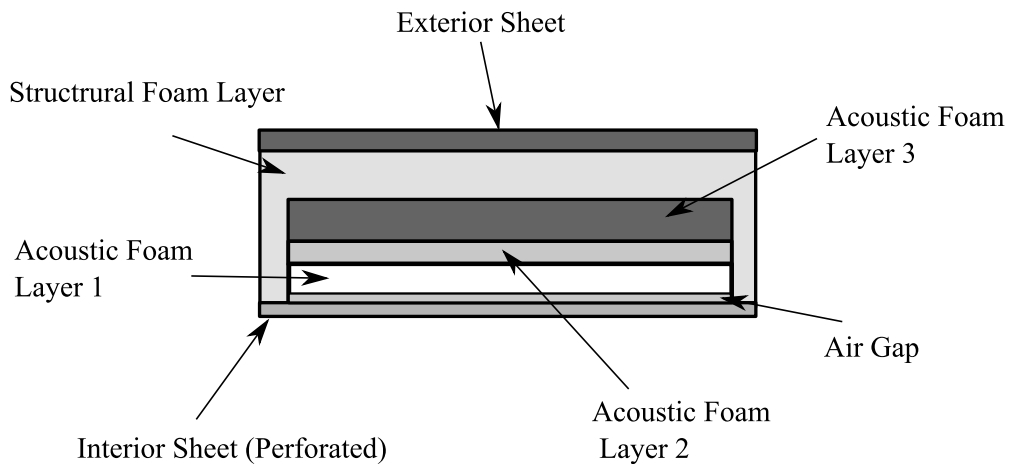
Figure 1: Cutaway view of panel concept

The exterior sheet of the panel is a glass fibre laminate. The acoustic foam treatment consists of three layers of open celled foam placed within a large pocket of structural foam in the centre of the panel. The interior sheet is a CSM glass fibre reinforced plastic perforated with circular holes in a rectangular pattern to allow fluid interaction between the passenger cavity and the acoustic foam in the sandwich panel. The air gap exists between the acoustic foam treatment and the interior sheet. An adhesive bond is assumed to exist between all layers of the structure, including between the interior sheet and the structural foam. Figure 1 shows a cutaway view of the proposed construction.

Model Description, Load Cases, and Boundary Conditions

The square panel was modelled using a one quarter model with symmetrical boundary conditions. NXNastran was used, and with the exception of the external sheet, wich was modelled using composite shell elements, all layers were modelled using 3D brick elements. Porous material properties

were described using Biot theory as implemented within CDH/EXEL[7, 8, 9, 10]. A fluid cavity was coupled to the interior side of the panel to represent the passenger compartment.

The first static analysis included a localized load of 150 N applied to the roof spread over a circular area of approximately 100 mm in diameter.

The second static load case involved a uniform distributed pressure across the entire outer surface of the panel equivalent to 1.25 times the vehicles weight.

The dynamic analysis was a normal modes analysis to calculate the frequency of the first mode of vibration of the panel.

Boundary conditions for all the structural analysis were as follows; along the sides of the panel, all edge nodes in all layers were constrained in x, y, z directions. Along the front and rear edge of the panel, the lowermost edge of the bottom face sheet was constrained in x, y, z.

For the acoustic analysis, the panel was excited using two phase-shifted dynamic forces at positions corresponding to where the a- and b-pillar (and due to symmetry also the c- and d-pillar) would introduce vibrations in the structure. As the acoustic panel only represents a part of the entire roof the layers were constrained in the x- and y-direction along the edges.

Results and Observations

Previous work on optimization of similar structures has yielded a panel of reduced mass in comparison to the conventional solution, while maintaining structural constraints, and exhibiting a large potential for acoustic improvements[5, 11]. The current method of optimization is expected to yield similar results, with improved acoustic performance via inclusion of design variables with a strong influence on acoustic behaviour.

Concluding Remarks

Simultaneous structural and acoustic optimization of complex, multifunctional vehicle structures represents the next generation of vehicle design.The results of this type of optimization yield a significant reduction in mass, in comparison to the conventional solution, and promising acoustic performance while maintaining structural integrity. The advanced finite element software used within this work is an enabler for high level multi-disciplinary design including structural and acoustic requirements. This type of design strategy offers new possibilities for vehicle manufactures, and may in fact be required in order for to reduce weight, maintain performance, and increase comfort of new vehicles while maintaining or reducing the amount of resources necessary for production in future generations of passenger carrying vehicles.

References

[1] M. D. Rao. Recent applications of viscoelastic damping for noise control in automobiles and commercial aeroplanes. *Journal of Sound and Vibration*, **262**, 457–474, (2003).

[2] S.M.Beane, M.M.Marchi, and D.S.Snyder. Utilizing optimized panel damping treatments to improve powertrain induced nvh and sound quality *Applied Acoustics*, **45(2)**, 181–187, (1995).

[3] J.Bienert. Optimisation of damping layers in car bodies *Proceedings of the 2002 International Conference on Noise and Vibration Engineering,ISMA*, 2005–2010, (2002).

[4] P. Göransson. Tailored acoustic and vibrational damping in porous solids – engineering performance in aerospace applications, *Aerospace Science and Technology*, **12**, 26–41, (2008).

[5] C. J. Cameron, E. Lind, P. Wennhage, and P. Göransson. Material property steered optimization of a multifunctional body panel to structural and acoustic constraints *Proceedings of ICCM-17, 17th International Conference on Composite Materials, Edinburgh, Scotland*, (2009)

[6] K. Svanberg. The method of moving asymptotes-a new method for structural optimization *International Journal for Numerical Methods in Engineering*, **24**, 359–373, (1987).

[7] M.A.Biot. Theory of propagation of elastic waves in a fluid saturated porous solid. i. low frequency range *J. Acoust. Soc. Am.*, **28**, 168–178, (1956).

[8] M.A.Biot. Theory of propagation of elastic waves in a fluid saturated porous solid. ii. higher frequency range *J. Acoust. Soc. Am.*, **28**, 179–191, (1956).

[9] M.A.Biot. Theory of deformation of a porous viscoelastic anisotropic solid *J. Appl. Phys*, **27**, 459–467, (1956).

[10] CDH AG. *Poroelastic material modelling and analysis with CDH\EXEL*, (2007).

[11] C. J. Cameron, E. Lind, P. Wennhage, and P. Göransson. Proposal of a methodology for multidisciplinary design of multifunctional vehicle structures including an acoustic sensitivity study *Int. J. Vehicle Structures & Systems*, **1(1-3)**, 1–13, (2009).

Implementation of molding constraints in topology optimization

S. Marx and A. Kristensen*

Esbjerg institute of Technology
Aalborg University, Aalborg, Denmark
e−mail: sm1076@student.aaue.dk, ask@civil.aau.dk

Key words: Topology optimization, injection molding, manufacturing constraints

Summary In many cases the topology optimization method yield inadmissible solutions in respect to a particular manufacturing process, e.g. injection molding. In the present work it is chosen to focus on the most common injection molding parameters/factors determining the quality of the mold geometry, i.e. uniform thickness, filling of the die and ejection of the molded item, i.e. extrusion. The mentioned injection mold parameters/factors are introduced in the topology optimization by defining a centerline of the initial domain and then penalize elements in respect to the distance to the defined centerline of the domain.

Introduction

One of the widely used processes for manufacturing is injection molding. In this paper an effort is made to implement constraints given by the process of injection molding into the process of topology optimization. Introduction of manufacturing constraints have been considered by Ishii et al [3] which proposes a modified frame based unit cell approach providing symmetrical cross sections. Also commercial topology optimization software include methods to impose manufacturing constraints as devised by Schramm et al. [4], [5] suggesting a coupled topology-size approach. In the present work the topology optimization method developed by Bendsøe et al. [1] is used as basis.

Algorithm to impose injection molding constraints in topology optimization

An algorithm implementing molding constraints in the process of topology optimization is described shortly in the following. The approach is to define the structures center lines on the background of topology optimization and using those lines to weaken the sections, which would make the injection molding of the solution difficult or impossible.

The use of lines

By defining the center lines of the structure the following constraints of the injection molding process can be easily implemented:

- Filling of the die: I there are a uninterrupted lines from the user defined placement of the injection nozzle to all parts of the structure, than the liquid material can fly in all parts of the structure in the molding process.
- Direction of draw: If the lines are limited in a way that respects the direction of draw, the possible ejection of the item is guaranteed.
- Uniform thickness and no intermediate densities: If all elements, which center point is closer to the line than half the thickness, are assigned with the density 1 and all others with the density 0 (or a very small value to avoid singularities), then the resulting item is of uniform thickness and does not contain intermediate densities.

The definition of lines

At each step of iteration the lines are defined subsequently starting at the user defined placement of the injection nozzle by adding the neighboring node, which both respects the angle of draw and is assigned with the highest density. The nodes are assigned with the average density of the elements, which center points are within the circle with the diameter of the thickness.

The node is not obtained in the line, if the assigned density is lower than a certain value, in the used cases 0.2.

If two neighboring nodes have the same assigned density, the circle's diameter is increased.

Adjusting the compliance sensitivity

The compliance sensitivity of an element is adjusted in respect to the distance between its center point and the line:

$$\frac{\partial obj\ \rho_e}{\partial \rho_e} = \begin{cases} \dfrac{\partial obj\ \rho_e}{\partial \rho_e} & \text{if } dist_e \leq \dfrac{t}{2} \\[2em] \dfrac{\partial obj\ \rho_e}{\partial \rho_e} \cdot \left(\dfrac{t}{2 \cdot dist_e} \right)^{\max\ 1;n_{\text{it-steady}} - 30} & \text{if } dist_e > \dfrac{t}{2} \end{cases} \tag{1}$$

In this equation the expression $\dfrac{\partial obj\ \rho_e}{\partial \rho_e}$ is the adjusted sensitivity for the element 'e',

$\dfrac{\partial obj\ \rho_e}{\partial \rho_e}$ is the unadjusted sensitivity for the element 'e', t is the user defined thickness, $dist_e$

is the distance form element 'e' to the line, $n_{it-steady}$ is the numbers of steps of iteration where the line was kept unchanged.

Definition of the volume fraction

The volume of the structure is defined by the sum of all elements' volume, which centre point is closer to the line than half of the thickness and a tenth or a thousandth of the other elements volume, if the line length is increasing or steady respectively.

$$v_{fr} = \frac{\sum\limits_{i=1}^{N_{el}} v_i \cdot \rho_{\langle 0/1 \rangle i}}{\sum\limits_{i=1}^{N_{el}} v_i} \text{, with the function } \rho_{\langle 0/1 \rangle i} = \begin{cases} \begin{cases} 0.1 & \text{if } n_{\text{steady}} \leq 30 \\ 0.001 & \text{if } n_{\text{steady}} > 30 \end{cases} & \text{if } dist_i > \dfrac{t}{2} \\[1.5em] 1 \text{ if } dist_i \leq \dfrac{t}{2} \end{cases} \tag{2}$$

Advantages of this algorithm

The solution from this algorithm is always an item, which easily can be manufactured by the process of injection molding, has uniform thickness and the ejection is possible. It is optimized by the process of topology optimization within the limits given by the manufacturing constraints.
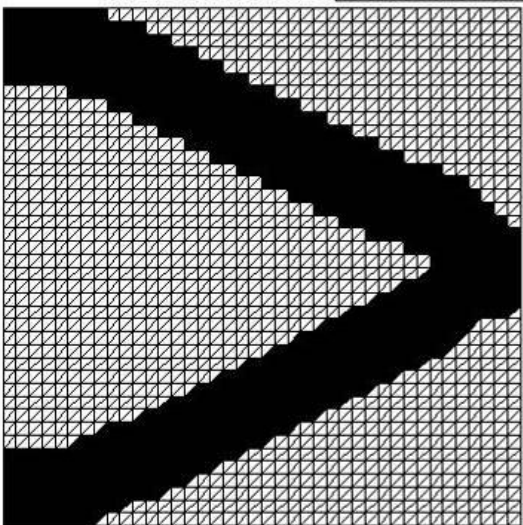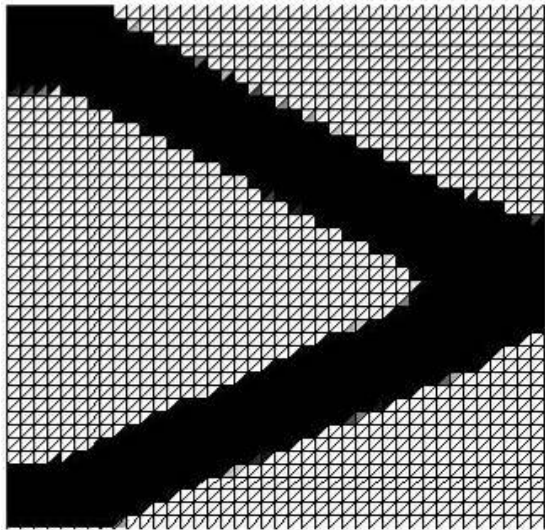
Because the combination of line and thickness defines, which elements are kept and which elements are left out of the solution, the method of SIMP is dispensable.

Disadvantages of this algorithm

The algorithm increases the calculation time, because the line has to be built up sequentially in every step of iteration and this includes assigned nodes with density. Afterwards the compliance sensitivity of all elements is adjusted in respect to the distance between the element's centre point and the line. The calculation time is not increase heavily compared to other filtering methods.

Verification of the algorithm

The algorithm is verified by a standard case, a quadratic cantilever beam with the force applied in the center of the free side. The algorithm's result is compared to the result found by the topology optimization process with Esbjerg filtering and the SIMP-penalty of 3.5.

New algorithm	Esbjerg filtering SIMP-penalty p=3.5
After 83 steps: Overall change of density < 1/10,000	After 122 steps: Overall change of density < 1/10,000
Compliance: 20.6321-20.6810	Compliance: 19.8397-20.1115

The solution of the Esbjerg algorithm has a compliance of ca. 20, while the new algorithm is a little weaker with compliance of 20.7. In the Esbjerg filtering the higher value of the compliance is the value shown after optimisation, still under the SIMP penalty. The lower value is cleaned for this influence. The little difference shows, that a few elements have intermediate densities.

The lower value in the new algorithm is the compliance of all the elements assigned with the density 1, while the higher value is the compliance for all elements.

In respect to the limitations to the new algorithm this seems reasonable. The difference in the compliance can be explained with the areas above and below the centre of the right edge. Here the Esbjerg filtering has material, which violates the limitation of uniform thickness. Therefore these areas are not a part of the solution of the new algorithm. At the upper right corner there is an area below the dark area, which is dark in the solution of the topology optimisation using the Esbjerg filtering. This area and the similar and the lower left corner violate the direction of draw and are therefore not a part of the new algorithm's solution.

Concluding remarks

The new algorithm might be a useful tool for developing and optimizing items, if it is integrated in commercial software. Instead of strengthening or weakening individual elements, the process works on sections.

References

[1] Bendsøe, M.P. and Sigmund, O., Topology Optimization, Theory, Methods and Applications, 2nd edition, Springer Verlag, 2002, p 1-68, 261-302

[2] Georgsen, L.S., Mortensen, L., Topology Optimization, Implementation of a Dynamic objective, Aalborg Universitet Esbjerg, 2007

[3] Ishii, K. and Aomura, S., Topology Optimization for the Extruded Three Dimensional Structure with Constant Cross Section, JSME International Journal, Series A, Vol. 47, No. 2, 2004

[4] Schramm, U., Thomas, H.L., Zhou, M. and Voth, B., Topology optimization with Altair OptiStruct, in Proceedings of the Optimization in Industry II Conference, Banff, CAN (1999).

[5] Altair OptiStruct, User's Manual v7.0, Altair Engineering Inc., Troy, MI (2003).

A General Type Nonlinear Buckling Optimization Procedure of Composite Structures

E. Lindgaard[*] and E. Lund

Department of Mechanical Engineering
Aalborg University, Aalborg, Denmark
e–mail: elo@me.aau.dk[*] & el@me.aau.dk

Summary   The paper presents an approach to general type nonlinear buckling fiber angle optimization of laminated composite shell structures. The approach accounts for the geometrically nonlinear behaviour of the structure by utilizing response analysis up until the buckling point, i.e. bifurcation or limit point. The proposed procedure handles bifurcation and limit point stability simultaneously and optimizes the buckling point first to arrive on the equilibrium path and thereby avoid problems related to mode or stability type switching during optimization. The optimization is formulated as a mathematical programming problem and solved using gradient-based techniques.

Introduction

Polymeric resin fibre reinforced materials (FRPs or composite materials) are being used increasingly for structural applications where properties such as high strength, high stiffness and low weight are determining design parameters. The driving force behind the development and application of these materials has been the demands posed by the aerospace industry, but the use of advanced composite materials is expanding rapidly to other industrial sectors including marine/offshore, wind turbines (blades), automotive, train and civil engineering applications. Designing structures made out of composite material represents a challenging task, since both thicknesses, number of plies in the laminate and their relative orientation must be selected. The best use of the capabilities of the material can only be gained through a careful selection of the layup. This work focuses on optimal design of laminated composite shell structures i.e. the optimal fiber orientations within the laminate which is a complicated problem. One of the most significant advances of optimal design of laminate composites is the ability of tailoring the material to meet particular structural requirements with little waste of material capability. Perfect tailoring of a composite material yields only the stiffness and strength required in each direction.

Stability is one of the most important objectives/constraints in structural optimization and this also holds for many laminated composite structures, e.g. a wind turbine blade. In stability analysis the buckling behaviour is often considered by linearized eigenvalue analysis at an initial pre-buckling point (linear buckling analysis) without any consideration to the type of buckling and the buckling load is generally overestimated. [1] studied buckling optimization of structures with geometrical nonlinear behaviour and found that formulations based on linear buckling analysis may lead to unreliable design results. Certain types of nonlinear buckling optimization of laminated composites have been investigated, see [2] and [1], but there are absence in optimization procedures that handles a general type of stability.

This paper focuses on the development of an integrated nonlinear buckling optimization procedure that handles a general type of buckling of composite structures. Different buckling behaviour is defined and characterized by a simple numerical example of a point loaded cylindrical shell, first introduced by [3] and later used extensively in the literature to investigate advances in finite elements for handling load and/or deflection reversals in nonlinear buckling problems. The numerical example will be used as the foundation for discussing and defining the challenges that

may be encountered while optimizing geometrically nonlinear structures with respect to a general type of stability. The proposed procedure and optimization formulation that handles a general type of nonlinear buckling includes the nonlinear response by a path tracing analysis, here by the arc-length method after [4], using the Total Lagrangian formulation. The nonlinear path tracing analysis is stopped when a buckling point is encountered and the buckling load is approximated at a precritical load by an eigenvalue analysis on the deformed configuration. Design sensitivities of the critical load factor are obtained semi-analytically by the direct differentiation approach on the approximate eigenvalue problem described by discretized finite element matrix equations. The proposed optimization procedure that handles a general type of nonlinear buckling will be presented at NSCM22 together with numerical results obtained by applying the proposed procedure to optimize fiber orientations in composite laminated structures.

Buckling Behaviour of the Point Loaded Cylindrical Shell

The cylindrical shell example, see figure 1, introduced by [3] is used to illustrate the complicated behaviour that may be encountered in shell buckling. The isotropic thin circular cylindrical shell panel, modelled by 200 equivalent single layer solid shell finite elements, is transversely loaded undergoing large deformations including buckling and post-buckling. The panel is supported by its two straight axial edges having a pinned fixture that cannot move, i.e. the mid-surface of the axial edges are restrained in displacements and rotations in u, v, w, Rx, Ry but free to rotate about the z-axis.

$r = 2540mm$	$E = 3.10275GPa$
$l = 508mm$	$G = 1.19337GPa$
$t = 6.35mm$	$\nu = 0.3$
$\alpha = 0.1rad$	$S = 508mm$
$R = 2400N$	
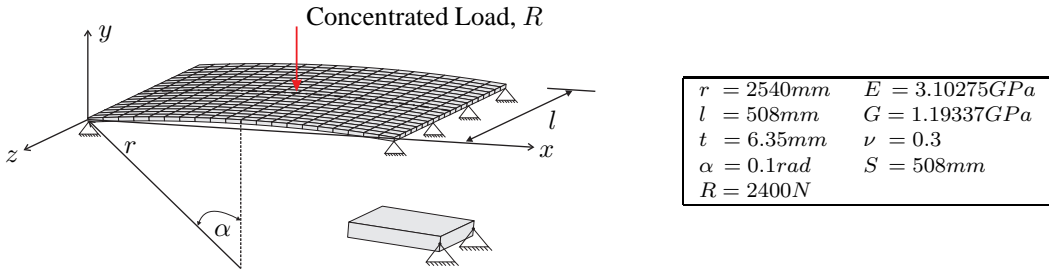
Figure 1: Geometry, loads, boundary conditions, and material properties for the cylindrical shell example. The hinged support is related to the mid surface of the shell, which is realized by multi point constraints (MPC) between the top and bottom edge nodes. The segment is loaded by two point loads in the negative y-direction, at the top and bottom node in the centre of the segment. All dimensions refer to the mid surface, where the thickness is denoted by t and the length of the curved edges is denoted by S.

Two solutions exist for the model, a symmetric and an asymmetric, see figure 2. The symmetric solution, introduced by [3] and later reported by many authors, may be obtained by geometric nonlinear analysis upon the original perfect system. The stability limit is characterized by a load limit point. A path tracing algorithm as the arc-length method after [4] is needed for this solution as both load and deflection reversals occur. Snap-through would occur at the load limit point in load control, and snap-down/snap-back at the deflection limit point in deflection control. Spanwise mode shapes along the shell centerline are symmetric about the centerline and loading point for the symmetric solution.
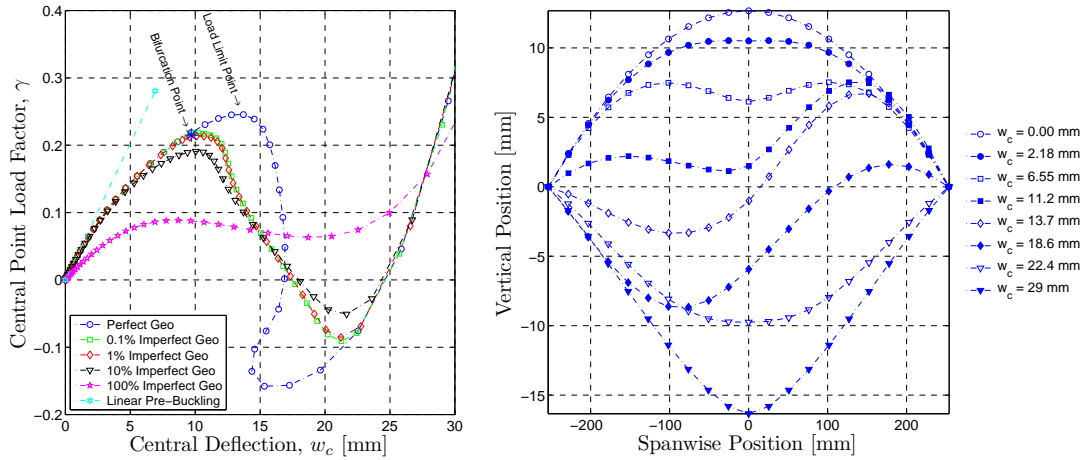
Figure 2: Left: Load-deflection response solutions of the perfect and imperfect systems together with the linear pre-buckling solution. Right: Central spanwise mode shapes at different values of center deflection, w_c, obtained by FEA on the imperfect system with imperfection amplitude of 0.1%.

Lately, [5] discovered that the symmetric solution of the shell benchmark problem was incorrect and concluded by numerical analyses and related experiments that there exists an asymmetric solution to the problem. The symmetric solution of the problem makes the assumption that limit point buckling will occur and does not consider bifurcation and an associated asymmetric buckling mode. At a bifurcation point the system have multiple solutions and a secondary equilibrium path may exist which at the point of bifurcation branches away from the fundamental path (the equilibrium path for the perfect system). Bifurcation points are commonly predicted by either linear pre-buckling analysis or geometrically nonlinear analysis of a slightly distorted imperfect system which may be accomplished by introducing a geometric imperfection in the form of the first linear buckling mode with some prescribed amplitude. Such a bifurcation point exists for this model and occurs approximately 12% below the load limit point for the symmetric solution, thus this is the preferred lower energy path. The linear pre-buckling analysis yields a very poor prediction of the bifurcation point which is caused by the inherent assumption that the structure is assumed to behave linearly up until the buckling point. Several imperfect systems have been analyzed with different amplitudes where the imperfection amplitude is defined as the largest translational component of the first linear buckling mode with respect to the shell thickness. The use of imperfections as a method to discover bifurcation points and associated branches may not always be trustworthy. It can be observed by the equilibrium paths of the imperfect systems in figure 2 that the imperfection amplitude has to be lower than approximately 1% in order not to change the problem and thereby the solution of the original problem which demonstrates the difficulty in discovering bifurcation point, i.e. the imperfection amplitude has to be large enough to induce bifurcation but also small enough so as not to change the problem. The same difficulties apply in the selection of the imperfection mode.

The two reliable imperfect equilibrium paths show a limit point in the region of the bifurcation point which indicates that the bifurcation point is unstable, i.e. the bifurcation path is unstable in load control thus the tangent stiffness is negative directly after bifurcation. The bifurcation response does not exhibit a deflection limit point but rejoins the equilibrium path with the symmetric response at large values of center deflection. In this region the response is dominated by membrane streching with symmetric modes, see figure 2 right.

Challenges in General Nonlinear Buckling Optimization

The starting point for a reliable nonlinear buckling optimization procedure is the ability to evaluate the point of stability with reasonable precision. As exemplified by the proceeding numerical example, linear pre-buckling analysis is not valid for determining buckling of general type and in cases where geometric nonlinearity cannot be ignored, thus geometrically nonlinear analysis is required. Furthermore, the analysis procedure should be able to handle and discover bifurcation as limit point instability, depending on what type of stability is first to arrive on the equilibrium path. It is desirable only to analyse the perfect structure and not apply imperfections as a method for predicting bifurcation points due to the problems in selecting a reasonable imperfection mode and amplitude. During optimization the stability type may even change and the chosen imperfection for the system may no longer be valid for inducing the structure to bifurcate. Finally, in case of a stable bifurcation point the buckling point may simply disappear with the introduction of imperfections and thereby not be identified during the analysis.

During optimization, mode or stability type switching may occur, i.e. the first buckling point to arrive on the equilibrium path may change from a bifurcation point to a limit point or vice versa, and should be considered in the optimization formulation.

For effective treatment of the optimization problem it should be formulated as a mathematical programming problem that is solved by gradient based optimizers, thus design sensitivities must be derived and calculated in an efficient way. This will be outlined in the presentation at NSCM22.

Concluding remarks

There is a need for development of an integrated approach that reliably optimizes structures with respect to a general type stability, i.e. simultaneously handles bifurcation and limit point stability, and especially in cases where geometrically nonlinear effects cannot be ignored. This study addresses these issues and presents a unified optimization procedure that solves these problems. This allows the material utilization of buckling critical laminated structures to be pushed to the limit in an efficient way in order to obtain lighter and stronger structures.

References

[1] E. Lindgaard and E. Lund. Nonlinear buckling optimization of composite structures. *Submitted*, (2009).

[2] J.S. Moita, J.I. Barbosa, C.M.M. Soares, and C.A.M. Soares. Sensitivity analysis and optimal design of geometrically non-linear laminated plates and shells. *Computers and Structures*, **76**, 407–420, (2000).

[3] A.B. Sabir and A.C. Lock. The application of finite elements to the large deflection geometrically non-linear behaviour of cylindrical shells *Variational Methods in Engineering* (Proceedings of an International Conference held at the University of Southampton, Sep. 25, 1972), edited by C.A. Brebbia and H. Tottenham, Southampton University Press, **2**, 7/66–7/75, (1973).

[4] M.A. Crisfield. A fast incremental/iterative solution procedure that handles "snap-through". *Computers and Structures*, **13**, 55–62, (1981).

[5] B.L. Wardle. The incorrect benchmark shell buckling solution. *Collection of Technical Papers - AIAA/ASME/ASCE/AHS/ASC Structures, Structural Dynamics and Materials Conference 8*, AIAA journal, 5263–5273, (2006).

Stress Constraints for Discrete Material Optimization

Christian G. Hvejsel[*] and Erik Lund

Department of Mechanical Engineering
Aalborg University, Aalborg, Denmark
e–mail: cgh@me.aau.dk and el@me.aau.dk

Summary Stiffness maximization is a well–described problem in structural design optimization. In this paper we consider stress-constrained multi–material design of composite structures. Constraining stresses requires interpolation schemes that have an unambiguous representation of stress in the mixed–phase computational material. We propose an averaged interpolation scheme for the effective failure function for mixtures.

Introduction

Optimal design of laminated composite structures is a challenging field for a number of reasons. The complexities associated with *modeling and analysis* of laminated composites makes *design* an even more complicated task. However, not only modeling poses difficulties, but also non-convexity of the resulting optimization problem is a challenge if ply orientations are used as design variables in e.g. compliance minimization. Alternatively, the lay-up design problem may be formulated as a *material selection problem* using a different parameterization, and in this paper the so-called Discrete Material Optimization (DMO) approach is applied. This approach is based on ideas from multi-phase topology optimization where the discrete material selection problem is relaxed to a continuous problem by expressing intermediate material properties as weighted sums of user-defined candidate material properties allowing for the use of gradient based mathematical programming techniques. Computationally, the optimization models coming from such formulations are very large scale in terms of number of design variables and criteria functions combined with large shell finite element models. The methodology has been applied successfully to problems involving global criteria functions such as compliance, see e.g. [5], but may as well be extended to problems involving local criteria functions such as constraints on the allowable stresses and strains. This includes criteria on the local strength leading to designs that perform well not only from a stiffness point of view but also have sufficient strength in terms of satisfaction of some failure criterion of the chosen materials. In this paper we investigate different multi-material interpolation schemes. The stiffness and strength of mixtures is deduced from physical interpretations of the mixing rules. The aim is to obtain consistent failure criteria for the mixture rules on basis of the failure behavior of the individual constituent phases. First, a mechanical interpretation of two interpolation schemes is given, followed by the formulation of consistent first-constituent failure criteria. In a relaxed material selection problem, the concern is not the microstructural realization of intermediate densities as in e.g. [1], but rather the physical behavior that a given mixture rule represents and that it eventually leads to a distinct material selection in order to enable a manufacturable physical interpretation of the final result. Also, interpolations should be reasonably simple and computationally efficient since the resulting optimization problems are very large scale. Various schemes fulfilling these are formulated and studied. One class of interpolations are special SIMP-like weighting functions which have been used with DMO to solve compliance minimization problems, [5]. These weighting functions use penalization of intermediate densities to avoid mixtures. However, the penalization is not always enough to drive the design to full convergence (0/1 solutions) due to a necessary scaling that flattens the design space and consequently the optimizer gets stuck for certain problems. Convergence to a distinct material choice turns out to be

of utmost importance since a final rounding to 0/1-designs has been shown to severely affect the result when local failure criteria are included, contrary to the situation with only global criteria functions where rounding typically is reasonable. In this work the hybrid Voigt-Reuss scheme proposed by [6, 7] provides a physically based mixing rule that leads to solutions closely fulfilling the 0/1-constraint of the originally discrete problem. This scheme has been adopted for DMO and turns out to be well suited for a number of reasons. The scheme has some desirable properties in terms of an unambiguous representation of the stress and strain state within each phase of the mixed material which allows for a consistent evaluation of the failure index of each phase. To assess failure of the mixed–phase material we propose an averaged failure criterion.

Problem Formulation

Given a number of predefined materials, n^e, with known constitutive properties and material strengths the goal is to minimize some objective function subject to constraints. In general, failure measures may be included in the objective function but may as well appear as constraints.

A material selection variable $x_{ij} \in \{0, 1\}$ is introduced to represent the selection of a given material for each candidate material, i, in every design domain, j.

$$x_{ij} = \begin{cases} 1 & \text{if material } i \text{ is chosen in design domain } j \\ 0 & \text{if not} \end{cases} \tag{1}$$

A (design) subdomain may for instance be a single layer in an element, a layer covering multiple elements, multiple layers within a single element etc.

In each subdomain we require only one material to be chosen. This is modeled by the following equality constraint.

$$\sum_{i=1}^{n^e} x_{ij} = 1 \quad \forall j \tag{2}$$

Material selection is parametrized by the decision variables introduced in (1). These variables are originally binary (0 or 1) but by allowing intermediate values between 0 and 1 the selection problem can be treated as a continuous sizing problem. If the solution to the continuous relaxation is binary, a useful solution has been found to the original problem. However, during optimization the variables take intermediate values and consequently interpolation of the material properties is needed to handle this. These interpolation schemes should preferably favor discrete selections over mixtures such that the continuous result converges to a discrete solution.

Material interpolation

In this work we use the so-called hybrid Voigt–Reuss material interpolation scheme [6, 7]. This scheme bases the stiffness interpolation on an unambiguous representation of the stress and strain state within the individual constituents of the mixed–phase material. The scheme forms the effective stiffness as a linear combination of pure Voigt and Reuss behavior respectively. The hybridization parameter α controls the amount of Voigt behavior and the remaining $1 - \alpha$ is Reuss behavior. The stiffness obtained with the Voigt scheme assumes that all phases in the mixture are exposed to the same state of strain contrary to the Reuss scheme that represents the stiffness of a mixed material where all phases are exposed to the same state of stress. Consequently the stiffness obtained with the hybrid Voigt–Reuss scheme is associated with an unambiguous state of stress and strain in each phase of the mixture.

Failure definition

As a measure of failure we use the so-called inverse load scaling factor or inverse reserve factor, k. If the reserve factor R is defined as the proportional scaling of the load until failure, the inverse load scaling factor is $k = \frac{1}{R}$. This formulation is completely general and failure may be predicted by any known failure criterion such as Tsai–Wu, Von Mises, etc. [2, 3, 4] recommend the use of this form of the failure criterion for optimization since direct minimization of e.g. the Tsai-Wu failure index might lead to non-optimal designs. It has the property that it takes on the value zero for the unloaded state ($R = \infty$) and unity for a failure load ($R = 1$). More importantly a value of $k = \frac{1}{2}$ means that the applied load may be doubled before failure. This number is regarded as a more meaningful measure of failure compared to the value of the failure index function. For instance the value of the Tsai–Wu failure criterion may take on *negative values* for certain combinations of load and material strength parameters. Clearly, this is undesirable since no physical meaning is associated with a negative failure index.

Mixed–phase failure averaging

To asses the amount of failure of a mixed–phase material we propose to use the weighted average of the inverse reserve factors.

$$\langle k \rangle = \alpha \sum_{i=1}^{n^e} x_i k_i^V + (1 - \alpha) \sum_{i=1}^{n^e} x_i k_i^R \tag{3}$$

where $k_i^V = k_i(\sigma_i^V, S_i)$ is the inverse reserve factor of the i'th phase in the Voigt part and $k_i^R = k_i(\sigma_i^R, S_i)$ is the inverse reserve factor of the i'th phase in the Reuss part.

Illustrative Example

To illustrate the concepts outlined above we study a simple example where the problem is to select the best orientation among two available material orientations for different loading situations.
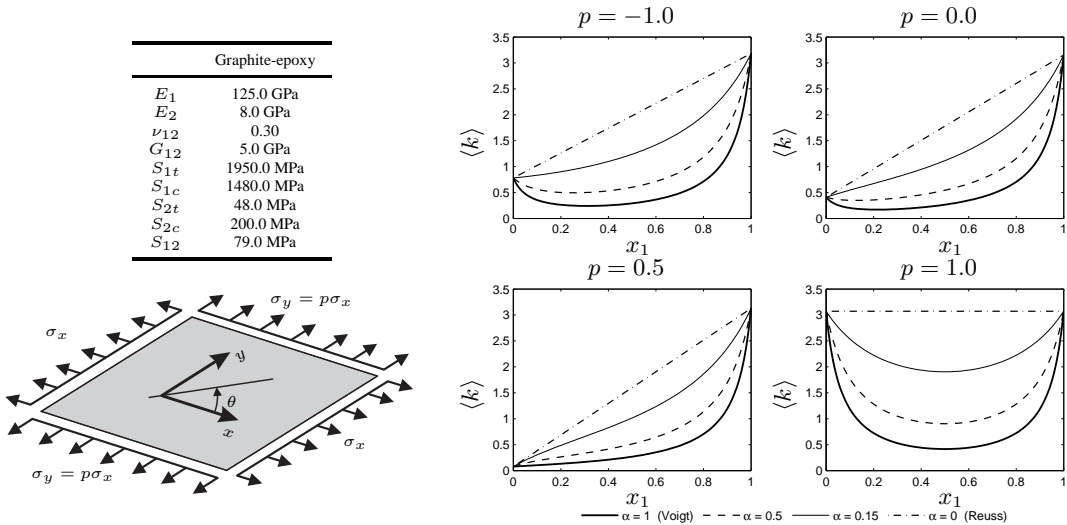
Figure 1: Left: Material properties and bi-axial stress states with coordinate system. Right: Averaged inverse reserve factor (wrt. Tsai-Wu failure prediction) with hybrid Voigt–Reuss scheme for different bi-axial stress states.

The approach outlined above is used to select the best of two orthotropic materials with identical properties, oriented at $\theta = \theta_1 = 90°$ and $\theta = \theta_2 = 0°$, respectively. This selection problem can be parametrized by x_1 using the material selection constraint from Equation (2) to eliminate x_2. The bi-axial state of stress is illustrated in Figure 1 along with the corresponding interpolated inverse reserve factor. The example illustrates a number of features of the proposed averaging scheme. First we note that the scheme is interpolatory, i.e. it recovers the known failure index of distinct material choices ($x_1 = 0$ and $x_1 = 1$) for all values of the hybridization parameter α. The scheme provides a continuous and differentiable failure function that is consistent with the stiffness parametrization from which the load sharing between the phases is given. The scheme handles differences in tensile and compressive strength through use of an appropriate failure criterion in the averaged measure, which is seen from the top left plot in Figure 1.

Concluding remarks

This work presents a general framework for handling of stress- and strain-based failure criteria within continuous multi–material optimal design problems. The paper proposes to use a weighted average of the failure measure in each constituent phase. The failure measure is based on a hybrid Voigt–Reuss scheme with a stress/strain state which is consistent with the interpolation used for the stiffness. This is not a limitation of the principle of using the weighted average of failure measures based on consistent-stress failure evaluation.

References

[1] M.P. Bendsøe and O. Sigmund. Material interpolation schemes in topology optimization. *Appl. Mech. Rev.*, 69:635–654, 1999.

[2] A.A. Groenwold and R.T. Haftka. Optimization with non-homogeneous failure criteria like Tsai–Wu for composite laminates. *Struct. Multidiscip. O.*, 32:183–190, 2006.

[3] CW Kim, SR Song, W. Hwang, HC Park, and KS Han. On the failure indices of quadratic failure criteria for optimal stacking sequence design of laminated plate. *Appl. Comp. Mat.*, 1(1):81–85, 1994.

[4] K.S. Liu and S.W. Tsai. A progressive quadratic failure criterion for a laminate. *Compos. Sci. Technol.*, 58(7):1023–1032, 1998.

[5] J. Stegmann and E. Lund. Discrete material optimization of general composite shell structures. *Int. J. Num. Meth. Eng.*, 62:2009–2027, 2005.

[6] C.C. Swan and J.S. Arora. Topology design of material layout in structured composites of high stiffness and strength. *Struct. Multidiscip. O.*, 13:45–59, 1997.

[7] C.C. Swan and I. Kosaka. Voigt–Reuss topology optimization for structures with linear elastic material behaviours. *Int. J. Num. Meth. Eng.*, 40(16):3033–3057, 1997.

Meso-level material modelling of compacted graphite iron and machining process simulation

Goran Ljustina* and Ragnar Larsson

Department of Aplied Mechanics
Chamers University, Göteborg, Sweden
e−mail: goran.ljustina@chalmers.se

Summary   The development of a meso-level model of Compacted Graphite Iron (CGI) based on micrographs has been developed. The modelling at the meso-level combines pearlitic grains with graphite nodules to produce compacted graphite iron structures. The behaviours of pearlite and graphite are described individually using the Johnson-Cook elasto-viscoplastic model describing continuous as well as discontinuous (fracture) deformation. Models are then used for finite element method simulation of orthogonal machining process.

Introduction

The development of models to predict physical behaviour during metal cutting has been a major preoccupation within the machining research community over the past 60 years. However, when new product materials like CGI with their sometimes heterogeneous microstructure are introduced, the simulation tools need to be modified in terms of the new mechanical properties that characterize the material. Usually, the finite element models are developed for simulations of homogeneous materials. Such models are not able to accurately describe local behaviour of highly heterogeneous materials like cast irons. This paper proposes a modelling procedure that simulates the material behaviour of heterogeneous materials on a microstructure-level scale. The meso-level models identify the role and behaviour of individual constituents which is not possible with macroscopic machining models. The use of this model is demonstrated on CGI. More specifically, the approach taken in the project, in order to account for the specific material structure of CGI (fig 1), is based on the explicit modelling of the suitably chosen meso-scale of the heterogeneous material. Of particular concern in the present context is the mechanical modelling of CGI with respect to relevant mechanisms within machining operations. The paper is concluded by a numerical simulation of the fracture process during orthogonal cutting. We also intend to consider the sensitivity of the cutting force with respect to the nodularity degree.

Simulation of microstructure

Compacted Graphite Iron contains primarily a mixture of pearlite, ferrite and graphite. The graphite phase in two dimensions appears as "worm-shaped" or vermicular particles. The particles are randomly oriented as in gray iron, however they are shorter and thicker, and have rounded edges. In three dimensions the individual worms are connected to their nearest neighbours and form the complex coral-like morphology which gives rise to thermal and mechanical properties between those of gray and ductile iron.
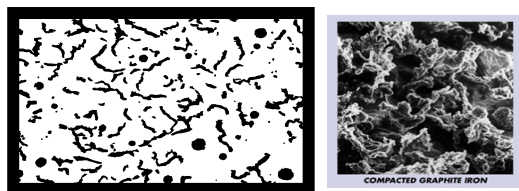
Figure 1: Microstructure of CGI in 2-D and 3-D

In order to analyse the heterogeneous microstructure of CGI the mesh based on micrograph was created through the software. OOF2 allows for the generation of a two-dimensional mesh with plane strain triangular elements representing the different phases observed in digitalized micrographs, cf. [1]. This mesh represents two separated groups of elements, each one associated with each of the two most important phases, graphite and pearlite. The CGI microstructures used in the industrial applications contain only small amounts of ferrite. The mesh is more refined in regions along the graphite/pearlite interfaces in order to increase the accuracy of calculations in those regions due to significant influence of graphite form on cast iron machinability (fig 2).
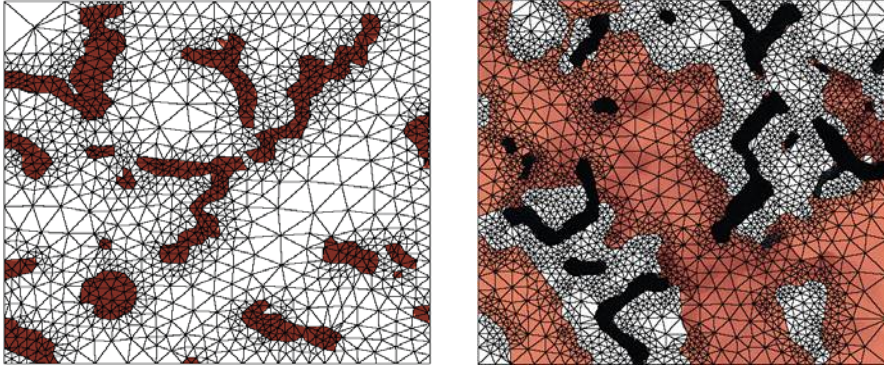
Figure 2: Example of meshes based on CGI micrographs

Material model

During machining the work-peace material is subjected to considerable levels of strain, strain rate, temperature and pressure. The constitutive model suitable for machining simulations should be able to describe stress-strain response together with its dependence on factors influencing flow stress, cf. [2] The Johnson-Cook (JC) constitutive model is used in this work due to good accessibility of material constants in literature, relatively low number of material constants, the fact that the JC model is often already implemented in commercial software and the JC damage model is used in analysis. JC model is suitable for high-strain-rate deformation of many materials, including most metals and is typically used in adiabatic transient dynamic simulations. The JC model assumes that the equivalent flow stress σ_{eq} is a function of the accumulated plastic strain ε_{eq}, plastic strain rate $\dot{\varepsilon}_{eq}$ and temperature T written as:

$$\sigma_{eq} = \left[A + B(\varepsilon_{eq}^{pl})^n \right] * \left[1 + C\ln\left(\frac{\dot{\varepsilon}_{eq}^{pl}}{\dot{\varepsilon}_0} \right) \right] * \left[1 - \hat{\theta}^m \right] \tag{1}$$

Each bracket in (1) describes flow stress dependence on different behaviour. The first one defines dependence on strain with respect to isotropic hardening. Second and third expresses the effects of strain rate and temperature, respectively. No data on JC related constants for

pearlite and graphite are available. Only "static" material properties can be found in ref. [3]. Therefore, the material constants are borrowed from materials with similar carbon content and mechanical properties. The JC model itself cannot predict the adiabatic phenomenon. To model an adiabatic process, a governing equation of converting deformation work to thermal energy has been used.

Fracture model

In this work the Johnson-Cook ductile fracture model is used. The JC model has been often used in simulations of metal cutting to obtain insight of chip formation. According to Johnson and Cook [4] the fracture strain for a constant stress state can be expressed by three uncoupled factors. For this model five parameters need to be calibrated. The material fracture is simply described by the element removal technique, where a fracture state is obtained as soon as the damage measure has reached a critical value. The damage measure is defined as:

$$D = \sum \frac{\Delta \bar{\varepsilon}^{pl}}{\bar{\varepsilon}_f^{pl}} \qquad (2)$$

Simulation

The material model described above was used to simulate orthogonal machining of compacted graphite iron. The geometry is shown in fig. 3. The tool has 0 deg rake angle, 3.5 deg clearance angle, and 50 micrometer edge radius. The tool moves with a constant speed of 160m/min. The model outputs include forces, displacements, strains, stresses, and temperatures.
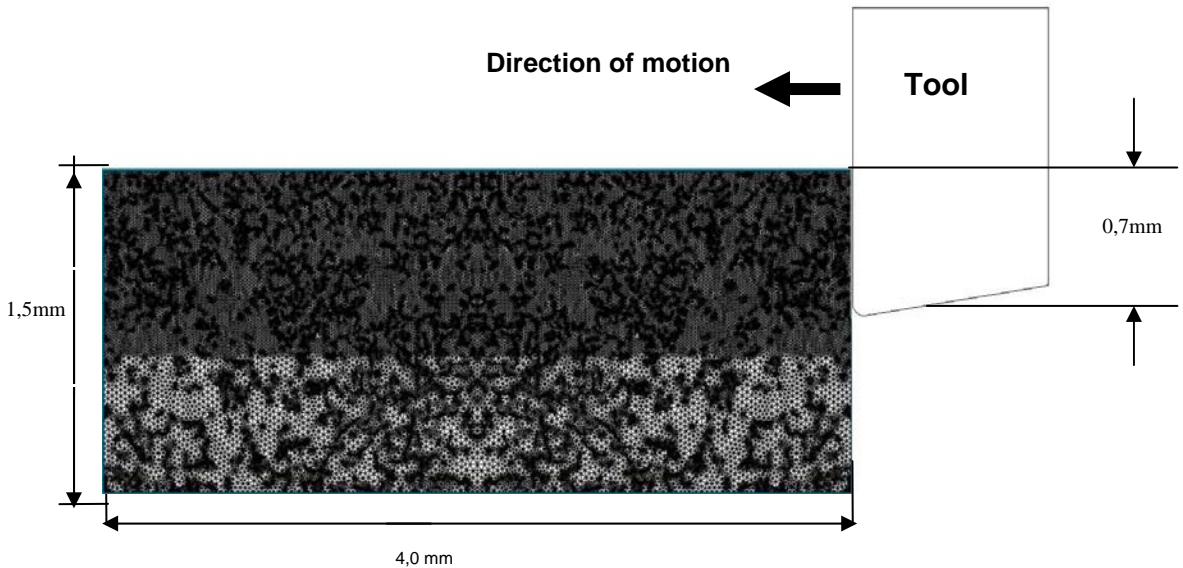
Figure 3: Problem geometry

Results and concluding remarks

The present model allows for determining the behaviour of different kinds of cast iron materials once the proper material models for pearlite, ferrite and graphite are provided. The development of simulation model is ongoing and only preliminary results are available at this point. Due to complexity of material behaviour during machining many issues remains to be considered. The orthogonal cutting process on CGI material has earlier been studied by Quick Stop Tests and external longitudinal turning operations in related project [5]. A comparison regarding chip formation is made and described simulation shows good agreement with experimental results.

Figure 4: Results from Quick stop experiments
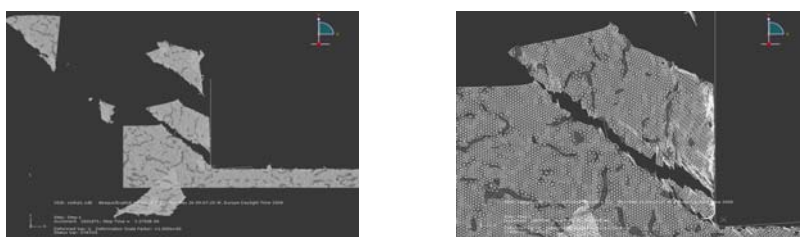
Figure 5: Simulation results

In the future the model will be used for cutting simulations of pieces with different nodularities. Nodularity is important parameter in CGI material. Variations in nodularity results in variations of mechanical properties and leads to decreased machinability of material. Comparison of different levels of nodularity in CGI material behaviour during machining with focus on chip morphology, cutting forces and temperatures is of great interest for industry.

References

[1] Langer, S.A., Fuller Jr., E.R. Carter, W.G., 2001, "OOF: An image-based finite-element analysis of material microstructures", Comput. Sci. Eng. 3 15-23

[2] Soo, S. L., Aspinwall, D. K., 2007, "Developments in modelling of metal cutting processes" Proc. IMechE Vol. 221 Part L: J. Materials: Design and Applications pp. 197-211

[3] Chuzhoy, L., DeVor, R. E., Kapoor, S. G. and Bammann, D. J., 2002, "Microstructure-Level Modeling of Ductile Iron Machining" ASME J. Manuf. Sci. Eng., 124, pp. 162-169.

[4] Johnson, G. R., Cook, W.H., 1985, "Fracture characteristics of three metals subjected to various strains, dtrain rates, temperatures and pressures" Ing. Fracture Mech. Vol. 21, No. 1, pp. 31-48.

[5] Grenmyr, G., 2008, "Investigation on the influence of nodularity in machining of CGI" Lic. thesis no 41/2008, Dep. of Materials and Man. Tech., Chalmers University of Technology, Göteborg, Sweden

On the modeling of deformation induced anisotropy of pearlitic steel

N. Larijani, E. Lindfeldt, M. Ekh, G. Johansson

Department of Applied Mechanics
Chalmers University of Technology, Gothenburg, Sweden
e–mail: nasim.larijani@chalmers.se

Summary   In this contribution, different types of homogenization methods of a micromechanically based plasticity model for pearlitic steel are investigated. The model was proposed in [**?**] and takes into account large strains as well as deformation induced anisotropy. The initially randomly oriented cementite lamellas in the pearlitic steel will tend to align with the deformation which causes a development of anisotropy.

Introduction

Pearlite is a two-phase material where each grain has a preferred direction that is determined by the cementite lamellas. The hard and brittle cementite lamellas are embedded in a softer ferrite matrix. Each grain can be considered to be transversally isotropic. The initial random orientation of the cementite lamellas gives an isotropic pearlitic material. After shear deformation, the orientations of individual grains tend to align with each other which causes a development of anisotropy.

In this contribution, the modelled anisotropy on the macroscopic length scale is obtained from homogenization procedures of a micromechanical model of "crystal plasticity"-type, proposed in [**?**], of the pearlitic microstructure. In this model the plasticity is assumed to be driven by shear stress of the ferrite between the cementite lamellas, and the re-orientation of the cementite lamellas is assumed to be of areal-affine type, cf. [**?**] The two different homogenization procedures investigated in this paper are: the Taylor assumption where all grains in the microstructure are assumed to be subjected to the same deformation gradient, and a procedure where the yield function of the grains have been replaced by a macroscopic yield function motivated from the micromechanical yield function.

Finally, results showing the development of the yield surface, macroscopic stress-strain response for the different homogenization procedures are given and compared.

Micromechanical model

The point of departure is the micromechanical yield function Φ_μ which is formulated as follows:

$$\Phi_\mu = \tau_\mu^2/Y_\mu - Y_\mu \ , \quad \forall \ \mu \tag{1}$$

where Y_μ is the yield stress (taking into account hardening), and τ_μ is the projected shear stress on the cementite lamella plane (or rather the ferrite in between the cementite lamellas) defined as:

$$\tau_\mu = \bar{\boldsymbol{M}}_{\mu,\mathrm{dev}} : [\bar{\boldsymbol{m}}_\mu \otimes \bar{\boldsymbol{n}}_\mu] \ . \tag{2}$$

In this expression we introduced the deviatoric Mandel stress $\bar{\boldsymbol{M}}_{\mu,\mathrm{dev}}$ on the intermediate configuration (the multiplicative split of the deformation gradient $\boldsymbol{F}_\mu = \boldsymbol{F}_{\mu,\mathrm{e}} \cdot \boldsymbol{F}_{\mu,\mathrm{p}}$ is adopted) and the normal to the cementite lamella $\bar{\boldsymbol{n}}_\mu$. Further, the direction $\bar{\boldsymbol{m}}_\mu$ is defined as the closest projection of the traction stress $\bar{\boldsymbol{t}}_\mu = \bar{\boldsymbol{M}}_{\mu,\mathrm{dev}} \cdot \bar{\boldsymbol{n}}_\mu$ onto the cementite lamella plane.

The evolution of the cementite lamellas is assumed to be of an areal affine type determined by the plastic deformation gradient, i.e.

$$\bar{\boldsymbol{n}}_\mu = \frac{\boldsymbol{F}_{\mu,\mathrm{p}}^{-\mathrm{t}} \cdot \boldsymbol{n}_{\mu,0}}{|\boldsymbol{F}_{\mu,\mathrm{p}}^{-\mathrm{t}} \cdot \boldsymbol{n}_{\mu,0}|}, \tag{3}$$

with $\boldsymbol{n}_{\mu,0}$ being the initial normal to the cementite lamellas. We also propose to adopt an isotropic elastic law of Neo-Hooke type, an associative type of evolution law for the plastic deformation gradient, and a nonlinear hardening of the yield stress Y_μ.

To compute the response of a microstructure of pearlitic steel for a given macroscopic deformation gradient, a finite element analysis using the micromechanical model summarized above with proper boundary conditions can be performed. However, to save computational time we will investigate the performance of two simplified homogenization procedures denoted model j and model $j + 1$ below.

Model j

In this type of modeling we simply adopt the Taylor assumption for the model of the microstructure. This means that we only have to solve the micromechanical model for each grain μ and then the stress can be computed as the volume average of all μ, i.e.

$$\boldsymbol{P} = \frac{1}{V_{\mathrm{RVE}}} \sum_\mu \boldsymbol{P}_\mu V_\mu, \tag{4}$$

where the $\boldsymbol{P}_\mu$ is the first Piola-Kirchhoff stress obtained in grain μ.

Model $j + 1$

By homogenization of the micromechanical yield function Φ_μ and introducing an approximation (in the spirit of [?]) we obtain

$$\Phi = \langle \Phi_\mu \rangle \approx \frac{1}{Y} \left[\mathrm{tr} \left(\bar{\boldsymbol{a}} \cdot \bar{\boldsymbol{M}}^2 \right) - \bar{\boldsymbol{M}} : \bar{\boldsymbol{B}} : \bar{\boldsymbol{M}} \right] - Y, \tag{5}$$

with

$$\bar{\boldsymbol{a}} = \langle \bar{\boldsymbol{a}}_\mu \rangle = \langle \bar{\boldsymbol{n}}_\mu \otimes \bar{\boldsymbol{n}}_\mu \rangle \ , \quad \bar{\boldsymbol{B}} = \langle \bar{\boldsymbol{a}}_\mu \otimes \bar{\boldsymbol{a}}_\mu \rangle . \tag{6}$$

Preliminary results
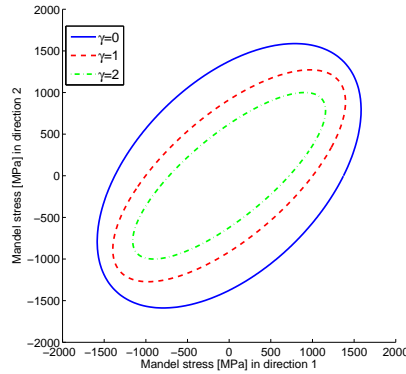
Figure 1: Yield surface in the development during simple shear.

Assume that an initially isotropic material is subjected to simple shear loading γ. In Figure **??** we illustrate how the yield surface (for the $1-2$ stress plane) develops from $\gamma = 0$ to $\gamma = 1$ and $\gamma = 2$. For this case, where we have assumed no isotropic hardening, the anisotropy development gives a shrinking and rotating yield surface.

References

[1] G. Johansson and M. Ekh. On the modeling of evolving anisotropy and large strains in pearlitic steel. *European Journal of Mechanics/A Solids*, **15**, 1041–1060, (2006).

[2] Y.F. Dafalias. Orientation distribution function in non-affine rotations. *Journal of Mechanics and Physics of Solids*, **49**, 2493–2516, (2001).

[3] T. Bohlke, A. Bertram, E. Krempl. Modeling of deformation induced anisotropy in free-end torsion. *International Journal of Plasticity*, **19**, 1867–1884, (2003).

Modeling of Continuous Dynamic Recrystallization in Aluminum

Håkan Hallberg*, Mathias Wallin, Matti Ristinmaa
Division of Solid Mechanics
Lund University, Lund, Sweden
e−mail: hakan.hallberg@solid.lth.se

Summary A constitutive model is presented, considering grain size refinement through continuous dynamic recrystallization together with an evolving dislocation density. The grain refinement is allowed to influence both the evolution of the dislocation density and the rate dependence of the material. The model is calibrated against experimental data on aluminum and numerical simulations of equal channel angular pressing (ECAP) material processing illustrates the capabilities of the model.

Introduction

The grain size is becoming an increasingly important parameter in industrial metal processing, such as in forming operations. Knowledge of the grain size allows better understanding of both hardness and ductility in the material being deformed and, perhaps more importantly, improved control the final product.

The recrystallization process is driven by a lowering of the energy stored within the material microstructure. This occurs through the migration of high-angle grain boundaries, leading to the formation of new grains of relatively lower internal dislocation density. Dislocations are, however, also to a great extent pinned at the extensively expanded grain boundary area as the grains are refined. In addition, dislocations are also trapped in subgrain structures in the new grains. The effect is a second-stage hardening of the material due to dislocation immobilization and storage. By founding a macroscopic, continuum mechanical, constitutive model on these micromechanical processes, it is possible to obtain a versatile tool suitable for simulations of metal forming.

Constitutive models of elasto-(visco)plasticity based on the dislocation density have been previously formulated by several authors. Some models, such as [1], also include the grain size in the dislocation density evolution law, but in many cases the grain size is treated as a constant parameter rather than a variable. The present constitutive model gives a coherent viscoplastic formulation suitable for large-scale simulations of materials undergoing continuous dynamic recrystallization. In addition, the present model allows the recrystallized grain size to influence both the evolution of the dislocation density and also the rate-dependence of the material. The latter characteristic has been observed in several different materials and also in aluminum, which is taken as example material in the calibration of the present model. The calibrated material model is employed as a user subroutine in Abaqus Explicit to allow for simulations, illustrating the workings of the model. As an example simulation, an equal channel angular processing (ECAP) setup is studied.

Constitutive model

The model is formulated within a thermodynamic framework giving a finite strain hyperelastic formulation. The inelastic response of the material is described by J_2 plasticity and the rate dependence of the model is established using a Perzyna-type overstress formulation. These macroscopic features of the model are based on a micromechanical reasoning where the evolution of the grain size D with viscoplastic deformation is described by

$$D = D_0 - \left(D_0 - D_f\right)\left[1 - \exp\left(-k_X\left\langle \tilde{\varepsilon}_{eff}^{\,p} - \varepsilon_c^{vp}\right\rangle^{c_X}\right)\right], \quad D_0 \leq D \leq D_f \tag{1}$$

where, D_0 and D_f are the initial and final values of the grain size, respectively. Using the McCauley brackets $\langle\cdot\rangle$, the recrystallization will not set in until the effective viscoplastic strain quantity $\tilde{\varepsilon}_{eff}^{\,p}$ exceeds a threshold value of ε_c^{vp}. This replicates the initial period needed for subgrain formation, dislocation accumulation at subgrain boundaries and build-up of enough stored energy, e.g. in terms of grain misorientation, to induce the recrystallization process. With k_X and c_X being model parameters to be calibrated against experimental data, the evolution of the effective viscoplastic strain quantity $\tilde{\varepsilon}_{eff}^{\,p}$ is defined as

$$\dot{\tilde{\varepsilon}}_{eff}^{\,p} = \left[1 - a\cos^2(3\theta)\right]\dot{\varepsilon}_{eff}^{\,p}, \quad \theta = \frac{1}{3}\arccos\left(\frac{3\sqrt{3}}{2}\frac{J_3}{J_2^{3/2}}\right), \quad a \in [0,1] \tag{2}$$

where θ is the Lode angle. This format is chosen as one possible way to reduce the evolution of recrystallization during purely uniaxial loading, motivated by experimental evidence. The parameter a allows control of the extent to which the deformation mode is permitted to influence the recrystallization.

Besides the grain size, the other microstructural variable important to the model is the dislocation density ρ_d which, after normalization with the initial dislocation density ρ_d^0, is assumed to evolve according to

$$\frac{\dot{\rho}_d}{\rho_d^0} = \left(d_1\sqrt{\frac{\rho_d}{\rho_d^0}} - d_2\frac{\rho_d}{\rho_d^0} + d_3\frac{D_0}{D}\right)\dot{\varepsilon}_{eff}^{vp} \tag{3}$$

In equation (3), dislocation generation and multiplication is dictated by the parameter d_1, dislocation annihilation by d_2 and the influence of grain size by d_3. Dislocation density evolution laws on the format (3) have been used previously in e.g. [2].

Considering the influence of the grain size according to the renowned Hall-Petch relation, the macroscopic static yield stress appears as

$$\sigma_y(\rho_d, D) = \sigma_{y0} + H\left(\sqrt{\frac{\rho_d}{\rho_d^0}} - 1\right) + k_D\left(\sqrt{\frac{D_0}{D}} - 1\right) \tag{4}$$

where σ_{y0} corresponds to the Peierls stress needed to overcome lattice friction, H is the generalized Taylor factor and k_D the stress intensity coefficient in the Hall-Petch relation.

Numerical Example - Simulation of ECAP

Since introduced by Segal in 1981, equal channel angular pressing (ECAP) has been a procedure frequently used to produce fine-grained materials through extensive plastic deformation, cf. [3]. A typical ECAP setup is shown in Fig. 1.
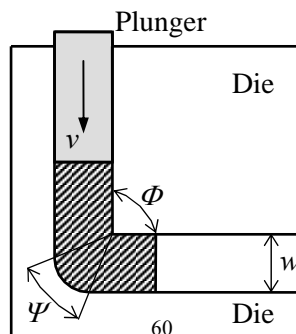
Figure 1: A typical ECAP setup with definition of the channel width *w*, plunger velocity *v*, die angle *Ψ* and

According to [4], the strain imposed on the workpiece by N_{pass} ECAP runs is approximately given by

$$\varepsilon_{eff}^{vp} = \frac{N_{pass}}{\sqrt{3}}\left[2\cot\left(\frac{\Phi}{2} + \frac{\Psi}{2}\right) + \Psi\csc\left(\frac{\Phi}{2} + \frac{\Psi}{2}\right)\right] \qquad (5)$$

where a channel angle $\Phi = 90°$ gives an effective plastic strain of approximately 1, quite independent of the die angle Ψ.

Simulations are performed assuming plane strain conditions and using an ECAP specimen with dimensions $20\times20\times150$ mm, a channel angle of $\Phi = 90°$, plunger velocity $v = 50$ mm/s and a channel width of $w = 20$ mm. The grain size distributions in the workpiece after one and two runs, respectively, through the die are shown in Fig. 2. Note that the workpiece is rotated 180° around its length axis in between the runs, representing a so-called "route C" ECAP run. As the figures show, apart from in the leading tip of the work piece and in the trailing, yet undeformed section, the grain size distribution is quite inhomogeneous after the first pass while the additional deformation exerted in pass two renders a more or less homogeneous grain size distribution corresponding to the final grain size D_f. This tendency to reach a saturation grain size quite rapidly with increasing plastic strain is clearly shown in experimental results on aluminium. This reduction of grain size is captured by the formulation given in equation (1).

Fig.3 shows the distribution of the dislocation density, corresponding to the grain size results in Fig. 2. Again it can be seen how the plastic deformation becomes increasingly homogeneous after subsequent ECAP passes. Note that the workpiece is rotated 180° around its length axis in between each pass, interchanging the Top and Bottom references. Varying the channel angle Φ to values >90° renders situations where one ECAP pass imposes an effective plastic strain less than 1, cf. equation (5). This is studied in the present work.
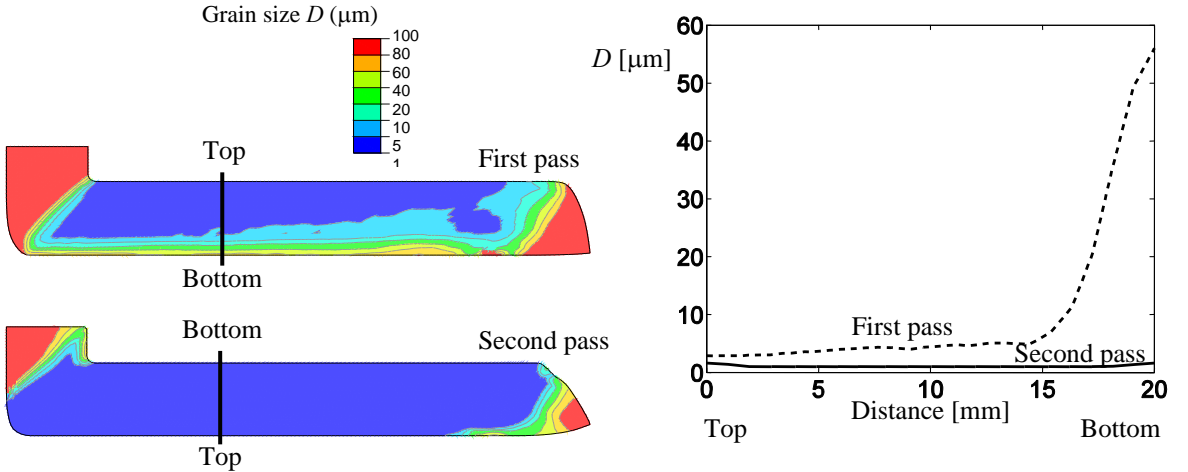
Figure 2: Grain size distribution in the ECAP specimen after one and two passes through the die.
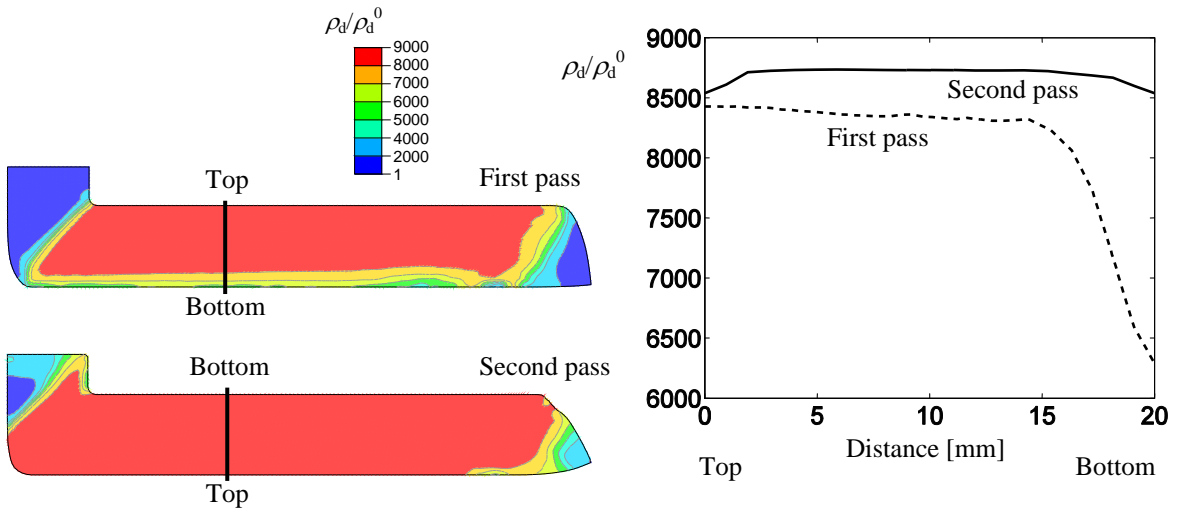
Figure 3: Distribution of normalized dislocation density in the ECAP specimen after one and two passes through the die.

Concluding remarks

Considering micromechanical processes such as the multiplication, interaction and annihilation of dislocations as well as the influence of continuous dynamic recrystallization, a micromechanically motivated constitutive model is formulated. The model recognizes the influence of grain size on the material behavior at both macro- and microlevel. The macroscopic yield stress is influenced by the grain size through a component corresponding to the Hall-Petch relation. In addition, the macroscopic rate dependence of the model is allowed to depend on the grain size. On the microlevel, recrystallization influences the evolution of the dislocation density since an increased amount of grain boundary area restricts the movement of mobile dislocations and since the recrystallization involves the nucleation of new, relatively dislocation-free, grains. By calibration of the model against experimental findings a micromechanically motivated and versatile tool for macroscale simulations of materials and conditions involving finite strain viscoplasticity and dynamic recrystallization is proposed.

References

[1] Y. Estrin and H. S. Kim. Modelling microstructure evolution toward ultrafine crystallinity produced by severe plastic deformation. *Journal of Materials Science*, **42**, 1512-1516, (2007).

[2] Y. Estrin. Dislocation theory based constitutive modelling: Foundations and applications. *Journal of Materials Processing Technology*, **80-81**, 33–39, (1998).

[3] V. M. Segal, V. I. Reznikov, A. E. Drobyshevskiy, and V. I. Kopylov. Plastic working of metals by simple shear. *Russian Metallurgy*, **1**, 99-105, (1981).

[4] Y. Iwahashi, J. Wang, Z. Horita, and M. Nemoto. Principles of equal-channel angular pressing for the processing of ultra-fine grained materials. *Scripta Materialia*, **35(2)**, 143-146, (1996).

Efficient Formulation of RVE-Problems with Application to Nodular Cast Iron

A. Holmström*, **F. Larsson and K. Runesson**

Department of Applied Mechanics
Chalmers Technical University, Gteborg, Sverige
e–mail: andreas.holmstrom@chalmers.se

Summary   Classical computational homogenization with a priori assumed scale separation is considered, whereby the macroscale response is obtained via averaging on Representative Volume Elements (RVE:s). Focus is placed on dimensional reduction from three-dimensional subscale representation within each RVE to one- or two-dimensional macroscale formats, a typical example being macroscale plane stress, which are applications of general mixed stress-strain control. For mixed stress-strain control a novel mixed variational format and single iteration strategy is proposed and compared numerically with the standard two-level (nested) iterative strategy based on strain control, that is commonly adopted for macroscale constitutive models.

Introduction

A classical approach to account for the effect of micro-heterogeneous material substructure in constitutive modeling is to employ fully "nested" macro-subscale modeling based on homogenization on a Representative Volume Element (RVE), c.f. Fish et al. [2], Miehe and coworkers [6, 5], Zohdi and Wriggers [7, 8], Kouznetsova et al. [3] or Aubry et al. [1]. The basic procedure is now quite well established, although many issues are still unresolved, for example in relation to the model assumptions that are (implicitly and explicitly) made as part of the computation.

In many situations it is of interest to analyze problems that are essentially one- or two-dimensional from the macroscopic viewpoint, while it is still desirable to take the three-dimensional subscale features into account. Typical examples are *macroscale uniaxial stress* and *macroscale plane stress*, as defined below. For example, macroscale uniaxial stress is (still) the predominant situation for most tests to evaluate the behavior of metallic materials. In such cases of *macroscale dimensional reduction* it is indeed possible to establish and exploit the results of RVE-problems that are fully three-dimensional (in the same spirit as fully three-dimensional macroscopic models are routinely used in, say, plane stress problems). These two cases obviously represent dimensional reduction from 3D on the subscale to 1D and 2D, respectively, on the macroscale.

A primitive version of dimensional reduction for macroscale plane stress was proposed by Lillbacka et al. [4], who carried out the RVE-analysis in 2D as well, while imposing the Taylor assumption on the out-of-plane deformation. Such a method is primitive in the sense that the three-dimensional features of the subscale structure are completely lost, since the subscale properties are then implicitly treated as homogeneous across the thickness of the (thin) plate.

In this contribution a novel mixed variational format and monolithic iteration strategy for mixed stress-strain control is proposed and compared numerically with the standard two-level (unified) iterative strategy based on strain control, that is commonly adopted for macroscale constitutive models.

Preliminaries

We introduce the complete orthonormal basis $\{\boldsymbol{N}_{ij}\}_{i,j=1}^{3}$ of base dyads for nonsymmetrical 2nd order tensors the displacement gradient, $\boldsymbol{H}$, and first Piola Krichhof stress, $\boldsymbol{P}$. We then introduce the index set $\mathbb{C} = \{11, 12, 13, 21, \ldots, 33\}$ and the split $\mathbb{C} = \mathbb{C}_{\mathrm{I}} \cup \mathbb{C}_{\mathrm{II}}$. For the definition of the RVE-problem, we shall adopt the convention that strain control is associated with components defined by $\mathbb{C}_{\mathrm{I}}$, whereas stress control is associated with the remaining set $\mathbb{C}_{\mathrm{II}}$. We thus decompose $\boldsymbol{H}$ and $\boldsymbol{P}$ as follows:

$$\boldsymbol{H} = \boldsymbol{H}_{\mathrm{I}} + \boldsymbol{H}_{\mathrm{II}}, \quad \boldsymbol{H}_{\alpha} = \sum_{ij \in \mathbb{C}_{\alpha}} \boldsymbol{N}_{ij} H_{ij}, \quad \alpha = \mathrm{I}, \mathrm{II} \tag{1}$$

$$\boldsymbol{P} = \boldsymbol{P}_{\mathrm{I}} + \boldsymbol{P}_{\mathrm{II}}, \quad \boldsymbol{P}_{\alpha} = \sum_{ij \in \mathbb{C}_{\alpha}} \boldsymbol{N}_{ij} P_{ij}, \quad \alpha = \mathrm{I}, \mathrm{II} \tag{2}$$

Finally, we introduce the split 4th order identity tensor

$$\mathsf{I}_{\alpha} \stackrel{\text{def}}{=} \sum_{ij \in \mathbb{C}_{\alpha}} \boldsymbol{N}_{ij} \otimes \boldsymbol{N}_{ij} \quad \alpha = \mathrm{I}, \mathrm{II} \tag{3}$$

which has the property that $\mathsf{I}_{\alpha} : \boldsymbol{H} = \boldsymbol{H}_{\alpha}$ and $\mathsf{I}_{\alpha} : \boldsymbol{P} = \boldsymbol{P}_{\alpha}$.

The same split can be stated for the macroscale (homogenized) quantities

$$\bar{\boldsymbol{P}} \stackrel{\text{def}}{=} \langle \boldsymbol{P} \rangle_{\square}, \quad \bar{\boldsymbol{H}} \stackrel{\text{def}}{=} \langle \boldsymbol{H} \rangle_{\square}, \tag{4}$$

where we introduced the average over the RVE $\Omega_{\square}$,

$$\langle \bullet \rangle_{\square} \stackrel{\text{def}}{=} \frac{1}{|\Omega_{\square}|} \int_{\Omega_{\square}} \bullet \, \mathrm{d}\Omega. \tag{5}$$
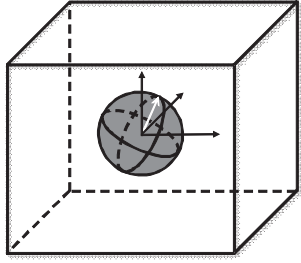
Figure 1: Geometry of a simplified RVE considered in the numerical example: A matrix material surrounding a soft spheroid inclusion.

Dirichlet boundary conditions

In order to formulate the monolithic iteration strategy an auxiliary constraint equation is introduced

$$c_{\square}^{(\mathrm{P})}(\boldsymbol{u}; \delta\bar{\boldsymbol{H}}) \stackrel{\text{def}}{=} \langle \boldsymbol{P} \rangle_{\square} : \delta\bar{\boldsymbol{H}} = \bar{\boldsymbol{P}} : \delta\bar{\boldsymbol{H}} \quad \forall \delta\bar{\boldsymbol{H}} \in \mathbb{R}^{3 \times 3} \tag{6}$$

With the use of the introduced form in Eq (6), the meso-scale problem can be written as follows: For given values of $\bar{\boldsymbol{H}}_{\mathrm{I}} \in \mathbb{R}_{\mathrm{I}}$ and $\bar{\boldsymbol{P}}_{\mathrm{II}} \in \mathbb{R}_{\mathrm{II}}$, find $\boldsymbol{u}^{\mathrm{s}} \in \mathbb{U}_{\square}^{\mathrm{D,s}}$ and $\bar{\boldsymbol{H}}_{\mathrm{II}} \in \mathbb{R}_{\mathrm{II}}$ such that

$$a_{\square}(\boldsymbol{u}^{\mathrm{M}}(\bar{\boldsymbol{H}}_{\mathrm{I}} + \bar{\boldsymbol{H}}_{\mathrm{II}}) + \boldsymbol{u}^{\mathrm{s}}; \delta\boldsymbol{u}^{\mathrm{s}}) = 0 \quad \forall \delta\boldsymbol{u}^{\mathrm{s}} \in \mathbb{U}_{\square}^{\mathrm{D,s}} \tag{7}$$

$$c_{\square}^{(\mathrm{P})}(\boldsymbol{u}^{\mathrm{M}}(\bar{\boldsymbol{H}}_{\mathrm{I}} + \bar{\boldsymbol{H}}_{\mathrm{II}}) + \boldsymbol{u}^{\mathrm{s}}; \delta\bar{\boldsymbol{H}}) = \bar{\boldsymbol{P}}_{\mathrm{II}} : \delta\bar{\boldsymbol{H}}_{\mathrm{II}} \quad \forall \delta\bar{\boldsymbol{H}}_{\mathrm{II}} \in \mathbb{R}_{\mathrm{II}} \tag{8}$$

Given a solution $\boldsymbol{u}^s, \bar{\boldsymbol{H}}_{\mathrm{II}}$ the stress can be solved as $\bar{\boldsymbol{P}}_{\mathrm{I}} \stackrel{\text{def}}{=} \langle \mathsf{I}_{\mathrm{I}} : \boldsymbol{P} \rangle_{\square} = \mathsf{I}_{\mathrm{I}} : \langle \boldsymbol{P} \rangle_{\square}$ in a "post-processing step".

Neumann boundary conditions

For Neumann boundary conditions with strain control an auxiliary condition is introduced in standard fashion using the bilinear form

$$c_{\square}^{(\mathrm{H})}(\boldsymbol{u}; \delta\bar{\boldsymbol{P}}) \quad \stackrel{\text{def}}{=} \quad \langle \boldsymbol{H} \rangle_{\square} : \delta\bar{\boldsymbol{P}}. \tag{9}$$

The monolithic iteration strategy follows from the use of the decomposition of $\bar{\boldsymbol{H}}$ and $\bar{\boldsymbol{P}}$ and the meso-scale problem can be stated as follows: For given values of $\bar{\boldsymbol{H}}_{\mathrm{I}} \in \mathbb{R}_{\mathrm{I}}$ and $\bar{\boldsymbol{P}}_{\mathrm{II}} \in \mathbb{R}_{\mathrm{II}}$, find $\boldsymbol{u} \in \mathbb{U}_{\square}^{\mathrm{N}}$ and $\bar{\boldsymbol{P}}_{\mathrm{I}} \in \mathbb{R}_{\mathrm{I}}$ such that

$$a_{\square}(\boldsymbol{u}; \delta\boldsymbol{u}) - c_{\square}^{(\mathrm{H})}(\delta\boldsymbol{u}; \bar{\boldsymbol{P}}_{\mathrm{I}}) = c_{\square}^{(\mathrm{H})}(\delta\boldsymbol{u}; \bar{\boldsymbol{P}}_{\mathrm{II}}) \quad \forall \delta\boldsymbol{u} \in \mathbb{U}_{\square}^{\mathrm{N}}. \tag{10}$$

$$c_{\square}^{(\mathrm{H})}(\boldsymbol{u}; \delta\bar{\boldsymbol{P}}_{\mathrm{I}}) = \delta\bar{\boldsymbol{P}}_{\mathrm{I}} : \bar{\boldsymbol{H}}_{\mathrm{I}} \quad \forall \delta\bar{\boldsymbol{P}}_{\mathrm{I}} \in \mathbb{R}_{\mathrm{I}} \tag{11}$$

Given a solution $\boldsymbol{u}$ the sought strain can be solved as $\bar{\boldsymbol{H}}_{\mathrm{II}} \stackrel{\text{def}}{=} \langle \mathsf{I}_{\mathrm{II}} : \boldsymbol{H} \rangle_{\square} = \mathsf{I}_{\mathrm{II}} : \langle \boldsymbol{H} \rangle_{\square}$ in a "post-processing step"

Results and Conclusion
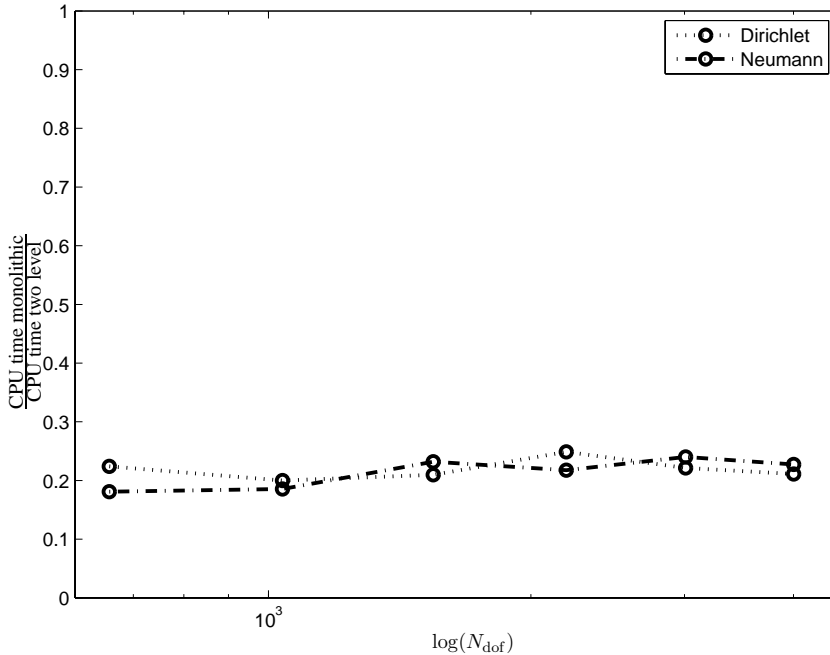
Figure 2: Relative calculation time for monolithic/two level iteration solution plotted against the number of degrees of freedom of the RVE, N_{dof}.

The proposed monolithic solution has been compared to the two level iteration strategy with respect to computational effort for a simple model problem. A rectangular Representative Volume Element consisting of a stiff matrix material with a soft spherical inclusion is considered, cf. Figure

1. Both material phases are modeled as elastic-plastic solids, using the von Mises yield criterion and mixed linear hardening, with different material parameters.

The load case is uniaxial stress, whereby we prescribe set $\bar{\boldsymbol{P}}_{\mathrm{II}} = \{\bar{P}_{22}, \bar{P}_{33}\} = \{0, 0\}$ and $\bar{\boldsymbol{H}}_{\mathrm{I}} = \{\bar{H}_{11}, \bar{H}_{12}, \bar{H}_{21}, \bar{H}_{13}, \bar{H}_{31}, \bar{H}_{23}, \bar{H}_{32}\} = \{1, 0, 0, 0, 0, 0, 0, 0\} \cdot \dot{\bar{H}}_{11} \cdot t$, where $\dot{\bar{H}}_{11} = 4 \cdot 10^{-3}\ \mathrm{s}^{-1}$ is a prescribed (constant) strain rate.

In Figure 2 the relative calculation time for the monolithic solution/two level iteration solution is plotted. As can be seen the reduction in computational time is considerable; the monolithic approach is between 3-5 times faster than the two level iteration strategy. There is no clear trend that the speed-up becomes less for higher number of degrees of freedom N_{dof}. The solution to the given problem is, of coarse, identical in the two formulations and the robustness appears to be unaffected (preliminary result).

References

[1] S. Aubry, M. Fago, and M. Ortiz. A constrained sequential-lamination algorithm for the simulation of sub-grid microstructure in martensitic materials. *Computer Methods in Applied Mechanics and Engineering*, 192:2823–2843, 2003.

[2] J. Fish, K. Shek, M. Pandheeradi, and M Shepard. Computational plasticity for composite structures based on mathematical homogenization: Theory and practice. *Computer Methods in Applied Mechanics and Engineering*, 148:53–73, 1997.

[3] V. Kouznetsova, M.G.D. Geers, and W.A.M. Brekelmans. Multi-scale constitutive modelling of heterogeneous materials with a gradient-enhanced computational homogenization scheme. *International Journal for Numerical Methods in Engineering*, 54:1235–1260, 2002.

[4] R. Lillbacka, F. Larsson, and K. Runesson. On the implementation of plane stress in computational multiscale modeling. *International Journal for Multiscale Computational Engineering*, pages 771–790, 2006.

[5] C. Miehe and A. Koch. Computational micro-to-macro transitions of discretized microstructures undergoing small strains. *Archive of Applied Mechanics*, 72:300–317, 2002.

[6] C. Miehe, J. Schröder, and J-Schotte. Computational homogenization analysis in finite plasticity simulation of texture development in polycrystalline materials. *Computer Methods in Applied Mechanics and Engineering*, 171:387–418, 1999.

[7] T. Zohdi and P. Wriggers. A model for simulating the deterioration of structural-scale material responses of microheterogeneous solids. *Computer Methods in Applied Mechanics and Engineering*, 190:2803–2823, 2001.

[8] T. I. Zohdi and P. Wriggers. *Introduction to Computational Micromechanics*. Springer, 2005.

A statistical method for structural damage identification using vibration data

Antti Huhtala

Department of Mathematics and Systems Analysis
Helsinki University of Technology, Espoo, Finland
e–mail: ahhuhtal@cc.hut.fi

Summary A change in modal parameters of a structure due to damage is related to both the extent and the location of the damage. Having a model of the structure and of the way damage changes it, the occured damage can be estimated from the measured changes in the parameters. This is, however, an inverse problem and thus ill-conditioned. In this work a regularization scheme based on Bayesian inference is investigated.

Introduction

Structural health monitoring has been under active research over the past 20 years [1, 2]. Many of the proposed methods are based on the fact that modal parameters of a structure change when it receives damage. This change is not only related to the extent of the damage, but also to its location [2].

The methods which seek also to locate the damage, in addition to just detecting its presence, are most often based on a model of the structure and on an assumption of the way damage changes that model. The simulated modal parameters of the structure model are compared against those measured from the actual structure. A damage state minimizing the difference is then sought for the model. This is an inverse problem and as such it is ill-conditioned, which means that some form of regularization has to be added in order to get any results.

As measurement noise and modelling error are always present in a realistic case, our approach is a statistical one. Using Bayesian inference, the posterior probability distribution, which states the probability density of the structure having a certain damage state given the measured parameters, is formed. The maximum a posteriori estimate of this distribution is then solved.

Damage identification

Modes of a structure

A discretized model of an undamped linear structure under free vibration is expressed as

$$M\ddot{U}(t) + KU(t) = 0, \tag{1}$$

where $M, K \in \mathbb{R}^{n \times n}$ are the mass matrix and stiffness matrix respectively. $U(t)$ is a vector containing the DOFs of the discretized displacement field as a function of time.

Solving the generalized eigenvalue problem

$$KX = MX\Lambda \tag{2}$$

gives a diagonal matrix of the eigenvalues Λ and a matrix of eigenvectors X.

By changing variables to the eigenbasis, given by

$$U(t) = X\eta(t), \tag{3}$$

equation (1) and the normalization of the eigenvectors give

$$\ddot{\boldsymbol{\eta}}(t) + \boldsymbol{\Lambda}\boldsymbol{\eta}(t) = \mathbf{0}. \tag{4}$$

As $\boldsymbol{\Lambda}$ is diagonal, equation (4) describes n independent harmonic oscillators. The oscillation frequencies are identified as the square roots of the eigenvalues and denoted as $\omega_i = \sqrt{\lambda_{ii}}$.

The solution to (1) is given by

$$\boldsymbol{U}(t) = \boldsymbol{X}\boldsymbol{\eta}(t) = \sum_{i=1}^{n} \boldsymbol{x_i}\eta_i(t), \tag{5}$$

which is a linear combination of independent vibration modes $\boldsymbol{x_i}\eta_i(t)$. Hence the eigenvectors $\boldsymbol{x_i}$ are the mode shapes corresponding to the DOFs.

Measurement model

The structure is observed using a number of measurement devices. In order to use the measurements, a model that relates the motions of the structure to the output of the devices is needed.

Any linear functional on the displacement field can be expressed as an inner product with the DOFs. Assuming that the measuring devices can be modelled as linear functionals of the displacement field, their measurements can be written as

$$\boldsymbol{Y}(t) = \boldsymbol{H}\boldsymbol{U}(t) = \sum_{i=1}^{n} \boldsymbol{H}\boldsymbol{x_i}\eta_i(t). \tag{6}$$

Presented with such time-domain data from the actual measurement devices, there exist methods for extracting some number, say m, of the modal frequencies ω_i and the corresponding observable mode shapes $\boldsymbol{H}\boldsymbol{x_i}$ [3]. Hence these quantities are used as the measured parameters. The measurement vector is defined as

$$\boldsymbol{m} = \begin{pmatrix} \omega_1 \\ \boldsymbol{H}\boldsymbol{x_1} \\ \vdots \\ \omega_m \\ \boldsymbol{H}\boldsymbol{x_m} \end{pmatrix}. \tag{7}$$

Damage model

Damage can be modelled as a loss of local stiffness in a structure [4]. The mass of the structure can be assumed to be not affected by the damage [1, 2, 4]. In the discretized model, this translates as a change in the stiffness matrix $\boldsymbol{K}$ and no change in the mass matrix $\boldsymbol{M}$.

Assuming a constant loss of stiffness within each element of the discretized model, the change in the stiffness matrix $\boldsymbol{\Delta K}$ can be expressed simply as

$$\boldsymbol{\Delta K} = -\sum_{i=1}^{N} d_i \boldsymbol{K_i^e}, \tag{8}$$

where the $\boldsymbol{K_i^e}$ are the individual element stiffness matrices. The parameters $d_i \in [0, 1]$ are element-wise damage parameters describing the amount of stiffness loss. The parameter value 0 indicates no damage and 1 is indicative of a complete loss of stiffness.

Forward model

The forward model combines the damage model with the measurement model. It simulates measurements for a given damage state. It is expressed simply as

$$\boldsymbol{m} = \boldsymbol{f}(\boldsymbol{d}), \tag{9}$$

where $\boldsymbol{d}$ is a vector containing the elementwise damage parameters and $\boldsymbol{m}$ is a vector of measurements as defined in equation (7) corresponding to the damage state $\boldsymbol{d}$.

Statistical inverse

In reality, the measurements differ from the forward model. This is because of measurement noise and modelling error. These effects are taken into account by adding a random error term to the forward model. In the Bayesian framework, all variables are thought as random variables. Using the convention that random variables are denoted by capital letters and their outcomes with corresponding lower case letters, the relation between the measurement, the damage state and the error term is written as

$$\boldsymbol{M} = \boldsymbol{f}(\boldsymbol{D}) + \boldsymbol{E}. \tag{10}$$

Assuming that $\boldsymbol{E}$ is multivariate normal distributed with covariance $\boldsymbol{\Sigma}$ and mean value $\boldsymbol{\epsilon_m}$, it has the probability density

$$p(\boldsymbol{E} = \boldsymbol{\epsilon}) = C \exp\left(-\frac{1}{2}(\boldsymbol{\epsilon} - \boldsymbol{\epsilon_m})^T \boldsymbol{\Sigma}^{-1}(\boldsymbol{\epsilon} - \boldsymbol{\epsilon_m})\right). \tag{11}$$

The statistics of $\boldsymbol{E}$ can be estimated from repeated measurements, given that the damage state of the actual structure is known. This is most easily done when the structure is still undamaged.

Assuming that $\boldsymbol{E}$ is independent of $\boldsymbol{D}$, which is to say the statistics of $\boldsymbol{E}$ stay the same regardless of the damage state, we can write the conditional probability density for obtaining measurement $\boldsymbol{m}$ under damage state $\boldsymbol{d}$, as

$$p(\boldsymbol{M} = \boldsymbol{m}|\boldsymbol{D} = \boldsymbol{d}) = p(\boldsymbol{E} = \boldsymbol{m} - \boldsymbol{f}(\boldsymbol{d})). \tag{12}$$

Using Bayes' formula, the posterior probability density is

$$p(\boldsymbol{D} = \boldsymbol{d}|\boldsymbol{M} = \boldsymbol{m}) = \frac{p(\boldsymbol{M} = \boldsymbol{m}|\boldsymbol{D} = \boldsymbol{d})p(\boldsymbol{D} = \boldsymbol{d})}{p(\boldsymbol{M} = \boldsymbol{m})}. \tag{13}$$

This is the conditional probability density of damage state $\boldsymbol{d}$ when the measurement is known to be $\boldsymbol{m}$. The density $p(\boldsymbol{D} = \boldsymbol{d})$ is a prior distribution, which encodes all the information known of the damage state prior to measurement $\boldsymbol{m}$.

The posterior density can be considered as the solution of an inverse problem, however point estimates are often more illustrative as they provide a single answer. Two common point estimates are the maximum a posteriori estimate and the conditional mean estimate. The maximum a posteriori estimate is presented here. It is simply defined as the maximum of the posterior probability density, that is

$$\boldsymbol{d}_{MAP} = \underset{\boldsymbol{d}}{\mathrm{argmax}} \frac{p(\boldsymbol{M} = \boldsymbol{m}|\boldsymbol{D} = \boldsymbol{d})p(\boldsymbol{D} = \boldsymbol{d})}{p(\boldsymbol{M} = \boldsymbol{m})}. \tag{14}$$

Since the measurement $\boldsymbol{m}$ is fixed, $p(\boldsymbol{M} = \boldsymbol{m})$ is a constant and acts only to normalize the distribution, hence it doesn't affect the optimization and the MAP estimate can be simplified as

$$\boldsymbol{d}_{MAP} = \underset{\boldsymbol{d}}{\mathrm{argmax}}\, p(\boldsymbol{M} = \boldsymbol{m}|\boldsymbol{D} = \boldsymbol{d})p(\boldsymbol{D} = \boldsymbol{d}). \tag{15}$$

Results

A steel cantilever beam 1400 millimeters long, 60 millimeters wide and 5 millimeters thick was measured with 7 accelerometers. The vibration of the beam was excited with a tap of a rubber hammer. A set of baseline measurements were taken from the undamaged beam, after which a slot was sawed to the beam with a hacksaw. The frequencies and mode shapes of the lowest 6 modes were identified in both cases. The mean of the relative standard deviations for the identified modal frequencies ended up being 0.05% whereas it was 0.97% for the observable mode shapes.

The beam was modelled using the finite element method as an Euler-Bernoulli beam discretized with 50 elements. A model updating scheme was used to update the FEM model to better reflect the baseline measurements. The remaining error was left to the error variable $\boldsymbol{E}$, the statistics of which were estimated from the measurements.

The prior distribution was chosen so that the damage parameters d_i were independent and identically distributed. The distribution needed to allow for values nearly zero, but no values below zero. It also had to give low probability for large damage. For this purpose the half-normal distribution, which has a single parameter, was chosen.

Figure 1 shows the MAP estimate of the damage parameters d_i. The location of the largest spike matches the location of the sawed slot. The parameter in the prior distribution is not critical, the damaged location is singled out over a large parameter range. In figure 1 it was chosen as $\sigma^2 = \frac{1}{2}$.
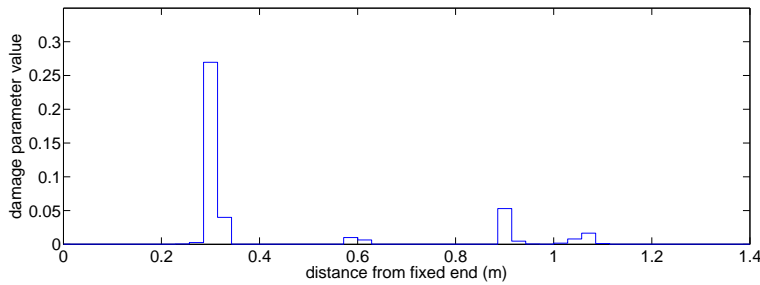
Figure 1: MAP estimate of the damage state in the beam. The largest spike matches with the actual damage.

Acknowledgements

References

[1] A. D. Dimarogonas. Vibration of cracked structures: A state of the art review. *Eng. Fract. Mech.*, **55**, 831–857, (1996).

[2] O. S. Salawu. Detection of structural damage through changes in frequency: a review. *Eng. Struct.*, **19**, 718–723, (1997).

[3] L. Mevel, A. Beneviste, M. Basseville and M. Goursat. Blind subspace-based eigenstructure identification under nonstationary excitation using moving sensors. *IEEE Trans. Signal Proc.*, **50**, 41–48, (2002).

[4] D. A. Castello, L. T. Stutz and F. A. Rochinha. A structural defect identification approach based on a continuum damage model. *Computers & Struct.*, **80**, 417–436, (2002).

Design of Resonant Control for Damping of Flexible Structures

Jan Høgsberg and Steen Krenk

Department of Mechanical Engineering
Technical University of Denmark, Kgs. Lyngby, Denmark
e–mail: jhg@mek.dtu.dk , sk@mek.dtu.dk

Summary Structural vibrations are typically governed by resonance, and thus damping of these vibrations can often be increased by using the resonant properties of these modes. In the present paper the basic principles of resonant absorbers are presented based on a general format in terms of sensors and actuators. A design procedure is developed for resonant displacement and acceleration feedback, respectively, introducing both 'equal modal damping' and almost equal response amplitudes of the two modes. In flexible structures the sensors and actuators also interact with background modes. A procedure is developed, in which a quasi-static representation of the higher modes is subtracted from the direct response. It is demonstrate that this explicit quasi-static correction procedure for resonant damping of flexible structures is very effective with high and nearly-equal damping around the resonance frequency.

Design of resonant control

The control problem is illustrated in Fig. 1. The structure is represented by a mass m with displacement $x(t)$. The external load on the structure is represented by the force $F(t)$. The control is accomplished via a sensor signal $y(t)$ used to control an additional force $F_c(t)$. Figure 1a illustrates the case of a flexible structure, with the first mode being represented by the mode shape vector $\mathbf{u}_1$ and the modal amplitude x_1. A single-degree-of-freedom representation is obtained, if this mode is considered without including interaction with higher modes. The governing equations can be written in the following general frequency format [2],

$$
\begin{aligned}
G_{xx}(\omega)\,x \,+\, G_{xy}(\omega)\,y &= F/m \\
G_{yx}(\omega)\,x \,+\, G_{yy}(\omega)\,y &= 0
\end{aligned}
\tag{1}
$$

introducing the frequency transfer functions $G_{xx}, G_{xy}, \cdots$. In the case without internal damping the structural response is governed by the following frequency function with natural frequency ω_s,

$$
G_{xx}(\omega) \,=\, \omega_s^2 - \omega^2
\tag{2}
$$

The controller consists of an oscillator defined by the second order filter function

$$
G_{yy}(\omega) \,=\, \omega_c^2 - \omega^2 + 2i\zeta_c\omega_c\omega
\tag{3}
$$

with characteristic frequency ω_c and bandwidth parameter ζ_c. The quality of the control is associated with its ability to limit the response of the structure around the resonance frequency ω_s.
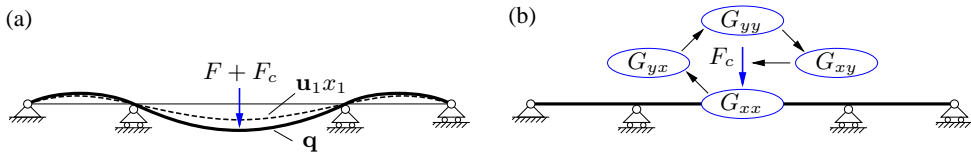
Figure 1: Structure with sensor and control force: (a) Flexible MDOF structure, (b) Control loop.

Parameter	Acceleration feedback	Displacement feedback
ω_c	$\omega_s/(1+\beta)$	$\omega_s/(1+\gamma)$
ω_0^2	$\omega_c\omega_s$	$\omega_c\omega_s$
α	β	$\gamma(1-\gamma)$
ζ_c^2	$\dfrac{1}{2}\dfrac{\beta}{1+\beta}$	$\dfrac{\gamma}{4}\dfrac{2+\gamma}{1+\gamma}$

Table 1: Optimal parameters for resonant damping in terms of β or γ.

Two types of resonant control are considered with generalized acceleration and displacement feedback, respectively. In the case of *acceleration feedback* the sensor function G_{yx} and the actuator function G_{xy} are conveniently formulated as

$$G_{yx}(\omega) = \omega^2 \quad , \quad G_{xy}(\omega) = \alpha\,\omega_c^2 + \beta\,2i\zeta_c\omega_c\omega \tag{4}$$

with gain parameters α and β. On the other hand *displacement feedback* can be written as

$$G_{yx}(\omega) = \omega_c^2 \quad , \quad G_{xy}(\omega) = \alpha\,\omega^2 + \gamma\,2i\zeta_c\omega_s\omega \tag{5}$$

introducing γ as the final gain parameter. For both acceleration and displacement feedback the system of equations contains four governing parameters to be determined: The filter parameters ω_c, ζ_c and the two gain parameters α, β (acceleration feedback) or α, γ (displacement feedback). The optimal calibration of the parameters is based on two desirable properties:

- Equal modal damping of the two associated vibration modes.

- Optimal frequency amplitude for both structural response and control force.

The equal modal damping property follows from a root locus analysis and determines of the optimal filter frequency ω_c and a reference frequency ω_0. The parameters α and ζ_c are determined to give a 'flat plateau' of the frequency amplitude around the resonance frequency, see [1, 2, 3]. The optimal design parameters are given in Table 1 with β and γ as gain parameters, respectively.

Resonant damping of flexible structures

Let a multi-degree-of-freedom system be represented by the stiffness matrix $\mathbf{K}$ and the mass matrix $\mathbf{M}$. The displacements are denoted $\mathbf{q}$ and the corresponding external loads $\mathbf{F}$. In addition to the external load an actuator with control signal η is connected to the structure as described by the connectivity vector $\mathbf{w}$. The corresponding frequency equation is

$$(\mathbf{K} - \omega^2\mathbf{M})\,\mathbf{q} = \mathbf{F} - \mathbf{w}\,G_{q\eta}(\omega)\,\eta \tag{6}$$

The actuator is controlled by the collocated signal η governed by the frequency equation

$$G_{\eta\eta}(\omega)\,\eta = -G_{\eta q}(\omega)\,\mathbf{w}^T\mathbf{q} \tag{7}$$

It is assumed that the response is dominated by the first vibration mode $\mathbf{u}_1$ with natural frequency ω_1. When introducing a modal representation, where the higher modes are represented quasi-statically [2, 4], the motion of the damper can be approximated as

$$\mathbf{w}^T\mathbf{q} \simeq -\left[\frac{\nu_1^2}{G_{qq}(\omega)} + \kappa_1\right]G_{q\eta}(\omega)\,\eta = \nu_1 x_1 - \kappa_1\,G_{q\eta}(\omega)\,\eta \tag{8}$$

where the modal amplitude over the damper link is $\nu_1 = \mathbf{w}^T\mathbf{u}_1$, and κ_1 representing the effect of the higher modes is defined as

$$\kappa_1 = \mathbf{w}^T\left(\mathbf{K}^{-1} - \frac{\mathbf{u}_1\mathbf{u}_1^T}{\omega_1^2}\right)\mathbf{w} = \mathbf{w}^T\mathbf{K}^{-1}\mathbf{w} - (\nu_1/\omega_1)^2 \tag{9}$$

The first term is the displacement between the degrees of freedom of the sensor for a unit force exerted by the actuator, and the second term subtracts the part associated with the first mode. It is convenient to introduce the normalized form $\kappa = (\omega_1/\nu_1)^2\kappa_1 = (\omega_1/\nu_1)^2\mathbf{w}^T\mathbf{K}^{-1}\mathbf{w} - 1$. The combined set of equations for the first mode and the controller then takes the form

$$\begin{aligned} G_{qq}(\omega)\,x_1 & + & \nu_1 G_{q\eta}(\omega)\,\eta & = & F_1 \\ \nu_1 G_{\eta q}(\omega)\,x_1 & + & \left[G_{\eta\eta}(\omega) - \kappa_1\,G_{\eta q}(\omega)G_{q\eta}(\omega)\right]\eta & = & 0 \end{aligned} \tag{10}$$

where the resonator frequency function $G_{\eta\eta}(\omega)$ is modified by the term $\kappa_1 G_{\eta q}(\omega)G_{q\eta}(\omega)$. The calibration procedure for the MDOF system consists in establishing an equivalence with the optimal control of the SDOF system in (1) with optimal parameters given in Table 1. The modal frequency function and the resonant controller are represented in the form

$$G_{qq}(\omega) = \omega_1^2 - \omega^2\,, \qquad G_{\eta\eta}(\omega) = \omega_\eta^2 - \omega^2 + 2i\zeta_\eta\omega_\eta\omega \tag{11}$$

In the case of *acceleration feedback* the sensor and actuator functions are given as

$$G_{\eta q}(\omega) = \omega^2\,, \qquad \nu_1^2 G_{q\eta}(\omega) = \alpha_\eta\omega_\eta^2 + \beta_\eta\,2i\zeta_\eta\omega_\eta\omega \tag{12}$$

The corresponding expressions for displacement feedback can be found in [2].

Example: Effect of flexibility

The efficiency and characteristics of filtered acceleration feedback are illustrated by the two cases in Figure 2: a force actuator F_c acting on the bottom floor of a 25 storey portal frame and a force actuator acting on a taut cable at 2% of the cable length from the support. In both cases the actuator is located where the amplitude of mode 1 is relatively small, implying a large influence from the higher modes and a large value of the correction factor; $\kappa = 11.76$ for the portal frame and $\kappa = 23.52$ for the cable. The optimal parameters and modal damping ratios are summarized in Table 2. The basis of the design is a desired damping ratio ζ_{des}. Because of the equal modal damping property the filter damping parameter is approximately twice the desired value: $\zeta_c \simeq 2\zeta_{des}$ [1]. It is seen from the table that the resulting damping ratios for the two vibration modes are both practically equal to the desired value. The last column gives the damping ratios for $\kappa = 0$, showing that without the correction for higher modes the equal modal damping property is lost, and one of the modes is only very lightly damped. The frequency response for a uniformly distributed harmonic load is shown in Fig. 3, exhibiting the desired flat plateau around resonance without any overshoot in the control force.
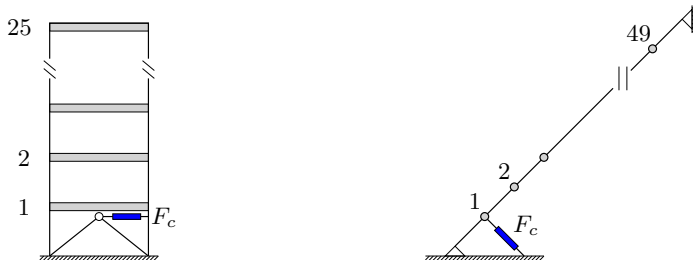
Figure 2: Portal frame and taut cable with force actuator.

Table 2: Mode 1 damping ratios for portal frame and taut cable.

ζ_{des}	ζ_c	β	ω_c/ω_1	β_η	α_η	ω_η/ω_1	ζ_η	$\zeta_1^{\mp}$	$\zeta_1^{\mp}|_{\kappa=0}$
				Portal frame with force actuator: $\kappa = 11.76$					
0.02	0.04	0.0032	0.9968	0.0031	0.0032	1.0160	0.0423	0.0202	0.0261
								0.0198	0.0117
0.04	0.08	0.0130	0.9872	0.0113	0.0130	1.0699	0.0999	0.0408	0.0505
								0.0394	0.0146
0.06	0.12	0.0297	0.9712	0.0220	0.0297	1.1856	0.1976	0.0626	0.0640
								0.0595	0.0146
				Taut cable with force actuator: $\kappa = 23.52$					
0.02	0.04	0.0032	0.9968	0.0030	0.0032	1.0364	0.0447	0.0205	0.0285
								0.0194	0.0072
0.04	0.08	0.0130	0.9872	0.0099	0.0130	1.1776	0.1245	0.0418	0.0470
								0.0376	0.0067
0.06	0.12	0.0297	0.9712	0.0175	0.0297	1.6607	0.3483	0.0647	0.0502
								0.0549	0.0055
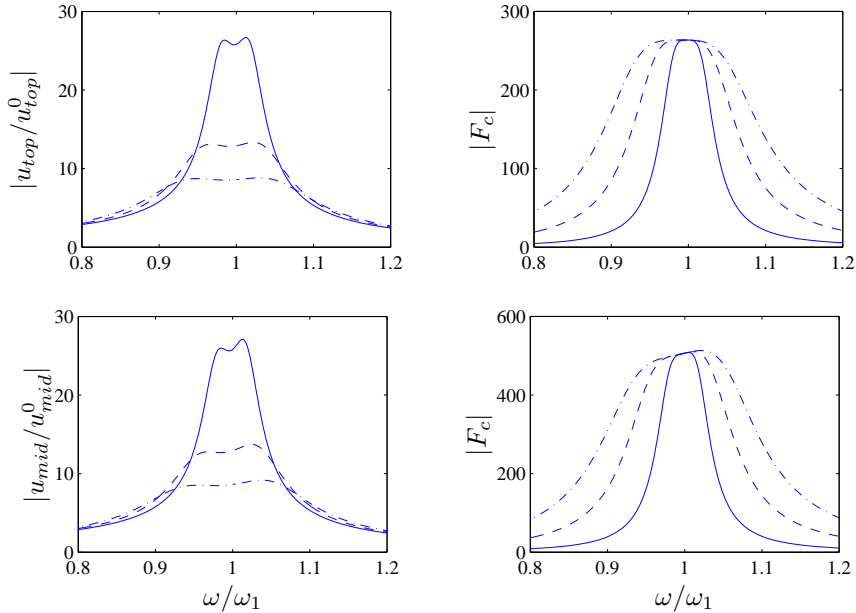
Figure 3: Frequency response of portal frame (top) and cable (bottom) for $\beta = 0.0032$ (——), 0.0130 (– – –) and 0.0297 (– · –).

References

[1] S. Krenk, Frequency analysis of the tuned mass damper, *Journal of Applied Mechanics ASME*, **72**, 936–942, 2005.

[2] S. Krenk, J. Høgsberg, Optimal resonant control of flexible structures, *Journal of Sound and Vibration*, **323**, 530–554, 2009.

[3] S. Krenk, J. Høgsberg, Resonant damping of flexible structures, *COMPDYN 2009*, Rhodes, Greece, June 22-24, 2009. (CD-Rom)

[4] O.E. Hansteen, K. Bell, Accuracy of mode superposition analysis in structural dynamics, *Earthquake Engineering and Structural Dynamics*, **7**, 405–411, 1979.

Resonant Vibration Control of Beams under Stationary Rotation

Martin N. Svendsen[*]**, Steen Krenk and Jan B. Høgsberg**

Department of Mechanical Engineering
Technical University of Denmark, Kgs. Lyngby, Denmark
e–mail: mns@mek.dtu.dk

Summary   The present paper deals with addition of damping to a specific vibration mode of a rotating beam using an active resonant controller. A recent general format for controller tuning is adopted and applied in a three-dimensional finite beam element formulation. The effects on controller tuning and performance due to changes in modal properties of a cantilever beam under different operational angular frequencies are investigated.

Introduction

Vibrations in rotating beams is a naturally occurring phenomenon in e.g. helicopter and wind turbine rotors. In some cases vibrations are concentrated on a single or a few lightly damped modes and it may be of practical interest to suppress these vibrations. The present paper deals with addition of damping to a specific vibration mode of a rotating beam using an active resonant controller. A resonant controller targets a specific mode by inherent resonant behaviour near the eigenfrequency of the mode. The principle was illustrated in an early, passive form as the tuned mass damper by Ormondroyd & den Hartog [1]. Recent work by Krenk & Høgsberg [2, 3] has provided a general format for tuning of a resonant, active device addressing a given mode of a flexible structure. This method is adopted here and applied in a three-dimensional finite beam element formulation where the controller can be attached at two arbitrary cross-section locations. Internal application of an active strut controller is illustrated in Fig. 1. A recent use of this type of controller is described by Preumont et al. [4].
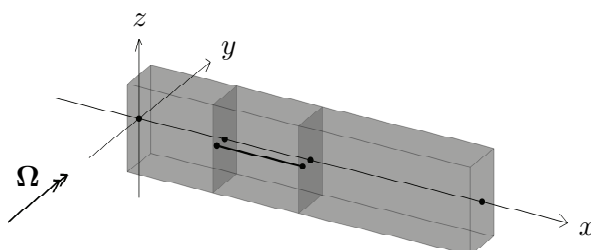
Figure 1: Active strut controller connected to two cross-sections of a beam.

As part of the resonant tuning the controller feedback system relates directly to physical system states. This differentiates the approach from control procedures where observers are used to estimate modal states, e.g. Khulief [5]. In cases where rotating machinery operates with different angular velocities, notable variations in eigenfrequencies due to centrifugal stiffening may occur, as illustrated by e.g. Maqueda et al. [6]. In the present paper the effects on controller tuning and performance due to changes in modal properties of a cantilever beam under varying operational angular frequencies are investigated.

Basic Equations

Linear structural equations of motion with nodal degrees of freedom $\mathbf{u}$, stiffness matrix $\mathbf{K}$, damping matrix $\mathbf{C}$, mass matrix $\mathbf{M}$ and external harmonic forces $\mathbf{f}_e$ with excitation frequency ω are

represented in the frequency domain by assuming a harmonic solution $\mathbf{u}e^{i\omega t}$,

$$\left(\mathbf{K} + i\omega\mathbf{C} - \omega^2\mathbf{M}\right)\mathbf{u} = \mathbf{f}_e - G_{q\eta}(\omega)\mathbf{w}\eta \tag{1}$$

where the controller force is represented by the controller feedback transfer function $G_{q\eta}$, the controller connectivity vector $\mathbf{w}$ and the controller state η. The controller state is governed by the equation

$$G_{\eta\eta}(\omega)\eta = -G_{\eta q}(\omega)\mathbf{w}^T\mathbf{u} \tag{2}$$

where $G_{\eta\eta}$ is the controller transfer function and $G_{\eta q}$ is the structural feedback transfer function. The beam is described in a local, rotating frame of reference with constant angular velocity and gyroscopic effects are neglected. Consequently, $\mathbf{M}$ is the classic beam element mass matrix, and the damping matrix $\mathbf{C}$ is omitted. System stiffness $\mathbf{K}$ is given as

$$\mathbf{K} = \mathbf{K}_e + \mathbf{K}_s + \mathbf{K}_c + \mathbf{K}_g \tag{3}$$

with constitutive stiffness $\mathbf{K}_e$, support stiffness $\mathbf{K}_s$, centrifugal stiffness $\mathbf{K}_e$ and geometric stiffness $\mathbf{K}_g$ based on an initial stress formulation.

Acceleration Feedback Controller

A controller operating with acceleration feedback has transfer functions of the form

$$G_{\eta\eta}(\omega) = \omega_\eta^2 - \omega^2 + 2i\zeta_\eta\omega_\eta\omega, \quad G_{\eta q}(\omega) = -\omega^2, \quad G_{q\eta}(\omega) = \frac{1}{\nu_1^2}\left(\alpha_\eta\omega_\eta^2 + \beta_\eta 2i\zeta_\eta\omega_\eta\omega\right) \tag{4}$$

where the resonant behaviour of the controller resides in the second-order filter $G_{\eta\eta}$. ω_η is controller eigenfrequency, ζ_η is controller damping and α_η and β_η are tuning parameters, including a background correction. Tuning of the controller (4) follows the procedure from [2, 3] where the desired additional modal damping ratio ζ_{des} and targeted natural modal eigenfrequency ω_n are specified,

$$\zeta_c = 2\zeta_{des}, \qquad \beta = \frac{2\zeta_c^2}{1 - 2\zeta_c^2}, \qquad \alpha_\eta = \beta, \qquad \beta_\eta = \frac{\beta}{1 + \kappa_n\beta},$$

$$\omega_\eta^2 = \frac{1}{1 - \dfrac{\kappa_n\beta}{(1+\beta)^2}}\left(\frac{\omega_n}{1+\beta}\right)^2, \quad \zeta_\eta = \frac{1}{\omega_\eta\left(1 + \kappa_n\beta\right)\left(1 - \dfrac{\kappa_n\beta}{(1+\beta)^2}\right)}\frac{\zeta_c\omega_n}{1+\beta} \tag{5}$$

The modal controllability depends on the amplitude of modal displacement over the controller. This is represented by the modal connectivity factor ν_n,

$$\nu_n = \mathbf{w}^T\mathbf{u}_n \tag{6}$$

where $\mathbf{u}_n$ is the targeted mode shape. Controller performance is affected by the presence of additional structural flexibility from higher modes at the location of the controller. This is represented by the modal quasi-static flexibility parameter κ_n,

$$\kappa_n = \left(\frac{\omega_n}{\nu_n}\right)^2\mathbf{w}^T\mathbf{K}^{-1}\mathbf{w} - 1 \tag{7}$$

The formulas (5) to (7) constitute the complete parameter tuning when the controller/structure connection has been chosen.

Active Strut Controller with Acceleration Feedback

Controller performance under different angular velocities is investigated in terms of a homogeneous, prismatic cantilever beam. The beam is oriented as shown in Fig. 1, i.e. fixed at $\{x, y, z\} = \{0, 0, 0\}$ and rotating about the y-axis with angular velocity $\boldsymbol{\Omega} = [\Omega_x, \Omega_y, \Omega_z]^T$, where Ω_y is the only non-zero component. Structural properties of the beam are given in terms of material density $\rho = 2700\text{kg/m}^3$, modulus of elasticity $E = 72\text{GPa}$, Poisson's ratio $\nu = 0.3$, length $L = 8.2\text{m}$, width $d_y = 0.035\text{m}$ and height $d_z = 0.35\text{m}$.

The mode shapes of mode 1 are shown in Fig. 2 where u_y are nodal displacements in the y-direction and φ_z are nodal cross-section rotations about the z-axis. It is seen that the centrifugal stiffening introduces a tensioning of the beam which straightens the free end of the beam. In Table 1 the development of ω_1 is given and notable variation is seen in the chosen interval for Ω_y.
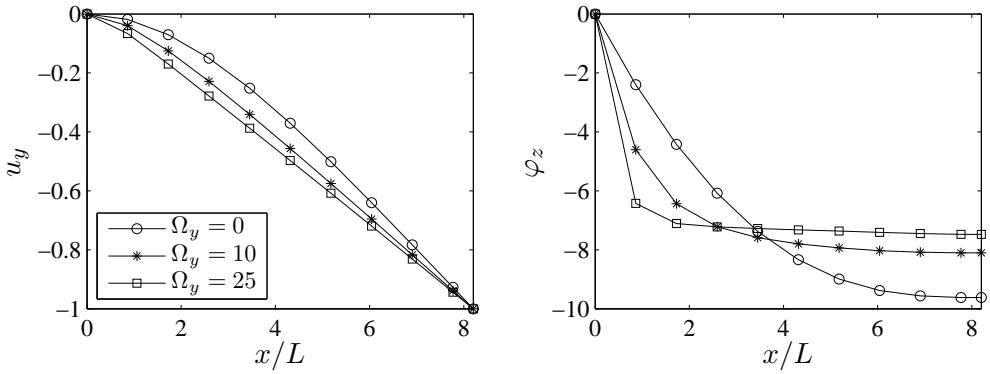
Figure 2: Mode 1: a) Transverse nodal displacements, b) Cross-section rotations.

The controller is an active strut located between the first and second node from the clamped beam end. The $\{y, z\}$-coordinates at both cross-sections are $\{-d_y, 0\}$, meaning that the controller is located on the beam surface.

Table 1: Mode 1 controller parameters.

Ω_y	ω_1	ω_η	$\nu_n \cdot 10^3$	κ	ζ_η	β_η	α_η	$\zeta_{1,1}$	$\zeta_{1,2}$	$\Delta\zeta_1$
0	2.7282	2.7266	0.178	1.9906	0.1308	0.0280	0.0297	0.0612	0.0609	0.0003
5	6.0250	6.2728	0.236	4.6415	0.1463	0.0261	0.0297	0.0618	0.0601	0.0017
10	10.885	11.665	0.316	6.3888	0.1575	0.0249	0.0297	0.0622	0.0593	0.0029
15	15.848	17.413	0.372	7.8182	0.1672	0.0241	0.0297	0.0624	0.0592	0.0032
20	20.831	23.605	0.405	9.4895	0.1794	0.0231	0.0297	0.0626	0.0592	0.0034
25	25.822	30.455	0.425	11.508	0.1955	0.0221	0.0297	0.0628	0.0593	0.0035

The controller is tuned at various angular velocities Ω_y using updated modal properties and a desired additional damping $\zeta_{des} = 0.06$. When the tuned controller is applied the targeted mode splits into two closely spaced modes. When the tuning is optimal the two new modes have identical damping ratios $\zeta_{n,1}$ and $\zeta_{n,2}$. It is seen from Table 1 that the modal connectivity factor ν_n increases with Ω_y. This is due to the increased difference in cross-section rotations at node 1 and 2 as seen in Fig. 2b. However, the modal quasi-static flexibility factor κ_n also increases, indicat-

ing increased interference from other modes. Consequently, the controller tuning becomes less efficient, as indicated by the increase in $\Delta\zeta_1 = \zeta_{1,1} - \zeta_{1,2}$.
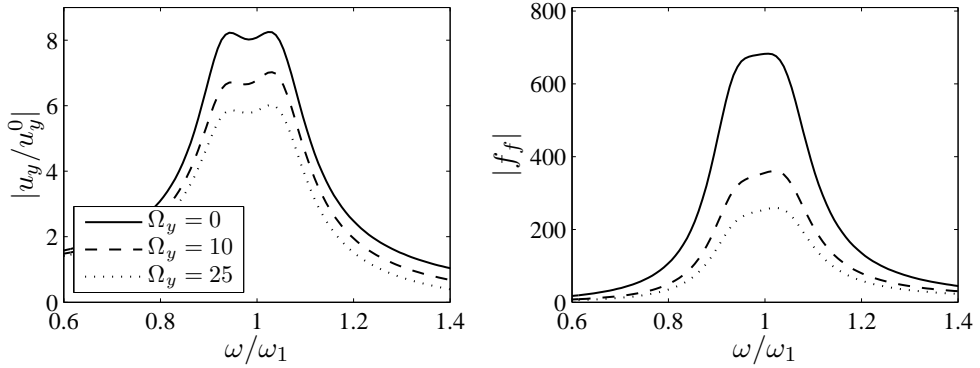
Figure 3: Frequency loading of free beam end: a) Displacement of beam end, b) Controller force.

In Fig. 3a the controlled frequency response to a unit load at the beam end is plotted for various angular velocities. The increasing effect of modal interference is clear, as the two resonant peaks are almost perfectly equal at $\Omega_y = 0$, while a slight loss of symmetry is seen for $\Omega_y > 0$. The controller force frequency response is seen in Fig. 3b. It is seen that controller effort is reduced with increasing angular velocity, corresponding to the observed increase in modal connectivity ν_n.

Concluding remarks

The tuning procedure from [2, 3] for an active resonant controller has been investigated for an active strut with acceleration feedback applied to a rotating beam under different angular velocities. In the present case the tuning procedure has been found to be quite robust, as it provides close to optimal tuning in all cases. The implication is that an active controller of the present type can be applied to machinery facing various operation conditions, if continuous change of controller parameters can be realized.

References

[1] J. Ormondroyd, J. P. den Hartog, The theory of the dynamic vibration absorber, *Trans. ASME*, **50**, 9–22 (1928).

[2] S. Krenk, J. Høgsberg, Optimal resonant control of flexible structures, *Journal of Sound and Vibration*, **323**, 530–554, (2009).

[3] S. Krenk, J. Høgsberg, Resonant damping of flexible structures, *COMPDYN 2009*, Rhodes (2009).

[4] A. Preumont, B. de Marneffe, A. Deraemaeker, F. Bossens, The damping of a truss structure with a piezoelectric transducer, *Computers & Structures*, **86**, 227–239, (2008).

[5] Y. A. Khulief, Vibration suppression in rotating beams using active modal control, *Journal of Sound and Vibration*, **242**, 681–699, (2001).

[6] L. G. Maqueda, O. A. Bauchau, A. A. Shabana, Effect of the centrifugal forces on the finite element eigenvalue solution of a rotating blade: A comparative study, *Multibody System Dynamics*, **19**, 281–302, (2008).

A numerical study of the aerodynamic admittance of bridge sections

Mads Mølholm Hejlesen[*1] **and Johannes Tophøj Rasmussen**[1]

[1]Department of Mechanical Engineering
Technical University of Denmark, Lyngby, Denmark
e–mail: s061937@student.dtu.dk and jtra@mek.dtu.dk

Jens Honoré Walther[1,2] **and Allan Larsen**[3]

[2]Computational Science and Engineering Laboratory, ETH Zürich, Switzerland
e–mail: walther@inf.ethz.ch
[3]COWI Consulting Engineers and Planners A/S, Lyngby, Denmark

Summary   Presented is a discrete vortex method of a turbulent oncoming flow with application to bluff body aerodynamics. The method is implemented in the DVMFLOW flow solver, enabling extended spectral analysis of the aerodynamic admittance used in bridge aerodynamics. A validation against thin airfoil theory and experimental results is provided. The numerical method provides a good agreement to experimental results, and captures significant aerodynamic effects such as vortex shedding and the effect of turbulence.

Introduction

Since the original Tacoma Narrows bridge collapsed in 1940 the study of bridge aerodynamics has been subject to intense research, and many resources is normally used conducting extensive wind tunnel tests in order to prevent a similar failure, when designing a new bridge. The main parameters when analyzing the aerodynamics of a bridge are the influence of static, periodic and random forces acting on the bridge i.e. the effect of steady wind, vortex shedding and turbulence in the oncoming wind.

Methods to derive the steady wind and vortex shedding parameters have been successfully applied in both wind tunnel tests and numerical computational calculations [6], however methods to investigate the effect of the turbulence are still of great interest.

The aerodynamic admittance function relates the turbulent oncoming wind and the resulting buffeting aerodynamic forces acting on the bridge. It has been well established that the aerodynamic admittance function vary significantly between different bridge designs, and the thin airfoil theory is due to non-negligible separation, inapplicable from a physical viewpoint.

The mesh free and re-meshed particle vortex method [5, 8, 10] is widely used in academia and industry to model two-dimensional flow past bluff bodies. The two-dimensional implementation DVMFLOW [10] is used by the bridge design company COWI to determine steady flow parameters and visualize the flow field around bridge sections. Presented in this paper is an implementation of turbulence in the oncoming flow into DVMFLOW, together with an extensive spectral analysis, enabling an improved aerodynamic analysis capturing the effect of turbulence.

In this paper the method is tested on a thin pate and two different bridge sections seen in figure 1. The results are validated against thin airfoil theory and experimental data.

(a) Thin plate   (b) Øresund bridge   (c) Busan-Geoje bridge
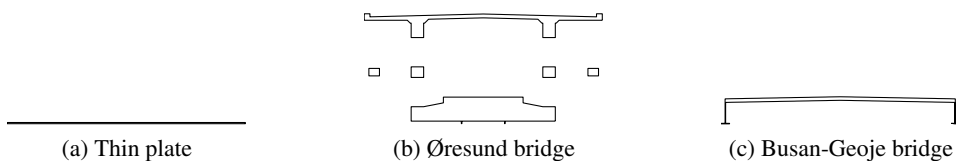
Figure 1: The three sections investigated.

Numeric method

The discrete vortex method

DVMFLOW applies a Lagrangian formulation to a two-dimensional discrete vortex method in order to form and develop a flow, consisting of vorticity particles. The fluid velocity is computed effectively using the adaptive Fast Multipole Method (FMM) [1]. To define the boundary conditions of the solid body a boundary element method is used to enforce a non slip boundary condition, and thereby creating surface circulation that is allowed to diffuse into the flow, forming the fluid boundary layer. To calculate the aerodynamic forces acting on the section a finite difference method is used calculating the total momentum of the particle cloud.

Turbulence modeling

To implement the unsteady oncoming flow, the turbulence is modeled as turbulent eddies moving freely as interacting vorticity particles. The resulting velocity signal induced by the particles represents the velocity fluctuations experienced by the section.

The oncoming turbulent flow is modeled using the statistical method proposed by [2]. The turbulent velocity field is generated from the velocity spectra [3] and the coherence function [4] defining the spatial correlations of the flow. The spectral representation of the velocity field is then Fourier transformed into a discrete time progressing vector field, and transformed into vortex particles carrying the circulation defined by the generated turbulent velocity field.

Simulation parameters

The simulations was performed at a Reynolds number $\frac{Uc}{\nu}$ of 10^4. The frequencies f of the velocity spectra is discretized using 4096 discrete frequencies with an upper and lower cut-off frequency of 5 83 and 1 42$10^{-3}$ reduced frequencies $k = \frac{fc}{U}$, respectively. Frequencies beyond this are considered to have negligible energy. This provides an adequate resolution and a turbulence intensity close to that, which is desired.

Spectral analysis

To create the spectra needed for the spectral analysis, Fourier transformation with basic signal processing techniques is used on the sampled force and velocity signals. The time signals are divided into subsamples with 50% overlap, and a Hanning window function is applied to each of the subsamples, to reduce the spectral leakage of the Fourier transform. After the Fourier transform, the spectra of the subsamples are averaged to create a reinforced spectra with less noise.

Aerodynamic admittance function

The aerodynamic admittance functions $_L(k)^2$ for lift and $_M(k)^2$ for pitching moment [9] is defined by the relations of the force spectrum for lift S_L or pitching moment S_M and the velocity spectra S_{uu} and S_{ww} normalized by the static coefficients C_L and C_M, and their the slope of lift or moment. is the density of the air, U the horizontal mean velocity and c the chord length.

$$_L(k)^2 = \frac{S_L(k)}{\left(\frac{1}{2}\ Uc\right)^2 \left[4C_L^2 S_{uu}(k) + \left(\frac{dC_L}{d\alpha} + C_D\right)^2 S_{ww}(k)\right]} \tag{1}$$

$$_M(k)^2 = \frac{S_M(k)}{\left(\frac{1}{2}\ Uc^2\right)^2 \left[4C_M^2 S_{uu}(k) + \left(\frac{dC_M}{d\alpha}\right)^2 S_{ww}(k)\right]} \tag{2}$$

Results

Velocity spectra

A validation of the method by simulating the turbulent flow past a flat plate Seen in figure 2 is the two spectra of the velocity components sampled in the simulation compared to the modified von Kármán spectra of [3] which are chosen as the predefined velocity spectra.
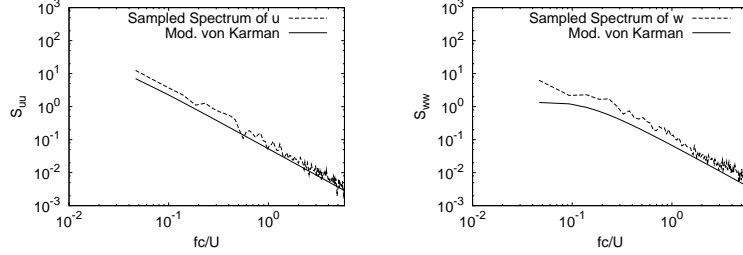
Figure 2: The simulated velocity spectra for the flow past Øresund bridge at a turbulence intensity of 5%. Sampled 6 chord lengths upstream of the bridge section

The sampled spectra of figure 2 correspond well to the input target spectra with slightly higher values at the lower frequencies. Further analysis shows that the velocity spectra is consistent and only varies spatially, when affected by the presence of a bridge. The velocity spectra is affected by numerical parameters such as the number of discrete frequencies and the width of the released particle cloud, whereas these parameters are selected sufficiently high to create converged spectra.

Aerodynamic admittance

The simulated aerodynamic admittance functions of the three sections are shown in figure 3.

(a) Lift Admittance - Thin plate

(b) Lift Admittance - Øresund

(c) Lift Admittance - Busan-Geoje

(d) Pitch Admittance - Thin plate

(e) Pitch Admittance - Øresund

(f) Pitch Admittance - Busan-Geoje
(no experimental data available)
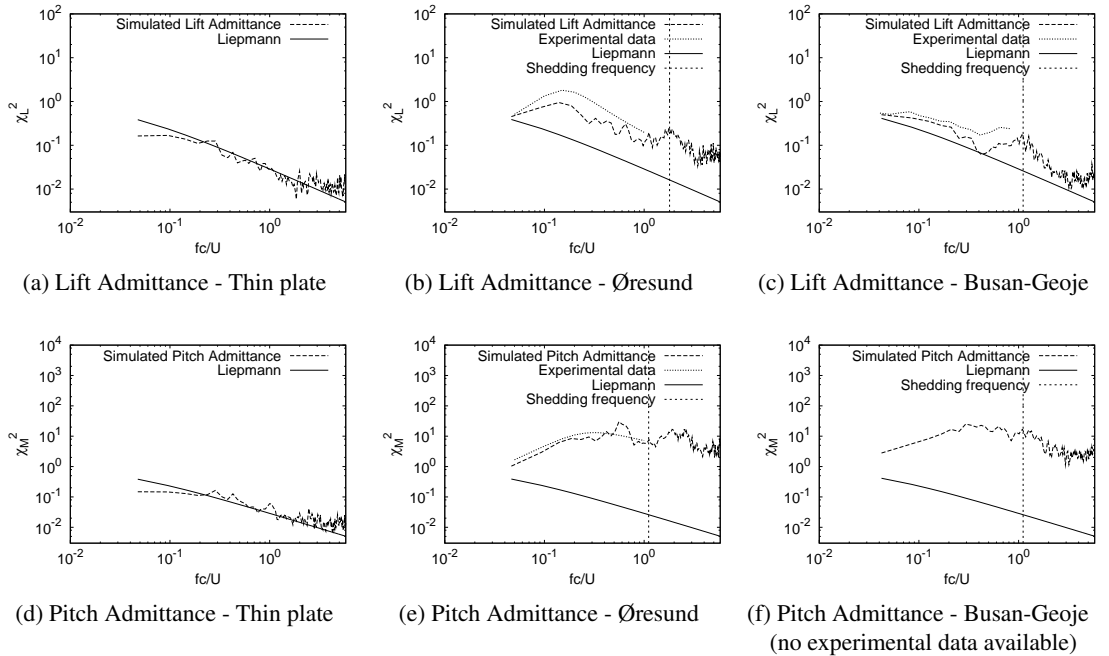
Figure 3: Admittance of the three sections at a turbulence intensity of 5%.

The aerodynamic admittance functions obtained by the simulation agrees well to the experimental data as well as the thin airfoil theory presented by Liepmann's approximation of the Sears function [7]. The thin plate shows no significant deviation from the Liepmann approximation whereas the bridge sections reveals a higher sensitivity towards turbulence especially regarding the pitching moment.

It is seen that the simulation provides results over a far wider frequency range than possible in wind tunnel tests, which suffers from restrictions regarding equipment. The wider frequency range reveals more information about aerodynamic characteristics of the section and enables an estimation of the vortex shedding frequency, as it is seen mainly in figure 3b and 3c. A study of different turbulence intensities can then be used to investigate the effect that turbulence has on other aerodynamic parameters, such as vortex shedding and the aerodynamic stability of the bridge section.

Concluding remarks

Presented is a method of implementation of a turbulent oncoming flow in DVMFLOW to derive the aerodynamic admittance of bridge sections. The method is tested on a thin plate and two bridge sections, which is validated against the theory of an infinitely thin plate, and experimental results of wind tunnel tests of the bridge sections, respectively. The method is also found useful to investigate other aerodynamic parameters, providing results where the effect of the turbulence is added.

Finally, the parameters of the simulation is easily adjusted so that many different scenarios can be investigated without extensive modifications, making the method a valuable tool when designing a bridge.

References

[1] J. Carrier, L. Greengard, and V. Rokhlin. A fast adaptive multipole algorithm for particle simulations. *SIAM Journal on Scientific and Statistical Computing*, 9:669, 1988.

[2] M. Di Paola. Digital simulation of wind field velocity. *Journal of Wind Engineering & Industrial Aerodynamics*, 74:91–109, 1998.

[3] ESDU. Characteristic of atmospheric turbulence near the ground, part II: single point data for strong winds (neutral atmosphere). Tech. Rep. 85020, 1993.

[4] G. K. Batchelor. *The theory of homogeneous turbulence*. Cambridge University press, 1953.

[5] P. Koumoutsakos and A. Leonard. High-resolution simulations of the flow around an impulsively started cylinder using vortex methods. *Journal of Fluid Mechanics*, 296:1–38, 1995.

[6] A. Larsen and J.H. Walther. Discrete vortex simulation of flow around five generic bridge deck sections. *Journal of Wind Engineering & Industrial Aerodynamics*, 77:591–602, 1998.

[7] H.W. Liepmann. On the application of statistical concepts to the buffeting problem. *Journal of the Aeronautical Sciences*, 19:793–800, 1952.

[8] G. Morgenthal and JH Walther. An immersed interface method for the Vortex-In-Cell algorithm. *Computers and Structures*, 85(11-14):712–726, 2007.

[9] RH Scanlan and NP Jones. A form of aerodynamic admittance for use in bridge aeroelastic analysis. *Journal of Fluids and Structures*, 13(7-8):1017–1027, 1999.

[10] J.H. Walther and A. Larsen. Two dimensional discrete vortex method for application to bluff body aerodynamics. *Journal of Wind Engineering & Industrial Aerodynamics*, 67:183–193, 1997.

Analytical results for wave propagation in compliant vessels

Leif Rune Hellevik
Department of Structural Engineering
Norwegian University of Science and Technology, Trondheim, Norway
Center for Biomedical Computing at Simula Research Laboratory, Lysaker, Norway
e–mail: leif.r.hellevik@ntnu.no

Summary   In this paper we revisit the Womersley-theory, and present a 1D approach for analytical estimates of the pulse wave velocity and the damping factor, which both may be useful for validation of FSI-codes.

Introduction

The development of reliable and stable fluid-structure interaction (FSI) solvers has been an important area of research in the recent years. FSI solvers may be applied in a wide range of disciplines e.g. [1, 5] as well as biomechanics [2]. In this contribution we revisit the Womersley theory and present a 1D-approach, which both predict a frequency dependent pulse wave velocity (pwv) and damping factor. These predictions may prove useful for validation of FSI-codes.

Methods

1D approximations   Following the lines of derivation in [3] the governing equations for one-dimensional wave propagation for incompressible fluids in compliant vessels may presented:

$$\frac{\partial A}{\partial t} + \frac{\partial Q}{\partial z} = 0 \tag{1a}$$

$$\frac{\partial Q}{\partial t} + (1+\delta)\frac{\partial}{\partial z}\left(\frac{Q^2}{A}\right) = -\frac{A}{\rho}\frac{\partial p}{\partial z} + A\,b_z + \frac{\pi D}{\rho A}\,\tau_w \tag{1b}$$

where the primary variables are cross-sectional area A, volume flow rate Q, ρ fluid density, and pressure p, whereas D is vessel diameter and δ a velocity-profile correction parameter. By introducing the compliance of the vessel as $C = \partial A/\partial p$, and disregarding body forces b_z, wall shear stress τ_w and the nonlinear convective term in equation (1b), one may find an expression for the pulse wave velocity by cross-derivation and subtraction:

$$c_0^2 = \frac{dp}{dA}\frac{A}{\rho} = \frac{1}{C}\frac{A}{\rho} = \frac{\eta\,h}{2\rho\,r_i} \tag{2}$$

The latter expression, commonly referred to as the Moens-Korteweg equation, follow by assuming a thin-walled Hookean structure, for which one may show $1/C = \eta h/2Ar_i$. To estimate τ_w, the velocity profile for fully developed straight pipe flow is employed [4]:

$$\hat{v}_z(r) = \frac{i}{\rho\omega}\frac{\partial \hat{p}}{\partial z}\left[1 - \frac{J_0(i^{3/2}\alpha r/r_i)}{J_0(i^{3/2}\alpha)}\right] \tag{3}$$

where J_0 is a Bessel-function of first kind, order zero. An approximation for the wall shear stress may be found by differentiation of equation (3):

$$\tau_w = -\frac{r_i}{2}F_{10}(\alpha)\frac{\partial p}{\partial z} \quad \text{and} \quad \tau_w = \mu\frac{\partial v_z}{\partial r} \tag{4}$$

where we have introduced the Womersley function:

$$F_{10}(\alpha) = \frac{2J_1(i^{3/2}\alpha)}{\alpha i^{3/2}\,J_0(i^{3/2}\,\alpha)} \tag{5}$$

Equation (4) may be substituted into the linearized form of equation (1), without body forces. Proposition of solutions of equation (1) on the form $Q = \hat{Q}\,e^{i(\omega t - kz)}$ and $\hat{A} = C\hat{p}$ yields:

$$\begin{bmatrix} i\omega C & -ik \\ \frac{-ik(1-F_{10})A_0}{\rho} & i\omega \end{bmatrix}\begin{bmatrix} \hat{p} \\ \hat{Q} \end{bmatrix} = 0 \tag{6}$$

which has non-trivial solutions if:

$$k\,c_0 = \pm\omega\,\sqrt{\frac{1}{1-F_{10}}} \quad \text{with} \quad k = \frac{\omega}{c} - i\frac{\gamma}{\lambda} = k_r + ik_i \tag{7}$$

The complex propagation factor k is related with the *pwv* c and the damping factor γ as given by equation (7) and thus:

$$\frac{c}{c_0} = \frac{\omega}{k_r c_0} = \pm\Re\left(\frac{1}{\sqrt{1/(1/F_{10})}}\right) \quad \text{and} \quad \gamma = -2\pi\frac{k_i}{k_r} \tag{8}$$

Axi-symmetric solution The following derivation is based the seminal report of Womersley [4].

The fluid

The momentum equations for a Newtonian fluid without convective terms, assuming axi-symmetric flow conditions may be presented:

$$\frac{\partial v_z}{\partial t} = -\frac{1}{\rho}\frac{\partial p}{\partial z} + \nu\left(\frac{\partial^2 v_z}{\partial r^2} + \frac{1}{r}\frac{\partial v_z}{\partial r}\right) \tag{9a}$$

$$\frac{\partial v_r}{\partial t} = -\frac{1}{\rho}\frac{\partial p}{\partial r} + \nu\left(\frac{1}{r}\frac{\partial}{\partial r}\left(r\frac{\partial v_r}{\partial r}\right)\right) \tag{9b}$$

The equation for conservation of mass takes the form in cylindrical coordinates:

$$\frac{\partial v_r}{\partial r} + \frac{v_r}{r} + \frac{\partial v_z}{\partial z} = 0 \tag{10}$$

Assume solutions on the form[1]:

$$p = \hat{p}e^{i\omega\,(t-z/c)}, \quad v_z = \hat{v}_z e^{i\omega\,(t-z/c)}, \quad v_r = \hat{v}_r e^{i\omega\,(t-z/c)} \tag{11}$$

Introduce the nondimensional scale $s = i^{3/2}\,\alpha\,y$, where $y = r/r_i$ and the Womersley parameter $\alpha = r_i\sqrt{\omega/\nu}$. The general solutions may be found, after some algebra, to be:

$$\hat{v}_z = \frac{C}{J_0(i^{3/2}\alpha)}\,J_0(s) + \frac{A}{\rho c\,(1-k^2)}\,J_0(ks) \approx \frac{C}{J_0(i^{3/2}\alpha)}\,J_0(i^{3/2}\alpha\,y) + \frac{A}{\rho c} \tag{12a}$$

$$\hat{v}_r = \frac{Cir_i\omega\,J_1(s)}{i^{3/2}\alpha c\,J_0(i^{3/2}\alpha)} + \frac{r_i A}{\mu i^{3/2}\alpha}\frac{k}{k^2-1}\,J_1(ks) \approx \frac{ir_i\omega}{2c}\left(\frac{2C\,J_1(i^{3/2}\alpha\,y)}{\alpha i^{3/2}J_0(i^{3/2}\alpha)} + \frac{A}{\rho c}y\right) \tag{12b}$$

by assuming $|k| \ll 1$[2]. The constants, denoted A and C, will be determined in the following. Further, by imposing continuity:

$$ks = \mp\frac{ir_i\omega}{c}y = \mp\frac{i\omega}{c}r \tag{13}$$

In order to match the solutions of the structure and the fluid (kinematic condition), it is convenient to provide expressions for the solutions of the fluid given in equation (12) at the vessel wall:

$$\hat{v}_z\Big|_{y=1} = C + \frac{A}{\rho c} \tag{14}$$

$$\hat{v}_r\Big|_{y=1} = \frac{ir_i\omega}{2c}\left(CF_{10}(\alpha) + \frac{A}{\rho c}\right) \tag{15}$$

For the evaluation of the wall shear stress the following can be found:

$$\frac{\partial \hat{v}_z}{\partial y}\Big|_{y=1} = -\frac{C}{2}i^3\alpha^2 F_{10}(\alpha) + \frac{1}{2}\left(\frac{\omega r_i}{c}\right)^2\frac{A}{\rho c} \tag{16}$$

---

[1]Note: This assumption will yield a complex c

[2]Note that here and in the sequel k has *not* the meaning as in equation (7).

84

The structure

The fundamental Cauchy equations in continuum mechanics: $\rho\,\mathbf{a} = \nabla\cdot\boldsymbol{\sigma} + \rho\,\mathbf{b}$, may be averaged over the over the cross-sectional area of a thin-walled structure to yield:

$$\rho_w\,a_z\,h = \frac{\partial\sigma_z}{\partial z}\,h + \tau_w \quad\text{and}\quad \rho_w\,a_r h = p - \frac{\sigma_\theta\,h}{r_i} \tag{17}$$

when body forces are neglected. Assuming a thin-walled vessel (i.e. plane stress) the constitutive equation for a thin walled vessel of a Hookean material, takes the form in cylindrical coordinates[3], and η for the Young's modulus and ν_p for the Poisson's ratio:

$$\sigma_z = \frac{\eta}{1-\nu_p^2}\left(\frac{\partial u_z}{\partial z} + \nu_p\frac{u_r}{r}\right) \quad\text{and}\quad \sigma_\theta = \frac{\eta}{1-\nu_p^2}\left(\frac{u_r}{r} + \nu_p\frac{\partial u_z}{\partial z}\right) \tag{18}$$

By assuming $a_z = \partial^2 u_z/\partial t^2$ and $a_r = \partial^2 u_r/\partial t^2$, i.e. neglecting convective terms, the averaged governing equations for a thin walled vessel may be obtained by substitution of equation (18) into (17):

$$\frac{\partial^2 u_z}{\partial t^2} = \frac{\eta}{(1-\nu_p^2)\rho_w}\left(\frac{\partial^2 u_z}{\partial z^2} + \frac{\nu_p}{r}\frac{\partial u_r}{\partial z}\right) + \frac{\tau_w}{\rho_w\,h} \tag{19a}$$

$$\frac{\partial^2 u_r}{\partial t^2} = \frac{p}{\rho_w\,h} - \frac{\eta}{(1-\nu_p^2)\,\rho_w}\left(\frac{u_r}{r^2} + \frac{\nu_p}{r}\frac{\partial u_z}{\partial z}\right) \tag{19b}$$

Assume solutions of the governing equations (19) for the vessel wall on the form:

$$u_r = De^{i\omega(t-z/c)} \quad\text{and}\quad u_z = Ee^{i\omega(t-z/c)} \tag{20}$$

where D and E are constants. Kinematic condition:

$$\frac{\partial u_z}{\partial t} = \hat{v}_z\Big|_{y=1} e^{i\omega(t-z/c)} \quad\text{and}\quad \frac{\partial u_r}{\partial t} = \hat{v}_r\Big|_{y=1} e^{i\omega(t-z/c)} \tag{21}$$

Fulfilment equation (21) of along with substitution of equations (20) into the governing equations (19) for the vessel wall yields:

$$\begin{bmatrix} \dfrac{1}{\rho\,c} & 1 & 0 & -i\omega \\[2mm] \dfrac{i\omega\,r_i}{2\rho\,c^2} & \dfrac{i\omega\,r_i}{2c}F_{10} & -i\omega & 0 \\[2mm] \dfrac{1}{\rho_w h} & 0 & \omega^2 - \dfrac{B}{\rho_w r_i^2} & \dfrac{iB\omega\,\nu_p}{\rho_w r_i c} \\[2mm] \dfrac{\rho}{\rho_w}\dfrac{\nu}{2r_i h}\left(\dfrac{\omega r_i}{c}\right)^2\dfrac{1}{\rho c} & -\dfrac{i\rho\,\omega\,r_i F_{10}}{2\rho_w h} & \dfrac{-iB\omega\,\nu_p}{\rho_w r_i c} & \omega^2\left(1-\dfrac{B}{\rho_w c^2}\right) \end{bmatrix} \begin{bmatrix} A \\ C \\ D \\ E \end{bmatrix} = 0 \tag{22}$$

Non-trivial solutions when:

$$\det(\mathbf{M}) = (1-F_{10})(1-\nu_p^2)\,x^2 - \left(k(1-F_{10}) + F_{10}\,(1/2 - 2\nu_p) + 2\right)\,x + F_{10} + 2k = 0 \tag{23}$$

which is a simple second order nonlinear equation with solution:

$$x = k\frac{\eta}{1-\nu_p^2}\frac{1}{\rho_w}\frac{1}{c^2} = \frac{h}{\rho r_i}\frac{\eta}{1-\nu_p^2}\frac{1}{c^2} \tag{24}$$

By substitution of the expression for c_0 in equation (2) in equation (24) and rearrangement we get as $c = c_r + ic_i$:

$$\frac{c}{c_0} = \left(\frac{(1-\nu_p^2)\,x}{2}\right)^{-1/2} \quad\text{and}\quad \frac{c_r}{c_0} = \Re\left(\frac{c}{c_0}\right) \quad\text{and}\quad \gamma = 2\pi\frac{c_i}{c_r} \tag{25}$$

---

[3]Engineering notation for stresses.

Results and discussion

In figure 1 the pulse wave predictions of the 1D approach are compared with the classical predictions of Womersley. Both approaches predict gross features of the c/c_0 dependency of the Womersley parameter α and the damping factor γ as a function of α. As most biological tissues are considered to be close to incompressible, the predictions with Poisson's ratio $\nu_p = 0.5$ are likely of most physiological relevance. The 1D-predictions were observed to under-estimate the c/c_0 ratio (for $\nu_p = $

(a) c/c_0 in lower α-range   (b) c/c_0 with log-scale for α

(c) γ in lower α-range   (d) γ with log-scale for α
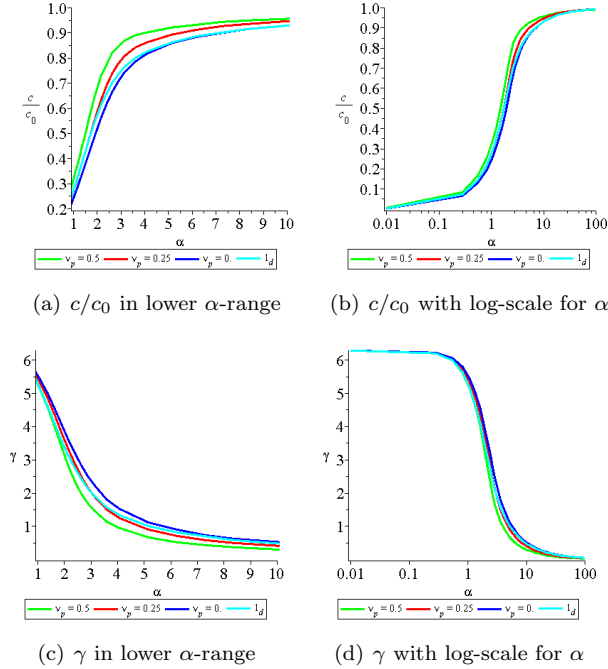
Figure 1: Pulse wave velocities for various Poisson's ratios ν_p and for 1D estimate.

0.5) consistently over the whole α-range. The relative error decrease monotonously with increasing α: from approximately 17% for $\alpha = 2$ to approximately 2.1 % for $\alpha = 10$. For high frequencies, the c/c_0-ration were found to approach 1. The opposite behavior is observed for the damping factor γ which has a relative over-prediction for the 1D-approach at $\alpha = 2$ of approximately 8%, whereas it is approximately 60% for $\alpha = 10$. In conclusion, both Womersley-theory for axi-symmetric flows, and the 1D approach in the present paper provide analytical estimates of the pwv and the damping factor in compliant vessels, which may be useful for validation of FSI-codes.

References

[1] C Farhat. CFD-based nonlinear computational aeroelasticity. In Hughes TJR Stein E, De Borst R, editor, *Encyclopedia of Computational mechanics*, volume 3, chapter 13. Wiley, NY, 2004.

[2] J-F Gerbeau, M Vidrascu, and P Frey. Fluid-structure interaction in blood flows on geometries coming from medical imaging. *Comput Struct*, 83:155–165, 2005.

[3] Thomas J. R. Hughes and J. Lubliner. On the one-dimensional theory of blood flow in the larger vessels. *Mathematical Biosciences*, 18:161–170, 1973.

[4] J.R. Womersley. An elastic tube theory of pulse transmission and oscillatory flow in mammalian arteries. Technical Report WADC Technical Report TR 56-614, Wright Air Development Center, Wright Patterson Air Force Base, Ohio, 1957.

[5] R Wüchner, A Kupzok, and Bletzinger K-U. A framework for stabilized partitioned analysis of thin membrane-wind interaction. *Int J Numer Methods Fluids*, 54:6–8, 2007.

The stability of finite-difference scheme for two-dimensional parabolic equation with nonlocal integral conditions

Svajūnas Sajavičius

Department of Computer Science II
Vilnius University, Vilnius, Lithuania
e–mail: svajunas.sajavicius@mif.vu.lt

Summary   We construct and analyse an alternating direction implicit method for a two-dimensional parabolic equation with nonlocal integral conditions. The main attention is paid to the stability of the method. We demonstrate that depending on the parameters of nonlocal conditions the proposed method can be stable or unstable. The results of numerical experiments with several test problems are also presented and they validate theoretical results.

Introduction

We consider the two-dimensional parabolic equation

$$\frac{\partial u}{\partial t} = \frac{\partial^2 u}{\partial x^2} + \frac{\partial^2 u}{\partial y^2} + f(x, y, t), \quad 0 < x < 1, \quad 0 < y < 1, \quad 0 < t \leqslant T, \tag{1}$$

subject to nonlocal integral conditions

$$u(0, y, t) = \gamma_0 \int_0^1 \alpha(x) u(x, y, t) \mathrm{d}x + \mu_1(y, t), \tag{2}$$

$$u(1, y, t) = \gamma_1 \int_0^1 \beta(x) u(x, y, t) \mathrm{d}x + \mu_2(y, t), \quad 0 < y < 1, \quad 0 < t \leqslant T, \tag{3}$$

boundary conditions

$$u(x, 0, t) = \mu_3(x, t), \quad u(x, 1, t) = \mu_4(x, t), \quad 0 < x < 1, \quad 0 < t \leqslant T, \tag{4}$$

and initial condition

$$u(x, y, 0) = \varphi(x, y), \quad 0 \leqslant x \leqslant 1, \quad 0 \leqslant y \leqslant 1, \tag{5}$$

where $f(x, y, t)$, $\mu_1(y, t)$, $\mu_2(y, t)$, $\mu_3(x, t)$, $\mu_4(x, t)$, $\alpha(x)$, $\beta(x)$, $\varphi(x, y)$ are given functions, γ_0, γ_1 are given parameters, and $u(x, y, t)$ is an unknown function.

The stability of implicit and explicit finite-difference schemes for a corresponding one-dimensional parabolic problem with nonlocal integral conditions is investigated in paper [1]. In that paper, the differential problem (1)–(5) is formulated as the example of problem for the possible extension of the proposed stability analysis technique.

The present work is devoted to the alternating direction implicit (ADI) method for the two-dimensional differential problem (1)–(5). Various ADI methods for two-dimensional parabolic problems with nonlocal integral condition (the specification of mass/energy) have been investigated by M. Dehghan (see [2] and references therein). Paper [3] deals with the ADI method for the two-dimensional parabolic equation (1) with Bitsadze-Samarskii type nonlocal boundary condition. We use the technique and argument of paper [3] in order to construct the ADI method for the differential problem (1)–(5) and to investigate the stability of this method.

The alternating direction method

To solve the two-dimensional differential problem (1)–(5) numerically, we apply the finite-difference technique and use the idea of alternating direction [4]. Let us define discrete grids with uniforms steps,

$$\omega_x^h = \{x_i = ih_1, i = 1, 2, \ldots, N_1 - 1, N_1 h_1 = 1\},$$
$$\omega_y^h = \{y_j = jh_2, j = 1, 2, \ldots, N_2 - 1, N_2 h_2 = 1\},$$
$$\omega^\tau = \{t^n = n\tau, n = 1, 2, \ldots, M, M\tau = T\},$$
$$\overline{\omega}_x^h = \omega_x^h \cup \{x_0 = 0, x_{N_1} = 1\}, \quad \overline{\omega}_y^h = \omega_y^h \cup \{y_0 = 0, y_{N_2} = 1\},$$
$$\overline{\omega}^\tau = \omega^\tau \cup \{t^0 = 0\}, \quad \omega = \omega_x^h \times \omega_y^h, \quad \overline{\omega} = \overline{\omega}_x^h \times \overline{\omega}_y^h.$$

We use the notation $U_{ij}^n = U(x_i, y_j, t^n)$ for functions defined on the grid $\overline{\omega} \times \overline{\omega}^\tau$ or its parts, and the notation $U_{ij}^{n+1/2} = U(x_i, y_j, t^n + 0.5\tau)$ (some of the indices can be omitted).

Now we explain the main steps of the ADI method for numerical solution of problem (1)–(5). First of all, we replace the initial condition (5) by equations

$$U_{ij}^0 = \varphi_{ij}, \quad (x_i, y_j) \in \overline{\omega}. \tag{6}$$

Then, for any n, $0 \leqslant n < M - 1$, the transition from the nth layer of time to the $(n+1)$th layer can be executed by solving two one-dimensional finite-difference subproblems:

1. For each $x_i \in \omega_x^h$, solve system

$$\begin{cases} \dfrac{U_{ij}^{n+1/2} - U_{ij}^n}{0.5\tau} = \delta_x^2 U_{ij}^n + \delta_y^2 U_{ij}^{n+1/2} + f_{ij}^{n+1/2}, & y_j \in \omega_y^h, \\ U_{i0}^{n+1/2} = (\mu_3)_i^{n+1/2}, \quad U_{iN_2}^{n+1/2} = (\mu_4)_i^{n+1/2}; \end{cases} \tag{7}$$

2. For each $y_j \in \omega_y^h$, solve system

$$\begin{cases} \dfrac{U_{ij}^{n+1} - U_{ij}^{n+1/2}}{0.5\tau} = \delta_x^2 U_{ij}^{n+1} + \delta_y^2 U_{ij}^{n+1/2} + f_{ij}^{n+1}, & x_i \in \omega_x^h, \\ U_{0j}^{n+1} = \gamma_0(\alpha, U)_j^{n+1} + (\mu_1)_j^{n+1}, \\ U_{N_1j}^{n+1} = \gamma_1(\beta, U)_j^{n+1} + (\mu_2)_j^{n+1}; \end{cases} \tag{8}$$

where

$$\delta_x^2 U_{ij} = \frac{U_{i-1,j} - 2U_{ij} + U_{i+1,j}}{h_1^2}, \quad \delta_y^2 U_{ij} = \frac{U_{i,j-1} - 2U_{ij} + U_{i,j+1}}{h_2^2},$$

$$(\alpha, U)_j^{n+1} = h_1\left(\frac{\alpha_0 U_{0j}^{n+1} + \alpha_{N_1} U_{N_1j}^{n+1}}{2} + \sum_{i=1}^{N_1-1} \alpha_i U_{ij}^{n+1}\right),$$

$$(\beta, U)_j^{n+1} = h_1\left(\frac{\beta_0 U_{0j}^{n+1} + \beta_{N_1} U_{N_1j}^{n+1}}{2} + \sum_{i=1}^{N_1-1} \beta_i U_{ij}^{n+1}\right).$$

Every transition is finished by calculating

$$U_{i0}^{n+1} = (\mu_3)_i^{n+1}, \quad U_{iN_2}^{n+1} = (\mu_4)_i^{n+1}, \quad x_i \in \overline{\omega}_x^h. \tag{9}$$

Thus, the procedure of numerical solution can be stated as follows:

procedure `The ADI Method`
begin
    Calculate U_{ij}^0, $(x_i, y_j) \in \overline{\omega}$, from Eqs. (6);
    for $n = 0, 1, \ldots, M - 1$
        for each $x_i \in \omega_x^h$
            Solve system (7) and calculate $U_{ij}^{n+1/2}$, $y_j \in \overline{\omega}_y^h$;
        end for
        for each $y_j \in \omega_y^h$
            Solve system (8) and calculate U_{ij}^{n+1}, $x_i \in \overline{\omega}_x^h$;
        end for
        Calculate U_{i0}^{n+1} and $U_{iN_2}^{n+1}$, $x_i \in \overline{\omega}_x^h$, from Eqs. (9);
    end for
end

The difference scheme (7), (8) can be written in the form

$$U^{n+1} = SU^n + \overline{F}^n, \tag{10}$$

where

$$S = \left(E + \frac{\tau}{2}A_1\right)^{-1}\left(E - \frac{\tau}{2}A_2\right)\left(E + \frac{\tau}{2}A_2\right)^{-1}\left(E - \frac{\tau}{2}A_1\right),$$

$\overline{F}^n$ is the vector of dimension $(N_1-1)\cdot(N_2-1)$, E is the identity matrix of order $(N_1-1)\cdot(N_2-1)$, $A_1 = -E_{N_2-1} \otimes \Lambda_1$, $A_2 = -\Lambda_2 \otimes E_{N_1-1}$, E_N is the identity matrix of order N, $A \otimes B$ denotes the Kronecker (tensor) product of matrices A and B,

$$\Lambda_1 = h_1^{-2}\begin{pmatrix} -2 + \gamma_0 h_1 a_1 & 1 + \gamma_0 h_1 a_2 & \gamma_0 h_1 a_3 & \ldots & \gamma_0 h_1 a_{N_1-2} & \gamma_0 h_1 a_{N_1-1} \\ 1 & -2 & 1 & \ldots & 0 & 0 \\ 0 & 1 & -2 & \ldots & 0 & 0 \\ \ldots & \ldots & \ldots & \ldots & \ldots & \ldots \\ 0 & 0 & 0 & \ldots & -2 & 1 \\ \gamma_1 h_1 b_1 & \gamma_1 h_1 b_2 & \gamma_1 h_1 b_3 & \ldots & 1 + \gamma_1 h_1 b_{N_1-2} & -2 + \gamma_1 h_1 b_{N_1-1} \end{pmatrix},$$

$$\Lambda_2 = h_2^{-2}\begin{pmatrix} -2 & 1 & 0 & \ldots & 0 & 0 \\ 1 & -2 & 1 & \ldots & 0 & 0 \\ 0 & 1 & -2 & \ldots & 0 & 0 \\ \ldots & \ldots & \ldots & \ldots & \ldots & \ldots \\ 0 & 0 & 0 & \ldots & -2 & 1 \\ 0 & 0 & 0 & \ldots & 1 & -2 \end{pmatrix}$$

are $(N_1 - 1) \times (N_1 - 1)$ and $(N_2 - 1) \times (N_2 - 1)$ matrices, respectively, and

$$a_i = \frac{1}{D}\left(\alpha_i - \frac{\gamma_1 h_1 \alpha_i \beta_{N_1}}{2} + \frac{\gamma_1 h_1 \alpha_{N_1} \beta_i}{2}\right),$$

$$b_i = \frac{1}{D}\left(\beta_i - \frac{\gamma_0 h_1 \alpha_0 \beta_i}{2} + \frac{\gamma_0 h_1 \alpha_i \beta_0}{2}\right),$$

$$D = \left(1 - \frac{\gamma_0 h_1 \alpha_0}{2}\right)\left(1 - \frac{\gamma_1 h_1 \beta_{N_1}}{2}\right) - \frac{\gamma_0 h_1 \alpha_{N_1}}{2} \cdot \frac{\gamma_1 h_1 \beta_0}{2}.$$

We assume that the grid step h_1 is chosen so that $D > 0$.

Analysis of the stability

A sufficient stability condition for the finite-difference scheme (10) is the inequality

$$\rho(S) = \max |\lambda(S)| < 1,$$

where $\lambda(S)$ is the eigenvalues of S and $\rho(S)$ is the spectral radius of S. To be precise, one can prove that the finite-difference scheme (10) is stable if $(-\Lambda_1)$ is a simple-structured matrix and $\lambda_1^{(i)} \geqslant 0$ or $\mathrm{Re}\lambda_1^{(i)} \geqslant 0$, where $\lambda_1^{(i)}$, $i = 1, 2, \ldots, N_1 - 1$, are real or complex eigenvalues of the matrix $(-\Lambda_1)$. As noted in [3], the finite-difference scheme (10) can be stable even if the matrix $(-\Lambda_1)$ has a negative eigenvalue or a complex eigenvalue with a negative real part.

Numerical experiments

In order to demonstrate the efficiency of the considered ADI method and practically justify the stability analysis technique, several test problems with different types of weight functions $\alpha(x)$ and $\beta(x)$ were solved. We used results related with the structure of the spectrum of the matrix $(-\Lambda_1)$ which were obtained in papers [1, 5], where the corresponding one-dimensional examples have been investigated. In all of our test examples, functions $f(x, y, t), \mu_1(y, t), \mu_2(y, t), \mu_3(x, t),$ $\mu_4(x, t)$ and $\varphi(x, y)$ were chosen so that the function $u(x, y, t) = x^3 + y^3 + t^3$ would be the solution to the differential problem (1)–(5). The ADI method was implemented in a stand-alone software application. However, for the numerical analysis of the spectrum of the matrix S, MATLAB (The MathWorks, Inc.) software package was used.

Numerical experiments with test problems and calculations of the maximum norm of computational errors allow us to estimate the accuracy of the numerical solution. We identify the ranges of the values of parameters γ_0 and γ_1 such that the proposed ADI method is stable. The stability domains are rather wider than the ranges of such the values of γ_0 and γ_1 that all real eigenvalues of the matrix $(-\Lambda_1)$ are non-negative or real parts of complex eigenvalues are non-negative.

Concluding remarks

We developed the ADI method for the two-dimensional parabolic equation with nonlocal integral conditions. Applying quite a simple technique (see, e.g., [1, 3, 5]) allow us to investigate the stability of this method. The technique is based on the analysis of the spectrum of the transition matrix of the finite-difference scheme. The results of numerical experiments with several test problems justify theoretical results. We demonstrate that the proposed ADI method can be stable or unstable depending on the parameters of nonlocal conditions.

References

[1] M. Sapagovas. On the Stability of a Finite-Difference Scheme for Nonlocal Parabolic Boundary-Value Problems. *Lith. Math. J.*, **48**(3), 339–356, (2008).

[2] M. Dehghan. A New ADI Technique for Two-Dimensional Parabolic Equation with an Integral Condition. *Comput. Math. Appl.*, **43**(12), 1477–1488, (2002).

[3] M. Sapagovas, G. Kairytė, O. Štikonienė, A. Štikonas. Alternating Direction Method for a Two-Dimensional Parabolic Equation with a Nonlocal Boundary Condition. *Math. Model. Anal.*, **12**(1), 131–142, (2007).

[4] D. W. Peaceman, H. H. Rachford. The Numerical Solution of Parabolic and Elliptic Equations. *J. Soc. Ind. Appl. Math.*, **3**(1), 28–41, (1955).

[5] M. P. Sapagovas. On Stability of Finite-Difference Schemes for One-Dimensional Parabolic Equations Subject to Integral Condition. *Obchysl. Prykl. Mat.*, **92**, 77–90, (2005).

$H(\mathrm{div})$-conforming Finite Elements for the Brinkman Problem

Juho Könnö* and Rolf Stenberg

Department of Mathematics and Systems Analysis
Helsinki University of Technology, Finland
e–mail: juho.konno@tkk.fi

Summary We study the non-conforming finite element approximation of the Brinkman problem with $H(\mathrm{div})$-conforming elements. Nitsche's method is applied to achieve consistency and stability in the mesh-dependent energy norms introduced. Furthermore, we present a numerically lightweight local postprocessing scheme for the pressure. Using the postprocessed pressure we are able to derive both an efficient and reliable a posteriori error estimator for the problem.

Introduction

We study the application of $H(\mathrm{div})$-conforming finite elements designed for the Darcy problem to the more complicated Brinkman problem. This constitutes a non-conforming approximation of the Brinkman problem. An extensive analysis of various conforming finite element approximations for the Brinkman equations has been recently presented in [1]. To get a stable method, we use the so-called Nitsche's method first introduced in [2], which in turn requires the use of a mesh-dependent bilinear form. The motivation for using a non-conforming approximation lies in the widespread use of $H(\mathrm{div})$-conforming elements in industrial applications for solving the Darcy equations. Thus, we aim at introducing an easy way of incorporating viscosity to the existing models and implementations.

The Brinkman model

The Brinkman model describes the flow of a viscous fluid in a porous medium. Let $\Omega \subset \mathbb{R}^n$, with $n = 2, 3$. Let $\boldsymbol{u}$ be the velocity field of the fluid and p the pore pressure. Denoting by the parameter t the effective viscosity of the fluid, the Brinkman equations are

$$-t^2 \Delta \boldsymbol{u} + \boldsymbol{u} - \nabla p = \boldsymbol{f}, \quad \text{in } \Omega \tag{1}$$

$$\mathrm{div}\, \boldsymbol{u} = g, \quad \text{in } \Omega. \tag{2}$$

For $t > 0$, the equations are formally a Stokes problem. The solution $(\boldsymbol{u}, p)$ is sought in $\boldsymbol{V} \times Q = H^1(\Omega) \times L^2(\Omega)$. For the case $t = 0$ we get the Darcy problem, and accordingly the solution is sought in $\boldsymbol{V} \times Q = H(\mathrm{div}, \Omega) \times L^2(\Omega)$. We define the following bilinear forms

$$a(\boldsymbol{u}, \boldsymbol{v}) = t^2 (\nabla \boldsymbol{u}, \nabla \boldsymbol{v}) + (\boldsymbol{u}, \boldsymbol{v}), \tag{3}$$

$$b(\boldsymbol{v}, p) = (\mathrm{div}\, \boldsymbol{v}, p) \tag{4}$$

and

$$\mathcal{B}(\boldsymbol{u}, p; \boldsymbol{v}, q) = a(\boldsymbol{u}, \boldsymbol{v}) + b(\boldsymbol{v}, p) + b(\boldsymbol{u}, q). \tag{5}$$

The Brinkman problem in the weak formulation then reads: Find $(\boldsymbol{u}, p) \in \boldsymbol{V} \times Q$ such that

$$\mathcal{B}(\boldsymbol{u}, p; \boldsymbol{v}, q) = (\boldsymbol{f}, \boldsymbol{v}) + (g, q), \quad \forall (\boldsymbol{v}, q) \in \boldsymbol{V} \times Q. \tag{6}$$

Mesh dependent norms

Let $\mathcal{K}_h$ be a triangulation of the domain Ω, and $\mathcal{E}_h$ the set of all the edges of $\mathcal{K}_h$. We introduce the following mesh-dependent norms for the problem. Note, that both of the norms are also parameter dependent. We denote the jump in the value of a generic function f on the edge E by $[\![f]\!] = f|_{K_1} - f|_{K_2}$, where $E = \partial K_1 \bigcap \partial K_2$. Similarly, we denote the average on the edge by $\{f\} = \frac{1}{2}(f|_{K_1} + f|_{K_2})$. For the velocity we use the norm

$$\|\boldsymbol{u}\|_{t,h}^2 = \|\boldsymbol{u}\|^2 + t^2 \sum_{K \in \mathcal{K}_h} \|\nabla \boldsymbol{u}\|_{0,K}^2 + t^2 \sum_{E \in \mathcal{E}_h} \frac{1}{h_E} \|[\![\boldsymbol{u} \cdot \boldsymbol{\tau}]\!]\|_{0,E}^2, \tag{7}$$

and for the pressure

$$\|\|p\|\|_{t,h}^2 = \sum_{K \in \mathcal{K}_h} \frac{h_K^2}{h_K^2 + t^2} \|\nabla p\|_{0,K}^2 + \sum_{E \in \mathcal{E}_h} \frac{h_E}{h_E^2 + t^2} \|[\![p]\!]\|_{0,E}^2. \tag{8}$$

Mixed finite element method

As a finite element approximation we use the following Brezzi-Douglas-Marini family of elements [3]

$$\boldsymbol{V}_h^{BDM} = \{\boldsymbol{v} \in H(\mathrm{div}, \Omega) \mid \boldsymbol{v}|_K \in [P_k(K)]^n \ \forall K \in \mathcal{K}_h\}, \tag{9}$$

$$Q_h = \{q \in L^2(\Omega) \mid q|_K \in P_{k-1}(K) \ \forall K \in \mathcal{K}_h\}. \tag{10}$$

By the definition of the spaces, the velocity is only continuous in the normal direction, thus resulting in a non-conforming method for $t > 0$. The spaces are chosen such that the following equilibrium property holds:

$$\mathrm{div} \, \boldsymbol{V}_h \subset Q_h. \tag{11}$$

To get a stable non-conforming method, we use Nitsche's method with a suitably chosen stabilization parameter α. We define the following mesh-dependent bilinear form

$$\mathcal{B}_h(\boldsymbol{u}, p; \boldsymbol{v}, q) = a_h(\boldsymbol{u}, \boldsymbol{v}) + b(\boldsymbol{v}, p) + b(\boldsymbol{u}, q), \tag{12}$$

in which

$$a_h(\boldsymbol{u}, \boldsymbol{v}) = (\boldsymbol{u}, \boldsymbol{v}) + t^2 \sum_{K \in \mathcal{K}_h} (\nabla \boldsymbol{u}, \nabla \boldsymbol{v})_K$$

$$+ t^2 \sum_{E \in \mathcal{E}_h} \{\frac{\alpha}{h_E} \langle [\![\boldsymbol{u}]\!], [\![\boldsymbol{v}]\!] \rangle_E - \langle \{\frac{\partial \boldsymbol{u}}{\partial n}\}, [\![\boldsymbol{v}]\!] \rangle_E - \langle \{\frac{\partial \boldsymbol{v}}{\partial n}\}, [\![\boldsymbol{u}]\!] \rangle_E\}. \tag{13}$$

Then the discrete problem is to find $\boldsymbol{u}_h \in \boldsymbol{V}_h$ and $p_h \in Q_h$ such that

$$\mathcal{B}_h(\boldsymbol{u}_h, p_h; \boldsymbol{v}, q) = (\boldsymbol{f}, \boldsymbol{v}) - (g, q), \quad \forall (\boldsymbol{v}, q) \in \boldsymbol{V}_h \times Q_h. \tag{14}$$

Let P_h be the L^2-projection onto Q_h. Assuming full regularity, we have the following a priori result:

$$\|\boldsymbol{u} - \boldsymbol{u}_h\|_{t,h} + \|\|P_h p - p_h\|\|_{t,h} \le Ch^{k+1}(\|\boldsymbol{u}\|_{k+1} + t\|\boldsymbol{u}\|_{k+2}). \tag{15}$$

We now have a superconvergence result for $\|\|P_h p - p_h\|\|_{t,h}$. This implies that the pressure solution can be improved by local postprocessing.

Postprocessing method

In this section we present a postprocessing method for the pressure in the spirit of [4]. We seek the postprocessed pressure in an augmented space $Q_h^* \supset Q_h$, defined as

$$Q_h^* = \{q \in L^2(\Omega) \mid q|_K \in P_{k+1}(K) \, \forall K \in \mathcal{K}_h\} \tag{16}$$

The postprosessing method is: Find $p_h^* \in Q_h^*$ such that

$$P_h p_h^* = p_h \tag{17}$$

$$(\nabla p_h^*, \nabla q)_K = (-t^2 \Delta \boldsymbol{u}_h + \boldsymbol{u}_h - \nabla p_h - \boldsymbol{f}, \nabla q)_K, \quad \forall q \in (I - P_h)Q_h^*|_K. \tag{18}$$

Thus, we use the finite element solution to improve the pressure approximation. Since the procedure is executed element-by-element, it adds very little computational complexity to the problem. Using the postprocessed solution, we have full convergence for both the pressure and the velocity:

$$\|\boldsymbol{u} - \boldsymbol{u}_h\|_{t,h} + \||p - p_h\||_{t,h} \leq Ch^{k+1}(\|\boldsymbol{u}\|_{k+1} + t\|\boldsymbol{u}\|_{k+2}). \tag{19}$$

A posteriori estimates

Finally, the postprocessing procedure allows us to introduce a residual based reliable and efficient a posteriori error estimator. The elementwise and edgewise estimators are defined as

$$\eta_K^2 = \frac{h_K^2}{h_K^2 + t^2}\| - t^2 \Delta \boldsymbol{u}_h + \boldsymbol{u}_h - \nabla p_h^* - \boldsymbol{f}\|_{0,K}^2 + (t^2 + h_K^2)\|g - P_h g\|_{0,K}^2 \tag{20}$$

$$\eta_E^2 = \frac{t^2}{h_E}\|[\![\boldsymbol{u}_h]\!]\|_{0,E}^2 + \frac{h_E}{h_E^2 + t^2}\|[\![p_h^*]\!]\|_{0,E}^2 + \frac{h_E}{h_E^2 + t^2}\|[\![t^2\frac{\partial \boldsymbol{u}_h}{\partial \boldsymbol{n}}]\!]\|_{0,E}^2 \tag{21}$$

The global estimator is

$$\eta = \left(\sum_{K \in \mathcal{K}_h} \eta_K^2 + \sum_{E \in \mathcal{E}_h} \eta_E^2\right)^{1/2} \tag{22}$$

We can show that this choice of estimator is both a lower and an upper bound for the error with constants independent of the viscosity parameter t.

Concluding remarks

It was shown, that elements tailored for the Darcy problem can be extended to cover the case of viscous flow in a porous medium. In addition, the pressure solution can be postprocessed with little computational cost to achieve optimal convergence for both of the variables. Postprocessing also allows us to introduce a well-behaving a posteriori error estimator.

Viitteet

[1] M. Juntunen Finite element methods for parameter dependent problems *Helsinki University of Technology Institute of Mathematics Research Reports*, **A573**, (2009).

[2] J.A. Nitsche Über ein Variationsprinzip zur Lösung von Dirichlet-Problemen bei Verwendung von Teilräumen, die keinen Randbedingungen unterworfen sind *Abhandlungen aus dem Mathematischen Seminar der Universität Hamburg*, **36**, 9–15, (1970).

[3] F. Brezzi and M. Fortin *Mixed and Hybrid Finite Element Methods*. Springer, (1991).

[4] C. Lovadina and R. Stenberg Energy norm a posteriori error estimates for mixed finite element methods *Math. Comp.*, **75**, 1659–1674, (2006).

On the Instability of an Axially Moving Elastic Plate

Tero Tuovinen[*] **and Juha Jeronen and Pekka Neittaanmäki**

Department of Mathematical Information Technology
University of Jyväskylä, Finland
e–mails:
tero.tuovinen@jyu.fi
juha.jeronen@jyu.fi
pekka.neittaanmaki@jyu.fi

Nikolai Banichuk

Institute for Problems in Mechanics
RAS, Russian Federation
e–mail:banichuk@ipmnet.ru

Summary Problems of stability of an axially moving elastic band travelling at constant velocity between two supports and experiencing small transverse vibrations are considered in a 2-D formulation. The stability of the plate is investigated with the help of an analytical approach. The results are illustrated via numerical examples, and it is observed that the transverse displacement becomes localised in the vicinity of free boundaries.

Introduction

This paper is devoted to application of analytical methods to instability analysis of an axially moving rectangular plate and to investigation of the dependence of the solution on the problem parameters. In the frame of the general dynamic approach, a functional expression for the characteristic index of stability is found and can be effectively used for frequency evaluation. It is proved that the loss of stability is realised for some critical velocity in a divergence mode, i.e.

$$V_0^{\text{div}} < V_0^{\text{fl}} \ .$$

Then a static analysis of instability is performed and the possible buckled forms of the plate (symmetric and antisymmetric) are studied as functions of geometric and mechanical problem parameters. In particular, we show that the buckled plate shape is symmetric and that the elastic deflections are localised in the vicinity of free edges of the plate.

Basic relations for transverse vibrations of axially moving elastic plate

Let us investigate the elastic stability of a band travelling with a constant velocity V_0 in the x direction between two rollers located at $x = 0$ and $x = \ell$.

The transverse displacement of the travelling band is described by the deflection function w which depends on the space coordinates x, y and time t. The differential equation for small transverse vibrations has the form

$$m\frac{\text{d}^2 w}{\text{d}t^2} = T_{xx}\frac{\partial^2 w}{\partial x^2} + 2T_{xy}\frac{\partial^2 w}{\partial x\partial y} + T_{yy}\frac{\partial^2 w}{\partial y^2} - D\Delta^2 w \tag{1}$$
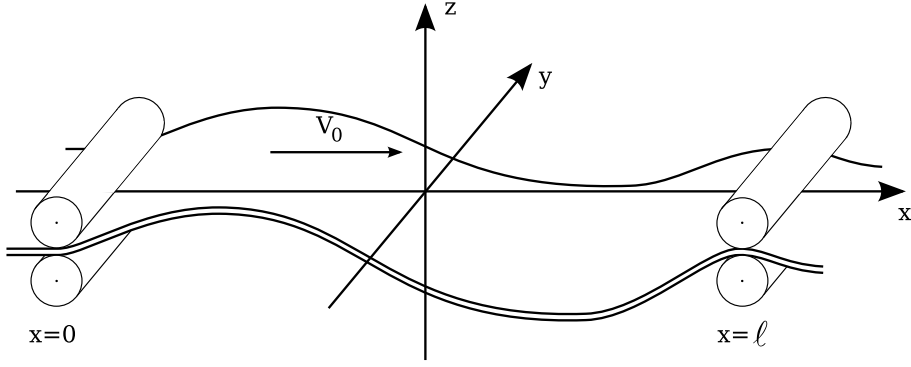
Figure 1: Open draw: Axially moving elastic plate between two rollers.

Here m is the mass per unit area of the middle surface of the plate, Δ^2 is the biharmonic operator, T_{xx}, T_{xy}, T_{yy} are in-plane tensions and

$$D\Delta^2 w = D\left(\frac{\partial^4 w}{\partial x^4} + 2\frac{\partial^2 w}{\partial x^2 \partial y^2} + \frac{\partial^4 w}{\partial y^4}\right), \quad D = \frac{Eh^3}{12(1-v^2)} \tag{2}$$

The in-plane tensions T_{xx}, T_{xy} and T_{yy} are assumed to satisfy the equilibrium equations

$$\frac{\partial T_{xx}}{\partial x} + \frac{\partial T_{xy}}{\partial y} = 0, \quad \frac{\partial T_{xy}}{\partial x} + \frac{\partial T_{yy}}{\partial y} = 0 \tag{3}$$

with the boundary conditions

$$T_{xx} = T_0, \quad T_{xy} = 0 \quad \text{at } x = 0,\ |y| \leq b \text{ and } x = \ell,\ |y| \leq b \,,$$

$$T_{yy} = 0, \quad T_{xy} = 0 \quad \text{at } y = \pm b, \quad 0 \leq x \leq \ell \,. \tag{4}$$

We assume that the deflection function w and its partial derivatives are small, and that they satisfy the boundary conditions corresponding to simply supported boundaries at $x = 0$, $|y| \leq b$, and $x = \ell$, $|y| \leq b$, and free boundaries at $|y| = b$, $0 \leq x \leq \ell$. That is (see, for example, Timoshenko and Woinowsky-Krieger 1959),

$$(w)_{x=0,\,\ell} = 0, \quad \left(\frac{\partial^2 w}{\partial x^2}\right)_{x=0,\,\ell} = 0\,, \quad -b \leq y \leq b \tag{5}$$

$$\left(\frac{\partial^2 w}{\partial y^2} + v\frac{\partial^2 w}{\partial x^2}\right)_{y=\pm b} = 0\,, \quad 0 \leq x \leq \ell \tag{6}$$

$$\left(\frac{\partial^3 w}{\partial y^3} + (2-v)\frac{\partial^3 w}{\partial x^2 \partial y}\right)_{y=\pm b} = 0\,, \quad 0 \leq x \leq \ell \,. \tag{7}$$

In the following we use stationary relations, i.e. it is supposed that $w = w(x,y)$ and all partial derivatives with respect to t are equal to zero. The following expressions for
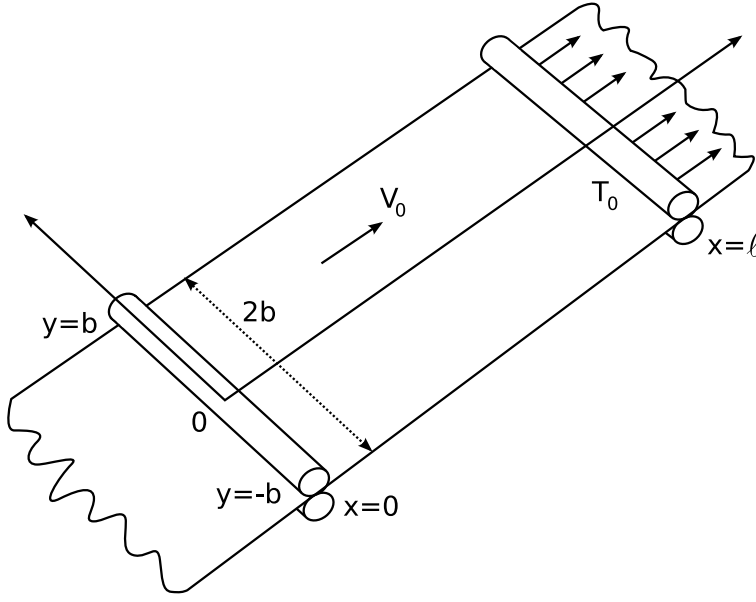
Figure 2: V_0 is velocity and T_0 is tension of the plate. Plate is simply supported at $x = 0$ and $x = \ell$.

in-plane forces are found using the boundary conditions (4) and the partial differential equations (3):

$$T_{xx}(x,y) = T_0, \quad T_{yy}(x,y) = T_{xy}(x,y) = 0 \quad (x,y) \in \Omega . \tag{8}$$

Thus, we have the following dynamic equation for small vibrations of the travelling plate:

$$\mathfrak{L}(w) = \frac{\partial^2 w}{\partial t^2} + 2V_0 \frac{\partial^2 w}{\partial x \partial t} + (V_0^2 - C^2)\frac{\partial^2 w}{\partial x^2}$$
$$+ \frac{D}{m}\left(\frac{\partial^4 w}{\partial x^4} + 2\frac{\partial^2 w}{\partial x^2 \partial y^2} + \frac{\partial^4 w}{\partial y^4}\right) = 0 , \quad C = \sqrt{\frac{T_0}{m}} . \tag{9}$$

As is seen from (5)-(9), our boundary-value problem is homogeneous and invariant with respect to the symmetry operation $y \to -y$, and consequently, all solutions of the problem can be considered as symmetric or antisymmetric functions of y, i.e.,

$$w(x,y,t) = w(x,-y,t) \quad \text{or} \quad w(x,y,t) = -w(x,-y,t) . \tag{10}$$

Concluding remarks

The loss of stability of axially moving plates was investigated in a two-dimensional formulation, taking into account their bending resistance and in-plane tension. The studies performed were mainly based on analytical approaches, and the basic relation characterising the behaviour of the plate at the onset of instability was found in an analytical form.

As the result of the general dynamic analysis performed, it was proved that the onset of instability takes place in a divergence (static) form for some critical value of the transport

velocity when the frequency of the plate vibrations is equal to zero. It was shown that the flutter modes arise only for higher values of the transport velocity.

Detailed analysis was performed in an analytical manner for static modes of instability. The critical divergence velocity and the corresponding buckling shapes were studied as functions of geometric and mechanical problem parameters. It was proved that the buckled plate shape is symmetrical, i.e. the antisymmetric shapes correspond to higher values of the transport velocity. It was shown that the meaningful elastic deflections are localized at the vicinity of free edges of the plate.

It is necessary to note that for some buckling problems for plates where the ratio of width to length, b/ℓ, is large, in practice a one-dimensional panel model is used. For this model, the critical parameter is equal to one ($\gamma_* = 1$). However, as was seen from our studies of the two-dimensional buckling problem, the limit of γ_* when the width to length ratio tends to infinity (panel limit) depends on the Poisson ratio, and is less than 1. For any meaningful Poisson ratio ($\nu > 0$), this difference is small but finite. The largest difference is obtained when the Poisson ratio is equal to 0.5. This unusual conclusion is important for rigorous estimation.

References

F. R. Archibald and A. G. Emslie. The vibration of a string having a uniform motion along its length. *ASME Journal of Applied Mechanics*, 25:347–348, 1958.

V. V. Bolotin. *Nonconservative Problems of the Theory of Elastic Stability*. Pergamon Press, New York, 1963.

S. Chonan. Steady state response of an axially moving strip subjected to a stationary lateral load. *J. Sound Vib.*, 107:155–165, 1986.

C. C. Lin. Stability and vibration characteristics of axially moving plates. *Int. J. Solids Structures*, 34(24):3179–3190, 1997.

C. C. Lin and C. D. Mote. Eigenvalue solutions predicting the wrinkling of rectangular webs under non-linearly distributed edge loading. *Journal of Sound and Vibration*, 197 (2):179–189, 1996.

W. L. Miranker. The wave equation in a medium in motion. *IBM J. R&D*, 4:36–42, 1960.

C. D. Mote. Dynamic stability of axially moving materials. *Shock Vib. Dig.*, 4(4):2–11, 1972.

A. Simpson. Transverse modes and frequencies of beams translating between fixed end supports. *J. Mech. Eng. Sci.*, 15:159–164, 1973.

R. D. Swope and W. F. Ames. Vibrations of a moving threadline. *J. Franklin Inst.*, 275: 36–55, 1963.

S. P. Timoshenko and S. Woinowsky-Krieger. *Theory of plates and shells*. New York : Tokyo : McGraw-Hill, 2nd edition, 1959. ISBN 0-07-085820-9.

J. A. Wickert. Non-linear vibration of a traveling tensioned beam. *Int. J. Non-Linear Mechanics*, 27(3):503–517, 1992.

J. A. Wickert and C. D. Mote. Classical vibration analysis of axially moving continua. *J. Appl. Mech.*, 57:738–744, 1990.

Instability Analysis of Axially Travelling Membranes and Plates Interacting with Axially Moving Ideal Fluid

Juha Jeronen[*] **and Tero Tuovinen and Pekka Neittaanmäki**

Department of Mathematical Information Technology
University of Jyväskylä, Jyväskylä, Finland
e–mail: juha.jeronen@jyu.fi

Nikolay Banichuk

Institute for Problems in Mechanics RAS, Moscow, Russian Federation

Summary   In this research, the statical instability problem for axially travelling membranes and plates interacting with surrounding axially moving ideal fluid was considered. The study was limited to the case of small cylindrical deformation, and the aerodynamic reaction was found analytically as a functional of the deformation function. The Fourier–Galerkin method was used for numerical computations, and some of the numerical results will be presented here.

Introduction

From the viewpoint of papermaking, the inherent mechanical instability of axially moving continua is an important question. An extensive amount of research has been conducted on the various aspects of travelling flexible strings, membranes, beams and plates, see e.g. [1] [2] [3] [4] [5] [6] [7] [8] [9] [10] [11, 12].

It is known from experimental studies and some theoretical estimations [13] that mechanical instability in a travelling paper web can arise at some critical velocities. These velocities are of both theoretical and practical interest, as they set an upper limit for the running speed of a paper machine. Under certain conditions, statical instability is known to occur first [14].

An important factor that affects the instability is the interaction between the elastic continuum and the surrounding medium. As has been noted [13], the critical velocities and eigenfrequencies obtained using the results from the vacuum case [15] may be up to 400% too high.

The simplest approach toward the fluid-structure interaction is to assume potential flow [16] [17]. Added-mass approaches have been used [13], usually in combination with a finite element solution [17]. A version with boundary layer theory was used in [18].

The potential flow problem, while not entirely accurate [18], is a standard reference case. It has been studied for axially moving materials in stationary air (e.g. [13]), and for stationary structures in axial flow (e.g. [19]). In this study, we have combined these two cases, solving the statical instability problem for a travelling web subjected to axial flow, with the assumptions of potential flow and cylindrical deformation.

We have used a Green's function approach to derive an analytical functional representation for the reaction of the ideal fluid, when axial motion is accounted for both the plate and the fluid. The form of the problem is similar to the problems of pipes conveying fluid, and stationary structures subjected to axial flow [20]. Indeed, a similar functional analytical solution has been found in the case of a stationary plate in axial flow [21].
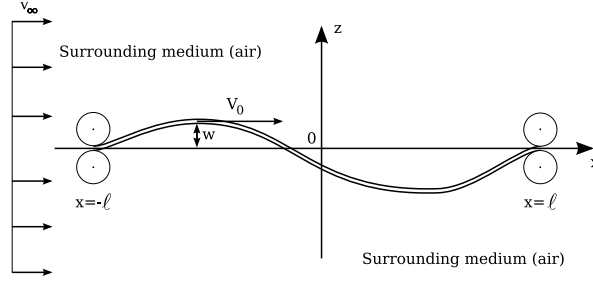
Figure 1: Plate travelling axially between two rollers at constant velocity V_0, submerged in ideal fluid moving axially at velocity v_∞.

Results

The idealised physical situation is shown in Figure 1. As is well known, small cylindrical deformations of the plate are described by the partial differential equation

$$m\frac{\partial^2 w}{\partial t^2} + 2mV_0\frac{\partial^2 w}{\partial x \partial t} + (mV_0^2 - T)\frac{\partial^2 w}{\partial x^2} + D\frac{\partial^4 w}{\partial x^4} = q_f \ . \tag{1}$$

In our study, simply supported boundary conditions were used. The main result of the study is an analytical functional representation for the aerodynamic reaction term q_f in equation (1). We present our result in dimensionless variables $x' \equiv x/\ell, \ x' \in [-1, 1]$ and $t' \equiv t/\tau, \ t' \in [0, \infty)$, where τ is an arbitrary normalisation constant for time. In our study, it was found that for the dynamic system (omitting the primes),

$$q_f = -\rho_f \left(\frac{1}{\tau}\frac{\partial}{\partial t} + \frac{1}{\ell}(v_\infty - V_0)\frac{\partial}{\partial x}\right) \int_{-1}^{1} N(\xi, x)\left[\frac{\ell}{\tau}\frac{\partial w}{\partial t}(\xi, t) + (v_\infty - V_0)\frac{\partial w}{\partial x}(\xi, t)\right] d\xi \ , \tag{2}$$

where the aerodynamic kernel N is defined as

$$N(\xi, x) \equiv \frac{1}{\pi}\ln\left|\frac{1 + \Lambda}{1 - \Lambda}\right| \ , \quad \text{where} \quad \Lambda(\xi, x) \equiv \left[\frac{(1-x)(1+\xi)}{(1-\xi)(1+x)}\right]^{1/2} \ . \tag{3}$$

For buckling analysis, the corresponding statical instability problem was formed (Figure 2). By solving the quadratic eigenvalue problem formed from the Fourier–Galerkin discretisation of the steady-state case, it was found that, as expected, the presence of ideal fluid decreases the critical velocity when compared to the vacuum case (Figure 3, left). In the case of stationary ideal fluid, the results support those of Pramila [13].

However, a difference was found upon computing the complex eigenvalues of the discretisation of the dynamic equation (1). It was found that unlike in the added mass approach, the scaling factors for the eigenfrequencies and critical velocities are different (Figure 3, right). Thus, couplings exist between the vacuum eigenmodes that cannot be reproduced by an added mass approach.
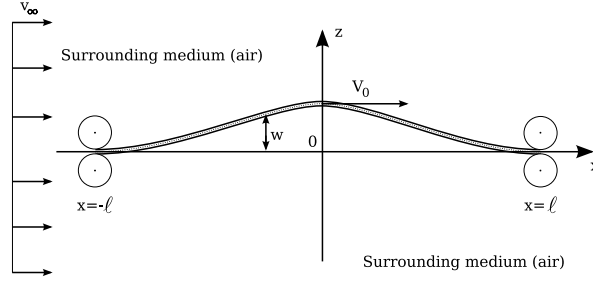
Figure 2: Axially travelling plate, submerged in axially moving ideal fluid, buckling at the lowest critical velocity $V_0 = V_0^{\text{div}}$.
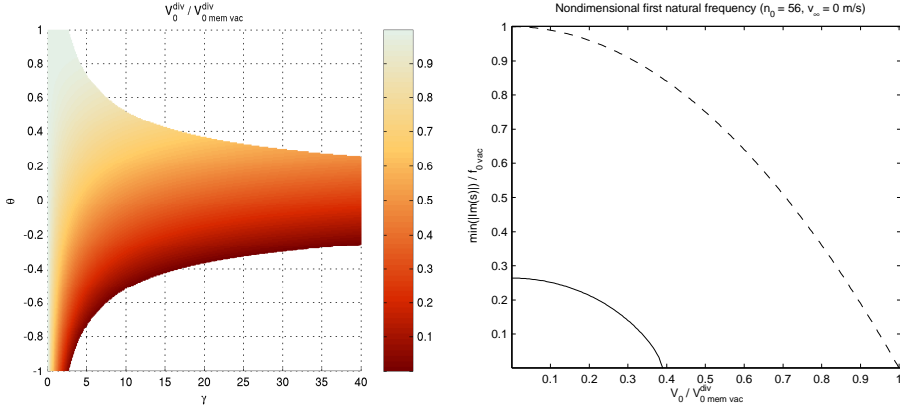
Figure 3: Some of the numerical results for an ideal membrane ($D = 0$). Left: Nondimensional critical velocity as a function of $\gamma \equiv \frac{\ell \rho_f}{m}$ and $\theta \equiv v_\infty / V_{0\,\text{mem vac}}^{\text{div}}$. Right: First nondimensional eigenfrequency as a function of the nondimensional velocity of the membrane. Dashed line, vacuum case. Solid line, with stationary ideal fluid.

Concluding remarks

The computations performed show that the surrounding fluid has a meaningful effect on the critical parameters of instability. Especially, it was found that when the plate is submerged in an external medium, even if this medium is ideal fluid, couplings exist between the vacuum eigenmodes that cannot be reproduced by an added mass approach.

It should be noted that the cylindrical deformation assumption is an approximation, due to the localisation of deformation near the free edges that has been observed in axially moving paper webs. Based on our comparison to earlier results [13], we conclude that the flat panel model is nevertheless a reasonable approximation for a narrow strip.

It should also be noted that due to the boundary layer, the critical velocities in viscous fluid may be significantly higher than those predicted by the ideal fluid model [18]. Thus, the present results should be primarily seen as academical basic research concerning axial flow phenomena and axially moving materials.

References

[1] F. R. Archibald and A. G. Emslie. The vibration of a string having a uniform motion along its length. *ASME Journal of Applied Mechanics*, 25:347–348, 1958.

[2] W. L. Miranker. The wave equation in a medium in motion. *IBM J. R&D*, 4:36–42, 1960.

[3] R. D. Swope and W. F. Ames. Vibrations of a moving threadline. *J. Franklin Inst.*, 275:36–55, 1963.

[4] A. Simpson. Transverse modes and frequencies of beams translating between fixed end supports. *J. Mech. Eng. Sci.*, 15:159–164, 1973.

[5] S. Chonan. Steady state response of an axially moving strip subjected to a stationary lateral load. *J. Sound Vib.*, 107:155–165, 1986.

[6] J. A. Wickert and C. D. Mote. Classical vibration analysis of axially moving continua. *J. Appl. Mech.*, 57:738–744, 1990.

[7] Ji Yao Shen, Lonnie Sharpe, and William M. McGinley. Identification of dynamic properties of plate-like structures by using a continuum model. *Mechanics Research Communications,*, 22(1):67–78, 0 1995.

[8] Xiaodong Wang. Instability analysis of some fluid-structure interaction problems. *Computers & Fluids,*, 32(1):121–138, 1 2003.

[9] Changho Shin, Jintai Chung, and Wonsuk Kim. Dynamic characteristics of the out-of-plane vibration for an axially moving membrane. *Journal of Sound and Vibration,*, 286(4–5):1019–1031, 9/22 2005.

[10] Ryszard Sygulski. Stability of membrane in low subsonic flow. *International Journal of Non-Linear Mechanics,*, 42(1):196–202, 1 2007.

[11] A. Kulachenko, P. Gradin, and H. Koivurova. Modelling the dynamical behaviour of a paper web. part i. *Computers & Structures*, 85:131–147, 2007.

[12] A. Kulachenko, P. Gradin, and H. Koivurova. Modelling the dynamical behaviour of a paper web. part ii. *Computers & Structures*, 85:148–157, 2007.

[13] A. Pramila. Sheet flutter and the interaction between sheet and air. *TAPPI-Journal*, 69(7):70–74, 1986.

[14] Y. B. Chang and P. M. Moretti. Interaction of fluttering webs with surrounding air. *TAPPI journal*, 1991.

[15] A. S. Mujumdar and W. J. M. Douglas. Analytical modelling of sheet flutter. *Svensk Papperstidning*, 79:187–192, 1976.

[16] J. Niemi and A. Pramila. Vibration analysis of an axially moving membrane immersed into ideal fluid by fem. Technical report, Tampere, 1986.

[17] A. Pramila. Natural frequencies of a submerged axially moving band. *Journal of Sound and Vibration*, 113(1):198–203, 1987.

[18] T. Frondelius, H. Koivurova, and A. Pramila. Interaction of an axially moving band and surrounding fluid by boundary layer theory. *J. Fluids Struct.*, 22(8):1047–1056, 2006.

[19] C. Eloy, C. Souilliez, and L. Schouveiler. Flutter of a rectangular plate. *J. Fluids Struct.*, 23(6):904–919, 2007.

[20] M. P. Païdoussis. The canonical problem of the fluid-conveying pipe and radiation of the knowledge gained to other dynamics problems across applied mechanics. *Journal of Sound and Vibration*, 310:462–492, 2008.

[21] A. Kornecki, E. H. Dowell, and J. O'Brien. On the aeroelastic instability of two-dimensional panels in uniform incompressible flow. *Journal of Sound and Vibration*, 47(2):163–178, 1976.

Identification of mass location on vibrating beams using Haar wavelets and neural networks

Helle Hein and Ljubov Feklistova*

Faculty of Mathematics and Computer Science
University of Tartu, Tartu, Estonia
e–mail: helle.hein@ ut.ee

Summary In this paper two procedures are suggested for estimating the location and/or magnitude of a concentrated mass attached to the isotropic vibrating beam. Artificial neural networks are applied to establish the mapping relationship between structural feature vector and status of the concentrated mass (location and magnitude). Seven different training methods are applied and compared.

Introduction

Several techniques for estimating the elastic parameters of beams, plates and shells have been proposed by a number of authors [1-3]. These methods include wave propagation measurements, eigenfrequency-based methods, genetic algorithms etc. In recent years, the artificial neural networks have become a powerful tool in the fields of forecast because of the special abilities to make mappings and simulations of complicate systems and functions. Artificial neural networks have been applied for solving the inverse prediction problems with non-linearity. The supervised multi-layer feed-forward neural network is one of the most popular architecture used today [4]. It is a universal approximator and is taken as the benchmark for comparing the performance of other neural network architectures. The structural parameter estimation based on neural networks includes the following steps: selection of network parameters, determination of network structure, collection and normalization of learning samples, initialization of network weight values, to perform the training in order to obtain the convenient accuracy.

In the present work, the dynamic response of vibrating beams with an attached mass is studied. Karlik and Ozkaya [5] applied neural networks to predict five natural frequencies of a beam if the mass ratios and locations were known. The basic idea in the vibration-based estimation is that these parameters depend on the physical properties of the systems structure. Changes in the mass ratio and location can result in detectable alterations in the natural frequencies, displacements or mode shapes. The key problem is how to extract useful features from the vibration signals for identification. However, successful network learning and its ability to generalise characteristic features of the system from input-output pairs requires large training sets.

The aim of the present research is to elaborate two methods which are capable of calculating: (i) the mass ratio if the position of the applied mass is known, (ii) the position of the attached mass if mass ratio is known, (iii) the ratio and position of the attached mass.

In the case of the first method the input vector of network consists of five natural frequencies of the system. The network is trained with different training algorithms. A comparison of the algorithms is done in order to find the most accurate method for solving the stated problem.

The second method uses the combined approach: the structural feature vector is calculated with the aid of Haar wavelets. Wavelet transform has been used in many fields including vibration-based damage detection of beams and plates [2, 6-8]. The wavelet packets and neural network identification were suggested by Hein [9] to inversely determine the elastic foundation parameters of delaminated vibrating beams. In most cases the continuous wavelet transform has been used. Non-sufficient attention has been paid to the discontinuous Haar functions, which are

mathematically the simplest wavelets. Nevertheless it has been demonstrated that the Haar wavelets can be successfully applied for solving differential and integral equations [10, 11].

In the present study the integrated method of Haar wavelets and neural networks is suggested. The main ideas of Chen-Hsiao method [10] are applied, according to which the derivatives of the functions were approximated for solving differential equations. This approach has been developed further by Lepik [11].

Dynamic response of vibrating beams carrying the concentrated mass

In this section, the analytical solution to the free vibration of a beam with a concentrated mass located at $x=a$ is formulated. The geometry of the beam is shown in Fig. 1.
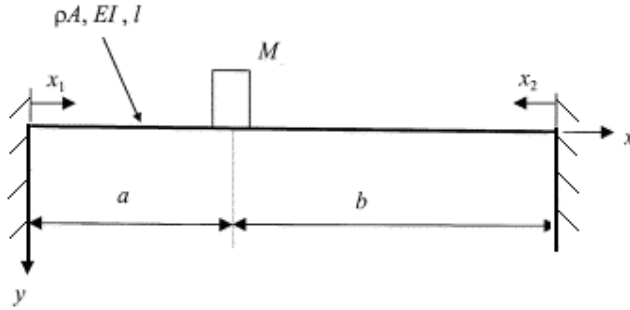
Fig. 1: The beam-mass system.

The differential equation associated with the present eigenvalue problem is [12]:

$$\frac{d^4V}{dx^4} - k^4V = 0, \quad k^4 = \frac{\rho A \omega^2}{EI}. \tag{1}$$

In (1) ρ denotes the beam's density, A is the cross-sectional area, E is Young's modulus and I is the moment of inertia.

The general solutions of the ordinary differential equation (1) can be presented as

$$\begin{cases} V_1(x_1) = C_1 \sin(kx_1) + C_2 \cos(kx_1) + C_3 \sinh(kx_1) + C_4 \cosh(kx_1), & x_1 \in [0,a] \\ V_2(x_2) = C_5 \sin(kx_2) + C_6 \cos(kx_2) + C_7 \sinh(kx_2) + C_8 \cosh(kx_2), & x_2 \in [0,b] \end{cases} \tag{2}$$

where V_1 and V_2 are the left and right transverse displacements with respect to the concentrated mass M and C_i ($i = 1, …, 8$) are the constants to be determined from boundary and continuity conditions. In the present work the following boundary conditions are considered: (i) $V = V' = 0$ (clamped end); (ii) $V'' = V'''' = 0$ (free end); (iii) $V' = V''' = 0$ (guided end). Here primes denote differentiation with respect to the spatial variable x. The compatibility conditions at the location of concentrated mass, which apply to all cases [13, 14], are given as follows:

$$V_1(a) = V_2(b),$$
$$V_1''(a) = V_2''(b),$$
$$V_1'(a) = -V_2'(b), \tag{3}$$
$$V_1'''(a) + V_2'''(b) + \alpha k^4 V_1(a) = 0.$$

where α is the mass ratio defined by $M/(\rho Al)$.

Identification using artificial neural networks

For identification problem the feed-forward back propagation network is used. The neural network contains only one hidden layer which neurons are assigned the log-sigmoid transfer function. The network is trained by seven different training algorithms in order to find out the most efficient one. In order to compare the performances of the network, trained by different methods, several criteria are used. These are the number of epochs, the mean squared error (MSE), training time, the mean absolute error ($MAE = (1/N)\Sigma|n_t - n_c|$), the variance account for ($VAF = 1 - \mathrm{var}(n_t - n_c)/\mathrm{var}(n_t)$) and the coefficient of multiple determination ($R^2 = 1 - \Sigma(n_t - n_c)^2 / \Sigma(n_t - n_m)^2$). Here n_t is the target output value, n_c is the computed value, n_m is the mean of the target values n_t, N is the number of patterns in the test set; *var* denotes the variance.

Performance assessment of the neural network models trained by natural frequencies

The accuracy of seven methods to predict the attached mass location on a beam with clamped ends is shown in Table 1. The most reliable forecasts have been made by the network which was trained by the Levenberg-Marquardt method. The network made 99.98 percent reliable predictions within 3.7 seconds. The least accurate methods were the steepest gradient methods. Among the conjugate gradient methods the most efficient was the Polak-Ribiére, whose variance account for was almost the same as the Levenberg-Marquardt's.

Table 1. Prediction of mass location on the beam with clamped ends.

	Sequential mode	Batch mode	Resilient method	Polak-Ribiére	Fletcher-Powell	Powell-Beale	Levenberg Marquardt
No of epochs	NA	1800	127	133	628	172	7
MSE	NA	0.0086	0.9903	0.9.954	0.9.991	0.0003	2.2e-5
Training time	1.0150	16.469	2.3590	2.7810	8.9070	3.3900	3.7030
MAE	0.0268	0.0102	0.0013	0.0012	0.0013	0.0018	0.0008
VAF	0.4425	0.9636	0.9991	0.9997	0.9991	0.9990	0.9999
R^2	0.2244	0.9559	0.9991	0.9994	0.9989	0.9987	0.9998

Performance assessment of the neural network models trained by Haar coefficients

First, the response of vibrating beam has been calculated numerically. Various possible combinations of beam parameters were considered. Second, the vibration responses (mode shapes) of the beam with and without concentrated mass were expanded into Haar series [10, 11]. A comparison of energy of vibration responses between beams with and without mass in some frequency bands will exhibit some remarkable difference. The input vectors for artificial neural networks have been calculated with the aid of energy values of sub-signals. The data training sets for artificial neural networks have been formed from input vectors and of corresponding mass locations and ratios.

Table 2. Predictions of the attached body location on a beam; $\alpha = 20$.

	Sequential mode	Batch mode	Resilient method	Polak-Ribiére	Fletcher-Powell	Powell-Beale	Levenberg-Marquardt
No of epochs	NA	1800	36	102	87	64	2
MSE	NA	0.0044	9.03e-5	9.97e-5	9.92e-5	9.74e-5	1.95e-6
Training time	0.7810	20.688	1.3440	1.8440	2.4380	1.6720	0.8910
MAE	0.1074	0.0115	0.0017	0.0008	0.0010	0.0005	0.0002
VAF	1.1348	0.9666	0.9995	0.9998	0.9998	1.0000	1.0000
R^2	0.8308	0.9976	0.9999	1.0000	1.0000	1.0000	1.0000

The results of the predictions made by the networks, trained by seven different methods, are presented in Table 2. During the learning nine-element patters were used. As a result, the

Levenberg-Marquardt and the steepest gradient methods showed the best results. Finally, the tests showed that the training time and number of epochs in second approach was smaller than in the case of previous method.

Concluding remarks

In this work two methods to inversely estimate the attached mass ratio and location on the vibrating beams were proposed. Numerical simulations showed that the integrated approach with Haar wavelets saved the computation time and showed the better accuracy.

Acknowledgement

References

[1] A.L. Araujo, C.M. Mota Soares, J. Herskovits and P. Pedersen. Parameter estimation in plate structures using gradient optimization and neural networks. *Inverse Problems, Design and Optimization Symposium*, Rio de Janeiro, Brasil, (2004).

[2] H. El Kadi. Modeling the mechanical behavior of fiber-reinforced polymeric composite materials using artificial neural networks – A review. *Computers and Structures*, **73**, 1-23, (2006).

[3] G.R. Liu, K.Y. Lam and X. Han. Determination of elastic constants of anisotropic laminated plates using elastic waves and a progressive neural network. *Journal of Sound and Vibration*, **252**, 239–259, (2002).

[4] S. Haykin. Neural networks: a comprehensive foundation. *Prentice Hall*, (1999).

[5] B. Karlik, E. Özkaya, S. Aydin, M. Pakdemirli. Vibration of beam-mass systems using artificial neural networks. *Computers and Structures,* **69**, 339–347, (1998).

[6] M. Rucka, K. Wilde. Application of continuous wavelet transform in vibration based damage detection method for beams and plates. *Journal of Sound and Vibration*, **297**, 536 – 550, (2006).

[7] L.H. Yam, Y.J. Yan and J.S. Jiang. Vibration.based damage detection for composite structures using wavelet transform and neural network identification. *Composite Structures*, **60**, 403–412, (2003).

[8] Y.J. Yan, L. Cheng, Z.Y. Wu, L.H. Yam. Development in vibration-based structural damage detecting technique. *Mechanical Systems and Signal Processing*, 21, 2198-2211, (2006).

[9] H. Hein. Determination of foundation characteristics of vibrating beams using wavelet transform and neural network. *Proc. SPIE*, 6763-8, (2007).

[10] C. F. Chen, C. H. Hsiao. Haar wavelet method for solving lumped and distributed-parameter Systems. *IEE Proc.-Control Theory Appl.*, **144**, 87-94, (1997).

[11] Ü. Lepik. Numerical solution of differential equations using Haar wavelets. *Mathematics and Computers in Simulation*, **68**, 127-143, (2005).

[12] S. Rao. Mechanical Vibrations, Addison Wesley, (1990).

[13] M.A. De Rosa, C. Franciosi, M. Maurizi. On the dynamic behaviour of slender beams with elastic ends carrying a concentrated mass. *Computers and Structures*, **58,** 1145–1159, (1996).

[14] K.H Low. A comparative study of the eigenvalue solutions for mass-loaded beams under classical boundary conditions. *International Journal of Mechanical Sciences*, **43,** 237–244, (2001).

Nonlinear Displacements of a Wind Turbine Blade based on a Multibody Formulation with a Local Observer Frame

K. Holm-Jørgensen and S.R.K. Nielsen

Department of Civil Engineering
Aalborg University, Aalborg, Denmark
e–mail: soren.nielsen@civil.aau.dk

Summary   The paper deals with different updating algorithms of the moving frame of reference parameters in a multibody formulation for flexible structures. The updating algorithms are based on the motion of one or two beam element nodes in the belonging substructure. An example of a clamped wind turbine demonstrates that the updating algorithm by the use of two beam element nodes is far superior.

Introduction

The basic idea of flexible multibody dynamics is to introduce a moving frame of reference to each substructure. Relative to the moving frame elastic displacements are relatively small, rendering linear analysis possible. This moving frame is defined by a position vector and a parameter vector defining the origin and rotation of the moving frame relative to a fixed frame of reference. In the floating frame of reference formulation these referential coordinates describe the rigid body translation and rotation of the structure and become a part of the degrees of freedom in the system vector of the multibody system, see e.g. Shabana [1]. The use of such a mixed set of referential and elastic coordinates leads to highly non-linear system equations. To circumvent these difficulties Kawamoto et al. [2, 3, 4, 5] suggested to let the moving frame of reference float in a controlled way relative to the moving substructure, so these are always sufficiently close to each other, in order for the small displacement assumption to be fulfilled. They named this type of moving frame a Local Observer Frame. Hereby, the system matrices do not depend on the degrees of freedom in the system vector by explicitly predicting the motion of the moving frame. To reduce or eliminate the gap between the predicted and actual motion, it is necessary to regularly update the motion of the moving frame of reference as demonstrated in Kawamoto et al. [5]. In Kawamoto et al. [2] the updating scheme is originally described, where the orientation, angular velocity, and angular acceleration of the moving frame are updated based on a local triad linked to four nodes in the body. The updating scheme of the moving frame of reference in the present paper follows the same principles as described in Kawamoto et al. [3]. A small change when updating the moving frame is presented, where the orientation of the moving frame is updated based on either the motion of one or two beam element nodes.

Multibody Formulation with a Local Observer Frame

The idea is to describe the motion of a substructure in a (x_1, x_2, x_3)-coordinate system, which is freely moving in the vicinity of the substructure. Further, a fixed $(\bar{x}_1, \bar{x}_2, \bar{x}_3)$-coordinate system is introduced common for all substructures. The origin of the moving frame is described by a position vector with the global components $\bar{\mathbf{x}}_c$, and its rotation is determined by the parameter vector (or pseudo vector) $\boldsymbol{\theta}$. In dynamic simulations the substructure may drift away from the moving frame, which requires sequential updating of the position, velocity and acceleration of the moving frame origin together with the rotation, angular velocity and angular acceleration vectors. In this paper only static simulations are in focus where the moving frames are updated to reduce the displacements of the substructure from the belonging moving frame in order for the small
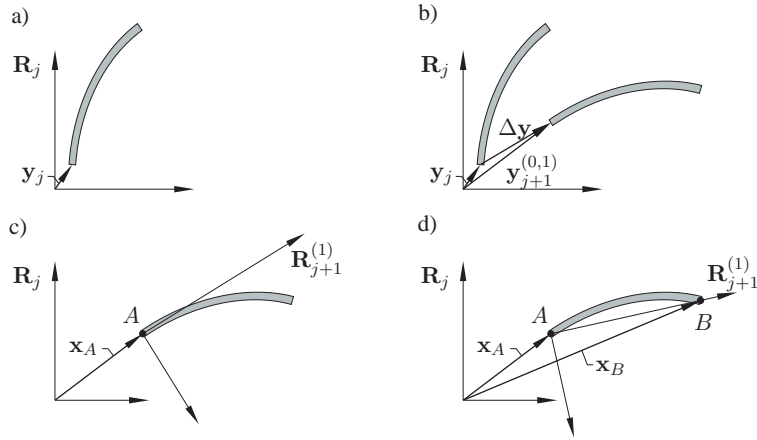
Figure 1: a) Moving frame and substructure at the load step j. b) Iterate the system vector for the load step $j + 1$. c) Updating of the moving frame based on the motion of the node at the origin. d) Updating of the moving frame based on the motion of two end nodes.

displacement assumption to be fulfilled. The equations of motion and updating algorithms for dynamic simulations are described in [6], which reduce to the static case when mass and damping terms are disregarded.

Update Algorithms for Static Analysis

In this section it is described how the moving frames are updated for use in static simulations. The reason for updating the moving frames in static analysis is to account for large nonlinear displacements. In Figure 1 a series of sketches are shown to illustrate the procedure when updating the moving frames in a static simulation. The lower index 'j' indicates a load step and an upper index (k_1) is used to specify the updating step of the moving frame of reference parameters within the load step. Similarly, an upper index (k_1, k_2) is used for the system vector, where k_2 indicates the iteration step of the system vector within the present updating step k_1 of the moving frame of reference. When determining the motion of the multibody system it is necessary that both the moving frame parameters and system vector have the same upper index k_1. In Figure 1a the moving frame and substructure are shown for the converged solution at load step j. In the next load step $j + 1$ the exterior load is changed, and the substructure is iterated to a new position within the moving frame, see Figure 1b. Due to the nonlinear rotational constraints several iterations may be necessary to obtain a residual which is within the specified convergency limits. When the solution has converged it is chosen to update the moving frame. In the present situation two methods are possible. In Figure 1c the node at the origin of the substructure is used to update the moving frame. Hereby, the moving frame obtains the same position and orientation as this node. Another possibility is demonstrated in Figure 1d, where the motion of the node at the origin and an arbitrary point, here the end node, are used to update the moving frame. At this point the updated moving frame and displacement vector do not correspond and it is therefore necessary to iterate the position of the substructure within the updated frame, similarly to Figure 1b.

Tip Displacement of a Clamped Wind Turbine Blade

In this section the accuracy of the updating methods for the multibody formulation are further investigated. A co-rotational beam formulation with 20 elements is used as the reference model,

which has been implemented by use of Krenk [7]. This type of formulation corresponds to having a moving frame for each beam element which is updated based on the motion of the end nodes in the respective elements. The examples are based on a clamped wind turbine blade where prismatic elements are used based on the mean value of the cross section parameters at the end points in the respective beam elements. The blade is discretized by a total of 20 elements with the same reference length. The total referential length of the blade is $L = 44.8\,\mathrm{m}$. The numeration of the nodes is chronological from the root to the tip. An exterior tip load in the flapwise $\bar{x}_1$-direction is applied so the tip displacement is approximately 20% of the undeformed blade length.

Convergency of Updating Algorithms

In this section the convergency of the two updating algorithms from section is investigated by increasing the number of substructures in the blade. In this example a constant reference length is used for each substructure. Because a total of 20 elements of equal reference length are used in the discretization of the blade the number of substructures become $n_{sub} = [1, 2, 4, 5, 10, 20]$. The tip position of the blade after deformation is shown in Figure 2 based on the two updating algorithms and the different number of multibodes. In Figure 2 it is shown that the updating algorithm based
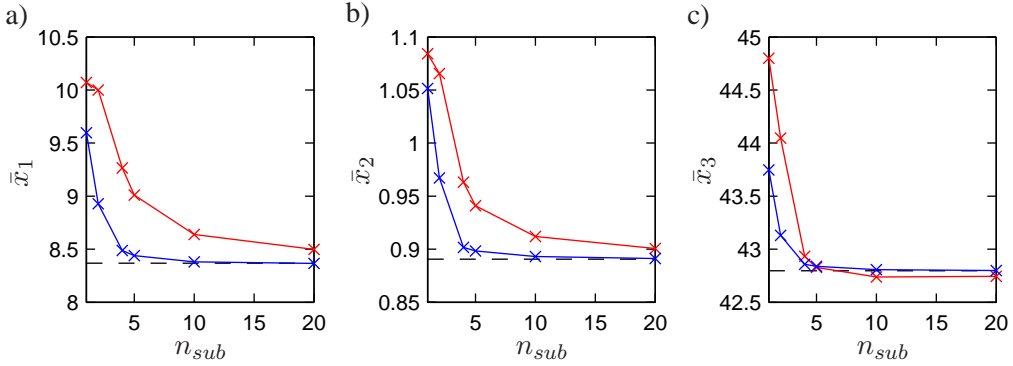
Figure 2: Tip position of the blade by use of 20 elements of equal reference length which are divided into a number of substructures n_{sub} of equal reference length. a) Tip position in $\bar{x}_1$ (flapwise). b) Tip position in $\bar{x}_2$ (edgewise). c) Tip position in $\bar{x}_3$ (spanwise). (——) Update based on node at origin. (——) Update based on end nodes. (– –) Co-rotating formulation by use of 20 elements.

on the motion of both end points in the substructure converges much faster than by only using the motion of one end point. 4 substructures updated based on the end points give similar results as by use of 20 substructures updated based on the motion of the node at the origin of the substructures. A total of 168 and 360 degrees of freedom, respectively, are used in these two cases. Moreover, far fewer moving frames need to be updated when only 4 substructures are present instead of 20 substructures.

Wind Turbine Blade Modelled by Two Substructures

In this section two substructures are used to model the blade. For both substructures the updating algorithm based on the position of the nodes at the ends of each substructure is used. It is examined how the best results are obtained by splitting the blade into the two substructures at different nodes throughout the blade. Because at least one element is necessary in each substructure it can not be split at node 1 and node 21. The results of the tip position by splitting the blade into two substructures at different nodes are shown in Figure 3. Here, the best results are obtained by
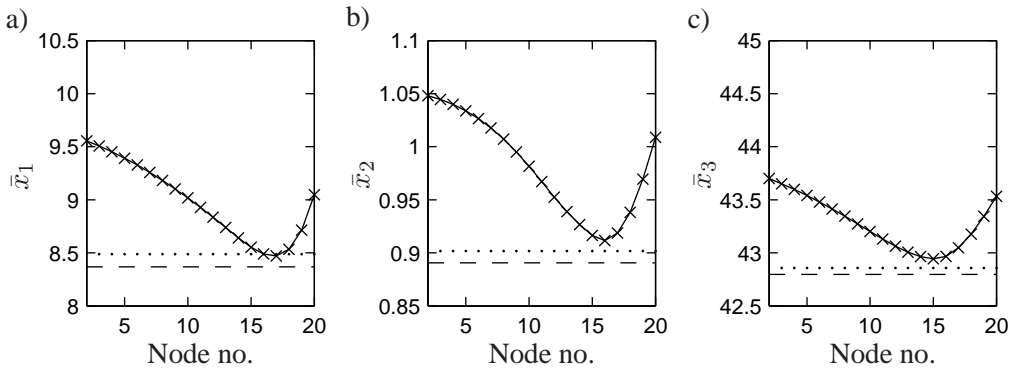
Figure 3: Position of blade tip when split into 2 substructures at different nodes throughout the blade. Both moving frames are updated based on the end nodes in the respective substructure. a) Tip position in $\bar{x}_1$. b) Tip position in $\bar{x}_2$. c) Tip position in $\bar{x}_3$. (——) 2 substructures. (⋯⋯) 4 substructures of equal reference length. (− −) Co-rotating formulation by use of 20 elements.

splitting the blade into two substructures at node 16. It is also shown that the results by use of these two substructures are almost identical to the co-rotating formulation and the case where four substructures of equal reference length are used.

Concluding Remarks

It can be concluded that the updating methods for the present multibody formulation and the co-rotating formulation both converge towards the same results. It is demonstrated that by updating the moving frame based on the motion of the end nodes in the substructure is far superior to just using the node at the origin of the substructure. For the clamped wind turbine blade it is demonstrated that by use of two substructures of unequal reference length makes it possible to absorb the non-linearities in an efficient way, which otherwise would require four substructures of equal reference length.

References

[1] A.A. Shabana, *Dynamics of Multibody Systems*, Third Edition, Cambridge University Press 2005.

[2] A. Kawamoto, M. Inagaki, T. Aoyama, K. Yasuda, Vibration of Moving Flexible Bodies (Formulation of Dynamics by using Normal Modes and a Local Observer Frame), *Proceeding of DETC99/VIB-8232 1999*.

[3] A. Kawamoto, S. Krenk, A. Suzuki, Flexible body dynamics in a freely floating local frame, *ECCOMAS Conference on Multibody Dynamics 2007*, Milan, Italy, 25-28 June 2007.

[4] A. Kawamoto, A. Suzuki, M. Inagaki, S. Krenk, Flexible-body dynamics in a floating frame with extraction of rigid body motion, *4th Asian Conference on Multibody Dynamics 2008*, ACMD, Jeju, Korea, August 20-23 2008.

[5] A. Kawamoto, S. Krenk, A. Suzuki, M. Inagaki, Flexible body dynamics in a local frame of reference with explicitly predicted motion, *International Journal for Numerical Methods in Engineering*, (2009) to appear.

[6] K. Holm-Jørgensen, S.R.K. Nielsen, A Component Mode Synthesis Algorithm for Multibody Dynamics of Wind Turbines, *Journal of Sound and Vibration*, **326**, 753–767, (2009).

[7] S. Krenk, *Non-Linear Modeling and Analysis of Solids and Structures*, Cambridge University Press, Cambridge, 2009.

Optimization of Rolling Bearing Parameters in Dynamic Flexible Application

Simon Kabus
Vestas Wind Systems A/S
E–mail: sikab@vestas.com

Ole Ø. Mouritsen
Department of Mechanical Engineering
Aalborg University, Aalborg, Denmark

Michael R. Hansen
Mekatronikk
Universitetet i Agder

Summary This study investigates the dynamic interaction between a flexible shaft and the rolling bearing support. The rolling bearing models have six degrees of freedom; include non-Hertzian stress recovery, crowning, clearance and pretension. A virtual test setup is evaluated, and characteristic bearing parameters are optimized to comply with structural requirements. The importance of including non-Hertzian edge effects in the contact modeling and the flexibility of the shaft is clearly demonstrated.

Introduction

Contact situations are classically divided into Hertzian and non-Hertzian contacts. The Hertzian contacts are further divided into line and point contacts with either uniform or elliptical pressure distributions. The latter describes the ball-raceway contact situations very well, and numerous textbooks treats this subject, e.g. [4]. Contrary to the elliptical contact for ball bearings, the Hertzian line contact for roller bearings is only a poor approximation of actual roller-raceway contact due to its missing ability to take into account misalignments of the bodies in contact as well as geometrical deviations such as the crowning of rollers or the raceway extending beyond the length of the rollers.

To include the influence of non-Hertzian pressure distributions in roller bearings, the roller is traditionally cut up into 30-100 imaginary cylindrical slices, denoted lamina. Each lamina has a radius corresponding to their coordinate along the length of the roller. The lamina are usually treated separately according to Hertzian line-contact theory, i.e. no transfer of forces between the individual laminae is considered. Despite this it is widely used (see e.g. [3], [4], [5]) even though it fails in predicting the roller edge effects. This matter is treated by various authors, e.g. [6], by introducing an influence coefficient matrix, that relates the deflections of individual slices. Although the usability of the slicing method is greatly improved by this approach, it is, as stated by the authors, not capable of predicting peak pressures at roller edges. This study propose the use of more complex methods for analyzing non-Hertzian concentrated contacts, as described by e.g. [7] and [8].

Contact pressure modeling

The contact area is discretised into a plane area divided into $N = Nx \times Ny$ rectangles, cut view shown in figure 1(a), each considered under constant contact pressure. The pressure vector, $\boldsymbol{p}$, containing the pressures in the N rectangles is calculated by the following set of linear algebraic equations:

$$\underset{[N \times N]}{\boldsymbol{C}} \cdot \underset{[N \times 1]}{\boldsymbol{p}} = \delta - \underset{[N \times 1]}{\boldsymbol{h}} \tag{1}$$

Where $\boldsymbol{C}$ is an influence coefficient matrix relating the pressures in the individual rectangles, taking into account the location of the individual rectangles, rectangle size and material properties, δ is the perpendicular penetration between the bodies in contact and $\boldsymbol{h}$ is the distance between the bodies at grid coordinates due to roller and raceway curvatures, crowning and contact misalignment. Solving eq. (1) requires iterations, since rectangles under negative pressure, i.e. tension,

must be removed from the influence coefficient matrix, C. Figure 1(b) shows eq. 1 solved for a $20mm$ roller at $\delta = 0.1mm$ deflection. Complete information about the calculation procedure is given in e.g. [7] and [8].

(a) Contact area between roller and plate.

(b) Contact pressure, $N = 24 \times 16$.
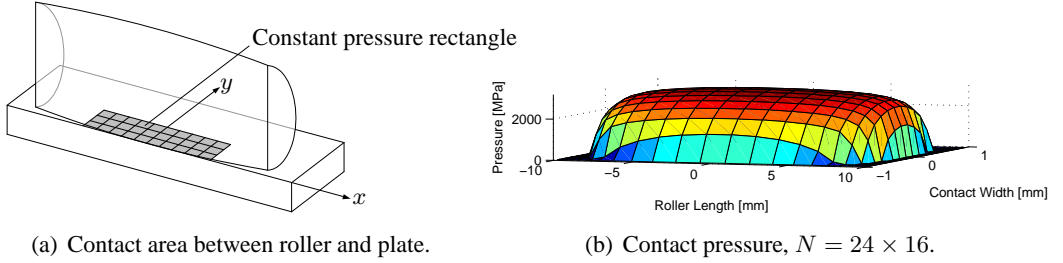
Figure 1: Discretized contact area and contact pressure results.

Although the solution of eq. (1), including iterations, is in the order of $1/100s$ at the fairly coarse mesh in figure 1(a), it is not an appropriate solution to include in a dynamic simulation including more bearings, several loaded rollers in each bearing, several roller-raceway equilibrium iterations against inner and outer raceway, system convergence iterations for each time step. Reference [9] approximates the number of iterations to $48e3/$(no. of bearings x time steps), and rejects this approach due to the potential high number of contact evaluations.

To include the precise pressure calculations described above, but reducing the number of contact evaluations to a minimum, this paper presents the idea of pre-processing series of contact situations, that are stored in look-up tables. During simulation, the necessary roller equilibrium calculations are hereby reduced to spline-fitting of the pre-processed results, which are orders of magnitudes faster than processing the individual contacts when needed.

Figure 2 shows such pre-processed contact situations, where the resultant force and moments are calculated by integrating the pressure results and figure 2(c) is the maximum contact pressure from each contact. Each grid point represents one preprocessed contact situation. The plot contains 13 misalignment angles and 20 deflections, hence a total of $13 \times 20 = 260$ contacts are simulated at respectively roller-inner raceway contact and roller-outer raceway contact.

(a) Resultant contact force.

(b) Resultant contact moment.

(c) Maximum contact pressure.
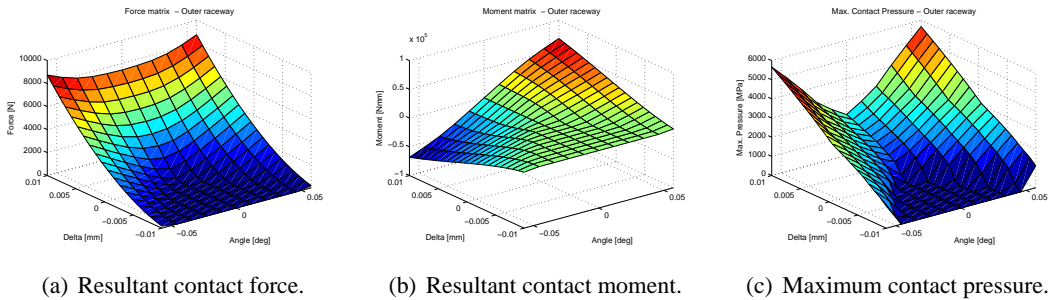
Figure 2: Pre-processed contact results.

At the 24×16 contact mesh size shown in figure 1(b), with the grid size unequally spaced along the roller length, potential edge effects are well captured, and increasing the resolution further has insignificant influence on the calculated pressure, even at significant edge loading. Due to the smoothness of the pre-processed results, the shown 13×20 contact simulations do indeed allow precise interpolation.

Implementation in Flexible Application

The method of including non-Hertzian contact theory in roller-raceway contacts is utilized in quasi static cylindrical and tapered roller bearing models with six degrees of freedom between the inner and outer bearing ring. At each time step, the displacement of the inner ring relative to the outer ring is used to calculate the contact deflection and misalignment at each roller position. From the proposed non-Hertzian method, the produced forces and moments of all rolling elements are summed to a six component reaction between the two bearing rings.

The tapered bearing model is identical to the one proposed by e.g. [5], except the roller-raceway contact uses the proposed non-Hertzian method instead of the slicing method. The cylindrical roller model follows the same principle, but without angular roller orientation and flange contact.

Bearing overview, design variables and test setup

Simple relations shown in figure 3 and design variables in table 1 have proved to be a design guideline with $error < \pm 15 pct$. The clearance of the cylindrical roller bearing is defined by SKF
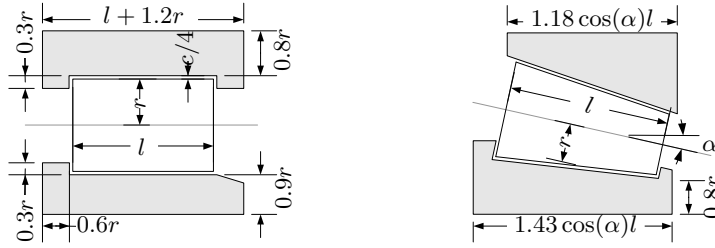
Figure 3: Design guidelines of the roller bearing models.

values from standard tolerance bearings. The design load is the loading, at which the crowned roller is subjected to a uniformly distributed contact pressure along the roller length. The logarithmic crown drop is designed as proposed by [2].

Cylindrical	$r_{bore}[mm]$	$r[mm]$	$l_{roller}[mm]$	Design load $[N]$	-	-
Tapered	$r_{bore}[mm]$	$r[mm]$	$l_{roller}[mm]$	Design load $[N]$	$\alpha[°]$	Pretension $[mm]$

Table 1: List of bearing design variables.

The test setup considered in this study is shown in figure 4, and loaded according to figure 5. The flexibility of the shaft is modeled by 9 Timoshenko beam elements.
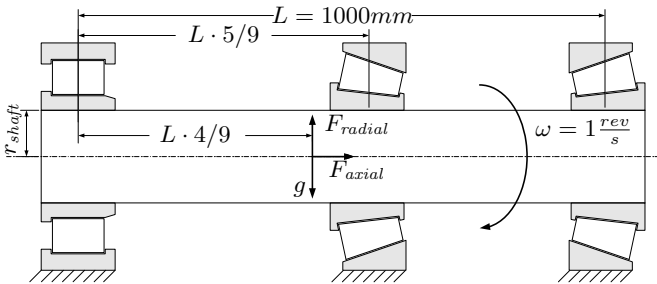
Figure 4: Test setup.
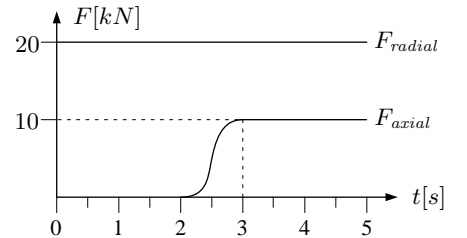
Figure 5: External forces.

Simulation and Optimization of model

The purpose of the optimization is to minimize the mass of the complete system. Reducing the dimension of the shaft will increase the deflection, causing larger angular deflections at the bearing positions, hence increasing the tendency to roller edge loading. Despite the system is rather simple compared to many bearing arrangements, the consequences of the individual choices is highly complex and non-trivial to predict, thus an obvious target for optimization.

The post-processing of the results can be expanded to include bearing life calculations, but for simplicity, a side constraint that compares the maximum pressure with a maximum allowable value of $1600 MPa$ is used. The optimization can be stated as:

$$ min \left(m_{shaft} + \sum_{i=1}^{3} m_{bearing}(i) \right) \quad, \quad \text{subject to:} \quad max\left(\sigma_{max}(i) \right) < 1600 MPa \qquad (2) $$

Results

In order to investigate the effects of roller edge loading the system is simulated and optimized with both a flexible and rigid shaft. The results are summorized in table 2.

Model	$r_{shaft}[mm]$	$r(1/2/3)[mm]$	$l(1/2/3)[mm]$	Pretension $[mm]$	$\alpha(2/3)[°]$	$mass[kg]$
Flexible	22.3	5.20/10.9/1.33	26.6/38.0/27.2	0.0191	11.8/28.5	17.8
Rigid	8.55	1.58/1.50/1.36	7.26/83.4/55.5	0.0294	5.0/9.4	3.50

Table 2: Design variables at optimum.

The optimization clearly differentiates between the two models; the flexible model weighs 5.1 times the rigid model. The lower mass of the rigid model is due smaller shaft dimension and the bearings in the rigid model being much more needle-like. The needle bearings are much more sensitive to misalignments.

Concluding remarks

In this paper current methods for contact pressure computations are examined and a method well suited for time domain simulation, while capable of capturing the important edge loading, is introduced. The new method is used for optimization purposes. This optimization reveals the usefulness of the method as well as the importance of including flexibility of all components in order to capture a realistic roller loading.

References

[1] Hertz, H., Über die Berührung fester elastischer Körper, Journal für reine und angewandte Mathematik, **92**, 156-171. (1882).

[2] Lundberg, G. Elastische Berührung zweier Halbräume. Forschung auf dem Gebiete des Ingenieurwesens, **10(5)**, 201-211, (1939).

[3] DIN ISO 281, Dynammischer Tragzahlen und nominelle Lebensdauer, Deutsches Institut für Normung e.V. 1990

[4] Harris, T. A. *Rolling Bearing Analysis*. John Wiley & Sons Inc., Third edition, (1991)

[5] Bhowmick et. al. Quasi-Static Analysis of Tapered Roller Bearings and Comparison of Bearing Lives for Different Roller Surface Profiles

[6] Teutsch, R. and Sauer, B. An Alternative Slicing Technique to Consider Pressure Concentrations in Non-Hertzian Line Contacts.

[7] Johnson K. L. *Contact Mechanics* Cambridge University Press, (1985).

[8] Cretu et. al. The Study of Non-Hertzian Concentrated Contacts by a GC-DFFT Technique.

[9] Houpert, L. An Engineering Approach to Non-Hertzian Contact Elasticity-Part II

[10] Sopanen, J. and Mikkola, A. Dynamic model of a deep-groove ball bearing including localized and distributed defects.

An Improved Multibody Model of Closed Chains in Loop-sorter-systems

Søren E. Sørensen*

Product Engineering
Crisplant A/S, Denmark
E−mail: soeren.soerensen@crisplant.com

Ole Ø. Mouritsen

Department of Mechanical Engineering
Aalborg University, Aalborg, Denmark
E−mail: oom@me.aau.dk

Morten K. Ebbesen

Department of Engineering
University of Agder, Norway
E−mail: morten.k.ebbesen@uia.no

Summary An improved formulation for simulation of closed chains in loop-sorter-systems is presented. Previous models have shown that reasonable results can be reached using rigid multibody dynamic. The improvements done to the model has been aimed on increased accuracy, reduced evaluation time and improved pre and post processing of simulation data. The evaluation time is reduced significantly although the presented results show only minor improvements to the accuracy.

Introduction

Poor dynamic performance in the chain of a loop-sorter-system can result in premature wear on vital mechanical components. This can lead to huge expenses on replacing worn down parts. Therefore, having the ability to simulate the dynamic of the chain of carts in an early stage of the design phase makes it feasible to avoid poor layouts.

Two vital components in the loop-sorter-system are the chain and the track. The track is composed of different building blocks like straight elements, horizontal curves, level curves etc. A closed chain of carts runs in the track with a constant speed as sortation is performed along the track. Depending on the sortation task the length of the track may vary from 100 [*m*] up to 3000 [*m*]. A cart is shaped like a T, see Figure 1 left. The cart has a connection point at each end of the main profile and two guiding wheels at each end of the end-profile. All carts are coupled by connecting the rear link to the front link of the following cart. Depending on the task the cart length may vary from 0.5 [*m*] up to 1.25 [*m*]. The chain is actuated by a number of linear motors placed along the track using an iron core at the bottom of the cart to drive the chain forward.

[1], [2], [3] developed a simulation model capable of determining forces in the chain of carts. To obtain a reasonable computation time [1] based the model on a multibody dynamic approach assuming all tracks and carts to be rigid bodies. To describe the flexibility of the chain, connections between the bodies were modelled by a system of springs and dampers. Through verification tests the dynamic simulation model showed some accordance with measured forces in the chain. With the aim of improving the accuracy, [4] build an extended simulation model where the flexibility of the track and supports was taken into account. The model incorporates a beam finite element model of the track and supports which runs in parallel with the multibody formulation given by [1]. In every time step reaction forces from the multibody model are send to the FE-model that returns the position and velocity of the track. Results were a model with only minor increase of the accuracy and a model with a lot of new parameters to deal with.

By the experiences gained from [1] and [4] an improved version of the multibody simulation tool has been developed. The conducted improvements have been aimed on higher accuracy, reduced computation time and improved pre and post processing of the simulation data. In this paper the basic theory in the simulation tool is presented in short terms along with a discussion on some of

the main improvements made. Results from simulations on two layouts are presented and compared with results form [1] and [4].

Methods

The model is based on [5] theory for unconstrained multibody dynamics where solving the equations of motion numerically impose the movement of each body. The track is modelled as a fixed rigid body on which each cart is an individual body, see Figure 1 right. Seven points on each cart defines the contact between the carts and the track. To approximate the cart stiffness a penalty formulation is used in the contact points by applying the force through a linear spring and a viscous damper. To model the friction a Coulomb friction model has shown to be sufficient. Defining the contact between the carts and the track [1] has constructed a kinematic model that, based on a Newton-Raphson solver, determines the position of each cart relative to the track.
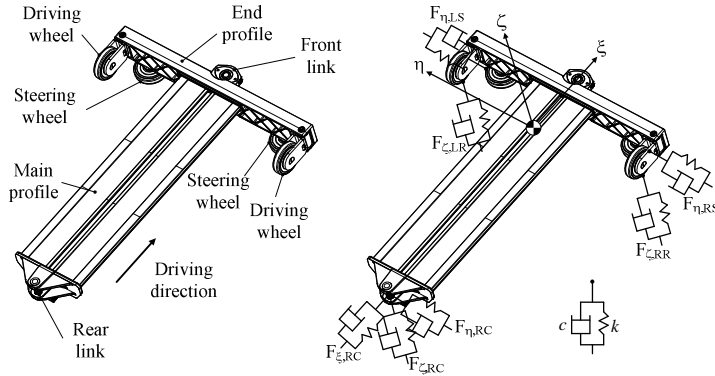
Figure 1: Left: Main components of a cart. Right: The rigid cart is connected in seven points using a linear spring and viscous damper.

Several improvements have been made to the simulation model. Manny of these involve reduction of the computation time and improvements of the pre and post processing of data. This is done in order to make the tool easier and faster to use and to prepare it as an evaluation method for optimization of the track layout. Reduced evaluation time has especially been achieved through rearranging the code and by rearranging the track and contact formulation developed by [1]. In total the evaluation time has been reduced by a factor of thousand. This factor is expected to increase as a new kinematic model without a the Newton-Raphson solver is being developed.

To increase accuracy and reduce the evaluation time a new ordinary differential equation (ODE) solver has been implemented. A survey on different ODE solvers has shown that some solvers are far from accurate when solving stiff problems. The survey showed that the fifth order Cash-Karp Runge-Kutta method with an adaptive stepsize control can handle the stiff problems in a robust and fast way. A routine for this ODE solver is found in [6].

To increase the accuracy a new formulation of the force applied by the motors has been implemented. This formulation uses a varying reaction point at the bottom face of the cart. This has increased the accuracy, especially for forces in the ζ-direction.

Results

Tests of the simulation model have been conducted on two different sorters denoted "Figure Eight Sorter" and "Oval Sorter". The figure eight sorter is 63.3 [m] long and has a chain of 52 carts each 1.248 [m]. Four linear motors are distributed along the track, see Figure 2. The track consists of an

upper and lower part where the incline and decline is made by the use of level curves. Further information on the cart setup and the layout is found in [4].
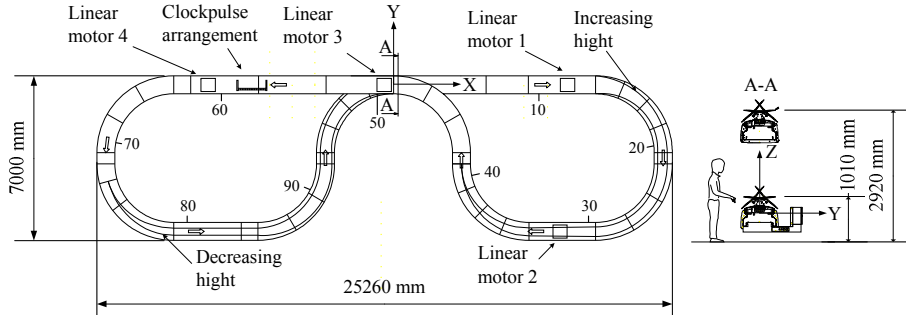
Figure 2: Layout of the figure eight sorter.

The oval sorter is 37.6 [*m*] and consists of two 180 [°] curves with two straight sections in between. The chain is driven by three motors located along one of the straight sections. The chain consists of 47 carts each 0.8 [*m*]. Further information on the setup is found in [1].

Evaluation of the simulation is done by comparing results with measurements conducted on the two layouts. Forces in the rear link were logged using the transducer described in [1]. An example of the measured and simulated force in the ξ-direction with a sorter speed at 2.0 [*m/s*] on the figure eight sorter is shown in Figure 3.
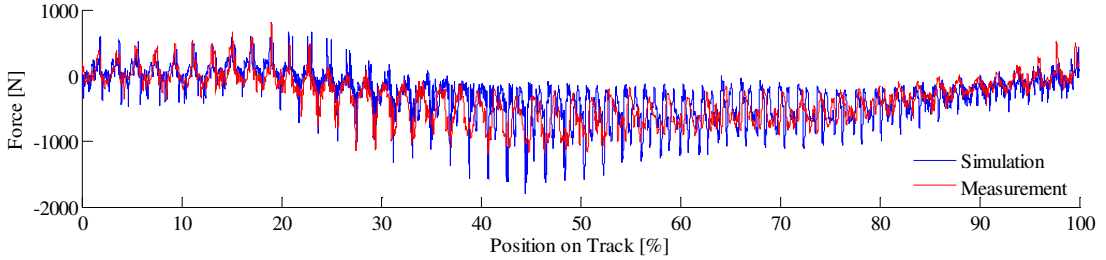
Figure 3: Measured and simulated force in the rear link in ξ-direction on the figure eight sorter.

In Table 1 results from four conducted simulations are shown. Three simulations were performed on the figure eight sorter with the chain speeds: 1.0, 2.0 and 3.0 [*m/s*]. On the oval sorter one simulation was made at 2 [*m/s*]. To evaluate the simulation tool results from [1] and [4] are included. Evaluation is done using Rain Flow Counting (RFC) [7] and the Root Mean Square Deviation (RMSD). The RFC is used to evaluate the systems lifetime by the number of reversals n_{rev} and the equivalent force F_{eq}. The cut-off is set to 80 [*N*] for simulations on the figure eight sorter and 50 [*N*] for data on the oval sorter. The RMSD provide the correlation between the simulated data and the measurements as the percentage deviation.

In Table 1 it is shown that only minor improvements in the precision have been achieved by the improved simulation model compared to results from [1] and [4]. The number of reversals in the simulation data is about twice the number of reversals in the measured data. Also, the equivalent force range seems to be larger in the simulated data than in the measured data. However, a FFT analysis shows a fine correspondence between the main frequencies. Tests have shown that varying some of the design variables may improve the results. An enlarged parameter study may therefore be able to reduce the deviation even further. The RMSD is generally lower for the new

simulations. Particular forces in ζ-direction have improved due to the enhanced formulation for the applied motor force.

		Figure Eight Sorter							
		Measurement		Improved formulation			Simulations by [4]		
Speed [m/s]	Force Direction	n_{rev}	F_{eq} [N]	n_{rev}	F_{eq} [N]	$RMSD$ [$\%$]	n_{rev}	F_{eq} [N]	$RMSD$ [$\%$]
1.0	ξ	650	342	1436	683	18.0	764	377	16.6
	η	23	129	269	240	9.0	31	261	25.9
	ζ	184	208	421	1112	16.5	13	270	12.0
2.0	ξ	544	490	1094	604	14.6	848	734	11.1
	η	142	150	245	275	8.7	104	200	22.8
	ζ	113	327	551	963	11.7	29	222	14.0
3.0	ξ	459	646	915	781	20.1	595	884	9.2
	η	212	172	282	263	7.4	157	249	39.5
	ζ	118	371	431	974	10.0	28	326	20.2
		Oval Sorter							
		Measurement		Improved formulation			Simulation by [1]		
2.0	ξ	386	214	123	291	18.1	91	279	28.0
	η	26	95	16	120	10.3	7	106	5.0
	ζ	9	172	7	119	18.3	1	53	18.2

Table 1: RFC and RMSD results from verification test conducted on the figure eight and oval sorter.

Concluding remarks

Work has been carried out to improve the accuracy, reduce computation time and improve the use of the multibody simulation model presented by [1]. Improvements have in particular been achieved through reduced computation time and improved pre and post processing of data. Results have shown that computation time is reduced by as much as a thousand times.

Results from simulations performed on two sorter layouts show that accuracy only has improved by a small amount. To further improve the accuracy a detailed parameter study should be performed together with studies on how to develop the contact formulation.

References

[1] M. K. Ebbesen. Optimal Design of Flexible Multibody Systems. Ph.D thesis. Department of Mechanical Engineering, Aalborg University, Denmark, (2008).

[2] M. K. Ebbesen, M.R. Hansen and N.L. Pedersen. Design Optimization of Conveyor Systems. ECCM 2006, Lisabon, Portugal (2006).

[3] M. K. Ebbesen, M.R. Hansen and N.L. Pedersen. A Modular Approach to Analysis of Large Scale Baggage Handling Systems. NSCM-17, pp. 23-26, KTH, Mechanics, Royal Institute of technology, Stockholm, Sweden, (2004).

[4] G. Petersen and J. Kofman. Simulation of Multibody Systems with Flexible Boundaries. Master Thesis. Department of Mechanical Engineering, Aalborg University, Denmark (2009).

[5] P.E. Nikravesh. Computer-Aided Analysis of Mechanical Systems. Prentice Hall, (1988).

[6] W.H. Press, S.A. Teukolsky, W.T. Vetterling and B.P. Flannery Numerical Recipes in Fortran 90: The art of Parallel scientific Computation, Cambridge University Press, 2. edition, (1996).

[7] R. Stephens, R.L. Hoffmann, A. Fatemi and H.O. Fuchs. Metal Fatigue in Engineering. Wiley Interscience, 2. edition, (2001).

Constant parameter identification of multi-body systems from motion data

Michael S. Andersen [*] **and John Rasmussen**

Department of Mechanical Engineering
Aalborg University, Aalborg, Denmark
e–mail: {msa,jr}@me.aau.dk

Michael Damsgaard

AnyBody Technology A/S
Aalborg, Denmark
e–mail: md@anybodytech.com

Summary   Scaling of cadaver study-based musculoskeletal models to a specific subject frequently involves trial-and-error to achieve reasonable results. In this study, we demonstrated an optimisation-based approach, which not only results in the best possible fit of the model to a dynamic trial, but also reduces the number of variables, which require user interaction.

Introduction

The musculoskeletal system of a human or an animal is frequently modelled as a multi-body dynamics model, where the bones are modelled as rigid segments connected by idealized joints and the muscles as lines from origin to insertion that may go through via. points or wrap over geometrical surfaces [1, 2]. Normally, a base model is defined from cadaver studies, where the bone lengths, segment inertia, mechanical properties of the muscles and so on are determined [3, 1]. Hereafter, scaling laws are defined such that the base model can be scaled to the size of a specific subject for which it is desired to perform an analysis of interest, for instance, to calculate the joint and muscle forces during gait [4].

Since the subject and the cadaver-based model are not identical, scaling the model to the subject is not trivial and frequently requires trial-and-error, which is both tedious and can result in large modelling errors. Recently, Andersen et al. [5] developed a general optimisation-based method to the determination of constant model parameters from given motion data for multi-body models subject to holonomic constraints. Among many other uses, this method can be used to compute the scaling of a musculoskeletal model such that it best fits measured motion, for instance, from a motion capture experiment. Therefore, in this study, we applied the method of [5] to identify the segment lengths and local marker coordinates of a multi-body model of the lower extremities from a gait trial measured using motion capture.

Methods

Computational method

The computational method that was applied to the parameter identification problem was originally described by [5]. This method was designed to determine the optimal model constants, d, as well as the time-dependent system coordinates, $q(t)$, given a system description by means of two sets of holonomic kinematic constraint equation: 1) a set of equations that are part of an objective function, $\Psi(q(t), d, t)$, and 2) a set which define the feasible set, $\Phi(q(t), d, t)$. Since the first set of constraint equations are allowed to be violated, these are refered to as soft, whereas the second set

of equations are refered to as hard constraint equations because they must be satisfied.

With these definitions, the large-scale parameter identification problem can be specified as [5]:

$$\min_{d,\, q(t_1), q(t_2),\ldots, q(t_N)} \quad \sum_{k=1}^{N} G(\Psi(q(t_k), d, t_k)) \tag{1}$$
$$\text{s. t.} \quad \Phi(q(t_i), d, t_i) = 0$$

where $i = 1, 2 \ldots, N$, where N is the number of analysis time steps and $G(\Psi(q(t_k), d, t_k))$ specifies the objective function evaluated for one time-step. In this study, we used a least-square objective function. The basic idea behind the method is to determine the model motion as well as constant model parameters such that the sum of soft constraint violations, as calculated by $G(\Psi(q(t), d, t))$, is minimized over all analysis time steps. For instance, if the soft constraint equations are specified as the vector difference between measured marker trajectories and the corresponding point on the model, the optimal solution is the set of model constants, which are made part of the problem, and model motion that makes the model follow the measured markers as well as possible.

As such, this optimisation problem is too large to solve directly due to all the variables in the problem. However, due to a special structure in the linearized Karush-Kuhn-Tucker (KKT) conditions, Andersen et al. [5], showed that the solution can be found efficiently using the following algorithm:

1. Specify an initial guess for the system coordinates at the first sample and an initial guess on the constant parameters.

2. Keep the initial guess on the constant parameters fixed at the initial guess and determine the system coordinates at all samples.

3. Solve the optimization problem in equation (1):

    (a) Initialize the iteration counter and set the initial conditions.

    (b) Check if the KKT conditions are satisfied if they are, break and return the result else go to (c).

    (c) Calculate a new search direction.

    (d) Calculate a new step length using a backtracking line search.

    (e) Update the variables.

    (f) Update the iteration counter and go to (b).

In the algorithm, for computational efficiency, the computation of the new search direction in step 3(c) relies on a specific structure in the linearized KKT conditions. Please see [5] for full details about the method. The method has been implemented in the AnyBody Modelling System version 4.1, which was used in this study.

Lower extremity model

The method has been applied to determine the segment lengths of a multi-body mechanical model of the lower extremities of a human based on the cadaver study of [1]. The motion of the model was specified from a motion capture experiment for a gait trial with a Helen Hayes marker protocol.

Since the placement of the markers on the model was not precisely known, a number of the local coordinates of the markers were also treated as unknown constant parameters and optimised. All marker coordinates except the ASIS, y-coordinates of the PSI and ANK, and the TOE markers were optimised. The marker coordinates, which were not optimised were placed manually on the model bone geometry. To obtain symmetry in the model, the left and right side were scaled using the same constant parameters, e.g. left and right thigh were assumed equally long.

Results

The initial model in its initial position can be seen in Figure 1(a), the motion of the model given the initial segment lengths and local marker coordinates in Figure 1(b) and the motion of the model after optimisation in Figure 1(c). Please notice that the model in Figure 1(b) has reasonable guessses of the location of the markers on the model as well as segment lengths and yet the marker errors are significantly improved by the optimisation.

(a)   (b)   (c)
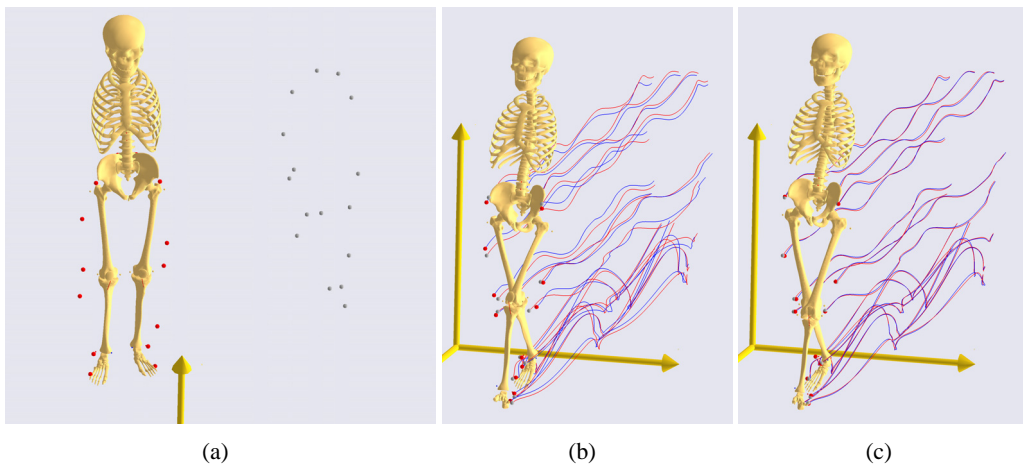
Figure 1: (a) The model with its initial segment lengths, markers (the red points) and in its initial starting position. The illustration also includes the measured markers at the first sample (the gray points). (b) Shows the marker trajectories before optimization. (c) Shows the marker trajectories after optimization. In both plots, the blue trajectories show trajectories of segment-fixed markers whereas the red trajectories show the trajectories of the measured markers.

The convergence history for the segment lengths, the maximum error on the KKT condtions, the step lengths as well as the objective function are shown in Figure 2.

The main thing to notice is that all segment lengths show small over-shoots before settling at their finale values. Additionally, the step length is initially reduced to $\frac{1}{4}$ but over the next two iterations is brought back to full step length from iteration three and forward. This behavior is likely explained by the nonlinearity of the problem. Finally, through the optimisation, the objective function is reduced from 1.06 m^2 to 0.072 m^2 after the ten iterations used.

Concluding remarks

This study demonstrated the possibility to scale a cadaver-based musculoskeletal model by optimising the best possible segment lengths as well as local marker coordinates over a dynamic trial.

In the study, a uniform scaling law, with only one parameter per segment, as well as the same
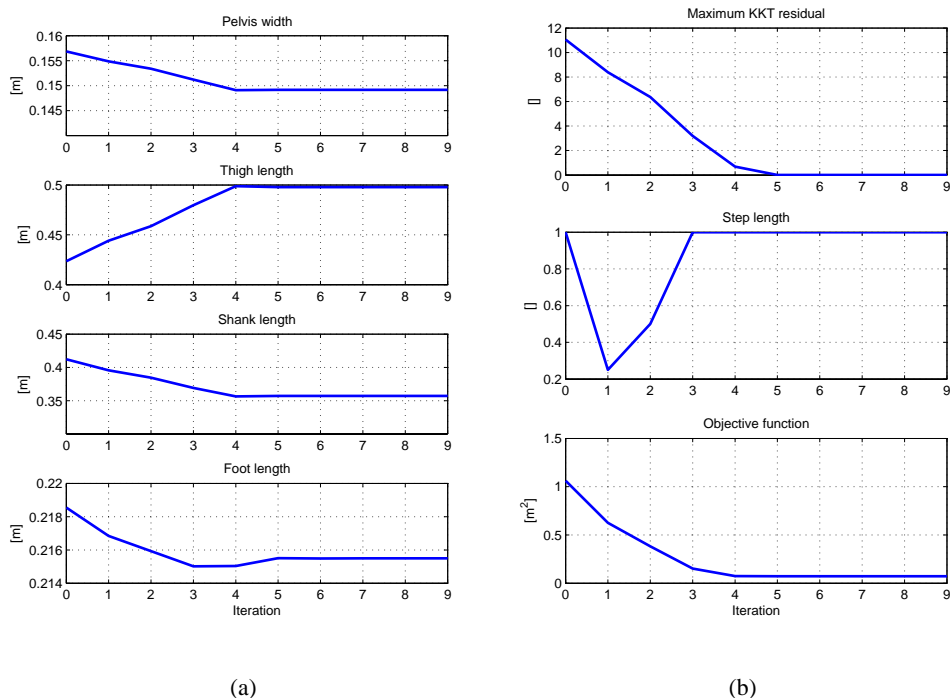
Figure 2: Optimiser convergens history. (a) Shows the convergens history of the segment lengths. (b) Shows the maximum error on the KKT conditions, the step length and the objective function at each iteration. A maximum error of 10^{-6} on the KKT condtions were used.

scaling parameters on the left and right side to ensure symmetry in the model, was used. Yet, after optimisation, the model successfully tracked measured marker trajectories relatively well.

Which scaling law to use to obtain the best results still requires further studies.

References

[1] M. D. Klein Horsman, H. F. J. M. Koopman, F. C. T. van der Helm, L. P. Pros and H. E. J. Veeger. Morphological muscle and joint parameters for musculoskeletal modelling of the lower extremity. *Clin. Biomech.*, **22**(2), 239–247 (2007).

[2] M. Damsgaard, J. Rasmussen, S. T. Christensen, E. Surma and M. de Zee. Analysis of musculoskeletal systems in the AnyBody Modelling System. *Sim. Mod. Prac. The.* , **14**(8), 1100–1111 (2006).

[3] S. L. Delp, J. P. Loan, M. G. Hoy, F. E. Zajac, E. L. Topp and J. M. Rose. An interactive graphics-based model of the lower extremity to study orthopedic surgical procedures. *IEEE Trans. Biomed. Eng.*, **37**, 757–767 (1990).

[4] J. Rasmussen, M. de Zee, M. Damsgaard, S. T. Christensen, C. Marek and K. Siebertz. A general method for scaling musculo-skeletal models. In Proceedings of the International Symposium on Computer Simulation in Biomechanics, Cleveland, Ohio, USA (2005).

[5] M. S. Andersen, M. Damsgaard, B. MacWilliams and J. Rasmussen. A computationally efficient optimisation-based method for parameter identification of kinematically determinate and over-determinate biomechanical systems. *Comput. Meth. Biomech. Biomed. Engin.*, DOI: 10.1080/10255840903067080 (In Press) (2009).

Selective Integration in the Material-point Method

Lars Andersen[*], Søren M. Andersen and Lars Damkilde

Department of Civil Engineering
Aalborg University, Aalborg, Denmark
e–mail: la@civil.aau.dk

Summary   The paper deals with stress integration in the material-point method. In order to avoid parasitic shear in bending, a formulation is proposed, based on selective integration in the background grid that is used to solve the governing equations. The suggested integration scheme is compared to a traditional material-point-method computation in which the stresses are evaluated at the material points. The deformation of a cantilever beam is analysed, assuming elastic or elastoplastic material behaviour.

Introduction

The material-point method (MPM) was proposed by Sulsky and coworkers [1, 2] as an alternative to the finite-element method (FEM) for analysis of problems in solid mechanics. The MPM can be described as a variation of the FEM, in which the material and any state variables are tracked at a finite set of material points that are allowed to move through a background grid of finite elements or cells. In contrast to a Lagrangian finite-element scheme, this allows the simulation of solids undergoing extreme deformation and displacements without mesh entanglement. Further, since the material follows the material points, mass diffusion occurring in Eulerian descriptions is avoided. Finally, the MPM automatically accounts for the exchange of momentum between adjacent bodies by solving the governing equations of motion a the nodes of the background grid.

Hence, apparently the MPM is useful for the analysis of problems in solid mechanics in which huge displacements and interaction between colliding bodies must be accounted for. However, in a standard MPM formulation, the stresses are evaluated at the material points. This may lead to *grid-crossing errors* as well as *parasitic shear*, in particular when linear interpolation functions are employed within the background grid.

Grid-crossing errors occur when a material point moves from one cell to another in a time step. This changes the sign of the stress contribution from that material point to the interior force at the adjacent grid nodes. As described by Bardenhagen et al. [3] this problem may be solved to some extent by smearing out the mass associated with a material point, leading to the so-called generalised-interpolation material-point (GIMP) method. Alternatively, higher-order interpolation may be applied as proposed by Andersen and Andersen [5].

Parasitic shear was reported by Cook et al. [4] in relation to linear quadrilateral elements applied to the analysis of bending. Thus, for first-order shape functions, the shear strains and stresses are only defined correctly at the centre of the element. Hence, full integration with two Gauss points in each direction may cause shear locking in bending. A similar effect occurs in the MPM since the material points are generally not placed at the centre of the computational cells. As described in this paper, it may therefore be advantageous to apply an integration scheme in the MPM corresponding to selective integration in the FEM.

Stress integration in the material-point method

The material-point method builds on the weak formulation. For the solid domain, Ω,

$$\int_\Omega \rho \mathbf{w} \cdot \mathbf{a} dV = -\int_\Omega \nabla \mathbf{w} : \rho \boldsymbol{\sigma}^s dV + \int_{\partial\Omega_\tau} \mathbf{w} \cdot \boldsymbol{\tau} dS + \int_\Omega \rho \mathbf{b} dV, \tag{1}$$

where $\mathbf{w} = \mathbf{w}(\mathbf{x},t)$ is the virtual field, $\mathbf{a} = \mathbf{a}(\mathbf{x},t)$ the material acceleration, $\rho = \rho(\mathbf{x},t)$ the mass density, $\boldsymbol{\sigma}^s = \boldsymbol{\sigma}^s(\mathbf{x},t)$ the specific stress, $\mathbf{b} = \mathbf{b}(\mathbf{x},t)$ the external body force field, and $\boldsymbol{\tau} = \boldsymbol{\tau}(\mathbf{x},t)$ signifies the surface traction on $\partial\Omega_\tau$ where mechanical boundary conditions are prescribed. Here, $\boldsymbol{\sigma}^s = \boldsymbol{\sigma}/\rho$ and $\boldsymbol{\tau} = \boldsymbol{\sigma} \cdot \mathbf{n}$ with $\mathbf{n}$ denoting the unit outward normal to the boundary of the domain.

The density field $\rho(\mathbf{x},t) = \sum_{p=1}^{N_p} M_p \delta(\mathbf{x} - \mathbf{x}_p)$ is employed, where M_p is the mass of material point number p, $p = 1,\ldots,N_p$, and $\mathbf{x}_p = \mathbf{x}_p(t)$ is its position. Further, linear interpolation within the computational background grid, discretization of time and lumping the mass at the grid nodes provide the following system of equations for node number i and time step k:

$$m_i^k \mathbf{a}_i^k = \boldsymbol{\tau}_i^k + \mathbf{b}_i^k - \sum_{p=1}^{N_p} M_p \boldsymbol{\sigma}_p^{s,k} \cdot \mathbf{G}_{ip}^k, \qquad m_i^k = \sum_{p=1}^{N_p} M_p \Phi_i(\mathbf{x}_p^k) \qquad (2)$$

where, for example, m_i^k is the mass associated with node number i at time step k. The interpolation function belonging to node i is denoted $\Phi_i(\mathbf{x})$, and $\mathbf{G}_{ip}^k = \nabla\Phi_i(\mathbf{x})|_{\mathbf{x}=\mathbf{x}_p^k}$. The first two terms on the left of Eq. (2) are identified as the external force on the body, whereas the final term represents the internal forces. In each time step, the velocities at the material points and nodes are updated as

$$\mathbf{V}_p^{k+1} = \mathbf{V}_p^k + \Delta t \sum_{i=1}^{N_n} \mathbf{a}_i^k \Phi_i(\mathbf{X}_p^k), \qquad m_i^{k+1} \mathbf{v}_i^{k+1} = \sum_{p=1}^{N_p} M_p \mathbf{V}_p^{k+1} \Phi_{ip}(\mathbf{x}_p^k). \qquad (3)$$

Subsequently, the strain increments at the material points are determined by

$$\Delta\boldsymbol{\varepsilon}_p^k = \frac{\Delta t}{2} \sum_{i=1}^{N_n} \left\{ \mathbf{G}_{ip}^k \mathbf{v}_i^{k+1} + (\mathbf{G}_{ip}^k \mathbf{v}_i^{k+1})^T \right\}, \qquad (4)$$

and the stresses are updated by a constitutive law. Two schemes are now compared: (1) a computation based on a standard MPM approach with the strain increments provided by Eq. (4), and (2) an alternative scheme with $\mathbf{G}_{ip}^k$ replaced by $\mathbf{G}_{ic}^k = \nabla\Phi_i(\mathbf{x})|_{\mathbf{x}=\mathbf{x}_c}$ for the determination of the shear strain increments, whereas Eq. (4) without modification for the computation of the normal strains. In the second approach, $\mathbf{x}_c$ denotes the coordinates of the point at the centre of the cell in which the material point resides. Hence, scheme no. 2 corresponds to selective integration.

Analysis of a cantilever beam

A cantilever beam is analysed by the MPM method, employing the explicit scheme described in the previous section. The length is $L = 8$ m in the x-direction, the height is $H = 2$ m in the y-direction and the beam has a mass density of $\rho = 10$ kg/m^3. The mesh size is 0.5 m and 2×2 material points are employed within each cell. Over a period of 0.5 s the beam is subjected to an increasing body force in terms of gravity with the final acceleration 10 m/s^2 in the negative y-direction. After this, the external force is kept constant.

Firstly, the analysis is carried out for an elastic material with Young's modulus $E = 10$ MPa and Poisson's ratio $\nu = 0$. Figure 1 shows the the normal and shear stresses, σ_{xx} and σ_{xy} after $t = 1$ s for Schemes 1 and 2, i.e. with standard MPM stress evaluation or 'selective integration'. Parasitic shear is clearly identified for σ_{xy} and, to some extent, the equivalent Mises stress σ_e. On the other hand, selective integration provides a smooth shear stress variation without reducing the accuracy of the normal stresses. However, the development of the mechanical energy is almost the same and only small differences are present in the displacement obtained with Schemes 1 and 2.

Standard material-point integration   **Selective integration**
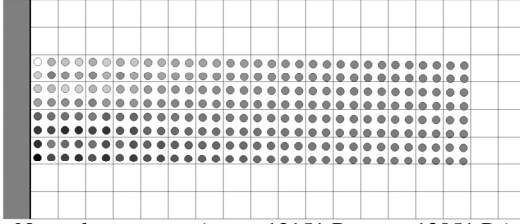
Normal stress, σ_{xx} ($\bullet = -7997$ Pa ; $\circ = 7988$ Pa)   Normal stress, σ_{xx} ($\bullet = -8174$ Pa ; $\circ = 8166$ Pa)

Shear stress, σ_{xy} ($\bullet = -1463$ Pa ; $\circ = 35$ Pa)   Shear stress, σ_{xy} ($\bullet = -978$ Pa ; $\circ = 11$ Pa)

Mises stress, σ_e ($\circ = 24$ Pa ; $\bullet = 8280$ Pa)   Mises stress, σ_e ($\circ = 25$ Pa ; $\bullet = 8230$ Pa)

Figure 1: Stresses in the elastic beam at the end of the simulation.

The second analysis concerns a von Mises material with the yield criterion $f = \sigma_e - \sigma_0 \leq 0$, where σ_0 is the yield stress ($\sigma_0 = 4$ kPa in this analysis). Otherwise, the parameters are the same as before. The results are illustrated in Fig. 2, and again parasitic shear occurs in the case of standard MPM integration of the stresses. Nonetheless, no significant change can be seen in the extent and shape of the plastified zone. This is likely a result of the fact that $\sigma_{xx} \gg \sigma_{xy}$ in the present case.

Concluding remarks

Selective integration in the material-point method provides a better approximation of the shear stress distribution in a beam subjected to bending than standard MPM analysis with shear stress evaluation at the material points. Nonetheless, for beams with a length-to-height ratio of more than 4, standard MPM integration does not degenerate the solution for plastic problems since the axial normal stresses are dominating in bending. However, for other classes of problems in which shear stresses dominate, selective integration may be necessary in order to have a physically sound transition from elastic into plastic response.

Figure 2: Stresses in the elastic-plastic beam at the end of the simulation.

References

[1] D. Sulsky, Z. Chen and H.L. Schreyer. A particle method for history-dependent materials. *Computer Methods in Applied Mechanics and Engineering*, **118**, 179–196, (1994).

[2] D. Sulsky, S.J. Zhou and H.L. Schreyer. Application of a particle-in-cell method to solid mechanics. *Compter Physics Communications*, **87**, 236–252, (1995).

[3] S.G. Bardenhagen and E.M. Kober. The generalized interpolation material point method. *Computer Modeling in Engineering and Sciences*, **5**(6), 477–495, (2004).

[4] R.D. Cook, D.S. Malkus and M.E. Plesha. *Concepts and Applications of Finite Element Analysis*. John Wiley & Sons, New York, Third edition, (1989).

[5] S.M. Andersen and L. Andersen. Material-Point Method Analysis of Bending in Elastic Beams. In *Proceedings of the Eleventh International Conference on Civil, Structural and Environmetal Engineering Computing*. Civil-Comp Press, Stirlingshire, Scotland, (2007).

Analysis of stress updates in the material-point method

Søren Andersen[*] **and Lars Andersen**
Department of Civil Engineering
Aalborg University, Aalborg, Denmark
e–mail: sa@civil.aau.dk

Summary   The material-point method (MPM) is a new numerical method for analysis of large strain engineering problems. The MPM applies a dual formulation, where the state of the problem (mass, stress, strain, velocity etc.) is tracked using a finite set of material points while the governing equations are solved on a background computational grid. Several references state, that one of the main advantages of the material-point method is the easy application of complicated material behaviour as the constitutive response is updated individually for each material point. However, as discussed here, the MPM way updating and integrating stresses in time is problematic. This is discussed using an example of the dynamical collapse of a soil column.

Introduction

The material-point point method is a new computational method for modelling large-stain dynamical engineering problems. The material-point method was originally developed by Sulsky and coworkers [1, 2]. An important extension, known as the generalized material point method (GIMP), is presented by Bardenhagen and Kober [3].

Theory

In the MPM a continuum problem is discretized by representing the domain of the problem, Ω, by a finite set $p = 1, ..N_p$ material points. Each material point is assigned a mass, stress, velocity and density, denoted $m_p, \boldsymbol{\sigma}_p, \mathbf{v}_p, \rho_p$, respectively. The domain associated with the material point, p, is denoted Ω_p and the volume of this domain is denoted V_p. In addition, a finite set grid nodes $i = 1, ..N_n$, are defined where the governing equations are solved. In the original MPM formulation the material points are represented using the Dirac delta function when forming the governing equations on the grid. Hence, the interpolation between the material points and the mesh is governed by the nodal shape functions $N_i(\mathbf{x})$. In the GIMP, further a particle characteristic function, $\chi_p(\mathbf{x})$, is defined for each material point.

The governing equation is the balance of momentum

$$\rho \frac{d\mathbf{v}}{dt} = \nabla \cdot \boldsymbol{\sigma} + \rho \mathbf{b}, \tag{1}$$

where $\rho = \rho(\mathbf{x}, t)$ is the current density, $\mathbf{v} = \mathbf{v}(\mathbf{x}, t)$ is the spatial velocity, $\boldsymbol{\sigma} = \boldsymbol{\sigma}(\mathbf{x}, t)$ is the Cauchy stress tensor and $\mathbf{b} = \mathbf{b}(\mathbf{x}, t)$ is the specific body force. Utilizing the GIMP formulation, the discrete equation becomes

$$m_i \frac{d\mathbf{v}_i}{dt} = \mathbf{f}_i^{int} + \mathbf{f}_i^{ext}, \tag{2}$$

where $m_i \frac{d\mathbf{v}_i}{dt} = \sum_p m_p \frac{d\mathbf{v}_p}{dt} \bar{N}_{ip}$ is the nodal momentum rate of change,

$$\mathbf{f}_i^{int} = -\sum_p \boldsymbol{\sigma}_p V_p \frac{\partial \bar{N}_{ip}}{\partial \mathbf{x}} \quad \text{and} \quad \mathbf{f}_i^{ext} = \int_{\partial \Omega_\tau} N_i \boldsymbol{\tau} dS + \sum_p m_p \mathbf{b}_p \bar{N}_{ip} \tag{3}$$

is the internal force and external forces, respectively.

The weighting and the gradient weighting function are defined by

$$\bar{N}_{ip} = \frac{1}{V_p} \int_{\Omega_p \bigcup \Omega} N_i \chi_p dV \quad \text{and} \quad \frac{\partial \bar{N}_{ip}}{\partial \mathbf{x}} = \frac{1}{V_p} \int_{\Omega_p \bigcup \Omega} \frac{\partial N_i}{\partial \mathbf{x}} \chi_p dV. \tag{4}$$

For comparison, if the particle function is defined by $\chi_p(\mathbf{x}) = \delta(\mathbf{x} - \mathbf{x}_p)$ the original MPM formulation is retrieved. Another comparison relevant for this discussion is that the MPM formulation is similar to a finite element formulation, where the Gauss points are replaced by material points.

Time-integration scheme

Equation 2 is the basic equation that using appropriate boundary conditions is integrated in time in order to find the evolution of the state variables, that are defined at the material points. This constitutes to updating the position, velocity, stress and density at the material points. The typical procedure applied here and in the references [1, 2] is to use explicit time integration. Hence, the time domain is divided into a finite set of timesteps and the size of the time-steps has to satisfy the Courant criterion.

The update of position and velocity is performed by

$$\mathbf{x}_p^{k+1} = \mathbf{x}_p^k + \Delta t \sum_{i=1}^{N_n} \bar{N}_{ip} \frac{m_i \mathbf{v}_i + \Delta t(\mathbf{f}_i^{int,k} + \mathbf{f}_i^{ext,k})}{m_i} \tag{5}$$

and

$$\mathbf{v}_p^{k+1} = \mathbf{v}_p^k + \Delta t \sum_{i=1}^{N_n} \bar{N}_{ip} \frac{(\mathbf{f}_i^{int,k} + \mathbf{f}_i^{ext,k})}{m_i}. \tag{6}$$

where the nodal mass and velocity are determined by

$$m_i^k = \sum_{p=1}^{N_p} m_p^k \bar{N}_{ip} \quad \text{and} \quad \mathbf{v}_i^k = \frac{\sum_{p=1}^{N_p} \mathbf{v}_p^k m_p \bar{N}_{ip}}{m_p}, \tag{7}$$

respectively.

Similarly, the strain increments at the material points are found by

$$\Delta \boldsymbol{\varepsilon}_p = \frac{\Delta t}{2} \sum_{i=1}^{N_n} \left(\nabla \bar{N}_{ip} \mathbf{v}_i + (\nabla \bar{N}_{ip} \mathbf{v}_i)^T \right). \tag{8}$$

Then the stress increments are found individually at each material point.

Problems regarding stresses

When considered at a specific time-step, the material point method is similar to a finite element method for the grid, but where the integration in now performed using the set of material points instead of using Gauss points. This leads to an inaccurate integration. In most implementations of MPM, the grid nodes are fixed spatially, while the material points will move in a dynamical problem. Hence, the material points move relatively to the grid between the different time steps,

which leads to a further loss of precision. Thus although initially optionally discretized, the integration involved in assembling Eq. 3 will not be complete. An effect of the relative motion is the co called grid-crossing error. Typically, the gradients of nodal shape-functions are discontinuous across element boundaries. Hence, as a material point that changes cell between to time-steps between two time-steps will contribute significantly differently to the internal force, when it moves relatively to the grid. The definition a particle characteristic function in the GIMP somewhat limit the grid-crossing error. As a result of this the material point will experience an unphysical acceleration according to Eq. 6 and an unphysical strain increment according to Eq. 8. However, due to the nature of the explicit time integration these effects will be smoothed spatially over time, and as has been shown realistic results can still be obtained.

However, for general problems the incremental stress update defined at the individual material points leads to unrealistic stresses. This is due to the sum over stress increments determined from strain increments which may generally be erroneous for the individual material points. The effect of this is shown in the following numerical example.

Example: Collapsing soil column

A rectangular soil column placed on a frictional surface is considered. The column is 8 metres high and 4 metres long and plane strain conditions are considered. The soil column is unsupported along the vertical boundaries. Further, the stresses are assumed to increase linearly with the distance from the top. As these stresses cannot be sustained on the vertical sides, a plastic collapse will occur. An elasto-plastic material model based on the Mohr-Coulomb yield criterion, using an explicit return mapping scheme as described by Clausen et al. [4] is applied to enforce the yield criterion.

The soil is described using the following set of material properties:

$$E = 20\text{MPa}, \quad \nu = 0.42, \quad \rho_0 = 10^3 \text{kg/m}^3, \quad c = 1\text{kPa} \quad , \phi = 42^o \text{ and } \psi = 0^o. \quad (9)$$

A frictional coefficient $\mu = 0.6$ is prescribed at the lower boundary.

An initial K_0-stress state is specified with the vertical and horizontal normal stress given by

$$\sigma_{yy}^0 = -dg\rho_0 \quad \text{and} \quad \sigma_{xx}^0 = \sigma_{zz}^0 = -dg\rho_0 K_0, \quad (10)$$

where $g = 9.8 m/s^2$ is the gravity and d is the distance from the top soil surface. where the earth pressure coefficient is given by $K_0 = \nu/(1 - \nu)$. Finally, $\sigma_{xy}^0 = 0$ is prescribed for all material points.

In order to visualize the collapse of the soil-column, each material is assigned a regular domain in the initial configuration. Further, a deformation tensor is prescribed for each material point with $\mathbf{F}_p^0 = \mathbf{I}$ at the start. The deformation tensor is integrated in time using the nodal velocities to track the deformation of the initially rectangular domains. The dynamic simulation is performed with a time step of $\Delta t = 0.001$s. The simulation is performed until the soil has reached a state of vanishing velocities. For the present model the time of the collapse is $t = 2.5$s. The initial configuration consists of 1800 material points. An adaptive scheme for splitting the material points in case of localized deformation is employed. The final configuration consists of 9402 material points.

In the MPM, the material points may be at arbitrary locations of the elements defined by the set of grid-nodes. The individual stresses may be unrealistic. Hence, combined with the effect of grid

crossing this completely degenerates the stress at an individual material point. In order to better understand the problems, a new way of visualizing the stresses are introduced. Firstly, grid-node stress tensors are defined by

$$\boldsymbol{\sigma}_i = \sum_{p=1}^{N_p} \frac{\boldsymbol{\sigma}_p \Phi_{ip} m_p}{m_i}, \tag{11}$$

where $\boldsymbol{\sigma}_i$ is the stress tensor, associated with grid node i, $\boldsymbol{\sigma}_p$ is the stress of material point p, Φ_{ip} is the interpolation function while m_i and m_p is the nodal and material point mass, respectively. Using the nodal stresses, a smoothed material point stress tensor is defined as

$$\boldsymbol{\sigma}_p^{smooth} = \sum_{i=1}^{N_n} \boldsymbol{\sigma}_i \Phi_{ip}, \tag{12}$$

Figure 1 shows the vertical normal stress during the collapse of the soil column. The left side of the figure shows the stresses at the individual material points, while the right side shows the stresses calculated by Eq. (12) in order to provide a better visualization.

The first thing to observe is that the deformation occur in a realistic fashion. As the pressure cannot be obtained, the soil column collapses until, it has reached a state, where its satisfies the yield condition (in a global sense) and the kinetic energy has dissipated due to the bottom friction and plastic dissipation. In the final configuration, it is still possible to observe the initial corners due to the small amount of cohesion present. As observed, the vertical normal stress during and at the end of the collapse varies in a very erratic fashion. This leads to a principle question: Can we trust the simulation, when the stresses at the individual material points are so unrealistic?

As seen, the deformation occurs as physically expected although the stresses are completely erroneous at the individual material points. From the mentioned analogy to the finite element method the material points plays the role as integration points when solving the governing equation of motion. Further, from finite element analysis it is common knowledge that special care need to be made regarding when interpreting stresses, as stresses as may only be realistic at certain locations within an element. As observed, the mapping via the grid nodes determines a stress field, that is physically realistic. Hence, in terms of the grid-nodes, where the equations are solved, the stress field is realistic.

Concluding remarks

The material-point method is a new promising numerical method for large strain continuum mechanic problems. As illustrated it is successfully able to capture in a realistic fashion problems involving very large deformations. However, this note provides an illustration of problematic issue for the method. This pertains to the fact that stress fields varies in a unrealistic fashion at the individual material points. As illustrated the overall solution may still be realistic, as the stresses are realistic at the grid nodes and realistic displacement and velocity fields are observed. However, in more complex problems the unrealistic stresses pose real problems as localized effects may be difficult to capture. Hopefully the presented results eventually can lead to a better algorithms for handling stresses within the MPM.
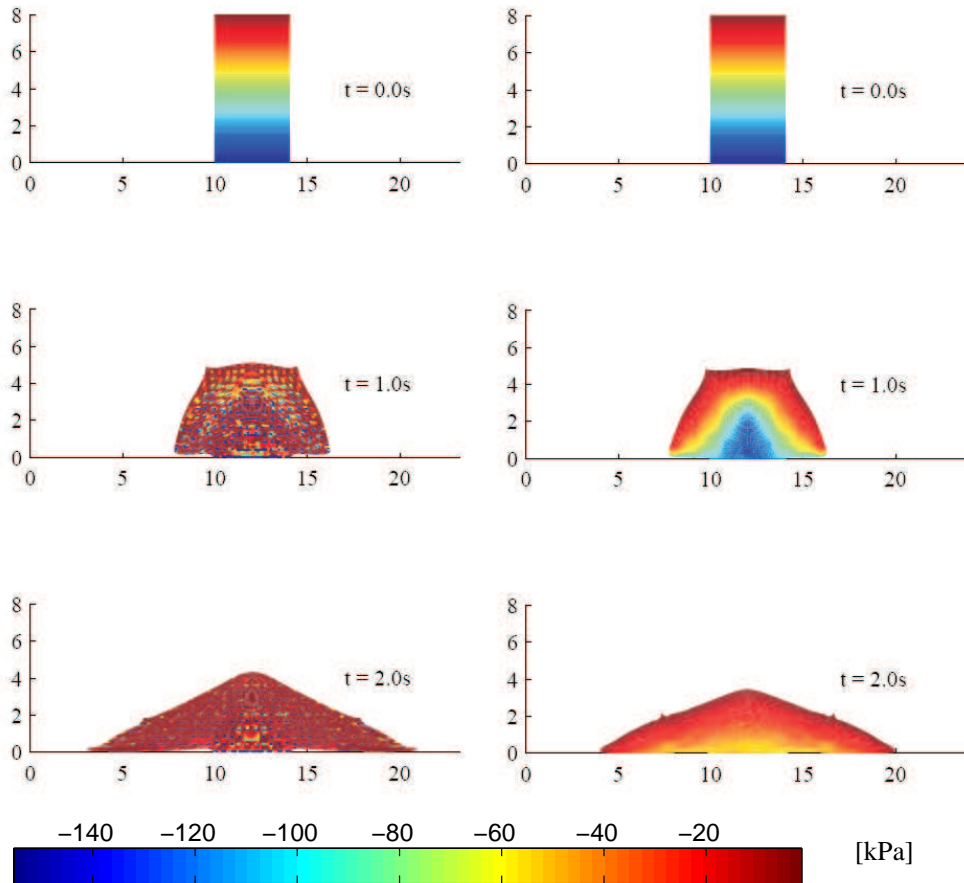
Figure 1: Vertical normal stresses during the collapse of the soil column. Left: The stresses at the individual material points. Right: A smoothing using Eq. (12) is introduced for a better visualization.

References

[1] D. Sulsky, Z. Chen and H.L. Schreyer. A Particle method for history dependent materials. *Comput. Methods. Appl. Mech. Engrg.*, **118**, 179–196, (1994).

[2] D. Sulsky, S.J. Zhou and H.L. Schreyer. Application of a particle-in-cell method to solid mechanics. *Computer Physics Communications.*, **87**, 236–252, (1995).

[3] S.G. Bardengagen and E.M. Kober.. The generalized material point method. *CMES*, **5**, 477–495, (2004).

[4] J. Clausen, L. Damkilde and L. Andersen An efficient return algorithm for non-associated plasticity with linear yield criteria in principal stress space. *Computers and Structures*, **66**, 1795–1807, (2007).

An efficient formulation of the elasto-plastic constitutive matrix on yield surface corners

Johan Clausen[*]**, Lars Andersen and Lars Damkilde**

Department of Civil Engineering
Aalborg University, Aalborg, Denmark
e–mail: jc@civil.aau.dk

Summary   A formulation for the elasto-plastic constitutive matrices on discontinuities on yield surfaces is presented, for use in finite element calculations. The formulation entails no rounding of the yield surface or the plastic potential, as it is done in most other formulations, and therefore exact analytical solutions can be approached. Computational examples are given with the Mohr-Coulomb, the Modified Mohr-Coulomb and the Hoek-Brown models.

Introduction

In practical geotechnical engineering most design calculations on soil structures are carried out with the Mohr-Coulomb material model, with the well-known hexagonal shaped yield criterion in principal stress space, see Fig. 1b. For clays the Tresca criterion, Fig. 1a, is used, and for rocks and concrete the Modified Mohr-Coulomb and the Hoek-Brown criteria are often used, see Fig. 1c and d.

As can be seen from the figure these criteria possess corners and apices, which explicitly have to be taken into account when formulating the constitutive matrices used for formulating the global stiffness matrix. This is especially true for 3D-calculations where all the different corner and apex discontinuities may come into play. One option of dealing with these discontinuities is to perform a local rounding of the yield criterion and/or the plastic potential, see e.g. [1, 2]. This option seems to work but the obtained numerical results do no longer converge towards the exact analytical results.
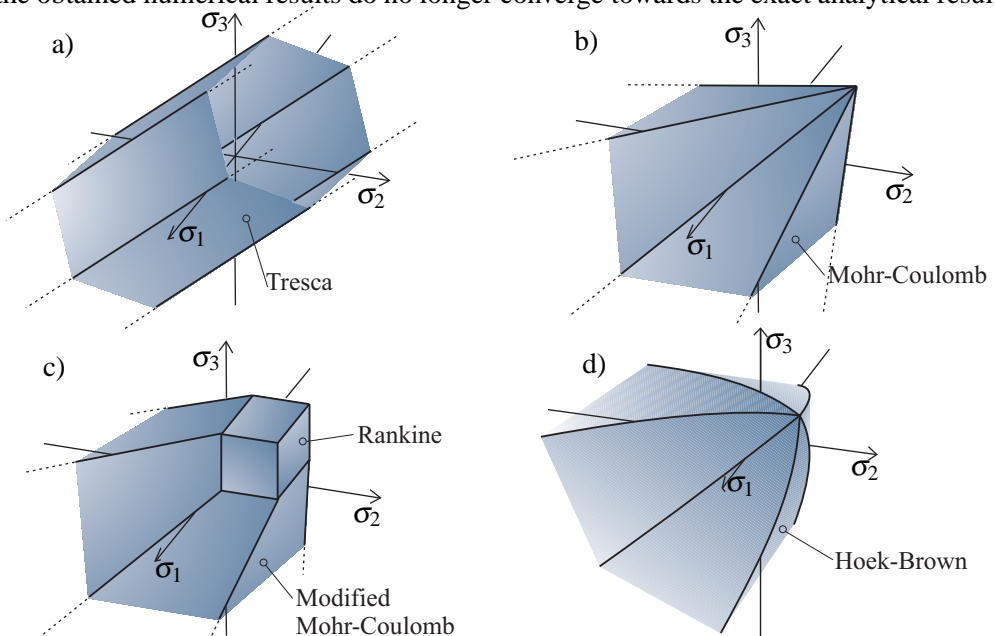
Figure 1: Examples of yield criteria with corners in principal stress space: a) The Tresca criterion. b) The Mohr-Coulomb Criterion. c) The Modified Mohr-Coulomb criterion. d) The Hoek-Brown criterion.

In this paper a formulation is presented that does not include a rounding of the corners or apices. It is also shown that the numerical solution for a footing on a Mohr-Coulomb soil converges towards the exact analytical solution.

Constitutive matrix on a surface

When a stress point is located on a yield surface the elasto-plastic constitutive matrix is found as

$$\mathbf{D}^{ep} = \mathbf{D} - \frac{\mathbf{D}\mathbf{b}^{\mathrm{T}}\mathbf{a}\mathbf{D}}{\mathbf{a}^{\mathrm{T}}\mathbf{D}\mathbf{b}} \tag{1}$$

where $\mathbf{a} = \partial f/\partial\boldsymbol{\sigma}$, $\mathbf{b} = \partial g/\partial\boldsymbol{\sigma}$ and $\mathbf{D}$ is the elastic constitutive matrix. f and g is the yield function and the plastic potential, respectively. Note that $\mathbf{D}^{ep}$ is singular with respect to $\mathbf{b}$, i.e. $\mathbf{D}^{ep}\mathbf{b} = \mathbf{0}$.

Constitutive matrix on a corner and an apex

When the stress point is located on a corner the constitutive matrix must be singular with respect to both $\mathbf{b}_1$ and $\mathbf{b}_2$. In Fig. 3 a direction vector of a yield surface corner, $\bar{\boldsymbol{\ell}}$ is shown. This can be regarded as a direction vector of any of the lines defining the yield criteria in Fig. 1. In Fig. 3 the direction vector of the plastic potential corner, $\bar{\boldsymbol{\ell}}^g$, is also shown. From these direction vectors it is shown in [3] that the doubly singular constitutive matrix on a line in principal stress space can be expressed as:

$$\bar{\mathbf{D}}_{\ell}^{ep} = \frac{\bar{\boldsymbol{\ell}}\,(\bar{\boldsymbol{\ell}}^g)^{\mathrm{T}}}{\bar{\boldsymbol{\ell}}^{\mathrm{T}}\bar{\mathbf{D}}^{-1}\bar{\boldsymbol{\ell}}^g} = \frac{(\bar{\mathbf{a}}_1 \times \bar{\mathbf{a}}_2)(\bar{\mathbf{b}}_1 \times \bar{\mathbf{b}}_2)^{\mathrm{T}}}{(\bar{\mathbf{a}}_1 \times \bar{\mathbf{a}}_2)^{\mathrm{T}}\bar{\mathbf{D}}^{-1}(\bar{\mathbf{b}}_1 \times \bar{\mathbf{b}}_2)} \tag{2}$$

The overbar indicates the the vectors and matrices are expressed with respect to the principal coordinates without the shear component terms, i.e. the vectors have three components and the matrices three by three. The $\times$ symbol indicates the cross product. The shear part is added,

$$\hat{\mathbf{D}}_{\ell}^{ep} = \begin{bmatrix} \bar{\mathbf{D}}_{\ell}^{ep} & \\ & \bar{\mathbf{G}} \end{bmatrix} \tag{3}$$

and the matrix is transformed from the principal stress coordinate system into the *xyz*-coordinate system. In the above equation the hat, $\hat{\,}$, signifies that the matrix includes all six by six components and is expressed in the principal coordinate system. The matrix $\bar{\mathbf{G}}$ is the shear part of the elastic constitutive matrix.

Figure 2: A direction vector, $\bar{\boldsymbol{\ell}}$, of an intersection line in principal stress space. The corresponding potential curve direction vector is denoted $\bar{\boldsymbol{\ell}}^g$. An elastic strain direction vector is denoted $\bar{\mathbf{e}}_{\ell}$. The vectors $\mathbf{b}_1$ and $\mathbf{b}_2$ are perpendicular to the direction vector of the plastic potential intersection line, $\bar{\boldsymbol{\ell}}^g$.

There are two different forms of constitutive matrix on an apex. If the stress point is located on an apex on the hydrostatic line the constitutive matrix must be singular with respect to all stress directions, i.e.

$$\hat{\mathbf{D}}_{a,1}^{ep} = \mathbf{D}_{a,1}^{ep} = \mathbf{0} \tag{4}$$

This is the case on the Mohr-Coulomb apex, the Hoek-Brown apex and one of the Modified Mohr-Coulomb apices, see Fig. 1. If, on the other hand, the stress point is located on an apex not on the hydrostatic line it is singular only in the normal directions, i.e. its composition in the principal coordinates is

$$\hat{\mathbf{D}}_{a,2}^{ep} = \begin{bmatrix} \mathbf{0} & \\ & \bar{\mathbf{G}} \end{bmatrix} \tag{5}$$

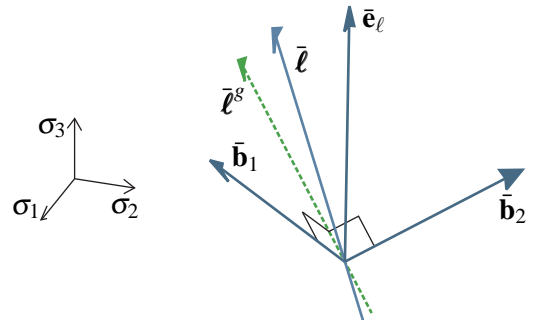This is the case for stress points located on the Modified Mohr-Coulomb apices outside the hydrostatic line, see Fig 1c.

Improved formulation

The formulations for the constitutive matrices given above works well for two-dimensional models where the (instant) friction angle is not too high, see e.g. [3, 4]. But for high friction angles and/or three dimensional problems the above formulations can cause the global stiffness matrix to become ill-conditioned. This is due to many stress points located on either corners or apices which add many singularities to the global stiffness matrix. This problem can be mended by adding a small stiffness in appropriate directions.

Improved formulation on the apex

When the elasticity of the material is linear the implicit stress integration can written in the "return mapping" formulation,

$$\bar{\boldsymbol{\sigma}}_C = \bar{\boldsymbol{\sigma}}_B - \Delta\bar{\boldsymbol{\sigma}}^p, \qquad \text{with} \quad \boldsymbol{\sigma}_B = \boldsymbol{\sigma}_A + \mathbf{D}\Delta\boldsymbol{\varepsilon} \quad \text{and} \quad \Delta\bar{\boldsymbol{\sigma}}^p = \bar{\mathbf{D}}\Delta\bar{\boldsymbol{\varepsilon}}^p \tag{6}$$

Here $\bar{\boldsymbol{\sigma}}_C$ is the updated stress point on the yield surface, $\bar{\boldsymbol{\sigma}}_B$ is the elastic predictor stress and $\Delta\bar{\boldsymbol{\sigma}}^p$ is the plastic corrector stress, all three expressed in the principal stress space as indicated by the overbar. The total strain increment is denoted $\Delta\boldsymbol{\varepsilon}$ and the plastic strain increment in principal coordinates is $\Delta\bar{\boldsymbol{\varepsilon}}^p$.

A key point of the elasto-plastic constitutive matrix is that it must be singular in the direction of the plastic strain increment. A simple method to add a little stiffness in the formulation of $\mathbf{D}^{ep}$ on the apex is given as

$$\bar{\mathbf{D}}^{ep}_{a,\text{mod}} = \frac{1}{\alpha}\left(\bar{\mathbf{D}} - \frac{\bar{\mathbf{D}}^T\,\Delta\bar{\boldsymbol{\varepsilon}}^p(\Delta\bar{\boldsymbol{\varepsilon}}^p)^T\bar{\mathbf{D}}}{(\Delta\bar{\boldsymbol{\varepsilon}}^p)^T\bar{\mathbf{D}}\Delta\bar{\boldsymbol{\varepsilon}}^p}\right) \tag{7}$$

This matrix is singular in the plastic strain direction and depending on the value of α poseses a small stiffness in other directions. In the presentation a study on the optimal value of α will be given.

Improved formulation on a corner

When the updated stress point is located on a corner the basic formulation for the constitutive matrix is given by Eq. (2). Again a simple formulation that adds a little stiffness is

$$\bar{\mathbf{D}}^{epc}_{\ell} = \frac{\bar{\boldsymbol{\ell}}(\bar{\boldsymbol{\ell}}^g)^T}{\bar{\boldsymbol{\ell}}^T(\bar{\mathbf{D}}^c)^{-1}\bar{\boldsymbol{\ell}}^g} + \frac{1}{\beta}\frac{\bar{\mathbf{c}}\,\bar{\mathbf{c}}^T}{\bar{\mathbf{c}}^T(\bar{\mathbf{D}}^c)^{-1}\bar{\mathbf{c}}} \tag{8}$$

The direction vector $\bar{\mathbf{c}}$ is the direction perpendicular to the plastic strain direction, $\Delta\bar{\boldsymbol{\varepsilon}}^p$, and the line defining the corner, $\bar{\boldsymbol{\ell}}$, see Fig. 2. In the presentation different results indicating the optimal value of the scalar β will be given. β controls the amount of stiffness that will be added. The Ref. [5].

Computational example

To assess the validity of the formulation a calculation is carried out with a rough circular footing resting on a cohesionless Mohr-Coulomb soil with a friction angle of $\varphi = 30°$, and a selfweight of $\gamma = 20$ kN/m^3. For symmetry reasons only a quarter of the footing is modelled, see Fig. 3a.
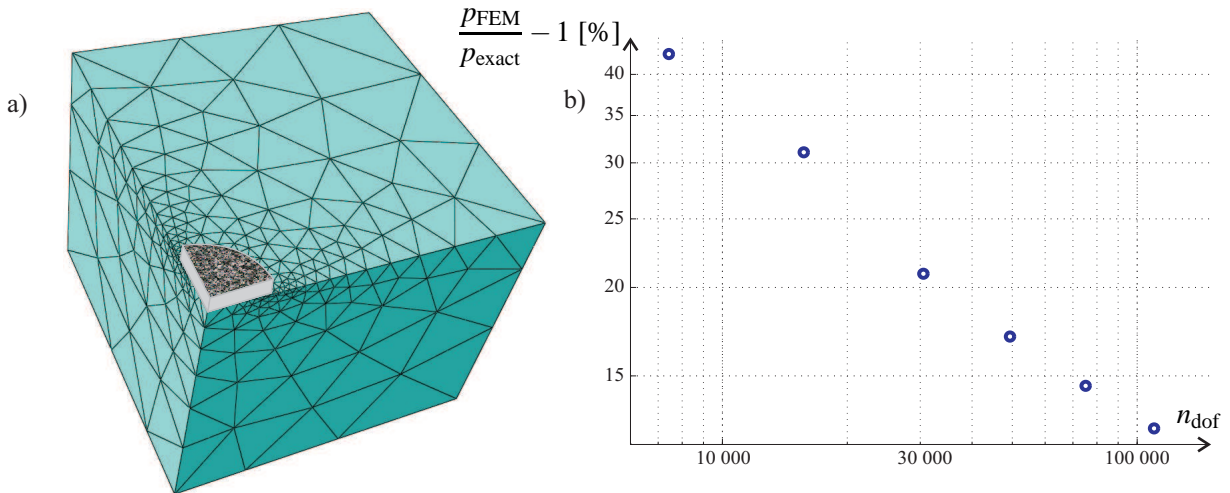
Figure 3: a) A quarter of a circular footing and an example of the element mesh with 7425 degrees of freedom. b) Results from the bearing capacity calculations compared to the exact value.

The elements are standard ten-node tetrahedrons. A vertical forced displacement is applied to the footing in steps and the bearing capacity is calculated from the sum of the maximum reaction forces at the footing nodes divided by the footing area. The exact bearing capacity is found in Ref. [6]. The result of the calculations can be seen in Fig. 3 for different mesh densities. It is seen that the calculated values converge toward the exact value. In the presentation results for the other material models shown in Fig. 1 will be given.

Conclusion

A formulation for elasto-plastic constitutive matrices on corner and apex singularities is given. The initial formulation is improved in order to make full 3D-calculations stable. It is shown that finite element calculations based on the formulation converge towards the exact solution.

References

[1] A. J. Abbo and S. W. Sloan. A smooth hyperbolic approximation to the mohr-coulomb yield criterion. *Computers & Structures*, 54(3):427–441, 1995.

[2] H. A. Taiebat and J. P. Carter. Flow rule effects in the tresca model. *Computers and Geotechnics*, 35:500–503, 2008.

[3] Johan Clausen, Lars Damkilde, and Lars Andersen. An efficient return algorithm for non-associated plasticity with linear yield criteria in principal stress space. *Computers & Structures*, 85:1795–1897, 2007.

[4] Johan Clausen, Lars Damkilde, and Lars Andersen. Efficient return algorithms for associated plasticity with multiple yield planes. *International Journal for Numerical Methods in Engineering*, 66(6):1036–1059, 2006.

[5] Johan Clausen. *Efficient Non-Linear Finite Element Implementation of Elasto-Plasticity for Geotechnical Problems*. PhD thesis, Esbjerg Institute of Technology, Aalborg University, 2007. http://vbn.aau.dk/fbspretrieve/14058639/JCthesis.pdf.

[6] C. M. Martin. User guide for ABC - analysis of bearing capacity, version 1.0. OUEL Report No. 2261/03, University of Oxford, 2004.

Testing program for modelling time dependent soft clay behaviour

Igor Mataic, Mr.Sc.*

Department of Civil and Environmental Engineering,
Helsinki University of Technology, Helsinki, Finland
e−mail: imataic@cc.hut.fi

Summary The paper defines extensive laboratory testing program perceived as a part of research project investigating delayed behaviour of soft structured clays. Tests are to be performed on HUT soft sensitive clay and include standard, long duration and constant strain rate oedometer tests, consolidated undrained triaxial tests in both compression and extension and triaxial creep tests. Tests results obtained are to be used for verification and enhancement of numerical capabilities of EVP SCLAY1S constitutive model.

Introduction

The behaviour of soft clay is very complicated. It exhibits several features such as: a significant degree of anisotropy developed during their deposition, sedimentation, consolidation history and any subsequent straining some apparent bonding which will be progressively lost during straining; time-dependent stress-strain relationship which has a significant influence on the shear strength and the preconsolidation pressure. Time dependency of stress-strain behaviour in particular still presents area of considerable uncertainty. Consequently additional efforts are necessity in order to develop sophisticated design methods and tools which could take into account the strain rate dependency of deformations and strength.[1] The laboratory testing program defined in this paper is a one more step in that direction and therefore presents continuation of previously conducted testing programs with an agenda to enhance understanding and improve engineering modelling capabilities of soft clay behaviour.[2, 3, 4] Based on the additional experimental results to be gathered in the testing programme verification and performance enhancement of existing EVP SCLAY 1S elasto-viscoplastic constitutive model is to be conceptualized. The model is one of the most sophisticated numerical tools developed for modelling stress-strain-strength behaviour of structured clays. Presently, it incorporates options to model specific soil behaviour effects of anisotropy, destructuration and viscosity. However, model performance still needs to be improved particularly in the area concerning formulation of time influence on destructuration process and strain softening, effects of creep and effects of viscosity. The interpreted laboratory results obtained within the proposed testing programme are to be used to simulate soft clay behaviour by the constitutive model and therefore used for its verification, consequently enabling improvement of numerical simulation capabilities and capacitating evaluation of the model performance in the field scale.

Testing program

Objective of the testing program is detail examination of effects of structure and time dependent stress-strain behaviour of soft sensitive clays. Testing program includes several specific types of soil tests performed in oedometer and triaxial apparatus, namely; standard oedometer tests, long duration odometer tests, oedometer tests at constant strain rate (CRS), anisotropically consolidated undrained triaxial tests in compression and extension (CAUC) and finally triaxial creep tests.

Soil Sampling

The tests anticipated in this study will be performed on HUT clay, a soft sensitive Finnish clay sampled in the area of Helsinki University of Technology (HUT). HUT clay is soft natural clay of

postglacial origin typical for Nordic Countries. All of the HUT clay samples are to be taken at the same location and at the same range of depth of 1,3 to 2,1 m. Unit weight of the material appears to be at about $\rho_t=1,6$ g/cm^3 and specific gravity is approximately of $\rho_s=2,7$ g/cm^3. Initial void ratio is typically very low being 1,7. Initial water content for HUT clay material is relatively low, ranging between 65 to 75 %. Typical value of water content in soft Finnish clays is 90 to 100%. Furthermore, organic content 0,75 % in HUT clay is low value as well. Below the value of 1.5% organic content has no effect on mechanical behaviour of clay. Initial pH value of samples was 6, the soil being almost neutral. Low pH data is logical considering that the organic content of HUT clay is very low. Typical value of initial plastic limit measured is 26,0 % and liquid limit is of 65,0 %. According to the plasticity chart these values position HUT clay below A-line in the area of organic clays.[5]

Oedometer tests

In order to obtain clear insight into compressibility and structure characteristics of soft clay standard incremental load oedometer tests are to be performed on natural and reconstituted clay samples. As shown on Figure 1a), oedometer tests on natural soils generally show compression curves appearing above the intrinsic compression line for the reconstituted material, with the post yield compression curve gradually converging with the intrinsic compression line as the bonding is progressively lost. Indeed, comparison of stress strain curves obtained on intact and remoulded samples allows insight and understanding of the effects of structure and progressive destructuration of bonds during inelastic strains, being the main objective of the specific test. The test results are to be used to determine yielding points and to define sensitivity characteristics of specific clay on the basis of preconsolidation pressure of undisturbed and remoulded samples. In addition, interrelation between destructuration process and secondary compression coefficient will be examined.

Long duration oedometer tests (10 days) are to be performed on natural soft clay samples in order to examine time and stress compressibility interrelationship by comparison of the characteristics of stress-strain curves obtained on samples with respect to different time duration of load increment. Indeed, as shown on Figure 1b) longer loading steep time does to certain extent influence stress-strain behaviour of clay [4]. Special attention is to be given to examining influence of loading time on values of preconsolidation pressure and values defining clay behaviour during secondary compression.

In order to analyse viscous effects of soft clay behaviour and relationship between preconsolidation pressure and strain rate, constant rate of strain oedometer test are to be performed on natural and reconstituted samples of soft clay. As an optimum, following strain rates have been selected: $1*10^{-4}$, $1*10^{-5}$, $1*10^{-6}$ and $1*10^{-8}$ s$^-$1. The test has two main objectives. Firstly, to study relationship between the preconsolidation pressure and actual level of strain-rate. As shown on Figure 2, by conducting CRS tests under considerable range of different constant strain rates and determining preconsolidation pressure at each strain rate, clear and confident definition of yield pressure strain rate interaction will be attained. Indeed, in the selected range of strain rates during CRS oedometer test a linear relationship between the logarithm of yield stress and the logarithm of strain rate can be established.[6] Second objective is to study influence of strain rate on destructuration process. Careful examination of previously conducted CSR test shows actual strain rate having significant influence on material softening behaviour [4].
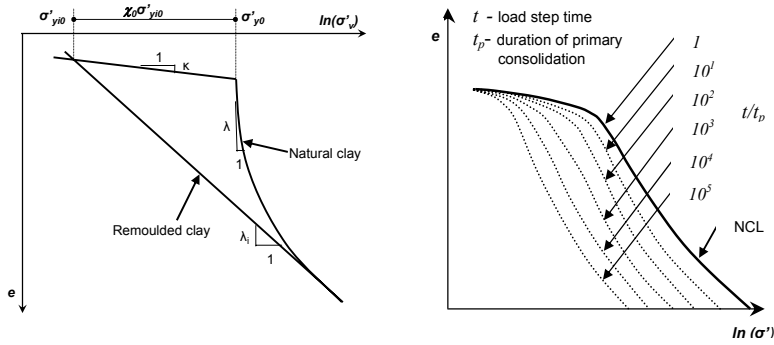
Figure 1: a) Compressibility of natural and remoulded clay and b) Influence of loading time duration on clay response in oedometer test [6, 7].
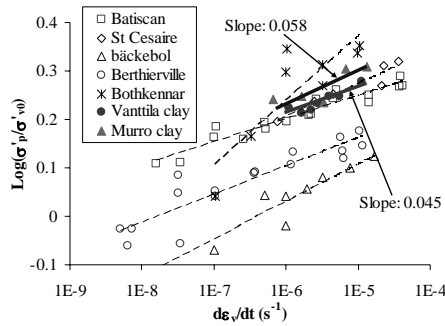
Figure 2: Strain rate effect on preconsolidation pressure in CRS oedometer test [4].

Triaxial tests

Drained triaxial compression tests at various consolidation and strain rate level are to be conducted on undisturbed and reconstituted soft clay samples. Main purpose of the tests is to examine progressive destructuration of bonding with time. In fact, the tests are performed on natural and reconstituted clay samples anisotropically consolidated to identical stress ratio level being η=0,2, 0,4 or 0,75 and at cell pressures of 20, 40 and 60 kPa. Indeed, in order to study influence of anisotropy, undrained compression tests are performed under distinctively different consolidation conditions. Furthermore, the compression tests include both tests performed at constant axial rate of strain and tests during which strain rate is varied several times during the actual test. In fact, during the tests considerable change of shear strain rate is to be imposed during unloading/reloading cycle. Selected strain rates to be applied are 6, 0,6 and 0,06 %/h. In addition to those in compression, supplemental anisotropically consolidated undrained triaxial tests in extension will be performed on undisturbed clay samples. In those tests samples will be anisotropically consolidated to stress ratio η= -0,2 and η= 0,75, respectively. Several tests are to be stopped entirely to allow sample test in relaxation, i.e. measurement of porepressures and deformations under state of no load applied. Objective of the tests is to identify influence of structure and shearing strain rate on sample compressive and extensive behaviour. On the basis of the results obtained, yield points corresponding to consolidation at different stress ratios and triaxial cell pressure are to be determined and resulting yield surface plotted together with clearly defined critical state in compression and extension for clay material tested. Furthermore, the results should enable plotting of intrinsic yield surface and determination of initial bounding

amount, as well. Finally, the tests will enable not only determination of yield surface rotation due to anisotropy level and yield surface shrinkage due to degradation of bonds but also a clear insight on a strain rate influence on both shape and size of yield surface and will therefore form adequate base for defining true time dependency of stress-strain-strength behaviour of soft clays (see Figure 3).

In order to study destructuration process during the creep deformations and evolution of strain rate during the undrained creep stage undrained triaxial creep tests will be performed. Undrained triaxial creep tests are to be performed on under different stress levels in undrained condition after an identical consolidation stage. Indeed, after saturation the samples are to be consolidated for one week so to ensure the identical initial stress states for the creep test as those defined for CAUC tests i.e. starting from the same consolidation points. At different deviator stress levels samples are to be sheared to failure in an undrained manner. Therefore, additional axial stresses are to be applied keeping the lateral stress constant. Objective of the test is to study destructuration process during the creep deformations and evolution of strain rate during the undrained creep stage.
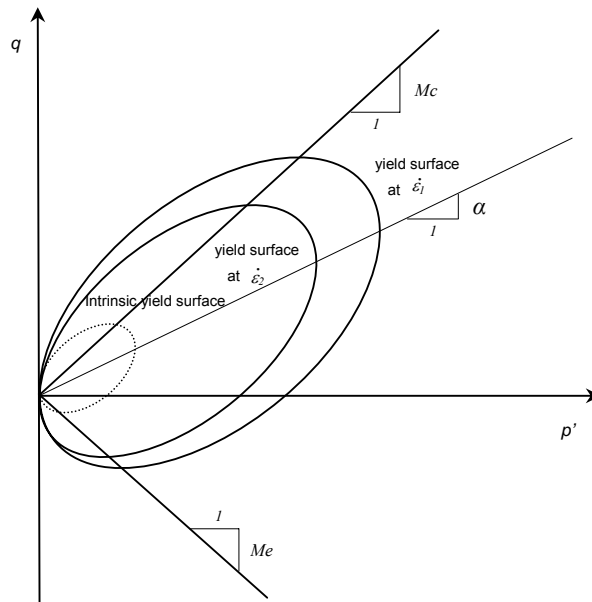
Figure 3: Influence of strain rate on shape and size of yield surface.

Concluding remarks

The testing programme proposed in this paper includes oedometer and triaxial tests on both natural and remoulded soil samples of HUT clay material, with varying rates of loading, with constant applied stresses by time (creep), and with constant applied strains by time (relaxation).[1] Conditions during standard, long duration and CRS oedometer tests are defined so to provide clear insight in; a) compressibility and structure characteristics of soft clay, i.e. sensitivity characteristics, progressive destructuration of bonds during inelastic strains, and interrelation between destructuration process and secondary compression coefficient ; b) time dependent compressibility characteristics of soft clay such as effect of loading time on values of

preconsolidation pressure and values defining clay behaviour during secondary compression; c) viscous characteristics of soft clay i.e. influence of strain rate level on the yield stress and destructuration process. Furthermore, undrained triaxial tests and triaxial creep tests are perceived so to provide substantial amount of data concerning influence of structure and shearing strain rate on soft clay behaviour and strength. The data will enable: a) determination of yield points corresponding to several consolidation conditions and definition of resulting yield surface with clearly defined critical state in compression and extension together with intrinsic yield surface defining initial anisotrophy level and initial amount of bonding; b) a clear insight on strain softening behaviour and strain rate influence on both shape and size of resulting yield surface, i.e. examination of destructuration effect with time and determination of yield surface rotation due to straining conditions and due to destructuration process; c) analyse of destructuration process during the creep deformations and evolution of strain rate during the undrained creep stage. To conclude, defined testing program enables simultaneous analysis of main aspects of soft clay behaviour being: anisotropy, bonding and destructuration, creep and time-dependency of stress-strain response and therefore forms adequate base for defining true time dependency of stress-strain-strength behaviour of soft clays.

References

[1] Karstunen, M., Yin Z.Y., Koskinen, M., Leoni, M. Vermeer, P. A. (2008). Some recent developments in constitutive modelling of soft clays. 12th International Conference of International Association for Computer methods and Advances in Geomechanics (IACMAG), 1-6 October, 2008. Goa, India.

[2] Wheeler, S.J., Näätänen, A., Karstunen, M., Lojander, M., (2003). An anisotropic elasto-plastic model for soft clays. Canadian Geotechnical Journal vol. 40, no. 2, pp. 403–418.

[3] Karstunen, M., Koskinen, M., (2008). Plastic anisotropy of soft reconstituted clays. Canadian Geotechnical Journal, vol. 45, no. 3, pp. 314-328

[4] Yin Z.Y., Chang C.S., Karstunen M., Koskinen M., Lojander, M.(2009). Time dependent behaviour of soft sensitive clay: experiment and modelling. In press.

[5] Mataic I. (2009). Behaviour of Stabilised soil. Helsinki University of technology, In press.

[6] Leroueil S., Hight D.W. (2003). Characteriation of soils for engineering purposes. Characterization and engineering properties of natural soils, (Tan et al. eds.), vol 1. Swets and Zeitlinger, Lisse, The Netherlands, 2003.

[7] Mesri G., Cepeda-Diaz A. F. (1986). Rezidual shear strength of clays and shales. Geotechnique vol 36, no.2, pp. 269-274.

Reducing Cross-Sectional Deformations in a Wind Turbine Blade

K. Branner∗, A. Roczek and F.M. Jensen

Wind Energy Division, Risø DTU
Technical University of Denmark, Roskilde, Denmark
∗e−mail: kibr@risoe.dtu.dk

Summary   Cross-sectional deformations in a wind turbine blade may cause peeling stresses that can result in failure of adhesive joints. Therefore, methods are needed to minimize the deformation of the cross-section. To address this problem, optimal solutions for the layup of materials used in a wind turbine blade trailing edge panel is studied.

FE-results are used to approximate the loading and boundary conditions for the studied panel. A composite layup optimization algorithm is implemented based on the plate problem solution. Several glass fiber layup solutions are implemented and analyzed in the blade model. The primary conclusion drawn from this study confirms significant improvement in the local behavior of the trailing edge panels obtained by rearranging the original layup of the material.
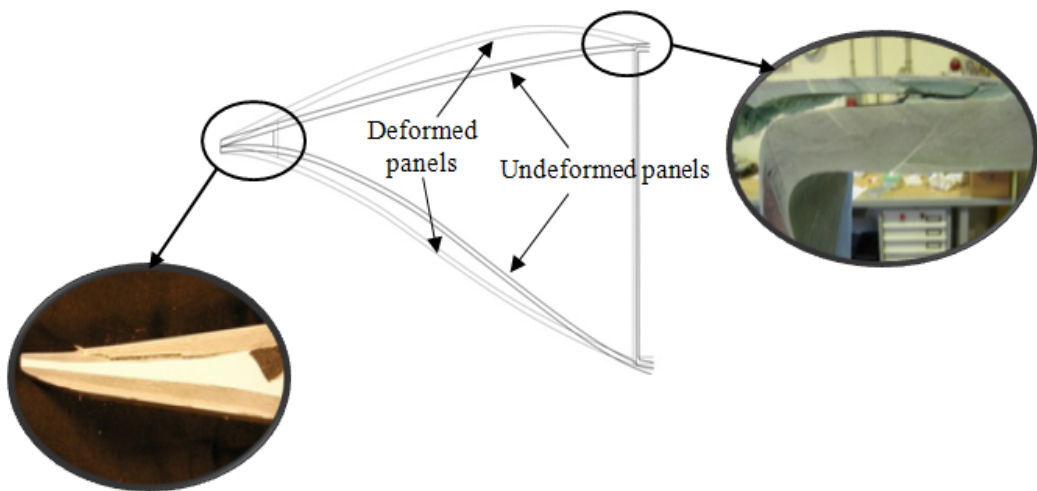
Figure 1: Sketch of trailing edge panels with out-of-plane deformations. The close ups show failure in the trailing edge and debonding of outer skin from the box girder.

Introduction

Recent full-scale tests on wind turbine blades performed at Risø DTU, have placed attention on failure mechanisms and loading configurations that often are not considered in wind turbine design [1]. Some of these recent tests indicate that failure modes can be directly related to large panel deformations, see [1] and [2]. Out-of-plane deformations of the panels between the load carrying box girder and the trailing edge can cause peeling stresses in the trailing edge connection, and this can lead to failure of the trailing edge adhesive joint as shown in Figure 1. Cross-sectional deformations will also change the aerofoil profile and may reduce the aerodynamic efficiency of the blade. It will therefore be beneficial to minimize this behavior and to keep the profile in the

aerodynamic region as close to the design shape as possible. Therefore, minimizing the out-of-plane deformation of the cross-sectional panels is needed in order to reduce these problems.

In this work a composite layup optimization algorithm is developed for sandwich panels. The objective is to minimize the out-of-plane deformation of the panel. Solutions for the layup of the trailing edge panels are studied in order to demonstrate the potential improvement that can be brought to the structural design without additional costs involved.

Method

The work is based on a finite element model of a 34m long wind turbine blade. The model consists of more than 160000 shell and solid elements. The forces are applied, as it is done in the full-scale test, in three positions from the root: 13.2m, 18.6m and 24.9m

Geometrical non-linearities are taken into account in the analysis and the numerical results are validated with experimental data confirming the occurrence of the out of plane deformation. See an example of comparison in Figure 2.

A composite layup optimization algorithm is developed for sandwich panels. The objective is to minimize the out-of-plane deformation of the panel. The algorithm is based on solutions to the plate problem with combined in-plane forces and lateral distributed load, provided partly by available literature (see [3],[4],[5] and [6]). The algorithm is then implemented using a searching engine based on Levenberg-Marquardt optimization method [7]. Also, a tailored simplified algorithm based on Discreet Material Optimization approach was used for comparison [8].

The results of non-linear out-of-plane deformations of the trailing edge panels are used to approximate the loading and boundary conditions for the panel. Each of the obtained layup solutions is implemented in the blade model and non-linear analyses are conducted focusing on out-of-plane deformation of the panels.
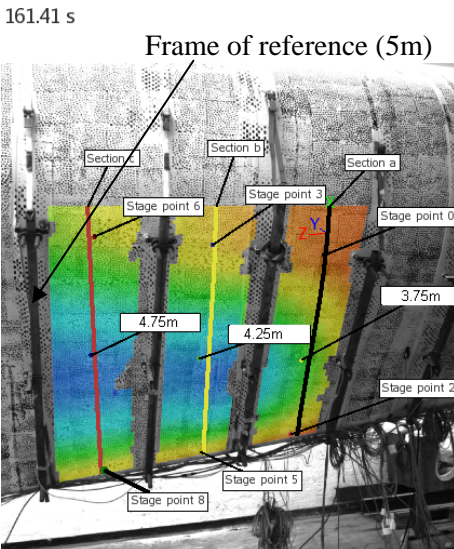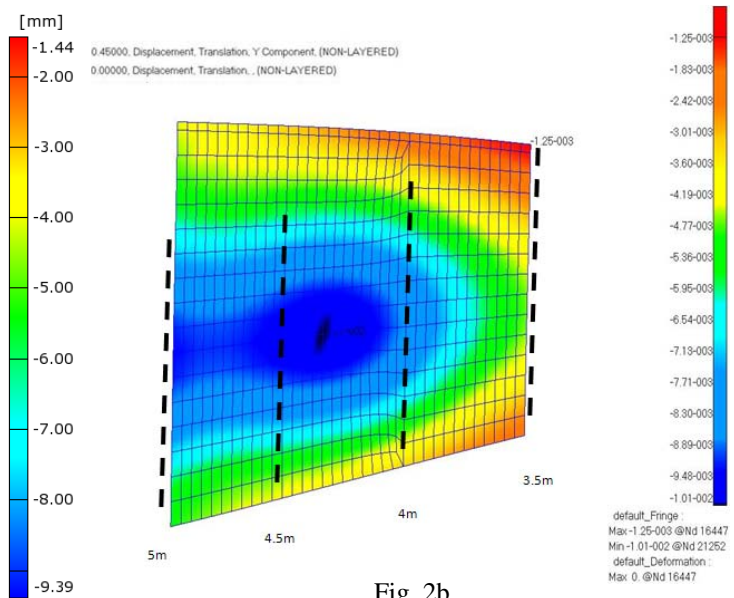
Fig. 2a   Fig. 2b

Figure 2: Comparison of experimental and numerical results for the out of plane deformation.
2a: Deformation distribution obtained with a digital image correlation system.
2b: FEM results from the corresponding load step in the same region.

Main Results

The main results from using the optimization algorithm, confirm that a significant improvement of the amplitude of the local deformation of the trailing edge panels can be obtained by rearranging the original layup of the sandwich used in the panels, see Figure 3. The improvement reached by rearrangement of the sandwich layup only was even 46%.

Designing a wind turbine blade is a trade-off between improved performance and reducing the weight of the blades. Thus, increasing the amount of material in the sandwich panels is not a particular efficient solution for reducing deformations.

Since the study demonstrated a promising improvement in the local behaviour of considered trailing edge panel in the edgewise loading, the result was implemented in other load cases in order to check the panel reliability under different, realistic loads for the blade. Tests in flapwise and combined load application directions, revealed no negative influence of the change in the considered sandwich panel's layup. Therefore, it was reasoned that the change in the plies' orientation in sandwich trailing edge panel suggested by the optimization algorithm indeed brought an improvement for the local behaviour of the root section of the blade.
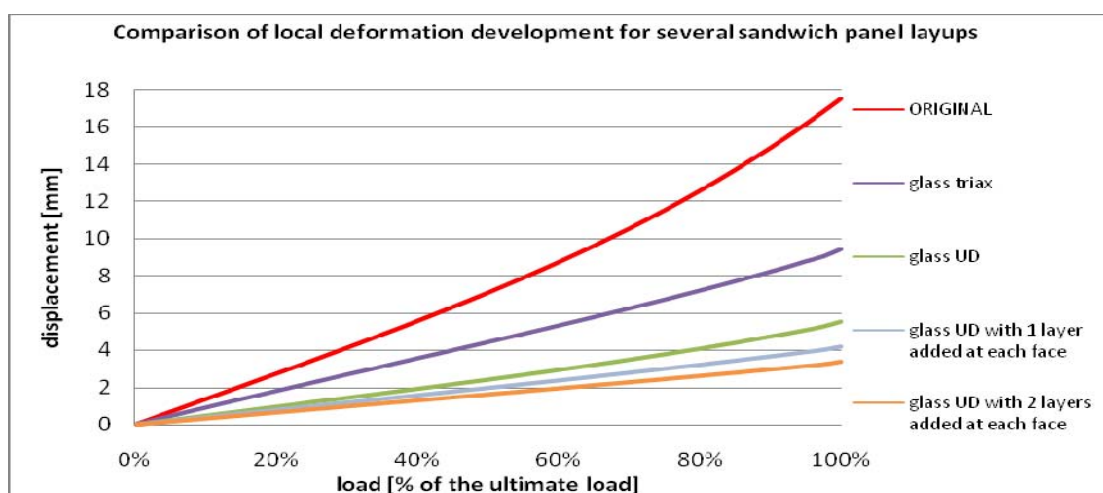
Figure 3: Comparison of local deformation of pressure side trailing edge panel at highest amplitude for optimized layups. The improvement was 82% for 2 layers added at each face, corresponding to almost doubling the thickness of the faces.

Conclusions

In the design and development of future wind turbine blades, there are several goals that the designers will try to meet. These goals can be to decrease the weight, to improve the materials and manufacturing process, to optimize the aerodynamic efficiency etc.

Studying wind turbine blades have shown that the out-of-plane deformation of trailing edge panels may cause peeling stresses in the adhesive joints in the trailing edge region. The aim of this work is to minimize out of plane deformation of the trailing edge panels by applying different solutions for layup of the materials used in wind turbine blade trailing edge panels. An optimization tool was created to demonstrate the potential improvement that could be brought to the structural design without increasing the weight and cost. The tool was prepared on basis of an analytical-

numerical solution derived for the plate problem in the established loading and boundary conditions.

The numerical study confirmed a significant improvement in the local behaviour of the trailing edge panel obtained by rearranging the original layup of this sandwich panel. A local deformation decrease by 46% was obtained only by changing the orientation of the layers present in the current design. A complete reorganization of the layup (without adding weight to the panel) brought an improvement of 65%.

References

[1] F.M. Jensen. *Ultimate strength of a large wind turbine blade*, Risø-PhD-34(EN), PhD thesis, Laboratory for Sustainable Energy, Technical University of Denmark, Denmark, (2008)

[2] F.M. Jensen, B.G. Falzon, J. Ankersen and H. Stang. Structural testing and numerical simulation of a 34m composite wind turbine blade, *Composite Structures*, **76**, (2006).

[3] C. Libove and S.B. Batdorf. A general small-deflection theory for flat sandwich plates, NACA Report 899, (1948)

[4] J.R. Robinsson. The buckling and bending of orthotropic sandwich plates with all edges simply supported, *Aero. Quart.*, **6**:2, (1955).

[5] S. Timoshenko and S. Woinowsky-Krieger. *Theory of Plates and Shells*, 2nd ed., McGraw-Hill Book Company, London, (1959).

[6] D. Zenkert. *An introduction to Sandwich Construction*, Chameleon Press. Ltd., London, (1995).

[7] K. Madsen and H.B. Nielsen. *Introduction to Optimization and Data Fitting*, DTU informatics – IMM, Technical University of Denmark, (2008).

[8] J. Stegmann and E. Lund. Discrete material optimization of general composite shell structures, *Int J Numer Meth Eng* **62**:14, (2005)

APPLICATION OF SOLID-SHELL ELEMENTS TO LAMINATED GLASS

Maria Fröling[*] **and Kent Persson**

Dept. of Construction Sciences

Lund University

P.O. Box 118

SE-221 00 LUND, Sweden

e–mail: maria.froling@byggmek.lth.se
e–mail: kent.persson@byggmek.lth.se

Summary   New so-called solid-shell finite elements are proposed for the accurate and efficient modelling of laminated glass. The elements are applied to a simple test example and the results are compared to 3D elasticity theory.

Introduction

It has become more common today to use glass as a structural material, although there is a lack of knowledge about the mechanical properties and structural behavior of glass compared to other structural materials [6]. This may result in erranous predictions of the glass strength and a greater risk for sudden failures of a structure.

The use of laminated glass instead of single layered glass is one means of increasing safety. Laminated glass consists of two layers of glass bonded with plastic inter layers, normally made of PVB. The use of laminated glass increases safety in two ways. Firstly, if the structure is properly designed, it should be allowed for one glass pane to break while the other glass panes can continue to carry the design loads. Secondly, fractured glass pieces can stick to the PVB layer and thereby prevent people from getting hurt.

Due to the combination of a very stiff material (glass) and a very soft material (PVB), a laminated glass pane displays a complicated structural behavior [1]. The introduction of a very soft PVB layer in a laminated glass unit leads to a structure whose layers are not perfectly bonded. For instance [8] reports on a decrease in stiffness of a laminated glass-PVB plate due to the relatively soft inter layer, compared to the case of a perfectly bonded plate. Moreover, discontinuous stress distributions may develop in laminated glass panes subject to certain loads and boundary conditions. The discontinuities are particularly pronounced around holes and edges and it is in these regions that the largest stress concentrations often occur.

The numerical modelling of laminated glass by means of the finite element method is difficult, taking the above mentioned features of laminated glass into account. A finite element model with 3D solid elements accurately determines displacements and stress distributions, but the fine mesh that is required in order to get the desired accuracy of the solution leads to very large models and great computational effort. Large real world structures with many point fixings are practically impossible to analyze using standard computational resources.

One alternative to the use of 3D solid elements is to use shell elements. However, the shell theories that are required in order to accurately determine the stress distributions in laminated glass structures are complicated.

In this work, a novel so-called solid-shell finite element, the M-RESS element [3], is implemented and applied to a simple test example. The element is developed for modelling composite structures with different material properties in each layer. The reason why the solid-shell element is

appropriate for the modelling of this type of composite structures is that the element only requires one element layer per material layer, but includes several integration points through thickness. This feature leads to great savings in terms of computational time, still preserving great accuracy. The implementation of the element is relatively straight-forward. Further advantages compared to shell-elements are that the full 3D constitutive laws are maintained, the use of rotational degrees of freedom is avoided and that contact situations are more easily modelled through the presence of physical nodes on top and bottom surfaces. The element has proven to be both robust and efficient through extensive testing.

The M-RESS solid-shell element

M-RESS stands for Modified Reduced (in-plane) integration, Enhanced strain field, Solid-Shell concept. The element name indicates several methods that have been used in order to make a standard (low-order) 3D solid element suitable for analysis of shell-like structures.

The geometry of the element is that of a 3D hexahedral solid element with 8 nodes and 3 translational degrees of freedom per node. A special reduced integration scheme is used in order to increase the computational efficiency. The reduced integration scheme uses one single element layer per material layer, but includes multiple integration points through thickness. The use of a reduced integration scheme leads to a stiffness matrix that is rank deficient and a physical stabilization procedure is thus required [2]. For instance the B-bar method [7] and the ANS method [5] are used to alleviate locking problems that occur due to the stabilization procedure.

Solid-shell elements are sensitive to several other types of locking phenomena. In the element formulation, the EAS method [9] plays an important role in preventing various types of locking problems. The crucial point of the EAS method is to enlarge the strain field, ε, through adding a new field of enhanced strain parameters, α. The displacement field, $\mathbf{u}$, is interpolated by the standard FEM strain-displacement matrix, $\mathbf{B_u}$. The enhanced strain parameters' field is interpolated by the matrix $\mathbf{B}_\alpha$. For each element, the enhanced part of the strain field, ε_α, is added to the standard strain field:

$$\tilde{\varepsilon} = \varepsilon + \varepsilon_\alpha = [\hat{\mathbf{B}}_{\mathbf{u}}\, \hat{\mathbf{B}}_\alpha] \left[\begin{array}{c} \mathbf{u} \\ \alpha \end{array} \right] = \tilde{\mathbf{B}}\tilde{\mathbf{u}}. \tag{1}$$

For linear applications, use of the EAS method leads to the following system of equations:

$$\left[\begin{array}{cc} \hat{\mathbf{K}}^{\mathbf{uu}} & \hat{\mathbf{K}}^{\mathbf{u}\alpha} \\ \hat{\mathbf{K}}^{\alpha\mathbf{u}} & \hat{\mathbf{K}}^{\alpha\alpha} \end{array} \right] \left(\begin{array}{c} \mathbf{u} \\ \alpha \end{array} \right) = \left(\begin{array}{c} \mathbf{f}^{ext}. \\ \mathbf{0} \end{array} \right). \tag{2}$$

The hat denotes evaluations in the local reference frame which is built at the centre of a standard element. Each of the sub-matrices in the above equation could be obtained as:

$$\hat{\mathbf{K}}^{\mathbf{uu}} = \int_\Omega \hat{\mathbf{B}}_{\mathbf{u}}^T \mathbf{C} \hat{\mathbf{B}}_{\mathbf{u}} d\Omega \tag{3}$$

$$\hat{\mathbf{K}}^{\mathbf{u}\alpha} = \int_\Omega \hat{\mathbf{B}}_{\mathbf{u}}^T \mathbf{C} \hat{\mathbf{B}}_\alpha d\Omega$$

$$\hat{\mathbf{K}}^{\alpha\mathbf{u}} = \int_\Omega \hat{\mathbf{B}}_\alpha^T \mathbf{C} \hat{\mathbf{B}}_{\mathbf{u}} d\Omega$$

$$\hat{\mathbf{K}}^{\alpha\alpha} = \int_\Omega \hat{\mathbf{B}}_\alpha^T \mathbf{C} \hat{\mathbf{B}}_\alpha d\Omega,$$

where $\mathbf{C}$ is the constitutive matrix. Static condensation of (2) leads to:

$$\hat{\mathbf{K}}^{\mathbf{u}+\alpha} = \hat{\mathbf{K}}^{\mathbf{uu}} - \hat{\mathbf{K}}^{\mathbf{u}\alpha}(\hat{\mathbf{K}}^{\alpha\alpha})^{-1}\hat{\mathbf{K}}^{\alpha\mathbf{u}}. \tag{4}$$

The displacement field can be determined as:

$$\mathbf{u} = (\hat{\mathbf{K}}^{\mathbf{u}+\alpha})^{-1}\mathbf{f}^{ext}. \tag{5}$$

It can be shown that the number of enhancing variables in the extra strain field is equal to one. The enhancing interpolation matrix could be written as:

$$\bar{\mathbf{B}}_1^T = [0 \ 0 \ \zeta \ 0 \ 0 \ 0], \tag{6}$$

where the bar indicates evaluations in the convective coordinate system which is a function of position within one element. ζ is the thickness coordinate in the local reference frame. The fact that only one enhancing parameter is needed contributes further to the computational efficiency of the element formulation.

Once the strain distribution has been determined through equation (1), the stress distribution is given by:

$$\sigma = \mathbf{C}\tilde{\varepsilon}. \tag{7}$$

The stresses are evaluated at the integration points. A method based on a quadratic least squares fit is used in order to extrapolate the stresses to the nodes [4]. This method requires a $3 \times 3 \times 3$ Gaussian integration scheme.

Numerical test

The M-RESS element is implemented and tested using a test problem comprising a cantilever beam of laminated glass subject to a point load at the tip of the beam. The x-y dimensions of the beam are 100×10. The laminate consists of two glass layers with a PVB inter layer. The thickness of the glass layers is 2 and the thickness of the PVB layer is 1. Glass and PVB are set to be linear elastic materials. The material parameters for glass are $E = 78$ GPa, $\nu = 0.23$ and for PVB $E = 6$ MPa, $\nu = 0.43$. The point load has the size 40000, and is directed in the negative z-direction. The beam is discretized using 50×5 elements in the x-y plane, and one element per layer in the z-direction.

The same structure is implemented in ABAQUS/CAE. The element type is a standard 8-node linear brick element (C3D8R). The mesh has the same discretization in the x-y plane as the above implementation and 4 elements per material layer in the z-direction.

Figure 1 shows the distribution of normal stress along the thickness coordinate at a cross section located at the center of the beam.

The M-RESS element is well capable of reproducing the stress distribution.

In comparison with the implementation in ABAQUS/CAE, the tip deflection in the z-direction and the normal stress component in the x-direction at a cross section located at the centre of the beam show small deviations.

Concluding remarks

Results from a simple test example show that the M-RESS element [3] can be used to reproduce discontinuous stress distributions for laminated glass. Compared to 3D elasticity theory, results for important structural mechanic variables correspond well. Further testing is required in order to fully evaluate the performance of the M-RESS element applied to laminated glass.
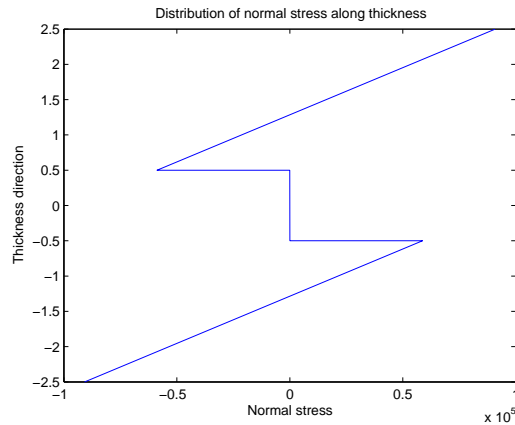
Figure 1: Distribution of normal stress along thickness.

References

[1] M.Z. Aşik and S. Tezcan. A mathematical model for the behavior of laminated glass beams. *Computers and Structures.*, **83**, 1742–1753, (2005).

[2] R.P.R. Cardoso, J.-W. Yoon, J.J. Gracio, F. Barlat and J.M.A. Cesar Sa. Development of a one point quadrature shell element for nonlinear application with contact and anisotropy. *Computer Methods in Applied Mechanics and Engineering*, **191**, 5177–5206, (2002).

[3] R.P.R. Cardoso, J.W. Yoon, M. Mahardika, S. Choudhry, R.J. Alves de Sousa and R.A. Fontes Valente. Enhanced assumed strain (EAS) and assumed natural strain (ANS) methods for one-point quadrature solid-shell elements. International Journal for Numerical Methods in Engineering, **75**, 156–187, (2008).

[4] D.J. Chen, D.K. Shah and W.S. Chan. Interfacial stress estimation using least-square extrapolation and local stress smoothing in laminated composites. *Computers and Structures*, **58**, 765–774,(1996).

[5] E.N. Dvorkin and K.J. Bathe. A continuum mechanics based four-node shell element for general nonlinear analysis. *Engineering and Computations*, **1**,77–88, (1984).

[6] P. Foraboschi. Behavior and failure strength of laminated glass beams. *Journal of Engineering Mechanics.*, **133**, 12, 1290–1301, (2007).

[7] T.J.R. Hughes. *The Finite Element Method: Linear Static and Dynamic Finite Element Analysis*. Dover Editions, New Jersey, Second edition, (2000).

[8] P. Krawczyk. Nonlinear analysis of layered structures with weak interfaces. PhD thesis, Ecole Polytechnique Fédérale de Lausanne, 2006.

[9] J.C. Simo and M.S. Rifai. A class of mixed assumed strain methods and the method of incompatible modes. *International Journal for Numerical Methods in Engineering*, **29**, 1595–1638, (1990).

Numerical modeling of a wave energy point absorber

Lorenzo Banos Hernandez[*] and Peter Frigaard

Department of Civil Engineering
Aalborg University, Aalborg, Denmark
e–mail: lbh@civil.aau.dk

Poul-Hening Kirkegaard

Department of Civil Engineering
Aalborg University, Aalborg, Denmark
e–mail: phk@civil.aau.dk

Summary   The present study deals with numerical modelling of the Wave Star Energy WSE device. Hereby, linear potential theory is applied via a BEM code on the wave hydrodynamics exciting the floaters. Time and frequency domain solutions of the floater response are determined for regular and irregular seas. Furthermore, these results are used to estimate the power and the energy absorbed by a single oscillating floater. Finally, a latching control strategy is analyzed in open-loop configuration for energy maximization.

Introduction

Recent studies conclude that 0.2% of untapped ocean energy would be sufficient to cover the entire world consumption needs [9]. During the past 10 years the deployment of devices such as different buoy concepts, the OWC plants [5] and the Pelamis have given Wave Energy certain credit. For the Danish case, the Wave Star Energy device is one of the outstanding concepts [2]. This 1:10 multipoint absorber consists of 40 semispherical floaters with 20 units along each side of a squared 24m x 5m platform. Latter test rig has been grid connected near-shore with rated 5.5 kW since 2006. Hereby, the sequential floaters oscillation in heave is converted via a Power Take Off (PTO) hydraulic system into electricity. Similar to the application of pitch and stall regulation in wind energy turbines [6], the control of such a PTO is primordial. A major advantage nowadays with respect to the right control implementation is that of being able to predict down to 48h in advance the next coming waves [7].

Wave Star Energy model

In the next figure, a view of the Nissum Bredning 1:10 scale is presented in storm protection mode.

Figure 1: left: WSE view at the pier (Nissum Bredning, DK); right: WSE Floater back view

On the right figure a single floater is held fixed while water is dropping over the surface. The system is simplified through an arm around the xz plane. Hence, the floater is assumed in the following as an abstraction of a SDOF mass spring damper, with an initially free oscillating floater

mass. The excitation force F_w caused by the waves is given through $F_w = F_e + F_h + F_r$, where F_e is the excitation force, F_h the hydrostatic buoyancy force and F_r the radiation force . They are frequency dependent, and are being determined over the BEM code. Adding an explicit definition of the excitation force the governing equation of motion becomes

$$M\ddot{z} = \int_0^t h_e(t-\tau)\eta(\tau)d\tau - (\int_0^t k_r(t-\tau)\dot{z}(\tau)d\tau + A_{r\infty}\ddot{z} + k_h z). \qquad (1)$$

The right hand side of (1) contains first the excitation force as a product over the Dirac impulse h_e and the surface elevation $\eta(t)$. Second and third terms constitute the radiation force due to the generated waves by the oscillation $z(t)$. It is noted that $k_r(t)$ is the radiation impulse function and $A_{r\infty}$ is the added mass value of $A(\omega)$ due to inertia, when $\omega \mapsto \infty$. The fourth term describes the Archimedes buoyancy force F_h . Latter integral terms are subject to a causal memory effect coming from the history of the waves in convoluted form over t. The calculation of the integrals is simplified over the Prony method [4]. The solution of the differential equation is the floater response $z(t)$ via a Newmark Algorithm and a Runge-Kutta Algorithm for a defined sea state over $\eta(t)$ and $F_e(t)$ to the initial conditions $z(t_0) = 0$ m and $v(t_0) = 0\frac{m}{s}$.

Floater response

The floater response is determined with respect to the mean water level regarding the following considerations. The oceanic constraints are settled through North Sea conditions, that means short crested, $\frac{H}{L} << 1$, shallow waters $\frac{H}{D} << 1$ (water depth $\approx 2m$).The Cummins decomposition of wave forces [3] is used for a unidirectional JONSWAP wave spectra (through the yz plane), whereas zero friction viscous losses apply.

Furthermore, the input values for the Boundary Element code are a geometry with a semisphere (symmetry to x,y), the diameter of $1m$ and a draught D of 0.5 m. Herewith, a quad mesh with 256 panels and 297 points is generated over the wetted surface. For the numerical model the following parameters are used

- Floater mass: M = 235 kg

- Significant Wave Height H_s : $1.2m$

- Wave Period T ranging from 0.1 : 0.27 : 21 s

For the later control implementation, a mechanical Stiffness for the floater arm is defined over $K_c = 10000\frac{kg}{s^2}$. Thereby, the mechanical damping C_c is first exerted as a constant($C_c = 10000\frac{kg}{s}$) and then as a non-linear damping ($C_c sign(\dot{z})|\dot{z}|$).

Power absorption

The power absorbed by the oscillating floater is calculated for a resonant situation. The next equation reflects the solution of Eq.(1) for a complex floater response, where the mechanical resistance is damped out by the water ($C_c = C_h$):

$$H(j\omega) = \frac{\hat{F}_e(\omega)\hat{\eta}(\omega)}{-(m+m_h(\omega))\omega^2 + j\omega(C_c + C_h(\omega)) + k_h(\omega) + k_c} \qquad (2)$$
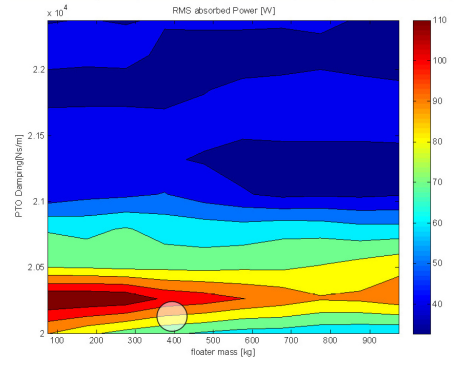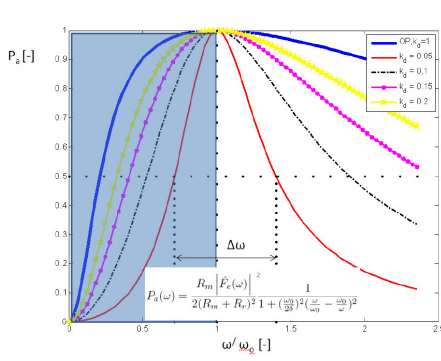
Figure 2: non-dimensionalized Absorbed Power for variable damping ratios k_d

Figure 3: Absorbed RMS [W] over floater mass M and mechanical damping C_c

Fig.(2) shows the non-dimensionalized behavior of absorbed power P_a over the frequency range $\frac{\omega}{\omega_0}$. Therefore, the damping ratio k_d is varied linearly in 0.05 steps up to the operating range (blue curve), corresponding to the regular sea state of latter simulations. The higher the damping ratio, the faster the power increases up to resonance frequency, where $\frac{\omega}{\omega_0} = 1$. For higher frequencies, this linearization also results in a wider bandwidth ($\Delta\omega$). In order to quantify the Power absorbed, the Root mean square RMS is calculated as a function of mass and PTO damping. The contour plots are shown in Fig. (3)

Maximal Power between 110 W and 165 W is obtained for a mass variation of 70 - 500 kg (x-axis). The PTO damping on the y-abscissa variates from 2 - 2.05 $\frac{kg}{s}$ for exciting loads ranging from -72.47 N to 226.98 N.

Finally, a latching control system strategy is applied for the linear damping case in regular waves, that locks and releases the body motion within given intervals. The objective is to tune the velocity to be in phase with the excitation force, while keeping the resonance condition. Results to this discrete phase control are presented in the next graphs.
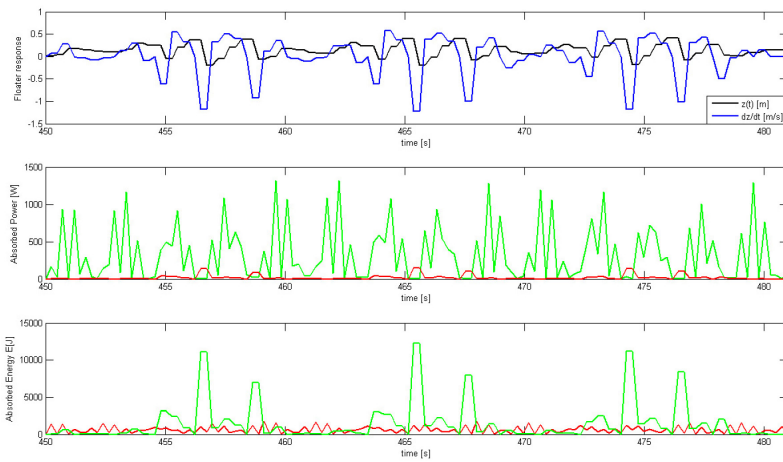
Figure 4: Floater response [m], Instantaneous absorbed Power [W] and available Energy [J])

The simulation results are fixed to a 31s interval after the transient of the floater response vanishes (nearly 450 s, with $\delta t = 0.24s$). As it can be seen in Fig. (4) the position is held constant during almost 1s latching intervals. The Power absorbed in the second plot compares the uncontrolled case

(red curve) with the latched strategy (green curve). Same procedure applies on the third subplot, where the wave energy absorption in J is compared for both cases. It is noted that the position, the absorbed power and wave energy correlate closely for time intervals with peak performance (e.g. at $t = 457, 459$ or $466s$).

Conclusion

The study introduces a standarized approach within the field of control algorithms for point absorbers. In time domain, the single body model performs with increased computational efficiency in comparison to previous analysis done in FORTRAN. The hydrodynamics coefficients acquisition is similar to commercial software examples, like WAMIT [1]. The floater response reveals the characteristic behavior of a second order delay system in control theory. Moreover, the power absorption ratio on Fig.(2) shows the significance of fitting the operative range of the device to a narrow bandwidth close to resonance frequency. The parametrization of mass and damping indicate that an increase of the mass might avoid possible floater slamming for maximum power. For instance a mass of nearly 400 kg and a damping value of nearly $2e4\frac{kg}{s}$ can still achieve 80-100 W(RMS) per floater (white circle on Fig. (3)). Through the applied control strategy, it can be seen that the power can be amplified significantly (in the order magnitude of 2-3 times the latched RMS power). Though, the peaks of nearly 1 kW per floater are quite unrealistic in comparison to the range calculated over Fig. (3). Despite of the stability analysis done, further improvements may be achieved through other control strategies that might be applied in order to smoothen the power output. Furthermore, the extension to the multibody formulation and the inclusion of stochastical disturbances is of interest for the WSE development [8].

References

[1] Falnes, J. Ocean Waves and Oscillating Systems. *Cambridge*, ISBN 982-207-002-0, (2002).

[2] Kramer,M. Internal Reports on Hydrodynamics and Structural design. Wave Star Energy, (2004-2009).

[3] Cummins, W.E. The impulse response function in ship motions. *Schiffstechnik*, 491-502, (1962).

[4] de Backer, G. Basics in numerical time domain simulation of a heaving point absorber. *Ghent University, Trainee report*, , (2007).

[5] Heath,T.V. The Development of a Turbo-Generation System for Application in OWC Breakwaters. *Proceedings of the 7th European Wave and Tidal Energy Conference*, Wavegen, (2007).

[6] Chen, Z., Blaabjerg, F., Ackermann, T. et al. Offshore Wind Power. *Twidell*, ISBN 982-207-002-0, (2009).

[7] Rhinefranka, K. Agamloha, E.B.et al. Novel ocean energy permanent magnet linear generator buoy. *OSU,School of Electrical Engineering*, p.1-5, (2005).

[8] Wave Star Energy A/S http://www.wavestarenergy.com.

[9] Brekken, T. The promise of wave power. IET Presentation, AAU. *Oregon State University*, p.1-3, (2009).

Periodicity effects in straight elastic pipes with inertial attachments: boundary integral equations method versus Floquet theory

Sergey V. Sorokin∗

Department of Mechanical Engineering
Aalborg University, Aalborg, Denmark
e−mail: svs@me.aau.dk

Ole Holst Jensen

Minus10dB
Stokrosevej 29 DK 8330 Beder, Denmark
e−mail: ole.holst@minus10db.dk

Summary   The paper addresses the theoretical analysis of possibilities to suppress the mechanical energy transmission in a pipe at relatively low excitation frequencies by employing a small number of equally spaced inertial inclusions. The methodology of boundary integral equations is used to obtain an exact solution of the problem in vibrations of a compound pipe. The power flow analysis in a pipe with and without equally spaced inertial attachments is performed and the effect of suppression of the energy transmission is demonstrated. These results are put in the context of predictions from the classical Floquet theory for an infinitely long periodic structure.

Introduction

Control of the vibro-acoustic energy transmission in pipes is an important and challenging problem in various industrial and civil applications. The ability to carry out a 'quiet design' of, for example, a heating system in houses is necessary to meet the modern regulations. Alongside, the noise and vibration levels in oil- and gas-transporting industrial pipelines should remain within the allowable limits. Therefore, various tools of 'anechoic termination' have been developed to suppress the wave propagation in piping systems. As is shown in recent publications by one of the co-authors, the presence of a small number of periodically located continuous inclusions in an otherwise homogeneous wave guide (an elastic plate or cylindrical shell) is capable to produce a substantial attenuation of the transmitted waves. The methodology of boundary integral equations has been developed to analyse the elastic wave propagation in compound thin-walled structures with continuous inclusions. The level of suppression of the wave propagation is controlled by a number of the 'periodicity cells' embedded in a wave guide. An excellent agreement between the Floquet theory predictions and the results of the energy transmission analysis has been found in the considered semi-infinite compound structures. If a few 'periodicity cells' composed as suggested by the Floquet theory are embedded in a wave guide and the excitation frequency lies within a predicted stop band, then the energy transmission is severely suppressed. In opposite, the same excitation of the same structure at a frequency outside any stop band produces a power flow virtually unaffected by the non-homogeneity of the wave guide. This conference paper is based on the reference [1] and is concerned with periodicity effects produced by inertial attachments ('block masses') in the framework of same methodology.

Modelling

Consider a straight pipe of the circular cross-section, which may be connected at one end (for definiteness, the left edge) to a relatively large structure (or it may be free as well) and extended to

sufficiently far distance at the other end (for definiteness, the right edge). The boundary conditions at the right edge mimic connection to an outer piping system or a radiator. In the situation, when these boundary conditions are 'non-reflecting', the pipe may be regarded as being extended to infinity. The source of the vibro-acoustic energy injected into the pipe is located in the vicinity of its left edge. It is modelled as an inertial attachment exposed to given driving forces. These forces have components acting in three orthogonal directions and each component is characterised by its spectral density. Therefore, all types of waves – longitudinal, torsion and flexural – may be excited in this mechanical system. Due to the linearity of its response, the superposition principle is valid and the energy transmission at each individual frequency may be considered independently. It also allows one to apply the methodology of Green's functions and boundary integral equations method.

There is no interaction between waves of different types in a homogeneous semi-infinite pipe and it is a trivial task to calculate the vibro-acoustic power injected by each component of the driving force at each frequency. As soon as several inertial attachments are mounted at a pipe, longitudinal, torsion and flexural waves become coupled due to the eccentricity of inertial attachments. If these attachments are aligned to be in the same plane (the obvious situation is masses hanging in the vertical plane), then the wave interaction is 'factorised'. Specifically, the flexural wave motion in the vertical plane is coupled with the axial wave motion and the flexural motion in the horizontal plane is coupled with the torsion wave motion. Violation of alignment of the inertial attachments into the same plane results in the full coupling of all four types of waves.

The boundary integral equations method is consistently used as a tool of analysis of time harmonic response of a pipe with inertial attachments. The following distinctive features of this method should be observed:
- it yields algebraic rather then integral governing equations, and, therefore, it gives the exact solution of any one-dimensional problem
- it is equally applicable for solving problems in the time harmonic response of infinitely long uniform structures and of structures composed of continuous segments with different properties
- it is equally applicable to consider travelling waves in infinite/semi-infinite structures and standing waves in structures of finite dimensions
- inasmuch as Green's matrices are set up with radiation and decay conditions being taken into account, the algorithm of solving problems in time-harmonic response by boundary integral equations method is inherently stable

The standard tool to study wave propagation in infinite periodic structures is provided by the Floquet theory. It is a straightforward matter to use this theory in the framework of the boundary integral equations method. Indeed, for a given segment of the pipe, boundary equations are readily available. The continuity conditions at the inertial inclusion are formulated for neighbouring segments. Since it is assumed that an infinitely long pipe is composed of repeating identical segments and inclusions, periodicity conditions with Bloch parameter K_B are introduced. It is an easy task to apply the Floquet theory for analysis of the wave guide properties of a pipe with inertial attachments, because its formulation implies the perfect alignment of inclusions and facilitates factorization of the problem into analysis of the coupled flexural-axial wave propagation in the vertical plane and the coupled flexural-torsion wave propagation in the horizontal plane.

All technical details of the theory very briefly outline here are presented in the reference [1].

Results

The steel pipe has the following dimensions: $d_{outer} = 33.6mm$; $d_{inner} = 27mm$. Aluminium inertial attachments are of height 206 mm, width 100 mm, length 80 mm and eccentricity 142 mm each. The results of calculations of insertion losses (IL) are shown in Figure 1. Triangle-mark, rhomb-marked and continuous curves are plotted for the cases when three, five and seven inclusions are mounted on a pipe. There is a perfect agreement between these results and predictions of the Floquet theory, which are illustrated in Figure 2, see thick dotted curves. Attenuation is most pronounced exactly in the frequency range of the first stop band, from 160Hz to 281Hz as shown in Figure 1 and reproduced in Figure 2. Furthermore, there is the second stop band readily predicted by the Floquet theory, see Figure 2 and its zoomed fragment in Figure 3. It is relatively narrow and it extends from 448Hz to 455Hz. To gain a better insight into the wave interaction phenomena involved in the formation of the frequency stop bands, it is helpful to consider two complimentary cases and put the results into the context of those already presented. This task is accomplished by inspection into the three sets of curves in Figures 2-3. Curves marked by thick dots present Bloch parameters computed for the coupled flexural-longitudinal wave motion in an infinite uniform pipe with inertial attachments in a broad frequency range. Triangle-marked curves are plotted for the simplified model of flexural wave propagation uncoupled from the axial wave. Thin dotted line presents Bloch parameter for the opposite situation: the axial wave uncoupled from the flexural wave. It is clearly seen that in the relatively low frequency range, approximately up to 140 Hz, the eccentricity-induced coupling of flexural and axial waves is very weak. However, this interaction plays the key role in formation of the frequency stop bands. In the uncoupled formulation (eccentricity is absent), curves presenting propagation constants intersect each other at frequencies of 171 Hz and 454 Hz. To avoid these intersections in a coupled waveguide, the purely real propagation constants acquire imaginary parts at 161 Hz and at 448 Hz and, therefore, the stop bands emerge. It is interesting to see how this narrow stop band emerges in Figure 8, when the number of inertial attachments increases. Exactly the same phenomenon has been reported for the case of a compound cylindrical shell with and without heavy fluid loading.
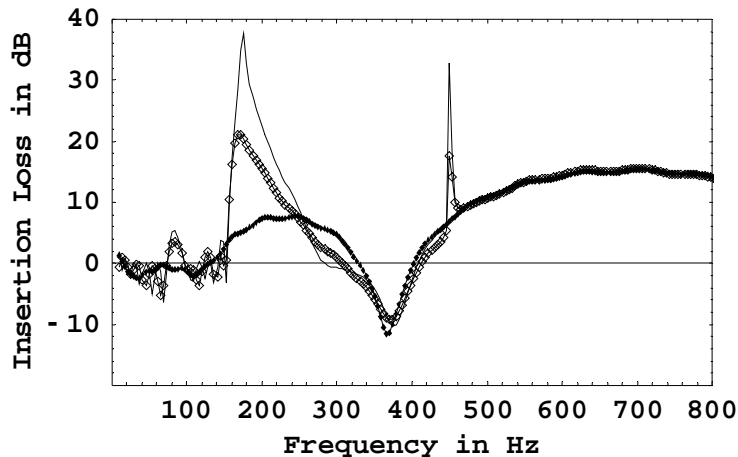
Figure 1: The effect of number of equally spaced (700 mm spans) masses.
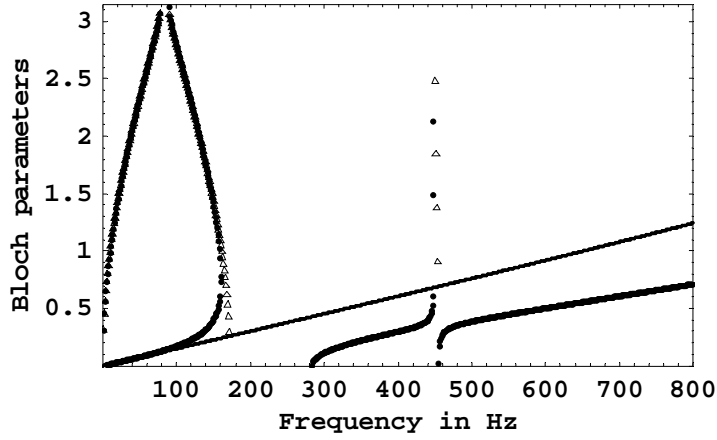
Figure 2: Bloch parameters ($\operatorname{Im} K_B = 0$, $\operatorname{Re} K_B > 0$) in the broad frequency range.
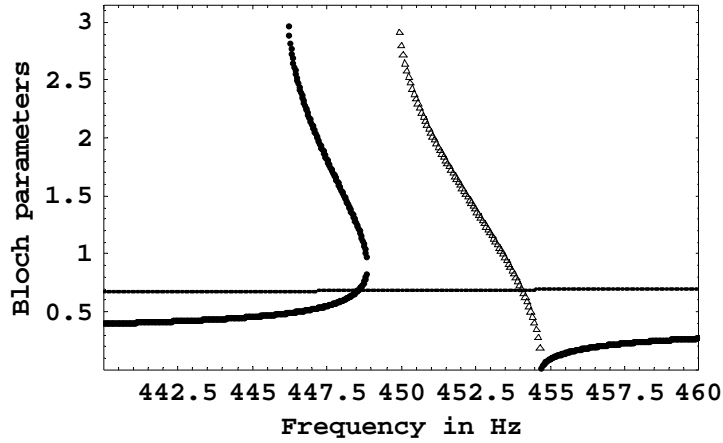
Figure 3: Bloch parameters ($\operatorname{Im} K_B = 0$, $\operatorname{Re} K_B > 0$) in the second frequency stop band.

Concluding remarks

The results reported in this paper demonstrate that the 'frequency band gap' effect in an elastic pipe may be achieved within a practically meaningful frequency range by use of the small number of inertial elements. Obviously, the location of the band gaps is controlled by the parameters of a pipe as well as by the parameters of the inertial inclusions. Although it is influenced by the impedance conditions at the point, where a pipe is connected to the outer part of a piping system, a reasonable 'first guess' for the choice of parameters of the inertial inclusions can be made by using the classical Floquet theory.

References

[1] O. Holst Jensen and S.V. Sorokin. On suppression of transmission of mechanicsl energy in straight elastic pipes by use of equally spaced inertial attachments. *Journal of Sound and Vibration*, JSV-D-09-00541 (2009).

Modelling of a Multi-parallel-path Transmission for Load-sharing Analysis

Shaoping Bai

Department of Mechanical Engineering
Aalborg University, Denmark
e-mail:shb@me.aau.dk

Abstract

Transmissions with multiple parallel paths can be used in special applications where high toques are to be transmitted. The uneven load sharing among all paths is an inherent problem for such kinds of transmissions. The paper presents an analytical model for transmissions with single input and multiple outputs. In the model, the elasticity of gear teeth and the stiffness of shafts and bearings are considered. The model takes also into account of factors including gear geometric errors and operational conditions. Simulation results show primarily the load-sharing difference due to variations of these factors.

Keywords Multi-parallel-path transmission, load-share gears, multi-body dynamics

1 Introduction

A multi-parallel-path transmission refers to a parallel shaft gearing arrangement in which the input gear meshes with multiple output gears, or, visa versa, multiple output gears mesh an output gear. Multi-parallel-path transmissions have some promising features such as high capability of torque transmission, low complexity of mechanism, and compact in size. They can be used in applications requiring high torque in a compact structure, such as helicopters and wind turbines.

While multiple-parallel-path transmissions have the potential to effectively transmit power, a fundamental problem is the uneven load-sharing among all paths. As a matter of fact, the load applied on the transmission cannot be equally shared by all paths, due to influences including the nonlinearty of the gear teeth, the manufacture and assembly error, and backlash, etc. The uneven load sharing increases the noise level, reduces the efficiency and more seriously, shortens significantly the life expectancy. To make the load is equally distributed among gears is a big concern in the design and development of multi-parallel-path transmissions.

The multi-parallel-transmissions are relatively new compared with traditional transmissions like planetary gear trains. White proposed to use a transmission with split-path arrangement in helicopters [1, 2]. Krantz developed a static model to analyze the load sharing of split-path transmissions [3]. A dynamics model was developed using rigid-body and lumped mass approximation by Dama, etc. [4].

In this paper, a dynamic model of transmission is developed by taking into account of the elasticity of gear teeth and stiffness of shafts and bearings. Operational conditions and gear geometric errors such as backlash are considered. Simulations are conducted using the developed model. It is found from the simulation that the material, the geometric error all contribute to the inequality in load sharing.

2 Dynamics Model

A model of multi-parallel-path transmission system is depicted in Fig. 1. In the system, power/torque from one motor is transmitted via multiple parallel paths to load. Only two paths are shown in the figure for clarity.

Let ϕ_m and θ_s be the rotations of the motor and the sun gear, while $\phi_{l,i}$ and $\theta_{p,i}$ be the rotations of the load the the ith output gear (planet gear). The motion equation of the system can be developed as

$$J_m\ddot{\phi}_m + C_{sm}(\dot{\phi}_m - \dot{\theta}_s) + K_{sm}(\phi_m - \theta_s) = T_m \tag{1}$$

$$J_s\ddot{\theta}_s + C_{sm}(\dot{\theta}_s - \dot{\phi}_m) + K_{sm}(\theta_s - \phi_m) + \sum_{n=1}^{3} F_{b,n}R_{b0} = 0 \tag{2}$$

$$J_{p,i}\ddot{\theta}_{p,i} + C_{sl,i}(\dot{\theta}_{p,i} - \dot{\phi}_{l,i}) + K_{sl,i}(\theta_{p,i} - \phi_{l,i}) + F_{b,i}R_{b,i} = 0, \quad i = 1,2,3 \tag{3}$$

$$J_{l,i}\ddot{\phi}_{l,i} + C_{sl,i}(\dot{\phi}_{l,i} - \dot{\theta}_{p,i}) + K_{sl,i}(\phi_{l,i} - \theta_{p,i}) = T_{l,i} \tag{4}$$

where
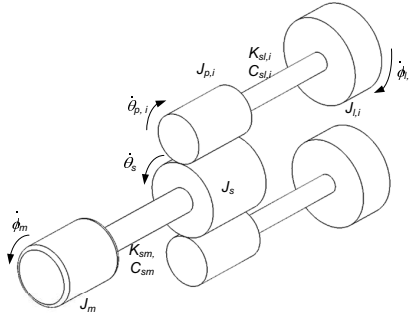
Figure 1: A multi-path transmission system

J_m and $J_{l,i}$ — moments of inertia of the motor and the equivalent load applied to the i-th planet gear

R_{b0} and $R_{b,i}$ — radii of the base circles of the sun gear and the i-th planet gear

C_{sm} and K_{sm} — damping factor and the torsional stiffness of the motor shaft

$C_{sl,i}$ and $K_{sl,i}$ — damping factor and the torsional stiffness of the shaft connected to the i-th planet gear

$F_{b,i}$— gear meshing force along the line of action

$T_m, T_{l,i}$—motor torque and the load applied at the i-th output

In deriving the system of equations, each gear is considered as a rigid body. The elastic nature of gear teeth is included in the determination of gear meshing force. This means that the changes of moments of inertia of gears are neglected in this model. It is noted that there is another approach as reported in [5], where each teeth is treated as a separated body connected to the gear body by means of springs.

The solving of the system depends on available gear meshing force $F_{b,i}$. The force is highly non-linear and discontinuous , due to the non-uniform gear profile and operational conditions. A method for the determination of the meshing force is outlined presently. In the method, the gear deflection and the gear meshing stiffness are calculated separately. The meshing force is then found as the product of gear meshing stiffness and gear deflection.

3   Gear teeth stiffness in gear meshing

The gear meshing stiffness is nonlinear due to facts such as the moving contact point, non-uniform gear tooth profile, the periodic engagement of tooth-pairs, the variation of contact ratio, etc.

A gear meshing model developed by Cornell [6] is adopted in this work. Cornell's model takes into account of three major factors: (1) the tooth deflection when treated as a cantilever beam, (2) the deflection due to the fillet and foundation, and (3) the local deflection due to surface compliance, or contact stiffness.

More details of this model are omitted due to space limit. An example of gear meshing stiffness is shown in Fig. 2 for a pair of gears with teeth numbers of $n_1 = 33$ and $n_2 = 18$.
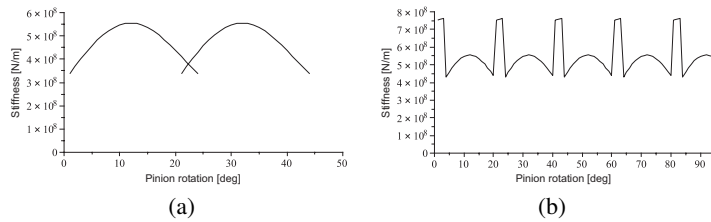
Figure 2: Gear meshing stiffness, (1) stiffness curve for two gear meshing pairs, (2) teeth stiffness for continuous rotation.

4 Gear meshing force

The gear meshing force $F_{b,i}$ is in principle equal to the product of gear meshing stiffness and gear tooth deflection. However, it is also subjected to the operational conditions, which are closely related to the gear backlash. Let δ_b denote the backlash and $\delta\theta = R_{b0}\theta_s - R_{b,i}\theta_p$ the rotation difference between two meshing gears. Three conditions can be classified according the gear meshing

1. Positive working condition, for which $\delta\theta < 0$. This is a situation in which sun gear drives planet gears.

2. Negative working condition, for which $\delta\theta > \delta_b$. In such a situation, a planet gear is in contact with the backside of the driving gear.

3. None-engagement condition, for which $0 < \delta\theta < \delta_b$. In this condition, gear teeth from both the driving and driven gears are separated. Thus no meshing force is generated.

Based on the three operational conditions, the forces generated in gear meshing can be calculated by

$$F_b(j) = \begin{cases} k(j)\delta p & \text{if } \delta\theta < 0 \\ -k(j)\delta p & \text{if } \delta\theta > \delta_b \\ 0 & \text{if } 0 < \delta\theta < \delta_b \end{cases} \tag{5}$$

where δp is the compression between meshing teeth. Referring to fig. 3, the compress is calculated by

$$\delta p = (p_x^2 + p_y^2)^{1/2} \tag{6}$$

with

$$p_x = (R_{b0}\theta_s - R_{b,i}\theta_{p,i})\cos\alpha_i + x_s; \quad p_y = (R_{b0}\theta_s - R_{bi}\theta_{p,i})\sin\alpha_i + y_s \tag{7}$$

where (x_s, y_s) are displacement of sun gear support or bearing. Moreover, α_i is the angle between the line of action and the selected x axis. Let α_0 be the angle from the line passing centers of the first planet gear and the sun gear to x-axis, then α_i is found as

$$\alpha_i = \alpha_0 + \pi/2 \pm \phi + 2\pi i/n \tag{8}$$

where ϕ is pressure angle and n the number of planet gears which are assumed to be placed symmetrically around the sun gear. The sign of ϕ in the right side of Eq. (8) depends on the rotational direction of the sun gear.
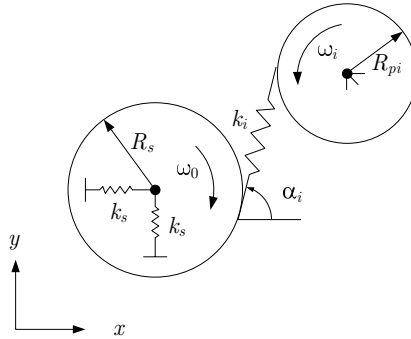
Figure 3: Equivalent gear meshing mechanism

So far, we have formulated the dynamics equations of the multi-parallel-path transmission, which is readily to be solved with parameters defined.

5 Results

An example is given for a transmission system consisting of one sun gear and three planet gears. The motor characteristics is assumed as ideal one for AC motors. The system starts running from all parts being rest. The maximum backlash is set to $\delta_b = 0.0005mm$. For simplicity, the gear meshing stiffness is approximated by square waves, with

Table 1: Gear Parameters

	planet gear	sun gear
Number of teeth	35	18
module[mm]	5	5
addendum [mm]	2.75	4.4
pressure angle[deg]	20	20
teeth width [mm]	50	50
MOI [kg.m^2]	0.19	0.056

Table 2: Simulation parameters

damping ratios [N/s]	$C_{sm} = 5.0 \times 10^2$; $C_{sl} = 1.0 \times 10^3$
shaft stiffness[N.m/rad]	$K_{sm} = 1.0 \times 10^4$; $K_{sl} = 2.0 \times 10^4$
starting position [rad]	$\theta_s = \theta_{p1} = 0.0$; $\theta_{p2} = \theta_{p3} = 0.0001$
payload [N.m]	$T_l = 100$

a lower bound of $2.5 \times 10^7 N.m$ and a upper bound of $4.5 \times 10^7 N.m$. Other parameters are listed in Tables 1 and 2. Note that the support for the sun gear is assumed to be rigid. The resultant torques at each gear are displayed in Fig. 4. The rms values of the torque at each planet are found as 171.0, 172.7 and 158.3 $N.m$ for three planet gears, respectively. They stand for $34.0\%, 34.4\%$ and 31.5% of the average torque transmitted through the transmission. The difference of load sharing in this example is not so significant, but still noticeable.

The load sharing is influenced by many factors. One more simulation is conducted by changing the gear meshing stiffness. With a lower limit of $2.5 \times 10^8 N.m$ and a upper limit of $4.5 \times 10^8 N.m$, the load shares for planet gears become $33.7\%, 33.4\%$ and 32.7%. It is noted the simulation cannot reach a conclusion that more rigid gears will get better load sharing. More simulations and analyses are required.

(a) gear 1   (b) gear 2   (c) gear 3
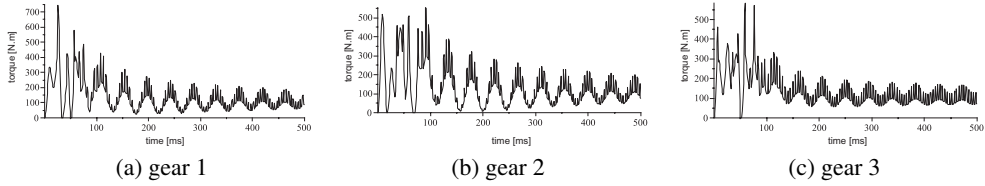
Figure 4: Variations of applied toques on planet gears

6   Conclusions

A multibody dynamics model of multi-parallel-path transmissions is developed. The model takes into account of factors including the gear deflection, shaft stiffness, gear backlash, and operational conditions. Numerical examples are included, which show that the model is able to reveal the difference of load-sharing among paths, hence can be used for further analysis of systems with multi-path transmissions.

References

[1] G. White. New family of high-ratio reduction gear with multiple drive paths. *Proc. Instn. Nech. Engrs.*, 188:281–288, 1974.

[2] G. White. Design study of a 375-kw helicopter transmission with split-torque epicyclic and bevel drive stages. *J. Mech. Eng. Sci., Part C*, 197:213–224, 1983.

[3] T.L. Krantz, et. al Split-torque transmission load sharing. Technical Report 92-C-030, NASA, Lewis Research Center, Cleveland, Ohio, U.S.A, 1992.

[4] R. Dama, D.A. Streit, and L. Chang. Modeling and analysis of a high-speed transmission with multi-path, elastomeric load-share gears. *Mechanism and Machine Theory*, 32(3):295–312, 1997.

[5] S. Ebrahimi and P. Eberhard. Rigid-elastic modeling of meshing gear wheels in multibody systems. *Journal Multibody System Dynamics*, 16(1):55–71, 2006.

[6] R. W. Cornell. Compliance and stress sensitivity of spur gear teeth. *ASME J. Mechanical Design*, 103(2):447–459, 1994.

Modelling of Spatial Pipe Systems Containing Finite Element Sub-Segments using Boundary Integral Equations

Alf Søe-Knudsen

Department of Mechanical Engineering
Aalborg University, Aalborg, Denmark
e–mail: ask@me.aau.dk

Summary A methodology of analysis of time harmonic motion is described for arbitrarily shaped spatial pipe systems consisting of interconnected slender straight and curved segments. It is validated by comparison of eigenfrequencies with FEM solutions in ANSYS. Results of the energy flux analysis for a system containing five repeated substructures are compared with stopband predictions obtained by use of standard Floquet theory.

Introduction

Spatial pipe systems are widely used in domestic and industrial applications. A by-product of the operational effect of pumps and valves, on such pipe systems, is generation of vibro-acoustic energy, which may be transmitted in the structural part of a pipeline over long distances and emit undesirable noise, for example, from a distant radiator. Because a spatial pipe system typically contains straight and curved slender pipe segments connected via more compact details, e.g. fixtures and flanges, it is of practical relevance and theoretical interest to analyze structural energy flux in such a compound system. An appropriate methodology for the slender straight and curved segments is boundary integral equations method (BIEM). These boundary integral equations (BIE) are obtained by use of Greens matrix and reciprocity theorem. For modeling of vibration of fixtures and flanges, finite element method (FEM) is suited better, than BIEM. In this paper a methodology to integrate finite element (FE) models into BIE is proposed. Standard Floquet theory is applied for analysis of stopband behavior in infinitely long structures composed of periodic repeated substructures, modeled by this combined method.

Methodology

Linear theory of vibration and wave motion in slender elastic rods is used. Green's matrix is derived as a response of an infinitely long element to a unit point excitation. Somigliana's identities are derived for the given element from reciprocity theorem with Green's matrix being used. These identities contain element boundary values, which are displacements, rotations, forces and moments at its endpoint cross sections. BIE are derived from Somigliana's identities by letting the observation point move to the boundaries.

The FE models of the compact segments yield stiffness and mass matrices from a commercially available program (in this case ANSYS11 with shell93 elements).These matrices are put into a FE sub-segment formulation which fits into the used BIE formulation. The global set of algebraic equations contains BIE's, FE sub-segment equations and boundary/interfacial conditions for all segments. All boundary values are hereafter found by solving this global set of equations. When the boundary values are known, displacements, rotations, forces and moments within each slender pipe segments can be found from Somigliana's identities. It is therefore possible to calculate energy flux in an arbitrary slender pipe cross-section of a semi-infinite global pipe system. By setting determinant of the global set of equations equal zero, eigenfrequencies of a finite pipe system can also be found.

An infinitely long periodic freely vibrating compound structure can be modeled by use of standard Floquet theory if it consists of repeated substructures. The application of this theory on a single substructure generates an eigenvalue problem, and its solution predicts existence of stopbands in dynamical response of the compound structure. A more detailed description of modeling straight and curved pipe segments by means of boundary integral equations can be found in [3] and [4].

Finite element sub-segment formulation

Stiffness matrix **K** and mass matrix **M** are available from the FE program. When time harmonic solutions are assumed, following system of equations of motion can be formulated for the sub-segment

$$\begin{Bmatrix} \mathbf{p}_c \\ \{0\} \end{Bmatrix} = \begin{bmatrix} \mathbf{K} - \omega^2 \mathbf{M} \end{bmatrix} \begin{Bmatrix} \mathbf{u}_c \\ \mathbf{u}_i \end{Bmatrix} \tag{1}$$

Here $\mathbf{p}_c$ are nodal forces at the connecting cross section surfaces, $\mathbf{u}_c$ are nodal displacement at the same nods and $\mathbf{u}_i$ are all the inner nodal displacements. Note that there are assumed no external forces at inner nodes. The dynamic stiffness matrix $\mathbf{S} = \mathbf{K} - \omega^2 \mathbf{M}$ is split into following four sub-matrices: $\mathbf{S}_{cc}$, $\mathbf{S}_{ii}$, $\mathbf{S}_{ic}$ and $\mathbf{S}_{ci}$. Equation (1) is reformulated by help of these sub-matrices into a system of equations independent of inner displacements $\mathbf{u}_i$ [1].

$$\begin{Bmatrix} \mathbf{p}_c \\ \{0\} \end{Bmatrix} = \begin{bmatrix} \mathbf{S}_{cc} & \mathbf{S}_{ci} \\ \mathbf{S}_{ic} & \mathbf{S}_{ii} \end{bmatrix} \begin{Bmatrix} \mathbf{u}_c \\ \mathbf{u}_i \end{Bmatrix} \Leftrightarrow \mathbf{p}_c = \mathbf{S}_{cc} - \mathbf{S}_{ci} \mathbf{S}_{ii}^{-1} \mathbf{S}_{ic} \mathbf{u}_c \tag{2}$$

Shell displacements at a node k, in the cross section j, are linked to the cross section j's beam node displacements by a transformation matrix $\mathbf{Q}_k$. This matrix employs the Bernoulli-Euler constrains (plane cross section assumptions) between these two nods, see equation (3). These constrains are defined by help of the node k's local in-plane cross section j coordinates (x_k, y_k). Note that the node k's shell displacements $\mathbf{u}_k$ and local beam displacements at the cross section j $\mathbf{u}_{bj}$, are given in the same local coordinate system for the cross section j, see Figure 1.

$$\mathbf{u}_k = \mathbf{Q}_k \mathbf{u}_{bj} \quad where \ \mathbf{Q}_k = \begin{bmatrix} 1 & 0 & 0 & 0 & 0 & -y_k \\ 0 & 1 & 0 & 0 & 0 & x_k \\ 0 & 0 & 1 & y_k & -x_k & 0 \\ 0 & 0 & 0 & 1 & 0 & 0 \\ 0 & 0 & 0 & 0 & 1 & 0 \\ 0 & 0 & 0 & 0 & 0 & 1 \end{bmatrix}, \mathbf{u}_k = \begin{Bmatrix} u_k \\ v_k \\ w_k \\ \alpha_k \\ \beta_k \\ \gamma_k \end{Bmatrix} and \ \mathbf{u}_{bj} = \begin{Bmatrix} u_{bj} \\ v_{bj} \\ w_{bj} \\ \alpha_{bj} \\ \beta_{bj} \\ \gamma_{bj} \end{Bmatrix} \tag{3}$$

Transformation between the global and the local FE sub-segment coordinate system is done by help of matrix $\mathbf{R}_D$ and between the local FE sub-segment and the local cross section j's coordinate system by the transformation matrix $\mathbf{R}_{Fj}$, see Figure 1. By help of $\mathbf{Q}_k$, $\mathbf{R}_D$ and $\mathbf{R}_{Fj}$ it is possible to formulate the global transformation matrix for the node k as $\mathbf{T}_k = \mathbf{R}_{Fj}^T \mathbf{Q}_k \mathbf{R}_{Fj} \mathbf{R}_D$. By help of $\mathbf{T}_k$ for all the N_j nodes at cross section j it is possible to reformulate equation (2) to a system only dependent on beam nodal forces $\mathbf{p}_b$ and displacements $\mathbf{u}_b$, both given in the global coordinate system [1].

$$\mathbf{p}_b = \mathbf{T}^T \begin{bmatrix} \mathbf{S}_{cc} - \mathbf{S}_{ci} \mathbf{S}_{ii}^{-1} \mathbf{S}_{ic} \end{bmatrix} \mathbf{T} \mathbf{u}_b \quad where \ \mathbf{T}^T = \begin{bmatrix} \begin{bmatrix} \mathbf{T}_1^T, \cdots, \mathbf{T}_{N_1}^T \end{bmatrix} & \cdots & 0 \\ \vdots & \ddots & \vdots \\ 0 & \cdots & \begin{bmatrix} \mathbf{T}_1^T, \cdots, \mathbf{T}_{N_j}^T \end{bmatrix} \end{bmatrix} \tag{4}$$

Equation (4) can then easily be transformed into a form applicable for the BIE formulation.

$$\{0\} = \begin{bmatrix} -\mathbf{I} & , & \begin{bmatrix} \mathbf{T}^T \begin{bmatrix} \mathbf{S}_{cc} - \mathbf{S}_{ci} \mathbf{S}_{ii}^{-1} \mathbf{S}_{ic} \end{bmatrix} \mathbf{T} \end{bmatrix} \end{bmatrix} \begin{Bmatrix} \mathbf{p}_b \\ \mathbf{u}_b \end{Bmatrix} \tag{5}$$
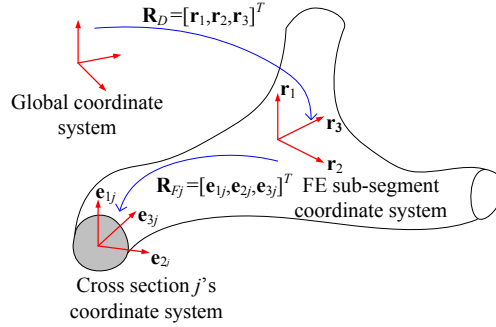
Figure 1: Sketch of FE sub-segment and its coordinate systems and transformation matrices. Vectors $\mathbf{r}_1$, $\mathbf{r}_2$ and $\mathbf{r}_3$ are given in the global coordinate system and $\mathbf{e}_{1j}$, $\mathbf{e}_{2j}$ and $\mathbf{e}_{3j}$ in the segment coordinate system.

Results and discussion

To verify the codes, free vibrations of the compound substructure shown in Figure 2 left, are considered. The methodology is checked by comparing eigenfrequencies, obtained by the described method and by means of complete FE modelling in Ansys11 using its shell93 elements. As the next step in verification, Floquet theory is employed to find frequency stopbands in an infinite structure consisted of the same sub-structures. Structural energy flux through a chain of five repeated substructures is mapped and compared with these Floquet theory predictions
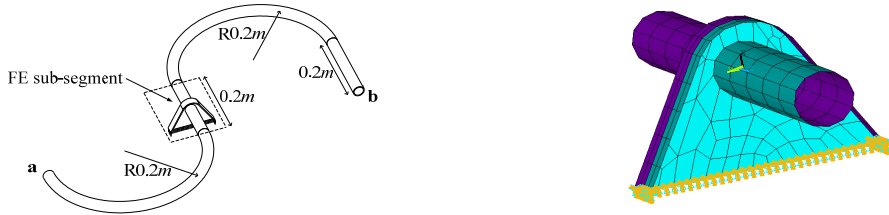
Figure 2: At left; sketch of the used sub-structure. At right; shell mesh of the used FE sub-segment. All outer pipe diameters is 28mm, wall thickness for all the structures is 2mm. Material data; E=219GPa, $v = 0.3$ and $\rho = 7800$ kg/m^3.

As seen from Table 1, the obtained eigenfrequencies are in good agreement.

ANSYS	24.2	28.4	45.6	54.2	74.5	89.5	145.7	158.2	289.8	296.5	400.0	521.0	593.6	800.1	828.6
BIE	25.0	29.2	44.1	54.9	73.4	90.4	145.4	160.2	293.3	297.2	408.9	523.4	601.3	807.8	837.9

Table 1: the 15 first eigenfrequencies in Hz obtained, by help of ANSYS11 and its shell93 elements and by help of the described combined method, of the structure illustrated on Figure 2

Accordingly to the Floquet theory [2] periodicity conditions, $\lambda\mathbf{a} = \mathbf{b}$ are employed, where $\mathbf{a}$ and $\mathbf{b}$ are vectors containing boundary state variables on each side of the substructure and $\lambda = \exp(iK_B)$. Free wave propagation is therefore impossible and filtering effects is achieved then all the solutions for λ fulfil the condition that $|\lambda| \neq 1$. The obtained results are given on Figure 3 left.
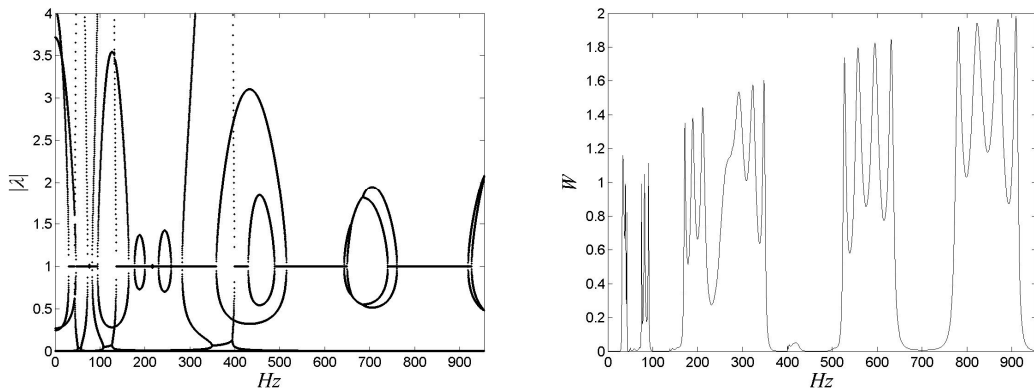
Figure 3: At left; |λ| for infinitely many reiterations of the substructure illustrated at Figure 2, mapped for frequencies between 1 and 955*Hz*. At right; total energy flux through the five repeated substructures on Figure 2 at excitations frequencies from 1 to 955*Hz*

Energy flux through a cross section to the right from the chain of five repeated substructures, connected at both ends of the chain to a semi-infinite long straight pipe segment, excited at left by transversal and axial harmonic forces of 10*N* and a torque of 1*Nm* are mapped at Figure 3 right. As is seen, minima in energy flux at Figure 3 right match the predicted stopbands at Figure 3 left.

Concluding remarks

A methodology for time harmonic analysis of compound straight and curved pipe segments modeled with BIE combined with FE modeling of sub-segments is described. This methodology is validated, firstly by comparison of eigenfrequencies of an individual substructure with results of its FE analysis, and secondly by mapping of the frequency dependence of the energy flux through a structure containing five repeated substructures to stopband predictions from standard Floquet stopband analysis of an infinite chain of the same substructure.

Acknowledgment

References

[1] S. Gopalakrishnan, J.F. Doyle. Spectral super-elements for wave propagation in structures with local non-uniformities. *Comput. Methods Appl. Mech. Engrg.,* 121, 77−90, (1995).

[2] S.Y. Lee, H.Y. Ke, M.J. Kao. Flexural Waves in a periodic Beam. *Journal of Applied Mechanics,* 57, 779-783, (1990).

[3] S.V. Sorokin, N. Olhoff, O.A. Ershova. Analysis of energy transmission in spatial piping systems with heavy internal fluid loading. *Journal of sound and Vibration,* 310, 1141-1166, (2008).

[4] A. Søe-Knudsen, Modeling of spatial fluid filled pipe system containing both straight and curved segments using boundary integral equations. M. Papadrakis, N.D. Lagaros, M. Fragiadakis eds. *2nd International Conference on Computational Methods in Structural Dynamics and Earthquake Engineering (COMPDYN 2009),* Rhodes Island, Greek, (June 22-24, 2009).

Optimization of elastic cylindrical shells

J. Lellep

Institute of Mathematics
Tartu University, Tartu, Estonia
e−mail: jaan.lellep@ut.ee

P. Nestler and W. Schmidt

Institute of Mathematics and Computer Science
Ernst-Moritz-Arndt University of Greifswald, Greifswald, Germany
e−mail: nestler.peter@googlemail.com; wschmidt@uni-greifswald.de

Summary Axisymmetric deflections and vibrations of circular cylindrical shells are considered. The problem of optimal design of elastic shells is formulated as an optimal control problem. A discrete approximation method resorting to the Bellman's principle is developed.

Introduction

Optimization of structures has obviously great theoretical and practical importance. Many valuable results have been obtained for shells subjected to various loadings. However, the most of studies are concerned with quasistatic loading or vibration due to initial excitation. In the present paper a discrete approximation method is suggested for optimization of cylindrical shells with stepped cross sections. The shell is subjected to external loading which intensity varies in time.

Formulation of the problem and basic equations

Consider axisymmetric deformations of circular cylindrical shells of length 2ℓ. Let the radius of the middle surface of the tube be denoted by R. Assume that the thickness h of the shell is piece wise constant. Let $h = h_j$ for $x \in (a_j, a_{j+1})$ where $j = 0,\ldots,n$ and h_j stand for fixed constants in the case of the direct problem. However, in the case of an optimization problem h_j and a_j are design parameters.

We shall confine our attention to small deformations and small displacements of the circular cylindrical shell. In this case the equilibrium equations of a shell element are for $x \in (a_j, a_{j+1})$ (see Soedel, 2004)

$$\frac{\partial N_x}{\partial x} = \rho\, h_j \frac{\partial^2 u}{\partial t^2}$$

$$\frac{\partial^2 M_x}{\partial x^2} - \frac{N_\theta}{R} + p - \rho\, h_j \frac{\partial^2 w}{\partial t^2} = 0 \tag{1}$$

In (1) N_x and N_θ stand for membrane forces in the axial and circumferential directions, respectively, and M_x is the axial bending moment whereas ρ is the material density. The quantities u and w are displacements of the middle surface in the axial and transversal directions, respectively, and $p = p(x,t)$ stands for the intensity of the distributed transverse loading, t being time.

Strain components corresponding to assumptions of the present study are (see Soedel, 2004; Ventsel and Krauthammer, 2001)

$$\varepsilon_x = \frac{\partial u}{\partial x}, \quad \varepsilon_\theta = \frac{w}{R}, \quad \kappa_x = -\frac{\partial^2 w}{\partial x^2} \tag{2}$$

The material of shells is pure elastic obeying Hooke's law. Generalized Hooke's law can be presented as (Reddy, 2007)

$$\left\{ \begin{matrix} N_x \\ N_\theta \\ M_x \end{matrix} \right\} = \frac{Eh}{1-v^2} \begin{bmatrix} 1 & v & 0 \\ v & 1 & 0 \\ 0 & 0 & \frac{h^2}{12} \end{bmatrix} \cdot \left\{ \begin{matrix} \varepsilon_x \\ \varepsilon_\theta \\ \kappa_x \end{matrix} \right\} \tag{3}$$

Here E and v stand for Young's and Poisson's modulus, respectively and $h = h_j$ for $x \in (a_j, a_{j+1})$. It easily follows from (2) and (3) that

$$N_x = \frac{Eh_j}{1-v^2}\left(u' + v\frac{w}{R} \right), \quad N_\theta = \frac{Eh_j}{1-v^2}\left(vu' + \frac{w}{R} \right), \quad \kappa_x = -\frac{Eh_j^3}{12\left(1-v^2\right)} \tag{4}$$

where prims denote the differentiation with respect to x. In the practically important case when $N_x = 0$ one has

$$u' = -\frac{v}{R}w \tag{5}$$

According to (1), (4), (5) one obtains for $x \in (a_j, a_{j+1})$

$$\frac{\partial^4 w}{\partial x^4} + \frac{12\left(1-v^2\right)}{R^2 h_j^2}w = -\frac{12\rho\left(1-v^2\right)}{Eh_j^2}\frac{\partial^2 w}{\partial t^2} + \frac{12\left(1-v^2\right)}{Eh_j^3}p \tag{6}$$

Eigenfrequencies of vibrating shells

Consider now the case of dynamic behaviour of shells whereas $p = 0$. Now we are looking for the solution of (6) for $x \in (a_j, a_{j+1})$ in the form

$$w(x,t) = X_j(x)\,T(t) \tag{7}$$

where $X_j(x)$ and $T(t)$ are unknown functions. Substituting (7) in (6) yields for $x \in (a_j, a_{j+1})$

$$X_j^{IV}(x)\,T(t) + \frac{12\left(1-v^2\right)}{R^2 h_j^2}X_j(x)\,T(t) = -\rho\frac{12\left(1-v^2\right)}{Eh_j^2}X_j(x)\,T(t) \tag{8}$$

Separating variables in (8) one obtains equations

$$\ddot{T}(t) + \omega^2 T(t) = 0 \tag{9}$$

and

$$X_j^{IV}(x) - r_j^4 X_j(x) = 0 \tag{10}$$

where

$$r_j^4 = \frac{12(1-v^2)}{h_j^2}\left(\frac{\omega^2}{E} - \frac{1}{R^2}\right) \tag{11}$$

for $x \in (a_j, a_{j+1})$; $j = 0,\ldots,n$. In (11) ω stands for the frequency of free vibrations. Evidently, the solution of (9) satisfying initial conditions $T(0) = 0, \dot{T}(0) = T_0\,\omega$ is

$$T = T_0\,sin\,\omega t \tag{12}$$

The general solution of (9) can be presented as

$$X_j(x) = A_j\,sin\,r_j x + B_j\,cos\,r_j x + C_j shr_j x + D_j chr_j x \tag{13}$$

for $x \in (a_j, a_{j+1})$.

Discrete approximation of the problem of optimization

Let us study an optimization problem which consist in the minimization of the cost function (t_0 is a fixed time instant)

$$J = \int_0^\ell w(x,t_0)dx \tag{14}$$

so that at each x and t governing equations (1) and (6) are satisfied and the material volume of the shell

$$V = \sum_{j=0}^n V_j \tag{15}$$

is fixed. Here V_j stands for the material volume of the segment of the tube of constant thickness h_j. If the radius of the internal surface of the tube is R, then $V_j = \pi h_j(h_j + 2R)$. Thicknesses h_j are assumed to be bounded, e.g.

$$h_{0j} \le h_j \le h_{1j} \tag{16}$$

where h_{0j} and h_{1j} are the lower and upper bounds, respectively.

Let us introduce the grid points x_j^i at each section of the shell so that $x_j^i \in \left[a_j, a_{j+1}\right]$ for each $i = 1,\ldots,q_j$ where $q_j \in N$ for $j = 0,\ldots,n$ and let us define the differential operators

$$A_j^m(w) = \frac{\partial^m w}{\partial x^m} \tag{17}$$

for $x \in (a_j, a_{j+1})$; $j = 0,\ldots,n$. It is reasonable to use an equidistant grid where

$$x_j^{i+1} = x_j^i + \Delta_j \tag{18}$$

and $\Delta_j = (a_{j+1} - a_j)/q_j$.

Evidently, $x_{j+1}^0 = x_j^{q_j}$, $x_0^0 = 0$, $x_n^{q_n} = \ell$.

Making use of (17), (18) one can present (6) as

$$\ddot{w}\left(x_j^i,t\right)=-\frac{1}{\mu_j}\left(d_j\,A_j^4 w\left(x_j^i,t\right)+b_j w\left(x_j^i,t\right)+p\left(x_j^i,t\right)\right)\qquad(19)$$

where $i=0,\dots,q_j;\;\;j=0,\dots,n$ and

$$\mu_j=\rho\,h_j,\quad b_j=E\frac{h_j}{R},\quad d_j=\frac{Eh_j^3}{12\left(1-\nu^2\right)}$$

The problem (14) - (19) is solved with the aid of Bellman's optimality principle. Computational methods appropriate to Bellman's principle and Bellman's equation are presented by several authors. Here we are following the papers by Azmyakov, Lellep and Schmidt (2008) and Nestler (2008).

Numerical results

The posed problem was solved by different methods. Nestler and Schmidt solved the control problem by direct methods. Therefore they approximate the original problem by a discrete one. The PDEs concerning to admissible controls are solved by means of FEM-methods. A gradient algorithm is applied to calculate the optimal solution of the discrete problem. The numerical solutions are checked to fulfill the first order optimality conditions derived for the PDE-problem. Results of calculations are presented in Fig. 1, 2.
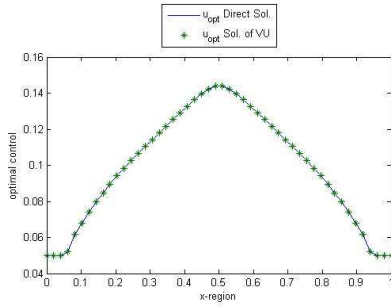
Figure 1: Optimal thickness for $p = x/\ell(1\text{-}x/\ell)$
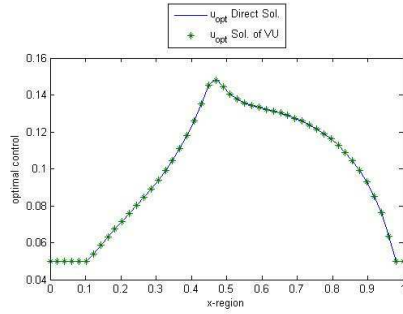
Figure 2: Optimal thickness for $p = sin(x/\ell)$

Acknowledgements

References

[1] V. Azmyakov, J. Lellep and W. Schmidt. *A computational approach to the optimal design of elastic shells*. (in preparation).

[2] P. Nestler. *Calculation of deformations of a cylindrical shell*. Greifswald, (2008).

[3] J.N. Reddy. *Theory and Analysis of Elastic Plates and Shells*. CRC Press, Boca Raton, (2007).

[4] W. Soedel. *Vibrations of Plates and Shells*. Marcel Dekker, New York, (2004).

[5] E. Ventsel and T. Krauthammer. *Thin Plates and Shells. Theory, Analysis and Applications*. Marcel Dekker, New York, (2001).

Lower Bound Limit State Analysis using the Interior-Point Method with Spatial Varying Barrier Function

Christian Frier* and Lars Damkilde

Department of Civil Engineering
Aalborg University, Aalborg, Denmark
e–mail: cf@civil.aau.dk

Summary A method of conducting lower bound Limit State analysis is to apply the interior-point method. The aim of the paper is to refine the method by reducing the number of optimization variables considerably by eliminating the equilibrium equations a priori. Another new idea is to adapt a spatially varying barrier function. Significant gains are made regarding computational speed and robustness of the algorithm.

Introduction

Limit State analysis has been used in design for decades e.g. the yield line theory for concrete slabs, [1]. The Limit State analysis is very well suited for manual methods especially the upper-bound methods and is therefore used in practical engineering design calculation. Analysis of elastic structures was around 1960 revolutionized by the introduction of computers and the Finite Element concept. Soon after the first attempts to solve Limit State problems by computers were implemented, see [2]. However, the methods did not penetrate into practice in the same impressive way as the linear Finite Element analysis did. The field of Computerized Limit State analysis did grow and extended the applications from frame and slabs also to include geotechnical problems, see e.g. [3] and reinforced plates, see e.g. [4]. In the last decade the main developments have been in the optimization procedure, where the interior point method in various formulations has increased the performance considerably, see e.g. [5].

The lower-bound formulation results in a non-linear convex optimization problem. The variables consist of the stress state in the elements and a load parameter. The object function will in this context be the load carrying capacity. The restrictions are linear equilibrium equations and non-linear convex yield criteria. The most effective solution methods are based on variants of Karmarkar's interior point method. In order to have a more efficient implementation two remedies can be used. The first is to eliminate the equality constrains a priori. This gives a considerably reduction in the number of variables. The method has in previous studies shown its capability, see [6]. The second is to deal with the non-linear yield criteria directly and in this respect avoiding the large number of linear inequalities, see e.g. [7]. Recently, both aspect as been implemented with success in [8]. In the present work the method is improved in terms of computational efficiency and improvements on the optimization algorithm. In the interior-point method a barrier function is used to ensure that the optimization variables stays feasible during the iterative solution process. It is suggested to use a spatial varying barrier function for which the barrier is different for each stress point. More details and further improvements on the optimization algorithm is to appear in [9]. In the paper the method is illustrated by a single example used by other researchers. However, the method is fully general and can be used for all types of limit state problems. The method is illustrated on a plane strain problem, but it is fully general.

Computational aspects

A lower bound solution is a stress state where equilibrium is satisfied and the yield criteria are not violated. The problem is discretized by the traditional Finite Element concept with stress-based

elements, and in this context only plane strain problems are considered. A triangular element with 9 stress parameters first formulated by Sloan is used, see [3], with the formulation from [10] adapted. The lower bound optimization problem can be formulated as:

$$
\begin{aligned}
\text{maximize} \quad & \alpha \\
\text{subject to} \quad & \mathbf{H}\boldsymbol{\beta}_{\mathbf{s}} = \alpha \mathbf{R} + \mathbf{R_0} \\
& f_j(\boldsymbol{\beta}_j) \leq 0, \quad j = 1, 2, \ldots, p
\end{aligned}
\tag{1}
$$

where $\mathbf{H}$ is the global flexibility matrix, $\boldsymbol{\beta}_s$ are stress parameters for the whole system, $\mathbf{R}$ are global nodal forces scalable by the load parameter, α, and $\mathbf{R_0}$ are constant global nodal forces independent of the load parameter. f_j are non-linear yield criteria evaluated in the jth stress point with stress parameters, $\boldsymbol{\beta}_j$, of p in total.

In order to reduce the problem size and improve the numerical stability the equilibrium equations can be eliminated a priori. The elimination is a standard Gauss elimination which reduces the number of independent stress parameters from $\boldsymbol{\beta}_s$ to $\boldsymbol{\beta}_f$, the so-called free stress parameters. The relation between the stress variables can be written:

$$
\boldsymbol{\beta}_s = \mathbf{B}\boldsymbol{\beta} + \mathbf{c}
\tag{2}
$$

where $\mathbf{B}$ is a matrix and $\mathbf{c}$ is a vector of constant elements relating the free stress variables, $\boldsymbol{\beta} = \begin{bmatrix} \boldsymbol{\beta}_f & \alpha \end{bmatrix}^T$, to the entire set of stress variables, $\boldsymbol{\beta}_s$, which are obtained during the Gauss elimination process. Note that the load multiplier for the sake of convenience has been included in the set of stress variables.

The optimization problem, can be solved by the interior-point method. A barrier function, μ_j, is added to the objective function in (1), see e.g. [11]. Furthermore, non-negative Slack variables, $\mathbf{s}$, are added to transform the non-linear inequality constrains into equality constrains. The Lagrangian of the augmented optimization problem can then be formulated:

$$
\mathcal{L}(\boldsymbol{\beta}, \mathbf{s}, \boldsymbol{\lambda}) = \mathbf{b}^T \boldsymbol{\beta} + \sum_{j=1}^{p} \mu_j \log \mathbf{s}_j - \boldsymbol{\lambda}^T (\mathbf{f}(\boldsymbol{\beta}) + \mathbf{s})
\tag{3}
$$

where $\mathbf{b} = \begin{bmatrix} \mathbf{0} & 1 \end{bmatrix}^T$ and $\mathbf{f}$ is the vector of the yield criteria, evaluated in all material points, $\mathbf{0}$ is a vector of zeros and $\boldsymbol{\lambda}$ is a vector of non-negative Lagrange multipliers.

The idea behind the barrier function is to prevent the gradient search process to end too close to the boundary. A new idea in the present work is to use a barrier function which differs between the stress points, thus hopefully increasing the convergence rate of the algorithm. The barrier functions are chosen as either of the following:

$$
\mu_j = c\delta^k \quad , \quad \mu_j = c \left[\max(s_j - s_{max}, 0.1)\delta \right]^k
\tag{4}
$$

where c is a scaling factor, δ is a constant controlling the speed by which the barrier is reduced, and k is the iteration number. The constant c is chosen such that the initial barrier parameter is just below one, in this work $c = 0.95$ and $\delta = 0.7$ is chosen. s_{max} is the largest slack variable.

The Kuhn-Tucker conditions states that the gradient of the Lagrangian must vanish at the optimum. By differentiation of (3), a non-linear equation system is to be solved for variables $\boldsymbol{\beta}$, $\mathbf{s}$ and $\boldsymbol{\lambda}$. This can be done by Newton's method, where increments on the variables are found iteratively. During the iterations, the barrier function, (4), is reduced and the iterations are started from an initial feasible point, i.e. $\boldsymbol{\beta} = \mathbf{0}$, $\mathbf{s} = \mathbf{e}$ and $\boldsymbol{\lambda} = \mathbf{e}$. Here, $\mathbf{e}$ is a vector of ones. Line search is conducted in order for the increments to be feasible, i.e. non-negative values of $\mathbf{s}$ and $\boldsymbol{\lambda}$ and the stress state, $\boldsymbol{\beta}$, must be within the yield criteria. After calculating the increments, they are multiplied by a factor below one, in this work 0.8 is used. The iterations are stopped when the duality gab between the slack variables, $\mathbf{s}$, and the lagrange multipliers, $\boldsymbol{\lambda}$, becomes sufficiently small.

Numerical example

As a test example the slotted block in plane strain, shown in Figure 1 is considered.
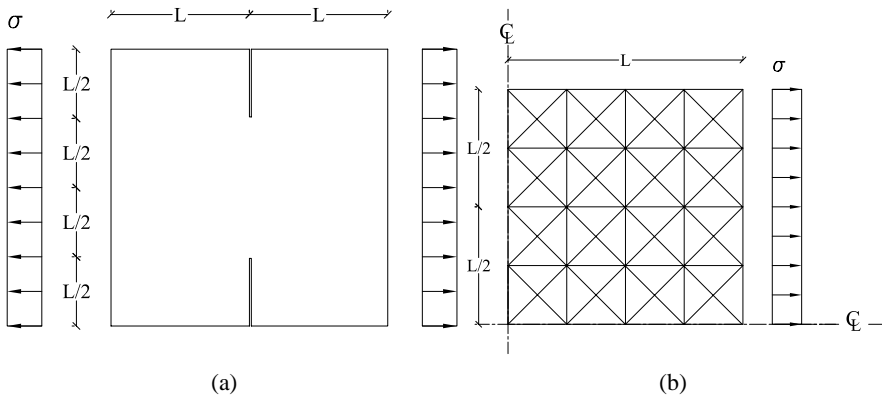
Figure 1: Slotted block problem (a) and element discretization, $N = 4$ (b).

The example has been treated by Andersen and Christiansen [12] and by Krabbenhoft and Damk-ilde [7]. The square block has two notches as shown in Figure 1.(a). The material is governed by the von Mises yield criterion in plane strain, with a yield stress $f_0 = \sqrt{3}$. In Figure 2 is shown the result of the optimization process in terms of the convergence of the load multiplier α as a function of the iteration number. Results are shown for both $N = 4$, as shown in Figure 1.(b), and for $N = 12$. The optimization process has been conducted with both the conventional constant barrier function and the new spatial varying barrier function in (4). It can be observed, that the load multiplier converges in all cases towards a value that does not differ much, suggesting that the $N = 12$ discretization is adequate in the present case. However this might not be a general conclusion for other structures. An interesting conclusion is, that the convergence is faster when using the spatial varying barrier function, suggesting that it is favorable.

Concluding remarks

In this paper the interior-point method is used to conduct Limit State analysis with the lower bound method for structural problems in plane strain. Focus is on improvements on the optimization algorithm in two different aspects. First, the equality constrains are eliminated prior to the optimization, reducing the number of optimization variables and constrains. Secondly, a spatially varying barrier function is suggested in order to speed up the convergence of the algorithm. Both suggestions improve the convergence of the optimization algorithm.
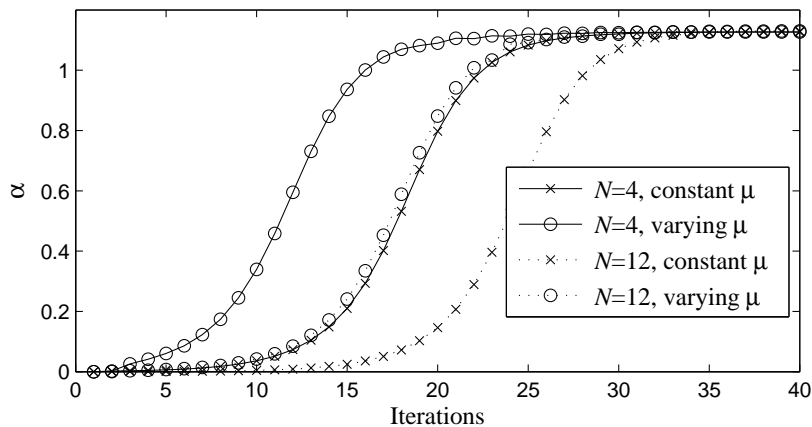
Figure 2: Convergence of load multiplier, computed for $N = 4$ and $N = 12$ as shown in Figure 1.b. Both a constant and a spatial varying barrier function is considered.

References

[1] K. W. Johansen. *Yield-line formulae for slabs*. Cement and Concrete Association, London, England, 1972.

[2] E. Anderheggen and H. Knöpfel. Finite element limit analysis using linear programming. *International Journal of Solids and Structures*, 8:1413–1431, 1972.

[3] S. W. Sloan. Lower bound limit analysis using finite elements and linear programming. *International Journal for Numerical and Analytical Methods in Geomechanics*, 12:61–77, 1988.

[4] A. F. Ashour and C. T. Morley. The numerical determination of shear failure mechanisms in reinforced-concrete beams. *The Structural Engineer*, 72(23, 24):395–400, 1994.

[5] S. Mehrotra. On the implementation of a primal-dual interior point method. *SIAM Journal on Optimization*, 2:575–601, 1992.

[6] L. Damkilde and O. Høyer. An efficient implementation of limit state calculations based on lower-bound solutions. *Computers & Structures*, 49(6):953–962, 1993.

[7] K. Krabbenhoft and L. Damkilde. A general non-linear optimization algorithm for lower bound limit analysis. *International Journal for Numerical Methods in Engineering*, 56:165–184, 2003.

[8] L. Damkilde and L. Juhl Schmidt. An efficient implementation of non-linear limit state analysis based on lower-bound solutions. In B. H. V. Topping, editor, *Proceedings of the Tenth International Conference on Civil, Structural and Environmental Engineering Computing*, Stirlingshire, UK, 2005. Civil-Comp Press.

[9] C Frier and L. Damkilde. An improved lower bound limit state method, using the interior point method. *To appear in: Communications in Numerical methods in Engineering*.

[10] P. N. Poulsen and L. Damkilde. Limit analysis of reinforced concrete plates subjected to in-plane forces. *International Journal of Solids and Structures*, 37:6011–6029, 2000.

[11] S. G. Nash and A. Sofer. *Linear and nonlinear programming*. McGraw-Hill, New York, N.Y., 1996.

[12] E. Christiansen and K. D. Andersen. Computation of collapse loads with von Mises type yield condition. *International Journal for Numerical Methods in Engineering*, 45:1185–1202, 1999.

Conceptual design of the reinforcement for concrete structures using topology optimization

Michael Bogomolny
Technical University of Denmark (DTU), Lyngby, Denmark
e-mail: m.bogomolny@mat.dtu.dk

Summary The main idea of the paper is to introduce advanced numerical methods for conceptual design of reinforcement for reinforced concrete structures. These methods will be based on optimization techniques providing an optimal placement of the reinforcement inside an arbitrary concrete domain.

Introduction

Typical concrete mixes have high resistance to compressive stresses. However, due to its quasi-brittle nature, any appreciable tension (e.g. due to bending) will cause fractures in the cementitous binding material resulting in cracking and separation of the concrete. Therefore concrete is typically reinforced by steel bars that have high strength in tension. Usually the reinforcing steel bars are located in the regions where tension is expected; therefore reinforced concrete (RC) can be considered a composite material.

Modeling of concrete is based on the fact that the compression and tension failure criteria are different. Therefore the failure criteria usually include combinations of different yield surfaces. The criteria are usually based on the Mohr-Coulomb criterion or the Drucker-Prager criterion in the compression region and the Rankine criterion in the tension region [4, 7]. Figure 1 [7] shows the combined yield surface between the Drucker-Prager criterion in the compression region, and the Rankine criterion in the tension region.
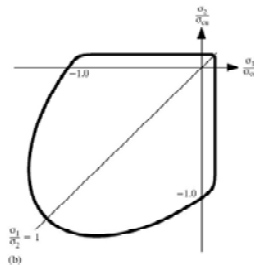
Figure 1. Combined yield surface

The classical *Topology Optimization* problem finds the optimal distribution of the isotropic material that gives the stiffest structure for a given set of boundary conditions and a given set of loads. Using certain interpolation schemes [3] the optimal distribution of 2 different materials can also be found. This procedure has been implemented for linear elastic isotropic materials. The typical result of this scheme is a composite "sandwich" structure with soft core and stiff facesheets (see Figure 2). Black color means stiffer material, white color – softer material. However, the "sandwich" structure does not fit the Reinforced Concrete elements requirements.
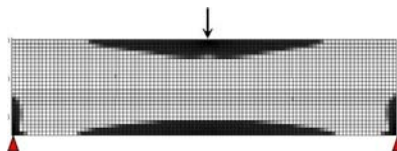
Figure 2. Topology optimization – 2 different isotropic materials (not published)

Layout of abstract

Material Interpolation

In the proposed paper, an interpolation scheme between two nonlinear materials (concrete and steel) with different properties and failure criteria is introduced. Concrete is introduced as an elasto-plastic material when the yield condition is based on the Drucker-Prager criteria (different in compression and tension region) described by

$$\alpha I_1 + \sqrt{J_2} \leq K_c \tag{1}$$

And steel is introduced as an elasto-plastic material when the yield condition is based on the von Misses criteria described by

$$\sqrt{J_2} \leq \sigma_{ys} / \sqrt{3} \tag{2}$$

When I_1 is a first stress invariant and J_2 is a second deviator invariant. σ_{ys} - is a yield stress of steel and K_c – is a function of yield compression stress of concrete.

Graphical introduction of von Misses criteria and Drucker-Prager criteria in principal stress space.
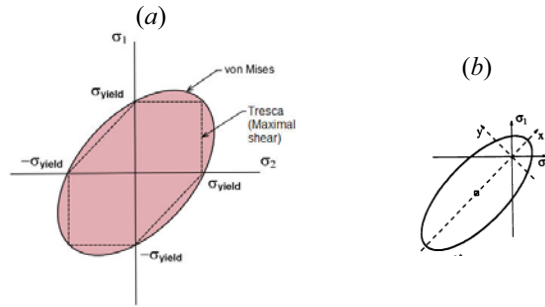
Figure 3. (*a*) von Mises   (*b*) Drucker-Prager

The final result of the optimization problem will be the optimal distribution of a steel inside a concrete domain. Therefore, the design variables of the optimization problem, densities x changing from 0 to1, will indicate which material is used including its material properties and yield surface. The interpolation scheme between the materials is offered as follows:

The modulus of elasticity

$$E = E_s x^{P_1} + E_c \left(1 - x^{P_1}\right) \tag{3}$$

And the yield criteria

$$\left(1 - x^{P_2}\right)\alpha I_1 + \sqrt{J_2} \leq \left(1 - x^{P_2}\right)K_c + x^{P_2}\left(\sigma_{ys} / \sqrt{3}\right) \tag{4}$$

For example, if $x = 0$ – we have a concrete with the Drucker-Prager yield surface and if $x=1$ – steel with the von Misses yield surface. The intermediate densities introduce equivalent hybrid artificial material, that hopefully disappears at the end of the optimal design process, when 0-1 design (or close to this) is achieved.

For illustration, we introduce a simply supported 2D plane-stress beam under the self weight. Figure 4 shows effective plastic strain of the beam for 3 cases: $x=0$, $x=1.0$ and $x=0.5$.

(*a*)

(*b*)

(*c*)
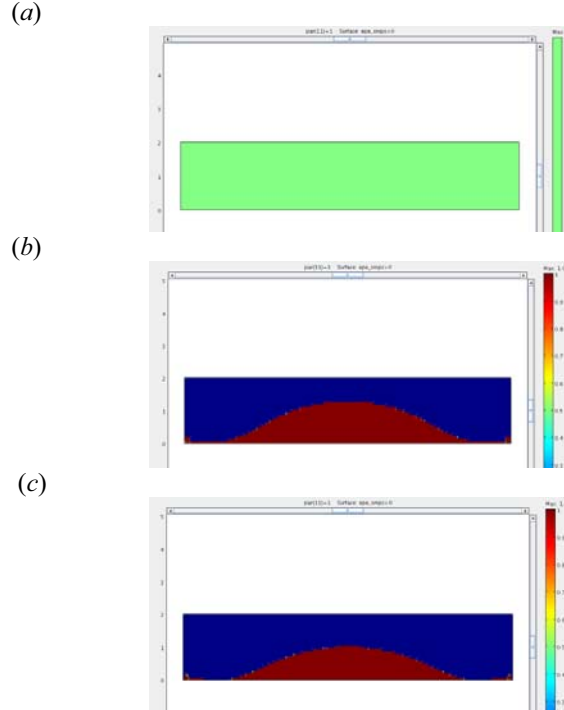
Figure 4. Effective plastic strain (a) x=1.0 – steel no plasticity, (b) x=0.0 and (c) x=0.5

Optimization

General definition of the optimization problem is:

$$\min \int_{\Omega} 0.5 \sigma_{ij} \varepsilon_{ij} \, \partial\Omega$$

$$s.t.$$

$$\sum_{e=1}^{N} x_e \leq V$$

$$0 < x_{e,\min} \leq x_e \leq 1 \qquad e=1,2,...,N$$

When the material behavior is according to eqs. (4) and (5). The system of nonlinear static equations is solved using an iterative Newton-Raphson method.

Example 1

Given a simply supported beam and loaded by an equally distributed loading. The final design is introduced in Figure 5, when the volume fraction *V*= 0.2. Steel, described by a black colour, is located where tension stresses are expected.
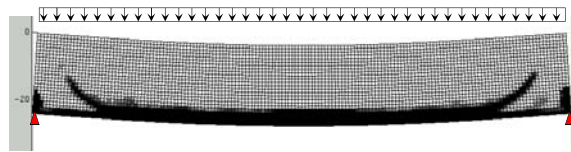
Figure 5. Simply supported beam.

Example 2

Given a beam supported by 3 restrains (2 spans) and loaded by 2 concentrated loads at the middle of each span (see Figure 6). The final design is introduced in Figure 6, when the volume fraction $V= 0.2$. Steel, described by a black colour, is located where tension stresses are expected.
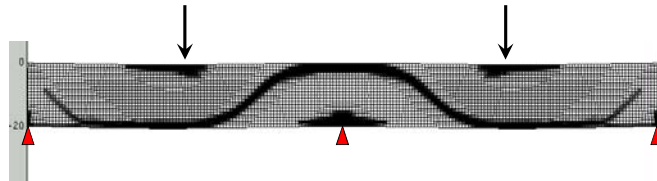
Figure 6. Simply supported beam.

References
1. Bendsøe M.P. and Sigmund O. (2002) – "Topology optimization. Theory, Methods and Applications", *Springer*.
2. Pravida J. and Wunderlich W. (2002) – "A plasticity based model and an adaptive algorithm for finite element analysis of reinforced concrete panels", *Int. J. Numer. Meth. Engng.*, **53**, pp. 2445-2462.

Nonlinear FE Model of the CFRP/ Concrete Interface in retrofitted beams

Yasmeen T Obaidat, Ola Dahlblom and Susanne Heyden

Division of Structural Mechanics, Lund University, Lund, Sweden

e-mail: Yasmeen.Obaidat@byggmek.lth.se, Ola.Dahlblom@byggmek.lth.se,
Susanne.Heyden@byggmek.lth.se

Summary: This paper presents a finite element analysis which is validated against laboratory tests of eight beams strengthened with externally bonded carbon fibre reinforced plastic (CFRP) plates. The commercial numerical analysis tool Abaqus was used. Cohesive elements were used to model traction and shear behaviour of the concrete/CFRP interface. The results are presented and discussed in terms of loading capacity. The results obtained from the finite element analysis show good agreement with the experimental results.

1 Introduction

The use of CFRP to repair and rehabilitate damaged steel and concrete structures has become increasingly attractive due to the well-known good mechanical properties of this material.

Researchers have, however, observed new types of failures that can reduce the performance of CFRP when used in retrofitting structures [3]. These failures are often brittle, and include debonding of concrete layers, delamination of CFRP and shear collapse. Brittle debonding has particularly been observed at laminate ends, due to high concentration of shear stresses at discontinuities, where shear cracks in the concrete are likely to develop. Thus, it is necessary to study and understand the behaviour of CFRP strengthened reinforced concrete members, including those failures.

While experimental methods of investigation are extremely useful in obtaining information about the composite behaviour of CFRP and reinforced concrete, the use of numerical models helps in developing a good understanding of the behaviour at lower costs. In most previous FE studies the interaction between of the Concrete/CFRP interface was neglected by either assuming perfect bond or using simple solid element for the interface [2, 5, and 7]. This can affect the accuracy of the results obtained from the FE model.

The subject of this work is to model the behaviour of reinforced concrete beams retrofitted using CFRP by the FE model, using a cohesive model for the bond between CFRP and concrete, and compare this with a perfect bond model.

2 Experimental work

Eight beams studied by Obaidat [6] were used to validate the finite element model in this paper. The beams were identical in geometry and tested in four point bending, Fig. 1. Two beams were tested as control beams and the rest were tested until cracks started to propagate and then the beams were retrofitted with various CFRP strengthening designs, see Fig. 2, and retested until debonding occurred.
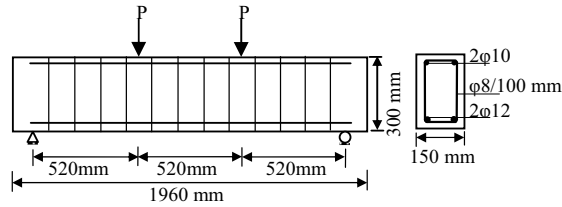
Figure 1: Geometry, arrangement of reinforcement and loading of the tested beams.

(a) RB1   (b) RB2   (c) RB3
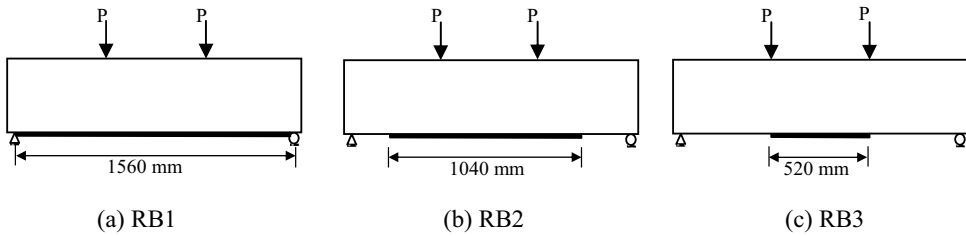
Figure 2: Length of CFRP laminates in test series RB1, RB2, and RB3.

3 Finite element analysis

The simply supported beam in four point bending experimentally studied by Obaidat [6], has been numerically analysed with nonlinear finite-element model by using Abaqus [4].

A plastic damage model was used to represent the concrete in compression and in tension. Two different models were used to represent the interface between concrete and CFRP. In the first model the interface was modelled as a perfect bond, as in previous work by Obaidat et al. [7], while in the second it was modelled using a cohesive zone model. The CFRP composite was assumed to be a linear elastic isotropic material and the constitutive relation of steel was an elastic-plastic model. In addition, perfect bond between steel and concrete was assumed. The material properties adopted for concrete and steel were obtained from the work by Obaidat [6], [1] and literature.

4-node linear tetrahedral elements were used for the reinforced concrete, reinforcement, steel plates at supports and under the load, and CFRP in this model. 8-node 3-D cohesive elements were used to model the interface layer. One quarter of the specimen was modelled, as shown in Fig. 3(a), by taking advantage of the double symmetry of the beam. The FE mesh is shown in Fig. 3(b).

(a)   (b)
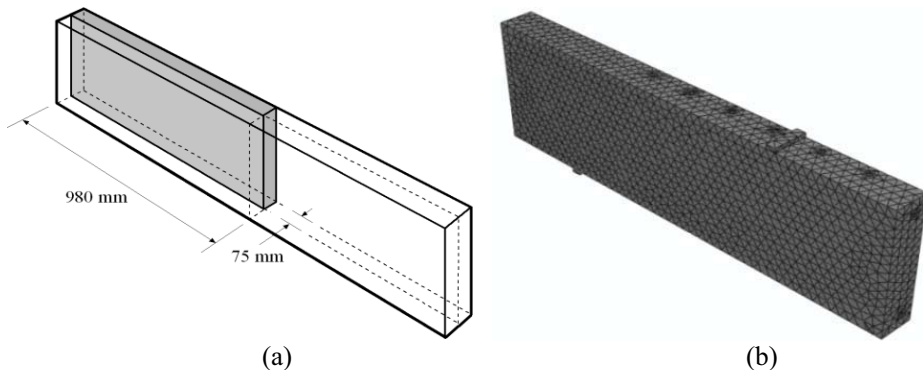
Figure 3: Geometry and elements used in the numerical analysis: (a) By use of symmetry, one quarter of the beam was modelled, (b) Finite element mesh of quarter of beam.

4 Results

Load-deflection curves obtained for control beam and retrofitted beams from experiments and FEM analysis are shown in Fig. 4. There is good agreement between FEM simulations and experimental results for the control beam, Fig. 4(a). The FEM analysis predicts the beam to be slightly stiffer and stronger, probably because of the assumed perfect bond between concrete and reinforcement.

When comparing Fig. 4 (b-d) it can be seen that the length of the CFRP significantly influences the behaviour of the beam. The longer CFRP, the higher is the maximum load.

For the retrofitted beams, the results from the two FEM models are also slightly stiffer than the experimental results and close to identical during the first part of the curve, Fig. 4 (b–d). After cracks start appearing, the perfect bond model increasingly overestimates the stiffness of the beam as in the previous work by Obaidat et al. [7]. This is due to the fact that the perfect bond does not take the shear strain between the concrete and CFRP into consideration.

The perfect bond models also fail to capture the softening of the beam, a fact that is most obvious for RB1. Debonding failure, which occurred in the experiments, is not possible with the perfect bond model. Thus, it is possible to increase the load further until another mode of failure occurs, in this case shear flexural crack failure or CFRP rupture. The cohesive bond model show good agreement with the experimental results.

(a) Control Beam   (b) RB1

(c) RB2   (d) RB3
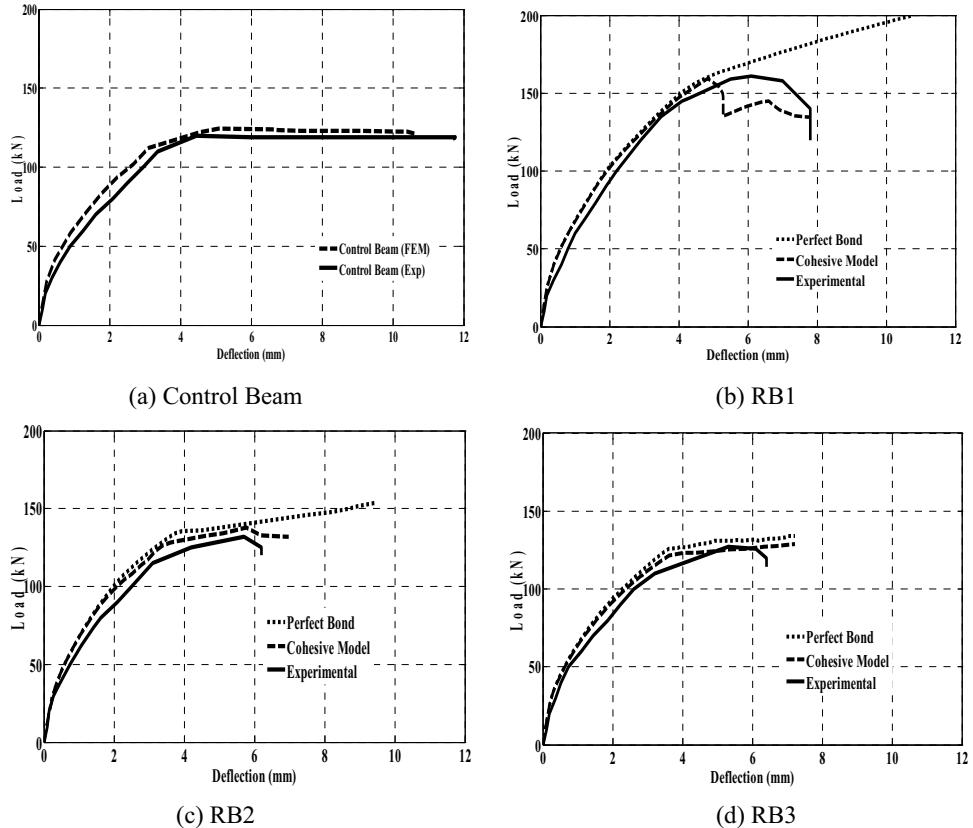
Figure 4: Load-deflection curves of beams, obtained by experiments and finite element model.

5 Conclusions

The finite element results show good agreement with the experimental results. A cohesive model was used to describe the interfacial behaviour between CFRP and concrete. The following conclusions can be drawn from this study:

- The behaviour of the retrofitted beams is significantly influenced by the length of CFRP. This is clear in experimental results as well as in numerical analysis. The ultimate load increases with the length of the CFRP.
- The perfect bond model failed to capture the softening of the beams.
- The cohesive model proved able to represent the bond behaviour between CFRP and concrete. The predicted ultimate loads and the debonding failure mode were in excellent correlation with the experimental work.

6 References

[1] ACI Comitte 318. Building Code Requirements for Structural Concrete and Commentary (ACI 318-99). American Concrete Institute Detroit, MI, 1999.

[2] Ebead, U. and Marzouk, H. Tension - stiffening model for FRP strengthend RC concrete two-way slab. Materials and Structures 2004; 193-200.

[3] Esfahani, M., Kianoush, M. and Tajari, A. Flexural behaviour of reinforced concrete beams strengthened by CFRP sheets. Engineering Structures 2007; 29: 2428-2444.

[4] Hibbitt, Karlsson, Sorensen and Inc. ABAQUS Theory manual, User manual Example Manual, Version 6.7. Providence, RI, 2000.

[5] Lundquist, J., Nordin, H., Täljsten, B. and Olafsson, T. Numerical analyis of concrete beams sterengthened with CFRP- A Study of anchorage lengths. In: FRP in Construction, Proceeding of The International Symposium of Bond Behaviour of FRP in Structures. 2005; 247-254.

[6] Obaidat,Y. Retrofitting of reinforced concrete beams using composite laminates, Master Thesis, Jordan University of Science and Technology. 2007.

[7] Obaidat,Y., Dahlblom, O. and Heyden, S. Retrofitting of reinforced concrete beams using composite laminates, 21 Nordic Seminar on Computational Mechanics NSCM-21. 2008.

Simulation of Nanoindentation Response of Viral Capsids

Aylin Ahadi

Department of Mechanical Engineering
Lund University, Lund, Sweden
e−mail: aylin.ahadi@mek.lth.se

Alex Evilevitch

Department of Physics
Carnegie Mellon University, Pittsburgh, USA
e−mail: alex.evilevitch@biochemistry.lu.se

Summary The nanoindentation response of empty viral capsids is modelled using three dimensional finite element analysis. Simulation with two different geometries, spherical and icosahedral, are performed using the finite element code Abaqus. The capsids are modeled as non-linear Hookean elastic and both small and large deformation analysis is performed. Force-indentation curves for three different viral capsids are directly compared to experimental data and the Young's modulus is determined by calibrating the force-indentation curve to data from atomic force microscopy (AFM) experiments. Predictions are made for two additional viral capsids. The results from the simulation showed a good agreement with AFM data, see [1].

Introduction

Viruses are the simplest biological structures. They have no metabolism and their only function is to reproduce them self by infecting cells. Viruses consist of DNA strings inside a shell called capsid. The viral capsid protects the DNA inside and it is built of protein chains in an ordered cyclic structures. Modelling the mechanical response of viral capsids has become a very active research area recently. Experimental results in combination with simulations have created the necessary conditions for better understanding the complex behaviour of biological systems such as viral capsids. Almost all capsids of spherical viruses have the symmetry of an icosahedron. Capsids of different sizes can be assembled from varying numbers of protein subunits. The complex structure of the capsid leads to mechanical properties which are not clearly understood and described in detail. Our knowledge of the mechanical behaviour of capsids is based almost entirely on experimental data gathered by nanoindentation probing performed using atomic force microscopy (AFM). AFM nanoindentation studies of empty viral capsids reveal unique mechanical properties for different classes of viruses which can, in turn, be directly correlated to the virion's life cycle. Besides from high resolution imaging of viral particles in liquid, as the nanometer size tip of the cantilever scans the specimen surface, it can apply force on single viral particle in order to obtain real-time force-distance curves. Probing with an AFM tip on phage capsids generally results in two outcomes: reversible deformations usually observed when force below a certain value is applied, and irreversible rupturing when the applied force is above that value. This enables us to obtain different parameters describing capsid mechanical properties. i) Information about the capsid's mechanical limits and strength of capsomer-capsomer bonds is provided by the threshold force beyond which the interactions between capsid proteins collapse, referred to as 'breaking force' and also by the maximum indentation distance before the capsid breaks. ii) due to the nearly linear response to deformation observed for some viruses, the spring constant can be obtained by linear fit to the force-distance curves. However, capsid response to deformation is not allways linear. iii) Using more general continuum model and finite element simulation, Young's modulus, E, can also be obtained. The spring constant and Young's modulus are measures of the capsid's elasticity, and while k is dependent on the material's geometry, E is

an intrinsic geometry-independent material property. However, as will be shown in this work, calibrating the Young's modulus value will depend strongly on the choice of the model used to describe the AFM data. The nanoindentation response of empty viral capsids is simulated using three dimensional finite element analysis. Simulation with two different geometries, spherical and icosahedral, are performed using the finite element code Abaqus. The capsids are modelled as non-linear Hookean elastic and both small and large deformation analysis is performed. The Young's modulus is determined by calibrating the force-indentation curve to data from AFM experiments. In particular, it is shown that capsids with dominantly spherical shape exhibit nearly linear relationship between force and indentation, which has been experimentally observed on the viral shell studies so far. However, we predict that capsids with significant faceting and thus more pronounced icosahedral shape will exhibit rather non-linear deformation behaviour.

Model description

The classical linear Hookean model for infinitesimal strain linear elasticity relates linearly the Cauchy stress T to the linearized strain tensor as $T = \lambda(\operatorname{tr}\varepsilon)\,I + 2\mu\,\varepsilon$, where λ and μ are the Lame constants and, $\varepsilon = (H + H^T)/2$, is linearized infinitesimal or small strain tensor. The nonlinear Hookean model is obtained from the same relation by replacing the infinitesimal strain with the logarithmic strain, $T = \lambda(\operatorname{tr}\varepsilon_{\ln})\,I + 2\mu\,\varepsilon_{\ln}$, where $\varepsilon_{\ln}$ is the logarithmic strain defined as $\varepsilon_{\ln} = \ln\sqrt{FF^T}$. H and F are the displacement and deformation gradient respectively.

Experimental results have shown that the deformation of the capsids is completely recoverable for small indentations below capsid failure, i.e. an elastic material model can be chosen to represent the capsids. The simplest continuum material model is the Hookean elastic model described by two material parameters. In the following we choose to use the Young's modulus, E, and the Poisson's ratio, ν. The Young's modulus, E is expressed in terms of λ and μ by $E = \mu(3\lambda + 2\mu)/2(\lambda + \mu)$.
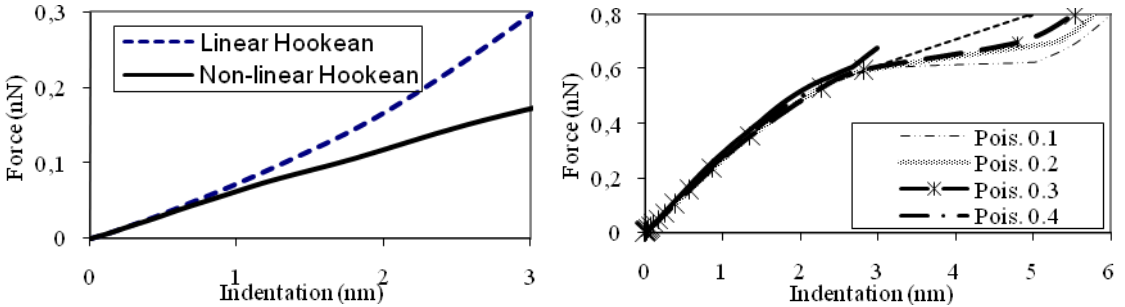
Figure 1: a) Force indentation curves for linear and non-linear models. b) Sensitivity to Poisson's ratio.

Fig.1 shows the results obtained by using linear and non-linear Hookean models of bacteriophage λ viral capsid deformation. As is seen, within a small range of deformation, up to 1 nm, it could be acceptable to use a linear Hookean model, but the experimental results from AFM indentation test on phage λ show that the capsid was deformed about 6 nm in height, before capsid rupture, which is more than 3 times larger than the thickness of the capsid (~1.8 nm). Even more complex elastic models could be used, but the response obtained is similar to that using the non-linear Hookean model and it is more significant to use large deformation formulation i.e., non-linear analyses, rather than the particular elastic material chosen. Therefore in this work the non-linear Hookean model is chosen since it is the simplest one, while providing sufficiently accurate results. A parametric study is performed in order to investigate how different values affect the shape of the

curve. The capsid is assumed to be slightly compressible and values of 0.3 or 0.4 are reasonable to use. In this study all the following simulations are performed with a Poisson ratio of 0.3. Two different geometries are investigated, namely, the sphere and the icosahedron. For the icosahedral models, two different positions of the capsid are considered, i.e., one pushing along a 5-fold symmetry axis and the other, pushing along a threefold symmetry axis (Fig. 2 b,c). The three geometrical models investigated here show different deformation characteristics. The spherical model is characterized by strong local deformation, (Fig. 2a). When a local deformation is present, the region bellow the tip is subjected to considerable deformation, whereas the rest of the capsid remains almost not deformed. The load transfer mechanics in this case is dominated by in plane stretching in the region bellow the tip and results in a nonlinear force-indentation curve. For the icosahedral model with pushing along a 3-fold symmetry axis, the deformation is initially local but transforms into a global. Initially the load transfer mechanics is dominated by in plane stretching and we have only local deformation, but eventually transverse bending becomes more significant resulting in a global deformation of the capsid. The last icosahedral model, loading along the 5-fold symmetry axis, has a somewhat different deformation behaviour compared to the two models above. This geometry exhibits almost no local initial deformation. The whole capsid is deformed already from the beginning and the load transfer mechanics is dominated by transverse bending. This is also clearly seen from the force-indentation curve (Fig. 3b), which starts with a linear regime representing the global deformation and a sudden increase in stiffness, where the local deformation starts to affect the curve. This sharp transition point from global to local deformation is not observed in the two cases described above.
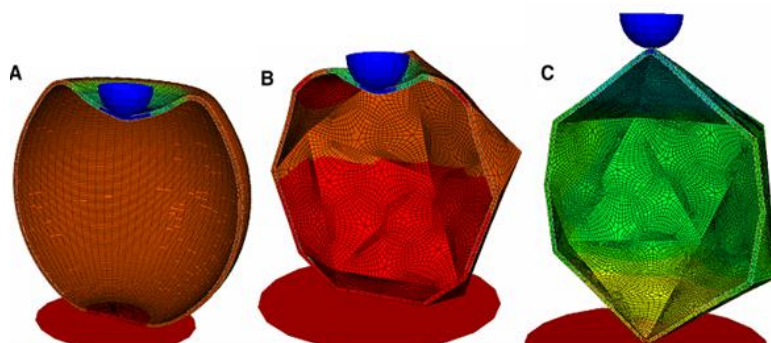
Figure 2: Three different models.

Results and discussion

The experimental AFM data from (2) are used to calibrate the models. Phage λ has an icosahedral capsid. The mature protein shell has a wall thickness of about 1.8 nm and an outer diameter of 63 nm. The breaking force for an empty capsid is about 0.8 nN for an indentation of ~6 nm. The typical curve presenting the experimental data from an AFM indentation test shows the deformation of the cantilever plus the deformation of the capsid (Fig.3). The deformation of the cantilever, however, is much larger in comparison to the indentation of the capsid. Since the cantilever deformation is linear while the capsid deformation is very small, and both indentation curves are superimposed in the standard data representation, the capsid deformation appears to be linear as well, while that is not necessarily the case. The results in Fig. 4 shows λ capsid deformation data only by subtracting cantilever deformation curve from the deformation curve for the capsid and cantilever combined. Fig. 4b shows the results from the spherical capsid model. Simulations with three different values of the Young's modulus are directly compared to the

experimental data, in an attempt to match the maximum indentation point before capsid failure. Results from the simulation of the indentation of the capsid as an icosahedron are presented in Fig. 4b.The simulation pushing along the fivefold symmetry axis is not very realistic since in the experiment, the viral capsid is attached to the tail that usually lies in a plane with the capsid on the glass surface (as explained above). The tail is attached to one vertex which implies that the capsid cannot be laying in that position on a surface. In the most stable position for the phage capsid, it is pushed by the cantilever tip along the 3-fold symmetry. The obtained value of the Young's modulus differs considerably between the models with these spherical versus icosahedral geometries. The two E values of 3 GPa for the sphere model and 0.65 GPa for the icosahedron can be considered as upper and lower limits.
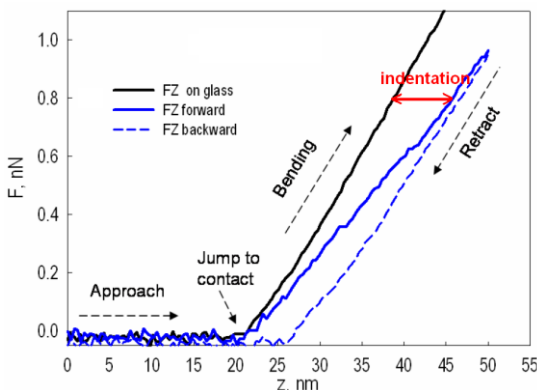
Figure 3: Typical results obtained from AFM.
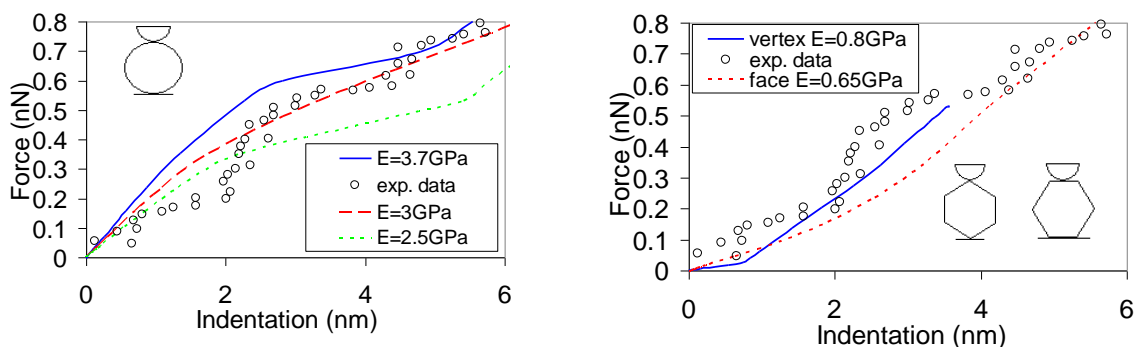
Figure 4: Nanoindentation response for λ phage. Simulations and experimental results.

References

[1] A. Ahadi, J. Colomo and A. Evilevitch, Three Dimensional Simulation of Nanoindentation Response of Viral Capsids. Shape and Size Effects. *The Journal of Physical Chemistry B,* **11**, 337 - 3378, (2009).

[2] I. Ivanovska, G. Wuite, B. Jönsson and A. Evilevitch, Internal DNA pressure modifies stability of WT phage. *Proceedings of the National Academy of Sciences of the United States of America,* **104**, 9603-9608, (2007).

Semi-Continuum Modeling of a Graphene Lattice Based on Tersoff-Brenner Atomistic Potential

K. Samadikhah[*] and R. Larsson

Department of Applied Mechanics. Division of Material and Computational Mechanics
Chalmers University of Technology, Gothenburg, Sweden
e–mail: ragnar.larsson@chalmers.se

Summary   The present contribution deals with the modeling of the graphene lattice. The importance of the graphene membrane modeling is to understand the lattice behavior. In this work, we use Tersoff-Brenner (TB) potential explanation for the atomic interactions. The resulting static lattice behavior of the graphene Representative Lattice Unit (RLU) is presented and compared with the first order CBN model for an RLU subjected to tension .In addition, anisotropic behavior of the lattice is discussed with respect to the lattice chirality.

Introduction

The graphene membranes have significant electrical and mechanical properties used for nanotechnology. Resonators, force/mass sensors and nanoswitches are some important examples. Considering graphene membrane as a homogenized graphene monolayer on the macroscopic structure [1], may not be accurate enough to model the molecular deformations. Because of the application for nanotechnology, relaxation of the Carbon atoms of the RUL are playing a significant role in whole the membrane configuration. Tersoff-Brenner (TB) atomic potential description is well stabilised for the modeling of carbonic structures in Molecular Dynamics (MD) and bigger scale simulation techniques. In the present paper, we focus on the formulation of the TB atomistic interaction as a multiscale problem. In fact the microscale consists of the atomistic lattice dictated by the TB potential subjected to the proper boundary conditions to allow for the angular dependencies. The resulting behavior is studied with respect to tension-compression tests for different unit cells. Considering the balance between computational cost, convergence of the microscopic solutions and desired accuracy of the homogenized behavior an appropriate RUL has been selected.The resulting anisotropic behavior of the lattice is completely explained as an effect due to chirality in the lattice configuration.

Macro-Micro homogenization

The principle of separation of scales is considered with respect to the membrane plane, meaning that the contribution from the macroscopic placement to the microscopic placement field within the underlying RUL is obtained by formulated it in terms of the total placement $\mathbf{x}_j$ and the relative atom-to-atom placement $\mathbf{r}_{ij}$. Subindex of j refers to the nearest neighbor atoms of i, while k refers to the next nearest neighbors of atom i. As to notation, to distinguish microscopic and macroscopic quantities, we shall denote the macroscopic fields by a superimposed bar, e.g.$\bar{\bullet}$.

$$\mathbf{r}_{ij} = \sum_{\alpha=1}^{2} \bar{\varphi}_{,\alpha} (\bar{\mathbf{G}}^{\alpha} \cdot \mathbf{R}_{ij}) + \mathbf{r}_{ij}^{f} \;\; where \;\; \mathbf{r}_{ij}^{f} = \mathbf{u}_{j}^{f} - \mathbf{u}_{i}^{f} \tag{1}$$

According to equation (1), $\mathbf{r}_{ij}$ is due to the of CBN first order mapping of a vector from atom i to its nearest neighbor atom j plus the microscopic fluctuation of the vector due to TB explanation. We also obtain the total placement of $\mathbf{x}_j$ as

$$\mathbf{x}_j = \bar{\mathbf{f}} \cdot (\mathbf{X}_i + \mathbf{R}_{ij}) + \mathbf{u}_j^f \tag{2}$$

where $\bar{\mathbf{f}} = \bar{\mathbf{g}}_\alpha \otimes \bar{\mathbf{G}}^\alpha$ is the in-plane deformation gradient, $\mathbf{x}_i$ is the initial coordinate of atom i and $\mathbf{R}_{ij}$ is the initial bond length between atoms i and j. $\mathbf{u}_i^f$ is introduced as microscopic displacement of atom j. The fluctuation displacements describe the inter-lattice relaxation and it is involved in the argument of the stored energy as according to the non-local TB potential [2] for the Carbon-Carbon bonds. The potential energy E for the entire lattice is defined by the summation over the bonds.

$$\psi = \sum_{i=1}^{N} \sum_{j=1}^{3} \psi_{ij} \text{ with } \psi_{ij} = \psi_{R_{ij}} - \psi_{A_{ij}} \bar{B}_{ij} \tag{3}$$

where $\psi_{R_{ijj}}$ and $\psi_{A_{ij}}$ are terms of potential energy for pairwise interaction, $\bar{B}_{ij}$ is a term of energy due to bond angle variation. N describes the total number of atoms in the lattice.It is also of significant for finite element method to derive the stiffness properties associated with the atomic motions δx_i.

Coupling of the micro and micro fields

In order to assess the homogenization of the stress resultants, The area region C_{0i} is introduced where the microscale fluctuation as defined in Eq.(2) is levaluated .This area region C_{0i} defined by the cut off radius R_m as shown in Figure 1. It is also illustrates an inner and an outer region used for the proper representation of boundary conditions for the microscopic fluctuation.
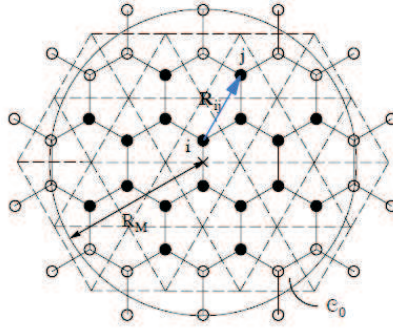
Figure 1: Representative graphene unit lattice C_0 defined by cut off radius R_M.Filled particles corresponds to particles allowed to relaxed within the lattice whereas hollow particles follows the CBN rule approximation.

In the example RUL in Figure 1, we have *32* number of atoms for the current cut off radius R_m. Please note that the the hollow particles denote particles of the boundary of the lattice where the Dirichlet boundary condition, i.e. $\mathbf{u}_i^f = 0$, is assumed to hold for the particle fluctuation. There is also an auxiliary outer set of particles outside the cutoff region, which are needed in order to properly evaluate the angular interaction forces of the TB potential in conjunction with the Dirichlet boundary condition.

Model evaluation and results

We present results for the lattice shown in Figure 1 based on the TB potential for graphene. To validate of our model we compute basic lattice deformation modes (*extension and compression*)numerically due to a tensile and a compressive loading. Due to the lattice structure graphene has anisotropic behavior. This means, the deformation of the material is sensitive to the orientation of the lattice relative to the loading direction. This well-known phenomenon is identified in the atomic interactions and their configurations of the lattice. Because of the sp^2 periodic aromatic structure of the graphene, the structure behaves dependently due to different angles of external applied forces in tension/compression test. Literally, this angular dependency comes from the $\bar{B}_{ij}$ in equation 3 . Chirality in the graphene structure can be divided in *Armchair* and *Zigzag*
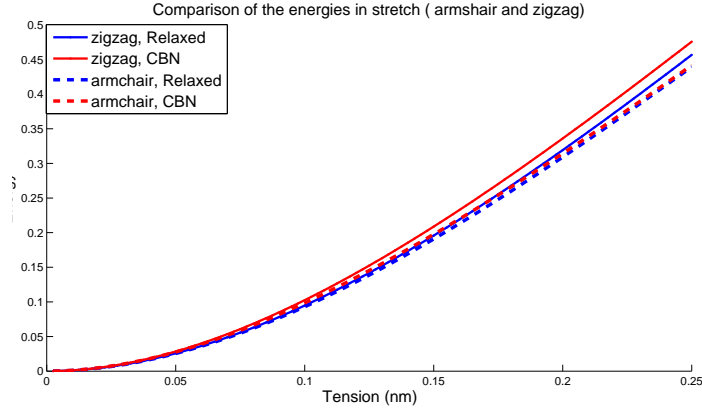
Figure 2: Tension comparison of zigzag and armchair graphene configuration for relaxed and not-relaxed models.
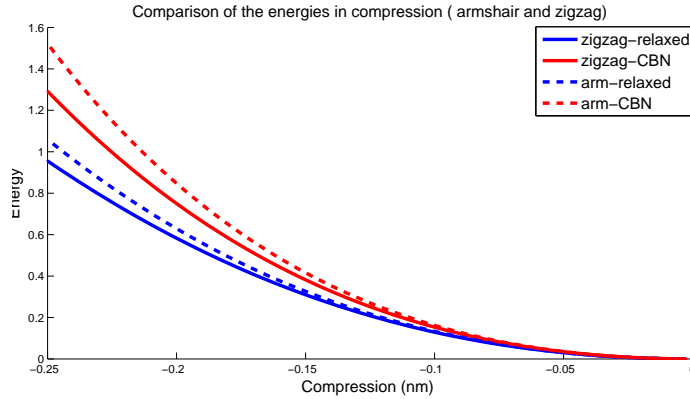
Figure 3: Compression comparison of zigzag and armchair graphene configuration for relaxed and not-relaxed models.

configurations. Each configuration has specific behavior in tensile test. We have presented relaxed and non-relaxed tension and compression tests for different sizes of RUL. The relaxed test is based on inter-lattice fluctuation; however, in non-relaxed model [3], we have used the first order CBN. In Figures 2 and 3, the comparison between these tests are illustrated. According to the figures

, the relaxed method shows lower level of energy and it reveals the error range of simple first order CBN modeling [3]. In addition, anisotropic property of graphene is fairly explainable in two different chiral configuration of the graphene. Moreover based on our results, we introduce the optimum size of the RUL. The chosen RUL is compensated by the optimum of the computation cost and application accuracy.

References

[1] R. Larsson and K. Samadikhah. Atomistic Continuum Modeling of Mono Layer Graphene Membranes. *21st Nordic Seminar on Compuational Mechanics* . (2008), 108–111.

[2] D.W. Brenner. Emperical potential for hydrocarbons for use in simulating the chemical vapor deposition of diamond films. *Physical Reviw B*, **42**, 9458–9470, (1990)

[3] J. Zhou and R. Huang Internal lattice relaxation of single-layer graphene under in-plane deformation *J. Mech. Phys. Solids*, **56**, (2008), 1609–1623

Effect of introducing flexible bodies in multi body dynamics

Morten Haastrup[*]

Mechanical Systems, Global Research
Vestas Wind Systems A/S
e–mail: mohaa@vestas.com

Ole Ø. Mouritsen

Department of Mechanical Engineering
Aalborg University, Aalborg, Denmark
e–mail: oom@me.aau.dk

Michael R. Hansen

Department of Engineering
University of Agder, Agder, Norway
e–mail: michael.r.hansen@uia.no

Summary   First, three models of a wind turbine gearbox is presented, each model with a different number of flexible shafts. The vibration of one bearing is analyzed, and the results are compared. It is observed that particularly the modelling approach of the shaft where the bearing is located has great influence on the vibrations.

Introduction

The numerical analysis plays a key role in the design process of wind turbine gearboxes; and the trend is going towards system simulation, where the entire wind turbine is modelled. With today's computational capacity it is possible to model all aspects of wind turbines: Aerodynamics, mechanics, electronics and control systems in the same simulation. Depending on the focus of the modelling, more effort can be put into some of the aspects. In this paper the significance of modelling the gearbox shafts as either flexible or rigid is investigated. For this purpose several models of the same gearbox are developed in the multi body simulation software Adams/View; each model with a different level of detail. In wind turbine gearboxes a major issue is bearing failure, therefore good modelling approaches are needed to foresee the fatigue loads on the bearings.

Model of the Gearbox

The gearbox considered originates from a 750kW wind turbine. Only the intermediate and the high speed stage of the gearbox are modelled, hence, the planetary stage is not explained in this study. Thereby three shafts and two gear pairs are modelled. Details of the gears are listed in table 1. The components of the gearbox model are shown in figure 1 along with the naming convention. The housing is hidden.

Gear pair	Teeth on pinion	Teeth on gear	ratio
Intermediate	23	82	3.5652
High speed	22	88	4.0000

Table 1: Details of the gear stages.

Bearings

The bearings are modelled by linear springs and dampers. The stiffness of each bearing is determined using finite element analysis and is linearized around a working point. There are three bearings on each shaft; one cylindrical roller bearing in the upwind end of the shafts and a pair of
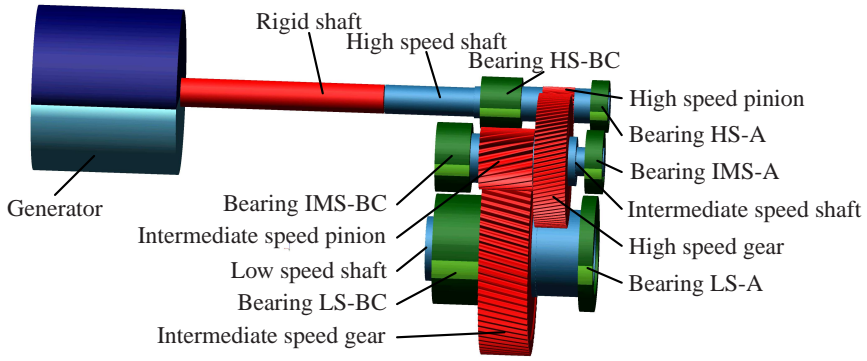
Figure 1: Components of the gearbox model.

tapered roller bearings in the downwind end. In the model each pair of tapered roller bearings are combined into one bushing. This simplifies the stiffness model because the bearing pair has equal stiffness in axial direction independent of the sign of the displacement. A pair of tapered roller bearings is able to take up some bending moment of the shaft which they are located on; this is accounted for by including torsional stiffness in the bushing model.

Loads

The rotor of the generator is modelled to avoid rotational oscillations of the high speed shaft of the gearbox. The nominal torque from the generator is applied as a constant torque. The mass moment of inertia is $J = 17[kg\ m^2]$ [2].

The power is transferred from the high speed shaft to the generator through a rigid shaft that is connected in both ends by bushings. The bushings allow some flexibility and damping to be introduced to the connections. The generator influences the gearbox by a rotational motion.

To keep the prescribed rotational speed of the low speed shaft a PI regulator is employed that controls the drive torque on the low speed shaft based on the deviation of the prescribed and actual rotational speed.

Flexible bodies.

Different models of the gearbox have been created with either no, one or all shafts flexible. The way flexible bodies are handled in Adams/View is by introducing shape functions, a set of eigenvectors that is scaled to approximate the deformation of the flexible body. The actual implementation of flexible bodies in Adams/View relies on the Craig-Bamptom method [1]. The flexible shafts are modelled with FEA in order to determine the modes. The shafts are meshed with relatively few 10 node tetrahedron elements because only the overall stiffness of the shafts is of interest.

Simulation settings

For all simulations the HHT solver in Adams is used with a maximum step size of $5 \cdot 10^{-5}$ and an error tolerance of 10^{-7}. The HHT is a predictor-corrector solver for differential equations.

Comparation parameters

To analyze the changes in response due to implementation of flexible shafts a Campbell diagram is created for each model. The data for the Campbell diagram comes from simulations where the
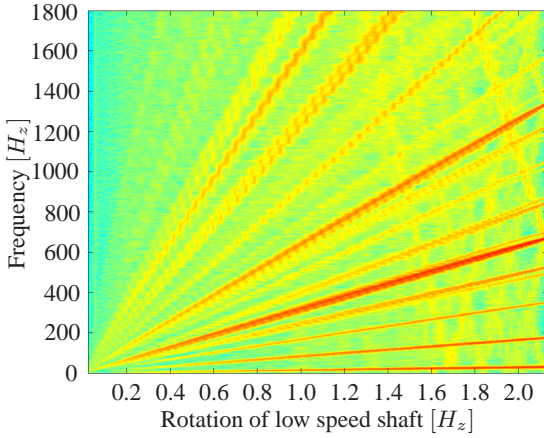
Figure 2: Campbell plot, rigid shafts.
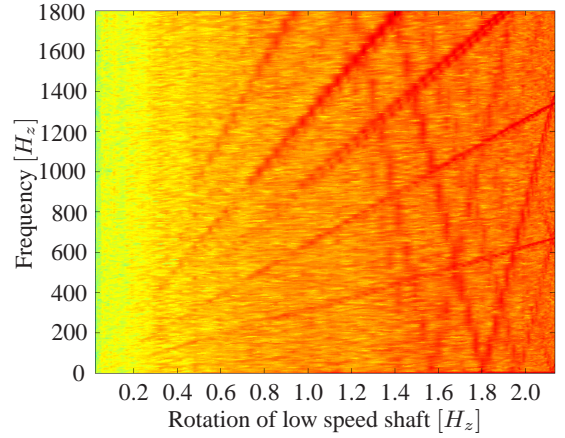
Figure 3: Campbell plot, flexible shafts.

gearbox is ramped up from stand still to speed at rated power production during $10s$. Afterwards the speed is ramped down again during $10s$. During all simulations, the gearbox is loaded at the generator by the torque corresponding to rated power production.

The signal considered in the following is the horizontal acceleration of the high speed shaft measured at the centre of the downwind bushing. The signal is measured by a virtual sensor in Adams/View.

The Campbell diagram of the model with rigid shafts shows narrow bands of frequencies that are excited (figure 2). If figures 2 and 3 are compared, it is observed that the lower frequencies are not present in 3. To investigate the possible origin of the frequencies present in the Campbell diagrams, the mesh frequencies are investigated.
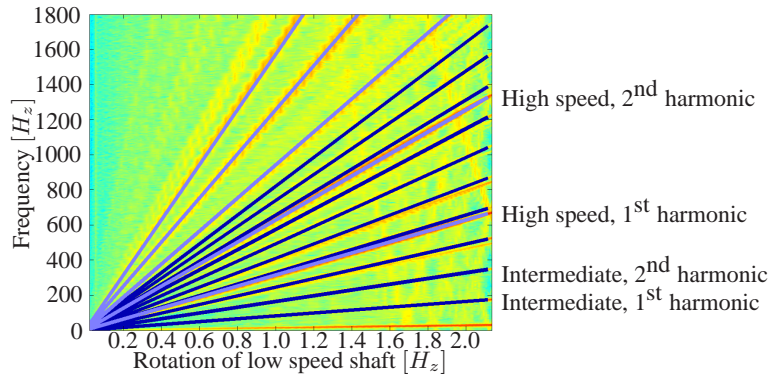
Figure 4: Harmonics of the gear meshes. Dark blue: Harmonics of the intermediate speed stage. Light blue: Harmonics of the high speed stage.

The mesh frequencies of the gears can be calculated if the rotational speeds of the shafts are known. The dependency of the gear mesh frequency of the i'th gear and the i'th shaft is

$$f_{mesh,i} = f_{shaft,i} Z_{gear,i} \qquad (1)$$

Where $Z_{gear,i}$ is the number of teeth on the gear and $f_{shaft,i}$ is the rotational speed of the shaft measured in hertz. Since the actual rotational speed of the shafts is known from the simulation

the mesh frequencies of the two gear pairs can be calculated and plotted on top of a Campbell diagram to investigate if the gear mesh frequency has influence on the measured signal. In figure 4 the fundamental frequencies of the two stages are plotted along with some of the overtones. The figure shows that there is a good correspondence between the mesh frequencies and the frequencies contained in the signal. The same plot can be viewed in figure 2 without mesh harmonics plotted. Actually most frequencies present in the signal is related to mesh harmonics.

In figure 3 it can be seen that only the harmonics of the high speed stage is clearly visible. One explanation is that the oscillations of the intermediate stage harmonics are not transmitted through the flexible high speed shaft. Another explanation is that oscillations of the high speed stage is less damped than with rigid shaft and therefore dwarfs the harmonics of the intermediate speed stage.

Model	RMS	CMC					
		HS-A	HS-BC	IMS-A	IMS-BC	LS-A	LS-BC
Rigid shafts	0.1319	9.7e3	72.8e3	11.3e3	135.7e3	19.5e3	178.2e3
Flexible LS shaft	0.0985	9.6e3	72.8e3	10.9e3	135.7e3	32.3e3	155.2e3
Flexible IMS shaft	0.0964	9.6e3	72.8e3	29.0e3	116.8e3	19.3e3	178.2e3
Flexible HS shaft	1.7822	31.4e3	46.5e3	9.8e3	135.6e3	18.7e3	178.1e3
All shafts flexible	1.7919	31.4e3	46.5e3	28.9e3	116.4e3	32.1e3	154.8e3

Table 2: RMS values of the acceleration signal and CMC values of the bearing forces.

To shed light on the matter the magnitude of the acceleration signal is investigated. The root mean square (RMS) values of the signals are computed. The RMS values of all five simulations are listed in table 2. From the table it is seen that when the flexible high speed shaft is introduced, the RMS value increases significantly. This implies that the harmonics of the high speed stages is enhanced rather than the harmonics of the intermediate speed stage is damped. In general, the results from table 2 clearly show the reaction forces are only influenced if the shaft it is supporting is flexible. The CMC-values where the supported shaft is flexible is highlighted.

Concluding remarks

Modelling of flexible shafts has great influence on the simulated vibrations of shafts and the loading of bearings. Further it is concluded that bearings are only affected by the shaft they are supporting regarding modelling of flexibility. If the loading of a bearing is to be determined, it is sufficient to model only the shaft supported by the bearing flexible.

References

[1] Gisli Ottarsson. Modal Flexibility Method in ADAMS/Flex. *Mechanical Dynamics, Inc.* , (2 August 2000)

[2] ABB. Product note Low voltage generators for diesel and gas engines Performance data. *ABB*, (2009)

[3] J. Sabot and J. Rerret-Liaudet. Effects of Gearbox Design Parameters On the Vibratory Response of Its Housing. *Laboratoire de Tribologie et Dynamique des Systmes, UMR 5513*, (1999)

[4] Robert G. Parker, Vinayak Agashe and Sandeep M. Vijayakar. Dynamic Response of a Planetary Gear System using a Finite Element/Contact Mechanics Model. *JOURNAL OF MECHANICAL DESIGN*, **Vol. 122**, (SEPTEMBER 2000)

An Adams/View-Matlab Computational Interface
for Clustered Optimization of Washing Machines

Thomas Nygårds and Viktor Berbyuk
Department of Applied Mechanics
Chalmers University of Technology, Göteborg, Sweden
e–mail: thomas.nygards@chalmers.se, viktor.berbyuk@chalmers.se

Summary   This paper describes an Adams/View-Matlab environment for parallel/clustered calculations running on ordinary workstations. The system was developed for sensitivity analysis and bi-objective optimization of washing machine performance by using a dynamic model built in the commercial multi-body software MSC.Software Adams\View. Together with statistics of performance of the system, results of a bi-objective optimization of a selection of structural parameters are presented.

Keywords: Bi-objective optimization, parallel computing, washing machine dynamics, vibration control

Introduction

Optimization of dynamical systems is often computationally demanding. Not seldom days or weeks of computational time have to be spent on solving an optimization problem. Several things influence on the CPU-time it takes to solve a specific problem. Always important are the number of parameters to be optimized and the complexity of the model which directly affect the time it takes to solve its equations. The number of conditions for which the model must be evaluated has also a strong influence on CPU-time. For instance, in the case of optimization of a car suspension it could be different road types or handling situations that the suspension needs to perform in. The amount of time it takes to prepare a model for simulation has also an effect on the time consumption. Sometimes heavy in data is needed to be loaded from disk before running.

The paper aims to present a developed computational environment for clustered bi-objective optimization of washing machine dynamics on a set of its operational conditions.

The washing machine model

A washing machine is an object familiar to almost everyone. Many people associate washing machines with noise and vibration, and locate their machine to remote parts of their house or apartment. With extreme cases of unbalanced load, which is the main reason to vibrations and noise, together with a fail of the unbalance detection electronics a washing machine behaviour called "walking" can occur. Walking happens when the normal forces of the floor become too low in relation to the lateral forces and the foot loses its grip.

To deal with these and other issues related to vibration analysis, control and dynamics optimization, a model of a modern in-production washing machine has been developed. Work has been performed during the last couple of years in collaboration with the washing machine manufacturer Asko Appliances AB [1, 2].

The work has resulted in a rigid multi-body model which has been implemented in the commercial software Adams/View. It can be seen together with relevant inner structural components of a physical machine in figure 1. Model parts are constructed using CAD drawings giving accurate inertia properties and joined with appropriate constraints. Remaining structural components of importance have been measured separately with dynamic measurement test-rigs resulting in separate sub models for dampers, springs, rubber bushings and feet. Details on the sub models can be found in [1, 2].
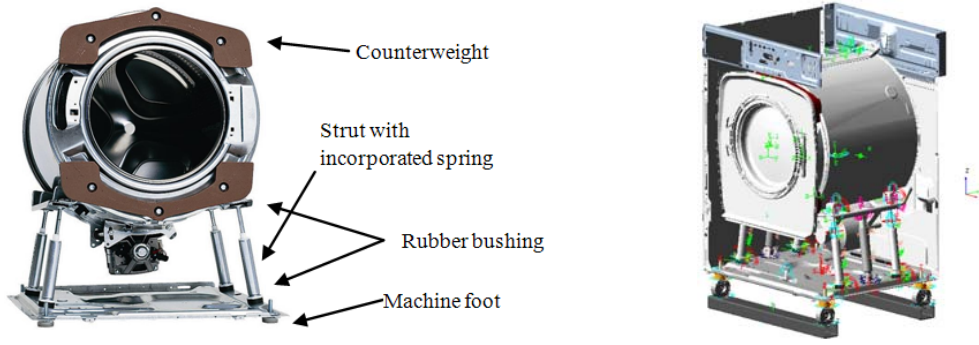
Figure 1: Some of the inner parts of a washing machine and the Adams\View model representation.

The optimization problem

In this paper two criteria of high importance in washing machine dynamics will be used. The first is to keep the tub free from hitting the housing during washing. The second is to limit the propagation of forces through the structure to minimize vibration impact on surroundings and to prevent the machine's walking behaviour [2]. The first objective to be minimized is defined as follows:

$$\mathfrak{I}_K = \max_p \left(\max_t \left(\Delta \mathbf{X}_p(t) - \Delta \mathbf{X}_p^{\max} \right) \right), p = 1, 2, 3 \ldots 9, \forall t \in [0, T] \tag{1}$$

where $\Delta \mathbf{X}_p$ and $\Delta \mathbf{X}_p^{\max}$ are movement and movement margins in three directions at the points p of the tub which have been defined as critical by the manufacturer. The second objective to be minimized is the sum of the RMS-values of the vertical forces F_i^z, (i=1,2,3,4) at the four feet of the machine during the simulation time T and is written as

$$\mathfrak{I}_D = \sum_{i=1}^4 \sqrt{\frac{1}{T} \int_0^T \left(F_i^z(t) \right)^2 dt} \tag{2}$$

To be a feasible product to sell, a washing machine has to be able to handle different amounts of load and different imbalances. To reflect these different operational conditions three critical load cases with respective drum rotational excitation schemes are defined as follows:
1. Constant load of 1kg placed in the front of the drum whilst spinning up to 800rpm with a gradient of 80rpm/s.
2. Constant load of 0.3kg placed in the middle of the drum whilst spinning up to maximum spin speed.
3. Maximal load of the machine distributed evenly in the drum with an exception of 1 kg, which is placed in the front of the machine.

The bi-objective optimization problem of washing machine vibration dynamics on a given set of operational conditions is stated as follows.

Problem A. It's required to determine the vector of structural parameters ξ_* and state vector $\mathbf{x}_*(t)$ which satisfy the variational equation $\min_{\xi, \mathbf{x}(t)} \{ \mathbf{F}[\xi, \mathbf{P}, \mathbf{x}(t)] \} = \mathbf{F}[\xi_*, \mathbf{P}, \mathbf{x}_*(t)]$ subject to the differential equations of motion $\dot{\mathbf{x}} = \mathbf{f}(\mathbf{x}, t, \xi, \mathbf{P})$ and constraints $\mathbf{B}_l \leq \xi \leq \mathbf{B}_u$. Here $\mathbf{F} = [\mathfrak{I}_K, \mathfrak{I}_D]^T$, $\mathbf{P} = [\mathbf{P}_1, \mathbf{P}_2, \mathbf{P}_3]^T$ where $\mathbf{P}_i$ is a vector of input parameters to the operational condition i, (i=1,2,3).

The computational environment and optimization results

To solve Problem A a computational environment has been created. It consists of one computer equipped with Matlab running an optimization algorithm. To this computer an arbitrary amount of computational processes, on the same or on other computers, running Adams/View can be connected through a developed interface.

The dynamical system model opened in Adams\View contains a macro which when it runs creates a unique ID for the program instance and registers it on a network path. It then loops waiting for commands or simulation in data. The in data for the simulations are created in Matlab by the optimizing algorithm and written to files by the developed interface which marks them with the ID of an available node. The interface enables parallel start of simulations if the optimizing algorithm can take advantage of this. One optimizer which works in parallel is the used MATLAB function *'gamultiobj'* from the 'Genetic Algorithm and Direct Search'. This optimizer creates a set of in data (called generation) at each optimization step and makes it available for the interface function to start. The interface searches for available computers to start simulations on, searches for and processes calculated files, sends status messages to the user and restarts crashed simulations when the Adams/View program or a computer is the reason for the crash.

As an example of a solution of Problem A the following results are presented. The resulting Pareto front visible on the left of figure 2 was obtained by the optimization algorithm after more than 3500 evaluations of sets of parameters ξ.
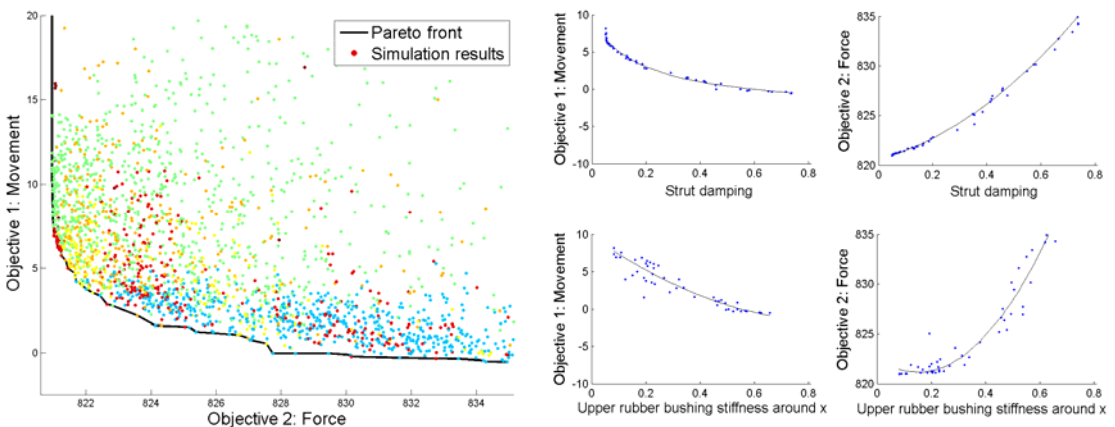
Figure 2: Resulting Pareto front from optimization together with a selection of resulting parameter values.

Together with the Pareto front some of the simulations are plotted with color depending on which of the points *p* where active in equation (1), i.e. at which point the maximum movement in relation to the allowed occurred. On the right side of figure 2 two of the variables which values results in optimal performance are plotted against the respective objective. The conflicting nature of the two objectives can clearly be observed.

Cluster performance

As a performance test a special simulation case (not connected to Problem A) was created. Here all parameters were held constant during simulation to enable predictable calculation time. Varying the time of simulation *T*, resulted in the relation for the cluster efficiency showed in figure 3 peaking at 96% for a *T*=251 s simulation. The data of each point is based on an average of 100 simulations. A curve is fitted to the points following the function *g(t)* in equation (3)

$$g(t) = 100 \times \left(1 - \frac{a}{t+b} - ct\right) \qquad (3)$$

where a=5.45, and b=5.44 and c=0.00101 giving a goodness value R^2=0.997.
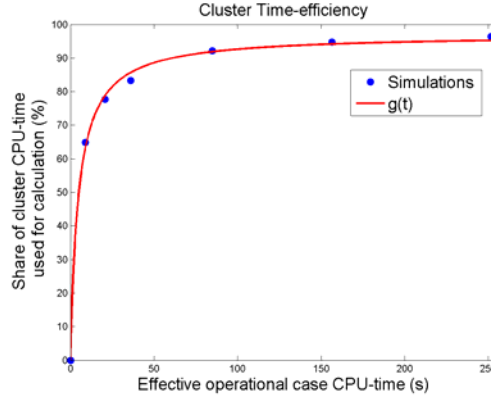
Figure 3: Efficiency of the cluster as a function of effective simulation time.

So, it can be stated that the average constant delay for results file administration for each simulation can be estimated to 5.44 seconds. The administration includes file reading and writing in Adams/View and input file-generation in Matlab. Included in this is a random delay which can be anything between 0 and 4 seconds depending on when for example Adams searches for files in relation to when it is written by Matlab. The random delay can be tuned further if found necessary. A file reading and writing time depending on the size of the output file is reasonable and represented here by coefficient c.

Concluding remarks

An Adams/View-Matlab based interface has been developed for parallelized computation and constrained multi-criteria optimization of washing machine dynamics on a set of critical operational conditions.

Implementation of the developed tools on ordinary workstations has proved calculation efficiency of up to 96% in case of optimization of the dynamics of a modern washing machine.

By using the developed interface and tools a Pareto front has been found giving the domain of realistic structural parameters with optimal dynamic and kinematic performance.

References

[1] T. Nygårds, V. Berbyuk, A. Sahlén: Modelling and Optimization of Washing Machine Vibration Dynamics. *Proceedings of the 9th International Conference on Motion and Vibration Control (MOVIC 2008)*, September 15-18, 2008, Technische Universität München, Munich, Germany.

[2] T. Nygårds, Modeling and Optimization of Washing Machine Vibration Dynamics during Spinning. Thesis for Licentiate Engineering 2009:1, Department of Applied Mechanics, CHALMERS, 2009.

Investigation of Hydraulic Motor Principle for Low Speed High Torque Applications

Rasmus Mørk Sørensen[*]
Department of Mechanical Engineering
Aalborg University, Aalborg, Denmark
e–mail: rms@me.aau.dk

Michael Rygaard Hansen
Department of Engineering
University of Agder, Agder, Norway
e–mail: michael.r.hansen@uia.no

Ole Ø. Mouritsen
Department of Mechanical Engineering
Aalborg University, Aalborg, Denmark
e–mail: oom@me.aau.dk

Per Fenger
Liftra Aps, Aalborg, Denmark
e–mail: pef@liftra.dk

Summary   A new hydraulic high torque low speed motor principle is introduced. The motor is characterized by a specific displacement that is at least an order of magnitude higher than that of commercially available motors. The basic geometry, design variables and governing equations are presented. Comprehensive leakage flow calculations and a detailed dynamic simulation has been used together with testing of a prototype to predict the performance of the motor.

Introduction

Hydraulic motors have some basic advantages that may be utilized in different applications. First of all, it is possible to have a high torque density. This enables hydraulic motors to deliver high torques without occupying large amounts of space. This advantage is further developed in the motor principle put forward in this paper. To examine the motor principle thoroughly, experiments have been carried out both on simulation models and on a physical prototype. The main purpose of this study is simply to highlight the motor principle and describe the derived design considerations that will be implemented on the next generation.

Motor Principle

The motor principle is like a rolling vane motor [2] and a Rolling Abutment Motor [3] in the general design, but is overall more simple because any outside timing is avoided. The main difference is that the vanes are moving in radial direction and the stops are fixed. The motor is illustrated in figure 1 using 4 chambers, however, it can be designed with n-chambers. The rotor is rotating because of pressure difference around the 5 (n+1) vanes. The stops form 4 chambers with either one or two vanes inside. To maximize displacement and output torque, the number of chambers should be maximized. The volumetric efficiency is due to internal leakage flow, why gaps between the individual parts must be kept as low as possible without introducing actual mechanical contact between the moving parts since this would introduce hydromechanical losses.

In figure 1 the basic design variables are shown and the motor displacement pr. rev. is:

$$D = 2 \cdot \pi \cdot n \cdot R \cdot S \cdot H, \tag{1}$$

where n is number of chambers.

Performance

The performance and efficiency are influenced by various parameters. In this work leakage flow has been investigated theoretically with a view to specify acceptable production tolerances. The 1. dimensional leakage flow Q around the vanes and stops is given as

$$Q = \frac{w \cdot h^3}{12 \cdot \mu \cdot L} \cdot \Delta p \quad [1], \tag{2}$$
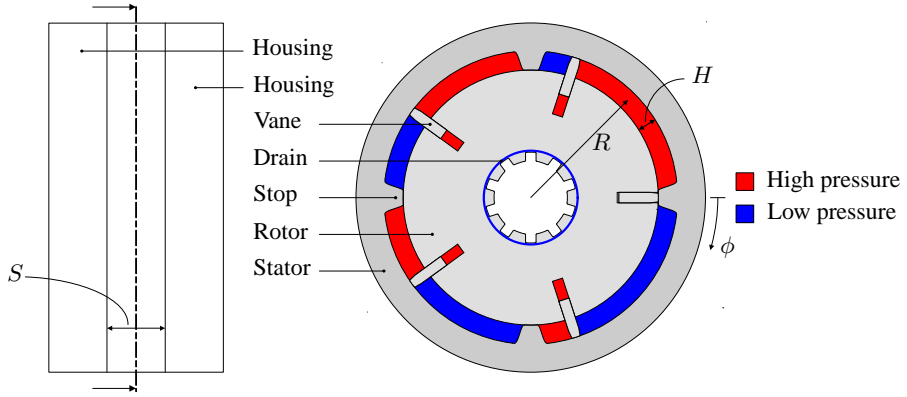
Figure 1: Motor principle with characteristic, design variables, name conventions and pressure volumes. A motor chamber is defined to consists of both the low- and the high pressure volume between 2 stops.

where w, h and L are the geometry of the leakage path and μ is the dynamic viscosity of the fluid. The leakage flow across both end planes of the rotor is 2. dimensional and thereby more complex to estimate. Reynolds equation in polar coordinates is used. For a constant gap height it yields the following differential equation:

$$\frac{\partial^2 p}{\partial r^2} + \frac{1}{r}\frac{\partial p}{\partial r} + \frac{1}{r^2}\frac{\partial^2 p}{\partial \beta^2} = 0, \tag{3}$$

where r is the radial coordinate and β is the angular coordinate. (3) solved for p by a numeric finite difference method to one rotor angle is illustrated in figure 2. Clearly, the pressure distribution varies when the rotor rotates, however, the leakage flow that is an integrated value has quite small variations. The pressure distribution obtained by solving (3) can be used to compute the leakage flow across the disc, in the r- and β direction respectively, as follows:
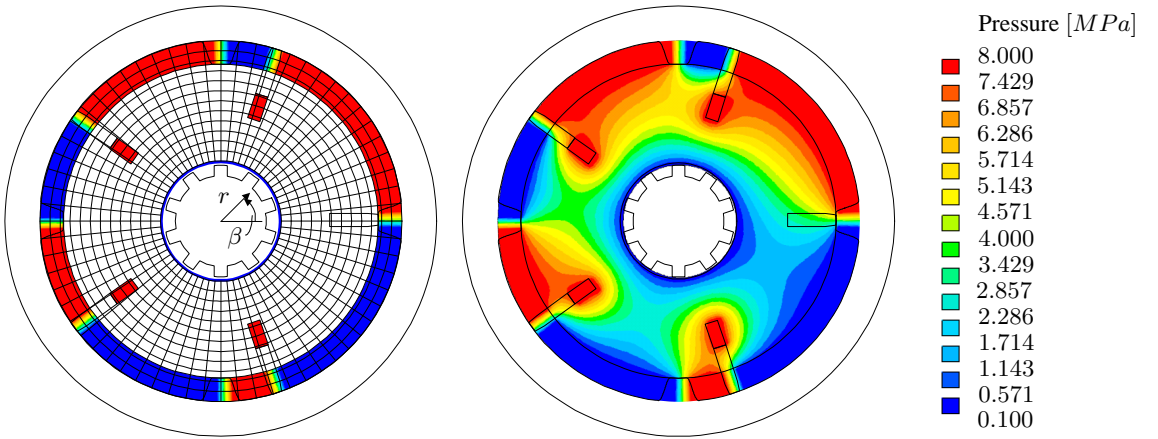
Figure 2: Left: Boundary conditions, coordinate system and unrefined finite difference mesh. Right: Pressure across rotor. (3) solved by the numeric finite difference method.

$$Q_r = -\frac{1}{12\mu} \cdot h^3 \cdot \frac{\partial p}{\partial r} \cdot r_k \cdot \Delta\beta \quad [4] \tag{4}$$

$$Q_\beta = -\frac{1}{12\mu} \cdot h^3 \cdot \frac{1}{r_k}\frac{\partial p}{\partial \beta} \cdot \Delta r + \frac{1}{2}h \cdot \omega \cdot r_k \cdot \Delta r \quad [4], \tag{5}$$

To scrutinize the behaviour of the motor principle, to specify production dimensions and tolerances and to get an overview of the coherence between different factors in the motor, the motor has

been subjected to a time domain simulation. The input to the dynamic simulation is a flow into the motor and the state variables comprise the pressure in the different chambers as well as the angular position and velocity of the rotor. The leakage flows from (2), (4) and (5) are used as lookup tables in this simulation. In figure 3 the result of the dynamic simulation is illustrated as power in and power out from the motor. This is with all gaps at $h = 0.02mm$ and without any influence from friction, i.e., all losses are volumetric. The irregularity after $\approx 6.5s$ is because the rotational direction is changing at that time by reversing the input flow. The small fluctuations in the curves are because of fluctuations in the leakage flow. The rotational speed in the dynamic simulation is $2\frac{rev}{min}$.
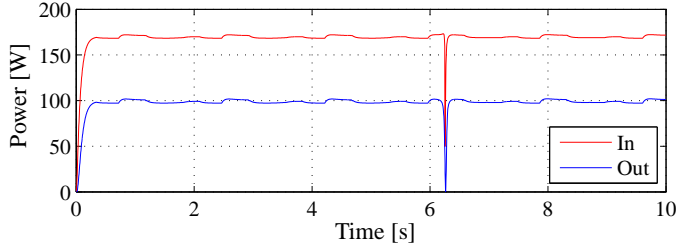
Figure 3: Power in (red) and out (blue) in the dynamic simulation. The efficiency is around 0.57.

Prototype

The prototype is designed with a displacement $D = 190\frac{cm^3}{rev}$. The motors outer dimensions is $200mm$ in diameter and $100mm$ in height. The specific displacement is $D' = \frac{D}{V} = 0.06\frac{1}{rev}$. Neither the size of the chambers nor the number of chambers have been optimized with respect to performance since the main purpose was to investigate the principle. Potentially, the performance, i.e., torque density, of the prototype could be increased by an order of magnitude simply by increasing S, H or N.

A picture of the prototype is shown in figure 4. The vanes are forced against the stator by springs and hydrostatic pressure and are therefore always sliding along the stator. The curvature of the stops is forcing the vanes in when passing a stop. There are

Figure 4: Prototype design.

one oil inlet and one outlet to each chamber, fitted in each stop. The rotor is perforated with small holes to ensure the same pressure at each end plane and therefore minimize mechanical friction.

Experimental Results

The Prototype is tested in a test bench, shown in figure 5. The load on the motor is added by a powder brake through a gearbox. The resistance torque in the test bench is proportional to a voltage signal supplied to the powder brake. To be able to calculate the motors efficiency, the test bench is fitted with different measurement devices; The oil flow into and returned from the motor are measured with flow transducers, the pressure in the oil into and returned from the motor are measured with pressure transducers, the output torque from the motor is measured with a full bridge strain gauge circuit mounted at the output shaft and the angular velocity of the motor is measured by a high resolution encoder. Testing has shown, that the internal friction is quite high
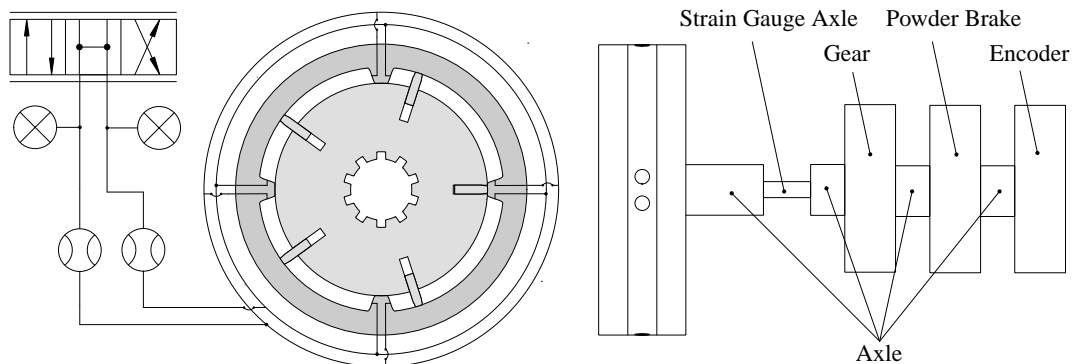
Figure 5: Test setup with all its components and their location. The parts named are just visualized by boxes, but their location is okay.

which affects the motion of the motor, however, the main focus has been on the leakage flow. In general, the leakage flow has increased with increased pressure level. In figure 6 the volumetric efficiency is shown together with the theoretical values obtained by means of simulation. The graphs fluctuates quite much because of irregularities in the angular velocity. The leakage flow is, in general, higher than expected. The main reasons for that are:

- the rotor is not radially balanced causing the leakage paths between stops and rotor/vane to be too high.
- the spring actuation of the vanes does not always function properly, i.e., the vanes are hanging.
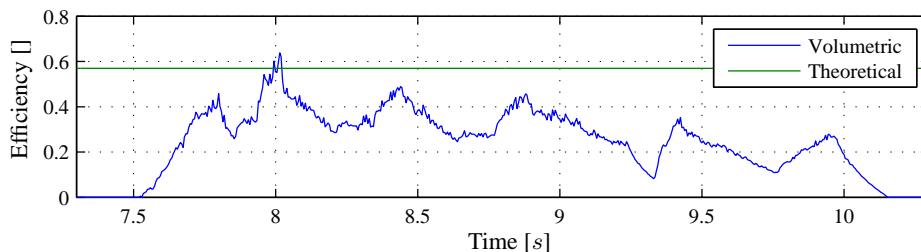
Figure 6: Prototype volumetric efficiencies during one rotation. Green is theoretical and blue is measured.

Concluding remarks

A hydraulic vane motor principle is presented. The motor principle is characterized by a very high torque density. Time domain simulation is carried out with a view to examine the volumetric efficiency as well as the general dynamic behavior of the motor during start, stop and reverse. The time domain simulation utilizes numerical results on leakage flows as lookup tables.

A prototype has been developed and tested. The prototype has a displacement of $D = 190 \frac{cm^3}{rev}$ and a specific displacement of $D' = 0.06 \frac{1}{rev}$. Simulation and measured results clearly indicate that the volumetric losses are higher in practice than in theory. The main reason for this has been identified as unbalanced radial force on the rotor as well as non-optimal vane behavior.

References

[1] M.R. Hansen and T.O. Andersen. *Notes on Fundamental Hydraulics*. Aalborg University, (2007).

[2] J. Ivantysyn and M. Ivantysynova. *Hydrostatic Pumps and Motors*. Technip Books International, New Delhi, First english edition, (2003).

[3] www.vonruden.com/hydraulic_motors/rolseal/rol-seal_cutaway.html. Von Ruden Manufacturing, Buffalo, Web page (12.08.2009).

[4] P.R. Trumpler. *Design of Oil Film Bearings*. MacMillian, (1966).

Design and Kinematics of a 5-DOF Light-Weight Anthropomorphic Robotic Arm

Lelai Zhou* and **Shaoping Bai**
Department of Mechanical Engineering
Aalborg University, Aalborg, Denmark
e–mail: {lzh,shb}@me.aau.dk

Michael R. Hansen
Department of Engineering
University of Agder, Norway
e–mail: michael.r.hansen@uia.no

Summary The kinematics of a 5-DOF light-weight anthropomorphic robotic arm for assisting disabled people is described in this paper. The mechanical design of this light-weight robotic arm is outlined. Forward and inverse kinematic equations are formulated with an aim to evaluate the dexterity of the robotic arm.

Introduction

Industrial robots have been widely used in automobile manufacturing industry and product assembly since the middle of the 20th century. They are used in well structured environments with high performance in terms of positioning accuracy and speed. Generally, the high positioning accuracy requires high stiffness at the cost of high weight relative to payload capacity. Contrary to industrial robots, light-weight robots, which are small, compact and light, are much more suitable for the assistance of activities of daily living (ADL).

The light-weight robots are the combination of light-weight motors, light-weight transmission and light structures. For service purpose, positioning accuracy is not as important as in the industrial field. FRIEND-I and FRIEND-II [1], KARES II [2], RAPTOR [3] and MANUS [4] are in the category of rehabilitation systems. DLR's robotics lab designed a 7-DOF torque-controlled light-weight robotic arm with load-to-weight ratio at 1:1 [5]. Jardon et al have designed a 5-DOF self-containing light-weight manipulator with a portable concept from wheelchair to docking stations in the room [6].

A light-weight robotic arm to support disabled people performing daily living is presented in this paper, as shown in Figure 1. As depicted in Figure 2, this is a 5-DOF system with two DOF at the shoulder, one at the elbow, and two at the wrist. This robotic arm uses harmonic drive^{TM} gears to set the motor and gears coaxially with the joint axis. The simplified construction of the arm links reduces the weight of robotic arm significantly. The total weight of the arm is $9kg$ with a payload capacity of $4kg$. The reachable distance is about $1m$.

Kinematics

Forward Kinematics

Following the Denavit and Hartenberg convention [7], a Cartesian coordinate system is attached to each link of the robotic arm, as shown in Figure 3. D-H parameters are defined as listed in Table 1. Under the established coordinate systems, the transformation matrix of two successive links, $^{i-1}A_i$, is given by

$$^{i-1}A_i = \begin{bmatrix} c\theta_i & c\alpha_i s\theta_i & s\alpha_i s\theta_i & a_i c\theta_i \\ s\theta_i & c\alpha_i c\theta_i & s\alpha_i c\theta_i & a_i s\theta_i \\ 0 & s\alpha_i & c\alpha_i & d_i \\ 0 & 0 & 0 & 1 \end{bmatrix} \tag{1}$$

Figure 1: A light-weight anthropomorphic robotic arm mounted on an electric wheelchair.

Figure 2: A 5-DOF light-weight anthropomorphic robotic arm.

where $c\theta$ stands for $\cos\theta$ and $s\theta$ for $\sin\theta$.
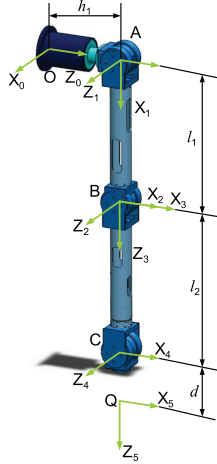
Figure 3: Robotic arm coordinate system.

Joint i	α_i	a_i	d_i	θ_i
1	$\pi/2$	0	h_1	θ_1
2	0	l_1	0	θ_2
3	$\pi/2$	0	0	θ_3
4	$\pi/2$	0	l_2	θ_4
5	$\pi/2$	0	d	θ_5

Table 1: D-H Parameters of the robotic arm.

The transformation matrix of the arm is given by

$$^0A_5 = {}^0A_1\,{}^1A_2\,{}^2A_3\,{}^3A_4\,{}^4A_5 \tag{2}$$

Inverse Kinematics

For inverse kinematics, the location of the end-effector is given and the problem is to find the joint variables necessary to bring the end effector to the desired location. In this work, the inverse kinematics problem is solved based on the methods presented in [8].

Note that the last two joint axes intersect at the wrist center point **C** as shown in Figure 3. Hence rotations of the last two joints do not affect the position of **C**.

To solve the inverse kinematics problem, the end effector location is given by Eq. (3).

Skipping details, a solution for θ_1 is found as

$$
{}^0A_5 = \begin{bmatrix} u_x & v_x & w_x & q_x \\ u_y & v_y & w_y & q_y \\ u_z & v_z & w_z & q_z \\ 0 & 0 & 0 & 1 \end{bmatrix} \tag{3}
$$

$$
\theta_1 = \arctan\left(\frac{p_y}{p_x}\right) \tag{4}
$$

where $p_x = q_x \quad dw_x$ and $p_y = q_y \quad dw_y$. Hence there are two solutions of θ_1. Specifically, if $\theta_1 = \theta_1^*$ is a solution, $\theta_1 = \theta_1^* + \pi$ is also a solution, where $0 \leq \theta_1^* \leq \pi$. We call $\theta_1 = \theta_1^*$ the front-reach solution and $\theta_1 = \theta_1^* + \pi$ the back-reach solution.

The solution of θ_3 is given as

$$
\theta_3 = \arctan\left(\pm\frac{\kappa_3 \quad \kappa_1}{\sqrt{\kappa_2{}^2 \quad (\kappa_3 \quad \kappa_1)^2}}\right) \tag{5}
$$

where $\kappa_1 = l_1^2 + l_2^2$, $\kappa_2 = 2l_1 l_2$, and $\kappa_3 = p_x^2 + p_y^2 + (p_z \quad h_1)^2$.

Equation (5) yields: (1) two real solutions if $\kappa_2^2 \quad (\kappa_3 \quad \kappa_1)^2 > 0$, (2) two solutions : $\pm\frac{\pi}{2}$, if $\kappa_2^2 \quad (\kappa_3 \quad \kappa_1)^2 = 0$, and (3) no real solutions if $\kappa_2^2 \quad (\kappa_3 \quad \kappa_1)^2 < 0$. If Eq. (5) yields no real solutions, the position is not reachable.

Once θ_1 and θ_3 are known, θ_2 can be obtained as

$$
\theta_2 = \arctan\frac{(\mu_2\eta_1 \quad \mu_1\eta_2)(\zeta_2\mu_1 \quad \zeta_1\mu_2)}{(\mu_2\zeta_1 \quad \mu_1\zeta_2)(\zeta_2\eta_1 \quad \zeta_1\eta_2)} \tag{6}
$$

where $\mu_1 = l_1 + l_2 s\theta_3$, $\zeta_1 = l_2 c\theta_3$, $\eta_1 = p_x c\theta_1 + p_y s\theta_1$, $\mu_2 = l_2 c\theta_3$, $\zeta_2 = l_1 + l_2 s\theta_3$, $\eta_2 = p_z \quad h_1$.

θ_5 takes the form of

$$
\theta_5 = \arccos\left(w_x c\theta_1 s\theta_{23} + w_y s\theta_1 s\theta_{23} \quad w_z c\theta_{23}\right) \tag{7}
$$

Assuming that $s\theta_5 \neq 0$, we can solve for θ_4 as follows.

$$
\theta_4 = Atan2(s\theta_4, c\theta_4), c\theta_4 = \frac{w_x c\theta_1 c\theta_{23} + w_y s\theta_1 c\theta_{23} + w_z s\theta_{23}}{s\theta_5}, s\theta_4 = \frac{w_x s\theta_1 \quad w_y c\theta_1}{s\theta_5}. \tag{8}
$$

Simulations

Based on the forward and inverse kinematics derived in last section, simulations have been conducted. With the given end-effector trajectory, the five joint variables of the robotic arm are solved as a function of time. The graphics package of MAPLE is used to draw the structure of the robotic arm, each link and joint are defined in each frame. The trajectory of the end-effector is defined as $x(t) = 250 \quad 150\cos(t)$, $y(t) = 350 + 30t$ and $z(t) = 50 + 120\sin(2t)$, x, y, z is that relative to X_0, Y_0, Z_0 in Figure 3. As shown in Figure 4, three frames are captured during the simulations.
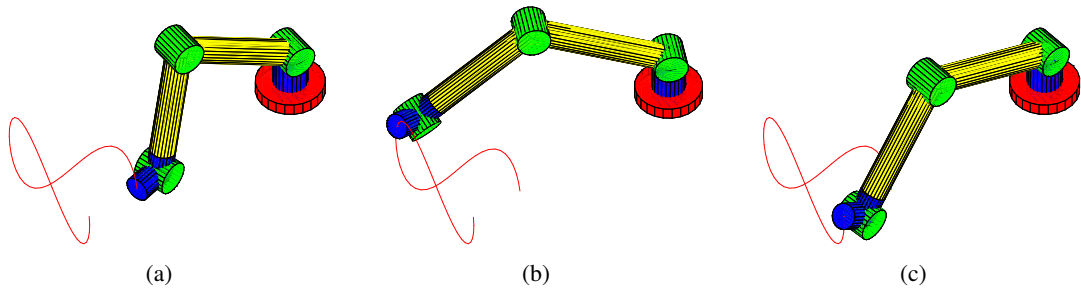
Figure 4: Kinematic simulation of the robotic arm.

Conclusions

In this paper, a 5-DOF light-weight anthropomorphic robotic arm is presented for the purpose of assistance of activities of daily living (ADL). The mechanism structure of this robotic arm is described. The forward and inverse kinematics problems are solved thoroughly, based on which kinematics simulations have been conducted. In the future works, dynamics analysis of this robotic arm will be carried out to set up the requirements needed to select appropriate motors and transmission elements. Moreover, system optimization will be done to maximize the payload capacity of the arm and to minimize the mass of the arm.

References

[1] O. Ivlev, C. Martens, and A. Graeser. Rehabilitation robots FRIEND-I and FRIEND-II with teh dexterous lightweight manipulator. *Technology and Disability*, 17:111–123, 2005.

[2] Z. Bien, M. J. Chung, P. H. Chang, and D. S. Kwon. Integration of a rehabilitation robotic system (KARES II) with human-friendly man-machine interaction units. *Autonomous Robots*, 16:165–191, 2004.

[3] M. S. Colello and R. M. Mahoney. Commercializing assistive and therapy robotics. *Universal Access and Assistive Technology*, pages 223–234, 2002.

[4] H. H. Kwee. Integrated control of MANUS manipulator and wheel chair enhanced by environmental docking. *Robotica*, 16(5):491–498, 1998.

[5] A. Albu-Schäffer, S. Haddadin, C. Ott, A. Stemmer, T. Wimböck, and G. Hirzinger. The DLR lightweight robot: design and control concepts for robots in human environments. *Industrial Robot*, 34(5):376–385, 2007.

[6] A. Jardon, A.Gimenez, R. Correal, R. Cabas, S.Martinez, and C.Balaguer. A portable light-weight climbing robot for personal assistance applications. *Industrial Robot*, 33(4):303–307, 2006.

[7] J. Denavit and R. S. Hartenberg. A kinematic notation for lower pair mechanisms based on matrices. *ASME J. Appl. Mech.*, 77:215–221, 1955.

[8] L. W. Tsai. *Robot analysis: The mechanics of serial and parallel manipulators*. John Wiley & Sons, 1999.

Simulations of optimal in-plane deployment of spinning space webs

Gunnar Tibert[*]**, Mattias Gärdsback, Rafael Ritterbusch and Pau Mallol**
Department of Mechanics
KTH, School of Engineering Sciences, Stockholm, Sweden
e–mail: tibert@kth.se

Summary   Existing control strategies for deploying large web by centrifugal forces seem to either consume excessive energy or cause oscillations. In this study, control laws are derived from the solution to relevant optimal control problems and existing controls. Simple on-ground experiments are being developed as a first step to an in-space experimental verification of the spin-deployment concept.

Introduction

Larger and lighter structures are required for many space technologies, e.g. solar sails and solar power systems. Flexible structures have the potential to keep the weight and package volume small and be deployed to the required size in orbit. One interesting method to deploy and stiffen flexible structures is to use the centrifugal force, which offers significant advantages compared to rigid alternatives: low mass, small package volume, low deployment power consumption, possible gyroscopic re-pointing, acceptable surface accuracy and presumably low cost.

Space webs, where spider-like robots are used to build large structures on a web platform in orbit, are considered by both the European and Japanese space agencies. With the aim to obtain a deployment that is easy to control, recent studies investigate the possibility to use the centrifugal force to deploy and stabilise webs in space [1, 2].

Strategies for optimal deployment control

Existing control strategies for centrifugal deployment of membranes and webs have not been obtained by mathematical analysis. Contrary, extensive research have been performed on the dynamics and control of deployment and retrieval of tethered satellite systems (TSS), which can be used as inspiration for modelling the spin deployment of membranes. We observe that optimal control of TSS models includes less variables than centrifugal deployment; the orbital angular velocity is constant and no torque is applied.

The aim of this study is to find control strategies for the deployment of membranes and webs, coiled on spools or coiled around a centre hub, that minimise the energy consumption and the presence of final oscillations. Because all the significant forces, both external and rotational inertia forces, are in the plane of rotation, it is enough to solve this problem in two dimensions, even though additional attitude control may be required to maintain the plane of rotation for a real case. The Legendre pseudospectral (PS) optimal control method is used to find optimal controls for different optimality criteria.

An optimal control is only optimal with respect to its optimisation criteria. For spin deployment of membranes the torque application is very important and elasticity of the web is less important [2]. An optimal spin deployment should: (i) cause a minimum of oscillations in the end, and (ii) require a minimum of control efforts, which could be to minimise the maximum power or torque, or minimise the total energy consumption or total change of angular momentum, or a combination. A third requirement could be that it should be completed within a specified time.

Deployment using the Melnikov–Koshelev law

The Melnikov–Koshelev (MK) law, Eq. (1), was used in [1] to control the deployment of the quadratic space web, initially coiled around the centre hub. The problem with this control law is that excessive torque is required to not induce oscillations. A control law that eliminates or decreases any oscillations is a requirement to obtain a tensioned web.

$$M = \widehat{M} \left(1 - \frac{\omega}{\omega_0} \right) \tag{1}$$

Derivation of new control laws from the optimal control results

One main advantage with the MK-law is that it is directly applicable, with appropriate parameters, to centrifugal deployment using folding patterns and deployment sequences that are difficult to model accurately, e.g. the one-step deployment of space webs used in [1]. The reason is that the MK law is not directly derived for a specific model, but based on the simple idea that more torque is required if the spin rate ω is low, thus making the torque linearly decreasing with increasing ω. The optimal control results suggest a nonlinear control torque that is smaller than the MK law when $\omega \gg 0$ and increases more rapidly when $\omega \to 0$, Fig. 1. To resemble the optimal control torque more, while keeping the simplicity, a power of the ω-dependent factor in the MK law was introduced:

$$M = \widehat{M} \left(1 - \frac{\omega}{\omega_0} \right)^{\gamma} \tag{2}$$

The parameter γ should be sufficiently large to give a small ω_f, yet sufficiently small to restrain the decrease of ω in the initial deployment phase. Eq. (2) is henceforth denoted as the MK power-law.

The main disadvantage with the MK power-law is that it does not include the final angular velocity. A different or supplementary control law is therefore required to reach the desired final spin rate. One option is to replace ω_0 with ω_f and ensure that M is non-negative:

$$M = \max \left[0, \widehat{M} \left(1 - \frac{\omega}{\omega_f} \right) \right] \tag{3}$$

Eq. (3) is denoted the modified MK law. For this law, $M = 0$ if $\omega \geq \omega_f$, i.e. in the initial and final phase of the deployment. Finite element (FE) simulations using the software LS-DYNA shows that the modified MK law require less energy and is effective to control the final spin rate, Fig. 2.

A first step to experimental verification of the deployment

So far, the control of the web deployment has only been performed numerically, but work is underway to get experimental data for the web deployment. A team of PhD and master students from the Department of Mechanics at KTH and the Departments of Mechanical and Aerospace Engineering at Glasgow University is working on the *Suaineadh* experiment under the ESA/SSC/DLR REXUS-8 programme [3]. The aim of the *Suaineadh* experiment is to centrifugally deploy a 2×2 m^2 web by launching the spacecraft containing the web with a sounding rocket from Esrange in Kiruna.

The KTH part of the *Suaineadh* team is responsible for the web manufacturing and deployment control. To verify the concept experimentally, a 0.6×0.6 m^2 web was manufactured from fishing line, an air hockey table was used to minimise the effects of gravity and a simple electric drill

was used to manually control the spin rate of the central hub, Fig. 3. The air hockey deployment experiment showed that the concept is feasible if the web material is more flexible and knot-free. Thus, the new web will be manufactured from a thin flexible fabric by cutting away material.
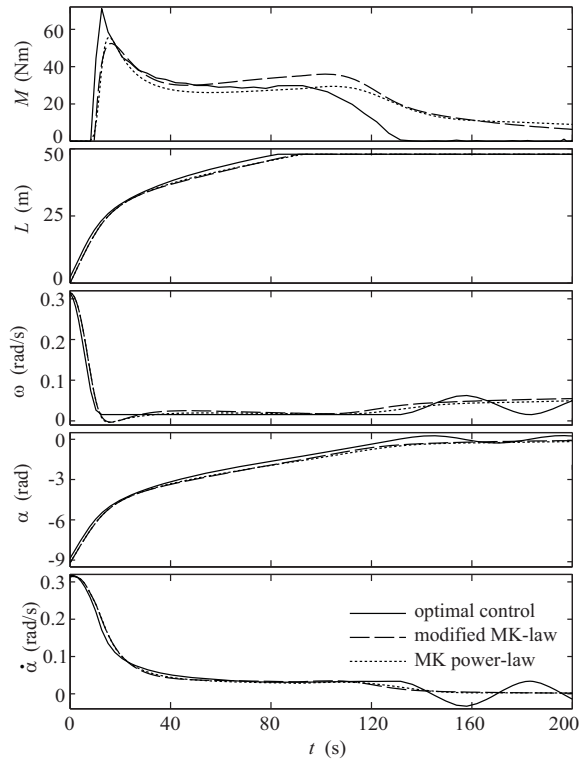
Figure 1: Comparison of control laws for space web deployment.
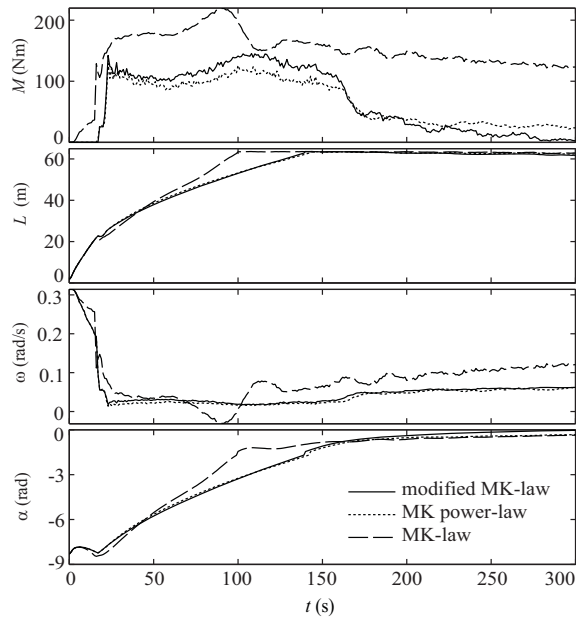
Figure 2: FE simulations of space web deployment.
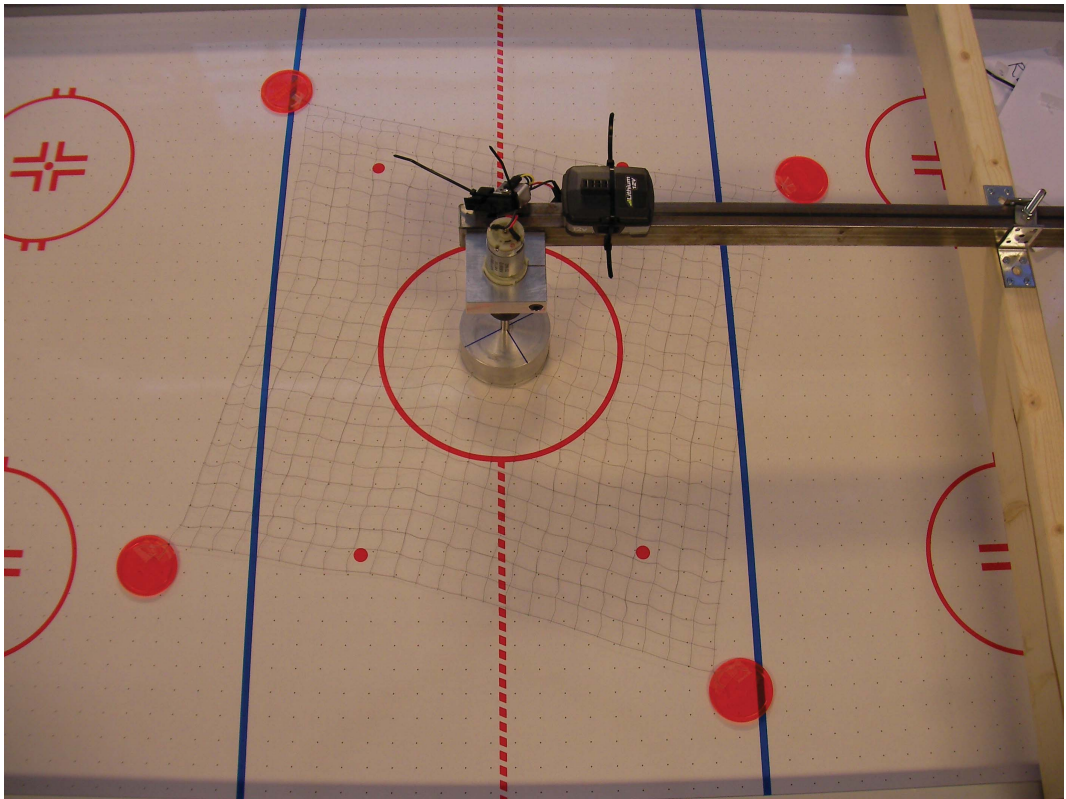
Figure 3: Experimental set-up for verification of the web spin-deployment: air hockey table, electric drill, fishing line web and corner pucks.

Concluding remarks

The developed optimal control strategies have been tested numerically and good agreement is found between a simple axisymmetric model and a FE model for in-plane deployment. To reach more solid conclusions about the feasibility of the spin-deployment concept and the optimal control strategies, experimental data is required and work is underway to get these data.

Acknowledgment

References

[1] M. Gärdsback and G Tibert. Deployment Control of Spinning Space Webs. *J. Guidance, Control & Dynamics*, **32**, 40–50, (2009).

[2] M. Gärdsback and G Tibert. Optimal Deployment Control of Spinning Space Webs and Membranes. *J. Guidance, Control & Dynamics*, **32**, 1519–1530, (2009).

[3] C. Murray, C. Maddock, N. Ismail, M. McDonald, P. Reynolds, A. Mathieson, C. Unsworth, R. Ritterbusch and P. Mallol *Suaineadh: Deployment of Spinning Space Web*. Student Experiment Documentation, Rocket Experiment for University Students (REXUS-8), August 20, (2009).

Predicting racket response during a badminton stroke

Maxine Kwan* and John Rasmussen

Department of Mechanical Engineering
Aalborg University, Aalborg, Denmark
e−mail: mak@me.aau.dk

Summary Badminton racket designs are currently developed using mostly industrial experience, without any real scientific basis. Design improvement is therefore difficult and unreliable. Assuming that racket performance is tied to the dynamic response of the racket, a simple model was developed and used to predict the deflection behaviour of different rackets. Peak deflections and deflections speeds were found to increase with lower racket frequencies, but validation of the model remains to be done.

Introduction

Modern badminton racket designs have largely been developed using heuristic methods, based on player intuition and experience, and racket performance is subsequently assessed by player feedback. From a scientific perspective, however, the interaction between racket and player remains poorly understood. By modelling the relationship between the kinematics of the stroke and the dynamic response of the racket, racket design can be done more efficiently and effectively.

During a stroke, the inertial forces generated from the high accelerations cause the racket to deform. As the racket is swung forward, the racket bends backward and then recovers forward, returning to its original shape as impact occurs. The velocity of this deformation contributes to the racket's total impact velocity. The elasticity of the racket is therefore advantageous only if the deformation velocity is in the same direction as the stroke motion at impact (i.e. both forward). The deformation behaviour of the racket can therefore play an important role in racket performance.

Using a simple uniform beam model, the racket is characterized here by its fundamental frequency, which is used to calculate the dynamic response during a stroke. The model is applied to measured data from a badminton stroke, and the predicted deflection curves are presented and discussed.

Model

The racket is modelled as a uniform cantilever beam of length L, as shown in Figure 1, subjected only to inertial loads which cause the racket to bend. The deflection of a beam can be represented analytically by the summation of the infinitely many natural modes of the beam [1]:

$$w(x,t) = \sum_{n=1}^{\infty} W_n(x)\, q_n(t) \tag{1}$$

where $W_n(x)$ and $q_n(t)$ represent the beam shape along x and the beam motion over time, for the nth mode of the beam. Assuming the first mode is dominant, such that $n=1$ gives:

$$w(x,t) = W_1(x)\, q_1(t) \tag{2}$$
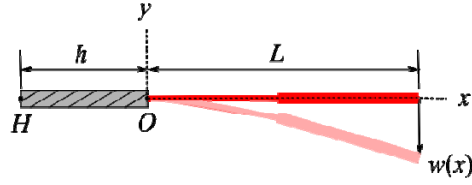
Figure 1: Beam model of racket.

For fixed-free boundary conditions, the beam shape function $W(x)$ is:

$$W_n(x) = \sin \beta_n x - \sinh \beta_n x - \alpha_n \left(\cos \beta_n x - \cosh \beta_n x \right) \tag{3}$$

where

$$\cos \beta_n L \cdot \cosh \beta_n L = -1 \tag{4}$$

$$\alpha_n = \frac{\sin \beta_n L + \sinh \beta_n L}{\cos \beta_n L + \cosh \beta_n L} \tag{5}$$

For $n = 1$, $\beta_n L = 1.8751$.

For a beam initially at rest, the dynamic response of the beam, $q_n(t)$, subjected to the forcing function $f(x,t)$ is given by:

$$q_n(t) = \frac{1}{\rho A b \omega_n} \int_0^t Q_n(\tau) \sin \omega_n (t - \tau) \, d\tau \tag{6}$$

where

$$\omega_n = \beta_n^2 \sqrt{EI / \rho A} \tag{7}$$

$$b = \int_0^L \left(W_n(x) \right)^2 \, dx \tag{8}$$

$$Q_n(t) = \int_0^L f(x,t) \, W_n(x) \, dx \tag{9}$$

Assuming the beam is subjected to inertial loads only, the forcing function can be expressed by $f(x,t) = \rho A \, a(x,t)$, where $a(x,t)$ represents the acceleration of a point along the beam. Focusing on the transverse direction only, the acceleration of a point along the beam is given by:

$$a(x,t) = a_H(t) + (x + h) \, \alpha_T(t) \tag{10}$$

where

$a_H(t)$ is the translational acceleration of point H (at the base of the handle)
$\alpha_T(t)$ is the rotational acceleration of the beam
h is the handle length, the distance from point H to point O

Combining the above equations, the deflection of the beam at a distance x_P along the beam can be expressed as a convolution:

$$w(x_P, t) = - W_n(x_P) \frac{2(\alpha_n + \beta_n h)}{b \omega_n \beta_n^2} \int_0^t \alpha_\varepsilon(\tau) \sin \omega_n (t - \tau) \, d\tau$$
$$= W_n(x_P) \left(\alpha_\varepsilon * g \right)(t) \tag{11}$$

with

$$\alpha_\varepsilon(t) = \frac{\beta_n}{\alpha_n + \beta_n h} a_H(t) + \alpha_T(t) \tag{12}$$

$$g(t) = -\frac{2(\alpha_n + \beta_n h)}{b\omega_n\beta_n{}^2} \sin\omega_n t \qquad (13)$$

Similarly, the deflection velocity of the beam is expressed by the convolution:

$$\dot{w}(x_P, t) = W_n(x_P)\left(\alpha_\varepsilon * \dot{g}\right)(t) \qquad (14)$$

where

$$\dot{g}(t) = -\frac{2(\alpha_n + \beta_n h)}{b\beta_n{}^2} \cos\omega_n t \qquad (15)$$

The term $\alpha_\varepsilon(t)$ can be thought of as a loading function, consisting of the rotational acceleration and a scaled contribution from the translational acceleration of the beam. The term $g(t)$ represents the influence of the racket's fundamental frequency on the dynamic behaviour during the stroke.

By varying the value of ω_n, the deflection behaviour of different rackets can be seen for a given player, assuming the racket does not affect how the player makes the stroke. The model therefore represents a one-way interaction between racket and player, i.e. the dynamic behaviour of the racket is affected by a change in racket properties, but the effects of the different racket properties on the player's stroke are not accounted for.

Implementation

The model requires two inputs: the fundamental frequency of the badminton racket ω_n, and the loading term $\alpha_\varepsilon(t)$. While the fundamental frequency ω_n of a badminton racket can be measured relatively easily, the accelerations of the racket are less straightforward to obtain. To avoid the need for motion capture equipment or several accelerometers, the loading term $\alpha_\varepsilon(t)$ may be deduced from a deflection measurements of a stroke using a racket with a known racket frequency, using Eq 11.

However, deflections are difficult to measure directly during a stroke, but strain measurements provide a nice alternative as they are directly proportional to the deflection and easier to measure. Strain is proportional to the second derivative of the deflection wrt x:

$$\varepsilon(x, t)/R = w''(x, t) = W_n''(x)\, q_n(t) \qquad (16)$$

where R is the radius of the shaft where the strain gage is placed, and

$$W_n''(x) = -\beta_n^2\left(\sin\beta_n x + \sinh\beta_n x - \alpha_n(\cos\beta_n x + \cosh\beta_n x)\right) \qquad (17)$$

From Eq 11, the deflection can be expressed as a convolution. Similarly, the expression for strain is given by:

$$\begin{aligned}
\varepsilon(x_{sg}, t) &= -R\, W_n''(x_{sg})\frac{2(\alpha_n + \beta_n h)}{b\omega_n\beta_n{}^2}\int_0^t \alpha_\varepsilon(\tau)\sin\omega_n(t - \tau)\, d\tau \\
&= R W_n''(x_{sg})\left(\alpha_\varepsilon * g\right)(t)
\end{aligned} \qquad (18)$$

Knowing the strains $\varepsilon(x_{sg}, t)$ and the racket frequency ω_n, the loading term $\alpha_\varepsilon(t)$ can then be solved for by a deconvolution of Eq. 18.

Results

Strain measurements during a stroke performed by a recreational player using a racket of frequency 16 Hz were taken from strain gages placed at the base of the shaft. The predicted deflection profiles at the racket head can be seen for a range of racket frequencies from 13 to 18 Hz in Figure 2. The calculated deflection velocities can be seen in Figure 3. Impact occurs at t=0.2833 s.
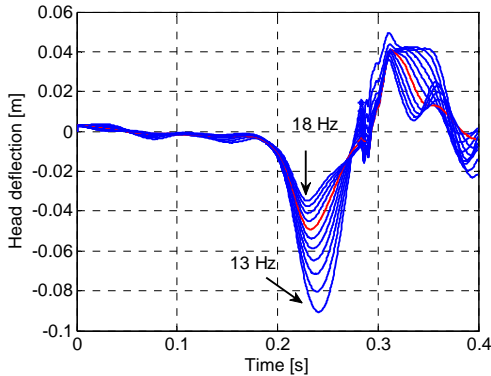
Figure 2: Predicted deflection profiles for racket frequencies ω_n = 13-18 Hz. Impact occurs at t=0.2833 s.
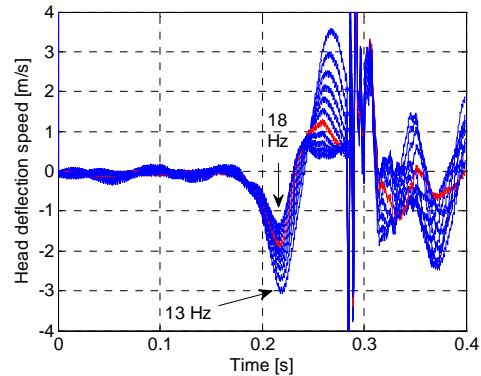
Figure 3: Predicted deflection velocity profiles for racket frequencies ω_n = 13-18 Hz. Impact occurs at t=0.2833 s.

Discussion

The results show the predicted deflection behaviour for rackets of different frequencies, essentially extrapolated from the measured dynamic response of a single racket, assuming the stroke motion is independent of the racket properties. In other words, the player swings all the rackets in exactly the same way. Rackets with lower fundamental frequencies show higher peak deflections and deflection speeds.

Further work includes validation of the model and increased complexity of the model. Model validation can be accomplished by comparing the predicted results against measured dynamic responses of several rackets of different frequencies. One major assumption in the model is the independence of the stroke motion from the racket properties. Studies in other sports such as baseball and tennis indicate that swing weight can greatly influence the stroke [2]. Inclusion of the swing weight effects on the stroke could significantly improve the accuracy of the model.

References

[1] S.S. Rao. *Mechanical vibrations*. Pearson Prentice Hall, Upper Saddle River, New Jersey. Fourth edition, (2004).

[2] R. Cross and R. Bower. Effects of swing-weight on swing speed and racket power. *Journal of Sports Science,* **24**, 23-30, (2006).

Finite element analysis of the mitral valve closure with active muscle fibres

V. Prot[1*] **and B. Skallerud**[2]
[1]Center for Biomedical Computing
Simula, Oslo, Norway
[2]Department of Structural Engineering
NTNU, Trondheim, Norway
e–mail: viktorpr@simula.no

Summary The mitral valve is an important valve of the heart preventing blood from flowing back into the left atrium during systole. In this study, we introduce a contractile element into our transversely isotropic hyperelastic material model [1] to investigate the role of the muscle fibres present in the mitral leaflets during the valve closure [2].

Introduction

The mitral valve located between the left atrium and left ventricle of the heart is one of the four valves of the heart. It prevents blood from flowing back into the atrium when the ventricle contracts. The mitral apparatus consists of two leaflets (anterior and posterior) attached to the annulus and the chordae tendinae. The chordae are further attached to the papillary muscles.

From a mechanical point of view, the mitral valve is often presented as a passive flap that opens and closes in response to the blood pressure gradient. However, several experimental findings showed that the mitral valve contains contractile cells such as cardiac and smooth muscle fibres.

If the mitral valve were only a passive structure, it would mean that the contractile tissue in the valve is functionless. Supporting this finding, our previous study (Prot and Skallerud [3]) showed that if the leaflets are modelled with a passive transversely hyperelastic material, the mitral valve is bulging too much in the left atrium at peak systole. This result agrees with Curtis and Priola [4] who studied the action the muscle fibres present in the anterior leaflet. They showed that when the muscle fibres are active, the mitral valve does not bulge into the left atrium and that in the case of passified muscle fibres the valve deflection was significantly increased at any left ventricular pressure value.

Therefore, our working hypothesis is that the contraction of the muscle fibres present in the mitral leaflets promotes the flat shape of the closed mitral valve during systole.

In this study, we present a transversely isotropic hyperelastic material model for solid elements based on the model described in Prot and Skallerud [3] for the mitral leaflets in which we add a contractile element in order to simulate the mechanical function of the muscle cells present in the leaflets. Then, finite element analyses of a porcine mitral valve are conducted in order to investigate the influence of the contractile force of the muscle fibres on the valve response between beginning and peak systole.

Methods

Finite element model

The geometry of the model is shown in Figure 1 and the modelling of the chordae tendinae is described by Prot et al. [5]. The shape of the annulus was measured at early systole from 3D ultrasound measurements and from anatomical measurements carried out on the same pig. The annulus
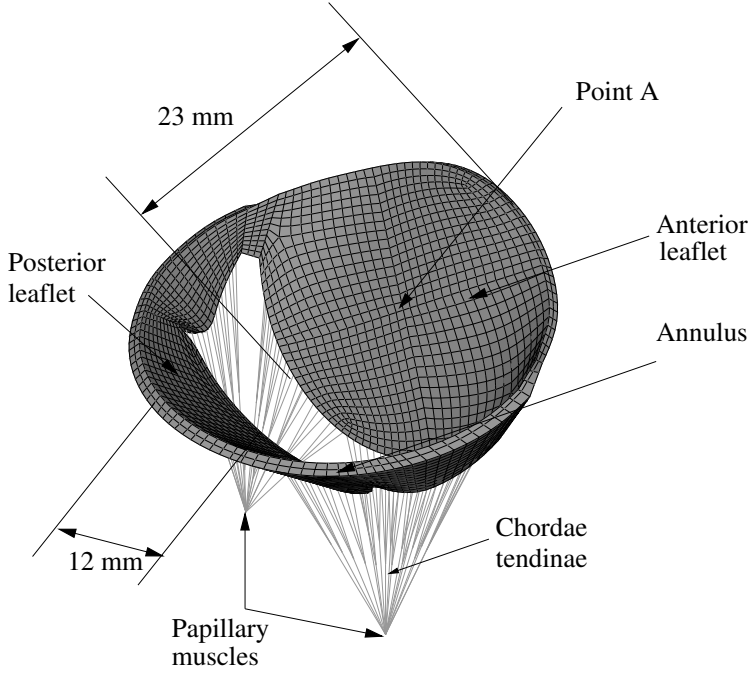
Figure 1: Initial geometry of the mitral valve at beginning of systole.

was idealized as a non-planar ellipse. The distance between the highest point of the anterior annulus to the highest point of the posterior annulus was 30.9 mm. The distance between the two commissures was 34.1 mm. The saddle height, defined as the distance between the highest point of the anterior annulus and the plane defined by the posterior annulus, was 4.81 mm. The maximum distance from the annulus to the free edge of the anterior and posterior leaflets were measured to be 23 mm and 12 mm, respectively, post mortem. The thickness of the leaflets was assumed to be constant and equal to 1 mm.

The collagen fibre orientation was set according to the mean collagen fibre direction map from SALS data shown by Einstein et al. [6]. Additionally, the muscle fibres were located in the central part of the anterior leaflet from the annulus to the middle of the leaflet and in the posterior leaflet along the annulus in a strip of 4 mm. The muscle fibre orientation was set perpendicular to the annulus.

The leaflets were meshed with eight noded brick hybrid elements (C3D8H ABAQUS type) and the chordae with truss elements (T3D2 ABAQUS type). The blood pressure from 0 to 120 mmHg was applied on the ventricular surface of the leaflets. The annulus and the two nodes representing the papillary muscles were constrained with respect to the translations but free to rotate.

Material models

In order to describe the anisotropic hyperelastic response of the mitral valve leaflets, we use the following strain energy function Ψ:

$$\Psi(\bar{I}_1, \bar{I}_4, \bar{I}_6, J) = \underbrace{c_0 \left(e^{c_1(\bar{I}_1-3)^2 + c_2(\bar{I}_4-1)^2} - 1 \right)}_{\bar{\Psi}_p:\ \text{passive isochoric part}} + \underbrace{\bar{\Psi}_a(\bar{I}_6)}_{\bar{\Psi}_a:\ \text{active isochoric part}} + \underbrace{\kappa(J-1)^2}_{\text{volumetric part}} , \quad (1)$$

where c_0, c_1, c_2 are material parameters, κ is a positive penalty parameter and $(J-1)^2$ is known as the penalty function. The idea is to approximate the material as slightly compressible by using

a large value of κ. $\bar{I}_4 = \bar{\mathbf{C}} : \mathbf{a}_0 \otimes \mathbf{a}_0$ and $\bar{I}_6 = \bar{\mathbf{C}} : \mathbf{b}_0 \otimes \mathbf{b}_0$ are pseudo invariants of the modified right Cauchy Green tensor $\bar{\mathbf{C}}$ related to the collagen fibres and muscle fibres, respectively. In the undeformed configuration, the collagen fibre and muscle fibre directions are represented by the unit vectors $\mathbf{a}_0$ and $\mathbf{b}_0$, respectively

Herein, $\bar{\Psi}_p$ and $\bar{\Psi}_a$ correspond to the passive behaviour ([7], [1]) and to the active behaviour of the leaflets due to the muscle fibres contraction in the leaflets, respectively.

$\bar{\Psi}_p$ describes the transversely isotropic mechanical behaviour of the mitral leaflets. As a first approach, we assume that $\bar{\Psi}_a$ is expressed as,

$$\bar{\Psi}_a = \frac{1}{2}\,\sigma_{max}\,f(t)\,(\bar{I}_6 - 1), \tag{2}$$

where σ_{max} is the maximum tetanization and $f(t)$ is a linear function of time including the muscle fibre activation time and the amplitude of the tetanization.

The Cauchy stress tensor σ is obtained as,

$$\boldsymbol{\sigma} = \frac{2}{J}\mathbf{F}\frac{\partial \boldsymbol{\Psi}}{\partial \mathbf{C}}\mathbf{F}^{T}. \tag{3}$$

The material model was implemented in the finite element program `ABAQUS` using the user subroutine `UMAT`.

The chordae were modeled as an incompressible hyperelastic material. The nonlinear stress-stretch behaviour was implemented from experimental data published in [8].

Results
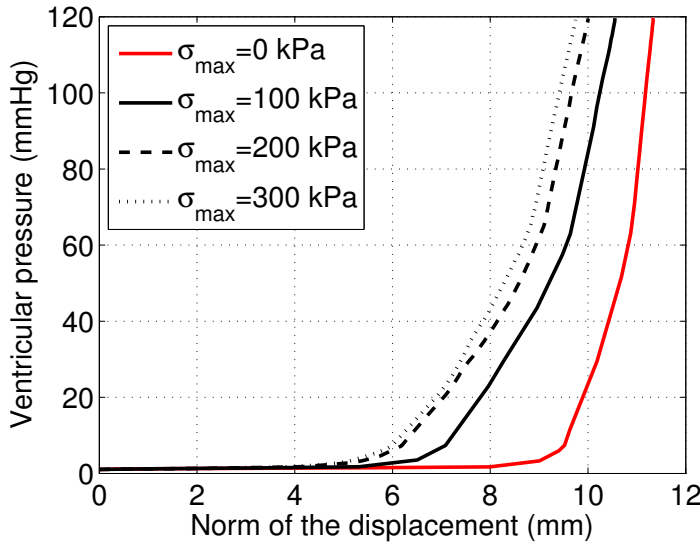
Figure 2: Norm of the displacement of point A (see Figure 1) against the left ventricular pressure for $\sigma_{max} = 0; 100; 200; 300\,\text{kPa}$.

Four finite element analyses were conducted with $\sigma_{max} = 0, 100, 200, 300\,\text{kPa}$. In Figure 2, the norm of the displacement of point A (see Figure 1) is plotted against the ventricular pressure. As can be seen, the displacement of point A decreases when the σ_{max} increases. This means that the deflection of the anterior leaflet decreases when the contraction force of the muscle fibres increases.

Concluding Remarks

Our simple approach to model the contractile cells in the leaflets shows that their contraction contributes to give a flat shape to the closed mitral valve. However, more data on the distribution of the different muscle fibres present in the mitral valve are needed for both human and porcine valves. Their activation time and their maximum tetanization warrant also further studies.

References

[1] V. Prot, B. Skallerud, G.A. Holzapfel. Transversely isotropic membrane shells with application to mitral valve mechanics. Constitutive modeling and finite element implementation. *Int. J. Numer. Meth. Eng.*, **71**, 987–1008, (2007).

[2] B. Skallerud, V. Prot, I.S. Nordrum. Modeling active contraction of mitral valve leaflets during systole. Submitted.

[3] V. Prot and B. Skallerud. Nonlinear solid finite element analysis of mitral valves with heterogeneous leaflets layers. *Comput. Mech.*, **43**, 353–368, (2009).

[4] B.C. Curtis and D.V. Priola. Mechanical properties of the canine mitral valve: effects of autonomic stimulation. . *J. Physiol.*, **31**, 56–62, (1992).

[5] V. Prot, R. Haaverstad and B. Skallerud. Finite element analysis of the mitral apparatus: annulus shape effect and chordal force distribution. *Biomech. Model. Mechanobio.*, **8**, 1617–7959, (2009).

[6] D.R. Einstein, K.S. Kunzelman, P. Reinhall, M. Nicosia, and R.P. Cochran. The relationship of normal and abnormal microstructural proliferation to the mitral valve closure sound. *J. Biomech. Eng.*, **127**, 134–147, (2005).

[7] K. May-Newman and F.C.P. Yin. A constitutive law for mitral valve tissue. *J. Biomech. Eng.*, **120**, 38–47, (1998).

[8] K.S. Kunzelman and R.P. Cochran. Mechanical properties of basal and marginal mitral valve chordae tendineae. *ASAIO Trans.*, **36**, 405–408, (1990).

A Simplified Missile Model Against Maneuvering Target

Sailaranta Timo* and Siltavuori Ari

Department of Applied Mechanics
Helsinki University of Technology, Finland
e−mail: timo.sailaranta@tkk.fi, ari.siltavuori@tkk.fi

Summary A simplified air-to-air missile simulation model is used to investigate the end-game against maneuvering target. The miss distances obtained against High-g Barrel flying target are compared with the results of [1] produced using fairly precise model. The simulation results show that even the miss distance can be estimated with reasonable accuracy based only on relatively simple weapon model.

Introduction

Missile design is a complex task and for example a very complicated aerodynamic model is needed to estimate the weapon dynamics at all possible flight conditions. However, this data is typically not available while existing missile properties are analyzed and simplified methods are needed to estimate the weapon performance. The objective of this paper is to study the capability of a simplified method to predict the end game miss distance.

Missile model

The missile data is listed in Table 1 and is based on the data of Ref. [1]. The missile diameter, engine mass flow and the aerodynamic model were not given [1] and some "typical values" are used instead. Also the autopilot time constant τ_a and missile response are estimated in this study.

Table 1: Missile parameters.

Missile mass	176 kg	Seeker head time constant, τ_1	0.1 s
Missile diameter	0.2 m	Signal processing time constant, τ_N	0.11 s
Thrust	5880 N	Autopilot time constant, τ_a	0.15 s
Rocket motor mass flow	2.6 kg/s	Missile response angular velocity, ω	18.3 rad/s ω_{damped}
Initial velocity	720 m/s		13 rad/s ($\tau_m \approx 0.078$ s)
Flight altitude	3000 m		
Pitch max acceleration	30 g	Missile damping, ζ	0.7
Yaw max acceleration	30 g	Axial force coefficient, C_A	0.5
Navigation gain, N_e	3	Normal force coefficient slope, C_{Z_α}	-20

The aerodynamic model is simplified as much as possible by assuming tetragonal symmetry and ignoring nonlinearities and control surface deflections. Also the missile speed is expected to be about constant and no Mach number effects are taken into account.

A 5th order model (5 lags) is used to describe the missile system dynamics with two time constants for the seeker-head and one for autopilot. The missile turning and lateral acceleration is modeled with a second order response according to formula 1. The 5th order model was used since the lower order systems do not describe the missile lag well enough in the case maneuvering target [2].

$$\frac{a}{a_c} = \frac{1}{\left(1 + 2\frac{\varsigma}{\omega}s + \frac{s^2}{\omega^2}\right)} \tag{1}$$

The autopilot poles were located in the frequency domain to define the three remaining lags (the two given lags are used to model the seeker head). In order to do that a separate acceleration autopilot model was created and some representative control surface aerodynamics was estimated. After that the poles were located to obtain reasonable gain and surface deflection rates. Later it was noticed that the distribution of the three autopilot poles does not affect much on the miss distances obtained with the simplified model. Finally the autopilot stability was checked by drawing the Bode-diagram [2].

The total lumped autopilot + missile time constant value about 0.23 was chosen to obtain the miss distances wished. The missile systems total time constant τ is about 0.44 as a sum of the component time constants (0.1+0.11+0.23). The time constant is fairly large and explains the large miss distances obtained (see results).

The pseudo 5 degree-of-freedom equations of motion were used to numerically integrate the trajectory of missile mass center. The word pseudo conveys the meaning of approximating the attitude dynamics with the linear differential equations of the transfer functions [3].

The navigation gain N_e value used is 3 even though the value in the simulations [1] is stated to be 4. It was not found any possible combination of initial data to reproduce the results [1] using the gain value 4 in the proportional navigation law including the closing velocity. However, the results wished were easily obtained using the representative missile data and the gain value 3. The value of the original paper [1] is assumed in this study to be a printing error.

Target maneuver and end game geometry

The target flies an ideal high-g barrel roll maneuver towards the missile at the flight altitude 3000 m. The end game geometry and the barrel pattern are depicted in Figs. 1 and 2 [1]. The target velocity is 290 m/s and the lateral sustained acceleration is 7 g. The effectiveness of the evasive maneuver is investigated also by varying the barrel roll rate. The roll rate values studied are 1 rad/s, 1.5 rad/s, 2 rad/s and 3 rad/s with different barrel diameters associated.
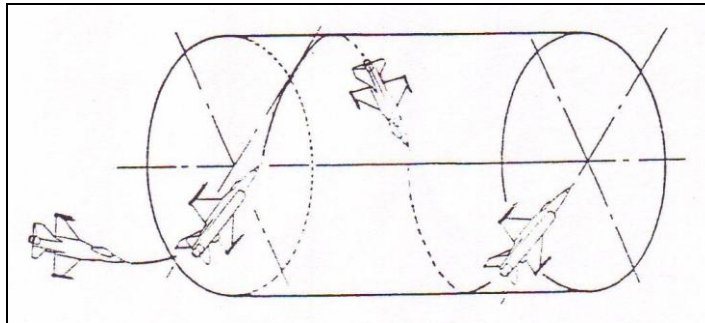
Figure 1: The ideal high-g roll pattern [1].

The missile is at the sustainer stage and flies straight towards the target in head-on geometry (Fig. 2).
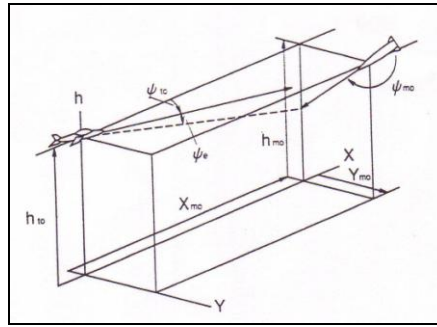
Figure 2: The end game geometry studied. The lateral shift Y_{mo} is 0 m in the case [1].

Results

The obtained miss distances are depicted in Fig. 3 as a function of time-to-go and the barrel roll rate. The time-to-go indicates the maneuver initiation time before interception. The curves were created by moving the initial position of the missile by about 200 meters and repeating the simulation run.

The results are comparable with the ones depicted in Fig. 4 [1].The correspondence of the results is fair taking into account the model simplifications and the partly missing initial data.

The results were checked by using an adjoint model [2]. The non-linear missile guidance model [2] resembles closely the one presented in Ref. [1]. The adjoint model is constructed by linearizing and reversing the original non-linear model [2]. The benefit of the adjoint model is capability to give all the results as a function of time-to-go in a single run. Only four runs were needed to get the results depicted in Fig. 5. The larger time-to-go adjoint miss distance results are constant and this is assumed to be caused by the model linearity.

The large miss distance at the small time-to-go values is due to the unrealistic target maneuver at the beginning of the simulation run. The target has an initial transverse velocity and acceleration since the trajectory is the ideal barrel without the target maneuver lag. This handicap can be eliminated easily by launching the missile to the intercepting course with a proper lead.
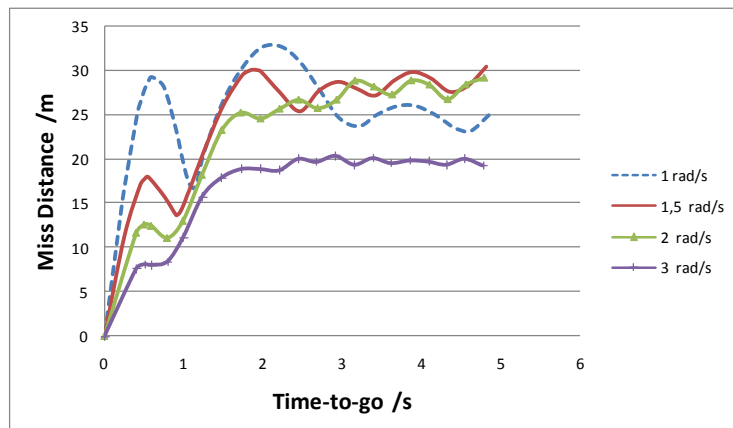
Figure 3: The miss distances obtained in this study using the simplified method.
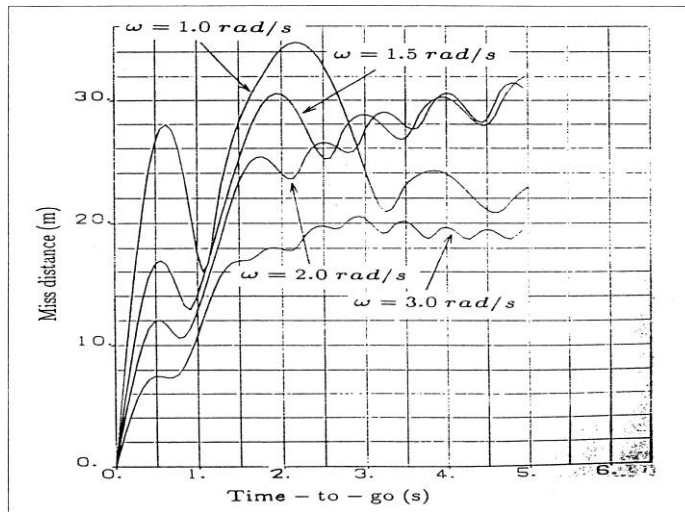
Figure 4: The miss distances obtained in Ref. [1].
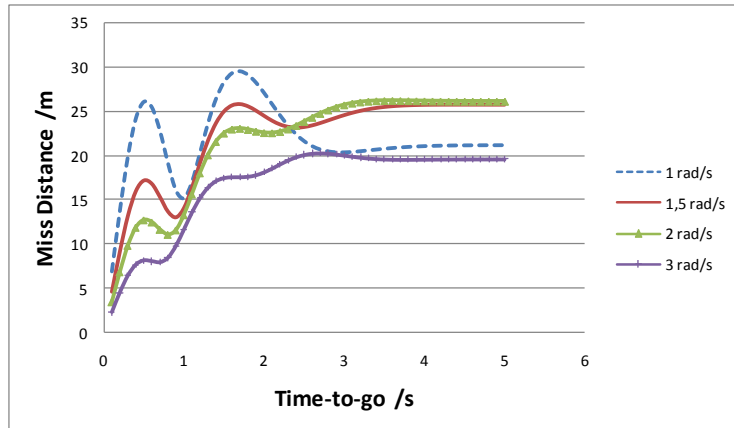
Figure 5: The miss distances obtained in this study using the adjoint model [2].

Concluding remarks

The correspondence of the miss distance results obtained is fair taking into account the simplifications and the partly missing initial data. The simple method seems to be good enough to predict the miss distance, at least in the end-game case studied. The adjoint model [2] verifies the results obtained.

References

[1] Fumiaki Imado and Susumu Miwa. Missile Guidance Algorithm Against High-g Barrel Roll Maneuvers. *J. of Guidange, Control and dynamics*,Vol 17 No1., 123–128, (1994).

[2] Paul Zarchan. *Tactical and Strategic Missile Guidance*. AIAA Progress in Astronautics and Aeronautics, Vol 176., VA USA, Third edition, (1997).

[3] Peter H. Zipfel. *Modeling and Simulation of Aerospace Vehicle Dynamics*. AIAA Education Series, (2000).

ForcePAD - A new user interface concept for design and optimisation

J. Lindemann

Division of Structural Mechanics
Lund University, Lund, Sweden
e−mail: jonas.lindemann@byggmek.lth.se

L. Damkilde

Esbjerg Institute of Technology
Aalborg University, Aalborg, Denmark
e−mail: ld@aaue.dk

Summary ForcePAD is a 2-dimensional finite element application that started as a concept application for finite element modeling. Over the course of 10 years the application has been evolved into an application that is used extensively in both an educational setting as well as a tool for design and engineering. In the latest version of ForcePAD an optimization module was added to enable to take advantage of topology optimization in the design process.

Introduction

The traditional finite element modeling process is complex involving several steps and iterations. The complexity is often needed to support the precision needed in the modeling real objects. In a design or architectural setting the need for precision is replaced with the need for quick iterations and the ability top quickly change a design analyse the effects of the changes. ForcePAD [1, 2, 3] is designed to support this development process, reducing the number of steps in the modeling process.

Analysis tools early in the design process

Early in the design process sketching is often used to iterate over several design concepts. Software supporting sketching is image-editing applications such as Adobe Photoshop [4], GIMP [5] or Paint.NET [6]. The design of ForcePAD is modelled after an image editing application, where color is replaced with stiffness, where black represent max stiffness and white no stiffness. To analyse the model the image is transferred to a finite element mesh, by sampling the image. The modelling workflow is shown in figure 1.
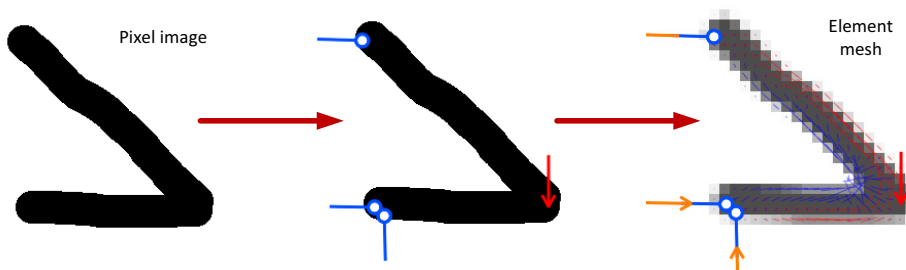
Figure 1: The sketch based modelling workflow of ForcePAD.

Topology optimisation for finding shapes

In the earlier versions of ForcePAD the user could do some "manual" optimisation by looking at the stress fields and removing unnecessary material. In the latest version of the software a topology optimisation algorithm was added based on work by Bendsoe and Sigmund [7] and Pederson et al. [8]. Using this algorithm topology optimisation can be applied to existing sketches aiding the designer in finding an optimal design. Figure 2 shows the algorithm applied to a rectangular model.
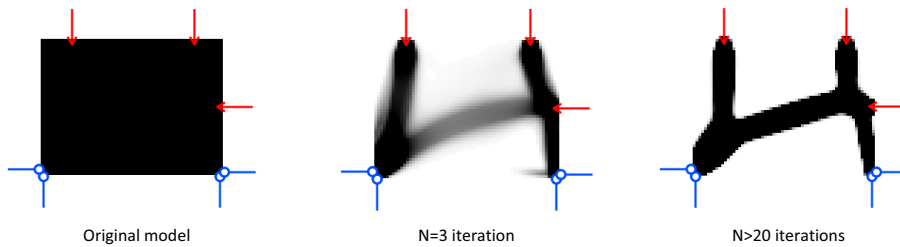
Figure 2: Topology optimisation in ForcePAD.

It is important to note that in this type of application the optimisation algorithm is used to provide the designer with ideas not the final solution. The user can stop the optimisation algorithm at any point and modify the model and restart the algorithm again.

User interface

To reduce the complexity of the ForcePAD user interface a task-oriented approach is used. This means that if the user is sketching, only tools relevant to that task are visible in the user interface, see **Error! Unknown switch argument.**.
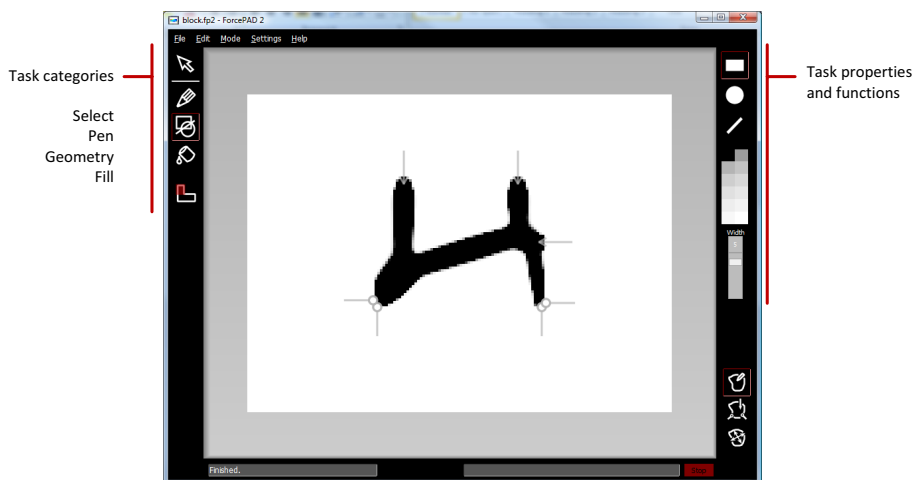
Figure 3: ForcePAD task oriented user interface.

There are 3 main modes in ForcePAD:

- Sketch mode – In this mode the model is created by painting with stiffness.
- Physics mode – In this mode the boundary conditions, such as loads and constraints are applied to the model.
- Action mode – In this mode analysis results can be viewed. It is also possible to modify loads and have the results updated in real-time.

Implementation

ForcePAD is C++ application that runs on Windows, Mac OS X and Linux. To enable this platform independence the FLTK user interface library [9] is used. The finite element code is implemented using the Newmat11 matrix library [10].

ForcePAD is an open source application [11] that can be downloaded from SourceForge.

Concluding remarks

ForcePAD provides a new user interface concept for modelling and optimisation that integrates well with the sketch based workflow of designers and architects. The user interfaces reduces the complexity of conventional finite element modelling, enabling easy updates of the model and quick feedback. The user interface is not limited to designers and architects; engineers can also use it as a tool for quickly illustrating design concept.

The reduced complexity also enables it to be effectively used in an educational setting, in which it also has been used for several years.

References

[1]   J. Lindemann et al, *An Approach to Teaching Architectural and Engineering Students Utilizing Computational Mechacnics Software ForcePAD*, ITcon Vol. 9, pg 219, 2004

[2]   J. Lindemann and G. Sandberg. *Design and Implementation of the Finite Element Software ForcePad*, Proceedings of 15th Nordic Seminar on Computational Mechanics, pp. 207–210, 2002.

[3]   J. Lindemann and G. Sandberg. *ForcePAD A New User Interface Metaphore for 2D Finite Element Modeling*, 9th US National Congress on Computational Mechanics, 2007.

[4]   Adobe Photoshop, http://www.adobe.com/products/photoshop/family, 2008

[5]   GIMP – GNU Image Manipulation Program, http://www.gimp.org, 2008

[6]   Paint.NET, http://www.getpaint.net, 2008

[7]   M. Bendsøe and O. Sigmund. *Topology Optimization - Theory, Methods and Applications,* Springer Verlag, Berlin Heidelberg New York, 2002

[8]   Pedersen, C. G., Lund, J. J., Damkilde, L. and Kristensen, A. S., *Topology optimization - Improved checker-board filtering with sharp contours,* Proceedings of 19th Nordic Seminar on Computational mechanics, pp. 4, 2006.

[9]   Fast Light Toolkit (FLTK), http://www.fltk.org, 2009

[10] R. Davies, *Newmat C++ matrix library*, http://www.robertnz.net/nm_intro.htm, 2008

[11] ForcePAD, http://forcepad.sourceforge.net/, 2009

Cost Optimization of Composite Aircraft Structures

Markus Kaufmann* and Dan Zenkert

Department of Aeronautical and Vehicle Engineering
Kungliga Tekniska Högskolan (KTH), Stockholm, Sweden
email: kaufmann@kth.se

Summary An integrated cost optimization framework for aircraft structures is presented and discussed by means of case studies. In particular, it is shown how the component design can be influenced by the introduction of the manufacturing cost, the inspection cost and a component specific fuel burn into the design process.

Introduction

Aircraft manufacturers aim to design airliners with the lowest possible direct operating cost (DOC). Looking at the drastic rise of the jet fuel price during the last decade, one can understand why a lot of efforts have been undertaken to lower the fuel consumption, whose cost is a substantial part of the DOC. One possible strategy to save fuel cost is to lower the structural weight. In order to lower the weight, manufacturers carefully introduced high-performance composite materials to the design of secondary and primary aircraft structures. The main advantages of carbon fiber reinforced plastics (CFRP) include the reduction of mass and number of parts, the option for complex and integrated shapes, improved fatigue life and generally improved corrosion resistance. The drawbacks of these materials are the higher manufacturing, repair and inspection costs, accompanied by a highly increased design complexity and complex damage tolerance management [1].

To some extent, the use of cost and weight data for the design optimization of aircraft structures was proposed in the literature [2–8]. Other information, such as producibility limits, post-production testing, or maintenance and repair issues were neglected, although they would impact the design decisions significantly. In this work, we included the material cost and the labor cost [8,9], cost for non-destructive testing [10] and an estimated lifetime fuel burn cost into one objective function, a simplified form of DOC. In addition, we examined the producibility of a design by simulating the draping of the prepreg material [11]. The overall framework is then exemplified by means of case studies.

Method

The problem was given as

$$
\begin{aligned}
min \qquad & DOC \text{ of a aircraft component} \\
subject\ to \qquad & \text{structural requirements} \\
& \underline{x}_i < x_i < \overline{x}_i, \quad i = 1 \ldots n.
\end{aligned}
\qquad (1)
$$

where DOC was the share of direct operating cost, x_i were design variables, and $\underline{x}_i$ and $\overline{x}_i$ were their lower and upper limits, respectively. The DOC were formulated as

$$ DOC = \alpha_1 C_{man} + \alpha_2 C_{\text{ndt,prod}} + N\alpha_3 C_{\text{ndt,serv}} + pW \qquad (2) $$

where C_{man} is the manufacturing cost of the component, and $C_{\text{ndt,prod}}$ and $C_{\text{ndt,serv}}$ are the cost for non-destructive testing in in-production and in-service inspection, p is a specific

fuel burn (in EUR/kg) and W the structural weight (in kg). The parameters α_i incorporate calibration factors due to depreciation, overhead cost and other adjustments, and N is the number of regular inspections during the lifetime of the component.
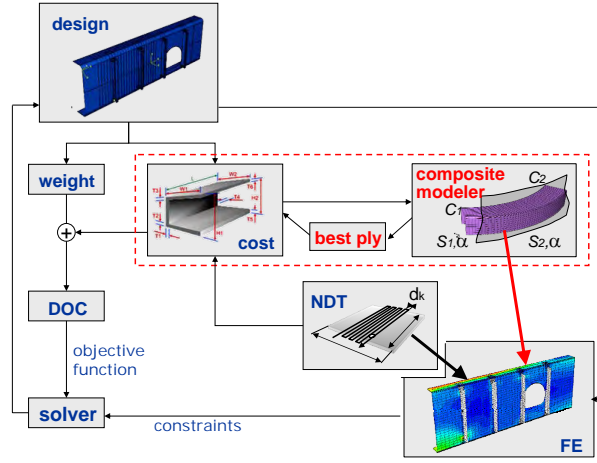
Figure 1: Proposed optimization framework

The proposed framework is shown in Fig. 1. As can be seen, it comprehends separate modules for the estimation of weight (ABAQUS/CAE), manufacturing cost (SEER-MFG) and structural performance (ABAQUS standard). The sequence of these estimations and the variables were handled by the solver (Xopt). In addition, the draping of the prepreg layers was modeled using a kinematic draping simulation (Composite Modeler, see Fig. 2). A set of best plies according to minimum material consumption or minimum fiber angle deviation rules was chosen from a previously generated draping knowledge database. The plies generated by Composite Modeler impacted then both the cost model (material consumption, ultrasonic cutting, number of plies needed) and the structural model (fiber angle after draping, number of plies).
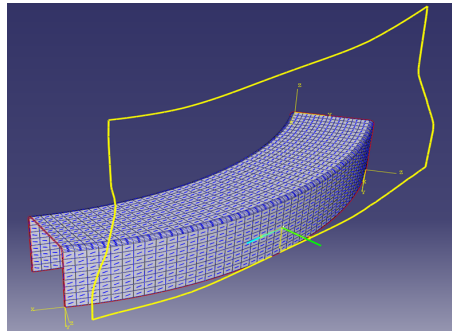
Figure 2: Simulated fiber angles in Composite Modeler

Another novel aspect was the implemented non-destructive testing model. This model affected again both the cost and the structural model, as the scan pitch of the ultrasonic scanner was varied throughout the optimization. On the cost side, the variable scan pitch influenced the scan cost, as less scan runs were anticipated during the post-processing of

the manufactured components. On the structural side, the scan pitch had an impact on the confidence of the testing in terms of quality assurance. For instance, a wider scan pitch lowered the confidence to find a defect of a certain size. This in turn lowered the strength of the material, as bigger flaws had to be taken into account for the design. Thus, the structural allowables were adjusted accordingly.

Results of the Case Studies

The optimization routine was implemented by means of the above mentioned tools and the scripting language Python. Using material data provided by Saab Aerostructures and Airbus, a series of case studies was performed.

Variable Weight Penalty

It could be shown that the design solution was dependent on the anticipated fuel cost during the lifetime of the aircraft. Stiffened panels, for example, underwent a change from a "coarsely stiffened skin with bulky stiffeners" to a "densely stiffened skin with fine stiffeners" configuration when the fuel cost was increased, see Fig. 3.

a) low-cost solution
(high weight, low C_{man}, C_{ndt})

b) low-weight solution
(high C_{man}, C_{ndt})
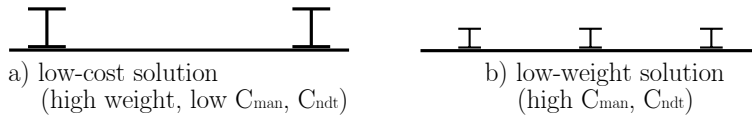
Figure 3: Change in stiffener configuration

Variable Laminate Quality

The implementation of non-destructive testing cost in the optimization framework allowed not only the cost/weight optimization of the panel, but also the optimization for an optimal quality level of the same. In particular, it was concluded that an optimized quality level tended towards much bigger flaws than commonly accepted today. Thus, the weight penalty of thicker structures was outweighed by the reduced testing cost (as a consequence of the lower quality level).

Sub-Optimization of Draping Parameters

Further, a draping knowledge database was generated for a double-curved C-spar as seen in Fig. 4. The C-spar was modeled and optimized using a M21/T800 prepreg material. For that prepreg material, one could again see the dependency of the solution on the fuel price. In particular, the "set of best plies" chosen would change from a solution with minimum material consumption to a solution with minimum fiber angle deviations (i.e. better structural performance) when the impact of the fuel price was increased during the design of the component

Concluding Remarks

We propose an optimization routine which includes various disciplines in the design of aircraft structures. These disciplines strongly interact with each other; the general objective of the framework, however, is to optimize for the lowest possible direct operating cost. The framework is promising and includes novel aspects not seen earlier in literature. In particular, the coupling between NDT and the structural model provides an interesting way to

include quality assurance already in the design process. Further, the implementation of a draping knowledge database enables the designer to optimize the layup with fiber angles closer to reality; it further influences the design with producibility constraints in an early design phase.
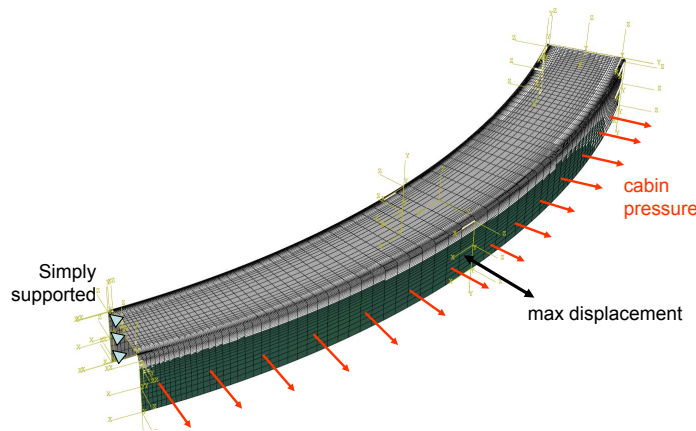
Figure 4: C-Spar modeled in ABAQUS/CAE

References

[1] C. Soutis. Fibre reinforced composites in aircraft construction. *Prog. Aerosp. Sci.*, **41(2)**, 143–151, (2005).

[2] T.S. Geiger and D.M. Dilts. Automated design-to-cost: Integrating costing into the design decision. *CAD Comput. Aided Des.*, **28(6-7)**, 423–438, (1996).

[3] B. Heinmuller and D.M. Dilts. Automated design-to-cost: Application in the aerospace industry. *In: Proceedings of Annual Meeting of the Decision Sciences Institute*, 1227–1229, (1997).

[4] M.G. Bader. Selection of composite materials and manufacturing routes for cost-effective performance. *Compos. Part A*, **33(7)**, 913–934, (2002).

[5] C.H. Park, W.I. Lee, W.S. Han and A. Vautrin. Simultaneous optimization of composite structures considering mechanical performance and manufacturing cost. *Compos Struct*, **65(1)**, 117–127, (2004).

[6] R. Curran, A. Rothwell and S. Castagne. Numerical method for cost-weight optimization of stringer-skin panels. *J. Aircraft*, **43(1)**, 264–274, (2006).

[7] A. Iqbal and J.S. Hansen. Cost-based, integrated design optimization. *Struct. Multidisc. Optim.*, **32(6)**, 447–461, (2006).

[8] M. Kaufmann, D. Zenkert and P. Wennhage. Integrated cost/weight optimization of aircraft structures. *Struct. Multidisc. Optim.*, doi 10.1007/s00158-009-0413-1, (2009).

[9] M. Kaufmann, T. Czumanski and D. Zenkert. Manufacturing process adaptation for the integrated cost/weight optimisation of aircraft structures. *Plast. Rubber Compos.: Macromol. Eng.*, **38(2)**, 162–166(5), (2009).

[10] M. Kaufmann, D. Zenkert and C. Mattei. Cost optimization of composite aircraft structures including variable laminate qualities. *Compos. Sci. Technol.*, **68(13)**, 2748–2754, (2008).

[11] M. Kaufmann, D. Zenkert and M. Åkermo. Cost/weight optimization of composite prepreg structures for best draping strategy. Accepted for publication in *Compos. Part A*, (2009).

Optimization of steel portal frames using genetic algorithms

Petr Hradil*, Matti Mielonen, Ludovic A. Fülöp

VTT Technical Research Centre of Finland
Espoo, Finland
e−mail: Ludovic.Fulop@vtt.fi

Summary   The study focuses on the optimization of steel portal frames, and on the proper use of different analytical methods including stability calculations. Our goal is to develop an effective tool which can produce optimal frame geometry and help designers to keep up with growing demands on price. Frames are analyzed in Abaqus/Standard or MS Excel and a real-coded genetic algorithm is used for finding optimal configurations satisfying Eurocode requirements.

Introduction

Low-rise commercial and industrial structures, utilizing portal frames (Figure 1), represent a very significant part of the steel construction market. As a consequence, portal frames are subjected to attempts of reducing their cost and increasing their efficiency [1]. Within the RFCS-PRECASTEEL project we use the latest improvements in computational resources, both in terms of hardware and FEA software, in order to make a step further in portal-frame optimization.
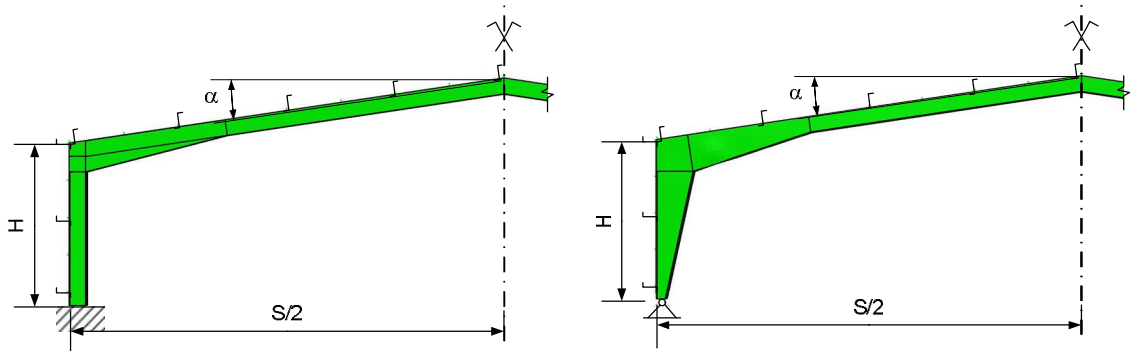
Figure 1: Basic frame types: hot-rolled sections (left) and welded (right)

Procedures used for the analysis of frames

One prerequisite of an optimization attempt is the existence of an analysis procedure, which produces results at a level of accuracy comparable to what is expected to be saved by the optimization. If the analysis procedure is too conservative, over-simplifying or not reliable, the optimization procedure can not be expected to compensate for the inadequacies of analysis produced. While, at first look, portal-frames appear simple they often conceal particular design difficulties. Therefore, in this study, special care has been placed on using adequate analysis procedures, even at a higher computational cost.

The analysis methods are divided into three levels according their accuracy, complexity and speed (Table 1). We developed automated scripts for Excel and Abaqus where the user can choose to load the models with vertical dead load, snow, wind and seismic actions. Results are expressed as

vertical load-carrying-capacity for ultimate limit state (ULS) and serviceability limit state (SLS), and they are passed to the optimization procedure which generates a new set of frames. Optimized frame geometry can usually be reached after several repetitions (Figure 2).

	Method 1	Method 2	Method 3
Software used	MS Excel	Abaqus/Standard	Abaqus/Standard
Geometry	2D wire model	2D wire model, 3D shell for buckling	3D shell model
Tapering	stepped – 4 divisions	stepped – 10 divisions and continuous shell	continuous shell
Global stability	sway imperfections	sway imperfections	sway imperfections
In-plane stability	reduction factors	deformed shape	deformed shape
Out-of-plane stability	reduction factors	global reduction factor	deformed shape
Material plasticity	plastic sect. resistances	elastic-plastic material	elastic-plastic mat.
Geometric non-linearity	linear calculation with 2nd order amplifier	non-linear calculation (when needed)	non-linear calculation
Calculation steps	1 step: LA	3 steps: LBA-y, LBA-z and GMNIA	2 steps: LBA and GMNIA
Calculation time	approx. 1 sec.	approx. 30 sec.	approx. 100 sec.

Table 1: Design methods

Method 1: Local member checks using interaction formulae (EN 1993-1-1, 6.3.3. [2])

The standard method often used by designers is based on individual checks of columns and rafters using internal forces from linear elastic analysis (LA). Load-carrying capacity can be predicted by design codes (e.g. EN 1993-1-1 [2]) in case of interaction of axial compression and major axis bending. However, the application of stability rules is difficult, especially when members have variable cross-sections, and/or the support conditions are non-conventional (e.g. not in the shear centre). If lateral torsional buckling (LTB) dominates, the critical load calculation becomes challenging. In practice, the factors corresponding to weak axis flexural buckling and LTB are doubtful when the member has eccentric supports, while the interaction factors and the meaning of axial and bending capacity are open to interpretation when the member has variable cross-section.

Method 2: General method (GM) for lateral buckling and LTB (EN 1993-1-1, 6.3.4. [2])

The general method is using the results of global (i.e. structure level) buckling and yield analyses to predict the capacity of the structure. The multipliers of loads corresponding to global buckling (α_{CR}) and yielding without buckling (α_{ult}) are the basis of calculating the load bearing capacity.

Method 3: Global nonlinear analysis

Global non-linear analysis (GMNIA) is used on the 3D shell model of the frame with imperfections obtained from the previous shell buckling analysis (LBA). The calculation is slower, but it provides complete load-deflection relationship including local and global stability.

Calculation performance

In order to reduce the run-time of the procedure, if multiple frames are submitted, the script is able to analyze several frames at the same time by redistributing computer memory and effectively using available processor cores. The procedure is also automatically maintaining a database of results, to avoid repeating calculations. Certain model simplifications are automatically selected when appropriate, and the script constantly monitors results of non-linear calculation in order to terminate the step when the data are enough to extract design values.
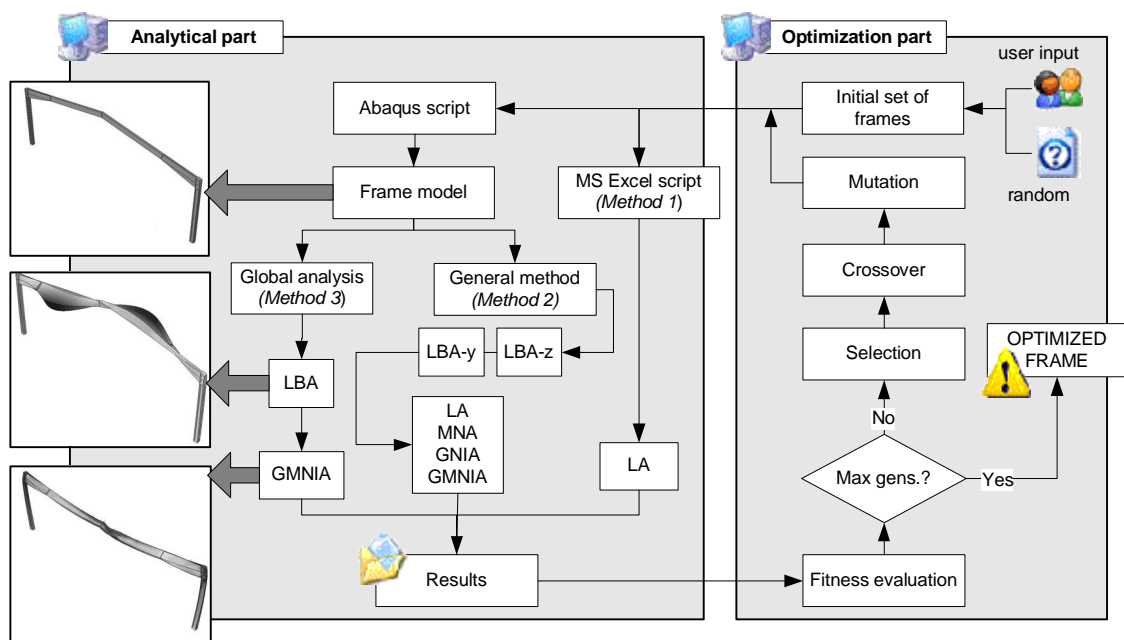
Figure 2: Analysis and optimization diagram

Optimization procedures using genetic algorithm (GA)

The optimization is using GAs, a procedure which tries to mimic natural evolution process. First, an initial population is created and analyzed and the fitness of each individual is evaluated. Second, a new population is created by favouring the fittest individuals and by applying genetic operators, such as crossover and mutation. The GA proceeds iteratively towards the optimal solution by creating a new population from the previous one. Elitism ensures that the best solution is kept during all of the genetic operations, and while no proof of convergence in finite time exists, good results are found in reasonable time.

Use of GAs for portal frame optimization

The portal-frame optimization is a mixed-integer non-linear problem. Classical direct and gradient-based methods have difficulties with these kinds of problems. On the other hand, GAs have been extensively used in structural optimization, having several advantages: multiple variables can be handled, parallel computing is possible, and coding procedure is straightforward.

A real-coded genetic algorithm (RCGA) can handle discrete and real variable types easily and has been chosen for this problem. With RCGA, the coding-decoding characterizing binary-coded GAs is also avoided. The obvious choices for optimization are the profiles of the column and beam, when the frames are made of hot-rolled sections (Figure 1.a). Cross-sectional dimensions can be selected as variables when the frames are made of welded sections (Figure 1.b). Other variables could be: the steel grade, the haunch ratio and the roof angle of the frame.

Optimization literature provides a large catalogue of different selection, crossover and mutation operators that can be combined to create a GA suited for the problem at hand. In this study, the well known simulated binary crossover (SBX) [3] and parameter based polynomial mutation operator [4] are compared with a new algorithm combining Laplace crossover and power mutation

[5]. Both crossover operators have a self-adapting behaviour, which favours creating children near to parents, when the parents are near to each other in the variable space.

The algorithm can be used with all of the analytical methods (Table 1). The objective function is quickly evaluated with the MS Excel tool, which enables a fast optimization of the desired configuration. The Abaqus based methods (Table 1) are considerably slower, even when reusing previously saved results from the database file, in order to avoid recalculating some objective functions. In both cases, the GA runs for predetermined number of generations, and the best configuration is given as an output.

Concluding remarks

In order to exemplify possible results, selected data gathered in the database file of a GA run using Method 3, is presented in Figure 3. The frame had the following parameters: S=20m, H=6m, T=6m, L_{Haunch}=3.6m, α=15%, G_k=380N/m^2, Q_k=750N/m^2, 3 + 5 purlins. Positive feasibility means that the frame fulfils both ULS and SLS criteria. In this case the mass/weight of the frame is accepted as measure of the performance, and it can be observed that the lightest feasible frame uses IPE500A column and IPE330 beam, and weights about 2.1 tons.
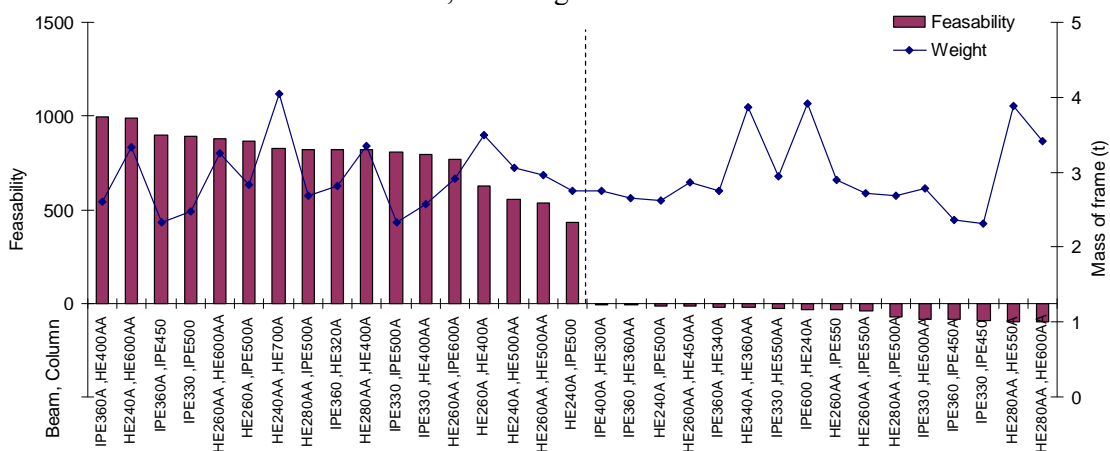
Figure 3: Possible configurations for a 20m span, 6m high, fixed base frame

References

[1]   Kravanja, S., and T. Zula. Cost optimization of industrial steel building structures. *Advances in Engineering Software* In Press, Corrected Proof. doi:10.1016/j.advengsoft.2009.03.005.

[2]   Eurocode 3: Design of steel structures – General rules and rules for buildings. EN 1993-1-1, Part 1-1. (2003)

[3]   Deb, K. & Agrawal, R.B. 1995. Simulated binary crossover for continuous search space. Complex Systems, , No. 9, pp. 115-148.

[4]   Deb, K. & Goyal, M. 1998. A Flexible Optimization Procedure for Mechanical Component Design Based on Genetic Adaptive Search. Journal of Mechanical Design, June 1998, , No. 2, pp. 162-164.

[5]   Deep, K., Singh, K.P., Kansal, M.L. & Mohan, C. 2009. A real coded genetic algorithm for solving integer and mixed integer optimization problems. Applied Mathematics and Computation, 6/15, Vol. 212, No. 2, pp. 505-518. ISSN 0096-3003.

Recent development of the CALFEM software

Per-Erik Austrell, Jonas Lindemann, Johan Lorentzon, Kent Persson, and Göran Sandberg

Department of Structural Mechanics

Lund University, Lund, Sweden
e−mail: calfem@byggmek.lth.se

Summary   Some new developments of the MATLAB based finite element software CALFEM are discussed. Functions making it possible to generate arbitrary triangular and quadrilateral meshes are currently being developed. Moreover, a stand-alone version of CALFEM is also in progress that makes use of the open source PYTHON environment. This version of the program is shortly discussed with an example of the syntax, to show the similarities. Finally a web site connection to improve the development work of CALFEM is discussed.

Introduction

The name of the finite element software CALFEM is an abbreviation of 'Computer Aided Learning of the Finite Element Method'. CALFEM has been used for several years in research and education at Lund University and in many other places worldwide. The down-loads of this open-source software are counted in thousands. CALFEM was originally developed at the division of structural mechanics and the first versions were written in FORTRAN. But since 1993 it has been adapted to MATLAB by a development work conducted at the division of Structural Mechanics and the division of Solid Mechanics at the department of Construction Science, Lund University.

Although CALFEM is now very much used in research, it was at the beginning developed to be used in education, for the purpose of giving a deeper understanding of the finite element method, without requiring too much programming efforts from the students. This was accomplished by FORTRAN subroutines, and is now accomplished by MATLAB-functions for the basic steps needed in solving problems by finite elements. For example, there are functions for creating element matrices, assembling them to a system of equations, and solving the global system for nodal quantities etc.

CALFEM is integrated in the education in several courses, given by Structural mechanics and Solid mechanics departments on under-graduate as well as post-graduate level. This means that students do exercises, projects and also master thesis works using CALFEM as the major tool. Moreover, post graduate students also use it as a tool in their thesis work.

This presentation concerns the recent development of the software. The major new features concerns mesh generation, a transcript of the code to PYTHON environment, and the use of the web-site SourceForge to take advantage of development work done in other places.

Mesh generation

When students use CALFEM in education and in master thesis or PhD-works they look at idealized model problems with simple geometry, but often also on more realistic problems with complex geometry. Until recently the support for mesh generation in CALFEM has been very limited. However, in a new development, one now has the option in CALFEM to generate two-dimensional triangular or quadrilateral meshes, based upon a triangular or quadrilateral surface topology.

The basic geometry in the mesh generation consists of vertices and segments, defined from an oriented polygon, i.e. the vertices are supposed to be oriented consecutively in clockwise direction on an arbitrary polygon. Two consecutive vertices define a segment.
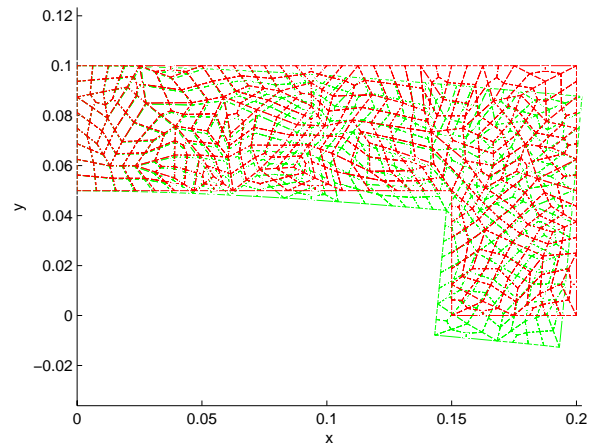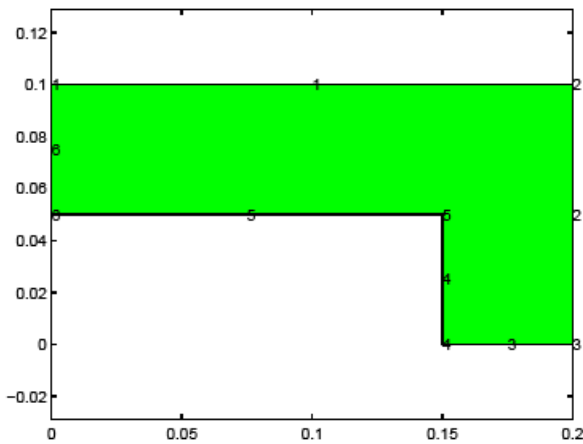
Figure 1. Example of unstructured quad mesh generation on an L-shaped consol.

From this basic geometry definition (left hand side in Figure 1) a structured or unstructured triangular mesh can be generated. The triangular mesh can then be further converted to a quadrilateral mesh. This is shown on the right hand side of the figure above, in the case of an unstructured triangular mesh as a base.

Tools to validate, extract degrees of freedom, smooth and correct the mesh provides the user with tools to refine and handle the generated mesh.

Example of new functions for mesh generation, in the L-shaped beam case (figure above), is as follows (preliminary syntax). The CALFEM code given here generates the geometry and the un-deformed mesh shown in Figure 1:

```
% ----------- basic geometry definition -------------------

l = 0.2; w = 0.05; h = 0.1;

vertices = [0.0 h; l h; l 0.0; l-w 0.0; l-w h-w; 0.0 h-w];

segments = [1 2 1; 2 3 1; 3 4 1; 4 5 1; 5 6 1; 6 0 1];

nen=3; dofsPerNode=2; maxArea=1e-4;

mp=[maxArea dofsPerNode nen];

geomdraw2(vertices,segments,mp)

% ----- generation of unstructured triangular elements ------

dbtri=unstri2d(vertices,segments,mp);

% ------ generation of quads from triangular elements -------

dbquad=tri2quad(dbtri);

% ------------- extraction of mesh quantities ---------------

[coord edof dof nen]=extractdb(dbquad);
```

A more complex example of two-dimensional meshing is shown in Figure 2. Several triangular ~~~ments
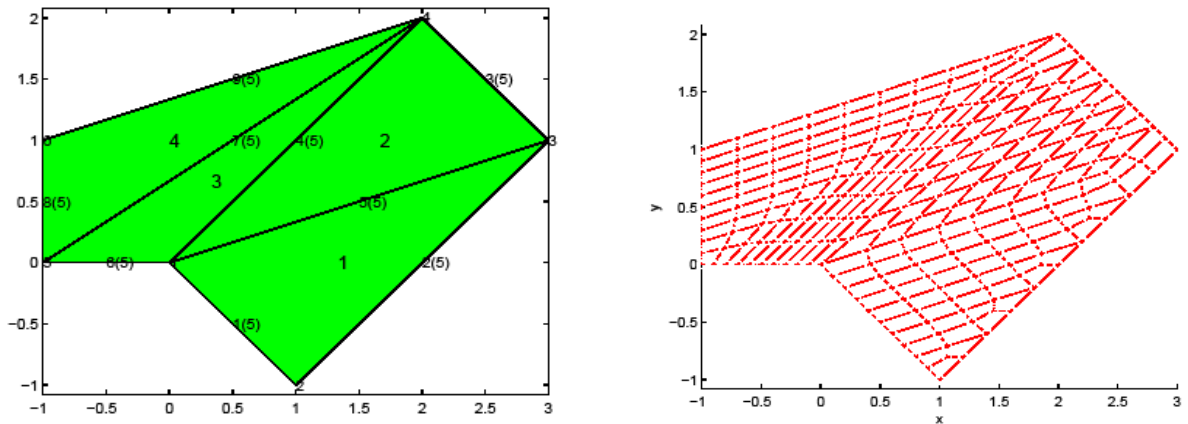
Figure 2. Several surfaces connected and meshed seamlessly along the edges.

CALFEM and Python:

To be dependent and connected to a big technical software like MATLAB, has advantages but also some apparent disadvantages. Although there are student versions of MATLAB for free use, it is a quite costly program for non students and say small companies that want to use it mainly for finite element analysis trough the use of CALFEM.

In order to circumvent this problem a special version of CALFEM, pyCALFEM, is under development. This version will implement all the CALFEM commands using the NumPy-library a Python module providing the necessary matrix support.

The following code illustrates the pyCALFEM use for a two-dimensional truss of 12 dofs:

```python
# -----------------------------------------------------------------
# PURPOSE:   Analysis of a plane 2D-truss structure
# -----------------------------------------------------------------

from numpy import *
from pycalfem import *

# ----- Topology, coordinate, and element properties ------------

K=zeros([12,12])

f=zeros([12,1]); f[10]=1e6

A=25.0e-4; E=2.1e11; ep=[E,A]

ex = array([
    [0., 2.],
    ...
    [0., 2.],
    [2., 4.]])

ey = array([
    [2., 2.],
    ...
```

239

```
        [2., 0.],
        [2., 0.]])

Edof = array([
    [1, 2, 5, 6],
    ...
    [1, 2, 7, 8],
    [5, 6, 11, 12]])

# --------- Assemble and solve the system of equations ----------

for elx, ely, eltopo in zip(ex, ey, Edof):
    Ke = bar2e(elx, ely,ep)
    assem(eltopo,K,Ke)

bc = array([1,2,3,4])
a, r = solveq(K,f,bc)

# ------------ Evaluate the element forces -----------------------

ed=extract(Edof,a);
N=zeros([Edof.shape[0]])

i = 0
for elx, ely, eld in zip(ex, ey, ed):
    N[i] = bar2s(elx,ely,ep,eld);
    i=i+1
```

CALFEM as a collaborative effort

To enable users to provide code as well as take advantage of new features which are not in the stable releases, CALFEM is now available on SourceForge. This web-site provides services for open source project such as:

- File release system for distributing stable packages.
- Source version management service providing source code control using subversion, enabling multiple developers to work on the code simultaneously.
- Detailed statistics on the number of downloads and code commits in the version management system.
- Forum for users of the package.

By using the SourceForge environment the development of CALFEM can be encouraged by third party developers by providing them access to development code as well as stable releases.

References

[1] O. Dahlblom and P-E Austrell et. al. CALFEM A finite element toolbox to MATLAB. *Department of Structural mechanics report TVSM 9001*, (1999).

[2] O.C. Zienkiewicz and R.L. Taylor. *The Finite Element Method*. McGraw-Hill, London, Fourth edition, (1989).

Designing with uncertainties

Tobias Lindberg and Kent Persson

Department of Construction Sciences
Lund University, Lund, Sweden
e−mail: tobias.lindberg@byggmek.lth.se

Summary   A computer-based methodology based on the Latin Hypercube Sampling technique is presented that is aimed at locating sensitive areas within the building industry where the tolerances need to be kept small. This methodology could also be a helpful tool for architects to find new designs and to find the influence the choice of material, form etc in the initial phase of the design process.

Introduction

Josephson and Saukkoriipi [1] found that 30-35% of the production cost for a building project in Sweden is wastage. Approximately 10% of this wastage could be related to production errors and controls and another 10% could be related to misuse of resources i.e. material wastage, downtime etc. These problems, specified above, could be related to one common denominator; imperfections.

Imperfections are defined as something - not perfect, defective or inadequate[1]. In this context imperfection is related to the probabilistic nature of reality i.e. it is not possible, or at least, very difficult and therefore very expensive to produce building components or structures that are perfect regarding dimensions, material properties etc. These imperfections may, or may not have a great influence on the functionality of the component or structure.

Imperfections can be either definable or indefinable;
Definable imperfections a.k.a. "*Tolerances*" are expected deviations within a pre-defined interval based upon experience e.g. manufacturing tolerances for building components or specification regarding the functionality. These intervals are regulated in Sweden by the Swedish building code, HusAMA.
Indefinable imperfections a.k.a. "*Errors*" are deviations outside any pre-defined tolerance interval.

In the building industry the concept of tolerances is widely known. The understanding of how tolerances, used locally, affect the global behaviour and in the end the functionality of the component or structure is, however, often vague.

It seems to be a general opinion within the building industry that there is nothing, or very little, to gain in optimization since, in the end, the methods used in the production phase and the environment at the construction sites are so rough that the delicate refinement is lost in the safety-margins needed.
However, there is a great demand from the building industry for techniques securing the esthetical and functionality (ex load-bearing capacity) directives specified for a building i.e. that the tolerances are observed.

---

[1] wordnet.princeton.edu/perl/webwn

Physical Uncertainties

The three components; material, structure (geometry and boundaries) and load can, to a certain degree, be seen as physical variables with semi-random characteristic. When looking at techniques for securing that the esthetical and functionality (ex load-bearing capacity) directives specified for a building are observed, focus is set on the semi-random characteristic of the structure solely.

To illustrate the role of the uncertainties, a frame with three columns and two beams is considered. A "block" is placed on respective beam with a specified distance, d_{init}, between them. See Figure 1. Due to imperfections at the foot of the column the location and inclination of respective column is decided from the three stochastic variables u, v and w.
Due to imperfections in the production the length of the columns and beams are not exact.
In Table 1 the input data as nominal value and the tolerance interval for each structural member is presented.
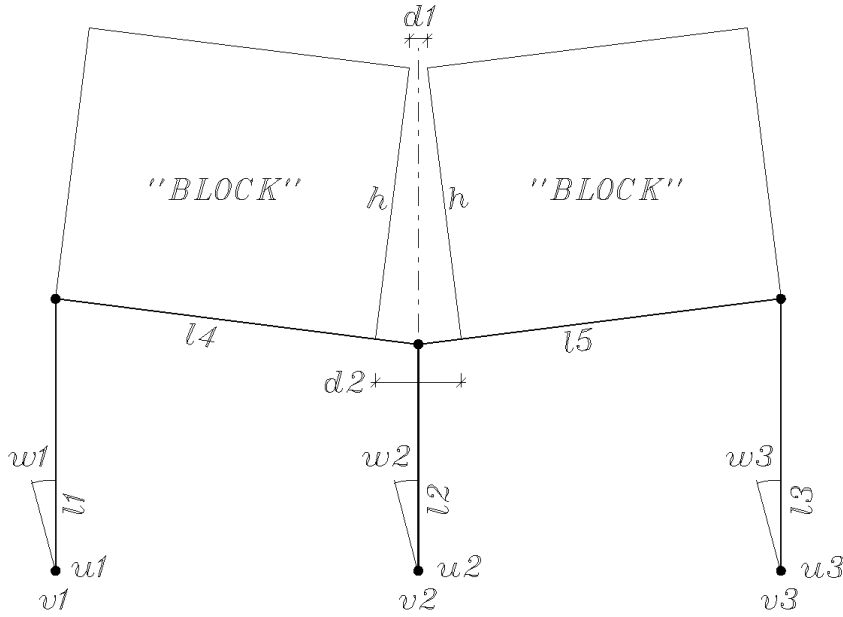
Figure 1: Geometry of the structure.

ID	u1	v1	w1	u2	v2	w2	u3	v3	w3
Nominal	0	0	0	0	0	0	0	0	0
±	5	5	5/1000	5	5	5/1000	5	5	5/1000

ID	l1	l2	l3	l4	l5	h	d_{init}		
Nominal	3000	3000	3000	4000	4000	3000	10		
±	2	2	2	2	2	0	0		

Table 1: Input data as nominal values and tolerance intervals given in millimetres.

If one assumes a discrete variation within each interval in even millimetres the number of possible combinations (samples) would be $11^9 \times 5^5 \approx 7369 \times 10^9$. By adopting the Latin Hypercube Sampling technique described in [2] it is possible to get a good representation of the stochastic field with considerably less number of samples.

From the different sets of input the distance between the two "blocks", d1 and d2, can be calculated as the output variables. Since the two "blocks" can not overlap each other the output variables d1 and d2 are adjusted so that the minimum distance is set to zero.

With 1×10^5 samples (approximately 5 minutes run-time on a Dell Precision M60) the following histogram, showing the distribution of the gap size at the bottom, is presented. See Figure 2.
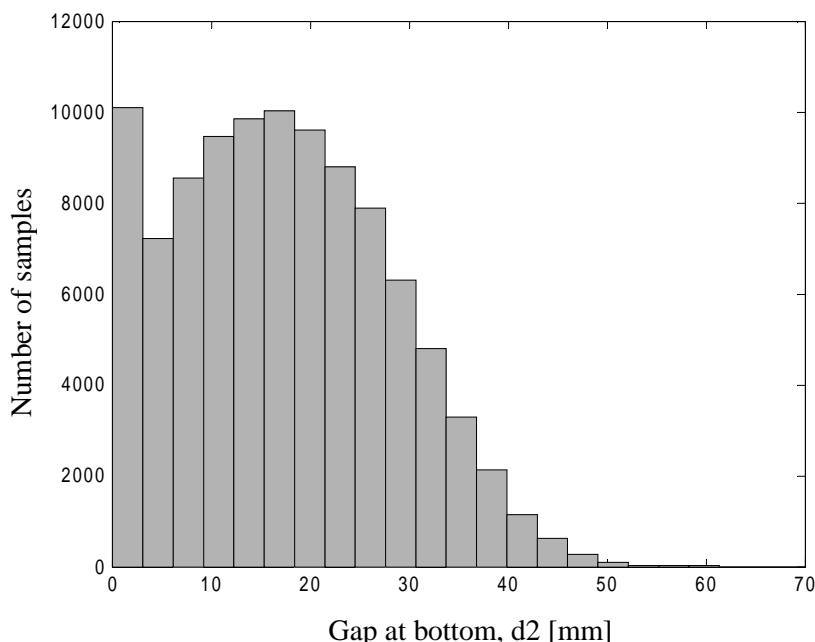
Figure 2: Distribution of the gap size at the bottom, d2.

The mean- and median value is approximately 17.4 mm and 16.8 mm respectively. The 95th percentile is approximately 36.0 mm meaning that the probability of getting a distance greater than 36.0 mm is 0.05 or less.

Most likely this magnitude of deviation from the prescribed value of $d_{init} = 10$ mm is unacceptable but with this computer-based methodology it is a simple task to perform a sensitivity analysis to identify where the tolerance should be more strict.

E.g. by setting the tolerance interval of the stochastic variable w to ±2.5/1000 instead of ±5/1000 the mean- and median value is approximately 13.2 mm and 12.8 mm respectively. The 95th percentile is approximately 18.4 mm which is considerably better.

In reality there are a lot more stochastic variables involved e.g. uncertainties in the loading and in the stiffness of the different members. By applying more sophisticated computational methods such as e.g. FEM it is possible to get a more complete picture of the structural behaviour due to the different uncertainties.

Architectural freedom

Another area in which this computer-based methodology comes in handy is when the prerequisites are vague. In this case it is also possible to add the material and the load as stochastic variables so that the architect/engineer has the possibility to "play around" with different materials, shapes etc.

Concluding remarks

By applying a computer-based methodology based on the Latin Hypercube Sampling technique it is possible to analyze where, in the structure, it is profitable and/or necessary to increase the tolerances. This methodology also gives the architect the artistic freedom to explore many different visions in the initial phase.

References

[1] Josephsson P-E and Saukkoriipi L. Slöseri i byggprojekt. *FoU-Väst Rapport*, **0507**, 7, (2005).

[2] Olsson A. *Probabilistic analysis and reliability of engineering structures*. LTH Lund, Sweden, (2002).

Uncertainty analysis of the mechanics of the heart

Harald Osnes*

Dept. of Mathematics, University of Oslo, Oslo, Norway
Also at Simula Research Laboratory, Fornebu, Norway
e–mail: osnes@math.uio.no

Stuart R. Clark and Joakim Sundnes

Simula Research Laboratory, Fornebu, Norway

Summary   This paper presents an uncertainty analysis of the passive behaviour of the left ventricle of the heart. By utilising a recently developed stochastic method, the probabilistic collocation method, we conducted several test cases for equations governing the passive filling phase of the cardiac cycle. We conclude that this stochastic method is well suited to be employed for the problem of consideration. In addition, it is more efficient than the Monte Carlo simulation method.

Introduction

In this paper, we add to a more than two decades of heart-mechanics research by solving for the uncertainty in the passive filling phase of the cardiac cycle. Such research includes advanced finite element solvers accounting for the relatively complex three-dimensional geometry of the ventricles, the anisotropic behaviour caused by the fibrous-sheet structure of the myocardium, and the geometric nonlinear effects due to the large deformation of the cardiac tissue [1, 2]. Furthermore, various nonlinear constitutive laws or stress-strain relations containing a set of material parameters have also been introduced. Due to the fact that the material coefficients govern the behaviour of the medium, the choice of parameter values is of great importance. Attempts on determining material parameters through biaxial tests of thin rectangular slices cut from the ventricular wall have been performed. However, it is known that such tests do not capture the entire three-dimensional *in vivo* behaviour of the myocardium [2]. Thus, the material properties are subjected to a considerable amount of uncertainty, which means that the problem is most consistently dealt with in a stochastic framework [3].

The most common way of solving stochastic differential equations numerically, is to apply the Monte Carlo simulation (MCS) method. However, due to the large number of realizations required, the method can be computationally intensive. In the present paper we investigate a recently developed technique, denoted the probabilistic collocation method (PCM). In the context of stochastic differential equations it has been applied in areas as for example computational fluid dynamics [4], porous media flow [3] and sedimentary basin modelling [5].

Mechanics of the heart

For simplicity, we consider only the equations governing the passive behaviour of the left ventricle of the heart. Thus, the analysis is restricted to the filling phase of the cardiac cycle. The governing partial differential equation reads

$$\nabla \cdot (\boldsymbol{F}\boldsymbol{S}) = \boldsymbol{0}, \quad \boldsymbol{x} \in H, \tag{1}$$

where $\boldsymbol{F}$ is the deformation gradient, $\boldsymbol{S}$ is the second Piola-Kirchhoff stress tensor, and H is the computational geometry. Following Vetter and McCulloch [1], Thorvaldsen et al. [6] and Osnes et

al. [7] we employ a transversely isotropic version of the exponential strain energy function

$$
\begin{aligned}
\Psi &= \frac{1}{2}C(e^W - 1) + K(J \ln J - J + 1), \\
W &= b_{ff}E_{ff}^2 + b_{xx}(E_{ss}^2 + E_{nn}^2 + E_{sn}^2 + E_{ns}^2) \\
&+ b_{fx}(E_{fn}^2 + E_{nf}^2 + E_{fs}^2 + E_{sf}^2).
\end{aligned}
\tag{2}
$$

Here C, b_{ff}, b_{xx}, b_{fx} and K are the uncertain material parameters, E_{ij} are components of the Green-Lagrange strain tensor, and J is the determinant of the deformation gradient $\boldsymbol{F}$. In the following we investigate the influence of the uncertainty in the material parameters upon several output quantities of the model.

Probabilistic collocation method

By considering the response variable as a polynomial expansion of the input parameters, uncertainty in the response function can be determined from the probability density functions of the input variables. Let $\boldsymbol{\xi} = (\xi_1, \xi_2, \ldots, \xi_N)^T$ be a vector of N independent random input variables. Then the stochastic output quantity y, for example the longitudinal displacement at apex or the end-diastolic cavity volume, may be expressed as an infinite polynomial chaos expansion [3]. In practical applications, the chaos expansion is usually truncated by finite terms. It can then be expressed as

$$
y(\boldsymbol{\xi}) = \sum_{j=1}^{P} b_j \Phi(\boldsymbol{\xi}),
\tag{3}
$$

where b_j are P deterministic coefficients to be determined, and $\Phi(\boldsymbol{\xi})$ are functions derived from the chaos expansion. Applying an expansion of degree d means that the number of terms P in (3) is given by

$$
P = \frac{(N + d)!}{N!d!},
\tag{4}
$$

where N still is the random dimension. Then we establish an equation system for the coefficients b_j in (3). In order to calculate the response parameter(s) of interest, the governing equation (1) must be solved. However, due to the random nature of the material parameters in (2), the partial differential equation is stochastic. The idea of the PCM and similar stochastic methods is to multiply the governing equation by a set of weighting functions $w_j(\boldsymbol{\xi})$ and taking the expectation. In the PCM, the weighting functions are defined by

$$
w_j(\boldsymbol{\xi}) = \delta(\boldsymbol{\xi} - \boldsymbol{\xi}_j), \quad j = 1, \ldots, P,
\tag{5}
$$

where δ is the Dirac delta function and $\boldsymbol{\xi}_j$ is a particular set of sampling points, typically determined as the most probable combinations of the roots of the function of order $d + 1$ from the chaos expansion [3]. This means that in the PCM the governing equation has to be solved P times, and in most problems P is several orders of magnitude smaller than the number of realizations required in the MCS method. Finally, the stochastic properties of the response quantity or quantities can be obtained through some simple analytical manipulations of (3) or by MCS of the same explicit algebraic formula, which is a very fast process.

Results and discussion

In this section we present some preliminary simulation results for the uncertainty analysis of the passive filling phase of the left ventricle. In agreement with Thorvaldsen et al. [6] and Usyk et al. [8] the ventricle is modeled as a truncated ellipsoid. A realistic fiber field is adopted; the angle between the fibers and the unit vector in the circumferential direction varies from -45° at the epicardium to $+45^o$ at the endocardium. The boundary conditions applied are as follows: At the basal (or equatorial) plane none of the nodes are allowed to move in the longitudinal direction. Furthermore, a limited set of base nodes is also restricted from displacement in one of the transverse directions. Finally, at the endocardium we apply a cavity pressure increasing from 0 to 2 kPa during the passive filling phase, while the normal stress at the epicardium is assumed to be zero.

Before running the simulations, the statistical properties of the uncertain material parameters in (2) must be determined. Since C and K are positive-valued multiplicative factors, they are assumed to be Log-Normally distributed, while Normal distributions are adopted for the rest of the parameters. The expectation values of the parameters are picked from [7]. As pointed out in the introduction, the uncertainty of the input parameters is considerable. Thus, the coefficient of variation (which is defined as the standard deviation divided by the expectation value) is set to 0.15 for all the variables. It should also be mentioned that we apply a polynomial chaos expansion of degree $d = 2$, which means that the number of terms P in the expansion (3) equals 21. This number also defines the number of realizations required. The stochastic results, along with the assumptions for the input parameters, are listed in Table 1, see the column denoted Case 1. It is seen that the uncertainty of the material parameters plays a crucial role on the longitudinal displacement at apex

Table 1: Statistical properties of the input and response (longitudinal displacement at the apex, u_{apex}, increase in cavity diameter near the base, Δd, and increase in cavity volume, ΔV_{cav}, during the filling phase) parameters. The expectation (E) and standard deviation (SD) are listed for the input parameters. For the response quantities the coefficient of variation (COV=SD/E) is also included.

Parameter	Case 1	Case 2	Case 3	Case 4	Case 5	Case 6
C (Pa) LogNormal	E=80.0 SD=12.0	E=80.0 SD=12.0	E=80.0 SD=0.0	E=80.0 SD=0.0	E=80.0 SD=0.0	E=80.0 SD=0.0
b_{ff} Normal	E=20.0 SD=3.0	E=20.0 SD=0.0	E=20.0 SD=3.0	E=20.0 SD=0.0	E=20.0 SD=0.0	E=20.0 SD=0.0
b_{xx} Normal	E=12.0 SD=1.8	E=12.0 SD=0.0	E=12.0 SD=0.0	E=12.0 SD=1.8	E=12.0 SD=0.0	E=12.0 SD=0.0
b_{fx} Normal	E=8.0 SD=1.2	E=8.0 SD=0.0	E=8.0 SD=0.0	E=8.0 SD=0.0	E=8.0 SD=1.2	E=8.0 SD=0.0
K (kPa) LogNormal	E=100.0 SD=15.0	E=100.0 SD=0.0	E=100.0 SD=0.0	E=100.0 SD=0.0	E=100.0 SD=0.0	E=100.0 SD=15.0
u_{apex} (mm)	E=4.07 SD=0.63 COV=0.15	E=4.00 SD=0.22 COV=0.055	E=4.01 SD=0.098 COV=0.024	E=4.04 SD=0.58 COV=0.14	E=4.02 SD=0.048 COV=0.012	E=4.00 SD=0.016 COV=0.0040
Δd (mm)	E=6.9 SD=0.24 COV=0.035	E=6.89 SD=0.11 COV=0.016	E=6.89 SD=0.090 COV=0.013	E=6.90 SD=0.12 COV=0.017	E=6.91 SD=0.15 COV=0.022	E=6.89 SD=0.0048 COV=0.0007
ΔV_{cav} (mm^3)	E=6244.6 SD=414.6 COV=0.066	E=6204.0 SD=183.3 COV=0.030	E=6211.6 SD=122.9 COV=0.020	E=6228.2 SD=314.0 COV=0.050	E=6225.1 SD=156.0 COV=0.025	E=6208.1 SD=2.62 COV=0.0004

(u_{apex}), while the increase in diameter of the cavity near the base (Δd) and cavity volume (ΔV_{cav}) are less influenced. Furthermore, in order to study the effect of each of the material parameters on the response quantities, a number of additional test cases has been run, see Case 2 to Case 6 in the table. In each of these test cases, only one of the material parameters is assumed to be stochastic, while the rest are considered deterministic. Now it is seen that the uncertainty in K only plays a minor role on the response, while the displacement at apex and the increase in cavity volume are mostly influenced by the parameter b_{xx}, which governs the elastic properties in the plane orthogonal to the local fiber direction.

Concluding remarks

Applying the probabilistic collocation method to a mathematical model describing the passive filling phase of the left ventricle has allowed us to calculate the uncertainty in the cavity volume, the longitudinal displacement at the apex (or the elongation of the ventricle) and the cavity diameter. By changing the number of uncertain input variables, we have been able to show the strength of relationships between input and response uncertainty. In general, the apex displacement is most strongly affected by uncertainty. The method has been implemented without a need to adjust the complicated partial differential equation to allow for input parameter stochasticity, leading to simpler implementation than for other stochastic methods, while not being as computationally expensive as the Monte Carlo simulation method, an alternative black box method.

Acknowledgements

References

[1] F.J. Vetter and A.D. McCulloch. Three-dimensional stress and strain in passive rabbit left ventricle: A model study. *Ann. Biomed. Engng.*, **28**, 781–792, (2000).

[2] K.D. Costa, J.W. Holmes and A.D. McCulloch. Modelling cardiac mechanical properties in three dimensions. *Phil. Trans. R. Soc. Lond.*, **359**, 1233–1250, (2001).

[3] H. LI and D. Zhang. Probabilistic collocation method for flow in porous media: Comparisons with other stochastic methods. *Water Resour. Res.*, **43**, 1–13, (2007).

[4] G.J.A. Loeven, J.A.S. Witteveen and H. Bijl. Probabilistic collocation: An efficient non-intrusive approach for arbitrarily distributed parametric uncertainties. In proceeding of *the 45th AIAA Aerospace Sciences Meeting and Exhibit*, Reno, Nevada, (2007).

[5] S.R. Clark, A.M. Bruaset, T.O. Sømme and T.M. Løseth. A flexible stochastic approach to constraining uncertainty in forward stratigraphic models. In proceeding of *the MODSIM09 International Congress on Modelling and Simulation*, Cairns, Australia, (2009).

[6] T. Thorvaldsen, H. Osnes and J. Sundnes. A mixed finite element formulation for a non-linear, transversely isotropic material model for the cardiac tissue. *Comput. Meth. Biomech. Biomed. Engng.*, **8**, 369–379, (2005).

[7] H. Osnes, T. Thorvaldsen, S. Wall, J. Sundnes and A.D. McCulloch. An operator splitting technique for integrating cardiac electro-mechanics. Submitted to *Biomech. Model. Mechanobiol.*, (2009).

[8] T.P. Usyk, R. Mazhari and A.D. McCulloch. Effect of laminar orthotropic myofiber architecture on regional stress and strain in the canine left ventricle. *J. Elast.*, **61**, 143–164, (2000).

Predicting Statistical Distributions of Footbridge Vibrations

Lars Pedersen* and Christian Frier

Department of Civil Engineering
Aalborg University, Aalborg, Denmark
e−mail: lpe@civil.aau.dk

Summary The paper considers vibration response of footbridges to pedestrian loading. Employing Newmark and Monte Carlo simulation methods, a statistical distribution of bridge vibration levels is calculated modelling walking parameters such as step frequency and stride length as random variables. The importance of modelling stride length and walking speed as random variables is evaluated, and results suggest that it is not necessary to model all parameters stochastically to produce fair response estimates.

Introduction

Vertical vibrations in footbridges generated by pedestrians are of concern as they may reach levels rendering bridges unfit for their intended use [1]. Basically vibrations may be perceived as unacceptable by bridge users. For evaluating the vibration serviceability limit state it is useful to employ numerical methods as, hereby, vibration levels may be predicted already at the design stage. As an add-on to this it is considered sensible to adapt a stochastic approach to modelling some of the walking parameters (parameters of the walking load model). Basically parameters such as step frequency and stride length (step length) may change from one pedestrian to the next and since there are proposals in the literature on the stochastic nature of these walking parameters [2], [3], they may be incorporated into numerical calculations predicting bridge vibrations to pedestrian loading. With this randomness implemented, the results of such calculations provide a statistical distribution of bridge vibration levels, and the paper provides an example of such result. As will be discussed in the paper this is a more refined and useful approach than the approach suggested in some current codes (for the British Standard [4]) addressing the serviceability limit state related to actions of walking.

Generally it might not be necessary to model the stochastic nature of all walking parameters for obtaining a fair estimate of the statistical distribution of bridge vibration levels. As an example illustrating this point, various approaches to modelling walking speed is considered in the paper. The walking speed depends on both step frequency and stride length, which are random variables. However, a deterministic model for walking speed is introduced, and the statistical distribution of bridge vibration levels calculated on this assumption is compared with that obtained by modelling step frequency and stride length as random variables.

In order to examine and illustrate the points outlined above, it is considered sufficient to employ a quite simple bridge model (SDOF model representing the first vertical bending mode of a pin-supported bridge) and to study only the response to single-person pedestrian loading.

Assumptions for the studies and study approaches

Bridge model

The modal characteristics of the bridge considered for the present studies are shown in Table 1.

f	M	ζ
2.00 Hz	39.500 kg	0.3%

Table 1: Dynamic characteristics.

The frequency of the bridge (f) is chosen such that it represents a bridge prone to react lively to actions of walking. The bridge damping ratio (ζ) is quite low, but yet realistic for bridges with low damping. The modal mass (M) is also believed to be quite realistic considering the frequency of the bridge, as is the length of the bridge, L, which is assumed to be 43 m (distance between the two pin supports).

Walking load

For the paper (and as often done for modelling the vertical excitation generated by a pedestrian [5]), the dynamic load acting on the bridge, $f(t)$, is modelled as shown in equation (1).

$$f(t) = \alpha W \cos(2\pi f_s t) \tag{1}$$

It is a harmonic load with a frequency, f_s, representing the step frequency of walking. The step frequency is assumed constant during the locomotion of the pedestrian whilst crossing the bridge. The amplitude of the load is αW, where α is the dynamic load factor where W is the static weight of the pedestrian.

Assuming that the mode space function of the first vertical bending mode of the bridge corresponds to a half-sine, it can be shown that the modal load on the bridge (first vertical bending mode) may be computed using either equation (2) or equation (3):

$$q(t) = \alpha W \cos(2\pi f_s t) \sin(\pi \frac{f_s l_s}{L} t) \tag{2}$$

$$q(t) = \alpha W \cos(2\pi f_s t) \sin(\pi \frac{v}{L} t) \tag{3}$$

In equation (2), l_s is the stride length (or step length) of the pedestrian. For a given pedestrian (bridge crossing) l_s is assumed to be a constant as is the step frequency, f_s. Hereby the walking velocity, v, is also a constant, and it can be computed from the equation $v = f_s l_s$. This relationship is used when setting up equation (2). Equation (3) represents a simplification of the load in which it is assumed that any pedestrian traverses the bridge using a constant and the same walking speed v. Such restricting assumption is not made in the load model in equation (2).

Approaches to predicting bridge response

For simulating load action two different approaches are considered:

Approach 1: In this approach it is assumed that the value of f_s will change from one pedestrian to the next and that also the value of l_s will change from one pedestrian to the next. The two parameters are modelled as independent random variables employing Gaussian distributions.

Proposals as for the mean value, μ, and standard deviation, σ, are available in literature. In this approach walking speed is a random variable. When simulating loads, equation (2) is employed. How α and W are modelled are explained later.

Approach 2: In this approach only f_s is modelled as a random variable (in the same way as in approach 1). For any pedestrian the walking speed, v, is set to 1.413 m/s. This is value in close proximity of 1.5 m/s, which is a figure often referred to as the walking speed associated with normal walk. The value 1.413 m/s is obtained using the equation $v = f_s\, l_s$ employing mean values of the random variables f_s and l_s. When simulating loads, equation (3) is employed. The parameters α and W are modelled in the same way as in approach 1.

Employing Monte Carlo simulation methods and a Newmark time integration scheme, bridge acceleration time-histories for a large amount of simulations (bridge crossings) are calculated; specifically, the vertical bridge acceleration at midspan. For every bridge crossing, the peak acceleration level, a, encountered at this position is extracted and this procedure provides a basis for calculating the probability distribution function for peak accelerations.

Inputs for calculations

Table 2 outlines the mean values (μ) and standard deviations (σ) employed for calculations.

Variable	Unit	μ	σ	Reference
f_s	Hz	1.99	0.173	[2]
l_s	m	0.71	0.071	[3]

Table 2:   Assumptions for walking parameters.

The static weight of the pedestrian, W, is set to 750 N. The dynamic load factor, α, is modelled to be conditioned on f_s, as results of measurements reported in [6] clearly reveal a relationship with f_s. The modelled relationship is:

$$\alpha = af_s^3 + bf_s^2 + cf_s + d \tag{4}$$

where

$$a = -0.2649 \quad b = 1.3208 \quad c = -1.7597 \quad d = 0.7613. \tag{5}$$

In equation (4), the unit Hz is to be used for f_s.

Results

Calculated statistical distributions of peak midspan accelerations are presented in Fig. 1.

From such distribution it may for instance be identified that there is a 5 % probability of reaching vibration levels above 0.54 m/s^2 (using approach 1 for this particular bridge). Hence for 1 out of 20 crossings an acceleration level above 0.54 m/s^2 is expected to occur. If employing the British Standard [4] for computing vertical bridge vibrations generated by a pedestrian, you would by default assume resonant action, and would not be provided with information on the probability of encountering the acceleration level calculated. The strength of modelling the stochastic nature of walking parameters (which is not done in [4]) in thus that it gives a more refined understanding of the likelihood of encountering various bridge vibration levels.
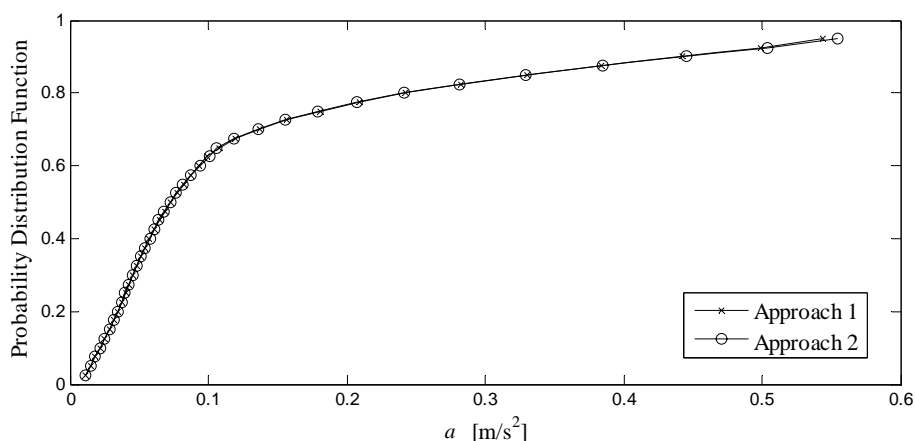
Figure 1: Statistical distributions of bridge vibration levels.

However, it might not be necessary to mode each and every parameter of the load model stochastically for obtaining a fair estimate of the statistical distribution of bridge response. The results in Fig. 1 suggest that the estimate obtained assuming the same walking velocity for every pedestrian provides a result which is in fair agreement with the result obtained when modelling walking speed as a random variable. In some way this suggests that it is not that important to model the stochastic nature of stride length. This conclusion is drawn based on examining only a single bridge (and using a quite simple bridge model). Additionally, multi-person pedestrian loading is a matter of concern, and it is not addressed or considered in this paper. Hence, care should be taken to generalise the conclusion.

Concluding remarks

The paper has illustrated the usefulness of employing a walking load model in which parameters are treated as random variables. Furthermore is has been shown that it is quite likely that not every single parameter of the load model need be modelled stochastically for obtaining a far estimate of the statistical distribution of bridge vibration levels.

References

[1] P. Dallard, A.J. Fitzpatrick, A. Flint, S. Le Bourva, S., A. Low, R.M. Ridsill-Smith, M. Wilford, The London Millennium Bridge, *The Structural Engineer*, **79**, 17-33, (2001).

[2] Y. Matsumoto, T. Nishioka, H. Shiojiri, and K. Matsuzaki, Dynamic design of footbridges, *IABSE Proceedings* , No. P-17/78: 1-15, (1978)

[3] S. Živanovic, Probability-based estimation of vibration for pedestrian structures due to walking, PhD Thesis, Department of Civil and Structural Engineering, University of Sheffield, UK, (2006).

[4] British Standard Institution, Steel, concrete and composite bridges. Specification for loads, BS 5400: Part 2, (1978).

[5] H. Bachmann, W. Ammann, *Vibrations in Structures – Induced by Man and Machines*, IABSE Structural Engineering Documents 3e, Zürich, Switzerland, 1987.

[6] S.C. Kerr, Human induced loading of staircases, PhD Thesis, University College London, Mechanical Engineering Department, UK, (1998).

Uncertainty on Fatigue Damage Accumulation for Composite Materials

Henrik Stensgaard Toft* and John Dalsgaard Sørensen

Department of Civil Engineering
Aalborg University, Aalborg, Denmark
e−mail: hst@civil.aau.dk

Summary   In the present paper stochastic models for fatigue damage accumulation for composite materials are presented based on public available constant and variable amplitude fatigue tests. The methods used for estimating the SN-curve and accumulated fatigue damage are presented.

Introduction

Damage accumulation models for composite materials exposed to fatigue loading have been widely considered in the literature, see e.g. [1] for a review. However, even though new empirical and physical models for the accumulation of damage are proposed, these models do not seem to perform much better than the linear damage accumulation proposed by Miner [2]. For this reason the accumulated damage is normally determined by Miners rule as recommended in [3] for wind turbine blades.

The uncertainties in damage accumulation based on Miners rule can in general be divided into three parts:

- Physical uncertainty on the SN-curves
- Statistical uncertainty on the SN-curves due to a limited number of tests
- Model uncertainty on Miners rule

The physical uncertainty on the SN-curves is due to the natural inherent uncertainty in the material and can not be reduced. The statistical uncertainty can be reduced by performing additional fatigue tests and the model uncertainty can in principle be reduced by adopting a better model.

In the present paper is the physical and statistical uncertainty on SN-curves for composite material determined based on a number of constant amplitude fatigue tests performed with different mean stresses. Based on variable amplitude fatigue tests for the same material using a standard load spectrum and the estimated SN-curves based on constant amplitude fatigue tests is the model uncertainty on Miners rule determined.

In most standards and regulations including [3] are fatigue design performed by using a deterministic design approach. However, calculation of the accumulated fatigue damage includes significant uncertainties for which reason a probabilistic design approach should be adopted in order to take the individual uncertainties into account in a rational manner. The stochastic models determined in the present paper forms the basis for a probabilistic modeling of the considered class of composite materials in fatigue loading.

Constant amplitude fatigue tests

The constant amplitude and variable amplitude fatigue tests used in the present paper are given in the OptiDAT database [4] for geometry R04 MD (MultiDirectional laminate). This geometry has been selected due to the many fatigue tests performed with this geometry. For composite materials the mean stress can have a significant influence on the fatigue properties which can be taken into

account by calculation of an SN-curve for different R-ratios and arranging these in a constant life diagram. The R-ratio is defined by:

$$R = \frac{\sigma_{\min}}{\sigma_{\max}} \tag{1}$$

where $\sigma_{\min}$ and $\sigma_{\max}$ are the minimum and maximum stress in a stress cycle respectively. Different types of SN-curves have been used for composite material, but no specific SN-curve have been recommended in [3]. In the present study is a log-log SN-curve used:

$$\log N = \log K - m \log \Delta\sigma + \varepsilon \tag{2}$$

where N is the number of cycles to failure, $\Delta\sigma$ is the stress range and ε is parameter which model the lack of fit and is assumed normal distributed with mean value zero and standard deviation σ_ε. The constants K and m are material parameters. By assuming that the residuals are normal distributed on a log-log scale the likelihood function in case of n constant amplitude tests and n_0 run-outs is given by:

$$L(\log K, \sigma_\varepsilon) = \prod_{i=1}^{n} \frac{1}{\sqrt{2\pi}\sigma_\varepsilon} \exp\left(-\frac{1}{2}\left(\frac{\log N_i - (\log K - m\log\Delta\sigma_i)}{\sigma_\varepsilon}\right)^2\right) \cdot \prod_{i=n+1}^{n+n_0} \Phi\left(\frac{\log N_i - (\log K - m\log\Delta\sigma_i)}{\sigma_\varepsilon}\right) \tag{3}$$

where N_i and $\Delta\sigma_i$ is the number of cycles to failure and stress range for test specimen number i respectively. The parameter m is determined by least square method and the parameters $\log K$ and σ_ε are estimated using the Maximum-Likelihood Method where the optimization problem $\max_{\log K, \sigma_\varepsilon} L(\log K, \sigma_\varepsilon)$ is solved using a standard nonlinear optimizer, e.g. the NLPQL algorithm [5]. In this paper is m assumed fixed determined by the least square method, but this parameter could also be included in the optimization. Since the parameters $\log K$ and σ_ε are estimated by the Maximum-Likelihood technique they become asymptotically Normal distributed stochastic variables with expected values equal to the Maximum-Likelihood estimators and covariance equal to, see e.g. [6]:

$$C_{\log K, \sigma_\varepsilon} = \left[-H_{\log K, \sigma_\varepsilon}\right]^{-1} = \begin{bmatrix} \sigma_{\log K}^2 & \rho_{\log K, \sigma_\varepsilon} \sigma_{\log K} \sigma_{\sigma_\varepsilon} \\ \rho_{\log K, \sigma_\varepsilon} \sigma_{\log K} \sigma_{\sigma_\varepsilon} & \sigma_{\sigma_\varepsilon}^2 \end{bmatrix} \tag{4}$$

where $H_{\log K, \sigma_\varepsilon}$ is the Hessian matrix with second order derivatives of the log-Likelihood function. $\sigma_{\log K}$ and $\sigma_{\sigma_\varepsilon}$ denote the standard deviation on $\log K$ and σ_ε respectively. $\rho_{\log K, \sigma_\varepsilon}$ is the correlation coefficient between $\log K$ and σ_ε. The Hessian matrix is estimated by numerical differentiation.

In table 1 are the estimated parameters shown and the SN-curves are fitted using all valid constant amplitude fatigue tests for the particular R-ratio and runouts are taken into account. The parameters $\log K$ and σ_ε can be assumed uncorrelated. It is noted that σ_ε represents the physical uncertainty and that $\sigma_{\log K}$ and $\sigma_{\sigma_\varepsilon}$ represents the statistical uncertainty. In table 2 are the static

tension and compression strength given. In figure 1 (left) is the constant life diagram containing the SN-curves and static strengths shown.

Table 1: SN-curves for different R-ratios for geometry R04 MD.

R-ratio	Tests n	Runouts n_0	m	$\log K$	σ_ε	σ_{logK}	$\sigma_{\sigma\varepsilon}$
0.5	15	0	10.541	27.768	0.358	0.092	0.065
0.1	45	2	9.508	27.191	0.259	0.039	0.027
-0.4	28	0	7.582	23.398	0.435	0.082	0.058
-1.0	84	3	6.719	21.359	0.878	0.094	0.068
-2.5	10	2	11.983	35.231	0.633	0.197	0.143
10.0	34	0	22.211	58.664	0.644	0.110	0.078
2.0	6	3	29.686	73.780	0.354	0.143	0.103

Table 2: Static tension strength (STT) and static compression strength (STC) for geometry R04 MD.

Test-type	Tests n	Mean [MPa]	Std. [MPa]
STT	66	556.5	64.2
STC	55	-458.6	33.2
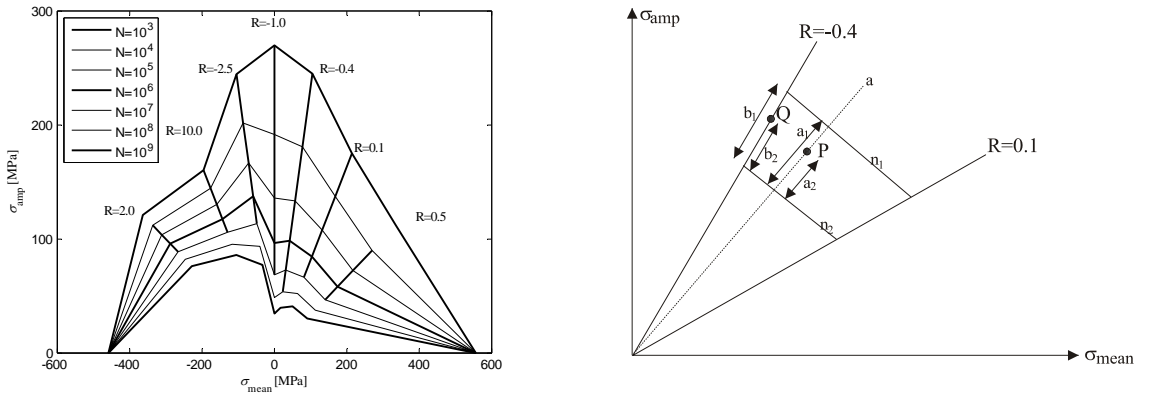
Figure 1. Left: Constant life diagram for geometry R04 MD. Right: Linear interpolation.

Variable amplitude fatigue tests

Variable amplitude fatigue tests are also performed with geometry R04 MD. The load spectrum used is the wisper and wisperx spectra developed for representing the flap bending moment of a wind turbine blade. In order to calculate the accumulated damage D Miners rule for linear damage accumulation is used:

$$D = \sum_{i=1}^{n} \frac{1}{N(\Delta\sigma_i)}$$

(5)

In order to calculate the accumulated damage at failure the number of cycles to failure N has to be determined for an arbitrary R-ratio. This is in the present paper done by linear interpolation in the constant life diagram using the procedure given in the following, see also figure 1 (right).

- The stress cycle P is located in the constant life diagram
- Draw a line a from the origin through and beyond the point P
- Identify the constant life lines closest to P, denoted n_1 and n_2
- Calculate the length a_1 on line a between the two constant life lines n_1 and n_2

- Calculate the length a_2 on line a between point P and the constant life line n_2
- Find the R-ratio closest to P and calculate the length b_1 between n_1 and n_2
- Calculate $b_2 = \dfrac{b_1 a_2}{a_1}$
- Determine the stress amplitude σ_{CLD} corresponding to point Q
- Determine the expected number of cycles to failure N using the SN-curve for the R-ratio

In table 3 are the conducted variable fatigue tests listed together with the mean and standard deviation on the accumulated damage at failure using the material parameters given in table 1 and 2. It is noted that COV_D represents the model uncertainty.

Table 3: Mean and standard deviation for estimated damage at failure for variable amplitude tests.

Spectrum	Tests N	Mean	Std.	COV_D
Wisper	10	0.9000	0.5355	0.595
Wisperx	13	0.2763	0.1982	0.717
Reverse Wisper	2	0.2020	-	-
Reverse Wisperx	10	0.3179	0.1576	0.496
Wisper, Wisperx	23	0.5474	0.4886	0.893
All	35	0.4621	0.4196	0.908

From table 3 it is seen that except for the wisper spectrum the estimated accumulated damage at failure is significantly below one. The uncertainty for fatigue damage accumulation are often modelled by a lognormal distribution in order two avoid negative values of Miners rule which are physical impossible. The mean and standard deviations given in table 3 can be used in a lognormal distribution.

Concluding remarks

In the present paper are stochastic models for the uncertainty related to fatigue damage accumulation for composite materials presented. The stochastic models are based on public available constant and variable amplitude fatigue tests and the procedure used for estimating the stochastic models are presented.

Acknowledgement

References

[1] Post NL, Case SW, Lesko JJ. Modeling the variable amplitude fatigue of composite materials: A review and evaluation of the state of the art for spectrum loading. International Journal of Fatigue 2008 Dec;30(12):2064-86.
[2] Miner MA. Cumulative Damage in Fatigue. Journal of Applied Mechanics-Transactions of the Asme 1945;12(3):A159-A164.
[3] IEC 61400-1. Wind turbines - Part1: Design requirements. 3rd edition. 2005.
[4] OPTIMAT BLADES. 2006. www.kc-wmc.nl.
[5] Schittkowski K. NLPQL: A FORTRAN Subroutine Solving Non-Linear Programming Problems. Annals of Operations Research 1986.
[6] Lindley DV. Introduction to Probability and Statistics from a Baysian Viewpoint. Cambridge University Press, Cambridge; 1976.

A Numerical Study of Vortex-Induced Vibrations (VIV) in an Elastic Cantilever

Johan Lorentzon[†,1], Per-Erik Austrell[2], Robert-Zoltan Szasz[1] and Johan Revstedt[1]

[1]Division of Fluid Mechanics
[2]Division of Structural Mechanics
Faculty of Engineering, Lund University, Sweden
e–mail:pi06jl6@student.lth.se[†]

Summary This study treats the subject fluid-structure interaction (FSI) for incompressible flow with small vibrations. The open source packages DEAL.II and OpenFOAM have been used to create a coupling between a finite element formulation for the structure and finite volume formulation for the fluid. A staggered solution algorithm have been implemented in C++ and verified against empirical data of Vortex-Induced Vibration (VIV) frequencies.

Introduction

A cantilever is placed in a domain of a velocity driven fluid. The traction differential acting upon the structure induce a deformation and the movement of the structure affects the fluid as well. This mutual influence referred to as fluid-structure interaction (FSI), is known to cause several interesting phenomena. Among such is vortex-induced vibration[1] (VIV), where the forced movement of a fluid around the structure gives upon point of release from the structure, an angular momentum manifested as a vortex in the fluid with an oscillating transversal force component.

Mathematical and Numerical Description

A physical domain consisting of fluid and structure is described by velocity field ($\mathbf{U}$,$\mathbf{v}$) and pressure p, displacement field ($\mathbf{q}$) and pressure in a continuum model. The equations governing the motion of an incompressible Newtonian fluid and an elastic structure ($D_{ijkl}\epsilon_{kl}$) with damping ($C_{il}v_l$) then takes the following form in reduced variables (*) in the fluid domain and state space formalism for the structure with small strain operator ($\epsilon(\mathbf{q})$),

$$\nabla^* \cdot \mathbf{U}^* = \mathbf{0}, \tag{1}$$

$$\frac{DU_i^*}{Dt^*} = -\partial_i p^* + \frac{1}{Re}\nabla^{*2}U_i^* + b_i^*, \tag{2}$$

$$\dot{q}_i - v_i = 0, \tag{3}$$

$$\partial_t v_i + C_{il}v_l - \partial_j D_{ijkl}\epsilon_{kl}(\mathbf{q}) = f_i. \tag{4}$$

The coupling boundary between fluid and structure is a traction term, i.e. the sum of the pressure force and the viscous force. Both PDE sets have the same character and therefore a monolithic approach is feasible [2]. However, the problem can become too large to handle or unstable, therefore a staggered algorithm is preferred where even the individually domains can further, by divide and conquer, be partitioned [4, 5]. In solving Eqn (2) and (4) it is assumed that the problem can be formulated in two steps, the solution of the physical domain in a steady state formalism, followed by semi-discretization in time.

---

[1]For an excellent review, C.H.K. Williamson and R. Govardhan, Vortex-induced vibrations. Ann. Rev.Fluid.Mech **36** (2004) 443-455.

Further, by assumption of fixed point solution the fluid domain is solved separately from the structure domain, using FVM respectively FEM.

```
Time Loop
 Staggered Loop
    Solve Fluid State
    Transfer Traction to Solid State Solver
    Solve Solid State
    Exit Staggered Loop if change of deformation < tolerance
    Transfer Deformation to Fluid State Solver
  End Staggered Loop
 End Time Loop
```

The norm for convergence is with respect to the displacement field. However, while combining two solvers the time must be adaptive with respect to the CFL condition in order to meet the convergence criteria. The open source packages used in this study are Open-FOAM[2]. and DEAL.II[3]. The staggered algorithm allows the FSI solver to be run on separate machines/threads. The test case and the staggered algorithm originates from a study using OpenFOAM [5]. The fix-point iteration to locate the quasi-static equilibrium point between the solvers use the Aitkens relaxation method[4] to accelerate the sub cycle loop, the staggered loop.

The Case Study

A cantilever of thickness $D = 0.2$ m and height of $10D$ is placed $5D$ from the inlet, $2.5D$ from the walls and $20D$ from the outlet. The wire frame of the rectangular domain is thus $(26 \times 6 \times 12.5) \cdot D$. The flow is velocity driven with uniform Dirichlet condition at the inlet $(\mathrm{mag}(\mathbf{U}))$ and Neumann conditions at the outlet. For the pressure a Neumann condition is used at the inlet and a Dirichlet condition at the outlet. At the walls, no-slip conditions are used. The unstructured grid in the fluid domain is created using scaled tetrahedral elements with a structured boundary mesh with size 0.02 m , growth rate 1.1 and 0.1 m as upper limit on cell size, while the structured grid for the structure domain $8 \times 8 \times 64$ cell partition.

Application to VIV

The following empirical expression for the Strouhal number (St) can be used to estimate the frequency of the VIV for a cantilever in an infinite domain,

$$St = \frac{fl}{U} = 0.198(1 - \frac{19.7}{Re}).$$ (5)

The result in table 1 presents the frequency of probes placed in respective domain, showing the synchronization between the frequency of the fluid motion (f) and the structure (f_s).

---

[2]*http://www.opencfd.co.uk/openfoam/*
[3]*http://www.dealii.org.*

It scales within the margin of error with Eqn (5). However, wall effects should also be accounted for. Table 2 gives the observed VIV in the nodamped cases with no fluid probes, note that for $U = 1$ two frequencies appear, where the higher is the first harmonic of the lower and it appears due to discretization error of a sinusoidal function. The VIV is masked

U (ms^{-1})	$f_s(Hz)$	$f(Hz)$	$f_i(Hz)$
1	0.7	1-1.3	1.7
10	8	7-14	11
25	15	17-25	11

Table 1: VIV frequency with damping from section 6.3 in [1].

U (ms^{-1})	$f_s(Hz)$
1	0.79, 0.74, 1.47, 1.53, 1.53, 1.53
10	6.3, 6.6, 5.2
25	17.07, 17.2

Table 2: VIV frequency without damping from table 6.1 in [1].

by the in-line frequency due to release of cantilever and for this reason a Rayleight damping was added with 0.1%. The in-line frequency f_i well match reported elsewhere [3]. Figure 1-2 is the FFT spectra for U=1 in table 1.

Conclusion

This study presents a method to resolve the fluid-structure interaction (FSI) using a fixed-point iterative scheme with a partitioned Gauss-Seidel technique accelerated with Aitkens relaxation method. The validation of the solver involves among others,

- reproduced frequency shift in in-line movement.

- matched frequency in VIV with probes of fluid and structure.

- reproduced VIV frequency with regard to Eqn (5).

The study implicates the need for damping in this model where frequency is obtained in a real time numerical experiment.
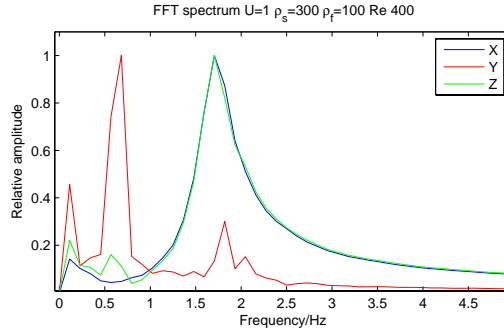
Figure 1: The FFT on marker point at U=1.
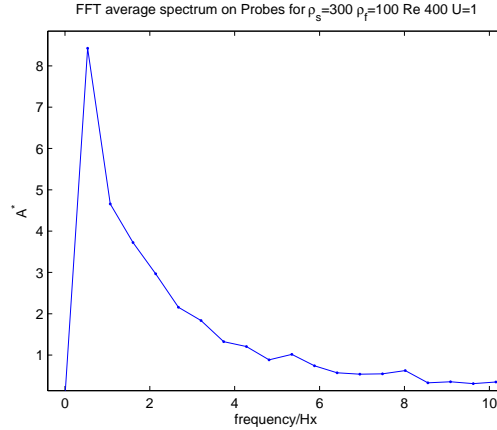
Figure 2: The averaged FFT spectrum for the fluid probes for U=1.

References

[1] Johan Lorentzon, *Fluid-Structure Interaction (FSI) case study of a cantilever using OpenFOAM and DEAL.II with application to VIV.* Master of Science Thesis, LTH, Lund, Sweden 2009, ISSN 0282-1990.

[2] Michael Stöckli, *A Unified Continuum Fluid-Structure Interaction Solver using an ALE finite Element Method. An Investigation on how to simulate blood flow.* Master of Science Thesis, KTH, Stockholm, Sweden 2007.

[3] Stefan Wagert, Markus Dreier and Martin Hegner, Frequency shifts of cantilevers vibrating in different various media. *Appl. Phys. Letter.* **69** (19), Nov 4. (1996) 2834-2836.

[4] Ulrich Küttler, Wolfgang A. Wall. Fixed-point fluid-structure interaction solvers with dynamic relaxation *Comput.Mech.* **43**(1) (2008) 61-72.

[5] Zeljko Tukovic Hrvoje Jasak, Updated Lagrangian finite volume solver for large deformation response of elastic body. *Transaction of Famena* **30**(2) (2007) 1-18.

Hydrodynamic interaction of a particle pair at Reynolds number 600.

A. Jadoon[*] and J. Revstedt

Department of Energy Sciences
Lund University, Lund, Sweden
asim.jadoon@energy.lth.se
johan.revstedt@energy.lth.se

L. Prahl

Department of Mechanics
Royal Institute of Technology, Stockholm, Sweden
prahl@mech.kth.se

Summary   In the current study the focus is on the flow and particle interaction effects in the chaotic regime. The influence on the forces (i.e drag and lift), wake structures and flow patterns from different inflow boundary conditions and varying separation distances of a particle pair in tandem is discussed at a particle Reynolds number of 600.

Introduction

Flow past a single sphere experiences different transitions with the increase in Reynolds number [1]. The first transition occurs at $Re = 20$ in which a steady attached vortex ring separates behind the sphere. The flow undergoes a second transition at $Re = 210 - 212$ where the flow changes to an asymmetric flow containing a plane of symmetry. During the third transition i.e. in the range of $270 \geq Re \leq 280$, the flow becomes unsteady however periodic. The vortices start to shed with a single dominant shedding frequency. The fourth transition occurs in the range of $Re = 375 - 420$ [2] [3] [4]. The flow becomes chaotic and a statistically axisymmetric wake is observed.

The introduction of second spherical particle in the wake of first one can substantially change the drag, wake structures and flow patterns. Numerical simulations for two spheres placed at different angular positions and separation distances were performed by Yoon and Yang [9]. The effect on drag, lift and pressure coefficients are discussed in detail. The change in wake structures and flow patterns for two spheres placed in tandem is reported by Zou et al. [8]. The above studies are reported for Reynolds number of 300. Previous studies by Prahl et al. [10] and by Jadoon et al. [11] suggest that the separation distance between particles is of major importance for the force loading on the respective particles as well as for the development of the wake structures.

The aim of the present study is to investigate particle pair in tandem, the influence on particle inter distance and flow structures in the chaotic wake region.

Numerical Method

The numerical technique used to represent the spherical object is the volume of solid (VOS) method [6] which is similar to the volume of fluid VOF method. In VOS the shear stress is assumed to be constant close to the solid surface. This assumption together with the linear relationship between the viscosity in a cell and the volume fraction of each phase, one may write the viscosity as a harmonic mean of the values of the two phases as:

$$\mu = \frac{1}{\frac{\alpha}{\mu_1} + \frac{1-\alpha}{\mu_2}} \tag{1}$$

The assumption of infinite viscosity in the solid (the second fluid) leads to a simple relation between the phase variable α and the viscosity. The phase variable representing the amount of fluid in each cell, $0 < \alpha < 1$. Complete details of the technique can be found in [6].

$$\delta\nu = \frac{\nu}{\nu_1} = \frac{\mu}{\mu_1} = \frac{1}{\alpha} \qquad (2)$$

With the definition of viscosity term as stated in equation (2), the governing equations for an incompressible flow can be written as;

$$\frac{\partial u_i}{\partial x_i} = 0 \qquad (3)$$

$$\frac{\partial u_i}{\partial t} + u_j \frac{\partial u_i}{\partial x_j} = -\frac{\partial p}{\partial x_i} + \frac{1}{R_e} \frac{\partial}{\partial x_j} \left(\delta\nu \left(\frac{\partial u_i}{\partial x_j} + \frac{\partial u_j}{\partial x_i} \right) \right) \qquad (4)$$

where $\delta\nu$ is viscosity ratio.

The governing equations are spatially discretised using first and second order basic finite-difference schemes on a staggered Cartesian grid. A single step defect correction method [7] is used to improve the accuracy to third order for convective terms and fourth order for remaining terms. A second order fully implicit scheme is used for temporally discretisation of the transient terms. Multi grid method is used to accelerate the computational efficiency

Problem Setup

In this study, two equally sized spheres with a diameter D are held fixed in a rectangular domain while changing the relative position in tandem between the spheres. In all simulations, the first (*reference*) sphere is placed fixed at $10D$ downstream of the inlet and in the middle in X and Y dimensions, whereas the second (*secondary*) sphere is moved to separation distances D_0 of $1.5, 2, 3, 4.5, 6$ and $9D$. The Reynolds number is 600. At the inlet, a uniform velocity profile i.e. stationary as well as pulsating with a strouhal number ($\text{Stin} = \text{fD}/U_{\text{in}}$) of 0.1 is applied (U_{in} is the mean inlet velocity).

In order to validate the accuracy, different domain sizes and grid resolutions were investigated. Regarding domain sizes, tests are performed both in stream-wise and lateral directions and grid of $[32, 32, 64]D$ corresponding to $[X, Y, Z]$ is selected (Z being the flow direction). The grid resolutions of $D/16$, $D/32$ and $D/64$ are examined and grid resolution of $D/64$ is chosen.

Results & Conclusions

The value of drag coefficient for *reference* sphere has a maximum reduction (about 10%) compared to the drag of single sphere at $D_0 = 3D$, Fig.1 (a). This is due to the change in wake structure and behaviour, as the chaotic flow is changed to a periodic flow at this separation distance. The *secondary* sphere shows a maximum reduction (negative value of drag) at $D_0 = 1.5D$ where after the drag increases as the gap is increased but it remains below the value for a single sphere even at $D_0 = 9D$ Fig.1 (a). The negative value of the drag is due to a low pressure region developed in front of the secondary sphere which in turn depends on the prolongation of the wake which, to a greater extent, enclose the secondary sphere in the wake of the reference sphere. For pulsating inflow, the drag of the *secondary* sphere follows the same trend except it remains a bit higher
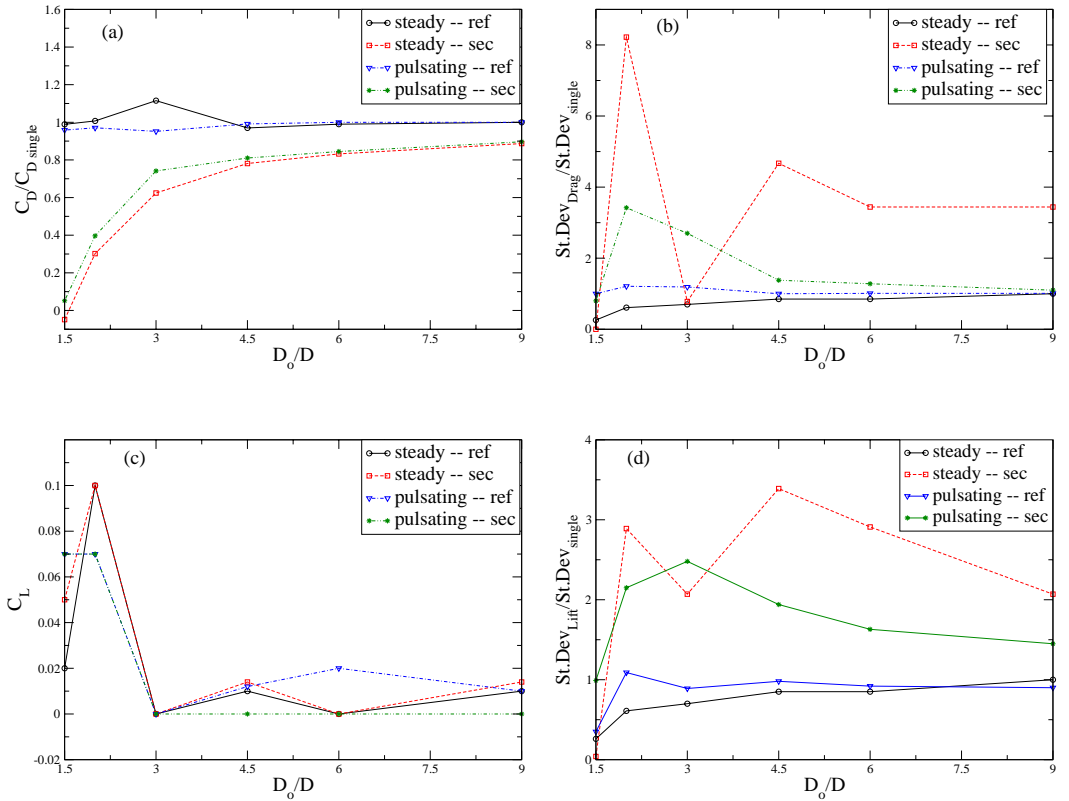
Figure 1: Drag coefficient C_D (a), Drag coefficient fluctuations (b), Lift coefficient C_L (c) and Lift coefficient fluctuations (d) at different separation distances. All the plots are normalized by the respective values for a single sphere except for (c) as $Cl_{single} = 0$. (**ref** and **sec** stands for **reference sphere** and **secondary sphere** respectively whereas **St.Dev** corresponds to **standard deviation**).

for all separation distances Fig.1 (a). The drag coefficient fluctuations have a maximum for the *secondary* sphere at $D_0 = 2D$ where it is 8 and 4 times greater compared to single sphere for uniform and pulsating inflow, respectively Fig.1 (b). The fluctuations are minimum at $D_0 = 1.5D$ for both cases.

The maximum lift experienced by both spheres is at $D_0 = 2D$ in both inflow conditions Fig.1 (c). The lift coefficient fluctuations are 2-3.5 times larger compared to a single sphere for the *secondary* sphere in the range of $D_0 \geq 2D$ Fig.1 (d).

In order to characterize the dynamics of the wake, different regimes have been defined based on the instantaneous lift coefficients: *unidirectional* for which the lift varies only in magnitude but direction is always along a line; *cyclic* for which magnitude and direction both varies periodically; *semi-chaotic* for which the lift has preferred direction with random fluctuations around that direction; *cyclic* for which there is no preferred direction and lift variation is randomly. The behaviour of the wake for both spheres based on above four definitions at different separation distances is tabulated in Table 1.

D_0	Uniform − inflow		
	$Wake(ref)$	$Wake(sec)$	$Flow − behaviour$
1.5D	plane-symmetric	plane-symmetric	Steady, Uni-directional
2D	plane-symmetric	plane-symmetric	Un-steady, Semi-Chaotic
3D	axi-symmetric	axi-symmetric	Un-steady, Uni-directional
4.5D	plane-symmetric	plane-symmetric	Un-steady, Chaotic
6D	axi-symmetric	axi-symmetric	Un-steady, Chaotic
9D	plane-symmetric	plane-symmetric	Un-steady, Chaotic
	Pulsating − inflow		
1.5D	plane-symmetric	plane-symmetric	Un-steady, Uni-directional
2D	plane-symmetric	plane-symmetric	Un-steady, Semi-Chaotic
3D	axi-symmetric	axi-symmetric	Un-steady, Uni-directional
4.5D	plane-symmetric	axi-symmetric	Un-steady, Chaotic
6D	plane-symmetric	axi-symmetric	Un-steady, Chaotic
9D	plane-symmetric	axi-symmetric	Un-steady, Chaotic

Table 1: Different wake structures and flow behaviours for both uniform and pulsating inflow conditions for different separation distances at Re= 600. (*ref* and *sec* stands for **reference sphere** and **secondary sphere** respectively).

References

[1] T. A. Johnson and V.C. Patel. Flow past a sphere up to a Reynolds number of 300. *J. Fluid. Mech.*, **285**, 69–94, (1995).

[2] V.A. Gushchin and R.V. Matyushin. Vortex formation mechanisms in the wake behind a sphere for $200 < Re < 380$. *Fluid. Dynamics*, **41(5)**, 795–809, (2006).

[3] H. Sakamoto and H. Haniu. A study on vortex shedding from spheres in a uniform flow. *Trans. ASME J. Fluids Eng.*, **112**, 386–392, (1990).

[4] H. Sakamoto and H. Haniu. The formation mechanism and shedding frequency of vortices from a sphere in a uniform shear flow. *J. Fluid. Mech.*, **287**, 151–171, (1995).

[5] J. Mittal, J.J. Wilson and F.M. Najjar. Symmetry properties of the transitional sphere wake. *AIAAJ.*, **40(3)**, 579–582, (2001).

[6] D. Lörstad, L. Fuchs. A volume of fluid (VOF) method for handling solid objects using fixed Cartesian grids. *Moving Boundaries VI - Computational Modelling of Free and Moving Boundary Problems.*, **Sarler, B. and Brebbia, C. A.**, Wessex Inst. of Techn. 143–152, (2001).

[7] J. Gullbrand, X.S Bai and L. Fuchs. High-order Cartesian grid method for calculation of incompressible turbulent flows. *Int. J. Num. Meth. Fluids.*, **36**, 687–709, (2001).

[8] J.F. Zou, A.L. Ren and J. Deng. Study on flow past two spheres in tandem arrangement using a local mesh refinement virtual boundary method. *Int. J. Num. Meth. Fluids.*, **49**, (2007).

[9] D.H. Yoon and K.S. Yang. Flow-induced forces on two nearby spheres. *Physics of Fluids.*, **19**, 465–488, (2005).

[10] L. Prahl, A. Jadoon and J. Revstedt. Interaction between two spheres placed in tandem arrangement in steady and pulsating flow. *Int. J. Multiphase Flows.*, **35**, 963–969, (2009).

[11] A. Jadoon, L. Prahl and J. Revstedt. Dynamic interaction of fixed dual spheres for several configurations and inflow conditions. *submitted for publication to Europen J. Mech.*, (2008).

Vortex Induced Vibrations of Multiple Cylinders

Alper Cesur* and Johan Revstedt

Department of Energy Sciences
Lund University, Lund, Sweden
alper.cesur@energy.lth.se
johan.revstedt@energy.lth.se

Summary This study is focused on the interaction among a group of four cylinders elastically mounted in a quadratical formation in a channel at $Re = 400$. The results show that the influence from variations in elasticity have a stronger effect on the amplitude of the downstream cylinders, whereas the staggering effect has the opposite effect in the synchronization range. Also, the amplitude of the downstream cylinders increase as the separation distance is decreased.

Introduction

Vortex induced vibrations (VIV) are of vital importance in many engineering problems, such as flow across the tube bank of a heat exchanger, offshore platforms and the flow around chimneys. According to Khalak and Williamson [1], at low mass and damping, the response of an elastically mounted single cylinder consist of three response branches, namely the initial, upper and lower branch. Govardhan & Williamson [2] and Morse & Williamson [3] have extended the work and further investigated the relationship between the existence of a critical mass and the resonance regime, and the effect of Reynolds number on the critical mass in VIV, respectively. Lazarkov and Revstedt [4] have also investigated the effect of a short cylinder confined in a channel flow, where no clear upper branch was found, which was probably due to confinement effects.

The wake instabilities, which characterize the vortex wake street, are affected in a different manner when a cylinder pair is exposed to VIV. Revstedt [5] has found that a pair of cylinders in tandem show similar vibrational response, but with enhanced oscillation amplitudes for the downstream cylinders, compared to the single cylinder case. Brika & Laneville [6] have shown that increasing spacing ratio, L/D, for a tandem arrangement, with fixed upstream cylinder and free downstream cylinder, has a reducing effect on the synchronization regime and the amplitude of oscillations.

The aim of the present study is to investigate how the vortex-induced vibrations are affected by the interaction of elastically mounted multiple cylinders confined in a rectangular channel. The effects of elasticity and separation distance are studied for equidistantly placed cylinders and also, the effect of staggering is examined. The single cylinder has served as a reference for the elasticity calculations.

Numerical method

The fluid under consideration is isothermal, incompressible and of Newtonian character. The flow is governed by the time-dependent, three-dimensional conservation equations of mass and momentum, which, in a nondimensional form, read as:

$$\frac{\partial u_i}{\partial x_i} = 0, \tag{1}$$

$$\frac{\partial u_i}{\partial t} + u_j \frac{\partial u_i}{\partial x_j} = -\frac{\partial p}{\partial x_i} + \frac{1}{R_e} \frac{\partial}{\partial x_j} \frac{\partial u_i}{\partial x_j} + \varphi_i. \tag{2}$$

The equation of motion of the cylinder is at each time step solved in addition to the governing equations of the fluid motion, (1) and (2), which in a nondimensional form can be written as:

$$m\ddot{x} + b\dot{x} + kx = C_x(t). \tag{3}$$

The system of governing equations (1) and (2) are discretized using finite difference approach on a staggered Cartesian grid. The level of accuracy for the convective and and remaining terms are improved to third and fourth-order, respectively, by introducing a single step defect correction [7]. A Multi-grid solver is used to enhance the computational efficiency.

The boundary conditions on the solid boundaries have been applied by replacing the boundary with momentum sources in (2), φ_i, such that the flow satisfy the required boundary condition. These source terms are then calculated based on the deviation of the fluid velocity from the boundary velocity on the surface. This method is called virtual boundary (VB) method and more detailed description can be found in [8].

Problem Setup

The computations, in this paper, have been performed for the case of flow past a confined cylinder in a rectangular channel at Reynolds number of 400, based on bulk velocity and cylinder diameter. The dimensions of the computational domain are 12D x 4D x 30D, in the x-, y- and z-directions, respectively. The flow direction is in the z-direction and the cylinders are only permitted to move in the transversal direction, i.e in the x-direction. Four cylinders are placed quadratically with the upstream cylinders placed 7.5D from the inlet. Two separation distances were studied, $L/D = 4$ and $L/D = 5$, maintaining the quadratical relationship between the cylinders. Finally, for staggered arrangement, the upstream cylinders were kept fixed at a position of 8D from the inlet while the downstream cylinders were positioned at several positions in the x-direction, maintaining the distance in the z-direction.

At the inlet, a uniform velocity profile is set, at the outlet a Neuman boundary conditions are used and the no-slip conditions are set for the walls. The computational grid consists of three global and two locally refined grids, yielding a grid resolution of h=D/32, close to the cylinder surfaces. The group of four cylinders are placed in the domain according to: $cylinder_{11}$ and $cylinder_{12}$ are positioned side by side upstream with $cylinder_{12}$ positioned at a higher x-coordinate. $Cylinder_{21}$ and $cylinder_{22}$ are the downstream cylinders, where $cylinder_{21}$ is in tandem with $cylinder_{11}$ and $cylinder_{22}$ is in tandem with $cylinder_{12}$, respectively.

Results and Conclusions

In this paper, the normalized data has been plotted against the reduced velocity, $U^\star = U/(f_N D) = 1/f_N^\star$, where $f_N^\star$ is the in vacuo natural frequency of the system, and the staggering angle β. The effects of multiple cylinder-interaction on the vortex-induced vibrations is shown in Figure 1. The influence of the vortex shedding of the upstream cylinders upon the downstream cylinder motion is strong. An amplitude of (at most) 80 % larger than the upstream and single cylinder is observed. Investigating Figure 1(a) closer, around $U^\star \approx 6$, one can see a dip in the oscillation amplitude. This is probably caused due to the complex interaction among the cylinders, however further investigation is needed to fully understand this phenomenon. This effect can also be seen in the upstream cylinder, however, the dip in this case is much more less pronounced, indicating that this might be a feedback from the downstream cylinders.

The character of Figure 1(a) reveals that only two response branches exist, which is the initial
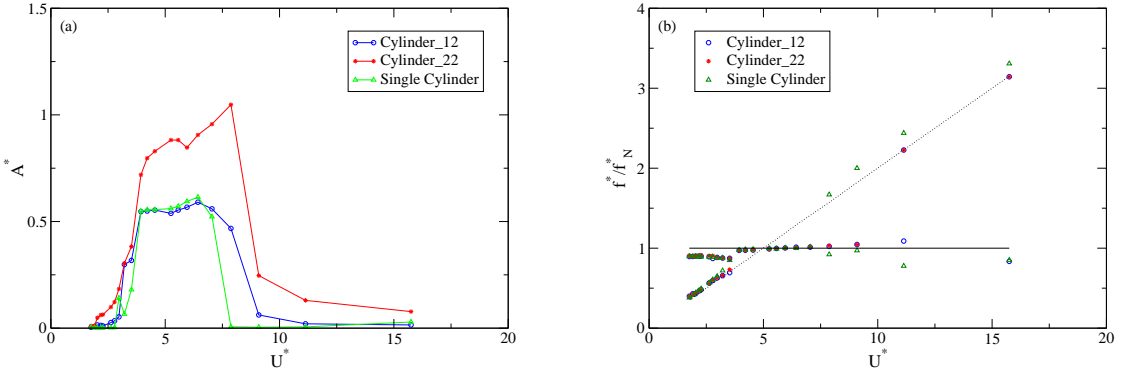
Figure 1: Amplitude (a) and frequency (b) of the cylinder motion for multiple and single cylinder configuration in the range of $U^\star = 1.761$ - $U^\star = 15.750$.

and the lower branches, also reported by Revstedt [5]. Additional effect of the multiple cylinder configuration, compared to the single cylinder case, is the range of synchronization velocities. As can be seen, both the upstream and downstream cylinders have a wider synchronization range than what is observed for a single cylinder.

Detailed investigation of the frequency response of the cylinders (Figure 1(b)) reveals that when decreasing the reduced velocity below $U^\star \approx 3$, the frequency of motion of the cylinders includes both the shedding frequency of a stationary cylinder and the natural frequency in a still fluid, i.e. also accounting for the hydrodynamic mass. The latter is according to Revstedt and Lazarkov [4] estimated to $0.87 f_N^\star$. This is a typical low branch response which is enhanced by the influence of the surrounding cylinders. For $U^\star > 3$, the commutative control of the frequency of motion disappears and now the cylinders are only locked into the in vacuo natural frequency. For values $U^\star > 8$ the cylinders are again commutatively locked into the shedding frequency of a stationary cylinder and the in vacuo natural frequency. The solid and dashed lines in Figure 1(b) represent the in vacuo natural frequency and the frequency of a stationary cylinder, respectively.

The behavior of the oscillations of multiple cylinder configuration as a function of the separation distance is tabulated in Table 1. The trend here is that the downstream cylinders achieve larger amplitudes for $L/D = 4$, going from the initial branch towards the lower branch. This trend might be expected since the cylinders are closer to each other giving rise to a stronger wake interference effects. However, no clear statement can be done for the upstream cylinders.

	$L/D = 4$				
	$U^\star = 7.044$	$U^\star = 4.547$	$U^\star = 3.937$	$U^\star = 3.215$	$U^\star = 2.273$
Cyl_{12}	$A^\star = 0.542$	$A^\star = 0.572$	$A^\star = 0.535$	$A^\star = 0.135$	$A^\star = 0.085$
Cyl_{22}	$A^\star = 1.188$	$A^\star = 0.862$	$A^\star = 0.755$	$A^\star = 0.433$	$A^\star = 0.075$
	$L/D = 5$				
Cyl_{12}	$A^\star = 0.559$	$A^\star = 0.554$	$A^\star = 0.546$	$A^\star = 0.298$	$A^\star = 0.011$
Cyl_{22}	$A^\star = 0.957$	$A^\star = 0.829$	$A^\star = 0.719$	$A^\star = 0.305$	$A^\star = 0.063$

Table 1: Vibration amplitudes $A^\star$ at two different separation distances, $L/D = 4$ and $L/D = 5$ for the upstream and downstream cylinders.

Figure 2 shows the effect of staggering for two different reduced velocities, $U^\star = 3.937$ and
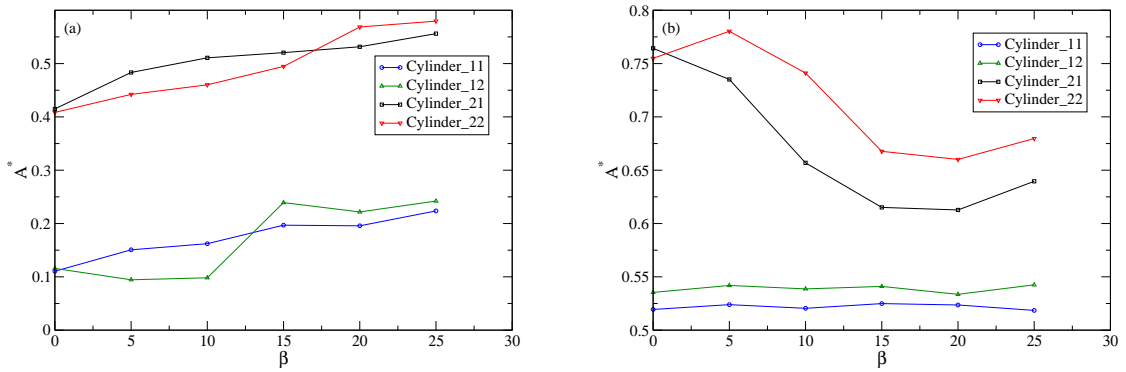
Figure 2: Effect of the staggering angle β on the response the multiple cylinder configuration for two different reduced velocities, $U^\star = 2.876$ (a) and $U^\star = 3.937$ (b).

$U^\star = 2.876$, one at the synchronized region and one nearly outside. For the latter case (Figure 2(a)), the results indicate that an increase in the staggering angle (β) increases the amplitude of oscillation gradually for all cylinders. The effect in the synchronization region (Figure 2(b)), on the other hand, has the opposite effect for the downstream cylinders, whereas the upstream cylinders maintain the same amplitude in average. However, there is an interesting behavior of the amplitudes of the downstream cylinders going from staggering angle $\beta = 20°$ to $\beta = 25°$. This phenomenon is probably related to that the lower downstream cylinder experiences the effect of both upstream cylinder wakes and will in turn enhance the motion of the upper downstream cylinder.

References

[1] A. Khalak and C. H. K. Williamson. Fluid forces and dynamics of a hydroelastic structure with very low mass and damping. *J. Fluid. Mech. Struct.*, **11**, 973–982, (1997).

[2] R. Govardhan and C. H. K. Williamson. Resonance forever: existence of a critical mass and an infinite regime of resonance in vortex-induced vibration. *J. Fluid. Mech.*, **473**, 147–166, (2002).

[3] T.L. Morse and C. H. K. Williamson. The effect of Reynolds number on the critical mass phenomenon in vortex-induced vibration. *Physics of Fluids*, **21**, 045105, (2009).

[4] M. Lazarkov and J. Revstedt. Fluid-induced motion of a short circular cylinder spanning a rectangular channel. *J. Fluid. Mech. Struct.*, **24**, 449–466, (2008).

[5] Johan Revstedt. Flow induced vibrations of dual cylinders in tandem formation in a channel flow. *Conference on Modelling Fluid Flow (CMFF'09). The 14th International Conference on Fluid Flow Technologies. Budapest, Hungary*, September 9-12, (2009).

[6] D. Brika and A. Laneville. The flow interaction between a stationary cylinder and a downstream flexible cylinder. *J. Fluid. and Struct.*, **13**, 579–606, (1999).

[7] J. Gullbrand, X. S. Bai and L. Fuchs. High-order Cartesian grid method for calculation of incompressible turbulent flows. *Int. J. Num. Meth. Fluids.*, **36**, 687–709, (2001).

[8] Johan Revstedt. A virtual boundary method with improved computational efficiency using a multi-grid method. *Int. J. Num. Meth. Fluids.*, **45**, 775–795, (2004).

Modelling of Flow around Two Aligned Cylinders

Ronnie R. Pedersen* and **Søren Leth**

Department of Civil Engineering
Aalborg University, Aalborg, Denmark
e–mail: rrp@civil.aau.dk

Summary   Flow around two cylinders is considered, where closed form solutions are compared to numerical results in order to justify the practical use of the theoretical solutions when the flow in front of the cylinders is analysed. For a relatively highly mutual distance between the cylinders the numerical and analytical results are comparable. Opposite, when the cylinders are closely placed the potential flow solutions become inadequate compared to the numerical findings.

Introduction

Modelling of flow around cylinders is of paramount importance in many engineering applications. Wind flow around wind turbine towers is one example. The presence of a wind turbine influences the wind flow locally which may develop into a turbulent flow. The turbulence in the wake behind the turbine is significantly different from the turbulence in front of the wind turbine. The wake effects behind the turbine is in particular important for the design of off-shore wind turbine farms [1] (annex D). The wind velocities at the blades depend on the position of the rotor plane i.e. if it is placed upwind or downwind. Tower shadow is another aerodynamic disturbance of the wind flow due to the presence of the tower [2]. During tower passage the blades hit a zone of stagnating and deflected mean wind velocities. The characteristics of the shadow zone is different in case of a downwind and upwind wind turbine. The complexity of these aerodynamic phenomena is further increased if the mono tower is thought replaced by a tripod configuration. Firstly, the question is if the disturbance from the interaction of the three cylinders is significant for the wind velocities. A second question is to what extent the analytical solutions properly estimate the wind velocities when compared to numerical results, where turbulence and wake effects are included. Therefore, in this paper we explore a closed form solution of the wind velocities around two aligned cylinders and compare the results to the wind velocities obtained from a computational fluid dynamic (CFD) model.

Closed form solution

The wind velocity components upstream in the vicinity of a single cylinder are determined from classical potential flow theory [5]. The wind velocity components for flow around multiple cylinders can be found from [3], where conformal mapping techniques are adopted. Here, we determine the velocity components based on the work by Alassar [4], where the problem is formulated in a bipolar coordinate system (ξ, η). The stream function for two cylinders reads

$$\psi = 2bU_0 \left(\psi_x \cos \gamma + \psi_y \sin \gamma \right), \tag{1}$$

where U_0 is the mean wind velocity, b is the mutual distance between the cylinders in the bipolar coordinate system and γ sets the direction of the incoming wind with respect to the cylinders, see Figure 1. The individual stream functions in equation 1 are

$$\psi_x = -\frac{\sinh(\xi)}{2(\cosh\xi - \cos\eta)} +$$

$$\sum_{n=1}^{\infty} \frac{\cos(n\eta)\exp(-n\xi_2)\sinh n(\xi - \xi_1)}{\sinh n(\xi_2 - \xi_1)} +$$

$$\sum_{n=1}^{\infty} \frac{\cos(n\eta)\exp(+n\xi_1)\sinh n(\xi - \xi_2)}{\sinh n(\xi_2 - \xi_1)} +$$

$$\sum_{n=1}^{\infty} \frac{\sinh n(\xi_2 + \xi_1)}{\sinh n(\xi_2 - \xi_1)},$$

$$\psi_y = \frac{\sin(\eta)}{2(\cosh\xi - \cos\eta)} -$$

$$\sum_{n=1}^{\infty} \frac{\sin(n\eta)\exp(-n\xi_2)\sinh n(\xi - \xi_1)}{\sinh n(\xi_2 - \xi_1)} +$$

$$\sum_{n=1}^{\infty} \frac{\sin(n\eta)\exp(+n\xi_1)\sinh n(\xi - \xi_2)}{\sinh n(\xi_2 - \xi_1)},$$

where indices x and y indicate flow parallel and perpendicular to the tripod legs, respectively, see Figure 1(left). In the following equations the radii R of the cylinders are identical. The distance
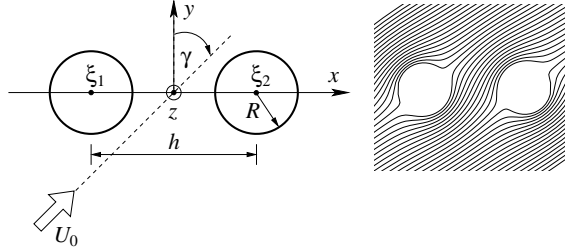

Figure 1: Orientation of free mean wind U_0 is controlled by the angle γ and the center of the cylinders is expressed in the bipolar coordinates ξ, whereas the physical distance between the cylinders is denoted h in Cartesian coordinates and b in the bipolar domain and the stream function ψ from equation (1) with $\gamma = \pi/6$.

between the cylinders in the bipolar coordinate system is defined as $b = R\sinh(\xi_2)$. The coordinate ξ_2 express the center of the second cylinder and is determined from $\xi_2 = \operatorname{arccosh}\frac{h}{2R}$. in which h is the physical distance between the cylinders and $\xi_1 = -\xi_2$ is the coordinate to the first cylinder. The stream function is illustrated in Figure 1(right), where $\gamma = \pi/6$ rad and $R = 1$ m. The relations between the bipolar and Cartesian coordinates are defined as [6]

$$x = \frac{b\sinh\xi}{\cosh\xi - \cos\eta}, \quad y = \frac{b\sin\eta}{\cosh\xi - \cos\eta}, \tag{2}$$

and after mathematically manipulations the inverse relations can be derived as

$$\xi = \operatorname{arccoth}\left(\frac{b^2 + x^2 + y^2}{2bx}\right), \quad \eta = \operatorname{arccot}\left(\frac{-b^2 + x^2 + y^2}{2by}\right). \tag{3}$$

The wind velocities are determined from

$$\left\{ \begin{array}{c} \frac{\partial\psi}{\partial x} \\[2mm] \frac{\partial\psi}{\partial y} \end{array} \right\} = \left[\begin{array}{cc} \frac{\partial x}{\partial\xi} & \frac{\partial y}{\partial\xi} \\[2mm] \frac{\partial x}{\partial\eta} & \frac{\partial x}{\partial\eta} \end{array} \right]^{-1} \left\{ \begin{array}{c} \frac{\partial\psi}{\partial\xi} \\[2mm] \frac{\partial\psi}{\partial\eta} \end{array} \right\}. \tag{4}$$

Numerical solution

The flow field is modelled with the incompressible Reynolds Averaged Navier-Stokes (RANS) equations with the $k - \epsilon$ turbulence model in a transient solution in ANSYS Flotran. A Courant number lower than one is ensured with a time step size $\Delta t = 0.05$ s, minimum element size 0.12 m and a maximum wind velocity 2 m/s.

Example with flow perpendicular to the cylinders ($\gamma = 0$)

The control domain is $(x, y) = [-15, 15]$ m and the centers of the two cylinders with radii $R = 1$ m are placed at the line $y = 0$ with a mutual distance $h = [3\,6\,9]$ m. The free mean wind velocity is $U_0 = 1$ m/s. The Reynolds number is Re $\approx 1.3 \cdot 10^6$ with a kinematic viscosity $\nu = 15.0 \cdot 10^{-6}$ m^2/s, which means the separation at the boundary layer remains laminar with a vortex shedding behind the cylinders. The theoretical and numerical wind velocity component
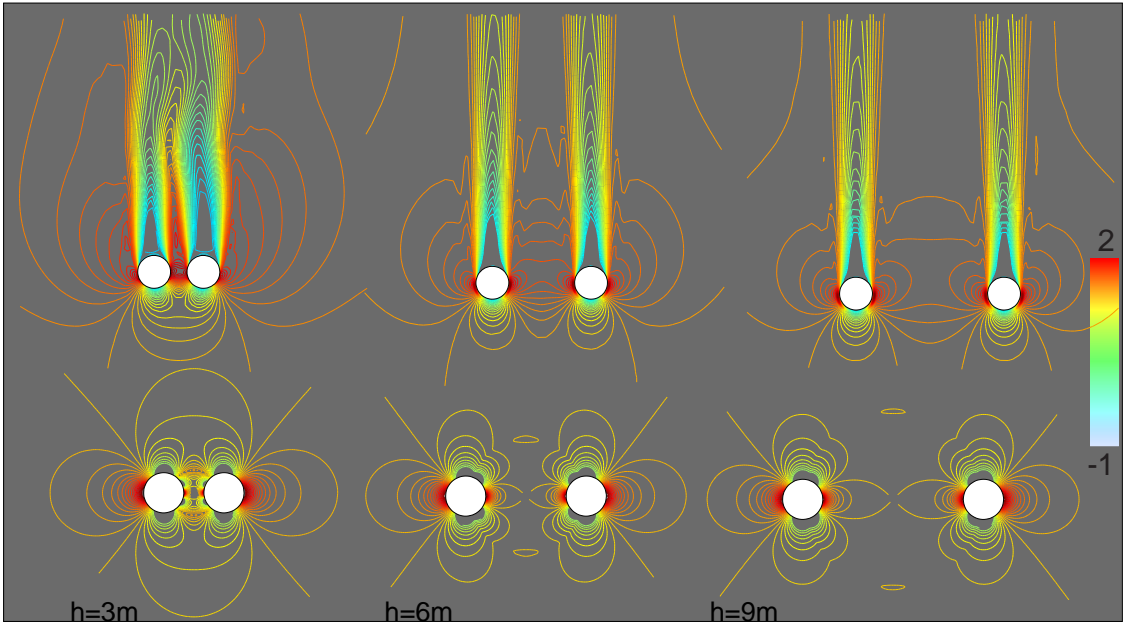
Figure 2: Contour plot of velocity component U_y [m/s] obtained from CFD computations (top) and analytical solution (bottom) with $\gamma = 0$ and different distances h between the cylinders.

$U_y(x, y)$ for $y = [-2, 2]$ m are presented in Figure 3, whereas Figure 2 shows the contour plots of U_y. We observe that the shadow zone (decreased velocity) is increased as the mutual distance of the cylinders is decreased. The potential flow theory underestimates the wind velocity in between the cylinders when compared to the numerical findings. Locally in front of the cylinders and at the exterior sides the velocity profiles are fairly comparable. However, behind the cylinders the potential flow theory is invalid as expected and negative velocities are found due to wake effects in the numerical simulations.

Concluding remarks

Wind flow around two aligned cylinders with arbitrary distance is considered. The purpose is to justify the use of potential flow theory to determine the wind velocities in front of the cylinders
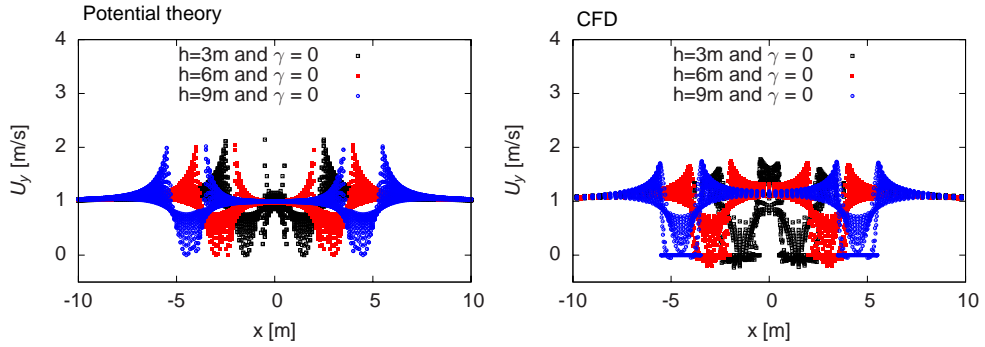
Figure 3: Wind velocity $U_y(x, y)$ ($y = [-2, 2]$ m) for $\gamma = 0$ coordinate and the distance h between the cylinders.

when compared to more realistic CFD computations.

The potential flow theory predicts the velocities well in front of the cylinders when compared to CFD simulations with turbulence included. However, in between the cylinders the theoretical velocities become inadequate when the mutual distance is lower than 6 m. Clearly, behind the cylinders the potential flow theory is invalid. Therefore, in case of a down wind turbine with a tripod tower configuration [2], the idea is to tabulate the wind velocities obtained from various CFD computations with flow passing multiple cylinders from different directions. With this database, more realistic wind velocities are imposed to the wind turbine blade and an accurate estimate of the fatigue life is possible.

Acknowledgements

References

[1] IEC. *Wind turbine - part 1 design requirement*. IEC 61400-1:2005(E) 3rd edition.

[2] P. Thoft-Christensen, R.R. Pedersen and S.R.K. Nielsen Numerical Estimation of Fatigue Life of Wind Turbines due to Shadow Effect. *Proceedings of the 10th International Conference on Structural Safety and Reliability*, eds: M. Dogaki and M. Sakano and S. Nishimura, Kansai University, Japan, (2009).

[3] D.G. Crowdy Analytical solutions for uniform potential flow past multiple cylinders. *J. Fluids Eng.*, **25**, 459–470, (2006).

[4] R.S. Alassar and M.A. El-Gebeily Inviscid flow past two cylinders. *J. Fluids Eng.*, **131**, 054501-1–054501-6, (2009).

[5] L.M. Milne-Thompson *Theoretical Aerodynamics*. Dover Publications, (1996).

[6] R.A. Ibrahim. *Liquid sloshing dynamics: theory and applications*. University Print, Cambridge, (2002).

Some models for numerical simulations of brittle failure

Kari Kolari and Juha Kuutti

VTT Technical Research Center of Finland
e–mail: firstname.lastname@vtt.fi

Juha Hartikainen and Reijo Kouhia*

Department of Structural Engineering and Building Technology
Helsinki University of Technology, Finland
e–mail: firstname.lastname@tkk.fi

Summary   One of the greatest challenges in the numerical analysis of quasi-brittle materials is the modelling the failure itself the continuous failure process due to material disintegration. Using advanced methods, analysis can be continued after complete material failure and failed sections can be retained in the model without violating the mass conservation. In this paper a new approach for the modelling of disintegration is proposed. In the approach the failure of material is modelled with anisotropic continuum damage mechanics (CDM) model. The CDM model is used to predict direction of a crack evolution while the proposed model update technique is applied to propagate the crack in FE geometry. The proposed approach has been applied in the simulation of tensile test and interaction of conical structure and level ice.

Introduction

The modeling of material disintegration is a fundamental issue in the modeling of continuous failure processes; e.g. ice structure interaction process cannot be simulated unless the material transition from continuous to discontinuous is taken into account because during the interaction process ice first fails and finally due to fracturing becomes discontinuous as shown in figure 1.

Models based on continuum damage mechanics (CDM) have been successfully applied in the modelling of anisotropic stiffness degradation due to damaging. The approach used in this paper enables phenomenological modelling of directional damaging as tensile cracking and axial splitting under uniaxial loading [2]. In the approach directional damage is modeled using damage vector based approach.

Most materials also exhibit rate-dependent inelastic behaviour. Increasing strain-rate usually increases the yield stress thus enlarging the elastic range. However, the ductility is gradually lost, and for some materials there exist a rather sharp transition strain-rate after which the material behaviour is completely brittle. A simple phenomenological approach to model ductile-to-brittle transition of rate-dependent solids is presented. The model is based on a consistent thermodynamic formulation using proper expressions for the Helmholtz free energy and the dissipation potential, which is additively split into damage and visco-plastic parts, and the transition behaviour is obtained through a stress dependent damage potential [1].

Modelling of disintegration

The CDM model provides data about the magnitude and orientation of damage in each element. Phenomenally the damage represents an actual crack inside the element. Using this information the finite element analysis is paused and mesh is updated so that the crack predicted by the CDM model is explicitly created in the mesh. After the update the analysis is continued with the updated
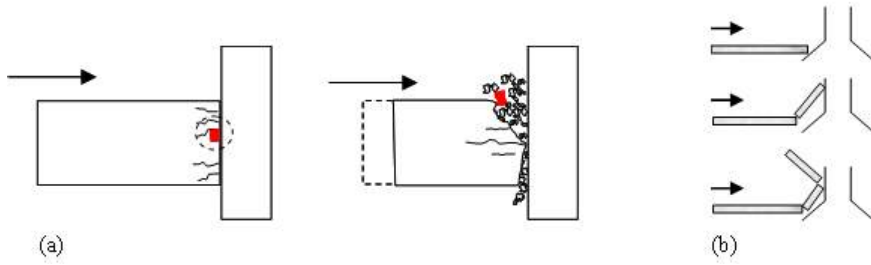
Figure 1: Material transition from continuous to discontinuous; a) crushing b) bending.

mesh. This technique is implemented into commercial finite element code Abaqus/Explicit using Python scripting.

The intersection points for the damage plane and each element edge is calculated separately, see figure 2. If the element is rectangular, this approach yields to four intersection points on opposite edges and element splitting can be done as specified by the damage vector. If the element is irregular but still 8 node, the intersection points can lay outside the element edges and splitting is not possible in the given direction. In this case splitting is done in a direction closest to the original vector that yields to two 8 node elements. A tolerance for the node proximity to the nearest original node is specified so that the side ratios in the created elements are allowable.
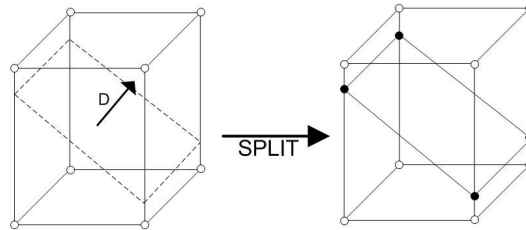
Figure 2: Element splitting based on the direction of the damage vector D.

Examples

Tensile test simulation

The example illustrates the effectiveness of the proposed model update technique in the simulation of tensile failure. The loading was velocity controlled with the velocity of 3 mm/s. The commercial FE-software Abaqus/Explicit was used in the simulation. The specimen was modelled with C3D8R elements. Two elements were used in the thickness direction and the total number of elements was initially 612, see figure 3.

Bending failure

Interaction of inclined structure with 30 cm thick level ice was analysed using the proposed model update technique. The number of C3D8R elements used was initially 792. Due to cracking new elements are created, therefore the number of elements is increased during the analysis, figure 4.
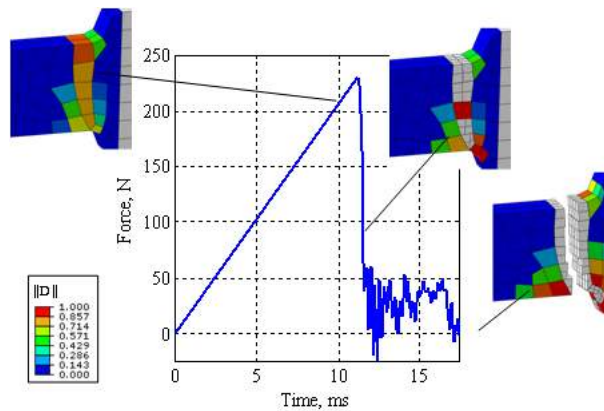
Figure 3: Axial force, damage evolution and crack propagation near the right end of the specimen.
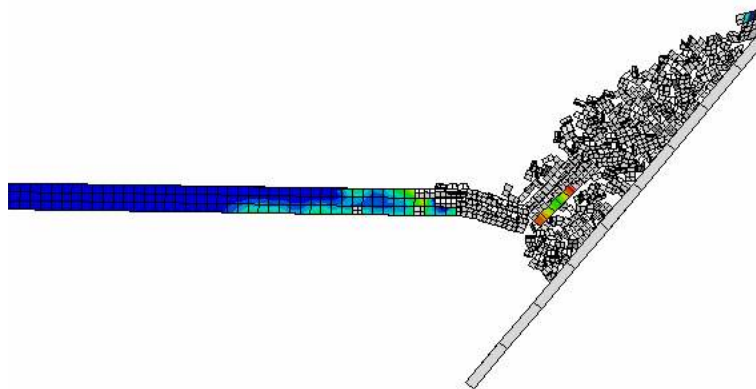
Figure 4: Evolution of particles due to disintegration during interaction, ice floe velocity is 10 cm/s.

References

[1] S. Fortino, J. Hartikainen, K. Kolari, R. Kouhia, T. Manninen, A constitutive model for strain-rate dependent ductile-to brittle-transition, *The IX Finnish Mechanics Days*, 13-14.6.2006, Lappeenranta, Finland, R. von Herzen and T. Halme (editors), pp. 652–662. http://www.hut.fi/Yksikot/Rakenteidenmekaniikka/julkaisut/2006/fortino_etal_smp06.pdf

[2] K. Kolari, *Damage mechanics model for brittle failure of transversely isotropic solids - Finite element implementation*, VTT Publications 628, Espoo 2007. http://www.vtt.fi/inf/pdf/publications/2007/P628.pdf

Propagation of a single crack under RCF conditions using the concept of material forces

Jim Brouzoulis*, **Johan Tillberg, Fredrik Larsson and Kenneth Runesson**

Department of Applied Mechanics
Chalmers University, Gothenburg, Sweden
e–mail: jim.brouzoulis@chalmers.se

Summary   This paper deals with the propagation of a single crack under RCF loading conditions. Two methods for propagating the crack are studied, both based on the concept of material forces for linear elastic material behavior. For these methods, the influence of surface friction conditions as well as that of initial crack inclination on the final crack path are investigated.

Introduction

Rolling Contact Fatigue (RCF) of rails is a major problem worldwide. Common RCF defects that can be observed in rails are *tounge lipping*, *head checks* and *squats*. However, only the development of head checks will be investigated in this paper. Head checks are typically closely spaced cracks which start out almost parallel. The cracks are initiated at the rail surface and are more common near the gauge corner in curves. Also the friction conditions affect the initiation of head checks. Cracks are more easily initiated under dry conditions (i.e. high friction coefficient) than in wet (i.e. low friction coefficient).

To properly simulate the propagation of a crack, we need to model how fast and in what direction it grows. A *generalized crack driving force*, abbreviated *GCDF*, will be derived from energy considerations in the material domain, giving rise to so called material forces. Based on the GCDF two different methods for propagating an existing crack will be presented. Furthermore, the proposed methods will be applied to the problem of simulating the development of a single head check crack under rolling contact fatigue (RCF) conditions.

Crack Driving Force

In order to establish the crack driving force, we study the change os rate of mechanical dissipation $\mathcal{D}(\delta\dot{\boldsymbol{X}})$ due to a variation of the domain $\mathcal{B}_X$, e.g. the extension of a crack. Following [1], this sensitivity can for a linear elastic body be expressed as

$$\mathcal{D}(\delta\dot{\boldsymbol{X}}) = \int_{\Omega_X} -\boldsymbol{\Sigma} : [\dot{\boldsymbol{X}} \otimes \boldsymbol{\nabla}_X]\, \mathrm{dV_X} \tag{1}$$

where the Eshelby stress tensor $\boldsymbol{\Sigma}$ is defined as

$$\boldsymbol{\Sigma} = \Psi_X \boldsymbol{I} - \boldsymbol{F}^{\mathrm{T}}\boldsymbol{P} \tag{2}$$

Here, Ψ_X is the volume specific strain energy, $\boldsymbol{I}$ is the identity tensor, $\boldsymbol{F}$ is the deformation gradient and $\boldsymbol{P}$ is the 1st Piola-Kirchhoff stress tensor.

Based on the rate of mechanical dissipation, the GCDF can be expressed as

$$\boldsymbol{\mathcal{G}} = \int_{\Omega_X} -\boldsymbol{\Sigma} \cdot (\varphi\boldsymbol{\nabla}_X)\, \mathrm{dV_X} \tag{3}$$

where φ is a suitably chosen weight function of unit value at the crack tip. In this manner, the GCDF is the change of rate of mechanical dissipation due to an advancement of the crack tip.

Crack Propagation Modeling

In the following simulations, a viscous propagation law has been adopted, whereby the rate of crack propagation is assumed proportional to the crack driving force. For sufficiently small time steps, this integration can be carried out in an explicit fashion.

Crack Extension Method I: Proportional Extension Method

Based on the GCDF for the existing crack, we may formulate a propagation law as

$$\dot{a} = \gamma < \Phi > \frac{\partial \Phi}{\partial \mathcal{G}} \tag{4}$$

with the constitutive parameter γ and the crack-driving potential Φ. The expression for the potential Φ is assumed as follows:

$$\Phi = |\mathcal{G}| - \mathcal{G}_{cr} \tag{5}$$

where $\mathcal{G}_{cr}$ is a parameter that describes the fracture toughness. By integrating eq. (4) in time, the propagation of the crack can be predicted. By the particular choice of Φ in (5), the crack tip velocity is proportional (in magnitude and direction) to the GCDF, see Fig. 1a. This simply means that the crack tip is incrementally extended in the direction of the GCDF. It is by far the fastest of the methods considered.

Crack Extension Method II: Virtual Crack Extension Method

Following of [2], a possible approach is to compute the energy release rate caused by a number of virtual extensions of the crack tip. The crack tip is extended a small increment in one of the predefined virtual directions, and the energy release in the corresponding direction is computed, cf. Fig. 1b. The direction with the largest energy release parallel to the virtual crack, $\mathcal{G}_{\parallel}^{vc}$, is taken as the propagation direction.
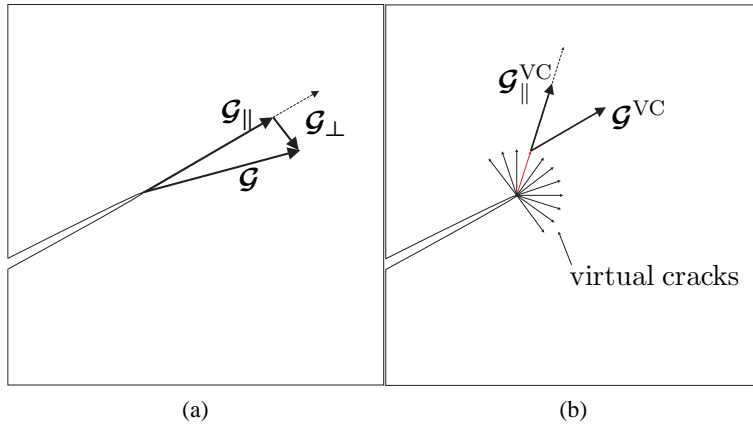
Figure 1: *Crack Extension Methods: a) Proportional Extension Method. b) Virtual Crack Extension Method.*

Problem description

To get an understanding of the characteristics of the propagation of a single surface crack in a piece of rail material subjected to a moving load, a simplified example is investigated. The material is

assumed to be linear elastic and in a state of plane strain. The normal load $P_N(x,t)$ is assumed to be given by an elastic Hertzian contact pressure, see e.g. [3]. Moreover, the traction stress $P_T(x,t)$ is obtained from the normal pressure $P_N(x,t)$ and the coefficient of friction μ by assuming full slip, i.e $P_T(x,t) = \mu P_N(x,t)$. The traction stress P_T is assumed to act in the direction opposite to the velocity of the wheel. Furthermore, the crack surfaces are assumed smooth (i.e. no friction). In Figure 2, the problem together with the resulting crack path for a crack of initial length 1 mm and with an initial inclination of $45°$, is shown.
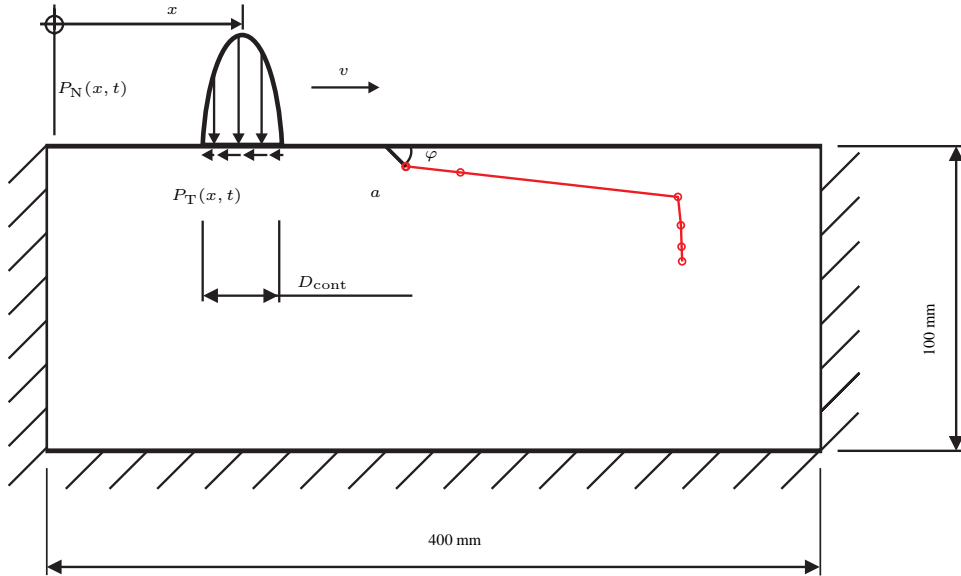
Figure 2: *2D model of a rail subjected to a moving contact load together with a example of simulated crack path.*

Concluding remarks and outlook

From the simulations it is concluded that the proportional extension method results in strongly mesh-dependent predictions and is, therefore, deemed as a less suitable method for crack propagation under RCF loading conditions. Preliminary parametric studies show that the prominent propagation direction is independent of the initial crack direction and surface friction condition. Furthermore, after reaching a critical length, the cracks changed direction and started to grow downward at a angle into the rail material.

References

[1] F. Larsson, K. Runesson and J. Tillberg. *On the sensitivity of the rate of global energy dissipation due to configurational changes. European Journal of Mechanics - A/Solids*, **28**, 1035-1050, (2009).

[2] T.K. Hellen. *On the method of virtual crack extensions. Int. J. Num. Meth. Eng.*, **9**, 187-207, (1975).

[3] K.L. Johnson. *Contact Mechanics*. Cambridge University Press, Cambridge, Ninth edition , (2003).

Effect of geometrical irregularity and scale on failure of wood-like cellular materials

Alp Karakoç ∗ and Jouni Freund

Department of Applied Mechanics
Helsinki University of Technology, FIN-02015, Espoo, Finland
e−mail: alp.karakoc@tkk.fi

Summary Micromechanical modeling and finite element simulation are used to study strength of honeycomb material. The effects of geometrical irregularity and scale are discussed by comparing the statistics of failure initiation for some different populations of specimen.

Introduction

Strength of wood originates from cellulose and hemi-cellulose matrix bound together with lignin [1]. This composite structure forms thin-walled, long cells, called tracheids, having roughly hexagonal cross sections (Figure 1). Early- and latewood (growth ring materials) have differences in density, cell wall thickness, cell wall configuration, and cell number per unit volume. In practice, wood is heterogeneous on scales of engineering interest, and, therefore statistical description is needed e.g. in strength predictions.
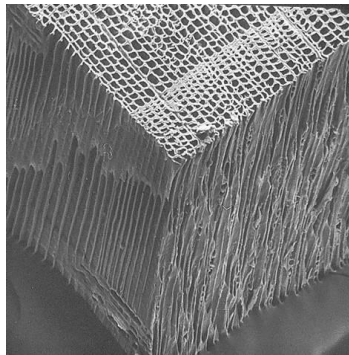
Figure 1: Tracheids forming early- and latewood [2].

The aim is to discuss the effect of geometrical features of cellular material and size of the specimen on statistics of failure initiation load by using micromechanical modeling. A square sample of wood-like honeycomb material with thin walls, is considered. In the simple model used, the walls are taken as slender beams, the material inside the cells is soft compared to the walls, and the walls are almost inextensible. Bending moment on a wall is chosen to be critical for failure. Also, as the length-to-thickness ratio of cells tends to be large (Figure 1), only the plane perpendicular to the long direction of cells is considered.

Micromechanical model

A square sample of the honeycomb material consisting of hexagonal cells is illustrated in Figure 2. In the micromechanical model, the walls of the cells are modelled by using Timoshenko beams with quadratic interpolation in order to provide applicability in a wider range, i.e., from slender to thick beams [3] and the material inside the cells is taken to be soft compared to the walls. Thickness to length ratio of the beams is assumed to be small.
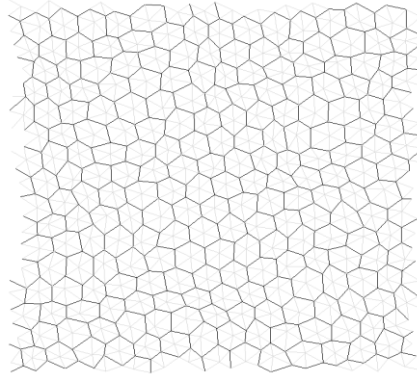
Figure 2: Rectangular specimen composed of irregular hexagonal cells.

The geometrical irregularity of the honeycomb is defined through construction in which the hexagons consist of six triangles. Triangles are grouped into four to form larger triangles whose vertices coincide with those of the small triangle. Then, the regular positions of the remaining three vertices of the small triangles are defined to be at the midpoints of the edges of the large triangle, and irregularity is measured as difference between the actual and regular positions. It is followed by grouping the larger triangles again to end up with a set of relative regularity measures. In mesh generation, reverse process with a given statistics of irregularity gives the geometry.

In micromechanical simulation of strength, first, a sample of specimen consisting of hexagonal cells is generated. Thereafter, finite element method is used to find the value of the external force acting on a specimen making at least one beam to fail. This is repeated for all specimens. Finally, obtained data is represented with a cumulative distribution function describing the probability of specimens to fail under chosen loading condition. Repetition of all the steps for different selections of geometrical parameters depicts the effect of scale and irregularity on failure initiation.

Case study: Effect of scale and irregularity on failure initiation

In the case study, $H \times H$ square specimens of honeycomb material having fixed cell size h were used. The geometrical irregularity of the honeycomb structure was generated by random sampling from the uniform distribution in range $\alpha[-h, h]$ (α is a parameter). The external force was chosen to be compressive distributed load f acting on opposite sides of the specimen. Finally, the bending moment with the limit value $\overline{M}$ was chosen to be decisive for failure initiation.

According to the weakest link theory [4], the cumulative density function of $fh^2 / \overline{M}$ satisfies

$$\mathrm{cdf}\,(\alpha,\frac{H}{\underline{H}}) = 1 - (1 - \underline{\mathrm{cdf}}(\alpha))^{(\frac{H}{\underline{H}})^2} \; . \tag{1}$$

in which the underscore for $\underline{H}$ denotes reference size of the specimen and $\underline{\mathrm{cdf}}(\alpha)$ is the corresponding cumulative density function of failure initiation. The results obtained through micromechanical simulations related with (1) and the effect of irregularity parameter, i.e. $\underline{\mathrm{cdf}}(\alpha)$, will be given in the presentation.

Concluding remarks

Statistical failure initiation model for wood-like cellular materials has been generated. Due to difficulties in physical experiments and setup, numerical experiments have been carried out on microcomputer by means of micromechanical model at this stage. As following steps, statistical model on failure will be developed and more precise physics, i.e. inclusion of layers of cell wall, mimicking natural formation, etc., will be considered.

References

[1] K. Persson. Modelling of wood properties by a micromechanical approach. *Report TVSM-3020*, University of Lund, Lund (1997).

[2] http://www.steve.gb.com/images/science/softwood.jpg

[3] Abaqus version 6.5 Documentation, *Analysis User's Manual*

[4] W. Weibull. A statistical theory of the strength of materials. *Ingenjörsvetenskapsakademiens Handlingar 151*, 1-45, (1939).

Evaluation of Geometrical Irregularity of Wood-like Hexagonal Structures

Johanna Sjölund* and Jouni Freund

Department of Applied Mechanics
TKK, Espoo, Finland
e–mail: johanna.sjolund@tkk.fi

Summary   Wood can be taken to be composed of honeycomb material containing geometrical features of various scales. A simple way to quantify the geometrical irregularity of a material sample is presented. Effects of sample size and scale are discussed by using an example with known statistics of irregularity.

Introduction

Wood can be taken to be composed of thin-walled, long cells having roughly hexagonal cross sections (Figure 1). Cells form growth rings with differences in e.g. density, cell wall thickness, cell wall configuration and cell number per unit volume. In addition, the cell structure contains geometrical features of various scales. As the mechanical properties of wood, such as strength depend on e.g. on the microstructure and scale, a material model should somehow include information on those. Although direct experimentation on the effect of cell structure regularity is not a realistic option, simulation by a micromechanical cell-scale model may be used to obtain qualitative understanding.
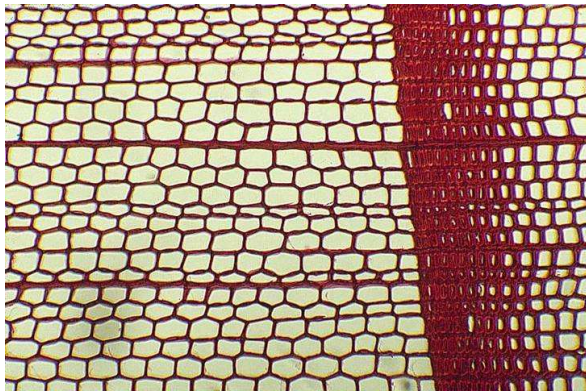
Figure 1: Softwood cell structure showing also the growth ring [1].

According to review [2] most micromechanical models of wood are based on a honeycomb, where a hexagonal cell is repeated in a more or less regular manner [3, 4]. Some of the models take into account the variation of the growth ring [5]. A few references consider the irregularity of wood by tracing the scanned image cell by cell [6, 7, 8]. However, to our knowledge, modelling the statistics of regularity to be used in generation of cellular material samples for finite element analysis has not been considered.

The aim is to discuss a simple way to quantify the geometrical irregularity of a given sample of honeycomb material so that modelled material has similar geometrical characteristics. Then one may generate a sample of specimen, use a micromechanical model, finite element method, and statistical analysis of results to improve the understanding on the effect of irregularity on macroscopic level.

Irregularity

Wood can have many different type of irregularities which need to be identified and modelled correctly by the analysis. As seen in Figure 2 the same type of irregularity forms completely different looking samples if applied to different scales. Morphing of the whole sample, for example continual cell growth of the growt ring in wood, cannot be analysed correctly. These type of irregularities need to be separately modelled.
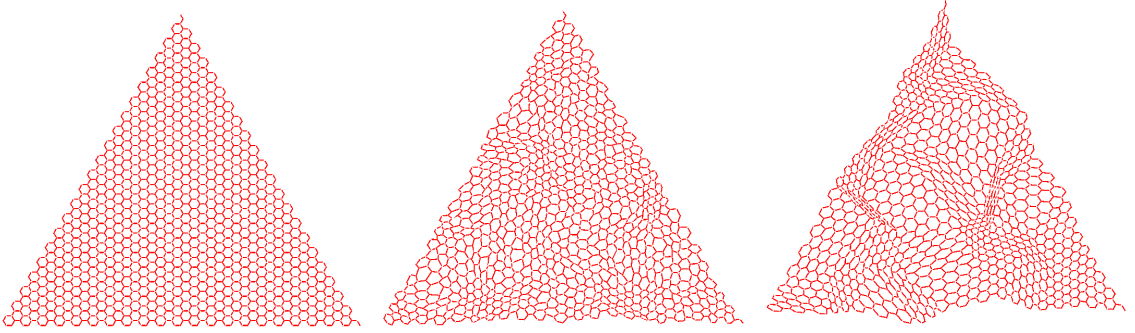
Figure 2: On the left, regular specimen. In the middle, specimen taken from a population having irregularities on various scales defined by the uniform distribution. On the right, specimen taken from a population having irregularities on one scale defined by the uniform distribution.

Method

A topologically regular honeycomb is assumed so that the actual geometry can be obtained by point mapping. In the analysis hexagons are taken to consist of six triangles. The reference geometries are formed by grouping four triangles into larger triangles and moving vertices following a certain rule. Quantification of irregularity is based on comparison of the actual and reference geometries. To be precise, deviations $\Delta\vec{x}_i$ (Figure 3) are used to form the experimental cumulative density function

$$cdf(a) = |\{a_i \in \Sigma : a_i < a\}| / |\Sigma| \tag{1}$$

in which a stands for Δx_i or Δy_i and $|a|$ denotes the size of set a. This is repeated as many times as needed to get information on irregularity on different scales.

Example

A sample, generated using known statistics of irregularity, is used to discuss the effect of sample size and scale of irregularity on the outcome of the analysis. The analysis of the sample can be used as a base to generate a population(Figure 4). The analysis also gives information on what type of irregularity has caused a certain geometry.

Concluding remarks

Finding the statistics on geometrical irregularities of the sample has been discussed. This procedure can be repeated multiple times to see if all features are analysed correctly. In the future also morphing will be included in the analysis. The ultimate goal is to automatically analyse a scanned image and use the result for strenght modelling.
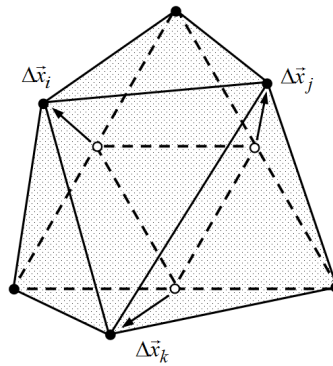
Figure 3: Element level coordinate mapping. Reference geometry in broken line. Actual geometry in solid line and shading.
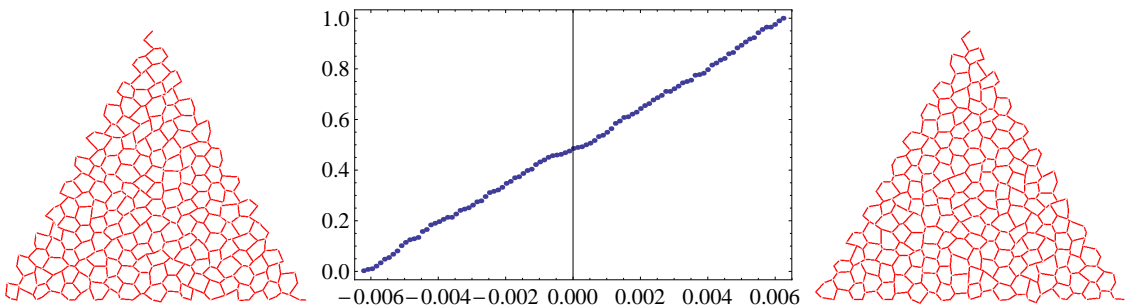
Figure 4: On the left a sample where a uniform distribution has been introduced in one scale. In the middle the cdf of the sample. On the right a sample generated using the statistics.

References

[1] http://www.steve.gb.com/images/science/softwood_rings.jpg

[2] L. Mishnaevsky Jr. and H. Qing. Micromechanical modelling of mechanical behaviour and strenght of wood: State-of-the-art review. *Comp. Mater. Sci.*, **44**, 363–370, (2008).

[3] l. J. Gibson and M. F. Ashby. *Cellular solids: Structure and properties*. Pergamon Press, Oxford, Second edition (1988).

[4] O.C. Zienkiewicz and R.L. Taylor. Transverse Youngs Moduli and Cell Shapes in Coniferous Early Wood. *Holzforschung*, **56**, 1–6, (2002).

[5] F. k. Wittel, G. Dill-Langer, and B. H. Kroplin. Modeling of damage evolution in soft-wood perpendicular to grain by means of discrete element approach. *Comput. Mater. Sci*, **32**, 594–603, (2005).

[6] K. Persson. *Micromechanical modelling of wood and fibre properties*. Doctoral thesis, Lund University, (1997).

[7] S. Holmberg, K. Persson, and H. Petersson. Nonlinear mechanical behaviour and analysis of wood and fibre materials. *Comput. Struct.*, **72**, 459–480, (1999).

[8] E. Kahle and J. Woodhouse. The influence of cell geometry on the elasticity of softwood. *J. Mater. Sci*, **29**, 1250–1259, (1994).

Isogeometric analysis for integration and performance

Trond Kvamsdal∗, Knut Morten Okstad and Vibeke Skytt

Department of Applied Mathematics
SINTEF ICT, Trondheim, Norway
e−mail: Trond.Kvamsdal@sintef.no, Knut.Morten.Okstad@sintef.no and Vibeke.Skytt@sintef.no

Geir Skeie

Veritas Research & Innovation
Veritasveien 1, 1322 Høvik, Norway
e−mail: Geir.Skeie@dnv.com

Summary An introduction to isogeometric analysis is given. Both its role as an enabling tool for integration of computer aided design and analysis and its numerical performance will be addressed.

Integration of computer aided design and analysis

The engineering process starts with designers encapsulating their perception using Computer Aided Design (CAD) tools. Thus, the geometry described in CAD systems is to be considered *exact* in the sense that it represents the projection from the designers perception of the desired object onto an electronic description. Today most CAD systems use spline basis function and often Non-Uniform Rational B-Splines (NURBS) of different polynomial order.

During and after the design stages different levels of numerical solid and fluid simulations are performed on the object. Very often this involves using the Finite Element Method (FEM) where the geometry is represented by piecewise low order polynomials. This practise introduce either significant approximation errors or fine FEM models with a large number of finite elements that make the numerical simulation computational costly. Furthermore, a huge amount of man-hours (***in some applications about 80% of total time is spent on mesh generation***, see Hughes *et al*. 2005) have to be spent in order to *remodel* the object into a suitable finite element mesh. This information transfer between models suitable for design (CAD) and analysis (FEM) is considered being a severe bottleneck in industry today.

To address this issue Hughes *et al*. (2005) introduced a analysis framework which is based on NURBS (Non-Uniform Rational B-Splines), which is standard technology employed in CAD systems. They propose to match the exact CAD geometry by NURBS surfaces, then construct a coarse mesh of *Spline Elements*. Throughout, the isoparametric philosophy is invoked, that is, the solution space for dependent variables is represented in terms of the same functions which represent the geometry. For this reason, they denote it isogeometric analysis.

Numerical performance

Recent studies have shown that finite elements based on the isogeometric concept have superior numerical performance compared to classical Lagrange finite elements. First of all we will mention that isogeometric finite elements result in lower approximation error than classical finite elements. The convergence order is the same for same order elements, but the actually error may be of one magnitude lower (i.e. the error is shifted downwards in a log-log plot). Furthermore, the conditioning of the resulting system matrix is also typically on order of magnitude lower, and this

is of importance when using iterative solvers. Finally, for eigenvalue problem the isogeometric elements performs significantly better both qualitatively (no divergence of the higher modes) and quantitatively (lower error in the lower modes).

Concluding remarks

In a project co-funded by the Research Council of Norway, Ceetron, Det Norske Veritas and StatoilHydro, SINTEF ICT and NTNU will make spline based elements (both NURBS and T-spline) available for integrated computer aided design and analysis (ICADA) of industrial relevant problems in civil, mechanical and naval engineering. In particular we will focus on stiffened thin walled structures and offshore pipelines. We will herein present results obtained by a prototype spline FE solver applied to cases relevant for ship engineering.

References

[1]   T. J. R. Hughes, J. A. Cottrell and Y. Bazilevs: Isogeometric analysis: CAD, finite elements, NURBS, exact geometry and mesh refinement, *Computer Methods in Applied Mechanics and Engineering*, 194: 4135-4195 (2005).
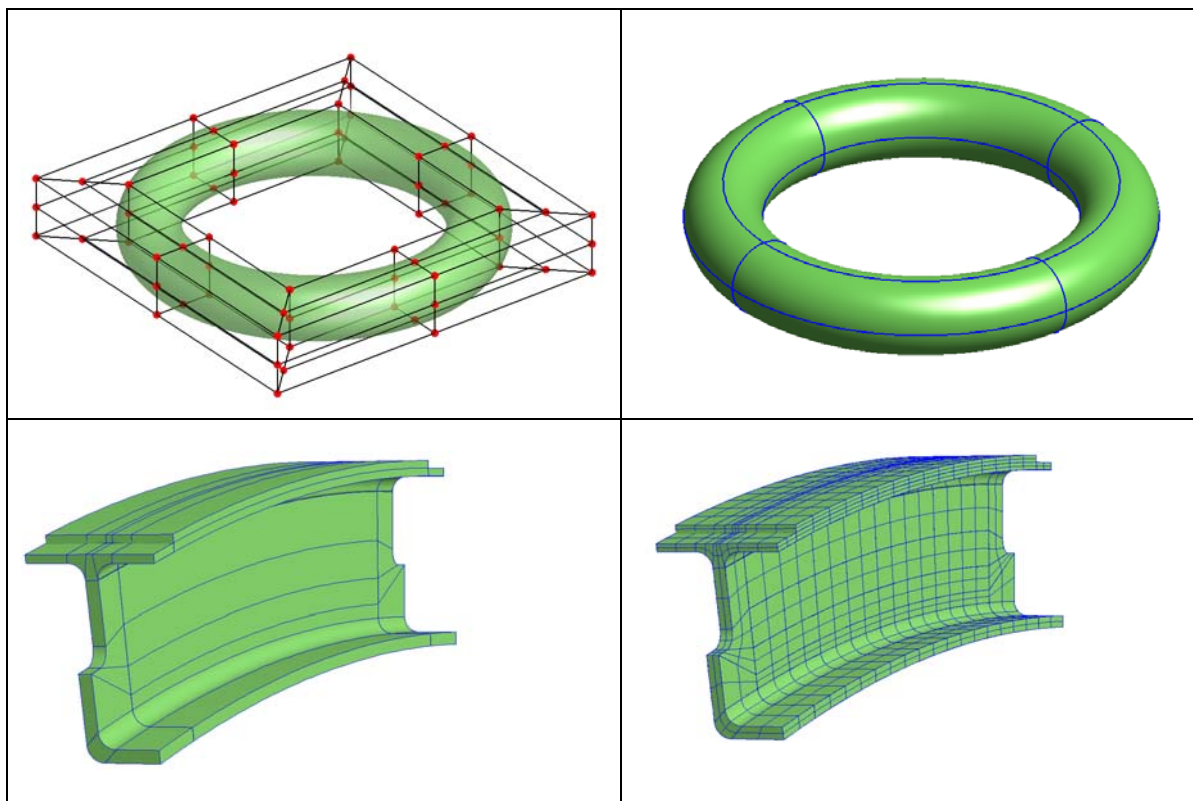
Figure 1. Examples on isogeometric representation and spline finite element meshes. *Upper left:* The control net for a toroidal surface. *Upper right:* The corresponding spline element net for the toroidal surface (notice that the geometry for the toroidal is exactly represented). *Lower left:* Coarse spline element mesh for a beam element. *Lower right:* Fine spline mesh for the same beam element (notice that the geometry is exactly the same for the two different spline meshes). (Courtesy Professor T. J. R. Hughes, UT-Austin, TX)

Adaptive isogeometric analysis using T-splines

Kjetil André Johannessen[*] **and Trond Kvamsdal**

Department of Mathematical sciences
Norwegian University of Science and Technology, Trondheim, Norway
e–mail: kjetijo@math.ntnu.no and Trond.Kvamsdal@math.ntnu.no

Summary We present an adaptive T-spline finite element solver in an isogeomtric setting. Traditional NURBS basis functions are tensor-product, while T-splines allow for true local refinement. This is proving superior to problems containing singularities. Moreover, T-splines is having a positive effect on smooth problems as well, since it will make the solver less prone to the choice parametrization.

Introduction

Hughes et al. [2] introduced the concept of isogeometric finite element method (FEM) solvers by using non-uniform rational B-splines (NURBS) as a basis. One of the main arguments is that modern computer aided engineering (CAE) is seeing a severe bottleneck in the construction of analysis suitable geometries. Hughes reports that as much as 20 percent of the time used in a CAE pipeline is used for creating a geometric model which for analysis is *possible*, while as much as 60 percent of the time is used creating a model which is *good* for analysis purposes. This totals a 80/20 factor of geometry construction versus actual analysis. Needless to say, it is a strong desire in the community to reverse this factor. NURBS basis functions itself might reduce the first 20 percent by allowing geometry construction to take place in existing computer-aided design (CAD) tools which have perfected this process for decades. T-splines along with adaptive refinement through a posteriori error estimates is what is making the last step superfluous by completely automating this process, allowing the designer to ultimately focus on the task at hand, which is making a model in which analysis is *possible*.

T-splines

For our solutions, we will be using T-splines as introduced by Sederberg et al. [5]. T-splines allow for local refinement as they are not restricted to tensor product configurations. While you will have to add an entire new row or column to your mesh when refining NURBS, the T-spline technology allows for T-joints and contains refining algorithms which exactly preserve the geometry [4].

Problems containing singularities

We will here present how the T-splines along with a posteriori error estimators perform on problems containing singularities.

Model problem

For our model problem containing a singularity, we are going to solve the stationary heat equation, or Laplace equation

$$
\begin{aligned}
\nabla^2 u &= f & \text{in } \Omega \\
u &= 0 & \text{on } \partial\Omega_D \\
\frac{\partial u}{\partial \boldsymbol{n}} &= g & \text{on } \partial\Omega_N
\end{aligned}
\tag{1}
$$

on an L-shape geometry with appropriate boundary conditions.

For the adaptivity we will need an estimate on what parts of the grid is contributing the most to the global error. For this purpose, we will devise a residual-based a posteriori error estimator. If we rewrite our original problem, we get

$$
\begin{aligned}
a(u, v) &= l(v) \\
a(u - u_h, v) &= l(v) - a(u_h, v) \\
a(e, v) &= \sum_{K \in \mathcal{P}} \int_K r v \, dA + \int_{\partial K \cap \partial \Omega_N} (g - \frac{\partial u_h}{\partial \boldsymbol{n}}) v \, dA - \int_{\partial K \backslash \partial \Omega} \frac{\partial u_h}{\partial \boldsymbol{n}} \, dS
\end{aligned} \tag{2}
$$

where in the last line we have partitioned the integral over the entire domain Ω into integrals over every element K, where $\mathcal{P}$ is the set containing every element such that $\cup K = \Omega$. Here $r = f - \nabla^2 u$ is the interior residual and $g - \frac{\partial u_h}{\partial \boldsymbol{n}}$ is the residual at the exterior edge. The last part of (2) is coming from the jump discontinuity in the flux of the solution due to interelement edges where the FE solution is C^0-continuous. By continued used of the Cauchy-Schwartz inequality and by replacing the test function v with the true error e we arrive at the result

$$
|||e|||^2 \leq C \left\{ \sum_{K \in \mathcal{P}} h_K^2 \|r\|_{L^2(K)}^2 + \sum_{\gamma \in \Gamma} h_K \|R\|_{L^2(\gamma)}^2 \right\}, \tag{3}
$$

where we have introduced the more compact notation for the edge residual

$$
R = \begin{cases}
g - \frac{\partial u_h}{\partial \boldsymbol{n}}, & \text{on } \partial \Omega_N \\
\left[\frac{\partial u_h}{\partial \boldsymbol{n}}\right]_K - \left[\frac{\partial u_h}{\partial \boldsymbol{n}}\right]_L, & \text{on } \partial K \cap \partial L \ \forall \ K, L \in \mathcal{P} \\
0, & \text{else}
\end{cases} \tag{4}
$$

For full details on the derivation of this result, see Ainsworth [1]. This allows us to quantify an error estimate for each element to be

$$
\eta_K^2 = h_K^2 \|r\|_{L_2(K)}^2 + h_K \|R\|_{L_2(\partial K)}^2 \tag{5}
$$

For comparison purposes, we provide four adaptivity strategies for refining the mesh.
a) Uniform refinement using NURBS.
b) Rule of thumb refinement, where we recursively refine the element closest to the singularity using NURBS.
c) Adaptive NURBS where we use the error estimator η_K to refine the x percent elements with the highest contribution to the error.
d) Adaptive T-splines where we use the error estimator η_K to refine the x percent elements with the highest contribution to the error.

Results

Due to the singularity the convergence rates of the uniform refinement is completely ruined. However the rule-of-thumb refinement keeps an optimal slope up until the point where the error from other parts of the grid than the singularity becomes dominant. The T-splines however gains an optimal convergence (using cubic basis functions). The most competitive NURBS refinement strategy, and most comparable, is of course the one where we are using the same a posteriori error estimator for refinement purposes. It is eventually beaten due to the fact that it is limited to tensor product refinements which generates many unwanted degrees of freedom.

(a) T-spline grid with adaptive solver

(b) Convergence rates for the four proposed refinement strategies
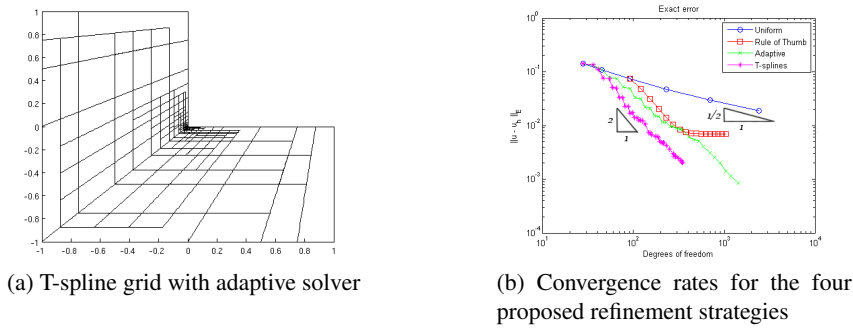
Figure 1: Results obtained from the singularity problem

(a) The parametrization control mesh

(b) The physical mapping
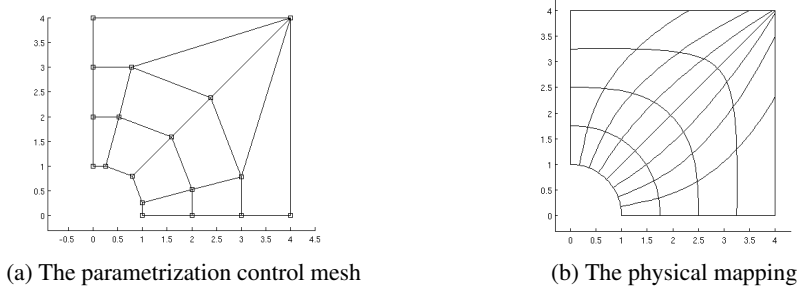
Figure 2: Parametrization of the hole problem

Smooth problems

In this section we take a look at a smooth problem, namely the static elasticity problem on an infinite plate with a circular hole. For full details on the problem see [3].

Parametrization

What is interesting here is the choice of parametrization. We will chose a particular parametrization which is depicted in figure 2. The traditional way of creating sharp corners using NURBS is by making the knot vector be interpolating by creating a knot with multiplicity p where p is the degree of the NURBS. However we have created the upper right corner by stacking p control points on top of each other. Multiple control points is making the derivatives vanish, much in the same manner as multiple knots and is thus allowing us to create the sharp corner. However the solution using this parametrization will not be well-behaved and the error estimator presented in the previous section is not applied. Instead we will use the exact error for adaptation purposes and argue that given an appropriate error estimator, then T-splines will demonstrate some remarkable properties, even for smooth problems without singularities.

The downside with our particular choice of parametrization for the hole-problem is that it is not uniform. That is a uniform refinement in the parametric domain, will result in a biased refinement in the physical space which is illustrated in figure 2b. We clearly see that the refinements are completely biased towards the upper right corner, leaving the lower left and upper right corners with unnaturally large elements. It is possible to bypass this by weighting the refinement in the parametric space, but this requires hand-tailoring by the implementer, which we want to keep to a bare minimum.

Refinement using T-splines

When using an adaptive T-spline refinement strategy, this will detect the large elements in the upper left and lower right corners and refine those as appropriate. This is a true local refinement

(a) Refined T-spline grid in the physical space

(b) Refined T-spline grid in the parametric space

(c) Convergence rates of T-splines versus uniform NURBS
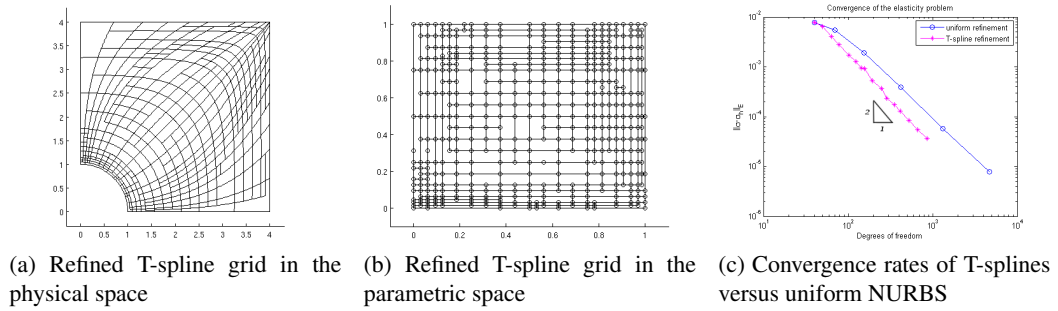
Figure 3: Results from solving a smooth problem

and will not spread out to the rest of the domain, resulting in a better refinement. T-splines is as such, *negating* the effect of the bad parametrization by enforcing a true uniform refinement in the *physical* space. This is shown in figure 3a where the physical T-mesh is illustrated. The parametric mesh corresponding to this is depicted in figure 3b. Note that there is three areas in the parametric space where the refinement is cluttered. The first two is the top left and right which are mapping to respectively the physical top left and bottom right corner. The third is the bottom row which is mapping to the inner circle, where the exact solution is most varying. The adaptive T-spline refinement strategy is biasing the parametric mesh, to allow for a more uniform physical mesh.

Results

Since this problem has a smooth solution, we expect the uniform NURBS refinement to be close to optimal. As was seen, however, the (parametric) uniform refinement scheme was not uniform at all when viewed in the physical space. This is then resulting in a non-optimal refining. The adaptive T-splines countered this, and is thus providing a better convergence rate. These are shown in figure 3c.

Concluding remarks

T-splines shows great promise as a basis for adaptive FEM. Not only do they display superior properties when it comes to true local refinement around singularities, but they also have the remarkable property of negating the effect of badly parameterized models.

References

[1] Mark Ainsworth and J. Tinsley Oden. A posteriori error estimation in finite element analysis. *Computer Methods in Applied Mechanics and Engineering*, 142(1-2):1 – 88, 1997.

[2] T. J. R. Hughes, J. A. Cottrell, and Y. Bazilevs. Isogeometric analysis: Cad, finite elements, nurbs, exact geometry and mesh refinement. *Computer Methods in Applied Mechanics and Engineering*, 194(39-41):4135–4195, October 2005.

[3] Trond Kvamsdal and Knut Morten Okstad. Error estimation based on superconvergent patch recovery using statically admissable stress fields. *Int. J. Numer. Meth. Engng.*, 42:443–472, 1998.

[4] Thomas W. Sederberg, David L. Cardon, G. Thomas Finnigan, Nicholas S. North, Jianmin Zheng, and Tom Lyche. T-spline simplification and local refinement. *ACM Trans. Graph.*, 23(3):276–283, 2004.

[5] Thomas W. Sederberg, Jianmin Zheng, Almaz Bakenov, and Ahmad Nasri. T-splines and t-nurccs. In *SIGGRAPH '03: ACM SIGGRAPH 2003 Papers*, pages 477–484, New York, NY, USA, 2003. ACM.

Static and linearized buckling Isogeometric Analysis using continuum and shell formulations

Geir Skeie*

DNV Research & Innovation
Høvik, Norway
e–mail: Geir.Skeie@dnv.com

Arne Christian Damhaug and Torgeir Rusten

DNV Software
Høvik, Norway
e–mail: Arne.Christian.Damhaug@dnv.com and Torgeir.Rusten@dnv.com

Summary   *Isogeometric Analysis* is a novel technique in *Finite Element Analysis* and its success depends on the performance in bridging the gap in modeling and analysis. The paper compares two options for doing analysis of thin-walled structures, namely, 3D solid modeling and reduced order models using the Mindlin-Reissner shell theory.

Introduction

Recently Isogemetric analysis was introduced by Hughes and coworkers [3]. This represents an interesting alternative to the ordinary finite element methods and it offers new opportunities related to the analysis of thin walled structures. Especially, the issues of C^1 continuity, shear locking in C^0 formulations including solids and the possibilities of avoiding large three dimensional rotations in large displacement analysis of shells are of interest.

Classically, reduced models have been used to analyze shells structures. However, the need to include physical effects generally outside the range of classical shell theory, like nonlinear material behavior including fracture, damage and failure, complex structures with stiffeners and intersection, connecting thin and thick regions, has resulted in higher order shell models and also the use of general three-dimensional theory to analyze shell structures. In later years, Bischoff and Ramm [1], there has been a vitalization of the question: Can we play the game over again? The question rises the issue of how to analysis thin walled structures within the new possibilities offered by the increase in computational capabilities and the gained knowledge on numerical methods, shell behavior and approximation theory.

The purpose of the paper is to compare the performance of solid elements and shell elements within the Isogeometric Analsysis approximation of linearized shell problem. The results are also compared with classical elements found in commercial packages like SESTRA[4].

Governing equations

The discrete problem consists in; find $\boldsymbol{u} \in \mathscr{U}$

$$\int_\Omega \boldsymbol{E} : \boldsymbol{\varepsilon}(\boldsymbol{u}) : \boldsymbol{\varepsilon}(\boldsymbol{v}) = \int_\Omega \boldsymbol{b} \cdot \boldsymbol{v} + \int_{\partial\Omega_t} \boldsymbol{t} \cdot \boldsymbol{v} \quad \forall \boldsymbol{v} \in \mathscr{U}_0 \tag{1}$$

where $\boldsymbol{E}$ denotes the elasticity tensor, $\boldsymbol{\varepsilon}(\cdot)$ is the symmetric part of the displacement gradient, $\boldsymbol{b}$ and $\boldsymbol{t}$ denotes the applied body force and surface traction field, respectively. In the one patch configuration the space $\mathscr{U}$ is constructed using tensor product B-splines. The space $\mathscr{U}_0$ is the subset of $\mathscr{U}$ of functions vanishing on $\partial\Omega \setminus \partial\Omega_t$. This result in an approximation similar to the one used in a classical finite element method

$$\boldsymbol{u}(x,y,x) = N_a(x,y,z)\boldsymbol{d}_a \tag{2}$$

where N_a denotes the B-spline shape functions and $\boldsymbol{d}_a$ is the (generalized) displacement vector at control point a, thus $\boldsymbol{u} \subset C^0(\bar{\Omega})$. Einsteins summation convention is used. The two-dimensional counterpart of N_a are shown in Figure 1 (left). The basis functions in higher dimensions are defined by tensor products of one dimensional basis functions.

Classical shell models are based on kinematic constraints. In order to simplify the presentation we assume a plate model, i.e. the midplane is the x–y plane and the transverse direction are in the z direction. The kinematic constraints are then

$$\boldsymbol{u}(x,y,z) = \boldsymbol{u}_0(x,y) + z\left(\theta_y(x,y)\boldsymbol{e}_x - \theta_x(x,y)\boldsymbol{e}_y\right) \tag{3}$$

Here $\boldsymbol{u}_0$ is the displacement field of the midplane, $\boldsymbol{e}_x$ and $\boldsymbol{e}_y$ are unit vectors in the x and y direction, while θ_1 and θ_2 are the components of the rotation vector

$$\boldsymbol{\theta} = \theta_x\boldsymbol{e}_x + \theta_y\boldsymbol{e}_y \tag{4}$$

The approximations of $\boldsymbol{u}_0$ and $\boldsymbol{\theta}$ are expressed in the form of Equation 2.

The geometric stiffness matrix may be generated through the expression

$$\int_{\Omega_0} \boldsymbol{\sigma} : \Delta\delta\boldsymbol{\varepsilon}\, dV = \delta\boldsymbol{d}_k^T \boldsymbol{K}_g \Delta\boldsymbol{d}_k = \delta\boldsymbol{d}_k^T \int_{\Omega_0} (\boldsymbol{\nabla N})^T \cdot \boldsymbol{\sigma} \cdot \boldsymbol{\nabla N}\, dV \Delta\boldsymbol{d}_k \tag{5}$$

where $\boldsymbol{d}_k$ are the control point values in translational direction k. Only the in-plane membrane forces are currently included in the geometric stiffness for the shell model.

Numerical example

The 3D continuum formulation and the Mindlin-Reissner formulation have been implemented in Mathematica [6] for easy verification and comparison. Two problems are solved for a simply supported plate; the static response of a uniform transverse load and the linearized buckling problem. The plate is depicted in Figure 1. The low order approximation of the plate is determined by the knot and control point vectors

$$\Xi = \mathscr{H} = \{0, 0, 5, 5\} \quad \text{and control points}$$
$$\boldsymbol{p} = \{\{0, 0, 0\}, \{10., 0, 0\}, \{0, 10., 0\}, \{10., 10., 0\}\} \tag{6}$$

Soft boundary conditions are used for the numerical simulation, see Cook *et al* [2]. Table 1 shows the convergence properties of the continuum model, the Mindlin-Reissner plate model for different order of field approximations. The second order thick shell formulation used in SESTRA is also included for comparison. The problem was also solved in Skeie and Rusten [5] using different Isogeometric approximations.

The results for linearized buckling problem using second order spline functions with $(18, 18, 5)$ control ponts and the loading $(N_x, N_y) = (1, 0)$ yield the eigenvalues shown in Table 2 where also the thin plate solution is taken as the reference solution.
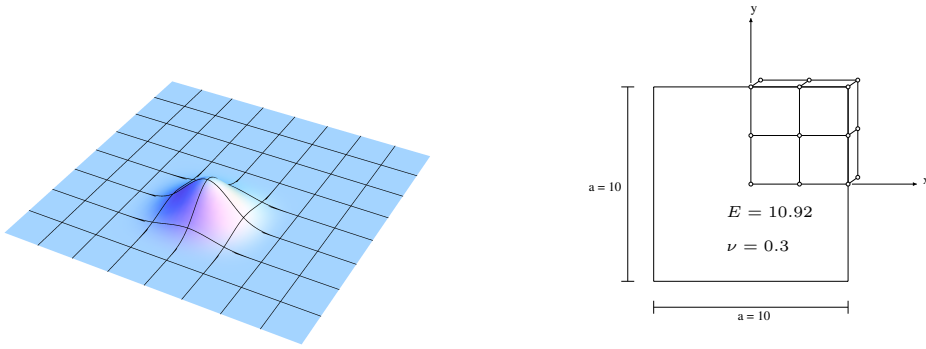
Figure 1: The simply supported plate.

	w/w_{ex} in % (Number of control points)				
Shell					
Linear	0.3(9)	1.1(25)	4.3(81)	15.1(289)	41.6(1089)
Quadratic	87.5(9)	87.5(16)	88.7(36)	96.8(100)	100.1(324)
Cubic	87.5(16)	89.7(25)	99.5(49)	100.3(121)	100.5(361)
Quartic	101.0(25)	101.0(36)	100.5(64)	100.4(144)	100.6(400)
Continuum					
Linear	0.0 (12)	0.2 (27)	0.9 (75)	3.6 (243)	12.8 (867)
Quadratic	87.5 (45)	87.5 (80)	88.5 (180)	96.3 (500)	100.0 (1620)
Cubic	87.5 (112)	89.3 (175)	99.2 (343)	100.3 (847)	
Quartic	101.0 (225)	101.0 (324)	100.5 (576)	100.3 (1296)	
Exact $w_{ex} = 40624$			100		

Table 1: Vertical midpoint displacement compared with exact solution as a function of control points. $t = 0.1$.

Concluding remarks

Initial calculations using both solid and shell formulations in thin walled structures show promising results. It is noted that the effect of shear locking seems to be pronounced only for the low order models.

Isogeometric analysis is a novel techniques still in its infancy and its use in the analysis of thin walled structures has to be investigated further.

References

[1] M. Bischoff and E. Ramm. Solid-like shell or shell-like solid formulation? A personal view. In W. Wunderlich, editor, *Solids, Structures and Coupled Problems in Engineering. Proceedings ECCM'99*, 1999.

[2] R. D. Cook, D. S. Malkus, M. E. Plesha, and R. J. Witt. *Concepts and Applications of Finite Element Analysis*. Number ISBN: 0-471-35605-0. John Wiley & Sons, Inc., 4th edition, October 2002.

Model	Mode number				
	λ_1	λ_2	λ_3	λ_4	λ_5
Mindlin-Reissner	3.95×10^{-4}	6.26×10^{-4}	1.15×10^{-3}	1.59×10^{-3}	1.91×10^{-3}
Continuum	3.95×10^{-4}	6.28×10^{-4}	1.17×10^{-3}	1.60×10^{-3}	1.92×10^{-3}
Exact	3.95×10^{-4}	6.17×10^{-4}	1.10×10^{-3}	1.58×10^{-3}	1.85×10^{-3}
(m,n)	$(1,1)$	$(2,1)$	$(3,1)$	$(4,1)$	$(3,2)$

Table 2: Buckling load for continuum and Mindlin-Reissner formulation compared with thin plate solution.

[3] T.J.R. Hughes, J. A. Cottrel, and Y. Bazilevs. Isogeometric analysis: CAD, finite elements, NURBS, exact geometry and mesh refinement. *Computer Methods in Applied Mechanics and Engineering*, 194:4135—4195, 2005.

[4] SESTRA. *SESTRA – Super Element Structural Analysis, User's Manual*. Veritas Sesam Systems, Høvik, Norway, March 1988.

[5] Geir Skeie and Torgeir Rusten. What is the future shell analysis? In B. Skallerud and H. I. Anderson, editors, *MekIT′09 - Fifth national conference on Computational Mechanics*, Trondheim, 2009. Tapir.

[6] Wolfram Research. *Mathematica*, 2008.

Free vibration and linearized buckling based on Isogeometric analysis

Knut M. Okstad* and Trond Kvamsdal

Department of Applied Mathematics
SINTEF ICT, N-7465 Trondheim, Norway
e–mail: Knut.Morten.Okstad@sintef.no, Trond.Kvamsdal@sintef.no

Geir Skeie

DNV Research & Innovation
Det Norske Veritas, N-1322 Høvik, Norway
e–mail: Geir.Skeie@dnv.com

Summary In this paper we look at eigenvalue analysis of thin-walled structures, based on isogeometric finite element analysis with splines and NURBS as basic functions. We test the methodology on linearized buckling analysis of a simply supported square plate.

Introduction

Currently, a lot of effort is being carried out in research communities using splines and non-uniform rational B-splines (NURBS) as basis functions in finite element analyses (FEA). The foundation for these kind of analyses was laid out by Hughes *et al.* [1]. In the current work we use spline-based continuum finite elements in eigenvalue analysis of thin-walled structures. We consider both free vibration and linearized buckling applications.

Isogeometric analysis was originally introduced in order to achieve efficient integration of computer-aided design (CAD) and FEA by introducing accurate geometry representations. However, as the method has been used and analyzed in more detail, it has become more and more evident that spline-based elements have several numerical advantages compared to classical finite elements.

Both B-splines and NURBS are composed by non-negative basis functions that inherit the so-called total variation diminishing (TVD) property. Finite elements based on the classical Lagrange polynomial basis functions do not inherit the TVD property and are prone to spurious oscillations (Gibbs phenomenon) nearby sharp fronts in dynamic problems.

Furthermore, Cottrell *et al.* have demonstrated in [2] that NURBS elements outperform classical finite elements when it comes to represent the spectrum of eigenvalues for dynamical problems. In fact, for higher order Lagrange elements the upper half of the spectrum is highly inaccurately represented whereas this is not the case for NURBS elements. Their results show that NURBS elements are more accurate than Lagrange elements throughout the entire spectrum.

Eigenvalue analysis

Free vibration

The weak form of the dynamic equation of motions for an elastic structure with neither body forces nor surface tractions is given by

$$\int_\Omega \rho\, \delta\boldsymbol{u}^{\mathrm{T}} \ddot{\boldsymbol{u}}\, \mathrm{d}V \;+\; \int_\Omega \delta\boldsymbol{\varepsilon}^{\mathrm{T}} \boldsymbol{\sigma}\, \mathrm{d}V \;=\; 0 \tag{1}$$

where ρ denotes the mass density, $\boldsymbol{u}$ is the displacement field, and $\boldsymbol{\varepsilon}$ and $\boldsymbol{\sigma}$ strains and stresses, respectively. Assuming simple harmonic motion in time and spatial discretization through a finite set of splines basis functions, $\mathbf{N}$, the displacement field can be written

$$\boldsymbol{u}(\boldsymbol{x}, t) = \sin \omega t \, \mathbf{N}^{\mathrm{T}}(\boldsymbol{x})\mathbf{v} \tag{2}$$

Inserting (2) into (1) and using the constitutive and kinematic relations between the stresses, strains and displacement, we obtain the matrix equation

$$\delta \mathbf{v}^{\mathrm{T}}(\mathbf{K} - \omega^2 \mathbf{M})\mathbf{v} = 0 \tag{3}$$

where $\mathbf{K}$ and $\mathbf{M}$ are the usual material stiffness- and mass matrices, respectively. Equation (3) may now be solved by standard eigenvalue solvers for eigenpairs $(\omega, \mathbf{v})$.

Linearized buckling

The equation governing the buckling phenomenon is derived by neglecting the first term of (1) and considering the second term to be non-linear. By linearizing this term we get

$$\Delta \int_{\Omega} \delta \boldsymbol{\varepsilon}^{\mathrm{T}} \boldsymbol{\sigma} \, \mathrm{d}V \; = \; \int_{\Omega} \delta \boldsymbol{\varepsilon}^{\mathrm{T}} \Delta \boldsymbol{\sigma} \, \mathrm{d}V \; + \; \int_{\Omega} \Delta \delta \boldsymbol{\varepsilon}^{\mathrm{T}} \boldsymbol{\sigma} \, \mathrm{d}V \; = \; 0 \tag{4}$$

We notice that the second term of (4) contains the current stress state, $\boldsymbol{\sigma}$. In the linearized buckling analysis, we assume that these stresses equals some reference state times a load factor, λ, i.e., $\boldsymbol{\sigma} = \lambda \boldsymbol{\sigma}_0$. Inserting this into the second term of (4), while carrying out the linearization of $\Delta \boldsymbol{\sigma}$ and $\Delta \delta \boldsymbol{\varepsilon}$ retaining first order terms only, and introducing a spatial discretization $\boldsymbol{u}(\boldsymbol{x}) = \mathbf{N}^{\mathrm{T}}(\boldsymbol{x})\mathbf{v}$, we obtain the matrix equation

$$\delta \mathbf{v}^{\mathrm{T}}(\mathbf{K} + \lambda \mathbf{K}_{\mathrm{g}})\mathbf{v} = 0 \tag{5}$$

where $\mathbf{K}_{\mathrm{g}}$ is the geometric stiffness matrix. Equation (5) may now be solved by standard eigenvalue solvers for eigenpairs $(\lambda, \mathbf{v})$. This is a similar kind of eigenvalue problem as (3). However, in contrast to the mass matrix $\mathbf{M}$, the geometric stiffness matrix is not necessarily positive definite, so the eigenvalue solver needs to account for that in the solution process.

Linearized buckling of a square plate

The spline-based isogeometric formulation has been tested on the plate problem depicted in Figure 1. It shows a rectangular plate subjected to constant in-plane loadings N_x and N_y in the x and y-directions, respectively. The plate is assumed to be simply supported around the boundary. This is achieved by constraining the out-of-plane deflection w to zero along the center line around the boundary. In addition, we add constraints in two of the corners in order to suppress the rigid body motions in the xy-plane of the plate.

Thin-plate solution

Based on Kirchhoff-Love thin plate theory, we find the buckling load for this plate problem as given by

$$N_x \left(\frac{m\pi}{a}\right)^2 + N_y \left(\frac{n\pi}{b}\right)^2 = D \left(\left(\frac{m\pi}{a}\right)^2 + \left(\frac{n\pi}{b}\right)^2\right)^2 \tag{6}$$

where m and n are integer values giving the number of half waves in the x and y directions of the plate, respectively, and D is the plate stiffness (see Figure 1). It should be noted that this solution does not account for transverse shear deformation, so when we are using volume elements we should expect convergence towards a somewhat more soft solution.
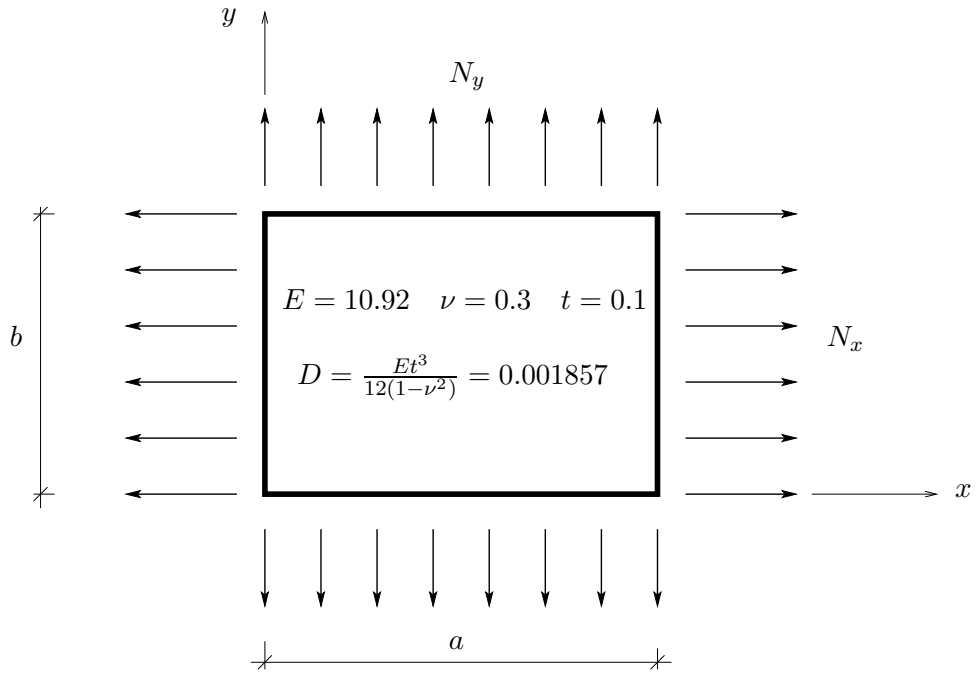
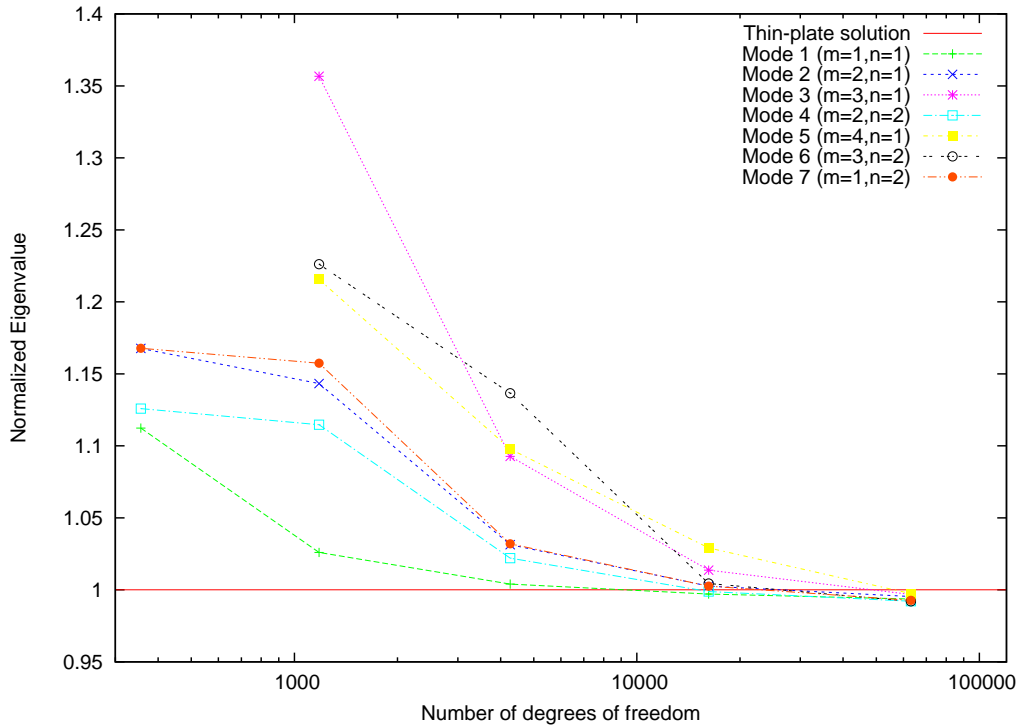Figure 1: Simply supported plate subjected to in-plane loading.

Figure 2: Normalized eigenvalues for the square plate.

Numerical results

In Figure 2 the convergence of the seven lowest eigenvalues (i.e., the buckling load N_x) are shown for the condition $N_y = 0.0$ and $a = b = 10.0$. The eigenvalues have here been normalized with the corresponding thin-plate solution. The results are obtained with quadratic spline elements ($p = 2$) and the number of control points (FE nodes) in x and y direction varying from 5 to 65. In the thickness direction 3 control points are used for each grid. In Figure 3, the four first mode shapes are depicted for the 33×33 grid.

The eigenvalue analysis is performed using the ARPACK library [3] (Buckling mode).
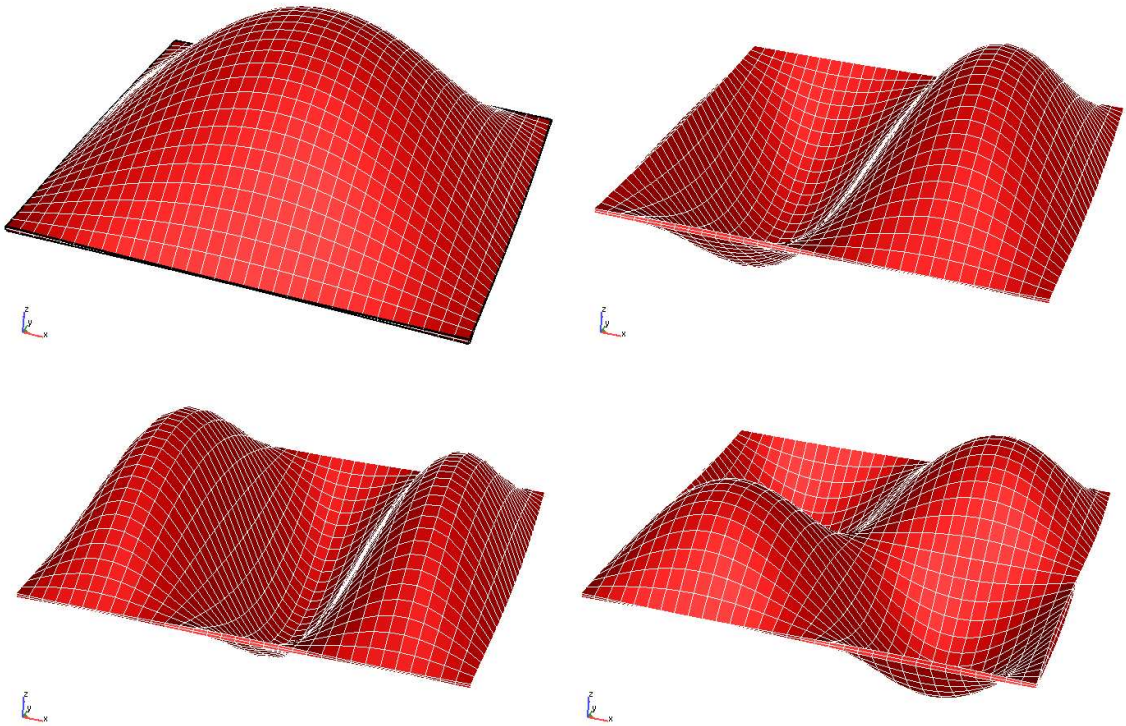
Figure 3: Mode shapes for the lowest four eigenvalues.

Concluding remarks

The results obtained so far look promising. We get good correlation with the thin-plate solution even for quite coarse meshes. We will also compare the performance with standard Lagrange finite elements to see whether spline basis is better for the same number of DOFs.

References

[1] T. J. R. Hughes, J. A. Cottrell, and Y. Bazilevs. Isogeometric Analysis: CAD, Finite Elements, NURBS, Exact Geometry and Mesh Refinement. *Computer Methods in Applied Mechanics and Engineering*, 194:4135–4195, 2005.

[2] J. A. Cottrell, T. J. R. Hughes, and Y. Bazilevs. *Isogeometric Analysis: Toward Integration of CAD and FEA*. John Wiley & Sons, Chichester, England, 2009.

[3] R. B. Lehoucq, D. C. Sorensen, and C. Yang. *ARPACK Users' Guide: Solution of Large-Scale Eigenvalue Problems with Implicitly Restarted Arnoldi Methods*. SIAM, 1998.

Structures and continua with uniform energy densities

Pauli Pedersen

Department of Mechanical Engineering, Solid Mechanics
Technical University of Denmark
Nils Koppels Allé, Building 404, DK-2800 Kgs.Lyngby, Denmark
e–mail: pauli@mek.dtu.dk

Summary   In optimal design the primary focus today is on mathematical programming in combination with finite element analysis. Here we put focus on the fact that the generality and versatility of optimality criteria methods are valuable from several point of views, and show recent solutions published on the basis of simple and few recursive redesigns.

Preface

This presentation is dedicated to Professor Niels Olhoff, appreciating his many years of work at DTU in Copenhagen, at AAU in Aalborg and in international societies.

Forty years ago Niels and I as Ph.D. students shared an office in Copenhagen. Niels used optimality criteria, expressed in differential equations, to optimize plates, while I used mathematical programming to optimize trusses; both believing strongly in our methods. Later we learned to use alternative methods and to put emphasis on sensitivity analysis.

Although practical problems call for finite element analysis and mathematical programming, the importance of optimality criteria methods should be kept in mind; here we focus on criteria in energy terms and with FE for analysis.

This is not a review paper and only few references are given. A list of the many papers by Niels Olhoff until 2003 is included in [1].

Introduction

In size optimization for minimum compliance with only active volume constraint, the necessary optimality criterion is uniform energy density, see [2]. This criterion also holds for non-linear power-law, anisotropic elasticity, see [3] and [4]. For eigenfrequency optimization with size parameters a similar criterion specifies constant difference between amplitudes of elastic energy density and kinetic energy density, see [5].

In shape optimization with prescribed size, say the thickness of a plate, we cannot expect constant energy density everywhere. For compliance minimization with only a single constraint on given volume the necessary optimality criterion is constant energy density at the boundary to be designed; see [2] and for extensions to non-linear power-law, anisotropic elasticity, and for the relations to strength optimization (stress constraints) see [6]. In shape optimization for eigenfrequency maximization a necessary optimality criterion, which expresses constant difference between amplitudes of elastic energy density and kinetic energy density at the designed boundary, is proofed in [7]. The boundary may be internal (holes) as well as external.

Optimality criteria are valuable from several points of view:

- Criteria give basic understanding
- Verify results by mathematical programming
- Analytical solutions
- Background for recursive design procedures
- Optimality criterion solution to initiate mathematical programming
- Criteria expressed in energy terms hold for 1D, 2D, 3D, for different models, for analytical as well as numerical treatment, for materials as well as for structures.
- Sensitivity analysis is a most important part

Table 1 presents an overview of the mentioned optimality criteria

Design variables / Problems	SIZE (thickness/density)	SHAPE (boundary)
Extremum COMPLIANCE	Specific elastic energy constant in design domains	Specific elastic energy constant on design boundary
Extremum EIGENFREQUENCY	Weighted elastic energy density minus kinetic energy density constant in design domains	Elastic energy density minus kinetic energy density constant on design boundary

Table 1: Optimality criteria for static single load cases and cases of non-multiple eigenfrequencies with size and/or shape design variables, and an active mass (volume) constraint.

Setting up the optimality criteria

A rather general optimization problem may be stated as

$$\text{Minimize } \Phi \quad \text{subjected to} \quad g = 0 \tag{1}$$

with t_e as design parameters, say element thicknesses. The necessary condition for optimizing a design is proportionality between the gradients of the objective Φ and the gradients of the constraint g

$$\frac{d\Phi}{dt_e} = \lambda \frac{dg}{dt_e} \tag{2}$$

with same λ for all domains (elements) e. In the case that Φ is energy and g is volume, then λ is interpreted in terms of the constant energy density.

The objective may be combined from multiple load cases, from eigenfrequencies, and from displacements.

$$\Phi = \sum_{k=1}^{K} \gamma_k \Phi_k^r \quad \Rightarrow \quad \frac{d\Phi}{dt_e} = \sum_{k=1}^{K} \gamma_k r \Phi_k^{r-1} \frac{d\Phi_k}{dt_e} \tag{3}$$

with user control parameters γ_k, r and gradients from design variation dt_e. Three examples expressed in elastic energy are compliance

$$\Phi_1 = U_l = \{D_l\}^T [S]\{D_l\} \quad \text{for load case} \quad l \tag{4}$$

and eigenfrequency by Rayleigh quotient

$$\Phi_2 = \omega_i^2 = \frac{U_i}{T_i} = \frac{\{D_i\}^T [S]\{D_i\}}{\{D_i\}^T [M]\{D_i\}} \quad \text{for eigenfrequency} \quad i \tag{5}$$

and displacements by cost combinations

$$\Phi_3 = \{\tilde{C}_j\}^T \{D_j\} = \tilde{U}_j = \{\tilde{D}_j\}^T [S]\{D_j\} \quad \text{,i.e., mutual energy for case} \quad j \tag{6}$$

where the artificial displacement vector $\{\tilde{D}_j\}$ results when treating the vector of combination factors $\{\tilde{C}_j\}$ as a load case.

Finding solutions to an optimality criterion

The applied recursive formula which is in agreement with the optimality criterion is an update of element densities by

$$(t_e)_{new} = (t_e)_{current} \left(\frac{(\lambda_e)_{current}}{\bar{\lambda}_{current}} \right)^{0.8} \left(\frac{\bar{V}}{V} \right) \tag{7}$$

assuming all $\lambda_e > 0$. With proper adjustment to limits $t_{min} \leq t_e \leq t_{max}$, and in an inner loop without FE analysis, iteratively updating the current active volume V and $\bar{V}$ (its corresponding part of the constraint), so that the total volume constraint is satisfied in each redesign.

An alternative version often applied by Niels Olhoff, includes move limits described by ξ, which introduce limits depending on the current design, i.e., $\alpha \leq t_e \leq \beta$ with

$$\alpha = max[(1 - \xi)(t_e)_{current}, t_{min}] \tag{8}$$
$$\beta = min[(1 + \xi)(t_e)_{current}, t_{max}] \tag{9}$$

The volume constraint is then determined in an inner iteration loop by means of e.g. bisection or a Newton-Raphson method.

Static 2D examples

A number of continua, designed to obtain uniform (or almost uniform) energy density, are presented. These designs, subjected to only one load case, are optimal with respect to stiffness as well as with respect to strength, assuming that the total volume $\bar{V}$ is not changed.

In addition to graphical illustrations of energy density fields and optimal thickness fields, a few relative numbers are needed to clarify the obtained results. The starting analysis with a uniform thickness design gives an initial total elastic energy U_0, from which an initial mean energy density $u_{mean0} = U_0/\bar{V}$ is given. Also this analysis for uniform thickness gives a maximum energy density u_{max0}, and an energy concentration factor, defined as u_{max0}/u_{mean0}. The total elastic energy of the optimized design is U and the goal of optimization is to obtain uniform energy density $u_{max} = u_{mean} = U/\bar{V}$, from which follows that a gain factor for improvement in stiffness can be

defined as $u_{mean0}/u_{mean} = U_0/U$, and a gain factor for improvement in strength can be defined as u_{max0}/u_{max}. Especially the upper bound t_{max} should also be seen in relation to the reliability of the finite element analysis. When the gradients of the thickness field get extended, the accuracy in modeling may be violated. The effect of the upper bound is that in most cases $u_{max}/u_{mean} > 1$ results even for the optimized continuum that gives almost uniform energy density. A good measure for the influence from the upper bound t_{max} is given by this ratio u_{max}/u_{mean}.

Figure 1 illustrates nine problems, for which we show thickness fields, that return almost uniform energy density. The pure beam problems and the pure bar problems might be solved with only half the models due to symmetry and skew-symmetry, but due to the bar-beam problems full models are used. The actual finite element models have 11042 degrees of freedom and 10800 design variables (thicknesses of 10800 triangular elements).
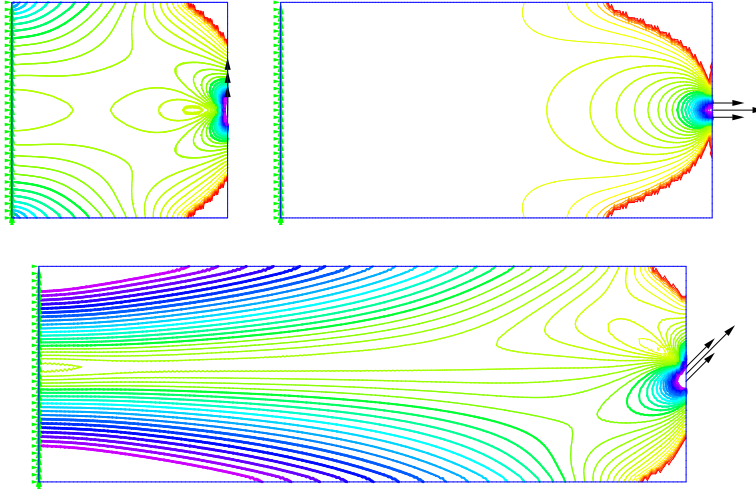
Figure 1: The basic models for optimization of bars, beams, and beam-bars in three different lengths, i.e. in combination 9 cases. Isolines for energy densities are shown for the uniform thickness design with the loads shown at the free ends. The color scale is red for low thickness values, green for medium thickness values and blue/violet for large thickness values.

Immediately, a suggested design for the bar problem would be a uniform bar only of the width corresponding to the area of uniform external load. However, such a design is questionable at the support where stress concentration can result. The isolines in Figure 1 for this case illustrate the complexity. Also the Saint-Venant principle is nicely illustrated in Figure 1, and in the solutions to follow.

Figure 2 shows some of the optimal designs and values are given in Table 2.

Static 3D example

An example of a 3D bridge model with moving loads is shown in Figure 3, that also shows optimized versions for the non symmetric four load case.

Figure 2: Optimal designs for 3×9 rectangular design domain. Top: a bar problem. Mid : a beam problem. Bottom: a combined ba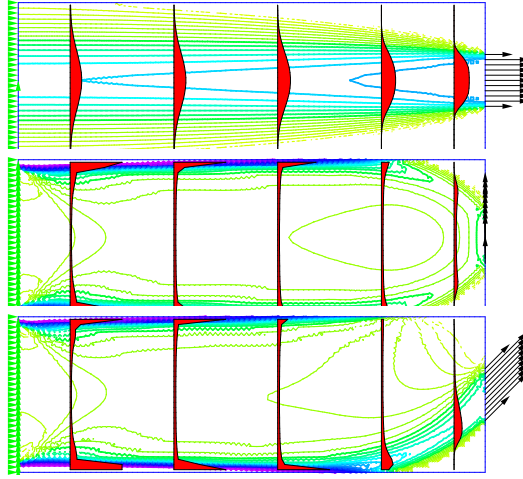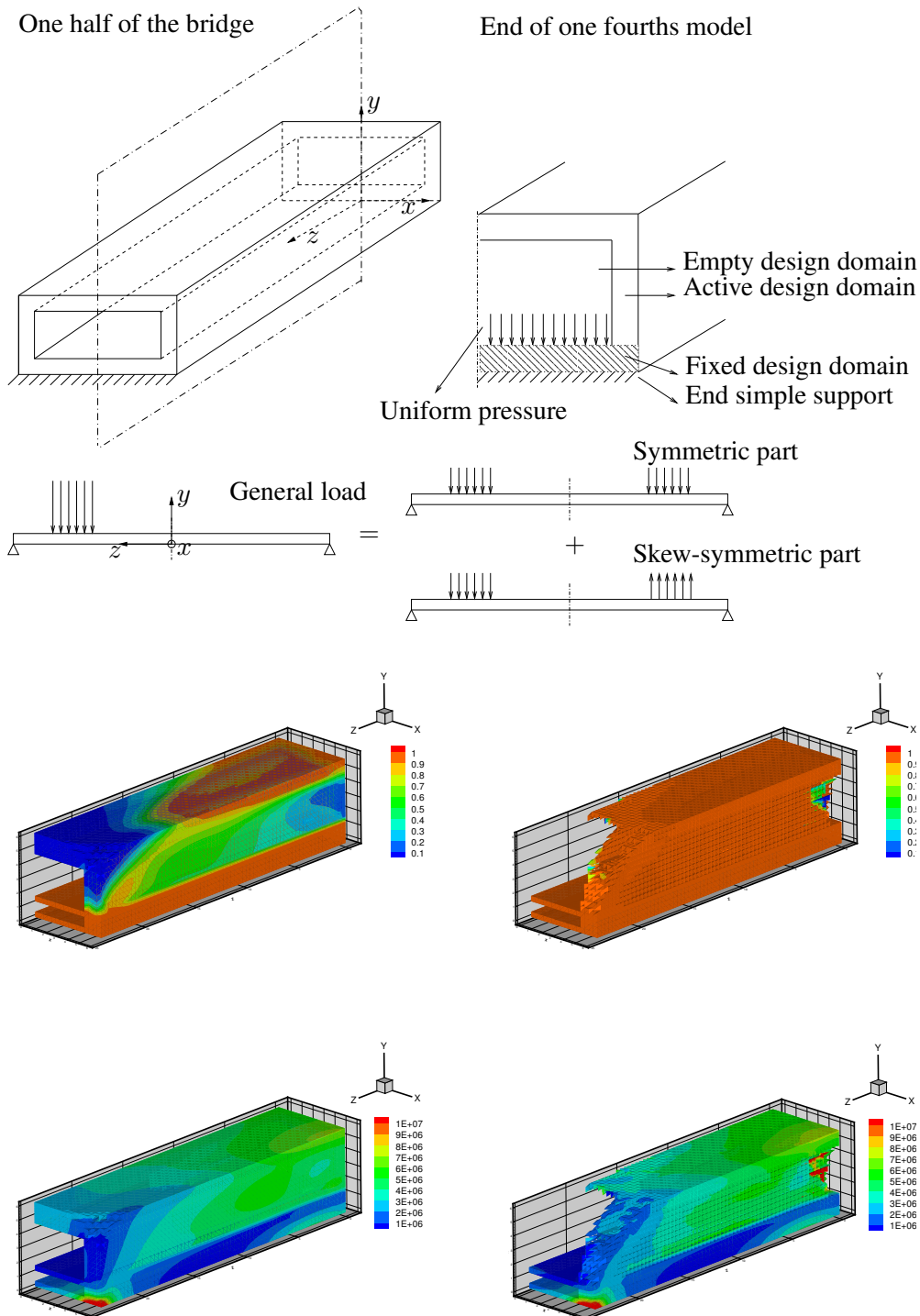r/beam load. Isolines for thicknesses and five cross-sectional "cuts" that more clearly show the thickness distribution. The resulting energy densities are almost uniform as seen in Table 2

BAR DESIGNS	Uniform thickness		Optimized design	
Resulting ratios	U_0/U	u_{max0}/u_{mean0}	u_{max0}/u_{max}	u_{max}/u_{mean}
Design domain 9×3	1.18	11.8	13.8	1.006
Design domain 6×3	1.27	11.1	14.0	1.006
Design domain 3×3	1.54	9.8	14.9	1.006
BEAM DESIGNS	Uniform thickness		Optimized design	
Resulting ratios	U_0/U	u_{max0}/u_{mean0}	u_{max0}/u_{max}	u_{max}/u_{mean}
Design domain 9×3	2.12	10.1	6.9	3.1
Design domain 6×3	1.80	10.5	5.5	3.4
Design domain 3×3	1.40	9.9	3.8	3.6
COMB. DESIGNS	Uniform thickness		Optimized design	
Resulting ratios	U_0/U	u_{max0}/u_{mean0}	u_{max0}/u_{max}	u_{max}/u_{mean}
Design domain 9×3	2.15	10.8	7.1	3.3
Design domain 6×3	1.87	11.2	5.9	3.6
Design domain 3×3	1.60	10.4	3.5	4.8

Table 2: Resulting ratios for energy and energy density, corresponding to nine different cases of bar and beam models. Uniform thickness design and optimized thickness design.

One half of the bridge

End of one fourths model

Empty design domain
Active design domain

Fixed design domain
End simple support

Uniform pressure

General load = Symmetric part + Skew-symmetric part

Figure 3: upper: Resulting optimized "bridge" designs, lower: Resulting distribution of von Mises stress, left: The graded (non-penalized) design, right: The almost solid (penalized) design.

Analytical described beam designs

Analytically described solutions for beam design are available for statically determinate cases, even based on Timoshenko beam. In a recent paper [8], which included valuable improvements suggested by Niels Olhoff, a large number of optimal designs are presented.

The primary step is to get the optimality criterion for the problem:

$$\text{Minimize compliance } \Phi \quad \text{for a given volume} \quad V = \int_0^L A(x)dx \quad \text{where}$$

$$\Phi = \int_0^L \phi(x)dx \quad \text{with} \quad \phi(x) = \beta \frac{T^2(x)}{GA(x)} + \frac{M^2(x)}{EI(x)} \tag{10}$$

all in traditional notation. The relation between cross sectional moment of inertia $I(x)$ and area $A(x)$ is presented in the form

$$I(x) = \gamma b^{2(2-n)} A^n(x) \quad \text{for} \quad n = 1, 2, \text{or } 3 \text{ with} \quad b \quad \text{as a cross sectional length} \tag{11}$$

and the optimality **criterion for the optimal area** $A^*(x)$ is derived to

$$\lambda = \alpha \frac{(T(x)/Q)^2}{(A^*(x)/b^2)^2} + n \frac{(M(x)/(Qb))^2}{(A^*(x)/b^2)^{n+1}} \tag{12}$$

The next step is to obtain analytical solutions to the optimality criterion 12, which in [8] is derived
Bernoulli-Euler beams

$$[A^*(x)]_{BE} \quad \propto \quad \sqrt[n+1]{(\frac{M(x)}{Qb})^2} \tag{13}$$

Timoshenko beams for $n = 1$

$$[A^*(x)]_{T,n=1} \quad \propto \quad \sqrt{\alpha(\frac{T(x)}{Q})^2 + (\frac{M(x)}{Qb})^2} \tag{14}$$

Timoshenko beams for $n = 2$

$$\left[\frac{A^*(x)}{b^2}\right]_{T,n=2} = \sqrt[3]{\frac{1}{\lambda}(\frac{M(x)}{Qb})^2 + \sqrt{\left(\frac{1}{\lambda}(\frac{M(x)}{Qb})^2)\right)^2 + \left(\frac{-\alpha}{3\lambda}(\frac{T(x)}{Q})^2\right)^3}} +$$

$$\sqrt[3]{\frac{1}{\lambda}(\frac{M(x)}{Qb})^2 - \sqrt{\left(\frac{1}{\lambda}(\frac{M(x)}{Qb})^2)\right)^2 + \left(\frac{-\alpha}{3\lambda}(\frac{T(x)}{Q})^2\right)^3}} \tag{15}$$

Timoshenko beams for $n = 3$

$$\left[\frac{A^*(x)}{b^2}\right]_{T,n=3} = \sqrt{\frac{\alpha}{2\lambda}(\frac{T(x)}{Q})^2 + \sqrt{\left(\frac{\alpha}{2\lambda}(\frac{T(x)}{Q})^2\right)^2 + \frac{3}{\lambda}(\frac{M(x)}{Qb})^2}} \tag{16}$$

Graphical displays of these solutions for specific distributions of shear force $T(x)$, moment $M(x)$, and cross sectional type b, n, α are presented in [8].

Eigenfrequency example

In the project [7] on shape optimization for maximum eigenfrequency we found great use of the information contained in the distributions of energy density over the structure/continuum. Three kinds of distributions are involved, the distribution of amplitude of elastic strain energy density, the distribution of amplitude of kinetic energy density, and finally and most important the distribution of difference between amplitude of elastic strain energy density and amplitude of kinetic energy density. The focus on the distribution of differences is due to the available optimality criteria for optimizing an eigenfrequency.

We exemplify primarily in relation to the model of a "knee" continuum shown in Figure 4 which also shows distributions of the specific energy difference z_e (Lagrange energy density) defined by

$$z_e = (U_e - T_e)/(V_e) \tag{17}$$

in the element e, where we have the elastic energy amplitude U_e, the kinetic energy amplitude T_e, and the volume V_e. Different z_e for the different elements in the model indicate that the eigenfrequency ω can be improved by thickness design. The objective is to maximize an eigenfrequency ω for given total mass M or volume V. The optimality criterion for this problem is a factor (problem depending) times the amplitude of elastic energy minus the amplitude of kinetic energy, corresponding to the mode of vibration. From [5] we cite *"The optimality criterion states that, for the fundamental mode, the difference between amplitude of the specific strain energy per unit stiffness and the amplitude of the specific kinetic energy of the structure (exclusive of the point masses) per unit stiffness is constant over the structure"*.

Conclusion

Thanks to Niels Olhoff for many years of cooperation on optimal design.

References

[1] G. N. I. Rozvany. Special issue to honour Niels Olhoff. *Struct. Multidisc. Optim.*, **25(5-6)**, 311–318, (2003).

[2] Z. Wasiutynski. On the Congruency of the Forming According to the Minimum Potential Energy with that According to Equal Strength. *Bull. de l'Academie Polonaise des Sciences, Serie des Sciences Techniques*, **8(6)**, 259–268, (1960).

[3] K. Dems and Z. Mroz. Multiparameter Structural Shape Optimization by Finite Element Method. *Int. J. Numer. Meth. Engng.*, **13**, 102–106, (1978).

[4] P. Pedersen. Some General Optimal Design Results using Anisotropic Power Law Non-linear Elasticity. *Structural Optimization*, **15**, 73–80, (1998).

[5] W. Prager and J. E. Taylor. Problems of optimal structural design. *J. of Applied Mechanics, Trans. ASME*, **35(1)**, 102–106, (1968).

[6] P. Pedersen. On Optimal Shapes in Materials and Structures. *Struct. Multidisc. Optim.*, **19(3)**, 169–182, (2000).

[7] P. Pedersen and N. L. Pedersen. An optimality criterion for shape optimization in eigenfrequency problems. *Struct. Multidisc. Optim.*, **29(6)**, 457–469, (2005).

[8] P. Pedersen and N. L. Pedersen. Analytical optimal designs for long and short statically determinate beam structures. *Struct. Multidisc. Optim.*, **39(4)**, 343–357 (2009).

A: Initial design

all $t_e = 1.0$

B: z_e-distribution

$\omega_1 = 1.00$ (ref.)

C: Design # 3

$0.1 < t_e < 5.0$

D: z_e-distribution

$\omega_1 = 1.4$

E: Design # 20

$0.1 \leq t_e \leq 5.0$

F: z_e-distribution

$\omega_1 = 2.9$

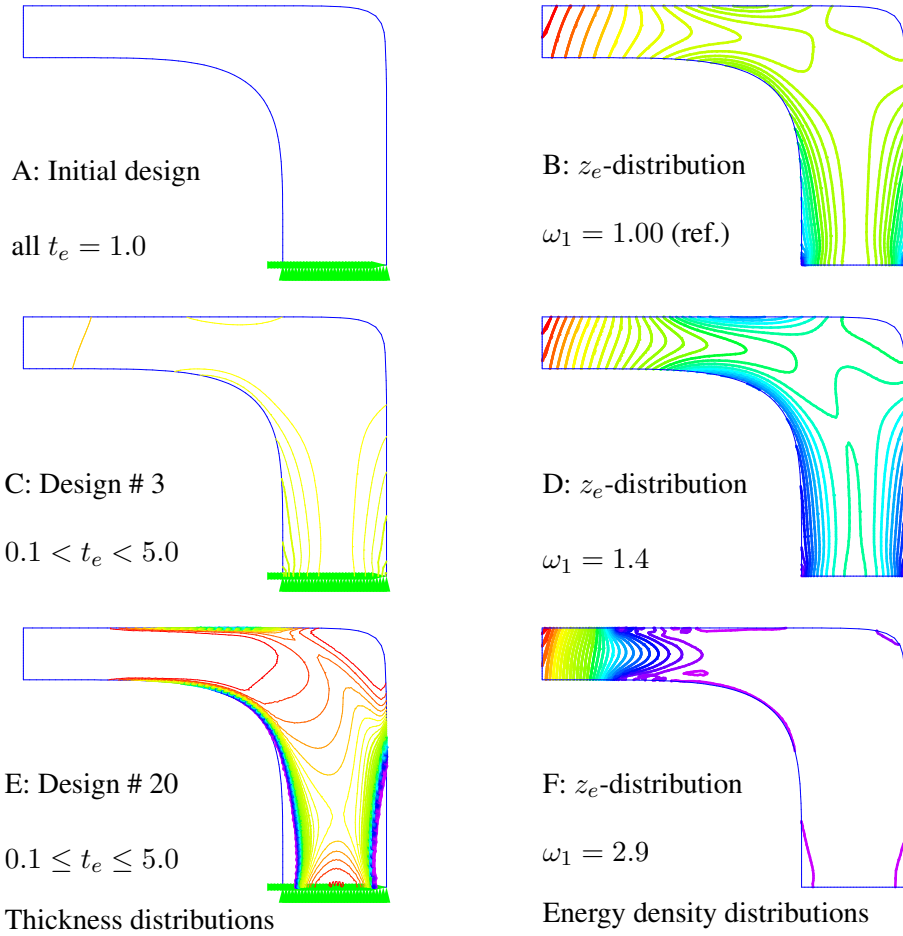Thickness distributions

Energy density distributions

Figure 4: Top: Initial uniform design. Middle: Design after 2 redesigns. Bottom: Design after 19 redesigns. Left: Thickness distributions with linear scale from minimum = 0.1 to maximum = 5.0. Right: Distribution of difference of energy density amplitudes.

Shape optimization of asymmetric gears

Niels L. Pedersen

Department of Mechanical Engineering, Solid Mechanics
Technical University of Denmark
Nils Koppels Allé, Building 404, DK-2800 Kgs. Lyngby, Denmark
e–mail: nlp@mek.dtu.dk

Summary Bending stress plays a significant role in gear design wherein its magnitude is controlled by the nominal bending stress and the stress concentration due to the geometrical shape. The bending stress is indirectly related to shape changes made to the cutting tool. This work shows that the bending stress can be reduced significantly by using asymmetric gear teeth and by shape optimizing the gear through changes made to the tool geometry. To obtain the largest possible stress reduction a custom tool must be designed depending on the number of teeth, but the stress reductions found are not very sensitive to small design changes. This observation could suggest the use of standard cutting tools.

Introduction

Gear strength is influenced by geometry as well as by material selection and production processes. Two primary fatigue related failure modes determine gear strength; failure due to bending stress and failure due to contact pressure. The focus of this work is on reducing bending stress levels whereby improving gear strength.

Gear design is in most cases conservative and specified by different standards. Almost all gears exhibit involute shape because the contact forces act along a straight line and a center distance variation due to, e.g. manufacturing tolerances or loadings, does not influence this fact. A center variation will neither influence the gear ratio. The only design variable that controls the involute shape is the pressure angle α; it is typically assigned the value $\alpha = \pi/9$. Only the gear region that is in contact with the other gear in the mesh is described by the involute shape. The root geometry or bottom land region, that connects two neighboring teeth, can be designed rather freely. The task of this paper, also done in [1], is to improve the gear strength by changing the gear geometry in a way that retains the involute shape.

Design changes of the gears are achieved indirectly by redesigning the cutting tool. Cutting tool parameterization includes the possibility of an asymmetric tooth; it is simple as it only requires four design parameters. Resulting optimized designs show that a significant reduction in the bending stress is possible. Furthermore, the cutting tool shape is described analytically and hence so is the cut teeth shape Thus, as discussed in [1], the maximum stress calculations can be trusted.

General aspects of gear design and analysis

Almost all gears are symmetric and defined according to the standard cutting tool. The cutting tool definition used in the present paper is based on the ISO profile and seen in Figure 1.

The shown profile has, as the ISO profile, an added top with the height of $M/4$, where M is the gear module which controls the gear teeth size and subsequent also the gear size (the pitch diameter d_p is given by $d_p = Mz$ where z is the number of teeth on the gear). Top radius ρ is chosen such that there is no jump in the slope. The bottom of the true cutting tooth profile is not identical to the bottom of the shown cutting profile based on the ISO profile. For the real cutting
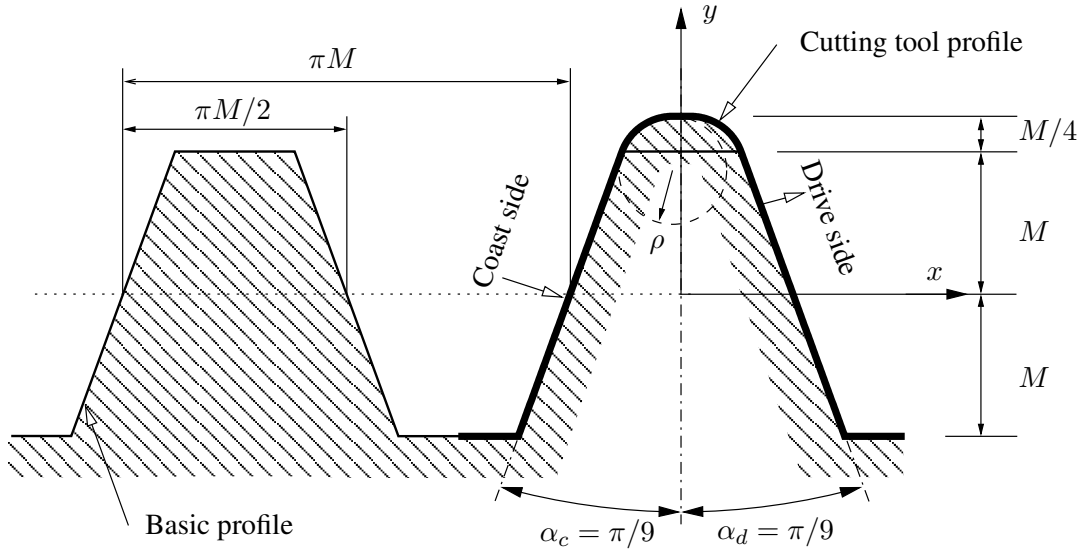
Figure 1: Cutting profile geometric definition and the basic profile based on the ISO profile, M is the gear module that defines the teeth size in the gear. The two sides of the tool are termed drive and coast side respectively. Pressure angles α_d and α_c are here shown with the same value. The coordinate system used is shown.

profile, the top of the cut teeth is assumed given by the initial steel blank diameter, which is equal to the addendum diameter. The shown profile has as envelope the full cut tooth, i.e., the envelope of the bottom part of the profile is the finished cut tooth top. Teeth cut with the ISO profile and teeth cut with the profile shown in Figure 1 are therefore identical.

Gears become symmetric when the cutting tool tooth is symmetric with respect to the y-axis as shown in Figure 1. Symmetry of the two involutes of a tooth follows a choice of identical pressure angles, $\alpha_d = \alpha_c$. Subscript d is used for drive side and subscript c is used for coast side. Two identical pressures angles imply that the two straight lines have opposite gradient, and that they go through the points $(-\pi M/4, 0)$ and $(\pi M/4, 0)$ respectively (the envelope of the straight side are the tooth involute).

If the object of gear design is to minimize the stresses the pressure angle should be as large as possible. The limiting factor is a needed minimum tooth top thickness.

The parameterization that remains is the tool top, the number of possible tool top design parameterizations is infinite. Here a variation of the parameterization used in [1] is applied, the central part is to use a variation of the super ellipse. Focus is on simplicity, although the optimization result should still be near to the optimal design. That a given parameterization is sufficiently flexible, i.e. that it can return optimal designs, can only be checked or verified after an actual optimization procedure. If the stress is constant along major parts of the surface then the shape is assumed optimal, see e.g. [2].

The parameterization presented fulfills the following constraints:

- The added tool tip height is fixed at $M/4$.

- The involute part of the tooth must not be penetrated on the drive side.

That the tool tip height is kept fixed is applied in order to allow for the same clearance in the optimized gears as is the case for the ISO gears. The involute part should be kept unchanged to allow the optimized gears to have the same functional qualities as the original involute gears.

A distinction is made between the tool top part that cuts the tooth root of the drive side (drive top) and the other part that cuts the tooth root of the coast side (coast top). As indicated in Figure 2 the coast side top is a simple circle (part of a full circle).
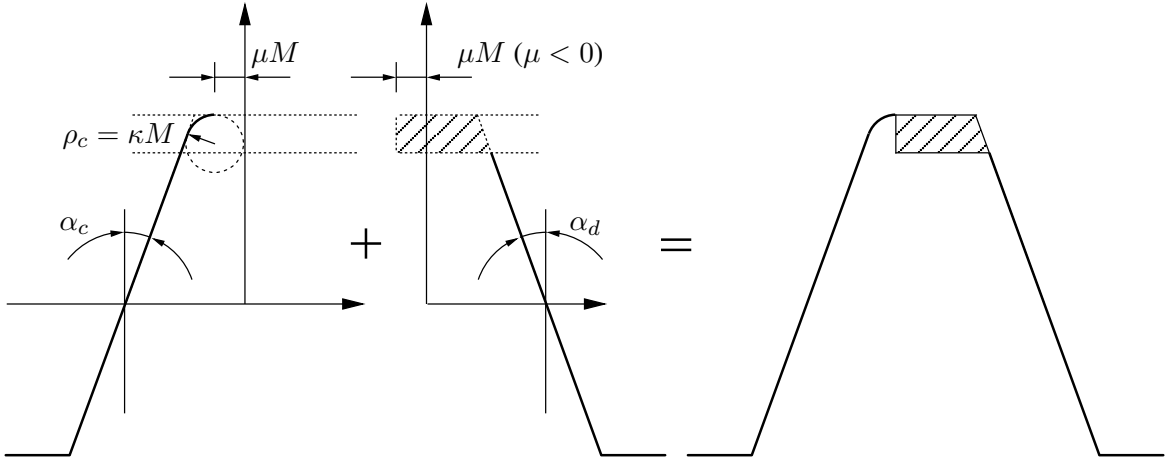

Figure 2: The design domain for the optimization shown as the hatched part. The coast side pressure angle and drive side pressure angle is shown together with the circle radius on the cutting tool coast side.

The radius of the circle is given as

$$\rho_c = \kappa M = \frac{4\mu + \pi - 5\tan(\alpha_c)}{4(\cos(\alpha_c) - (\sin(\alpha_c) - 1)\tan(\alpha_c))}M \tag{1}$$

and might be greater than or smaller than the ISO standard $\rho \approx 0.38M$ (see Figure 1). This also means that the involute on the costs side might not be as long as it would have been using the ISO cutting tooth, but this is ignored due to of the unidirectional loading assumption.

Final part to be parameterized is the drive top, this is done by a modified super elliptic shape. The design domain is shown as the hatched part in Figure 2 and enlarged in Figure 3. As seen in Figure 2 the design domain size is variable and controlled through the parameter μ, with the restrictions from the boundaries this parameter must fulfill.

$$\mu_{\min} = -\frac{\pi}{4} + \frac{5}{4}\tan(\alpha_c) \leqq \mu \leqq \frac{\pi}{4} - \frac{5}{4}\tan(\alpha_d) = \mu_{\max} \tag{2}$$

From the optimization presented in [1] it was found that in order to minimize the stress concentration it is important that the parameterization includes a straight part before entering the elliptical shape, but in that paper the teeth were symmetric. The idea used in the present paper is instead that the design domain can change size through the design parameter μ
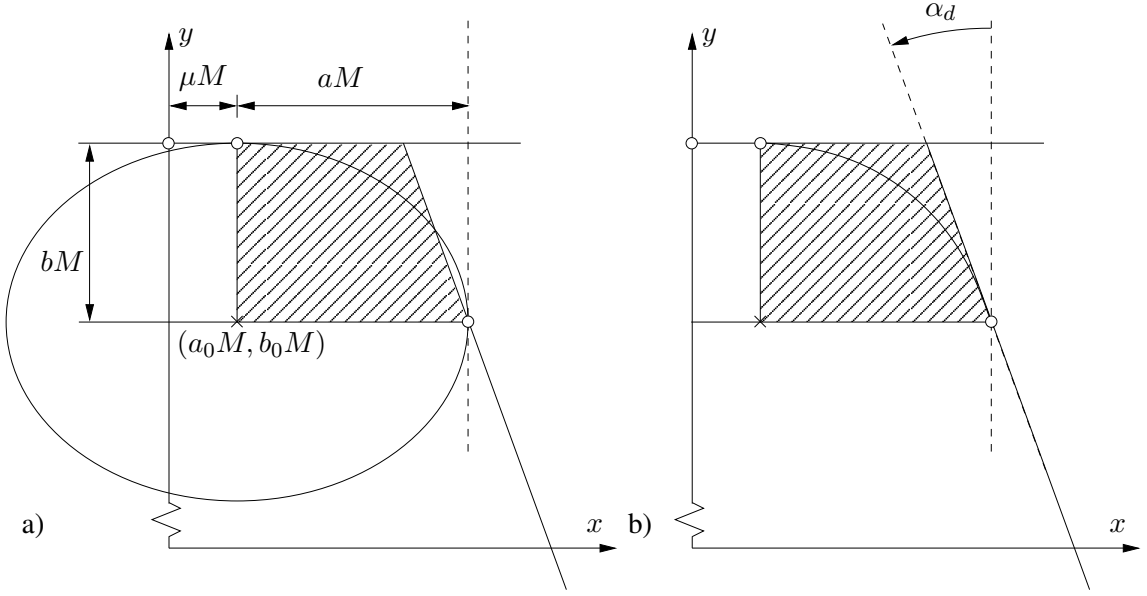
Figure 3: The tooth top parameterization that cuts the drive side tooth root, here shown for a positive value of μ. a) the parameterization of including a super ellipse is shown to be also outside the design domain. b) the super elliptical shape is forced back into the design domain by a distortion.

The remaining top part is as indicated in Figure 3a parameterized by a super elliptical shape, only the first quarter of the super ellipse is used. Parametric form of the super ellipse is

$$x = (a_0 + a_1 \cos(t)^{(2/\eta)})M, \qquad\qquad t \in [0 : \frac{\pi}{2}] \tag{3}$$

$$y = (b_0 + b_1 \sin(t)^{(2/\eta)})M, \qquad\qquad t \in [0 : \frac{\pi}{2}] \tag{4}$$

where the constants are given by

$$a_0 = \mu \,, \quad a_1 = (\frac{\pi}{4} - \tan(\alpha_d) - \mu) \,, \quad b_0 = 1 \,, \quad b_1 = \frac{1}{4}$$

As indicated in Figure 3a the super ellipse might potentially come outside the design domain, which is not wanted since this has an influence on the length of the involute of the cut tooth. To move the super ellipse back a distortion is added to the x position parameterization. The distortion is indicated in Figure 3b by rotating the dashed line. The quarter distorted super ellipse parameterization is given by

$$x = \left(a_0 + a_1 \cos(t)^{(2/\eta)}(1 - \frac{b_1}{a_1} \tan(\alpha_d) \sin(t)^{(2/\eta)}) \right) M, \qquad t \in [0 : \frac{\pi}{2}] \tag{5}$$

$$y = \left(b_0 + b_1 \sin(t)^{(2/\eta)} \right) M, \qquad\qquad t \in [0 : \frac{\pi}{2}] \tag{6}$$

316

Using the parameterization given by (5) and (6) it is possible both to achieve the design space upper limit by letting $\eta \to \infty$ or the lower boundary by letting $\eta \to 0$. The given parameterization fulfills that the gradient/slope is continuous, i.e., no jumps in the slope if $\eta \geqq 1$.

The presented total cutting tool tooth parameterization is in principle controlled by four parameters; the two pressure angles α_d and α_c, the length parameter μ and the super elliptic power η. As preciously stated one of the pressure angles are assumed given so the optimizations presented are parameter studies with only three parameters, μ, η and either α_d or α_c. It is shown that this simple parameterization is sufficiently flexible to achieve constant stress along a major part of the root.

Analytical description of the teeth shape

In shape optimization it is important to have a detailed or preferably analytical shape description. Analytical description also makes verification and comparison possible for other designs. Another reason is that it is known from shape optimization (see e.g. [3] and references therein) that we cannot use the nodes of the FE model as design parameters. In the present paper, we have made an analytical cutting tool parameterization and it is possible to find analytical descriptions for the envelope of the parameterizations in case of a gear with a finite number of teeth. This might not be as easy when using e.g. splines to parameterize the tool tip.

In [1] it is shown how the envelope can be found. In Figure 4 an example of a asymmetric tooth is given.
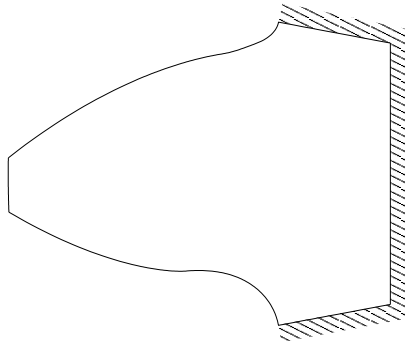

Figure 4: An asymmetric tooth.

Optimization of general spur gear

As discussed in [1] the design that minimizes the maximum bending stress in the tooth will depend on the position of the external loading on the tooth. Therefore in order to compare different designs the load must be applied in the same position. For consistency and for easy reference the choice made here is that the tooth is loaded at the pitch point where we have rolling contact. The load is not put at a single node but applied as a constant line load symmetrically around the pitch point.

In the examples the starting point is the ISO tooth with $\alpha_d = \alpha_c = \pi/9$, the load size is scaled so that the maximum of the largest principal stress is unity. To compare the bending stress of the optimized asymmetric teeth to the ISO tooth the transferred torque is kept constant, i.e., the load size on the optimized tooth is scaled relative to the ISO tooth load.

The example is with 17 teeth, i.e., $z = 17$, and we are at the limit of under-cutting. In Figure 5 a plot with iso-lines and gray scale of the largest principal stress is shown. The plot only shows

the stress at points where the numerical largest principal stress is positive, i.e., where there is predominating tension. If the numerical largest principal stress is negative, i.e., there is predominating compression, the color is white. In Figure 5 the external loading on the tooth is also shown together with the reaction forces at the clamped boundaries.
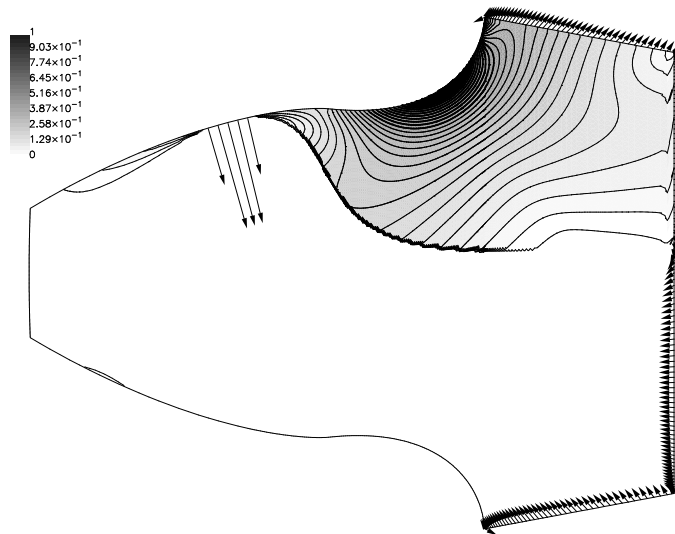

Figure 5: The ISO profile (symmetric) of a tooth for a gear with 17 teeth. Iso-lines and gray scale of the largest principal stress. In the plot the gray scale shows tension only while compressive larger principal stresses are white.

Figure 6 shows a close-up of the stress concentration zone of the ISO tooth. Figure 6b shows the iso-lines of the largest positive principal stress as in Figure 5 but now without the gray scale. Figure 6a shows the size of the largest principal stress along the part of the boundary where the stress concentration is present. The stress size is indicated by the gray area, the perpendicular thickness of the gray area corresponds to the stress level. A tensile stress is plotted under the boundary for illustrative purposes.

a) b)
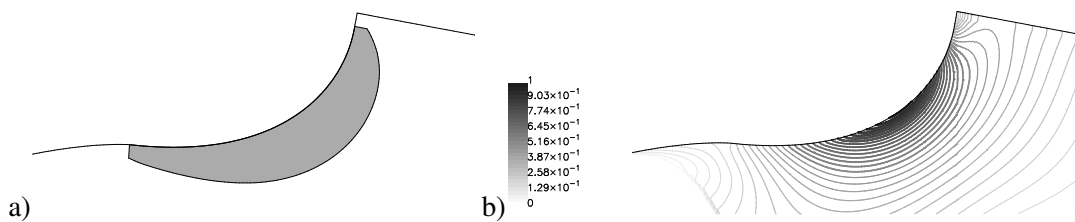
Figure 6: Close-up of the stress concentration zone for the ISO gear.

From the stress plot in Figure 6a it can be seen that there is a potential for improving the stress. However, the ISO tooth does have a rather nice stress distribution along the boundary, so the room for improvement through only shape optimization is limited. This was done in [1] where the best design for a symmetric gear with 17 teeth gave a stress reduction of 12.2% compared to the ISO tooth. With the asymmetric design we can also improve the stress by increasing the tooth root thickness.

Design of asymmetric tooth

Figure 7 is similar to Figure 5 but now with a asymmetric tooth. The design is optimized through a parameter study. Fixed value of this optimization is the coast pressure angle $\alpha_c = \pi/9$.
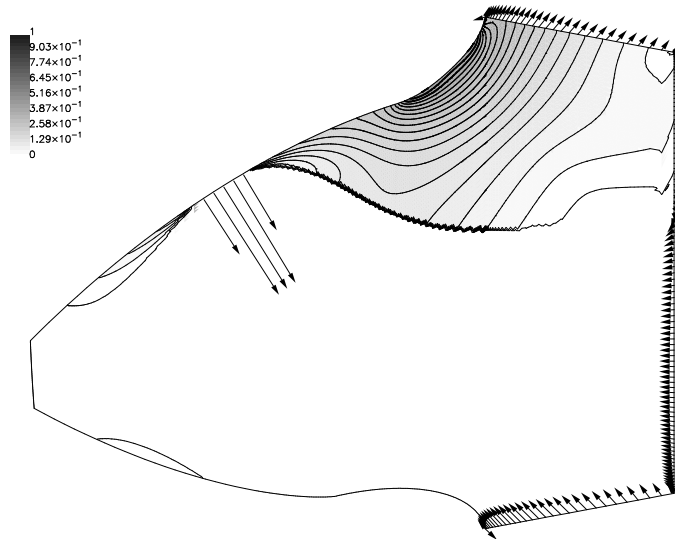

Figure 7: Full view of optimized tooth. The designed tooth is for a gear with 17 teeth, the optimized design variables are $\alpha_c = \pi/9$, $\alpha_d = 7\pi/36$, $\eta = 1.87$ and $\mu = \mu_{\min}$. The stress is reduced with 39.2% as compared to the ISO profile.

The optimized design in Figure 7 have the following design parameters $\alpha_c = \pi/9$, $\alpha_d = 7\pi/36$, $\eta = 1.87$ and $\mu = \mu_{\min}$. Stress is reduced with 39.2% as compared to the ISO profile. A close-up of the interesting tooth part is given in Figure 8. Since this optimization is a parameter study with only three design parameters there might be room for improvement with a more complicated boundary parameterization. From Figure 8a it is, however seen that the stress is constant over a long part of the boundary so any optimization relative to this design must give minor changes. The stress scale in Figure 6 and Figure 8 is the same so the reduction in the stress level is directly visualized.

Figure 8: Close-up of the stress concentration zone for the optimized gear ($\alpha_c = \pi/9$, $\alpha_d = 7\pi/36$, $\eta = 1.87$ and $\mu = \mu_{\min}$). The stress is reduced with 39.2% as compared to the ISO profile.

The prize we pay in this design relative to the original ISO tooth is a smaller contact ratio but this can be fixed through a possible longer tooth since the tooth top thickness is not near the limit. Alternatively to this we fix the drive side pressure angle at $\alpha_d = \pi/9$ and optimize the coast side pressure angle α_c instead, doing this will result in the same contact ratio as the ISO gear. Result of this optimization is presented in Figure 9.
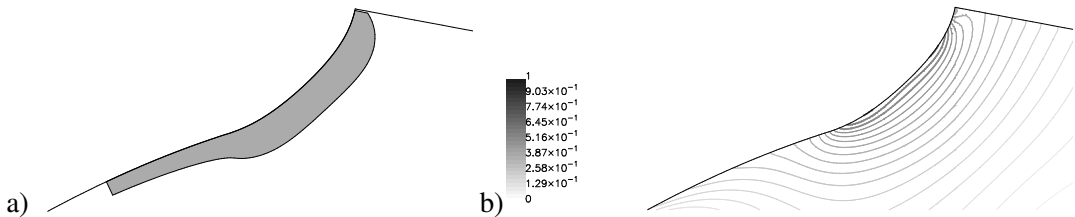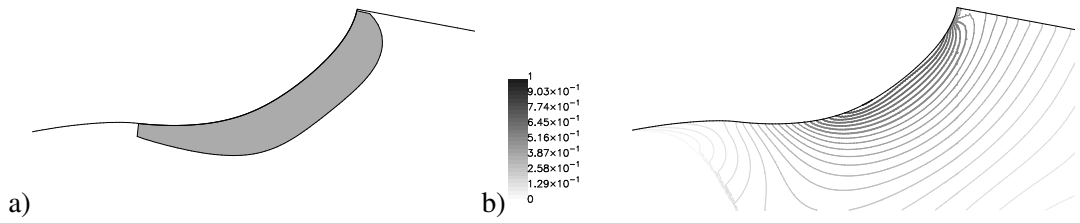
Figure 9: Close-up of the stress concentration zone for the optimized gear ($\alpha_c = 17\pi/90$, $\alpha_d = \pi/9$, $\eta = 1.57$ and $\mu = 0.07$). The stress is reduced with 23.2% as compared to the ISO profile.

Overall the improvements in the bending stresses are large. The largest stress improvement is possible with $\alpha_d > \alpha_c$, here we find almost twice the improvement found when $\alpha_d < \alpha_c$. The improvement of 39.2% and 23.2% should be compared to the result in [1] where the best design gave a stress reduction of 12.2%, so the influence from the enlarged tooth root thickness is clear. The choice of $\alpha_d > \alpha_c$ is similar to what is found in e.g. [4] while $\alpha_d < \alpha_c$ corresponds to the choice in e.g. [5]. With the latter choice the contact ratio is constant but some articles report that the teeth becomes too stiff while with the first choice the contact ratio goes down.

Concluding remarks

The results show that large improvements in the bending stress for gears can be found by the use of asymmetric gears. Bending stress reduction is achieved by two contributions, a thicker tooth root and a root shape change where we have the stress concentration. The factor that has the largest influence is here the enlargement of the root thickness.

The cutting tool is designed so the root shape optimization of the gear tooth is achieved in an indirect way. However the changes made to the cutting tool are directly related to the actual gear tooth. The design parameter choice of the optimization have been, that either the coast side pressure angle α_c or the drive side pressure angle α_d are fixed at $\pi/9$. For 17 teeth the maximum reported reduction in the bending stress is 39.2%, in this case we have a custom cutting tool specifically for a gear with 17 teeth.

References

[1] N. L. Pedersen. Reducing bending stress in external spur gears by redesign of the standard cutting tool. *Structural and Multidisciplinary Optimization*, 28(3):215–227, 2009.

[2] N. L. Pedersen and P. Pedersen. Design of notches and grooves by means of elliptical shapes. *Journal of Strain Analysis for Engineering Design*, 43(1):1–14, 2008.

[3] Y. Ding. Shape optimization of structures: A literature survey. *Computers and Structures*, 24(6):985–1004, 1986.

[4] A. Kapelevich. Geometry and design of involute spur gears with asymmetric teeth. *Mechanism and Machine Theory*, 35(1):117–130, 2000.

[5] G. Deng, T. Nakanishi, and K. Inoue. Bending load capacity enhancement using an asymmetric tooth profile (1st report, influences of pressure angle on tooth root stress and bending stiffness). *JSME International Journal, Series C: Mechanical Systems, Machine Elements and Manufacturing*, 46(3):1171–1177, 2003.

On relaxations and restrictions of structural topology optimization problems with stress constraints

Mathias Stolpe* and Marie-Louise H. Rasmussen

Department of Mathematics
Technical University of Denmark (DTU), Kgs. Lyngby, Denmark
e–mail: M.Stolpe@mat.dtu.dk and M.L.H.Rasmussen@mat.dtu.dk

Summary   We present a technique to determine upper and lower bounds on the objective function value for stress constrained structural topology optimization problems. The technique is based on concepts from global optimization, in particular relaxations and restrictions. The bounds are obtained by solving well-defined nonlinear programs on standard form which are suitable for modern mathematical programming methods such as sequential quadratic programming and interior point methods. The bounds can be used to determine how far away, in the worst case, a feasible point to the stress constrained problem is from global optimality. The technique is illustrated on a two-dimensional variable thickness sheet example.

Introduction

One of the many challenges with stress constrained structural topology optimization problems is that they are not stated on standard nonlinear programming form. If an element vanishes, i.e. if a design variable becomes zero, then the corresponding stress constraint should be removed from the problem formulation. The problems can be reformulated on standard form by multiplying the stress constraints with the corresponding design variable. Alternatively, they can be reformulated as mathematical programs with complementarity constraints [3]. In both cases, standard constraint qualifications such as linear independence constraint qualifications and Mangasarian-Fromovitz constraint qualifications [4] will not be satisfied. Constraint qualifications are always stated as assumptions in convergence theorems for nonlinear programming methods. Hence, with the lack of regularity it is unlikely that classical methods will be able to routinely solve large-scale stress constrained topology optimization problems. Stress constrained problems are difficult to solve, however, we can gain much information about them by solving other related problems.

The main objective of this article is to determine upper and lower bounds on the objective function value for stress constrained structural topology optimization problems. The objective is achieved by using concepts from global optimization, in particular relaxations and restrictions. The bounds are obtained by solving well-defined nonlinear programs on standard form which are suitable for modern mathematical programming methods such as sequential quadratic programming (SQP) [4] and interior point methods [10]. The bounds can be used to determine how far away, in the worst case, a feasible point to the stress constrained problem is from global optimality. Furthermore, the bounds can help to assess how much the stress constraints will influence the optimal design, i.e. to determine if the design is driven by stiffness or strength considerations.

Problem formulation and basic assumptions

We consider the following minimum volume (or weight) structural topology design problem with compliance constraints and design-dependent local stress constraints. The design variables $t \in \mathbb{R}^n$, where n denotes the number of design variables, can for example represent element thicknesses in the two-dimensional case and densities in the three dimensional situation. The state variables $u_k \in \mathbb{R}^d$, where d is the number of degrees of freedom, represent the displacements for the k-th load condition. Throughout, we will state and solve the considered problems using the approach

of simultaneous analysis and design. Problems stated in nested form are only used for establishing theoretical results.

$$v^* = \min_{t \in \mathbb{R}^n, u_1,\ldots,u_m \in \mathbb{R}^d} \sum_{j=1}^{n} t_j w_j$$

(P)
$$\text{subject to} \quad K(t)u_k = f_k \qquad k = 1,\ldots,m$$
$$f_k^T u_k \leq \gamma_k \qquad k = 1,\ldots,m$$
$$\frac{1}{2} u_k^T W_j u_k \leq \bar{\sigma} \quad k = 1,\ldots,m \text{ and } j : t_j > 0$$
$$t_j \in [0,1] \qquad j = 1,\ldots,n$$

In (P), $K(t) \in \mathbb{R}^{d \times d}$ denotes the stiffness matrix in global coordinates, $f_k \in \mathbb{R}^d$ is the k-th given external force, γ_k is the upper bound on the k-th compliance, and $\bar{\sigma}$ is an upper bound on the stress measure. Finally, $W_j \in \mathbb{R}^{d \times d}$ for $j = 1,\ldots,n$ are given symmetric positive semi-definite matrices which are used to compute the stress measure, for example the (square of the) von Mises stress. Notice that the problem formulation (P) is not on standard mathematical programming form due to the stress constraints. Hence, modern standard numerical optimization methods for nonlinear programming can not immediately be applied to the formulation (P).

Let $\mathcal{F}$ denote the feasible set of the problem (P), i.e.,

$$\mathcal{F} = \{(t, u_1,\ldots,u_m) \mid \quad K(t)u_k = f_k, f_k^T u_k \leq \gamma_k, \forall\, k, t \in [0,1]^n,$$
$$\frac{1}{2} u_k^T W_j u_k \leq \bar{\sigma},\ \forall\, k \text{ and } j : t_j > 0\}.$$

Throughout, we make the following basic assumptions which are variations of the assumptions stated in [1] and [5] for continuous minimum compliance problems with an upper bound on the volume of the structure.

(A-1) The external loads $f_k \neq 0$ for $k = 1,\ldots,m$.

(A-2) The stiffness matrix is linear in the design variables $t \in \mathbb{R}^n$, i.e.,

$$K(t) = \sum_{j=1}^{n} t_j K_j$$

where $K_j = K_j^T \succeq 0$ are the given scaled element stiffness matrices.

(A-3) The given constants w_j are non-negative for $j = 1,\ldots,n$.

(A-4) The stiffness matrix $K(e) \succ 0$, where $e \in \mathbb{R}^n$ is a vector of all ones.

(A-5) The compliance bounds γ_k satisfies, for some $0 < \alpha < 1$, the inequalities

$$f_k^T K^{-1}(\alpha e) f_k < \gamma_k < +\infty \text{ for } k = 1,\ldots,m.$$

Notice that due to assumptions (A-1) and (A-4) this implies that $\gamma_k > 0$.

The first assumption (A-1) is stated to avoid the situation that some of the external loads are zero and thus can be removed. The fourth assumption (A-4) guarantees that the ground structure is rich enough in the sense that if material is distributed in all elements the structure can carry any applied load. Notice that the assumption (A-2) allows for the introduction of linear density filters, see e.g. [8] and [12], in the formulation (P). The assumptions stated above, do however, not guarantee that the feasible set of (P) is non-empty.

We consider optimization problems on the form $\min_{x \in \mathcal{F}} f(x)$ where $f(x)$ is the objective function and $\mathcal{F}$ denotes the feasible set. A *relaxation* to this problem is defined as another optimization problem on the form $\min_{x \in \mathcal{F}_R} f(x)$ for which $\mathcal{F} \subseteq \mathcal{F}_R$. Similarly, we define a *restriction* to the problem as another optimization problem $\min_{x \in \mathcal{F}_C} f(x)$ for which $\mathcal{F}_C \subseteq \mathcal{F}$. The definition of the relaxation is slightly less general than normally seen in the global optimization literature [11], but it suffices for our purposes.

The relaxation

A natural approximation of the stress constrained problem (P) is obtained by removing the complicating stress constraints.

$$
\begin{aligned}
v_R^* = \quad & \underset{t \in \mathbb{R}^n, u_1, \ldots, u_m \in \mathbb{R}^d}{\text{minimize}} && \sum_{j=1}^n t_j w_j \\
\text{(R)} \quad & \text{subject to} && K(t)u_k = f_k && k = 1, \ldots, m \\
& && f_k^T u_k \leq \gamma_k && k = 1, \ldots, m \\
& && t_j \in [0,1] && j = 1, \ldots, n
\end{aligned}
$$

Let $\mathcal{F}_R$ denote the feasible set of the problem (R), i.e.,

$$
\mathcal{F}_R = \{(t, u_1, \ldots, u_m) \mid K(t)u_k = f_k, f_k^T u_k \leq \gamma_k, \, \forall \, k, t \in [0,1]^n\}.
$$

Due to assumptions (A-4) and (A-5) the feasible set of (R) is non-empty, i.e. $\mathcal{F}_R \neq \emptyset$. From the construction of the problem (R), it immediately follows that it is a relaxation of the stress constrained problem (P) and that the objective function in (R) underestimates the objective in (P).

Lemma 1 *The problem (R) is a relaxation of the problem (P), i.e. $\mathcal{F} \subseteq \mathcal{F}_R$, and hence $v_R^* \leq v^*$.*

An immediate consequence of this is the following.

Corollary 1 *If $(t^*, u_1^*, \ldots, u_m^*)$ is an optimal solution to the relaxation (R) and at the same time feasible to problem (P) then it is also optimal to (P).*

This situation is perhaps unlikely in practice since it shows that the stress constraints are not stringent enough to influence the optimal design (but notice that they may still very well be active).

The relaxation (R) is indeed a problem on standard form, but it is not certain that some classical constraint qualifications are satisfied.

Reformulations of the relaxation

The relaxation, as stated in (R), is non-convex due to the equilibrium equations. There are however several equivalent and convex reformulations of this problem. We reformulate the relaxation (R) as a linear semidefinite program (SDP) in the design variables t only. The reformulation is based on the ideas for (SDP) reformulations of minimum compliance problems presented in [6, 7].

$$
\begin{aligned}
&\underset{t\in\mathbb{R}^n}{\text{minimize}} && \sum_{j=1}^{n} t_j w_j \\
(\text{R}-\text{SDP}) \quad &\text{subject to} && K(t) \succeq \frac{1}{\gamma_k} f_k f_k^T \quad k=1,\ldots,m \\
& && t_j \in [0,1] \qquad\quad j=1,\ldots,n
\end{aligned}
$$

As a by-product of this reformulation, and the stated assumptions, we can show existence of solutions to (R) using strong SDP duality [14]. The dual of (R − SDP) is given by the linear semidefinite program [14]

$$
\begin{aligned}
&\underset{U_1,\ldots,U_m,\sigma\in\mathbb{R}^n}{\text{maximize}} && \sum_{k=1}^{m} \frac{1}{\gamma_k}\text{Tr}(f_k f_k^T U_k) - e^T\sigma \\
(\text{D}-\text{SDP}) \quad &\text{subject to} && \sum_{k=1}^{m}\text{Tr}(K_j U_k) - \sigma_j \leq w_j \quad j=1,\ldots,n \\
& && U_k \succeq 0, \qquad\qquad\qquad\quad k=1,\ldots,m \\
& && \sigma_j \geq 0 \qquad\qquad\qquad\quad\; j=1,\ldots,n
\end{aligned}
$$

Notice that due to the stated assumptions the feasible set of (R − SDP) is non-empty and in fact has interior points due to assumption (A-5), i.e. it satisfies the strong Slater constraint qualifications. Furthermore, the objective function in (R − SDP) is bounded from below by zero. The feasible set of the dual (D − SDP) is also non-empty and also has interior points. These regularity conditions are enough to guarantee that both the primal (R − SDP) and the dual (D − SDP) has optimal solutions and the optimal objective function values are equal [15]. A consequence of this is that also the relaxation (R) possesses an optimal solution.

The dual (D − SDP) can be reformulated as a non-convex all-quadratic program [13]. This reformulation is indeed useful for practical computations. In the numerical experiments we however instead treat directly the problem (R) even though it is non-convex and it is uncertain if some constraint qualifications are satisfied. The objective is to find a KKT point and, if necessary, attempt to modify this point to satisfy the optimality conditions to the primal-dual pair (R − SDP) and (D − SDP). Due to the regularity conditions, which are satisfied for these problems, the optimality conditions are given by

$$
\begin{aligned}
&K(t) - (1/\gamma_k)f_k f_k^T \succeq 0 && k=1,\ldots,m && \text{(Primal feasibility)} \\
&t_j \in [0,1] && j=1,\ldots,n && \text{(Primal feasibility)} \\
&\sum_{k=1}^{m}\text{Tr}(K_j U_k) - \sigma_j \leq w_j && j=1,\ldots,n && \text{(Dual feasibility)} \\
&U_k \succeq 0, && k=1,\ldots,m && \text{(Dual feasibility)} \\
&\sigma_j \geq 0 && j=1,\ldots,n && \text{(Dual feasibility)} \\
&U_k(K(t) - (1/\gamma_k)f_k f_k^T) = 0 && k=1,\ldots,m && \text{(Complementarity)} \\
&\sigma_j(t_j - 1) = 0 && j=1,\ldots,n && \text{(Complementarity)}
\end{aligned}
\tag{1}
$$

Let $\eta_k \in \mathbb{R}^d$ denote the Lagrange multipliers for the k-th equilibrium equations, $\xi_k \in \mathbb{R}$ the Lagrange multipliers for the k-th compliance constraint, and $\sigma \in \mathbb{R}^n$ the multipliers for the upper box constraints. The KKT conditions for the relaxation (R) can be stated as

$$
\begin{aligned}
K(t)u_k &= f_k & k &= 1, \ldots, m & \text{(Primal feasibility)} \\
f_k^T u_k &\leq \gamma_k & k &= 1, \ldots, m & \text{(Primal feasibility)} \\
t_j &\in [0,1] & j &= 1, \ldots, n & \text{(Primal feasibility)} \\
K(t)\eta_k &= -\xi_k f_k & k &= 1, \ldots, m & \text{(Stationarity)} \\
-\sum_{k=1}^{m} \eta_k^T K_j u_k - \sigma_j &\leq w_j & j &= 1, \ldots, n & \text{(Stationarity)} \\
\xi_k (f_k^T u_k - \gamma_k) &= 0 & k &= 1, \ldots, m & \text{(Complementarity)} \\
\sigma_j (t_j - 1) &= 0 & j &= 1, \ldots, n & \text{(Complementarity)} \\
\sigma_j &\geq 0 & j &= 1, \ldots, n & \text{(Dual feasibility)} \\
\xi_k &\geq 0 & k &= 1, \ldots, m & \text{(Dual feasibility)}
\end{aligned}
\tag{2}
$$

Let $(t, u_k, \eta_k, \xi_k, \sigma)$ be a KKT point to the relaxation (R). Since $(t, u_1, \ldots, u_m)$ is feasible to (R), the design variables t is feasible to the SDP formulation (R $-$ SDP). The KKT conditions (2) imply that the point $(U_1, \ldots, U_m, \sigma)$ with $U_k = \xi_k u_k u_k^T$ is feasible to the dual (D $-$ SDP). Notice that this choice of U_k makes it both symmetric and positive semi definite. Hence, if we also have no duality gap at this point, i.e. if $\sum_j w_j t_j = \sum_k \frac{1}{\gamma_k} \mathrm{Tr}(f_k f_k^T U_k) - e^T \sigma$, then the found KKT point is indeed a global minimizer to the relaxation (R). If on the other hand there is a duality gap, then we have numerically found a KKT point to (R) which is not a global minimizer. In this case we can use the objective function value from the dual (D $-$ SDP) to find a lower bound (this follows from weak duality).

The restriction

Another natural approximation of the stress constrained problem (P) is obtained by enforcing the stress constraints in all elements, regardless of the values of the design variables. We arrive at the problem

$$
\begin{aligned}
v_C^* = \quad &\underset{t \in \mathbb{R}^n, u_1, \ldots, u_m \in \mathbb{R}^d}{\text{minimize}} \quad \sum_{j=1}^{n} t_j w_j \\
\text{(C)} \qquad &\text{subject to} \quad K(t)u_k = f_k & k &= 1, \ldots, m \\
& \qquad\qquad\quad f_k^T u_k \leq \gamma_k & k &= 1, \ldots, m \\
& \qquad\qquad\quad \frac{1}{2} u_k^T W_j u_k \leq \bar{\sigma} & k &= 1, \ldots, m \text{ and } j = 1, \ldots, n \\
& \qquad\qquad\quad t_j \in [0,1] & j &= 1, \ldots, n
\end{aligned}
$$

Notice that the problem (C) is stated on standard form for nonlinear programming. Let $\mathcal{F}_C$ denote the feasible set of the problem (C), i.e.

$$
\mathcal{F}_C = \{(t, u_1, \ldots, u_m) \mid \quad K(t)u_k = f_k, f_k^T u_k \leq \gamma_k, \forall\, k, t \in [0,1]^n \\
\frac{1}{2} u_k^T W_j u_k \leq \bar{\sigma}, \ \forall\, k \text{ and } j \}.
$$

From the construction of the problem (C), it immediately follows that it is a restriction of the stress constrained problem (P) and that the objective function value in (C) overestimates the objective function value in (P).

Lemma 2 *The problem* (C) *is a restriction of the problem* (P), *i.e.* $\mathcal{F}_C \subseteq \mathcal{F}$, *and hence* $v_C^* \geq v^*$.

An immediate consequence of this is the following.

Corollary 2 *If* $(t^*, u_1^*, \ldots, u_m^*)$ *is a feasible point to the restriction* (C) *then it is also a feasible point to* (P).

Notice that the restriction (C) can be infeasible while the original problem (P) has a non-empty feasible set.

It is not known if the problem formulation (C) satisfies some constraint qualifications. It is however possible to perturb the lower bounds on the design variables in (C) by a $\delta > 0$ while maintaining the property that the problem is a restriction of (P). The perturbation guarantees that the stiffness matrix is positive definite for all t satisfying the box constraints. Hence the Jacobian of the equality constraints is full rank and at least part of the linear independence constraint qualifications [4] are satisfied. With this perturbation we expect to see a more robust behavior of standard optimization methods such as SQP and interior point methods when applied to instances of (C).

Measure of closeness to optimality

From the (global) optimal solution to the relaxation (R) a lower bound v_R^* on v^* is found. This lower bound will be strictly bigger than zero because otherwise the equilibrium equations cannot be satisfied. If a feasible point to the restriction (C) is found, then also an upper bound v_C^* on v^* is available. An optimal solution to the restriction (C) is of course desirable, since this gives the best bound. In summary, after attacking both (R) and (C) we can bound v^* by $v_R^* \leq v^* \leq v_C^*$ without actually treating the problem (P). If (C) is feasible and $v_C^* < +\infty$ then we can define the relative gap ν as

$$\nu = \frac{v_C^* - v_R^*}{v_R^*}.$$

If the relative gap ν is small then one can argue that the optimal design problem (P) is driven by stiffness rather than strength considerations. If the relative gap ν is large then either the design is driven by strength considerations, or a poor feasible point to the restriction (C) has been found.

Given a point $(t, u_1, \ldots, u_m)$ with objective function value v which is feasible to the stress constrained problem (P), one can improve on the relative gap and obtain a worst case measure how far away from a global minimum the point is. If $v > v_C^*$ then this point is clearly not optimal. If v is close to v_R^*, one can again argue that stiffness is more important than strength in the given design situation.

Method and implementation

The relaxation (R) and the restriction (C) are treated by a primal-dual interior point method [10]. Convergence is enforced by performing a backtracking line-search on an l_1-penalty function. The interior point method and all finite element routines including the sensitivity analysis are implemented in MATLAB. The majority of the computation effort resides in solving a saddle-point system at each iteration of the interior-point method. This is done by the LDL-factorization routine MA57 [9].

Numerical experiments

We consider a two-dimensional rectangular design domain with width 8 and height 5. The entire left hand side is fixed to a rigid wall. A single vertical uniform external load distributed over a distance of 0.2 is centered around the middle of the right hand side. The finite elements used in the numerical experiments are 4-node bilinear elements in plane stress and the stresses are computed in the Gauss points. The design domain is discretized into 80×50 elements with 8160 degrees of freedom. The modulus of elasticity is set to one and Poisson's ratio is set to 0.3. The compliance bound γ is determined as follows: First every element is assigned a thickness of 1/2 and the displacements and compliance are computed. The maximum allowed compliance is then set to 0.75 times the computed compliance. Then a KKT point to the relaxation (R) is computed using the interior-point method and we attempt to verify optimality through the optimality conditions (1) and by computing the duality gap. In this particular example all conditions were satisfied and the optimality gap was (numerically) zero. The optimal design to the relaxation is presented in Figure 1. The number of interior point iterations to solve the relaxation (R) is 38. The optimal volume is 47.9% of the total possible volume After solving the relaxation (R) the von Mises stress is com-
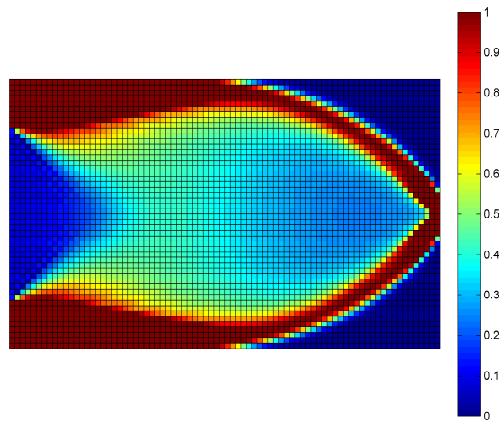

Figure 1: The optimal thickness distribution obtained by solving the relaxation (R).

puted. The upper bound on the von Mises stress $\bar{\sigma}$ is then set as 0.5 times the maximum stress from the optimal solution to (R) after excluding the elements to which the load is applied. The design found after treating the restriction (C) with this stress bound and the same compliance bound as above is presented in Figure 2. The number of interior point iterations to solve the restriction (C) is 63. The found volume for this design is 50.1% of the total possible volume. The relative optimality gap ν for this particular example is approximately 4.6%. For the presented example the relaxation (R) gives a fairly tight lower bound to the objective function of the stress constrained problem (P). However, there are clearly visible differences in the obtained designs.
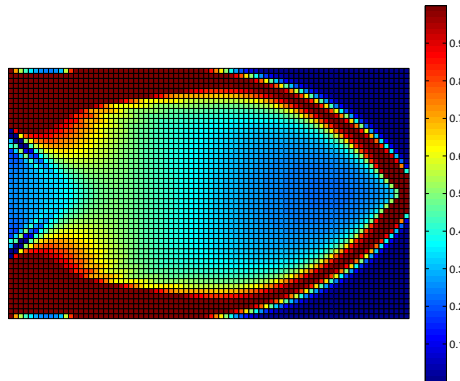
Figure 2: The thickness distribution obtained by solving the restriction (C).

References

[1] W. Achtziger and M.P. Bendsøe and A. Ben-Tal and J. Zowe. Equivalent displacement based formulations for maximum strength truss topology design *Impact of Computing in Science and Engineering*, **4**, 315 – 345, (1992).

[2] W. Achtziger. Multiple load truss topology and sizing optimization: Some properties of minimax compliance. *Journal of Optimization Theory and Applications*, **98**, 255 – 280, (1998).

[3] W. Achtziger. On non-standard problem formulations in structural optimization. *Proceedings of the Sixth World Congress of Structural and Multidisciplinary Optimization*, (2005).

[4] M.S. Bazaraa, C.M. Shetty, H.D. Sherali. *Non-linear Programming*. John Wiley and Sons, Second edition, (1993).

[5] A. Ben-Tal and M.P. Bendsøe. A new method for optimal truss topology design. *SIAM Journal on Optimization*, **3:2**, 322 – 358, (1993).

[6] A. Ben-Tal and A. Nemirovski Optimal design of engineering structures. *OPTIMA Mathematical Programming Society Newsletter*, **47**, (1995).

[7] A. Ben-Tal and A. Nemirovski Robust truss topology design via semidefinite programming. *SIAM Journal on Optimization*, **7:4**, 991 – 1016, (1997).

[8] B. Bourdin. Filters in topology optimization. *International Journal for Numerical Methods in Engineering*, **50:9**, 2143 – 2158, (2001).

[9] I.S. Duff. MA57 – a code for the solution of sparse symmetric definite and indefinite systems. *ACM Transactions on Mathematical Software*, **30:2**, 118 – 144, (2004).

[10] A. Forsgren, P.E. Gill, M.H. Wright. Interior Methods for Nonlinear Optimization. *SIAM Review*, **44:4**, 525 – 597, (2002).

[11] R. Horst and H. Tuy. *Global optimization: deterministic approaches*. Springer, Second edition, (1996).

[12] O. Sigmund. Morphology-based black and white filters for topology optimization. *Structural and Multidisciplinary Optimization*, **33:4 – 5**, 401 – 424, (2007).

[13] M. Stolpe and R. Stainko and M. Kočvara. Lower bounding problems for stress constrained discrete structural topology optimization problems. *PLATO–N Public Report PU–R–8–2007*, (2007).

[14] L. Vandenberghe and S. Boyd. Semidefinite programming. *SIAM Review*, **38:1**, 49 – 95, (1996).

[15] H. Wolkowicz. Some applications of optimization in matrix theory. *Linear Algebra and its Applications*, **40**, 101 – 118, (1981).

Simulation of the human musculoskeletal system: mechanics and optimization at work

John Rasmussen* and Michael Skipper Andersen
Department of Mechanical Engineering
Aalborg University, Aalborg, Denmark
*e−mail: jr@me.aau.dk

Mark de Zee
Department of Health Science and Technology
Aalborg University, Aalborg, Denmark
e−mail: mdz@hst.aau.dk

Summary   This paper outlines some of the optimization-related issues in simulation of musculoskeletal systems, more precisely handling of over-determinate motion specifications, statically indeterminate muscle equilibrium and modeling of the body's ability to adapt to different loading conditions. It is concluded that optimality principles seem to guide many aspects of living organisms and that an understanding of optimization processes is the key to understanding basic life processes.

Introduction

The idea that optimization principles guide the development and function of living organisms has been around at least since the time of Darwin. However, closer investigation reveals that optimization processes do not only guide genetic development of the species but can also explain adaptations of the individual organism to its environment in different time scales, i.e. from one moment to the next or over weeks or months. In this paper, we shall use musculoskeletal modeling techniques to predict the behavior of the human body in response to different living conditions and also as a means to impose experimentally measured movements on computer models and to identify unknown model parameters.

The AnyBody Modeling System

Development of "well-made" musculoskeletal models is challenging. The human musculoskeletal system is a very complex machine with literally thousands of components, each of which is described by many parameters that vary in a complex fashion between individuals and across populations. The AnyBody Modeling System [1] and the AnyScript model repository is an attempt to bring musculoskeletal modeling to a wider audience, to capture the similarity of body morphology between individuals, and to equip it with scaling laws that allow for reasonable scaling between individuals of different sizes. The model library was initiated by the AnyBody Research Group at Aalborg University in 1997 and has since received contributions in the form of anatomical data, model development or validation from a multitude of scientists in different countries with special expertise on different body parts. The library today contains the entire body with more than 1000 individually activated muscles as illustrated in Figure 1.
The model is developed in a high-level, object-oriented scripting language, AnyScript, particularly developed for the purpose. The need to describe such a model in terms of a programming language rather than as a database becomes evident when we consider that the model is not merely static data but must also encapsulate variations, scaling laws, and complex dependencies between its elements. The modeling language also has the advantage of not separating the basic information of the model from what the user sees. This means that the model is entirely open for scrutiny,

modification and validation by independent scientists and this has become the fundamental strategy for obtaining credibility of this novel technology with potentially critical applications. The contributions are numerous, for instance from Dubowsky et al [2], de Zee et al [3] [4], Nolte et al [5], Wu et al [6], Manders et al [7] and Wehner et al [8].

Figure 1: The current version of the AnyBody full body model comprising more than 1000 muscles.

The fact that the technology takes the form of a modeling system allows the user to connect the human model from the model repository to user-defined mechanisms such as bicycles, sports equipment, tools, workplaces, furniture, car driver environments and other situations of interest to occupational safety, ergonomics or performance. Figure 2 illustrates a number of such applications. The simulation method is based on inverse dynamic in which the motion, loads and external boundary conditions are specified and the system subsequently computes the detailed movement of all degrees-of-freedom (DoF) and the internal joint and muscle forces.
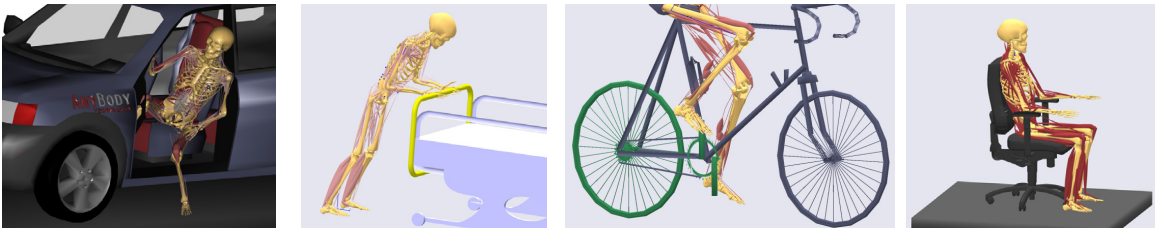

Figure 2: Typical applications of the musculoskeletal model.

Over-determinate kinematical systems

Motion input to inverse dynamics musculoskeletal analysis is usually provided through motion capture technology, in which a set of synchronized video cameras record optical markers attached to the body and the three-dimensional trajectories of these markers are subsequently reconstructed by photogrammetric techniques. This leaves the model with a number of kinematic constraints, requiring the skeletal points, corresponding to the marker positions, to follow the trajectories.

A mechanical system that is subject to holonomic constraints can be formulated as a set of m equations of the n_q-dimensional time-dependent system coordinates, $q(t)$, n_d-dimensional model constants, d, and time, t [16], [17].

$$\Gamma(q(t), d, t) = 0 \qquad (1)$$

Depending on the number of coordinates and the number of equations, these equations can either be under-determinate ($m < n_q$), determinate ($m = n_q$) or over-determinate ($m > n_q$). Due to the

setup of motion capture experiments and the nature of multibody systems, the number of measured trajectory coordinates will always exceed the number of DoFs in the system, i.e. the system will be kinematically over-determinate. Since over-determinacy means that there generally does not exist a solution to equation (1), some re-arrangement of the equations is required in order to define what constitutes a solution. Andersen *et al*. [17] introduced the concept of having the equations split into two sets: 1) $\Psi(q(t),d,t)$ a set of equations that only has to be solved "as well as possible" in some sense, and 2) $\Phi(q(t),d,t)$ a set of equations that has to be solved exactly:

$$\Gamma(q(t),d,t) = \begin{bmatrix} \Psi(q(t),d,t) \\ \Phi(q(t),d,t) \end{bmatrix} \tag{2}$$

This split of the equations into these two sets can be done in any way as long as the solution set of $\Phi(q(t),d,t)=0$ is non-empty. Typically, $\Psi(q(t),d,t)$ consist of the marker constraints, i.e., equations that specify that the marker position in the model must be equal to the measured position, whereas $\Phi(q(t),d,t)$ contain the joint constraints of the musculoskeletal system.

We shall start off by assuming that the constant model parameters are known and denote them by $\hat{d}$. If it is desired to solve equation (2) at N discrete time steps,

$$q_1 = q(t_1), q_2 = q(t_2),\ldots, q_N = q(t_N) \tag{3}$$

the solution can be found by solving the following nonlinear and non-convex optimization problem [17]:

$$\begin{aligned} q_i^* \quad &= \quad \arg\min \quad G(\Psi(q_i,\hat{d},t_i)) \\ &\qquad\quad q_i \\ &\qquad \text{s.t.} \quad \Phi(q_i,\hat{d},t_i)=0 \end{aligned} \tag{4}$$

for $i = 1,2,\ldots N$. The scalar objective function, $G(\Psi(q_i,\hat{d},t_i))$, has been introduced to express how violations of the $\Psi(q_i,\hat{d},t_i)$ equations are allowed. Andersen *et al*. [17] and Ausejo *et al* [18]. (2006) demonstrated the use of a weighted least-square objective function:

$$G(\Psi(q_i,\hat{d},t_i)) = \frac{1}{2}\Psi(q_i,\hat{d},t_i)^T W(t_i)\Psi(q_i,\hat{d},t_i) \tag{5}$$

The KKT conditions for the optimization problem in equation (4) at time step i are (refer, for instance, to [19]):

$$\begin{aligned} G_{q_i}^T + \Phi_{q_i}^T \lambda_i &= 0 \\ \Phi &= 0 \end{aligned} \tag{6}$$

When a Newton-based method is used to find a local minimizer, the linearized KKT conditions are required:

$$\begin{bmatrix} G_{q_i q_i}^T + (\Phi_{q_i}^T \lambda_i)_{q_i} & \Phi_{q_i}^T \\ \Phi_{q_i} & 0 \end{bmatrix} \begin{bmatrix} \Delta q_i \\ \Delta \lambda_i \end{bmatrix} = \begin{bmatrix} -G_{q_i}^T - \Phi_{q_i}^T \lambda_i \\ -\Phi \end{bmatrix} \tag{7}$$

where Δq_i and $\Delta \lambda_i$ denote the search direction at step i, which is found by solving the linear set of equations in equation (7). For well-conditioned systems, the matrix on the left hand side will be invertible, and the method can be shown to generally lead to improved transfer of the recorded motion to the model compared to manual method of reduction of the constraint set to a determinate system. However, the redundancy of information from the motion capture experiment can be used to further enhance the accuracy of the model. A musculoskeletal model contains many constant parameters that may not match the test subject of the experiment completely and which are very difficult to measure directly. It is therefore obvious to attempt the use of the redundant information

to determine these parameters. In principle, any constant parameter of the model may be subject to identification, but the relevant parameters for musculoskeletal models are in particular: segment lengths, joint axis orientations and local placement of markers on the segments. Inclusion of the constant parameters in the problem requires a split of the design variables into two groups. One group is the comprised of the time-dependent variables, i.e. the state variables of the kinematical system. The other group is the time-invariant parameters such as segment lengths etc. It turns out that this leads to a large-scale, non-convex and generally difficult optimization problem. It turns out, however, that it is possible to exploit a special structure in the problem and obtain a partial decoupling, which allows the problem to be solved very efficiently. Please refer to Andersen et al [20] for details.
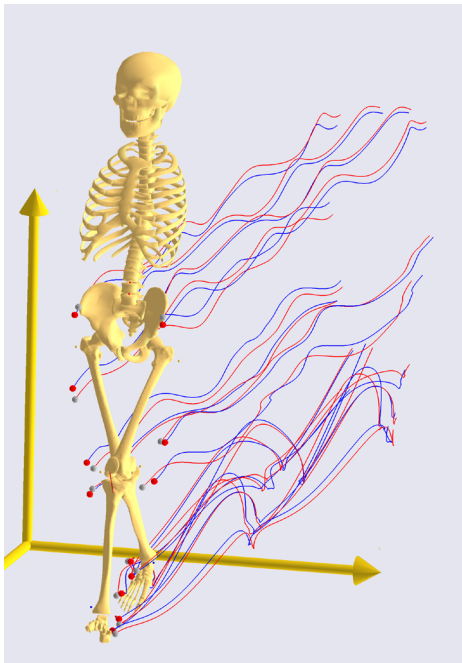

Figure 3: Measured (red) and realized (blue) marker trajectories before model parameter optimization.
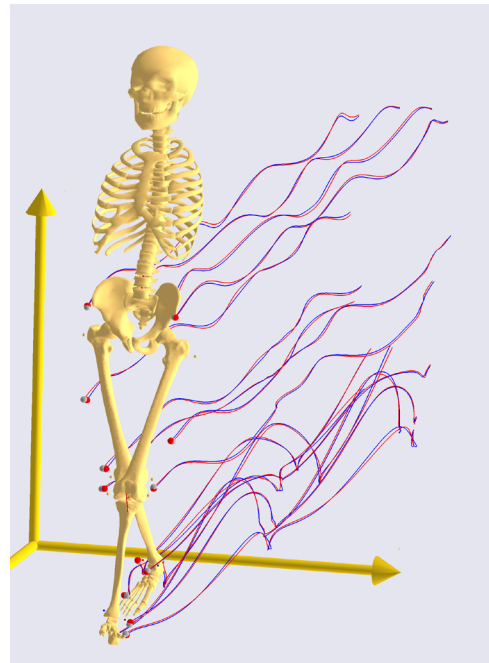

Figure 4: Measured (red) and realized (blue) marker trajectories after parameter optimization.

The implications of this finding are significant and very direct. It will now be possible, in a clinical setting, to conduct a relatively simple and non-invasive experiment on a patient and obtain valuable information about internal parameters that are very difficult to measure accurately. Furthermore, the method leads to much improved accuracy of musculoskeletal analysis because it provides better agreement between the test subject and the model parameters.

Muscle recruitment

Inverse dynamics presumes that a kinematic analysis has been performed to provide the motion, i.e., the acceleration of all segments in the system. If, furthermore, the masses are known, Newton's second law can be solved for the forces in the system, i.e. the muscle and joint forces. Inverse dynamics was first used in gait analysis, where measured ground reaction forces are applied to the end of open kinematic chains, i.e. the lower extremities, and simple equilibrium can then determine the necessary joint moments.

Muscle systems generally have more muscles than DoFs and the resulting equations are therefore indeterminate and must be solved by an optimization technique. Let us briefly review the formulation of the muscle recruitment problem:

Minimize

$$G(\mathbf{f}^{(M)}) \tag{8}$$

Subject to

$$\mathbf{Cf} = \mathbf{r} \tag{9}$$

$$f_i^{(M)} \geq 0 \tag{10}$$

where $\mathbf{f} = [\mathbf{f}^{(m)}, \mathbf{f}^{(R)}]$ is a vector of internal muscle (M) and joint reaction (R) forces respectively, and $\mathbf{r}$ is a vector of external forces. The two constraints express that the system must be in equilibrium and that the muscle part of the $\mathbf{f}$ vector is restricted in sign because muscles can only pull. The fact that the system has more muscles than degrees of freedom means that the coefficient matrix $\mathbf{C}$ is rectangular, and the equilibrium equations therefore have infinitely many solutions. The objective function, $G(\mathbf{f}^{(M)})$, is used to select the single optimal solution, and muscle recruitment therefore involves a discussion of which objective function, G, expresses the true physiology of the problem.

Several choices of objective function G (for a review, please refer to Rasmussen et al [21]) lead to realistic muscle forces and numerically benevolent problems, which can be solved for large systems with hundreds of muscles in a few seconds on an ordinary desktop computer. The disadvantage of this approach is that it presumes optimal activation of the muscles and therefore only works for voluntary movements. It is also difficult in inverse dynamics to take the rise and decay times of muscle forces into account, so the method has a limitation for fast movements. However, for most activities of daily living such as gait, good estimates can be expected from inverse dynamics as demonstrated by Anderson and Pandy [9], if the models are well-made and the motions are accurately recorded and imposed on the model.

One particular interesting choice of objective function is the maximum relative muscle load, i.e. maximum muscle activity:

$$G\left(\mathbf{f}^{(M)}\right) = \ \max \left(\frac{f_i^{(M)}}{N_i}\right)$$

where N_i is a normalization factor expressing the strength of the ith muscle. As observed by An et al. [10], this is equivalent to minimization of fatigue in the muscle system in the sense that it postpones fatigue in the highest loaded muscle as far as possible. The structure of the resulting optimization problem is remarkably similar to a class of problems in structural optimization described by Olhoff and Taylor [11]. These problems of maximization of multiple eigenfrequencies or minimization of maximum stress in a structure can be solved by observing that a simple reformulation can change the optimization problem from a nonlinear and non-differentiable form to a linear form with the same solution:

Minimize

$$\beta \tag{11}$$

Subject to

$$\frac{f_i^{(M)}}{N_i} \leq \beta \tag{12}$$

$$\mathbf{Cf} = \mathbf{r} \tag{13}$$

$$f_i^{(M)} \geq 0 \tag{14}$$

where β is an artificial design variable. The linear nature of this problem makes it possible to solve it for very large musculoskeletal systems in a few seconds per time step on an ordinary desktop or laptop computer. This computational efficiency enables more advanced applications of optimization as we shall see in the following section.

Adaptation of joint surfaces to changes in loading conditions

The human mandible with its two temporomandibular joints (TMJ) is a complex biomechanical system. The mandible can move with six DoFs due to the special construction of the TMJ, and it does so for a variety of functions like chewing, clenching, speech and swallowing, tasks are often a combination of high forces and precision. De Zee et al. [12] validated a generic mandible model built in the AnyBody Modeling System, and we shall now show a patient-specific version of the model applied to a load adaptation problem, which was described in more detail by De Zee et al. [22].

Trainor *et al.* [13] and Iwasaki *et al.* [14] were able to show that the mandible's articular eminence morphology is consistent with minimisation of joint loads for the normal population. This principle has also the potential to be used in prediction of the eminence shape in clinical cases before and after surgery where there is a major change of the geometry of the mandible like mandibular distraction osteogenesis (DO). The model used here represents the patient previously analyzed by Cattaneo *et al.* [15]. The model represents the patient before and after DO at shown in Figure 5, and the angles of the two articular eminences are subsequently varied and the joint forces are computed for each combination.
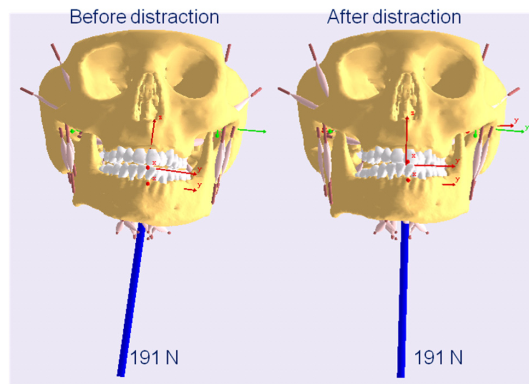

Figure 5: Patient-specific musculoskeletal model of the mandible before and after distraction osteogenesis.

Figure 6 shows the results of the parameter study before DO, i.e. the mean TMJ reaction force as a function of the two articular eminence angles. A minimum is located at 0 degree angle on the right hand side and 11 degrees on the left hand side, corresponding to an average TMJ load of 94 N. The measured eminence angles before distraction were 5 degrees on the right hand side and 15 degrees on the left hand side. In the model, the measured angle values of 5 and 15 degrees will lead to an average TMJ force of 96 N. Figure 7 shows the results of the parameter study after DO. The surface exhibits a rather large, flat area around 20 degree angles on both sides, corresponding to an average TMJ load of 82 N. The measured eminence angles after distraction were 15 degrees on the right hand side and 20 degrees on the left hand side. In the model, the measured angle values of 15 and 20 degrees will lead to an average TMJ force of 83 N, i.e. almost the same as the mathematical minimum.
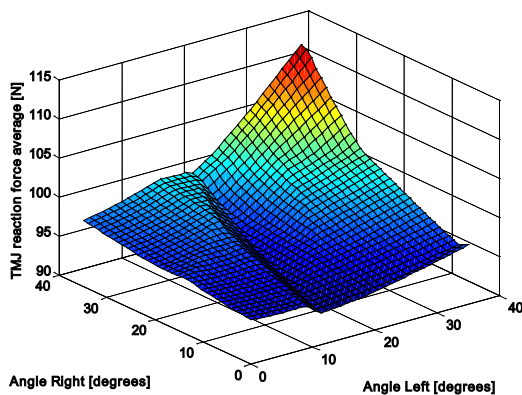
Figure 6: Average joint force as a function of the two articular eminence angles before OD.
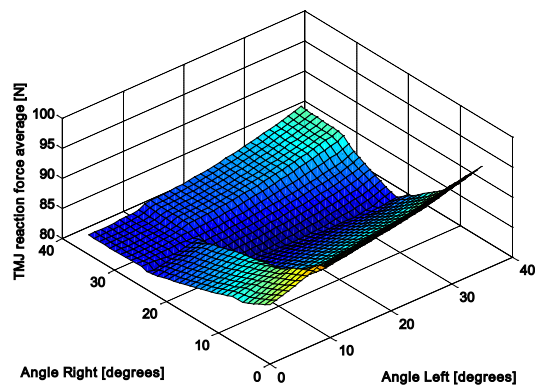

Figure 7: Average joint force as a function of the two articular eminence angles after OD.

Conclusions

Optimization principles seem to guide the development and behavior of the human body on several temporal scales, i.e. in terms of muscle recruitment from one instant to another, in the form of bony adaptation to loads in the time scale of months or years, and in the form of adaptation of the species to different conditions of living over millenniums. A basic understanding of optimality principles is therefore essential to our understanding of many aspects of life sciences, and an operational skill in formulation and implementation of efficient optimization algorithms is necessary to obtain effective and reliable tools to simulate human behavior. The current state-of-the-art in musculoskeletal simulation to a large extent builds on results of pioneers within structural and multidisciplinary optimization.

References

[1] M. Damsgaard, J. Rasmussen, S.T. Christensen, E. Surma and M. de Zee. Analysis of musculoskeletal systems in the AnyBody Modeling System. *Simulation Modelling Practice and Theory*, **14**, 1100-1111, (2006).

[2] S.R. Dubowsky, J. Rasmussen, S.A. Sisto, and N.A. Langrana (2008). Validation of a musculoskeletal model of wheelchair propulsion and its application to minimizing shoulder joint forces. *Journal of Biomechanics*, **41**, 2981-2988.

[3] M. de Zee, L. Hansen, C. Wong, J. Rasmussen, E.B. Simonsen, (2007). A Generic Detailed Rigid-Body Lumbar Spine Model. *Journal of Biomechanics*, **40**, 1219-1227.

[4] M. de Zee, P. Cattaneo, P. Svensson, T.K. Pedersen, B. Melsen, J. Rasmussen and M. Dalstra (2009). Prediction of the articular eminence shape in a patient with unilateral hypoplasia of the right mandibular ramus before and after distraction osteogenesis - a simulation study. *Journal of Biomechanics*, **42**, 1049-1053.

[5] A. Nolte, P. Augat and J. Rasmussen (2008). Analysis of the muscle and joint forces in the shoulder joint using the anybody simulation model. *Journal of Biomechanics*, **41**, S492.

[6] J.Z. Wu, K.-N. An, R.G. Cutlip, K. Krajnak, D. Welcome, R.G. Dong (2008). Analysis of musculoskeletal loading in an index finger during tapping. *Journal of Biomechanics*, **41**, 668-676.

[7] Catherine Manders, Andrew New, John Rasmussen (2008): Validation of Musculoskeletal Gait Simulation for use in Investigation of Total Hip Replacement. *Journal of Biomechanics*, **41**, S488

[8] T. Wehner, L. Claes, U. Simon (2009): Internal loads in the human tibia during gait. *Clinical Biomechanics*, In Press.

[9] F.C. Anderson and M.G. Pandy (2001). Static and dynamic optimization solutions for gait are practically equivalent. *Journal of Biomechanics*, **34**, 153-61.

[10] K.N. An, B.M. Kwak, E.Y. Chao and B.F. Morrey (1984). Determination of muscle and joint forces: a new technique to solve the indeterminate problem. *Journal of Biomechanical Engineering*, **106**, *364-367*.

[11] N. Olhoff, and J.E. Taylor (1983). On structural Optimization, *Journal of Applied Mechanics*, **50**, 1139-1151.

[12] de Zee, M., Dalstra, M., Cattaneo, P. M., Rasmussen, J., Svensson, P., Melsen, B., (2007). Validation of a musculo-skeletal model of the mandible and its application to mandibular distraction osteogenesis. Journal of Biomechanics 40, 1192-1201.

[13] Trainor,P.G., McLachlan,K.R., and McCall,W.D. (1995) Modelling of forces in the human masticatory system with optimization of the angulations of the joint loads. J Biomech. 28, 829-843.

[14] Iwasaki,L.R., Petsche,P.E., McCall,W.D., Jr., Marx,D., and Nickel,J.C. (2003) Neuromuscular objectives of the human masticatory apparatus during static biting. Arch.Oral Biol. 48, 767-777.

[15] Cattaneo,P.M., Kofod,T., Dalstra,M., and Melsen,B. (2005) Using the finite element method to model the biomechanics of the asymmetric mandible before, during and after skeletal correction by distraction osteogenesis. Comput.Methods Biomech.Biomed.Engin. 8, 157-165.

[16] Nikravesh, P. E. (1988). Computer-aided Analysis of Mechanical Systems. Prentice-Hall International, Inc.

[17] Andersen, M. S., Damsgaard, M., Rasmussen, J., (2009). Kinematic analysis of over-determinate biomechanical systems. Computer Methods in Biomechanics and Biomedical Engineering. 12, 371-384.

[18] Ausejo S., Suescun A., Celigueta J., Wang X. (2006). Robust human motion reconstruction in the presence of missing markers and the absence of markers for some body segments. In: Proceedings of Digital Human Modeling for Design and Engineering Conference; American Society of Automotive Engineers, Lyon, France.

[19] Boyd S., Vandenberghe L. (2004). Convex Optimization. Cambridge University Press.

[20] Andersen, M.S., Damsgaard, M., Mac-Williams, B., Rasmussen, J. (2009). A computationally efficient optimisation-based method for parameter identification of kinematically determinate and over-determinate biomechanical systems. Computer Methods in Biomechanics and Biomedical Engineering (accepted).

[21] Rasmussen, J., Damsgaard, M. Voigt, M. (2001), Muscle Recruitment by the min/max Criterion: A Comparative Numerical Study, Journal of Biomechanics, 34, 409-415.

[22] de Zee, M., Cattaneo, P., Svensson, P., Pedersen, T.K., Melsen, B., Rasmussen, J., Dalstra, M. (2009), Prediction of the articular eminence shape in a patient with unilateral hypoplasia of the right mandibular ramus before and after distraction osteogenesis - a simulation study. Journal of Biomechanics, 42, 1049-1053.

Topology optimization, dynamical systems, thermodynamics and growth

Anders Klarbring

Division of Mechanics
Institute of Technology, Linköping University, Linköping, Sweden
e–mail: anders.klarbring@liu.se

Summary   This note continues an investigation of the dynamical systems approach to the SIMP formulation of topology optimization. Three different views on the classical optimality criteria updating formula are given. It is also indicate how a Lyapunov property of the dynamical system relates to thermodynamics, which in turn leads to a topology design strategy that involves inflow of "biochemical" energy, or "nutrients", and which is closely related to growth or remodeling processes.

Introduction

Recently, in [1] and [2], we investigated the use of a dynamical systems approach to the SIMP formulation of topology optimization. Simply put, this approach to optimization means that we solve

$$\min_x f(x) \tag{1}$$

by defining a dynamical system that delivers $x = x(t)$, t being a time-like variable, such that

$$\frac{d}{dt} f(x(t)) \leq 0, \tag{2}$$

for all evolutions of the system. The property (2) holds if $f(x)$ is a Lyapunov function of the dynamical system. Many dynamical systems of this type, like

$$\frac{dx(t)}{dt} = -\nabla f(x),$$

will have the property that their equilibrium points coincide with the stationary points of (1), and in a region of space where $f(x)$ is convex the dynamical system will arrive at these points when integrated.

A first theoretical result of this approach was that the classical optimality criteria formula of structural optimization, see [3] or [4], could be seen as resulting from an explicit time discretization of a certain dynamical system. The derivation leading up to this conclusion is presented here together with two previous views on this formula: fixed point iterations and sequential convex approximations.

Furthermore, an interesting analogy connected with (2) is studied in this note: inequalities of this type (albeit, usually having a right hand side) appear also in thermodynamics under the name dissipation inequality. Gurtin [5] states the following interpretation of a general dissipation inequality: "*the rate at which the free energy increases cannot exceed the sum of working and the energy inflow due to mass transport*". This means that dynamical systems with the property (2), or generalizations of it, could be constructed following well established techniques developed in non-smooth thermodynamics, see [6]. This is exemplified in the following. The observation also produces the idea that structural design strategies can be developed from the property (2), instead

of using the pure optimization view based on (1). In fact, such an idea may have a close connection to traditional engineering thinking, where improvement and not necessarily the actual optimum is central. In the last section of this note, a dynamical system that represents a design strategy is modeled on the basis of a dissipation inequality, without stating an optimization problem. It concerns topology design where the design changes are effected by the available "biochemical" energy. It is inspired by the fact that the SIMP formulation is very close to a model for bone remodeling (or growth), see [1] and [2].

The SIMP model for stiffness optimization

The quasi-static equilibrium equation for linear discrete structures, where the stiffness depends on design variables, reads

$$\boldsymbol{F} = \boldsymbol{K}(\boldsymbol{\rho})\boldsymbol{u}. \tag{3}$$

Here $\boldsymbol{u}$ is the vector of nodal displacements and $\boldsymbol{F}$ is the corresponding force vector. The symmetric positive semi-definite stiffness matrix $\boldsymbol{K}(\boldsymbol{\rho})$ depends on a vector $\boldsymbol{\rho} = (\rho_1, \ldots, \rho_E)^T$ of design variables in the following way:

$$\boldsymbol{K}(\boldsymbol{\rho}) = \sum_{i=1}^{E} \rho_i^q \tilde{\boldsymbol{K}}_i \tag{4}$$

where E is the number of elements in the structure and $\tilde{\boldsymbol{K}}_i$ is an element stiffness matrix for a unit value of the design variable ρ_i. In topology optimization we seek methods that returns values (close to) 0 or 1 for ρ_i, and these values are interpreted as presence of material or holes in the structure. In the SIMP method this is achieved by letting the design variables be restricted to the set

$$K = \{\boldsymbol{\rho} \mid \epsilon \le \rho_i \le 1, \; i = 1, \ldots, E\}$$

and by letting the penalty parameter $q > 1$ (in practise, say, $q = 3$). Here, $\epsilon > 0$ is a small value that, by being non-zero, has the effect of making $\boldsymbol{K}(\boldsymbol{\rho})$ non-singular for all $\boldsymbol{\rho} \in K$.

The efficiency or goal function f generally depends on both displacements and design variables, i.e., $f = f(\boldsymbol{u}, \boldsymbol{\rho})$. We can base an optimization problem on the objective function

$$f_\mu = f_\mu(\boldsymbol{u}, \boldsymbol{\rho}) = f(\boldsymbol{u}, \boldsymbol{\rho}) + \mu \sum_{i=1}^{E} a_i \rho_i$$

where the second term represents the total mass or volume of the material, or possibly, depending on the nature of the a_i:s, a more general cost. The positive parameter μ regulates the relative importance of the two terms in f_μ. For a general function f we consider the following nested optimization problem:

$$\min_{\boldsymbol{\rho} \in K} \tilde{f}_\mu(\boldsymbol{\rho}), \tag{5}$$

where $\tilde{f}_\mu(\boldsymbol{\rho}) = f_\mu(\boldsymbol{u}(\boldsymbol{\rho}), \boldsymbol{\rho})$ and $\boldsymbol{u} = \boldsymbol{u}(\boldsymbol{\rho}) = \boldsymbol{K}(\boldsymbol{\rho})^{-1}\boldsymbol{F}$. When f is chosen as the compliance, problem (5) becomes

$$(\mathcal{C}) \quad \min_{\boldsymbol{\rho} \in K} f_C(\boldsymbol{\rho}) \quad \text{where} \;\; f_C(\boldsymbol{\rho}) = \frac{1}{2}\boldsymbol{F}^T \boldsymbol{u}(\boldsymbol{\rho}) + \mu \sum_{i=1}^{E} a_i \rho_i.$$

In the following we will need sensitivities of the objective function of $(\mathcal{C})$. Using (3) and (4) we find that

$$\frac{\partial f_C(\boldsymbol{\rho})}{\partial \rho_i} = \mu a_i - e_i(\boldsymbol{\rho}), \tag{6}$$

where

$$e_i(\boldsymbol{\rho}) = q\rho_i^{(q-1)}\frac{1}{2}\boldsymbol{u}^T\tilde{\boldsymbol{K}}_i\boldsymbol{u} \quad \text{and} \quad \boldsymbol{u} = \boldsymbol{u}(\boldsymbol{\rho}) = \boldsymbol{K}(\boldsymbol{\rho})^{-1}\boldsymbol{F}.$$

Three views on the optimality criteria (OC) formula

The traditional view of the optimality criteria (OC) formula (or method) is that it is an iteration rule for satisfying the optimality conditions of a structural optimization problem, see, e.g., [3]. However, another, lesser known, view is possible: it can be seen as a sequential convex approximation method where the approximation is obtained by linearizing in a certain intervening variable, in the same manner as in the CONLIN and MMA algorithms. This was explained for stiffness optimization in lecture notes by Joakim Petersson in 2000 and presented in the text book [4]. The equivalence is also shown in a more general setting in [7]. Recently a third view on the OC method was presented in [1] and [2]. It was shown that the OC method can be seen as resulting from an explicit time discretization of a certain dynamical system or ordinary differential equation. The objective function of the optimization problem is a Lyaponov function of this ODE. These three views on the OC formula will be shortly presented in the following.

Fixed point iteration

The optimality conditions for problem $(\mathcal{C})$ can be written as

$$0 \in \mu a_i - e_i(\boldsymbol{\rho}) + \partial I_{K_i}(\rho_i). \tag{7}$$

The last term in this expression is a subdifferential of an indicator function of the set $K_i = \{\rho_i \mid \epsilon \leq \rho_i \leq 1\}$. A fixed point iteration that should converge to a value of $\boldsymbol{\rho}$ that satisfies (7) is to first calculate

$$\hat{\rho}_i = \left(\frac{e_i(\boldsymbol{\rho}^n)}{\mu a_i}\right)^\eta \rho_i^n, \tag{8}$$

and then to put $\rho_i^{n+1} = \hat{\rho}_i$ if $\epsilon \leq \rho_i \leq 1$ and otherwise letting ρ_i^{n+1} be ϵ or 1 depending on which inequality is violated. The constant η is known as a damping coefficient.

Sequential convex approximation

We formulate an approximation of $(\mathcal{C})$ by linearizing the first term of f_C in the intervening variables $\rho_i^{-\alpha}$, $\alpha > 0$. If the linearization is made at the point $\boldsymbol{\rho}^n$ we obtain

$$f_C(\boldsymbol{\rho}) \approx \text{const.} + \sum_{i=1}^{E}\left[e_i(\boldsymbol{\rho}^n)\alpha^{-1}(\rho_i^n)^{1+\alpha}\rho_i^{-\alpha} + \mu a_i\rho_i\right]. \tag{9}$$

This approximation is separable and minimization can be performed one variable at a time. Assuming that the minimum is taken strictly inside the interval $\epsilon \leq \rho_i \leq 1$, we find a stationary point at

$$\rho_i = \left(\frac{e_i(\boldsymbol{\rho}^n)}{\mu a_i}\right)^{\frac{1}{1+\alpha}}\rho_i^n. \tag{10}$$

If this value is outside the interval, the minimization of the approximate optimization problem is taken at the boundary of the interval. Thus, letting $\eta = 1/(1 + \alpha)$ we have regained the OC formula (8).

Dynamical systems approach

The dynamical systems approach to $(\mathcal{C})$ consists in viewing the design $\boldsymbol{\rho}$ as evolving with a time-like variable t, i.e., $\boldsymbol{\rho} = \boldsymbol{\rho}(t)$, and defining a dynamical system such that

$$\frac{d}{dt} f_C(\boldsymbol{\rho}(t)) \leq 0. \tag{11}$$

Thus, we construct a system that has the objective function as Lyapunov function. There are many systems that meet the inequality (11), but the following one turns out to be related to the OC formula: $\dot{\rho}_i = 0$ if $\rho_i = 1$ and $\partial f_C / \partial \rho_i < 0$ or $\rho_i = \epsilon$ and $\partial f_C / \partial \rho_i > 0$, and otherwise

$$\mu a_i \dot{\rho}_i = -\lambda \rho_i \frac{\partial f_C(\boldsymbol{\rho})}{\partial \rho_i} = \lambda \rho_i (e_i(\boldsymbol{\rho}) - \mu a_i), \tag{12}$$

where a superposed dot indicates a time derivative and λ is a positive constant that has a physical dimension and also represents different time scales. By making a time discretization of (12) the relation to (8) or (10) becomes evident: We first rewrite (12) as

$$\frac{d}{dt} \ln \rho_i = \lambda \left(\frac{e_i(\boldsymbol{\rho})}{\mu a_i} - 1 \right). \tag{13}$$

Given a solution $\boldsymbol{\rho}(t)$ at time t, we like to calculate an approximation of the solution at time $t + \Delta t$. By an explicit time discretization of the left hand side of equation (13) we calculate test values $\hat{\rho}_i(t + \Delta t)$ from

$$\frac{\ln \hat{\rho}_i(t + \Delta t) - \ln \rho_i(t)}{\Delta t} = \lambda \left(\frac{e_i(\boldsymbol{\rho}(t))}{\mu a_i} - 1 \right),$$

which we rewrite, using standard formulas for logarithms, as

$$\left(\frac{\hat{\rho}_i(t + \Delta t)}{\rho_i(t)} \right)^{\frac{1}{\lambda \Delta t}} = \exp \left(\frac{e_i(\boldsymbol{\rho}(t))}{\mu a_i} - 1 \right) \approx \frac{e_i(\boldsymbol{\rho}(t))}{\mu a_i},$$

and where the approximation comes from using the first two terms in the Taylor expansion for the exponential. By letting $\eta = 1/(1 + \alpha) = \lambda \Delta t$ and by doing other appropriate identifications we obtain the OC formula (8) (or (10)).

Thermodynamic analogy

The inequality (11) is a condition that should be satisfied by all evolutions of a dynamical system. Thus, it has exactly the same role as the dissipation inequality of thermodynamics, where f_C would be a free energy. This observation implies that one could construct a dynamical system for topology optimization following the same procedure as when constructing governing equations of (non-smooth) dissipative mechanical systems, see, e.g., Frémond [6]. We develop this idea in the following and first observe that

$$\frac{d}{dt} f_C(\boldsymbol{\rho}(t)) = \sum_{i=1}^{E} \frac{\partial f_C}{\partial \rho_i} \dot{\rho}_i = -\sum_{i=1}^{E} r_i \dot{\rho}_i, \tag{14}$$

where the "thermodynamic forces" r_i satisfy

$$-r_i \in \frac{\partial f_C(\rho_i)}{\partial \rho_i} + \partial I_{K_i}(\rho_i). \tag{15}$$

The last term in this expression is a subdifferential of an indicator function of the set $K_i = \{\rho_i \mid \epsilon \leq \rho_i \leq 1\}$. This means that (15) is equivalent to

$$-r_i = \frac{\partial f_C(\rho_i)}{\partial \rho_i} + \underline{\lambda}_i + \overline{\lambda}_i, \quad \underline{\lambda}_i \geq 0, \ \epsilon \leq \rho_i, \ \underline{\lambda}_i(\epsilon - \rho_i) = 0, \quad \overline{\lambda}_i \geq 0, \ \rho_i \leq 1, \ \overline{\lambda}_i(\rho_i - 1) = 0.$$

It is easily shown, by taking the time derivative of $\underline{\lambda}_i(\epsilon - \rho_i) = 0$, that $\underline{\lambda}_i \dot{\rho}_i = 0$, and, similarly, that $\overline{\lambda}_i \dot{\rho}_i = 0$. This proves the last equality of (14). What now remains, in order to have equations that define evolutions satisfying (11), is a relation between r_i and $\dot{\rho}_i$ such that

$$\sum_{i=1}^{E} r_i \dot{\rho}_i \geq 0.$$

This inequality is satisfied for all evolutions if $r_i = k_i \dot{\rho}_i$ for some positive function k_i that could depend on $\boldsymbol{\rho}$, $\boldsymbol{c}$ and their time derivatives. Taking $k_i = \mu a_i / \lambda \rho_i$ we are back to equation (12), but other choices may also be investigated, e.g., one could think of a plasticity-type evolution of the design instead of the viscous behavior that is represented by (12).

Time dependent loads

When deciding to view optimization as a time evolution it becomes natural to consider time dependent loads. For such loads, i.e., $\boldsymbol{F} = \boldsymbol{F}(t)$, equation (3) implies that the displacement becomes an explicit function of both $\boldsymbol{\rho}$ and t, which has the implication that the first equality of (14) is replaced by

$$\frac{d}{dt} f_C(\boldsymbol{\rho}(t), t) = \dot{\boldsymbol{F}}^T \boldsymbol{u} + \sum_{i=1}^{E} \frac{\partial f_C}{\partial \rho_i} \dot{\rho}_i.$$

This means that if we define the same dynamic system as above, the inequality that it satisfies is

$$\frac{d}{dt} f_C(\boldsymbol{\rho}(t), t) \leq \dot{\boldsymbol{F}}^T \boldsymbol{u}.$$

Numerical result

Structural optimization involving several load cases is traditionally treated by using one state problem for each load case and by summing the contributions in the objective function, see [3]. However, in the present view this situation could also be treated by having a time varying load where the load cases act one at a time in an oscillating manner. In the left hand picture of Figure 1 two corner loads are shown. In the middle picture we show the design after having changed which load is active ten times back and forth, and in the right hand picture the traditional solution is shown. The oscillation of the load has to be fast compared to the evolution of the design in order to achieve what could be regarded as a converged state. It is also likely that a very quick change of load will result in a design that coincide with a traditional solution where both loads are simultaneously present.

Optimization and inflow of nutrients

In the previous sections evolutions towards optimally stiff structures are driven by a balance between the mechanical state of the structure and the cost of material. However, there is no consideration regarding how energy needed for "building" is transported to the structure. In a biological
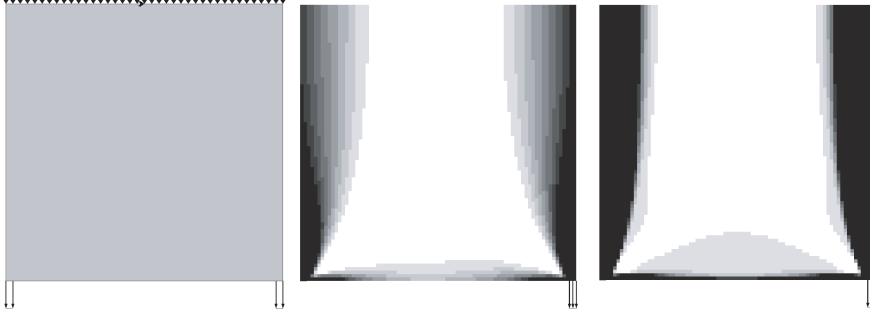
Figure 1: The left hand picture shows the definition of the problem. The middle picture is when the load is oscillating and the right hand picture is a traditional solution with two load cases. The SIMP exponent is set to one ($q = 1$) in order to avoid having a not well-posed continuum problem.

structure such energy is in the form of "biochemical" energy, or "nutrients" and we take inspiration from theories for biological growth, see [8], to extend our previous thermodynamic view of topology optimization in this direction. Part of the motivation for this section also comes from the fact that the SIMP model is very close to what has been used in bone remodeling theories, see [1] and [2].

Continuing along the lines of a discrete (or discretized) setting we introduce a vector $\boldsymbol{c} = (c_1, \ldots, c_N)^T$, representing nodal values of nutrient concentration. The number of nodes in the structure is N. Next, we assume that the "free energy", i.e., the objective function, depends on this concentration in an additative manner, so the extended objective function is

$$f_C^e(\boldsymbol{\rho}, \boldsymbol{c}) = f_C(\boldsymbol{\rho}) + \psi(\boldsymbol{c}).$$

The flow of nutrients satisfies the balance equation

$$\dot{\boldsymbol{c}} + \boldsymbol{B}^T \boldsymbol{h} = \boldsymbol{m} - \beta \boldsymbol{N} \dot{\boldsymbol{\rho}} \quad \Longleftrightarrow \quad \dot{c}_k + \boldsymbol{B}_k^T \boldsymbol{h} = m_k - \beta \sum_{i=1}^{E} N_{ki} \dot{\rho}_i, \qquad (16)$$

where $\boldsymbol{B}$ and $\boldsymbol{N}$ are constructed from the FE shape functions, and the transpose of the former is the discrete divergence operator; $\boldsymbol{m} = (m_1, \ldots, m_N)^T$ is the nodal inflow of nutrients and $\boldsymbol{h}$ is the nutrient flow vector; $\boldsymbol{B}_k$ is row k of $\boldsymbol{B}$ and N_{ki} is an element of $\boldsymbol{N}$. The constant β represents the relation between nutrient and material.

The evolution equations (dynamical system) should now satisfy the following dissipation inequality:

$$\frac{d}{dt} f_C^e(\boldsymbol{\rho}, \boldsymbol{c}) \leq \sum_{k=1}^{N} \tilde{\mu}_k m_k, \qquad (17)$$

where $\tilde{\mu}_k$ is a chemical potential that is such that the right hand side of the inequality represents the inflow of energy.

Eliminating m_k between (16) and (17) we find

$$\sum_{i=1}^{E} \left(\frac{\partial f_C(\boldsymbol{\rho})}{\partial \rho_i} - \beta \sum_{k=1}^{N} \tilde{\mu}_k N_{ki} \right) \dot{\rho}_i + \sum_{k=1}^{N} \left(\frac{\partial \psi(\boldsymbol{c})}{\partial c_k} - \tilde{\mu}_k \right) \dot{c}_k - (\boldsymbol{B} \tilde{\boldsymbol{\mu}})^T \boldsymbol{h} \leq 0, \qquad (18)$$

where $\tilde{\boldsymbol{\mu}}$ is a vector of chemical potentials. This inequality should hold for all evolutions of the system. If one assumes that $\tilde{\mu}_k$ depends on c_k only, it is therefore necessary that

$$\tilde{\mu}_k = \frac{\partial \psi(\boldsymbol{c})}{\partial c_k}, \tag{19}$$

implying that the second term of (18) vanishes. Once this is established one also concludes that it is necessary for satisfaction of (18) that

$$\beta \sum_{k=1}^{N} \tilde{\mu}_k N_{ki} - \frac{\partial f_C(\boldsymbol{\rho})}{\partial \rho_i} - \partial I_{K_i}(\rho_i) = \tilde{k}_i \dot{\rho}_i \tag{20}$$

where $\tilde{k}_i$ is a positive function of $\boldsymbol{\rho}$, $\boldsymbol{c}$ and their time derivatives. Finally, (18) implies

$$(\boldsymbol{B}\tilde{\boldsymbol{\mu}})^T \boldsymbol{h} \geq 0.$$

This inequality can be satisfied by assuming Fick's law for diffusion of nutrients. That is, there exists a positive definite matrix $\boldsymbol{E}(\boldsymbol{\rho})$ such that

$$\boldsymbol{h} = \boldsymbol{E}(\boldsymbol{\rho})\boldsymbol{B}\tilde{\boldsymbol{\mu}}. \tag{21}$$

In the isotropic case $\boldsymbol{E}(\boldsymbol{\rho}) = \sum_{i=1}^{E} \kappa(\rho_i)\boldsymbol{I}_i$, where $\kappa(\rho_i)$ is the diffusivity and $\boldsymbol{I}_i$ are identity-like matrices, the size of which depends on the number of integration point of finite elements. In order to suggest a simple dependence on ρ_i for the diffusivity, one could think of ρ_i as being a porosity-like variable, such that the diffusivity is close to zero when $\rho_i = 1$ (solid material) and having a fixed value κ_0 when ρ_i is small. Using then the small value ϵ we could write

$$\kappa(\rho_i) = (1 - \rho_i + \epsilon)\kappa_0. \tag{22}$$

To summarize, the dynamical system for stiffness optimization including flow of nutrients is defined by (16), (19), (20), (21) and (22). If, for simplicity, we take $\psi(\boldsymbol{c})$ to be a quadratic function defined by a constant γ, so that (19) becomes $\boldsymbol{c} = \gamma\tilde{\boldsymbol{\mu}}$, a simple OC-like iteration loop for finding an equilibrium point of this system would be

For $\boldsymbol{\rho}^n$ solve and update as follows:

1. solve $\boldsymbol{F} = \boldsymbol{K}(\boldsymbol{\rho}^n)\boldsymbol{u}$ for $\boldsymbol{u}$ and calculate $e_i(\boldsymbol{\rho}^n)$;

2. solve $\boldsymbol{m} = \boldsymbol{K}_c(\boldsymbol{\rho}^n)\boldsymbol{c}$, where $\boldsymbol{K}_c(\boldsymbol{\rho}) = \gamma\boldsymbol{B}^T\boldsymbol{E}(\boldsymbol{\rho})\boldsymbol{B}$, for $\boldsymbol{c}$;

3. calculate $\hat{\rho}_i^{n+1} = \left(\dfrac{e_i(\boldsymbol{\rho}^n) + \beta\gamma \sum_{k=1}^{N} c_k N_{ki}}{\mu a_i} \right)^{\eta} \rho_i^n$, do a projection onto K_i, set $\boldsymbol{\rho}^n = \boldsymbol{\rho}^{n+1}$ and go to Step 1.

References

[1] A. Klarbring and B. Torstenfelt. ODE Approach to Topology Optimization. *8th World Congress on Structural and Multidisciplinary Optimization*. June 1-5, 2009, Lisbon, Portugal, 1148

[2] A. Klarbring and B. Torstenfelt. Dynamical Systems and Topology Optimization. *submitted*.

[3] M.P. Bendsøe and O. Sigmund. *Topology optimization: theory, methods and applications*. Springer, Berlin (2003).

[4] P.W. Christensen and A. Klarbring. *An Introduction to Structural Optimization*. Springer (2009).

[5] M.E. Gurtin. Generalized Ginzburg-Landau and Cahn-Hilliard equations based on a microforce balance. *Physica D*, **92**, 178-192, (1996).

[6] M. Frémond. *Non-Smooth Thermomechanics*. Springer, Berlin, (2002).

[7] A.A. Groenwold and L.F.P. Etman. On the equivalence of optimality criterion and sequential approximate optimization methods in the classical topology layout problem. *International Journal for Numerical Methods in Engineering*, **73**(3), 297-316, (2008).

[8] D. Ambrosi and A. Guillou. Growth and dissipation in biological tissues. *Continuum Mechanics and Thermodynamics*, **19**(5), 245-251, (2007).

Eigenvalue sensitivity analysis and optimization in structural design problems

Erik Lund[*] **and Henrik Møller**

Department of Mechanical Engineering
Aalborg University, Aalborg, Denmark
e–mail: el@me.aau.dk

Summary The paper focuses on gradient based multi-material topology optimization of laminated composite structures with the objective of maximizing the lowest eigenfrequency or the buckling load factor. Details about efficient adjoint design sensitivity analysis of buckling load problems are emphasized.

Preface

This paper is dedicated to Professor Niels Olhoff who has been our inspiring friend and mentor in the field of structural optimization. The paper deals with some of the topics where Niels has been a leading researcher in the international community of structural optimization, that is, topology optimization and optimization of eigenvalue problems.

Introduction

The use of laminated composite structures with Glass and Carbon Fiber Reinforced Polymers (GFRP and CFRP) is popular for lightweight constructions due to their superior strength and stiffness characteristics. In order to fully exploit the weight saving potential of these multilayered structures, it is necessary to tailor the laminate layup and behavior to the given structural needs. In some design situations it is most cost effective to combine several different materials, such that a multi-material design problem is considered. An example of such a design problem is wind turbine blades where sandwich structures are used in many parts of the structure, and where many different materials are combined, for example GFRP, CFRP, birch wood, wood-carbon/epoxy, balsa wood, and different foam materials. In order to obtain a cost effective design, it is desirable to have a general computer aided tool that can generate a high performance topology in the initial design phase, and in this paper focus is on structural eigenvalue design optimization.

The design problem investigated in this work consists of optimal distribution of different materials in multi-layered composite shell structures, and the criteria functions considered are the lowest eigenfrequency of the structure or the lowest buckling load factor of the compressively loaded composite structure.

The finite element method is used for determining the structural response of the laminated composite. The laminated composite is typically composed of multiple materials and multiple layers, and the laminated shell structures may, in general, be curved or doubly-curved. The materials used in this work may be fiber reinforced polymers oriented at a given angle θ_k for layer k or it may be softer isotropic core materials. All materials are assumed to behave linearly elastic and the structural behavior of the laminate is described using an equivalent single layer theory.

The discrete material optimization approach

The design parametrization method applied is denoted Discrete Material Optimization (DMO), see [1], [2] and [3]. The basic idea in the DMO approach is to formulate an optimization problem using a parametrization that allows for efficient gradient based optimization on real-life problems while

reducing the risk of obtaining a local optimum solution when solving the discrete material distribution problem. The approach is related to the mixed materials strategy suggested by Sigmund and co-workers [4, 5] for multi-phase topology optimization, where the total material stiffness is computed as a weighted sum of candidate materials. By introducing differentiable weighting functions for the material interpolation, the topology optimization problem is converted to a continuous problem that can be solved using standard gradient based optimization techniques.

As in topology optimization the parametrization of the DMO formulation is invoked at the finite element level. The element constitutive matrix, $\mathbf{C}^e$, for a single layered laminate structure may in general be expressed as a sum over the element number of candidate material configurations, n^e:

$$\mathbf{C}^e \;=\; \sum_{i=1}^{n^e} w_i \mathbf{C}_i \;=\; w_1 \mathbf{C}_1 + w_2 \mathbf{C}_2 + \cdots + w_{n^e} \mathbf{C}_{n^e}, \quad 0 \le w_i \le 1 \tag{1}$$

where each candidate material is characterized by a constitutive matrix $\mathbf{C}_i$. The interpolation of mass density ρ is done in a similar way. The weight functions w_i must all have values between 0 and 1 in order to be physically allowable. Furthermore, in case of solving eigenvalue problems or having a mass constraint as in the optimization problems studied here, it is necessary that the sum of the weight functions is 1.0, i.e., $\sum_{i=1}^{n^e} w_i = 1.0$. If this demand is not fulfilled, incorrect mass densities will be obtained. Several new parametrization schemes have been developed, see details in [6, 1], and we give here a short outline of the most effective implementation. We apply for each element (or design domain in terms of a patch of finite elements) a number of design variables x_i^e, $i = 1, \ldots, n^e$, and write

$$w_i = \frac{\hat{w}_i}{\sum_{k=1}^{n^e} \hat{w}_k}, \quad i = 1, \ldots, n^e, \quad \text{where} \quad \hat{w}_i = (x_i^e)^p \prod_{j=1; \, j \neq i}^{n^e} \left(1 - (x_j^e)^p\right) \tag{2}$$

To push the design variables x_i^e towards 0 and 1 the SIMP method known from topology optimization has been adopted by introducing the power, p, as a penalization of intermediate values of x_i^e. The power p is typically set to 1 or 2 in the beginning of the optimization process and then increased by 1 for every 10 design iterations until p is 3 or 4.

Maximum lowest eigenfrequency / buckling load factor

The objective of the design problem considered is to maximize the lowest eigenfrequency or to maximize the linearized buckling load factor of the laminated composite structure. The free vibration analysis problem can be written as

$$(\mathbf{K} - \lambda_j \mathbf{M}) \, \mathbf{\Phi}_j = \mathbf{0}, \quad \lambda_j = \omega_j^2, \; j = 1, 2, \ldots \tag{3}$$

where $\mathbf{K}$ is the global stiffness matrix, $\mathbf{M}$ the global mass matrix, λ_j the eigenvalue, ω_j the eigenfrequency, and $\mathbf{\Phi}_j$ the corresponding eigenvector. The eigenvalues are assumed ordered by magnitude, such that λ_1 is the lowest eigenvalue.

In case of buckling load optimization, the starting point is to solve the static equilibrium equation

$$\mathbf{Ku} \;=\; \mathbf{p} \qquad \text{or written in residual form} \qquad \mathbf{r}(\mathbf{u}, \mathbf{x}) \;=\; \mathbf{Ku} - \mathbf{p} \;=\; \mathbf{0} \tag{4}$$

where $\mathbf{u}$ is the global displacement vector, $\mathbf{p}$ the global load vector, and $\mathbf{r}$ is the residual vector. Based on the displacement field the stress stiffening effects due to the mechanical loading can be

evaluated by computing the initial global stress stiffness matrix $\mathbf{K}_\sigma$ (also termed the geometric stiffness matrix), and the linearized buckling problem can be established as

$$\left(\mathbf{K} + \lambda_j \mathbf{K}_\sigma\right) \mathbf{\Phi}_j = \mathbf{0}, \quad j = 1, 2, \ldots \tag{5}$$

where the eigenvalues are assumed ordered by magnitude, such that λ_1 is the lowest eigenvalue, i.e., buckling load factor, and $\mathbf{\Phi}_1$ is the corresponding eigenvector.

It is a well known fact that the design sensitivity analysis of eigenvalues is problematic in the case of multiple eigenvalues, i.e., the case where two or more eigenvalues attain exactly the same value. In this case, the eigenvalues are no longer differentiable functions of the design in the normal Fréchet sense. In the following it is described how expressions for design sensitivity analysis (DSA) of both simple (distinct) and multiple (repeated) eigenvalues can be obtained.

Design sensitivity analysis of simple eigenvalues

The direct approach to obtain the eigenfrequency sensitivity is to differentiate (3) with respect to a design variable x_i, premultiply by $\mathbf{\Phi}_j^T$, make use of (3), and noting that the system matrices are symmetric, then the following expression is obtained for the eigenvalue sensitivity in case of a simple, i.e. distinct, eigenvalue λ_j, see, e.g., [7] and [8]

$$\frac{d\lambda_j}{dx_i} = \mathbf{\Phi}_j^T \left(\frac{d\mathbf{K}}{dx_i} - \lambda_j \frac{d\mathbf{M}}{dx_i} \right) \mathbf{\Phi}_j \tag{6}$$

where it is assumed that the eigenvectors have been $\mathbf{M}$-orthonormalized, such that $\mathbf{\Phi}_j^T \mathbf{M} \mathbf{\Phi}_j = 1$.

For the DMO parametrization proposed in this work the geometry is fixed and only the material is changed. Therefore the derivatives $\frac{d\mathbf{K}(x_i)}{dx_i}$ and $\frac{d\mathbf{M}(x_i)}{dx_i}$ only involve the derivative of the element constitute matrix $\mathbf{C}^e$ and the mass density ρ with respect to x_i. Thus, the derivative of the weight functions defined in (2) must be computed which is done analytically. Note that in a finite element implementation, all of these computations are performed on the element level, such that derivatives are only computed for elements depending on the given design variable x_i.

In a similar way the design sensitivity of a distinct buckling load factor is given as

$$\frac{d\lambda_j}{dx_i} = \mathbf{\Phi}_j^T \left(\frac{d\mathbf{K}}{dx_i} + \lambda_j \frac{d\mathbf{K}_\sigma}{dx_i} \right) \mathbf{\Phi}_j \tag{7}$$

where the eigenvectors have been $\mathbf{K}_\sigma$-orthonormalized, such that $\mathbf{\Phi}_j^T(-\mathbf{K}_\sigma)\mathbf{\Phi}_j = 1$.

The first of the derivatives $\frac{d\mathbf{K}(x_i)}{dx_i}$ is computed in the same way as when performing eigenfrequency sensitivity analysis. The second term $\frac{d\mathbf{K}_\sigma(x_i)}{dx_i}$ in (7) is a little more complicated because of the implicit dependence of the state variables $\mathbf{u}$, i.e. $\mathbf{K}_\sigma(x_i, \mathbf{u}(x_i))$. In case of using modern stabilized shell finite elements this analytical derivative is not straightforward to derive. Instead a direct numerical approach can be used to evaluate the term using finite differences, such that we approximate the derivative using, for example, a forward difference expression

$$\frac{d\mathbf{K}_\sigma(x_i, \mathbf{u}(x_i))}{dx_i} \approx \frac{\mathbf{K}_\sigma(x_i + \Delta x_i, \mathbf{u}(x_i) + \frac{d\mathbf{u}}{dx_i}\Delta x_i) - \mathbf{K}_\sigma(x_i, \mathbf{u}(x_i))}{\Delta x_i} \tag{8}$$

Note that the term $\frac{d\mathbf{u}}{dx_i}$ is the sensitivity of the state variables w.r.t. the design variable x_i. Thus, the displacement sensitivities $d\mathbf{u}/dx_i$ must be computed which is done efficiently using the direct

differentiation approach, i.e., the static equilibrium equation, (4), is differentiated with respect to a design variable x_i

$$\mathbf{K}\frac{d\mathbf{u}}{dx_i} = \frac{\partial\mathbf{p}}{\partial x_i} - \frac{\partial\mathbf{K}}{\partial x_i}\mathbf{u} \qquad \text{or written in residual form} \qquad \frac{\partial\mathbf{r}}{\partial\mathbf{u}}\frac{d\mathbf{u}}{dx_i} = -\frac{\partial\mathbf{r}}{\partial x_i} \qquad (9)$$

where the load sensitivity $\partial\mathbf{p}/\partial x_i$ is zero for the DMO material design variables used, unless volume forces are considered. Here it is worth noting that the sensitivity of the state variables is easily obtained analytically with the described design parametrization.

This direct approach is computationally demanding for the DMO approach as this parametrization yields many design variables. First it is necessary with a sensitivity solve for the state variables for each design variable, see (9). The time consumption for this is reasonable, since the pseudo load vector is sparse and thus the most time consuming part of the procedure is the back substitution into the already factored stiffness matrix. Notice, however, that the state variable sensitivity is a vector described over all the elements, so in order to get the buckling load sensitivity using the numerical approach, see (8), it is necessary to loop all the elements in the model for each of the design variables x_i. The time complexity of this task is $\mathcal{O}(n_e \cdot n_{dv})$ where n_e is the number of elements and n_{dv} is the total number of design variables.

In order to obtain a computationally more efficient approach in case of many design variables an adjoint approach is used. The approach is similar to the work presented in [9] and [10] but is nevertheless described here for completeness.

Applying the chain rule we have

$$\frac{d\mathbf{K}_\sigma(x_i, \mathbf{u}(x_i))}{dx_i} = \frac{\partial\mathbf{K}_\sigma(x_i, \mathbf{u})}{\partial x_i} + \frac{\partial\mathbf{K}_\sigma(x_i, \mathbf{u})}{\partial\mathbf{u}}\frac{d\mathbf{u}}{dx_i} \qquad (10)$$

Again, the first term is the partial derivative of $\mathbf{K}_\sigma$ and this term is computed on the element level in the same way as described in eigenfrequency sensitivity analysis for the term $\frac{d\mathbf{K}(x_i)}{dx_i}$. For reasons of computational efficiency the computation of these two terms are joined in our FE implementation.

The second term of (10) involving $\partial\mathbf{K}_\sigma/\partial\mathbf{u}$ is the difficult and costly part to compute and still requires evaluation of state variable sensitivities for all design variables. To make further progress, note that we are not *really* interested in computing the term, but instead it is to be pre- and post-multiplied with some eigenvectors in (7), i.e,

$$\mathbf{\Phi}_s^T\frac{\partial\mathbf{K}_\sigma(x_i, \mathbf{u})}{\partial\mathbf{u}}\frac{d\mathbf{u}}{dx_i}\mathbf{\Phi}_k = -\mathbf{\Phi}_s^T\frac{\partial\mathbf{K}_\sigma(x_i, \mathbf{u})}{\partial\mathbf{u}}\mathbf{\Phi}_k\frac{\partial\mathbf{r}}{\partial\mathbf{u}}^{-1}\frac{\partial\mathbf{r}}{\partial x_i} \qquad (11)$$

where the right hand side is arrived at by inserting the expression for state sensitivities $d\mathbf{u}/dx_i$ from (9) and regrouping terms exploiting symmetries. Note that the indices s and k for the eigenvectors are introduced as we later on in design sensitivity analysis of multiple eigenvalues will have different eigenvectors involved in the sensitivity expression.

It is now notational convenient to introduce the adjoint vectors $\mathbf{v}_{sk}$ given as

$$\mathbf{v}_{sk}^T = \mathbf{\Phi}_s^T\frac{\partial\mathbf{K}_\sigma(x_i, \mathbf{u})}{\partial\mathbf{u}}\mathbf{\Phi}_k\frac{\partial\mathbf{r}}{\partial\mathbf{u}}^{-1} \qquad (12)$$

Notice that $\mathbf{v}_{sk}$ is the same for all design variables, and thus only need to be computed once for each iteration in the optimization. When solving the linear systems of equations in (12) for the adjoint vectors $\mathbf{v}_{sk}$, the factored stiffness matrix $\partial \mathbf{r}/\partial \mathbf{u}$ can be reused. The term $\partial \mathbf{K}_\sigma /\partial \mathbf{u}$ is still a difficult (and costly) matrix to compute for stabilized shell finite elements, but we note that $\mathbf{K}_\sigma$ is a linear function of $\mathbf{u}$. Thus a forward difference approximation to the matrix will be numerically exact. In our implementation we compute the forward difference approximation by perturbing one element degrees of freedom (DOF) at a time and then compute $\mathbf{\Phi}_s^T (\partial \mathbf{K}_\sigma /\partial u_m) \mathbf{\Phi}_k$ at the element level. The element contributions are then summed.

By using (12) and (10) in (7) and regrouping terms, the buckling load factor sensitivity can be computed as

$$\frac{d\lambda_j}{dx_i} = \mathbf{\Phi}_j^T \frac{d\mathbf{K}}{dx_i} \mathbf{\Phi}_j + \lambda_j \left(\mathbf{\Phi}_j^T \frac{\partial \mathbf{K}_\sigma(x_i, \mathbf{u}(x_i))}{\partial x_i} \mathbf{\Phi}_j - \mathbf{v}_{jj}^T \frac{\partial \mathbf{r}}{\partial x_i} \right) \tag{13}$$

Notice that in comparison to the direct numerical approach described by (8) it is now only necessary to touch each element one time per associated design variable after $\mathbf{v}_{sk}$ has been computed, and that all computations are done on the element level.

Design sensitivity analysis of multiple eigenvalues

In case of multiple eigenvalues the corresponding eigenvectors are not unique, which complicates the sensitivity analysis and optimization due to the non-differentiability of the eigenvalues. In such situations the sensitivity analysis described in [11] and [12] is used. The result is outlined here.

When the solution of the generalized eigenvalue problem in (3) yields a N-fold multiple eigenvalue

$$\tilde{\lambda} = \lambda_j, \quad j = 1, \ldots, N \tag{14}$$

where, for convenience, the repeated eigenvalues have been numbered from 1 to N, then the computation of the sensitivities of this eigenvalue is not straight-forward. This is due to the fact that the eigenvectors $\mathbf{\Phi}_j, j = 1, \ldots, N$, of the repeated eigenvalues are not unique. Thus, any linear combination of the eigenvectors will satisfy the original eigenvalue problem (3).

In the sensitivity analysis we shall use such eigenvectors $\tilde{\mathbf{\Phi}}_j$ which remain continuous with design changes, see [7] and [11]. The result of the sensitivity analysis w.r.t. a single design variable x_i in case of buckling problems is the following sub-eigenvalue problem

$$\det \left| \mathbf{\Phi}_s^T \left(\frac{d\mathbf{K}}{dx_i} + \tilde{\lambda} \frac{d\mathbf{K}_\sigma}{dx_i} \right) \mathbf{\Phi}_k - \mu \delta_{sk} \right| = 0, \quad s, k = 1, \ldots, N \tag{15}$$

This is the main equation for determining the sensitivities $\mu_j, j = 1, \ldots, N$ of the multiple eigenvalue $\tilde{\lambda}$ with respect to changes Δx_i of a single design parameter x_i.

If we consider the general case when all the design variables $x_i, i = 1, \ldots, n_{dv}$, are changed simultaneously, then we need to determine the increments $\Delta \lambda_j, j = 1, \ldots, N$, of the N-fold eigenvalue $\tilde{\lambda}$ subject to a given vector $\Delta \mathbf{x} = (\Delta x_1, \ldots, \Delta x_{n_{dv}})$ of actual increments of the design variables $x_i, i = 1, \ldots, n_{dv}$. If the *generalized gradient vectors* $\mathbf{f}_{sk}$ of dimension n_{dv} are introduced

$$\mathbf{f}_{sk} = \left(\mathbf{\Phi}_s^T \left(\frac{d\mathbf{K}}{dx_1} + \tilde{\lambda} \frac{d\mathbf{K}_\sigma}{dx_1} \right) \mathbf{\Phi}_k, \ \ldots, \ \mathbf{\Phi}_s^T \left(\frac{d\mathbf{K}}{dx_{n_{dv}}} + \tilde{\lambda} \frac{d\mathbf{K}_\sigma}{dx_{n_{dv}}} \right) \mathbf{\Phi}_k \right) \tag{16}$$

then the resulting sensitivity expression becomes

$$\det \left| \mathbf{f}_{sk}^T \mathbf{\Delta x} - \delta_{sk} \Delta \lambda \right| = 0, \quad s, k = 1, \dots, N \tag{17}$$

If we solve this N-th order algebraic equation for $\Delta \lambda$, we obtain the increments $\Delta \lambda = \Delta \lambda_j, j = 1, \dots, N$, of the N-fold eigenvalue corresponding to the vector $\mathbf{\Delta x}$ of actual increments of the design variables.

The efficient adjoint approach described above for a distinct eigenvalue can be applied in a similar fashion for multiple eigenvalues. In case of an N-fold multiple eigenvalue we need to determine the adjoint vectors $\mathbf{v}_{sk}, s, k = 1, \dots, N$ given by (12), and then the terms in (16) can be determined.

It should be noted that the adjoint approach described can also be used for design sensitivity analysis of nonlinear buckling problems where the buckling load is approximated at a precritical load by an eigenvalue analysis on the deformed configuration determined using geometrically nonlinear analysis. In such cases the stiffness matrix $\mathbf{K}$ is replaced by $\mathbf{K} + \mathbf{K}_L$ where $\mathbf{K}_L$ is the displacement stiffness matrix.

The mathematical programming problem

The optimization problem of maximizing the lowest eigenfrequency ω_1 or buckling load factor λ_1 can be formulated using a bound formulation, see [13], as

$$
\begin{array}{ll}
\text{Objective :} & \max_{\mathbf{x}, \beta} \ \beta \\[1mm]
\text{Subject to :} & \lambda_j \geq \beta, \quad j = 1, \dots, N_\lambda \\
& \text{(state equations)} \\
& M \leq \overline{M} \\
& \underline{x_i} \leq x_i \leq \overline{x_i}, \ i = 1, \dots, I
\end{array}
\tag{18}
$$

where $\overline{M}$ is the upper limit on the mass M of the structure. By introducing the bound parameter β the lowest N_λ eigenvalues are considered when solving the max-min problem of maximizing the lowest eigenvalue, and the possibility of crossing eigenvalues (mode switching) and creation of multiple eigenvalues is taken into account during the optimization process. This optimization formulation can be solved directly using a gradient based algorithm in case of distinct eigenvalues, and in this work the Method of Moving Asymptotes by Svanberg [14] is used.

In case of multiple eigenvalues specialized optimization procedures like the one described in [12] and [15], see also [16] for another computational procedure, can be used.

Example: Eigenfrequency design of 16-layer clamped plate

The first example illustrate the potential of the DMO method for solving the combinatorial problem of proper choice of material, stacking sequence and fiber orientation simultaneously for maximum lowest eigenfrequency design of a clamped plate. The plate has dimension 0.1×0.1 m and consists of 16 layers of equal thickness 0.0003 m, yielding a total thickness of 0.0048 m. One candidate material is unidirectional glass/epoxy, i.e. an orthotropic material with $E_x = 5.4 \cdot 10^{10} \ Pa$, $E_y = E_z = 1.8 \cdot 10^{10} \ Pa, \nu_{xy} = \nu_{xz} = 0.25, \nu_{yz} = 0.29, G_{xy} = G_{xz} = 9.0 \cdot 10^9 \ Pa$, $G_{yz} = 3.4 \cdot 10^9 \ Pa$, and $\rho = 1900 \ kg/m^3$. The other candidate material is an isotropic polymer foam material and has $E_x = 1.25 \cdot 10^8 \ Pa, \nu = 0.3$, and $\rho = 100 \ kg/m^3$.
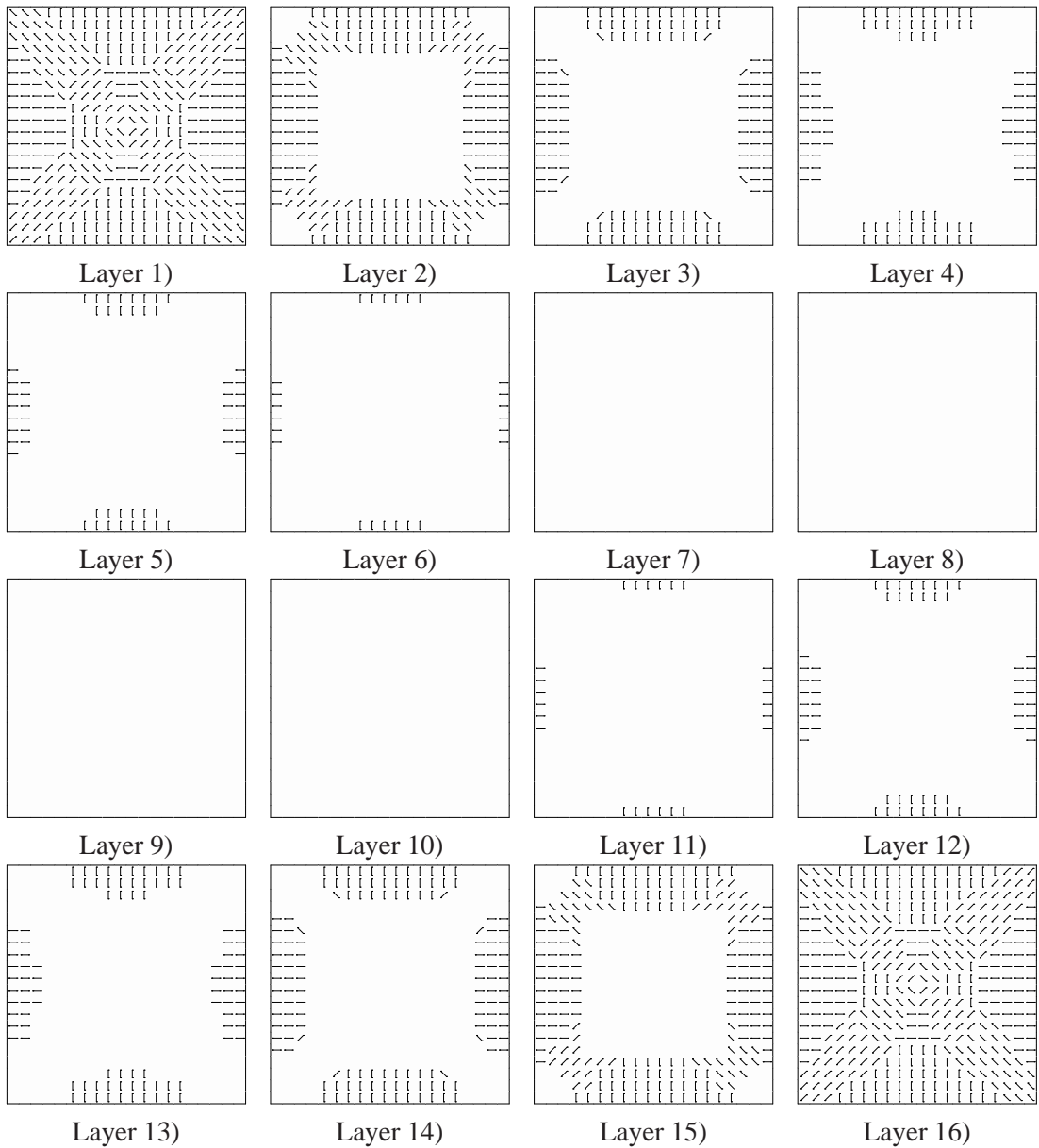
Figure 1: Optimized material directions (fiber angles) for maximum lowest eigenfrequency design of 16-layer clamped plate when 5 DMO variables per element are used (soft material together with orthotropic material oriented at $0°$, $\pm45°$, and $90°$). White means that the isotropic soft material has been selected.

The upper and lower layers have 4 DMO design variables per element associated with the orthotropic material oriented at $0°$, $\pm45°$, and $90°$, respectively, and the remaining 14 interior layers have 5 DMO variables, allowing the optimizer also to choose the soft isotropic material. The mass constraint is set such that $2/3$ of the total volume should be filled with soft material. A 20 by 20 mesh of 4-node shell elements is used, and the result of the optimization can be seen in Fig. 1.

The fiber directions for the orthotropic material in the upper and lower layers are quite similar to results published by other people for single layer plates made of unidirectional composites

using continuous fiber angles, see e.g. [17]. For the remaining 14 interior layers the DMO method suggests to put soft material in the middle of the plate as expected. Furthermore, the orthotropic material available should be put at the middle of the clamped edges, oriented perpendicular to the boundary.

Example: buckling design of trailing edge panel of wind turbine blade

The next example is related to buckling load maximization of a trailing edge panel of a generic wind turbine blade, and it is described in detail in [18]. A brief outline is given here.

Simplified model of the NACA 63_4 - 421 airfoil test section.
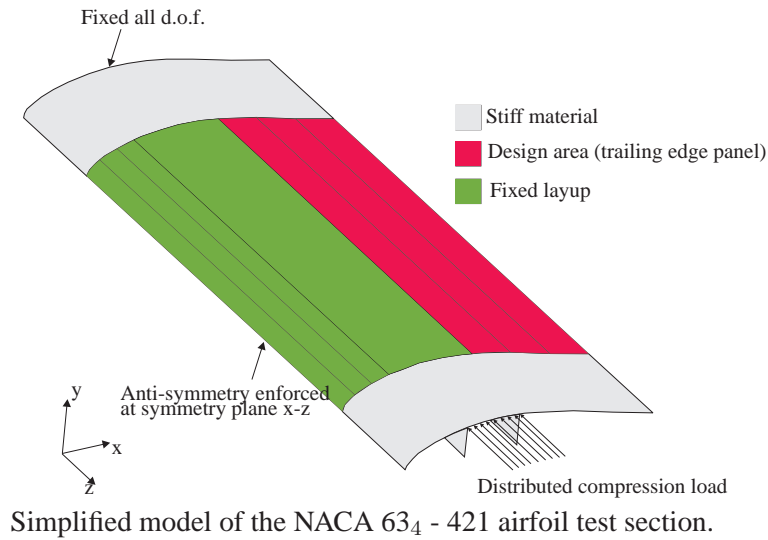
Figure 2: Simplified model of the NACA 63_4 - 421 airfoil test section. The design domain is the trailing edge panel. Antisymmetric boundary conditions are assumed.

The simplified analysis model shown in Fig. 2 is used for the example. The spar cap consists of wood-carbon/epoxy and 4 layers of $\pm 45°$ E-glass/epoxy (GFRP). The design area is the trailing edge panel which is divided into 14 patches, each having 12 layers, for DMO optimization. The candidate materials are unidirectional GFRP at $0°$ or $90°$ together with GFRP $\pm 45°$ angle-ply, and foam material. 2/3 of the design domain must be filled with foam material.

The analysis model consists of 1648 layered 9 node shell elements with up to 12 layers, and the time consumption for the analysis phase on a standard pc is as follows: the assembly of $[\mathbf{K}]$ takes 4.5 s, the factorization of $[\mathbf{K}]$ takes 0.6 s, a forward backward substitution takes 0.2 s, and the assembly of all matrices for the linearized buckling problem takes 23 s. The problem has 648 design variables and if the direct method, see (7), is used for buckling DSA of the three lowest buckling load factors, then the time consumption is 34260 s. In case of using the adjoint approach the computation of three adjoint vectors $\mathbf{v}_{sk}$, see (12) takes 1219 s and the sensitivities are computed using (13) in 1008 s, such that the total time for DSA becomes 2227 s, which is more than 15 times faster than the direct approach. In case of having a larger number of design variables, which is usually the case for DMO optimization models, the advantages of the adjoint formulation becomes even more pronounced.

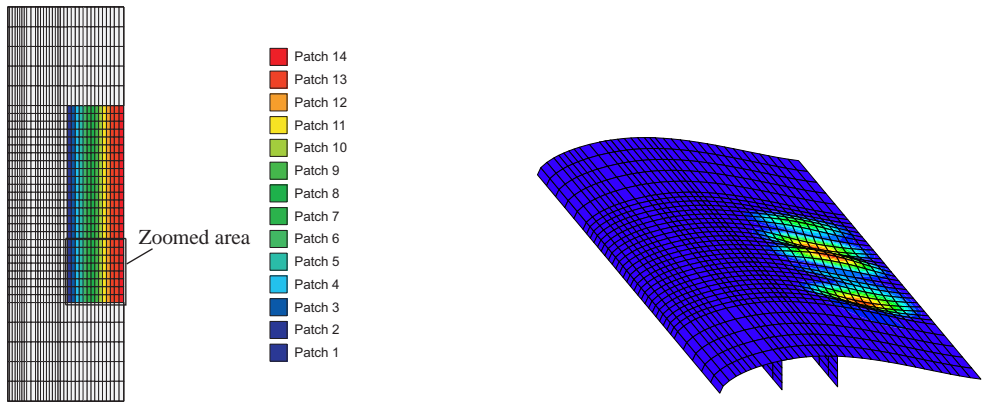The result of the optimization can be seen on Fig. 4.

Figure 3: Left: The design area (the trailing edge sandwich panel) is divided into 14 patches. Results of the topology optimization will be presented for the zoomed area. Right: Typical lowest buckling mode.
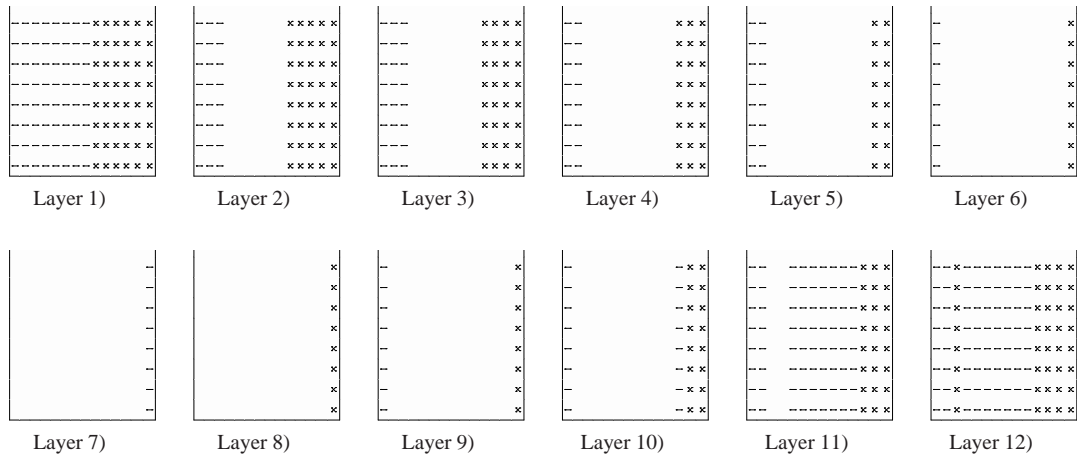

Figure 4: Case 2: Optimized material directions (fiber angles) for maximum buckling load factor design of 12-layer trailing edge panel of the test section when 4 DMO variables per patch are used (foam material together with GFRP unidirectional material oriented at $0°$ and $90°$ and GFRP $\pm 45°$ angle-ply). White means that the isotropic foam material has been selected. Layer 1 is the lower layer and layer 12 is the top (outer) layer. The results are shown for the zoomed area defined in Figure 3.

Conclusions

The Discrete Material Optimization (DMO) method for structural topology optimization of multi-material laminated composite shell structures has been presented with focus on eigenfrequency and buckling load optimization. The method makes it possible to solve the discrete problem of choosing the right material together with the fiber orientation and thickness distribution problem by introducing weighting functions, such that the total material stiffness (or density) is computed as a weighted sum of candidate materials. In this way the discrete problem is converted to a continuous problem that can be solved using gradient based optimization techniques. Efficient design sensitivity analysis of linear eigenvalue problem in the form of eigenfrequency and buckling load problems has been presented with focus on an adjoint approach for buckling load sensitivities, and two examples have illustrated the potential of the DMO approach.

References

[1] J. Stegmann and E. Lund. Discrete material optimization of general composite shell structures. *Int. Journal for Numerical Methods in Engineering*, 62(14):2009–2027, 2005.

[2] E. Lund and J. Stegmann. On structural optimization of composite shell structures using a discrete constitutive parametrization. *Wind Energy*, 8(1):109–124, 2005.

[3] E. Lund. Buckling topology optimization of laminated multi-material composite shell structures. *Composite Structures*, 91:158–167, 2009.

[4] O. Sigmund and S. Torquato. Design of materials with extreme thermal expansion using a three-phase topology optimization method. *Journal of the Mechanics and Physics of Solids*, 45:1037–1067, 1997.

[5] L.V. Gibiansky and O. Sigmund. Multiphase composites with extremal bulk modulus. *Journal of the Mechanics and Physics of Solids*, 48:461–498, 2000.

[6] J. Stegmann. *Analysis and optimization of laminated composite shell structures*. Ph.D. Thesis, Institute of Mechanical Engineering, Aalborg University, Denmark, 2004. Special report no. 54, available at www.ime.aau.dk/˜js.

[7] R. Courant and D. Hilbert. *Methods of mathematical physics*, volume 1. Interscience Publishers, New York, 1953.

[8] W.H. Wittrick. Rates of change of eigenvalues, with reference to buckling and vibration problems. *Journal of the Royal Aeronautical Society*, 66:590–591, 1962.

[9] H.C. Rodrigues, J.M. Guedes, and M.P. Bendsøe. Necessary conditions for optimal design of structures with a nonsmooth eigenvalue based criterion. *Structural Optimization*, 9:52–56, 1995.

[10] M.M. Neves, H.C. Rodrigues, and J.M. Guedes. Generalized topology design of structures with a buckling load criterion. *Structural Optimization*, 10:71–78, 1995.

[11] A.P. Seyranian, E. Lund, and N. Olhoff. Multiple eigenvalues in structural optimization problems. *Structural Optimization*, 8:207–227, 1994.

[12] E. Lund. *Finite element based design sensitivity analysis and optimization*. Ph.D. Thesis, Institute of Mechanical Engineering, Aalborg University, Denmark, 1994. Special report no. 23, available at www.ime.aau.dk/˜el.

[13] M.P. Bendsøe, N. Olhoff, and J.E. Taylor. A variational formulation for multicriteria structural optimization. *Journal of Structural Mechanics*, 11:523–544, 1983.

[14] K. Svanberg. The method of moving asymptotes - a new method for structural optimization. *Numerical Methods in Engineering*, 24:359–373, 1987.

[15] L.A. Krog and N. Olhoff. Optimum topology and reinforcement design of disk and plate structures with multiple stiffness and eigenfrequency objectives. *Computers and Structures*, 72:535–563, 1999.

[16] J. Du and N. Olhoff. Topological design of freely vibrating continuum structures for maximum values of simple and multiple eigenfrequencies and frequency gaps. *Structural and Multidisciplinary Optimization*, 34:91–110, 2007. See also Publisher's Erratum in *Structural and Multidisciplinary Optimization* (2007), **34**, pp. 545.

[17] N.L. Pedersen. On design of fiber-nets and orientation for eigenfrequency optimization of plates. *Computational Mechanics*, 39(1):1–13, 2006.

[18] E. Lund and L.S. Johansen. On buckling optimization of a wind turbine blade. In P.P. Camanho, C.G. Davila, S.T. Pinho, and J.J.C. Remmers, editors, *Mechanical Response of Composites, Computational Methods in Applied Sciences, Vol. 10*, pages 243–260. Springer Verlag, ISBN 978-1-4020-8583-3, 2008.

On Structural Topology Optimization Against Vibration and Noise

Niels Olhoff

Department of Mechanical Engineering
Aalborg University, Aalborg, Denmark
e−mail: no@me.aau.dk

Jianbin Du

School of Aerospace
Tsinghua University, Beijing, China
e−mail: dujb@tsinghua.edu.cn

Summary This paper presents a brief overview of applications of the methodology of topology optimization to passive design of elastic continuum structures against vibration and noise. The design objectives include maximization of specific eigenfrequencies and distances (gaps) between two consecutive eigenfrequencies of free structural vibrations, as well as maximization of the dynamic stiffness and minimization of the sound emission of structures subjected to forced harmonic vibrations. Results show that these design objectives enable us, in a very cost-efficient way, to move structural resonance frequencies far away from external excitation frequencies, such that high vibration and noise levels are avoided.

Introduction

The method of topology optimization of continuum structures was introduced in the literature in 1988 by the landmark paper [1] that addressed the problem of determining the distribution of an elastic material within an admissible design domain that yields the stiffest possible structure for a given static loading and prescribed volume of material. Since usual sizing and shape optimization methods generally cannot change the structural topology, the development of this method was a break-through in the field of engineering design, as the choice of the best topology generally has the most decisive impact on the gain that can be achieved by optimization. Topology optimization is therefore an important preprocessing tool for sizing and shape optimization [2].

During the last decade, the method has been extended to handle several other design objectives and constraints. Thus, topology optimization has become a standard tool for synthesis of parts or whole structures in the automotive and aerospace industries, and it is rapidly spreading into other engineering design disciplines. The reader is referred to the exhaustive textbook [3], the review article [4] and the proceedings [5] for recent developments and publications. A survey of topological design with vibration and noise emission objectives is available in [6].

1. Eigenfrequency optimization problems

Topology optimization with respect to structural eigenfrequencies of free vibrations of structures of given material volume and boundary conditions is, *a.o.*, undertaken in [7-14] and has the following significance. By optimizing with respect to the fundamental frequency [7-12,14], a minimum cost design against vibration resonance is obtained subject to all external excitation frequencies within the large range from zero and up to the particular fundamental frequency. Optimization with respect to a specific higher order eigenfrequency [7,12,14] is generally found to produce a considerable gap between this eigenfrequency and the adjacent lower eigenfrequency, and thereby offers a very competitive design for avoidance of resonance in problems where external excitation frequencies are confined within a large interval with finite lower and upper limits. However, for a band of external excitation frequencies of this type, the most efficient

design is, of course, obtained if the design objective is *directly* formulated as maximization of the difference (gap) between two consecutive eigenfrequencies of the structure, and this is done in the papers [7,13].

It is worth noting that the three kinds of problems just discussed in general require careful attention since the eigenfrequencies subject to optimization often become multiple eigenfrequencies which are not differentiable in the usual (Gateau) sense, but only directionally differentiable, a complexity that is taken into account in the analyses in [7,12,13].

1.1 Maximization of the fundamental eigenfrequency

Problems of topology design for maximization of fundamental eigenfrequencies of vibrating elastic structures without damping can be formulated as a max-min problem as follows, see e.g. [7]

$$\max_{\rho_1,\cdots,\rho_{N_E}} \{ \min_{j=1,\cdots J} \{\omega_j^2\}\} \tag{1a}$$

$$Subject\ \ to:$$

$$\mathbf{K}\boldsymbol{\varphi}_j = \omega_j^2\mathbf{M}\boldsymbol{\varphi}_j\ ,\quad j=1,\cdots,J, \tag{1b}$$

$$\boldsymbol{\varphi}_j^\mathrm{T}\mathbf{M}\boldsymbol{\varphi}_k = \delta_{jk}\ ,\qquad j\geq k,\quad k,j=1,\cdots,J, \tag{1c}$$

$$\sum_{e=1}^{N_E}\rho_eV_e - V^* \leq 0\ ,\quad V^* = \alpha V_0, \tag{1d}$$

$$0 < \underline{\rho} \leq \rho_e \leq 1\ ,\qquad e=1,\cdots,N_E. \tag{1e}$$

Here, ω_j is the *j*-th eigenfrequency and φ_j the corresponding eigenvector, and $\mathbf{K}$ and $\mathbf{M}$ are the symmetric and positive definite stiffness and mass matrices of the finite element based, generalized structural eigenvalue problem in the constraint (1b). The *J* candidate eigenfrequencies considered will all be real and can be numbered such that

$$0 < \omega_1 \leq \omega_2 \leq \cdots \leq \omega_J\ . \tag{2}$$

It is assumed that the corresponding eigenvectors are $\mathbf{M}$-orthonormalized, cf. (1c) where δ_{jk} is Kronecker's delta. In problem (1), the symbol N_E denotes the total number of finite elements in the admissible design domain. The design variables $\rho_{e,}\ e=1,\ldots,N_E$, represent the volumetric material densities of the finite elements, and (1e) specifies lower and upper limits $\underline{\rho}$ and 1 for ρ_e. To avoid singularity of the stiffness matrix, $\underline{\rho}$ is not zero, but assigned a small positive value like $\underline{\rho} = 10^{-3}$.

For single-material design problems, the symbol α in (1d) defines the volume fraction V^*/V_0, where V_0 is the volume of the admissible design domain, and V^* the given available volume of solid material. For a bi-material design problem, α defines the volume fraction of the available stiffer solid material *1, and the rest of the admissible design domain will be filled by the weaker solid material *2.

1.2 Bound formulations for maximization of the n-th eigenfrequency and the gap between two consecutive eigenfrequencies

Consider now the more general problem of maximizing the *n*-th eigenfrequency ω_n of given order of a vibrating structure, i.e., the fundamental eigenfrequency (*n*=1) or a higher order eigenfrequency (*n*>1). Employing a bound formulation (see [15,16]) involving a scalar variable β which plays both the role of an objective function to be maximized and at the same time a variable lower bound for the *n*-th and higher order eigenfrequencies (counted with possible multiplicity), the problem can be formulated as

$$\max_{\beta, \rho_1, \cdots, \rho_{N_E}} \{\beta\} \tag{3a}$$

Subject to:

$$\beta - \omega_j^2 \le 0, \qquad j = n, n+1, \cdots, J, \tag{3b}$$

Constraints: (1b-e) $\tag{3c}$

Here, as well as in problem (4) below, J is assumed to be larger than the highest order of an eigenfrequency to be considered a candidate to exchange its order with the *n*-th eigenfrequency or to coalesce with this eigenfrequency during the design process.

The problem of maximizing the gap (difference) between two consecutive eigenfrequencies of given orders *n* and *n–1* (where *n*>1) may be written in the following extended bound formulation, where two bound parameters are used,

$$\max_{\beta_1, \beta_2, \rho_1, \cdots, \rho_{N_E}} \{\beta_2 - \beta_1\} \tag{4a}$$

Subject to:

$$\beta_2 - \omega_j^2 \le 0, \qquad j = n, n+1, \cdots, J, \tag{4b}$$

$$\omega_j^2 - \beta_1 \le 0, \qquad j = 1, \cdots, n-1, \tag{4c}$$

Constraints: (1b-e). $\tag{4d}$

Note that if here we remove the bound variable β_1 and the corresponding set of constraints (4c) from the formulation, then the eigenfrequency gap maximization problem (4) reduces to the *n*-th eigenfrequency maximization problem (3), and in particular, for *n*=1, to the problem (1) of maximizing the fundamental eigenfrequency.

In problem (3) the eigenfrequency ω_n, and in problem (4) both the eigenfrequencies ω_n and ω_{n-1} of the optimum solution may very well be multiple, and the bound formulations in (3) and (4) are tailored to facilitate handling of this difficulty.

1.3 Design sensitivities of simple and multiple eigenfrequencies

If the *j*-th eigenfrequency ω_j is simple (also called unimodal or distinct), i.e., $\omega_{j-1} < \omega_j < \omega_{j+1}$, then the corresponding eigenvector $\mathbf{\varphi}_j$ will be unique (up to a sign) and differentiable with respect to the design variables ρ_e, $e = 1,\ldots,N_E$. The sensitivity (derivative) $(\lambda_j)'_{\rho_e}$ of the eigenvalue $\lambda_j = \omega_j^2$ with respect to a particular design variable ρ_e is then given by, cf. [17,18],

$$(\lambda_j)'_{\rho_e} = \mathbf{\varphi}_j^{\mathrm{T}} (\mathbf{K}'_{\rho_e} - \lambda_j \mathbf{M}'_{\rho_e}) \mathbf{\varphi}_j, \quad e = 1, \cdots, N_E \tag{5}$$

where the derivatives of the matrices $\mathbf{K}$ and $\mathbf{M}$ can be calculated numerically. If all the design variables are changed simultaneously, the linear increment $\Delta\lambda_j$ of $\lambda_j = \omega_j^2$ is given by the scalar product

$$\Delta\lambda_j = \nabla \lambda_j^{\mathrm{T}} \Delta\mathbf{\rho} \tag{6}$$

where $\Delta\mathbf{\rho} = \{\Delta\rho_1, \cdots, \Delta\rho_{N_E}\}^{\mathrm{T}}$ is the vector of small changes of the design variables, and

$$\nabla\lambda_j = \left\{ \mathbf{\varphi}_j^{\mathrm{T}} (\mathbf{K}'_{\rho_1} - \lambda_j \mathbf{M}'_{\rho_1}) \mathbf{\varphi}_j, \cdots\cdots, \mathbf{\varphi}_j^{\mathrm{T}} (\mathbf{K}'_{\rho_{N_E}} - \lambda_j \mathbf{M}'_{\rho_{N_E}}) \mathbf{\varphi}_j \right\}^{\mathrm{T}} \tag{7}$$

is the vector of sensitivities (or gradients) of the eigenvalue λ_j with respect to the design variables ρ_e, $e = 1, \ldots, N_E$.

Multiple eigenfrequencies may manifest themselves in different ways in structural optimization problems. Thus, an eigenfrequency subject to optimization may be multiple from the beginning of the design process, e.g., due to structural symmetry, but an originally unimodal (simple) eigenfrequency may also become multiple during the optimization process due to coalescence with one or more of its adjacent eigenfrequencies. In such cases, sensitivities of the multiple eigenfrequency cannot be calculated straightforwardly from (5) or (6), (7) due to lack of usual differentiability properties of the sub-space spanned by the eigenvectors associated with the multiple eigenfrequency. Sensitivity analysis of multiple eigenvalues (like eigenfrequencies or buckling loads) is dealt with in a number of papers, see e.g., [19] and papers cited therein. Following [19], the sensitivity analysis leads to the result that the increments $\Delta\lambda_j$ of an N-fold multiple eigenvalue $\tilde{\lambda}$,

$$\tilde{\lambda} = \lambda_j = \omega_j^2, \quad j = n, \cdots, n + N - 1 \tag{8}$$

associated with the N ($N > 1$) lowest eigenfrequencies ω_j appearing in the bound constraints (3b) and (4b)[*1] are eigenvalues of an N-dimensional algebraic sub-eigenvalue problem of the form

$$\det\left[\mathbf{f}_{sk}^{\mathrm{T}}\Delta\boldsymbol{\rho} - \delta_{sk}\Delta\lambda\right] = 0, \quad s, k = n, \ldots, n+N\text{-}1. \tag{9}$$

The N eigenvalues of this sub-eigenvalue problem, i.e., the increments $\Delta\lambda_j, j = n, \cdots, n + N - 1$, represent the directional derivatives of the multiple eigenvalue $\tilde{\lambda}$ in (17) with respect to small simultaneous changes $\Delta\rho_e$ (assembled in the vector $\Delta\boldsymbol{\rho}$) of the design variables $\rho_e, e=1,\cdots,N_E$. Moreover, in (9), δ_{sk} is Kronecker's delta and $\mathbf{f}_{sk}$ denote generalized gradient vectors of the form

$$\mathbf{f}_{sk} = \left\{\boldsymbol{\varphi}_s^{\mathrm{T}}(\mathbf{K}'_{\rho_1} - \tilde{\lambda}\mathbf{M}'_{\rho_1})\boldsymbol{\varphi}_k, \cdots, \boldsymbol{\varphi}_s^{\mathrm{T}}(\mathbf{K}'_{\rho_{N_E}} - \tilde{\lambda}\mathbf{M}'_{\rho_{N_E}})\boldsymbol{\varphi}_k\right\}^{\mathrm{T}}, \; s, k = n, \ldots, n+N\text{-}1. \tag{10}$$

According to the definition in (10), each $\mathbf{f}_{sk}$ is an N_E-dimensional vector, which means that $\mathbf{f}_{sk}^{\mathrm{T}}\Delta\boldsymbol{\rho}$ in (9) is a scalar product. The label 'generalized gradient vector' for $\mathbf{f}_{sk}$ becomes apparent when comparing (10) with the expression for the gradient vector $\nabla\lambda_j$ of a simple eigenvalue λ_j in (7). Note also that $\mathbf{f}_{sk} = \mathbf{f}_{ks}$ due to the symmetry of the matrices $\mathbf{K}$ and $\mathbf{M}$, and that the two subscripts s and k refer to the orthonormalized eigenmodes from which $\mathbf{f}_{sk}$ is calculated.

An efficient iterative computational procedure for solution of problems (1), (3) and (4) with simple and multiple eigenfrequencies is presented in [7]. Particular topics pertaining to the topology optimization like penalization models, filtering, and elimination of spurious eigenmodes, are also discussed in [7].

2. Examples of eigenfrequency optimization problems

As a first example [7], we consider the topology optimization of a single-material plate-like structure modeled by 8-node 3D brick elements with Wilson incompatible displacement models to improve precision. The admissible design domain is specified, and three different cases (a), (b) and (c) of boundary conditions and attached concentrated, nonstructural masses as shown and defined in Fig. 1 and its caption, are considered. The design objective is to maximize the fundamental eigenfrequency for a prescribed material volume fraction α = 50%. The material is isotropic with Young's modulus $E = 10^{11}$, Poisson's ratio υ = 0.3 and mass density γ_m = 7800 (SI units are used throughout this paper). The fundamental eigenfrequencies of the initial designs with the three

---

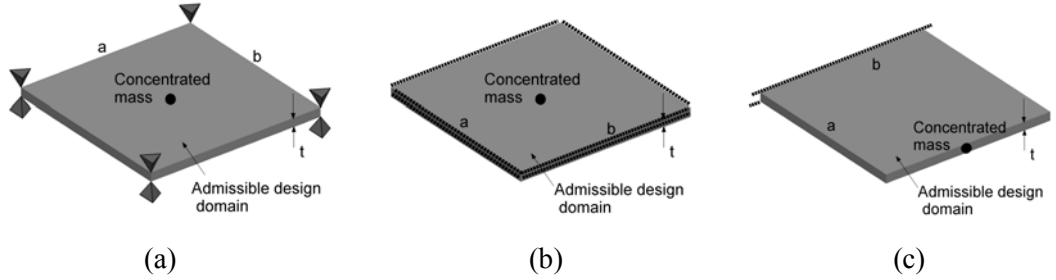[*1] Multiplicity of the largest eigenfrequency in (4c) can be treated similarly.

(a) (b) (c)

Figure 1: Plate-like 3D structure (a=0.020, b= 0.020 and t=0.001) with three different cases of boundary conditions and attachment of a concentrated nonstructural mass. (a) Simple supports at four corners and concentrated mass m_c at the center of the structure ($m_c = m_0/3$, m_0 the total structural mass of the plate). (b) Four edges clamped and concentrated mass m_c at the center ($m_c = m_0/10$). (c) One edge clamped, other edges free, and concentrated mass m_c attached at the mid-point of the edge opposite to the clamped one ($m_c = m_0/10$). The fundamental eigenfrequencies for the 3 initial designs (uniform distribution of material with density $\rho = 0.5$) are $\omega_{1a}^0 = 8.13$, $\omega_{1b}^0 = 31.07$ and $\omega_{1c}^0 = 3.46$.

(a) (b) (c)
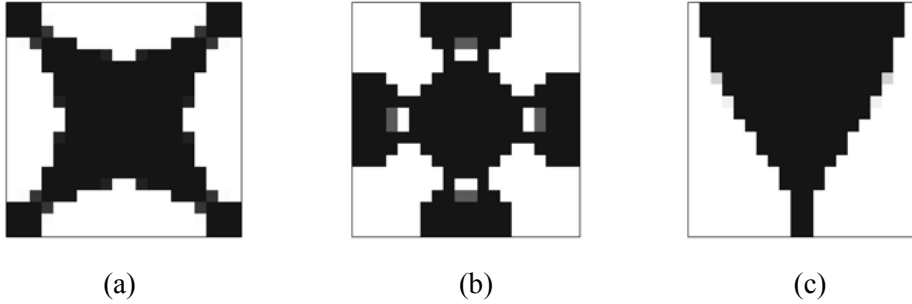
Figure 2: Optimized single-material topologies (50% volume fraction) with solid material shown in black and void in white for the three cases of boundary conditions and mass attachment in Figs.1(a-c). The optimum fundamental eigenfrequencies are found to be (a) $\omega_{1a}^{opt} = 16.38$, (b) $\omega_{1b}^{opt} = 65.42$, and (c) $\omega_{1c}^{opt} = 9.66$, i.e., they are increased by (a) 101%, (b) 111% and (c) 179% relative to the initial designs.

cases (a), (b) and (c) of boundary and mass conditions are given in the caption of Fig. 1. The optimized plate topologies are shown in Figs. 2(a-c), and the corresponding optimum fundamental eigenfrequencies are all unimodal with values given in the caption of Fig. 2.

In the next example [7], we apply topology optimization to maximize the difference (gap) between the 2nd and 3rd eigenfrequencies of two bi-material structures with the cases (a) and (c) of boundary conditions and concentrated mass attachment as shown in Fig. 1. Both of the two elastic materials used for each of the structures are isotropic. The stiffer material *1 is shown in black in Fig. 3, and has the Young's modulus $E^{*1} = 10^{11}$, Poisson's ratio $\upsilon = 0.3$ and specific mass $\gamma_m^{*1} = 7800$, while the weaker material *2 is shown in grey in Fig. 3 and has the properties $E^{*2} = 0.1E^{*1}$, $\gamma_m^{*2} = 0.1\gamma_m^{*1}$ and $\upsilon = 0.3$. We take the volume fraction of material *1 to be up to 50% of the admissible design domain and impose the condition that the remaining part of the admissible design domain is filled with material *2. The resulting optimum solutions are presented in Fig. 3.

(a)   (b)   (c)
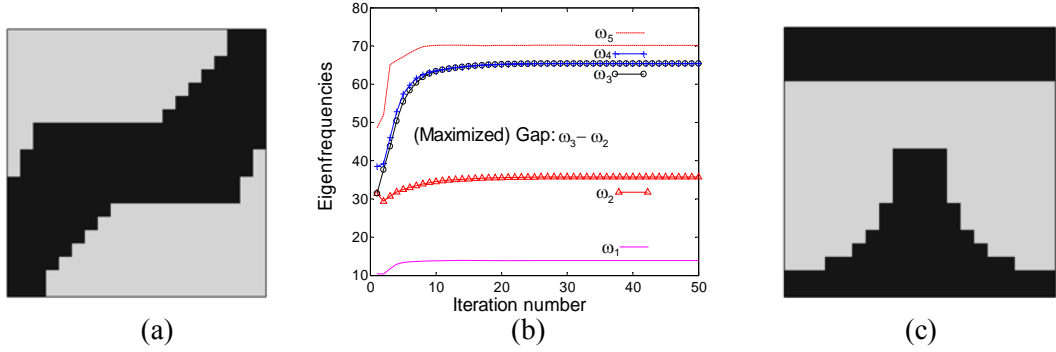
Figure 3: (a) Optimized topology of the plate-like structure with simple supports at four corners and a concentrated mass at the center, cf. Fig. 1(a). The gap between the 2nd and the 3rd eigenfrequencies is maximized. (b) Iteration histories for the first five eigenfrequencies associated with the process leading to the design (a). It shows that the second and the third eigenfrequencies form a double eigenfrequency for the initial design, but that they split as the design process proceeds, and the 3rd and the 4th eigenfrequencies end up being a double eigenfrequency of the final design. (c) Optimized topology of the plate-like structure with the upper horizontal edge clamped, other edges free, and a concentrated mass attached at the mid-point of the lower horizontal edge, cf. Fig. 1(c). The gap between the 2nd and the 3rd eigenfrequencies is maximized.

3. Minimization of the dynamic compliance of structures subjected to forced harmonic vibration

Optimization of the topology of an elastic continuum structure for minimum dynamic structural compliance has, *a.o.*, been undertaken in [20-23]. Following [23], where damping is neglected and a single external excitation frequency is assumed, the problem may be formulated as

$$\min_{\rho_e,\, e=1,\cdots,N_E} \{F = C_d^2\}$$

Subject to :

$$C_d = |\mathbf{P^T U}| \,,$$
$$(\mathbf{K} - \omega_p^2 \mathbf{M})\mathbf{U} = \mathbf{P} \,,$$
$$\sum_{e=1}^{N_E} \rho_e V_e - V^* \leq 0 \,, \qquad (V^* = \alpha V_0) \,,$$
$$0 < \underline{\rho} \leq \rho_e \leq 1 \,, \qquad (e = 1,\cdots,N_E) \,. \tag{11}$$

The symbol C_d stands for the dynamic compliance defined as $C_d = |\mathbf{P^T U}|$, where $\mathbf{P}$ denotes the vector of amplitudes of a given external time-harmonic mechanical surface loading vector $\mathbf{p}(t) = \mathbf{P}e^{i\omega_p t}$ with the prescribed excitation frequency ω_p, and $\mathbf{U}$ represents the vector of magnitudes of the corresponding structural displacement response vector $\mathbf{a}(t) = \mathbf{U}e^{i\omega_p t}$. Thus, $\mathbf{U}$ and $\mathbf{P}$ satisfy the dynamic equilibrium equation included in (11) for the steady-state vibration at the prescribed frequency ω_p. The two last constraint equations in (11) are the same as (1d,e). We note that the above expression for the dynamic compliance C_d represents the numerical mean value of the magnitudes of the surface displacement amplitudes weighted by the values of the amplitudes of the corresponding time-harmonic surface loading. For the case of static loading

360

($\omega_p = 0$), the expression directly reduces to the traditional definition of static compliance, i.e., the work done by the external forces against corresponding displacements at equilibrium.

3.1 Sensitivity analysis

The following convenient expression for the sensitivity of the objective function F in problem (11) with respect to the design variables ρ_e is obtained in [23] by usage of the adjoint method [24].

$$F' = 2(\mathbf{P}^T\mathbf{U})\left[2\mathbf{U}^T\mathbf{P}' - \mathbf{U}^T(\mathbf{K}' - \omega_p^2\mathbf{M}')\mathbf{U}\right]. \tag{12}$$

3.2 Example

We consider topology design for minimum dynamic compliance of a quadratic bi-material plate-like structure (side length 0.020, thickness 0.001) with clamped edges [23]. A time-harmonic, uniformly distributed, transverse external load $p(t) = P\cos\omega_p t$ with $P = 1$ and prescribed loading frequency ω_p is applied to the upper surface of the plate. The two materials available for the structure are the same as in the preceding example, and again the volume fraction of the stiffer material 1* is taken to be up to 50%. The plate is modeled by 3D 8-node isoparametric elements in a 40×40×1 mesh to ensure sufficient accuracy of the computational results. Six prescribed different loading frequencies, $\omega_p = 10, 100, 200, 300, 500$ and 1000 are considered, which cover the designs from lower frequency level to high frequency level. (The fundamental eigenfrequency of the initial design with a uniform mixing of the materials is $\omega_1 = 95$.) The results are shown in Fig. 4 with the stiffer and the weaker material indicated in black and grey, respectively.

For each of the optimized designs shown in Fig. 4 it is characteristic that the resonance frequencies are far from the prescribed excitation frequency ω_p, which implies efficient avoidance of resonance phenomena with large displacement amplitudes and low dynamic stiffness.

|(a) $\omega_p = 10$ | (b) $\omega_p = 100$ | (c) $\omega_p = 200$|
|(d) $\omega_p = 300$ | (e) $\omega_p = 500$ | (f) $\omega_p = 1000$|
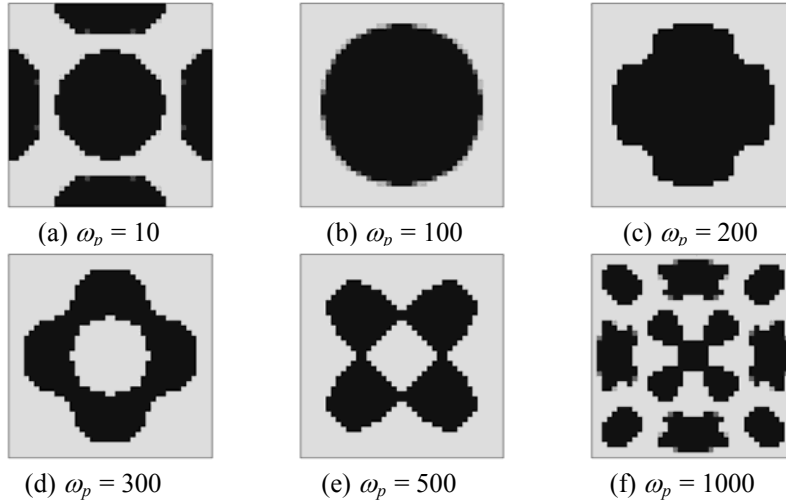
Figure 4: Topological designs of clamped, quadratic bi-material plate-like structures obtained by minimizing the dynamic compliance for six different values of the prescribed external excitation frequency ω_p.

4. Minimization of the sound radiation from a vibrating structure into an acoustic medium

In this section, we consider topological design optimization of a vibrating bi-material elastic structure with the objective of minimizing the total sound power (energy flux) $\prod$ radiated from the structural surface S into a surrounding acoustic medium. As in Section 3, the structural vibrations are assumed to be excited by an external, time-harmonic mechanical surface loading vector

$\mathbf{p}(t) = \mathbf{P}e^{-i\omega_p t}$ with prescribed excitation frequency ω_p and amplitude vector $\mathbf{P}$ on S or part thereof. Assuming that damping can be neglected, the corresponding structural displacement response vector can be stated as $\mathbf{U}e^{-i\omega_p t}$, and the problem of minimizing $\prod$ can be formulated as, cf. [25],

$$\min_{\rho_e} \left\{ \Pi = \int_S I_n dS = \int_S \frac{1}{2} \mathrm{Re}(p_f v_n^*) dS \right\}$$

subject to :

$$(\mathbf{K} - \omega_p^2 \mathbf{M})\mathbf{U} = \mathbf{P} + \mathbf{L}\mathbf{P}_f ,$$

$$\mathbf{C}_\alpha \mathbf{P}_f = \mathbf{G}\mathbf{U} - \mathbf{H}\mathbf{P}_f ,$$

$$\sum_{e=1}^{N_E} \rho_e V_e - V^{*1} \le 0 , \quad (V^{*1} = \alpha V_0) ,$$

$$0 \le \rho_e \le 1 , \quad (e = 1, \cdots, N_E) .$$

(13)

The symbols p_f and v_n^* in the expression for the total sound power $\prod$ represent the acoustic pressure and the complex conjugate of the normal velocity of the structural surface. The first two constraint equations in (13) represent the structural-acoustic coupling equations (without incoming waves). Here, $\mathbf{P}_f$ denotes the vector of amplitudes of the acoustic pressure on S, $\mathbf{L}$ represents the fluid-structural coupling matrix, and the matrices $\mathbf{G}$, $\mathbf{H}$ and $\mathbf{C}_\alpha$ can be generated by the discretized Helmholtz integral and calculation of the spatial angle along the structural surface (see e.g., [26]). These equations imply quite lengthy computations which must be carried out in each iterative step of the solution procedure. For simplification, one may consider the Rayleigh integral approximation if the vibration frequency has a sufficiently high value. Then the pressure and normal velocity on the structural surface approximately satisfy the linear relationship $p_a = \gamma_a c v_n$, where c is the sound speed and γ_a is the specific mass of the acoustic medium [27]. Considering air to be the acoustic medium, we may further ignore the acoustic pressure in the structural equation (i.e., assume weak coupling). This way, problem (13) can be simplified to a great extent, see [25].

4.1 Example

Consider now topological design for minimum sound radiation into air from a bi-material pipe-like structure with clamped ends and an external time-harmonic loading condition as shown in Fig. 5. The properties of the two materials and the volume fraction of material 1* are taken to be as in the example in Section 3. The specific mass of the air is $\gamma_f = 1.2$ and the sound speed c = 343.4.

The pipe is modeled by 3D 8-node isoparametric elements in a 40×20×1 mesh. The two materials 1* and 2* are uniformly mixed in the initial design, the fundamental eigenfrequency of
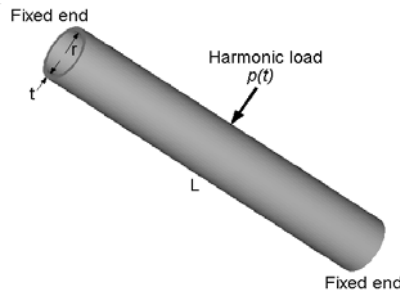

Figure 5: Clamped-clamped pipe-like structure (L=0.4, r=0.025, t=0.005) subjected to a concentrated harmonic load $p(t) = P\cos\omega_p t$ at the middle of its external surface.
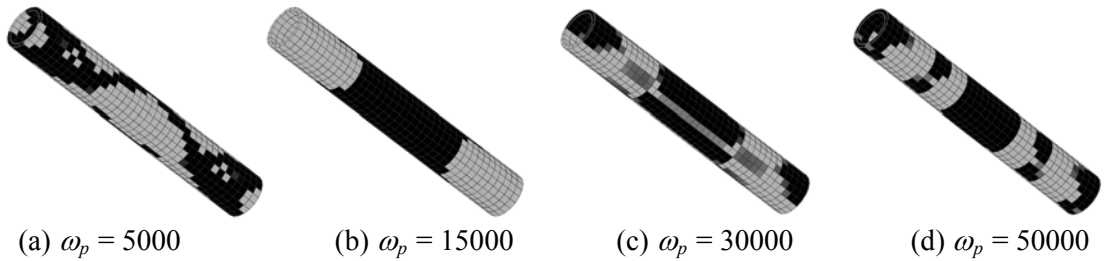
(a) $\omega_p = 5000$ (b) $\omega_p = 15000$ (c) $\omega_p = 30000$ (d) $\omega_p = 50000$

Figure 6: Optimum topologies of bi-material pipe-like structures for four different excitation frequencies ω_p .

which is found to be bimodal with $\omega_1 = \omega_2 = 10985$. The optimum topologies of the pipe for four different prescribed loading frequencies are illustrated in Figures 6 (a-d), where the stiffer material *1 is shown in black and the weaker material *2 in grey. In comparison with the initial design, the total sound power radiated from the optimum design is reduced from 8.14×10^{-7} to 4.11×10^{-8} for $\omega_p = 5000$, from 2.28×10^{-6} to 4.56×10^{-8} for $\omega_p = 15000$, from 1.25×10^{-4} to 2.32×10^{-7} for $\omega_p = 30000$, and from 2.39×10^{-6} to 7.87×10^{-8} for $\omega_p = 50000$.

Concluding remarks

A brief overview of the potential of applying topology optimization to passive design of structures against vibration and noise is presented in this paper. The design objectives include maximization of specific eigenfrequencies and distances between two consecutive eigenfrequencies of free vibrations, as well as maximization of the dynamic stiffness and minimization of the sound emission from structures subjected to forced harmonic vibrations. Numerical examples of topology optimization of some simple structures were carried out with these design objectives and confirmed that considerable reduction can be achieved of structural vibration and noise levels.

References

[1] Bendsøe, M.P., Kikuchi, N. (1988): Generating optimal topologies in structural design using a homogenization method, *Comp. Meths. Appl. Mech. Eng.*, **71**, 97-224.

[2] Olhoff, N., Bendsøe, M.P., Rasmussen, J. (1991): On CAD-intergrated structural topology and design optimization, *Comp. Meths. Appl. Mech. Eng.,* **89**, 259-279.

[3] Bendsøe, M.P., Sigmund, O. (2003): *Topology Optimization: Theory, Methods and Applications,* Springer-Verlag, Berlin.

[4] Eschenauer, H., Olhoff, N. (2001): Topology optimization of continuum structures: A review, *Appl. Mech. Rev.*, **54**, 331-389.

[5] Bendsøe, M.P., Olhoff, N., Sigmund, O. (2006): *Proc. IUTAM Symposium on Topological Design Optimization of Structures, Machines and Materials – Status and Perspectives*. Copenhagen, Denmark, Oct. 26-29, 2005. Springer-Verlag, Dordrecht, The Netherlands.

[6] Olhoff, N., Du, J. (2008): On Topological Design Optimization of Structures Against Vibration and Noise Emission. In: *Computational Aspects of Structural Acoustics and Vibrations* (eds. G. Sandberg and R. Ohayon), Springer Series: CISM Int. Centre for Mech. Sciences, Springer-Verlag, 217-276.

[7] Du, J., Olhoff, N. (2007): Topological design of freely vibrating continuum structures for maximum values of simple and multiple eigenfrequencies and frequency gaps, *Struct. Multidisc. Optim.,* **34**, 91-110. See also Publisher's Erratum in *Struct. Multidisc. Optim.* (2007), **34**, 545.

[8]   Diaz, A.R., Kikuchi, N. (1992): Solutions to shape and topology eigenvalue optimization problems using a homogenization method, *Int. J. Num. Meth. Engng.*, **35**, 1487-1502.

[9]   Ma, Z.D., Cheng, H.C., Kikuchi, N. (1994): Structural design for obtaining desired eigenfrequencies by using the topology and shape optimization method, *Comp. Systems Engng.*, **5**, 77-89.

[10] Diaz, A.R., Lipton, R., Soto, C.A. (1994): A new formulation of the problem of optimum reinforcement of Reissner-Midlin plates, *Comp. Meth. Appl. Mech. Eng.*, **123**, 121-139.

[11] Kosaka, I., Swan, C.C. (1999): A symmetry reduction method for continuum structural topology optimization, *Computers & Structures*, **70**, 47-61.

[12] Krog, L.A., Olhoff, N. (1999): Optimum topology and reinforcement design of disk and plate structures with multiple stiffness and eigenfrequency objectives, *Computers & Structures*, **72**, 535-563.

[13] Jensen, J.S., Pedersen, N.L. (2006): On maximal eigenfrequency separation in two-material structures: the 1D and 2D scalar cases, *J. Sound and Vibration*, **289**, 967-986.

[14] Pedersen, N.L. (2000): Maximization of eigenvalues using topology optimization, *Struct. Multidisc. Optim.*, **20**, 2-11.

[15] Bendsøe, M.P., Olhoff, N., Taylor, J.E. (1983): A variational formulation for multicriteria structural optimization, *J Struct Mech,* **11**, 523-544.

[16] Taylor, J.E., Bendsøe, M.P. (1984): An interpretation of min-max structural design problems including a method for relaxing constraints, *Int J Solids Struct,* **20**, 301-314.

[17] Wittrick, W.H. (1962): Rates of change of eigenvalues, with reference to buckling and vibration problems, *J. Royal Aeronautical Society,* **66**, 590-599.

[18] Lancaster, P. (1964). On eigenvalues of matrices dependent on a parameter, *Numerische Mathematik*, **6**, 377-387.

[19] Seyranian, A.P., Lund, E., Olhoff, N. (1994): Multiple eigenvalues in structural optimization problems, *Struct. Optim.,* **8**, 207-227.

[20] Ma, Z.D., Kikuchi, N., Cheng, H.C. (1995): Topological design for vibrating structures, *Comp. Meth. Appl. Mech. Eng.*, **121**, 259-280.

[21] Jog, C.S. (2002): Topology design of structures subjected to periodic loading, *J. Sound and Vibration*, **253**, 687-709.

[22] Jensen, J.S. (2007): Topology optimization of dynamics problems with Padé approximants. *Int. J. Num. Meth. Engng.*, **72**, 1605-1630.

[23] Olhoff, N., Du, J. (2009): Topological design for minimum dynamic compliance of continuum structures subjected to forced vibration, *Struct. Multidisc. Optim.* (accepted).

[24] Tortorelli, D., Michaleris, P. (1994): Design sensitivity analysis: overview and review, *Inverse Problems in Engineering,* **1**, 71-105.

[25] Du, J., Olhoff, N. (2007): Minimization of sound radiation from vibrating bi-material structures using topology optimization, *Struct. Multidisc. Optim.,* **33**, 305-321.

[26] Christensen, S.T., Sorokin, S.V., Olhoff, N. (1998). On analysis and optimization in structural acoustics – Part I: Problem formulation and solution techniques, *Struct. Optim.,* **16**, 83-95.

[27] Herrin, D.W., Martinus, F., Wu, T.W., Seybert, A.F. (2003): A new look at the high frequency boundary element and Rayleigh integral approximations, *Society of Automotive Engineers, Inc*.

Author Index